

nature

HORSE CODE

The genetic origins of the modern domesticated horse



Gain of function

What do we learn by giving dangerous microbes extra abilities?

Battling the bootlegs

How to tackle the Hydra of predatory publishing

Thirsty work

The global potential for harvesting drinking water from the air

Nature.2021.10.30

[Sat, 30 Oct 2021]

- [This Week](#)
- [News in Focus](#)
- [Books & Arts](#)
- [Opinion](#)
- [Work](#)
- [Research](#)
- [Amendments & Corrections](#)

This Week

- **[The answer to the biodiversity crisis is not more debt](#)** [26 October 2021]
Editorial • Funding pledges from China and other countries need to be given in grants — which must include research grants — and not as a reward for taking out loans.
- **[The COVID pandemic must lead to tuberculosis vaccines](#)** [27 October 2021]
Editorial • The coronavirus crisis has halted decades of progress on TB. But the speed of COVID vaccines shows there can still be hope for advances against neglected diseases.
- **[This digital-hygiene routine will protect your scholarship](#)** [26 October 2021]
World View • Simple, regular checks could squelch some pernicious practices by unscrupulous publishers and preserve your digital presence.
- **[Moulded or folded, this wood stays strong](#)** [22 October 2021]
Research Highlight • By tinkering with the structure of wood fibres, scientists have boosted the material's flexibility and strength.
- **[A COVID vaccine elicits a middling but durable immune response](#)** [21 October 2021]
Research Highlight • Antibody levels drop sharply six months after mRNA jabs, but remain stable well after receipt of Johnson & Johnson's vaccine.
- **[A battery that's not just greener but better](#)** [14 October 2021]
Research Highlight • Lithium-ion batteries that incorporate a recycled material outperform those made with a commercial version.
- **[How ancient reptiles were streamlined for flight](#)** [18 October 2021]
Research Highlight • Pterosaurs, which soared overhead while dinosaurs stomped the land, had muscles that provided an aerodynamic profile.
- **[Mutant enzymes give ordinary bacteria unnatural powers](#)** [22 October 2021]
Research Highlight • Common bacteria make a compound not found in nature after being kitted out with an artificial enzyme.

- **Defeating the genome's guardians boosts a DNA-editing tool** [21 October 2021]
Research Highlight • A promising alternative to the CRISPR system works better when scientists shut down the target cell's DNA repair systems.
- **A mysterious object is beaming radio waves into the Milky Way** [20 October 2021]
Research Highlight • The emissions profile measured on Earth does not match that of any known type of space body.

| [Next section](#) | [Main menu](#) |

- EDITORIAL
- 26 October 2021

The answer to the biodiversity crisis is not more debt

Funding pledges from China and other countries need to be given in grants — which must include research grants — and not as a reward for taking out loans.



The Alichur Valley in Tajikistan is among a number of ecologically sensitive areas that researchers say could be affected by China's Belt and Road Initiative. Credit: Alamy

Funding for biodiversity is getting some attention at last.

In September, nine philanthropic organizations, most of them in the United States, pledged a total of US\$5 billion over a decade towards projects that will help to preserve the richness of Earth's species.

This month, Chinese President Xi Jinping announced the allocation of 1.5 billion yuan (\$235 million) to the new Kunming Biodiversity Fund. This will have a goal of funding projects, such as protected areas, that will contribute to slowing down and eventually reversing the loss of species and ecosystems.

More details are awaited from China, along with further information on a promise made by the European Union to double its funding for biodiversity. Contributions to the Kunming fund should be given as grants, not loans; they should have a research component; and they should be pooled and managed through international organizations. Moreover, the rules for access need to be transparent and fair to all applicants. These are important factors to emphasize, because there seems to be a trend towards providing environmental finance as loans — many of them to some of the world's poorest countries, which are often already highly indebted.



[The broken \\$100-billion promise of climate finance – and how to fix it](#)

The pledges were timed to coincide with the first part of the China-hosted United Nations biodiversity conference, COP15, which ended on 24

October. Collectively, the sums, although not insignificant, will amount to little more than a 1–2% increase on the roughly \$133 billion a year that the world currently spends on biodiversity. Well over half of this is spent by China, the EU, Japan and the United States.

Spending on biodiversity needs to increase in all regions, according to a report by the UN Environment Programme, published in May (see go.nature.com/3ekaopk). For comparison, money earmarked for tackling climate change totalled \$632 billion per year in 2019–20, according to a *Nature* analysis ([*Nature* 598, 400–402; 2021](https://doi.org/10.1038/nature29131)).

The reasons that finance for biodiversity is lower than that for its climate cousin include a relative dearth of finance in low- and middle-income countries and the fact that more than half of all climate funds take the form of loans. Both public and private investors know that in financing projects such as solar energy plants or batteries research and development, they will probably see a return on their investments. By contrast, protecting a watershed or a wetland is more of a public service — and so is more likely to be funded from taxation. Partly as a result, some 86% of biodiversity funding currently comes from public sources, in the form of grants.

But that might be about to change. Researchers, corporations, bankers and policymakers have been exploring how to create financial investment products — from both private and public sources — in biodiversity, as well as how to better protect nature from the negative environmental impacts of big infrastructure projects. Most industrial sectors rely on biodiversity to some extent. Food producers, forestry, clothing manufacturers and hydropower, for example, would all struggle without healthy soils, pollinators or predictable water supplies. If nature continues to degrade, the world's economic output will begin to suffer sooner or later.



Global climate action needs trusted finance data

One idea being studied is how to create an internationally agreed reporting system so that any entity — a bank, a government or a corporation — would need to publish data on whether its investments could lead to ecological damage. Such disclosures would probably prompt financiers to think twice before taking on investments that might be environmentally harmful. Earlier this year, an organization called Taskforce on Nature-related Financial Disclosures began work to develop such a system. It is co-chaired by Elizabeth Mrema, the executive secretary of the UN biodiversity convention secretariat, and is based in Montreal, Canada.

Another idea under study is called Nature Performance Bonds (NPBs). According to this model, indebted countries would be eligible for more-favourable loan repayment terms if they could commit to spending the cash saved on environmental protection.

Last month, a study commissioned by the China Council for International Cooperation on Environment and Development, an organization of policymakers that advises China's government, recommended that China become a global leader in NPBs (see go.nature.com/3pekzk7). The study says that some 52 low- and middle-income countries owe China a combined total of more than \$100 billion in loans. These include loans for projects that are part of China's Belt and Road Initiative (BRI) to upgrade energy sources,

roads, railways and airports, mainly in low- and middle-income countries. Many of China's BRI investments are in ecologically sensitive areas.

The terms of China's \$235-million biodiversity announcement have not yet been confirmed. But it would be wise if this funding were not linked to the debts of countries whose biodiversity is being affected by BRI projects. Otherwise it would seem that China's main motivation is the greening of its own investments, when, as the host of COP15, it needs to think and act more globally, and work towards creating a fund by and for all nations.



Where climate cash is flowing and why it's not enough

The Kunming Biodiversity Fund needs to be a stand-alone grant fund, ideally managed by a mechanism involving all countries, and with transparent rules of access. It also needs to have a dedicated research component — something that is not possible through loan finance. And other nations must contribute.

The need for research funding is especially acute. There are often few funding opportunities from national research bodies for researchers in low- and middle-income countries that are rich in biodiversity. The UN's official biodiversity funder, the Global Environment Facility, based in Washington DC, does not have a dedicated research facility. It does fund some science,

but that is a part of a small-grants programme (see go.nature.com/3mgu8io) that is mainly focused on funding for conservation.

It is clear that biodiversity will be getting more finance. But loan finance must not crowd out or replace grant funding. There is a precedent for this. It is already happening in climate finance, for which a much-delayed \$100 billion pledged to be provided annually to low- and middle-income countries will be [mainly in the form of loans](#).

A step change in biodiversity finance is needed and the Kunming Biodiversity Fund will be a welcome move in the right direction. But it will be inequitable if most of the promised finance ends up committed to loans. Finding an answer to the biodiversity crisis should not mean the poorest countries having to take on yet more debt.

Nature **598**, 539-540 (2021)

doi: <https://doi.org/10.1038/d41586-021-02891-y>

This article was downloaded by **calibre** from <https://www.nature.com/articles/d41586-021-02891-y>.

| [Section menu](#) | [Main menu](#) |

- EDITORIAL
- 27 October 2021

The COVID pandemic must lead to tuberculosis vaccines

The coronavirus crisis has halted decades of progress on TB. But the speed of COVID vaccines shows there can still be hope for advances against neglected diseases.



A tuberculosis patient consults with their doctor in Indonesia. Diagnosis and treatment of the disease has been severely affected by the COVID-19 pandemic. Credit: Jefri Tarigan/Anadolu Agency/Getty

Researchers and clinicians are upset and frustrated that decades of work in diagnosing, treating and researching tuberculosis (TB) have massively

stalled. The slowdown means the world is losing ground against a disease that kills 1.5 million people every year.

As the International Union Against Tuberculosis and Lung Disease held its annual conference online last week, Guy Marks, the union's president, spoke for many when, comparing efforts against COVID-19, he said: "Many of us who work in the [TB] field feel robbed that equivalent efforts to develop a TB vaccine have never been as well committed or funded."

Marks added: "The failure to deliver COVID-19 vaccines to low- and middle-income countries and end tuberculosis are two sides of the same coin — a devaluation of human life in poor countries." He has a point. But it doesn't need to be this way.



How COVID hurt the fight against other dangerous diseases

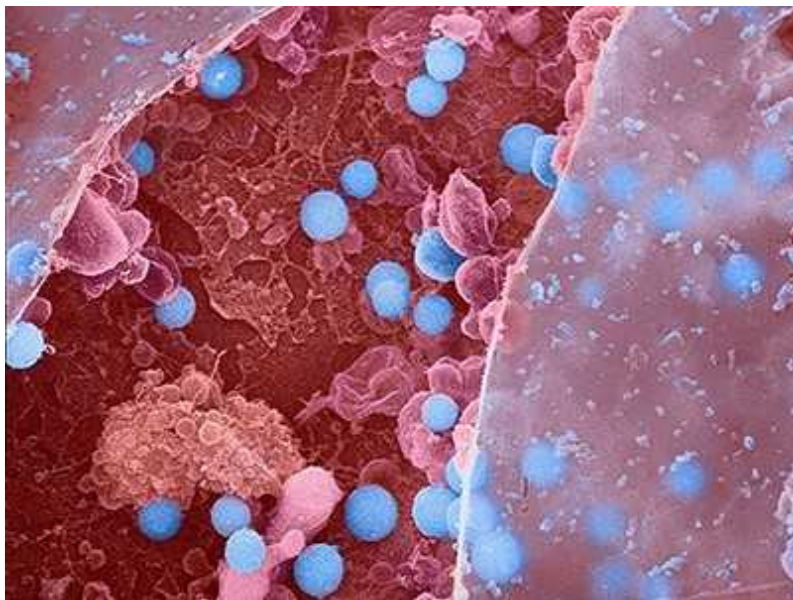
Researchers are again urging decision-makers to revive diagnosis, treatment and research programmes for TB and other infectious diseases, such as malaria. And they are saying that much can be learnt from how the creation of COVID-19 vaccines was fast-tracked.

Researchers have been warning that even more people will die from TB and other infectious diseases, such as malaria and HIV, if health systems continue to neglect these infections because of the continuing focus on

coronavirus (see [Nature 597, 314; 2021](#)). And they are pleading with funders and governments not to drop the ball on TB work.

But their warnings are not being heeded. Not only are more people dying of the disease, but a target to reduce deaths by 90% from 2015 levels by 2030 — part of the United Nations Sustainable Development Goals — is now in peril. According to research published this month, this failure will also lead to profound economic and health losses in the trillions of dollars — with the greatest impact in sub-Saharan Africa ([S. Silva et al. Lancet Glob. Health 9, E1372–E1379; 2021](#)).

A crucial problem is that fewer medical professionals have been available to diagnose and treat TB. As a result, the number of people diagnosed with the disease fell from 7.1 million in 2019 to 5.8 million in 2020. India, Indonesia and the Philippines are the most affected countries, according to the World Health Organization's (WHO's) latest TB report, published this month (see [go.nature.com/3re4n6j](#)).



[Nature Index 2021 Infectious disease](#)

At the same time, funding has also shrunk. Global spending on TB diagnostic, treatment and prevention services dropped from US\$5.8 billion to \$5.3 billion in 2020. Moreover, this overall spending is less than half of the WHO's global target of \$13 billion annually by 2022. TB research

funding is also half of what it needs to be. The WHO set a separate target for this of \$2 billion annually for 2018–22. In 2019, funding for TB research totalled only \$901 million. By contrast, the US National Institutes of Health alone has set aside \$4.9 billion for research on COVID-19. Published research in TB seems to be holding up for now, according to an analysis published this week in *Nature* Index (see [Nature 598, S10–S13; 2021](#)).

Some conference delegates spoke of lowering the targets for diagnosing and treating TB (and for other infectious diseases) to account for these and other ground realities. But that would be inadvisable. Although the COVID-19 pandemic is the highest priority for political leaders, wealthier nations and philanthropic donors, the pandemic has also shown how it is possible to boost both research into an infectious disease and treatment — and to do so at speed, which has led to COVID-19 vaccines in record time.

Lessons from COVID-19 must be applied to the fight against TB and other infectious diseases — from extraordinary resource mobilization to the use of emerging technologies, such as messenger RNA and other platforms to create vaccines. Advances in rapid and reliable diagnostics, advanced computation, sequencing and clinical-trial capacity for new vaccines and treatments can all be harnessed for TB and other infectious diseases.

The TB vaccine in use today is essentially the same as the Bacillus Calmette–Guérin (BCG) vaccine introduced in July 1921. The COVID-19 pandemic has shown that it's possible to produce new vaccines in one year, not 100 — provided that there is funding and political will.

Nature **598**, 540 (2021)

doi: <https://doi.org/10.1038/d41586-021-02892-x>

This article was downloaded by **calibre** from <https://www.nature.com/articles/d41586-021-02892-x>

- WORLD VIEW
- 26 October 2021

This digital-hygiene routine will protect your scholarship



Simple, regular checks could squelch some pernicious practices by unscrupulous publishers and preserve your digital presence.

- [Guillaume Cabanac](#) 0

A few years ago, one of my mentors was surprised when he realized he shared a name with a porn star. He wrote to Google to request that queries under his name not turn up racy images. Another adviser had learnt that a former junior colleague had added his name to a conference submission without his knowledge, presumably to enhance its prestige, and my adviser found himself accused of undisclosed conflicts of interest.

Such stories are common across academia — and are as likely to arise from malpractice as from mix-ups. Scholars' names, work or both are used by

crooked individuals or institutions to deceive others. The scope of the problem dismays me. I shiver when imagining my university's research-integrity officer coming to me with a pile of buggy papers — that I've never seen before — bearing my name.

Funders, publishers and institutions all bear responsibility to craft policies that stymie scholarly abuse. But individual scholars have some power — and a duty — to do so, too. I propose a 'hygiene routine' that scientists should repeat regularly — much like getting a haircut or a dental check-up. The threat of detection and broader community awareness of abuse could shrink [established predatory practices](#) and nip emerging ones in the bud.



[Predatory publishers' latest scam: bootlegged and rebranded papers](#)

Every other month or so, I do my own scholarly check-up. These tasks not only protect my own reputation, but also discourage abuse in general. If researchers everywhere adopt such a habit, we can keep abuse from becoming rampant.

As part of my digital-hygiene routine, I search my own name and affiliation in an online search engine to make sure I'm not on editorial boards of predatory journals or conference committees I've never heard of. I check whether I have received unconsented acknowledgement, a form of authorship abuse, which 'credits' your support and contribution to a paper

without your knowledge and suggests the work represents your views. If anything turns up, you can contact the publisher or the corresponding author of the study, copying in your own university administrators or research-integrity officers.

Another part is consulting your researcher profile on bibliographic databases, including Dimensions and Google Scholar. Better still, subscribe to alerts and contact Dimensions, Scopus or Web of Science if your work is attributed to another scientist with your name, or vice versa. Use citation alerts to correct misrepresentations of your results.

This monitoring will help you find opportunities, too. Liaise with researchers you've worked with. Telling your co-authors about who has cited your work (and why) can strengthen ties and revitalize idle collaborations. When members of my team saw researchers putting software we'd written to use, we updated it to screen for problematic papers and improved how it scanned for 'tortured phrases' — which are produced by paraphrasing software to conceal plagiarism — such as 'p-esteem' (instead of '*p*-value').



[Illegitimate journals scam even senior scientists](#)

Reviewing activities also demand care. When reviewing a paper, be aware of techniques to evade plagiarism detection and point them out to editors. In

the ‘related work’ section, look for pasted strings of paragraphs that have been computationally modified to evade plagiarism detectors and mimic an original synthesis of ideas. Reject submissions with such content.

Part of your routine should be highlighting your pro bono, good-faith efforts in reviewing. How many reviewers have read a published paper and wondered whether the authors even saw their critiques that took hours? Sometimes they don’t: journal editors might not know how to address reviews, or be pressured to get papers published quickly.

To make your effort visible, add the relevant parts of your evaluation report to PubPeer. Post a comment (signed or not) stating that you had offered this criticism but never saw the authors’ rebuttal. This will demonstrate that the journal editors either did not deliver valuable comments or let them go unaddressed. Authors (or other readers) can then deliver a point-by-point public response, should they wish to. Perhaps researchers will find ways to consider these comments in meta-analyses, or manuscript editors could use them to get a sense of how articles published in their journals are perceived.

As a scholar, become aware and keep yourself informed of how scammers deceive editors, reviewers and authors. Skim through PubPeer and Retraction Watch. Stay alert for predatory publishers and their flattering schemes. When you do notice a problem in a publication, such as erroneous formulae, fabricated data or manipulated images, post a comment on PubPeer to notify the authors so that they can clarify the situation. This will help reviewers and authors to see the problems that routinely crop up at certain journals. Praise counts, too. If you realize an approach could work beyond the applications described, say so.

These check-ups aren’t cure-alls for predatory publishers, deceptive practices, unheeded reviews or simple mistakes. Think of it like cleaning up a beach: more litter will wash in, but the more that’s removed, the cleaner the beach is and the more pollution is discouraged.

Researchers no longer accept that their duties are over once a paper is published. If everyone monitors their corpus, a scourge of abuses will be squelched — and productive collaborations will rise in its place.

Nature **598**, 541 (2021)

doi: <https://doi.org/10.1038/d41586-021-02901-z>

This article was downloaded by **calibre** from <https://www.nature.com/articles/d41586-021-02901-z>

| [Section menu](#) | [Main menu](#) |

- RESEARCH HIGHLIGHT
- 22 October 2021

Moulded or folded, this wood stays strong

By tinkering with the structure of wood fibres, scientists have boosted the material's flexibility and strength.



A sheet of wood treated to make it flexible can be folded in half. Credit: Liangbing Hu

A quick bath in water helps to make a sheet of treated wood as pliable as paper, allowing it to take on complex forms that have much more strength than natural wood¹.

Access options

Subscribe to Journal

Get full journal access for 1 year

\$199.00

only \$3.90 per issue

[Subscribe](#)

All prices are NET prices.

VAT will be added later in the checkout.

Tax calculation will be finalised during checkout.

Rent or Buy article

Get time limited or full article access on ReadCube.

from \$8.99

[Rent or Buy](#)

All prices are NET prices.

Additional access options:

- [Log in](#)
- [Learn about institutional subscriptions](#)

Nature **598**, 542 (2021)

doi: <https://doi.org/10.1038/d41586-021-02861-4>

References

1. 1.

Xiao, S. *et al.* *Science* **374**, 465–471 (2021).

This article was downloaded by **calibre** from <https://www.nature.com/articles/d41586-021-02861-4>

| [Section menu](#) | [Main menu](#) |

- RESEARCH HIGHLIGHT
- 21 October 2021

A COVID vaccine elicits a middling but durable immune response

Antibody levels drop sharply six months after mRNA jabs, but remain stable well after receipt of Johnson & Johnson's vaccine.



A health-care worker in Bogota gives a dose of the Johnson & Johnson vaccine against COVID-19. Credit: Raul Arboleda/AFP/Getty

Immune responses to SARS-CoV-2 decline sharply within eight months of the second jab of the Pfizer–BioNTech or Moderna vaccines, but remain relatively stable after a single shot of the vaccine produced by Johnson & Johnson.¹.

Access options

Subscribe to Journal

Get full journal access for 1 year

\$199.00

only \$3.90 per issue

[Subscribe](#)

All prices are NET prices.

VAT will be added later in the checkout.

Tax calculation will be finalised during checkout.

Rent or Buy article

Get time limited or full article access on ReadCube.

from \$8.99

[Rent or Buy](#)

All prices are NET prices.

Additional access options:

- [Log in](#)
- [Learn about institutional subscriptions](#)

Nature **598**, 542 (2021)

doi: <https://doi.org/10.1038/d41586-021-02838-3>

References

1. 1.

Collier, A. Y. *et al.* *N. Engl. J. Med.*
<https://doi.org/10.1056/NEJMc2115596> (2021).

This article was downloaded by **calibre** from <https://www.nature.com/articles/d41586-021-02838-3>

- RESEARCH HIGHLIGHT
- 14 October 2021

A battery that's not just greener but better

Lithium-ion batteries that incorporate a recycled material outperform those made with a commercial version.

 Examples of NMC particle cross sections from the recycled sample and the control sample

Particles (left two objects) of recycled lithium-based material are bigger and have more voids than particles made of pristine material, giving the recycled materials a performance edge. Credit: X. Ma *et al./Joule*

Recycled battery materials can outperform conventional components¹.

Access options

Subscribe to Journal

Get full journal access for 1 year

\$199.00

only \$3.90 per issue

[Subscribe](#)

All prices are NET prices.

VAT will be added later in the checkout.

Tax calculation will be finalised during checkout.

Rent or Buy article

Get time limited or full article access on ReadCube.

from \$8.99

[Rent or Buy](#)

All prices are NET prices.

Additional access options:

- [Log in](#)
- [Learn about institutional subscriptions](#)

Nature **598**, 542 (2021)

doi: <https://doi.org/10.1038/d41586-021-02814-x>

References

1. 1.

Ma, X. *et al.* Joule <https://doi.org/10.1016/j.joule.2021.09.005> (2021).

This article was downloaded by **calibre** from <https://www.nature.com/articles/d41586-021-02814-x>

- RESEARCH HIGHLIGHT
- 18 October 2021

How ancient reptiles were streamlined for flight

Pterosaurs, which soared overhead while dinosaurs stomped the land, had muscles that provided an aerodynamic profile.



A pterosaur (artist's impression) sliced easily through the air thanks in part to muscles that formed an aerodynamic covering between its wings and neck. Credit: Alex Boersma

Pterosaurs were the first vertebrates to fly, ruling the skies for more than 160 million years during the time of the dinosaurs. Now a beautifully preserved fossil has revealed a pterosaurian trick for reducing drag during flight: a curved aerodynamic profile courtesy of muscles connecting the wings to the neck¹.

Access options

Subscribe to Journal

Get full journal access for 1 year

\$199.00

only \$3.90 per issue

[Subscribe](#)

All prices are NET prices.
VAT will be added later in the checkout.
Tax calculation will be finalised during checkout.

Rent or Buy article

Get time limited or full article access on ReadCube.

from \$8.99

[Rent or Buy](#)

All prices are NET prices.

Additional access options:

- [Log in](#)
- [Learn about institutional subscriptions](#)

Nature **598**, 542 (2021)

doi: <https://doi.org/10.1038/d41586-021-02822-x>

References

1. 1.

Pittman, M., Barlow, L. A., Kaye, T. G. & Habib, M. B. *Proc. Natl Acad. Sci. USA* <https://doi.org/10.1073/pnas.2107631118> (2021).

This article was downloaded by **calibre** from <https://www.nature.com/articles/d41586-021-02822-x>

- RESEARCH HIGHLIGHT
- 22 October 2021

Mutant enzymes give ordinary bacteria unnatural powers

Common bacteria make a compound not found in nature after being kitted out with an artificial enzyme.



With a little bioengineering, *Escherichia coli* bacteria (artificially coloured) can churn out useful chemicals not found in the natural world. Credit: Steve Gschmeissner/SPL

Adding an artificial enzyme to bacteria¹ allows them to carry out unnatural reactions that produce novel chemical compounds from sugars.

Access options

Subscribe to Journal

Get full journal access for 1 year

\$199.00

only \$3.90 per issue

[Subscribe](#)

All prices are NET prices.

VAT will be added later in the checkout.

Tax calculation will be finalised during checkout.

Rent or Buy article

Get time limited or full article access on ReadCube.

from \$8.99

[Rent or Buy](#)

All prices are NET prices.

Additional access options:

- [Log in](#)
- [Learn about institutional subscriptions](#)

Nature **598**, 543 (2021)

doi: <https://doi.org/10.1038/d41586-021-02839-2>

References

1. 1.

Huang, J. *et al.* *Nature Chem.* <https://doi.org/10.1038/s41557-021-00801-3> (2021).

This article was downloaded by **calibre** from <https://www.nature.com/articles/d41586-021-02839-2>

- RESEARCH HIGHLIGHT
- 21 October 2021

Defeating the genome's guardians boosts a DNA-editing tool

A promising alternative to the CRISPR system works better when scientists shut down the target cell's DNA repair systems.



The editing of DNA (artist's illustration) by a next-generation DNA editor is vastly more efficient if cellular repair systems are inhibited. Credit: Science Photo Library

By tweaking a process that cells use to repair DNA, researchers have boosted the efficiency and precision of 'prime editing', a genome-editing method that offers some advantages over the popular CRISPR–Cas9 technique¹.

Access options

Subscribe to Journal

Get full journal access for 1 year

\$199.00

only \$3.90 per issue

[Subscribe](#)

All prices are NET prices.
VAT will be added later in the checkout.

Tax calculation will be finalised during checkout.

Rent or Buy article

Get time limited or full article access on ReadCube.

from \$8.99

[Rent or Buy](#)

All prices are NET prices.

Additional access options:

- [Log in](#)
- [Learn about institutional subscriptions](#)

Nature **598**, 543 (2021)

doi: <https://doi.org/10.1038/d41586-021-02837-4>

References

1. 1.

Chen, P. J. *et al.* *Cell* <https://doi.org/10.1016/j.cell.2021.09.018> (2021).

This article was downloaded by **calibre** from <https://www.nature.com/articles/d41586-021-02837-4>

- RESEARCH HIGHLIGHT
- 20 October 2021

A mysterious object is beaming radio waves into the Milky Way

The emissions profile measured on Earth does not match that of any known type of space body.



Radio waves from an unknown source (white circle; artist's illustration) near the Galactic Centre have been recorded by observatories in Australia and South Africa. Credit: Sebastian Zentilomo/University of Sydney

Astronomers have detected an intermittent source of radio waves near the centre of the Galaxy that doesn't seem to fit the profile of any known astrophysical phenomenon¹.

Access options

Subscribe to Journal

Get full journal access for 1 year

\$199.00

only \$3.90 per issue

[Subscribe](#)

All prices are NET prices.

VAT will be added later in the checkout.

Tax calculation will be finalised during checkout.

Rent or Buy article

Get time limited or full article access on ReadCube.

from \$8.99

[Rent or Buy](#)

All prices are NET prices.

Additional access options:

- [Log in](#)
- [Learn about institutional subscriptions](#)

Nature **598**, 543 (2021)

doi: <https://doi.org/10.1038/d41586-021-02836-5>

References

1. 1.

Wang, Z. *et al. Astrophys. J.* **920**, 45 (2021).

This article was downloaded by **calibre** from <https://www.nature.com/articles/d41586-021-02836-5>

News in Focus

- **[COVID reinfections, asteroid mission and tuskless elephants](#)** [27 October 2021]
News Round-Up • The latest science news, in brief.
- **[Attempt to charge Mexican scientists with ‘organized crime’ prompts international outcry](#)** [19 October 2021]
News • The Mexican government has accused 31 scientists and officials of organized crime and money laundering — allegations that they deny and that many claim are politically motivated.
- **[Physicists make most precise measurement ever of neutron’s lifetime](#)** [15 October 2021]
News • But decades-long mystery of how long the particles live persists.
- **[Ancient DNA points to origins of modern domestic horses](#)**
[22 October 2021]
News • Genetic analysis shows that the ancestors of all modern horses lived in the Western Eurasian steppes more than 4,000 years ago.
- **[Climate change: Nature readers say their fears are growing](#)**
[22 October 2021]
News • Poll shows that 80% of respondents are more concerned in the run-up to the COP26 climate meeting than they were ahead of the Paris conference 6 years ago.
- **[COVID vaccine makers brace for a variant worse than Delta](#)** [20 October 2021]
News • Companies are updating vaccines and testing them on people to prepare for whatever comes next in the pandemic.
- **[‘Politicians shouldn’t meddle’: new chief of Europe’s major research funder shares priorities](#)** [25 October 2021]
News Q&A • Developmental geneticist Maria Leptin hopes to keep the European Research Council true to its founding mission.
- **[The shifting sands of ‘gain-of-function’ research](#)** [27 October 2021]
News Feature • The mystery of COVID’s origins has reignited a contentious debate about potentially risky studies and the fuzzy terminology that describes them.

- **The secret lives of cells — as never seen before** [26 October 2021]

News Feature • Cutting-edge microscopy techniques are allowing researchers to spy on the innards of cells in all their crowded glory.

| [Next section](#) | [Main menu](#) | [Previous section](#) |

- NEWS ROUND-UP
- 27 October 2021

COVID reinfections, asteroid mission and tuskless elephants

The latest science news, in brief.



The Lucy spacecraft, shown here in an artist's rendering, will fly by six Trojan asteroids near Jupiter. Credit: NASA

First mission to Jupiter's asteroids lifts off

A NASA spacecraft has [begun its journey](#) to a realm of the outer Solar System that has never before been visited: a set of asteroids orbiting the Sun near Jupiter. The rocks are “the last unexplored but relatively accessible

population of small bodies” circling the Sun, says Vishnu Reddy, a planetary scientist at the University of Arizona in Tucson.

The US\$981-million Lucy mission, which launched from Cape Canaveral, Florida, on 16 October, will spend the next 12 years performing gravitational gymnastics to swoop past six of the asteroids, known as Trojans, to snap photos and determine their compositions. Scientists think the Trojans will reveal information about the formation and evolution of the Solar System. The mission’s name reflects their hopes: Lucy is the 3.2-million-year-old hominin fossil unearthed in 1974 in Ethiopia that unlocked secrets of human origins.

Powered by two 7.3-metre-wide solar panels, Lucy will whizz past each asteroid at 6 to 9 kilometres per second. It won’t reach its first target, the asteroid Eurybates, until 2027. Whatever the mission finds will almost certainly rewrite textbook entries on the Trojan asteroids, Reddy says. “We might throw all our formation models out the window.”



Elephants without tusks had an advantage in areas where ivory poaching was prevalent.Credit: Peter Chadwick/Getty

Ivory poaching drives evolution of tuskless elephants

African elephants have [evolved towards tusklessness](#) in an area where they were intensively hunted for ivory, finds a study of elephants' traits and genetics in Mozambique ([S. C. Campbell-Staton *et al. Science* 374, 483–487; 2021](#)).

The finding could have implications for the recovery of elephant populations in the country.

Ivory trading was used to finance a civil war in Mozambique from the late 1970s to early 1990s. Poaching caused the elephant population in the country's Gorongosa National Park to crash by more than 90%, from more than 2,500 animals down to around 200 in the early 2000s.

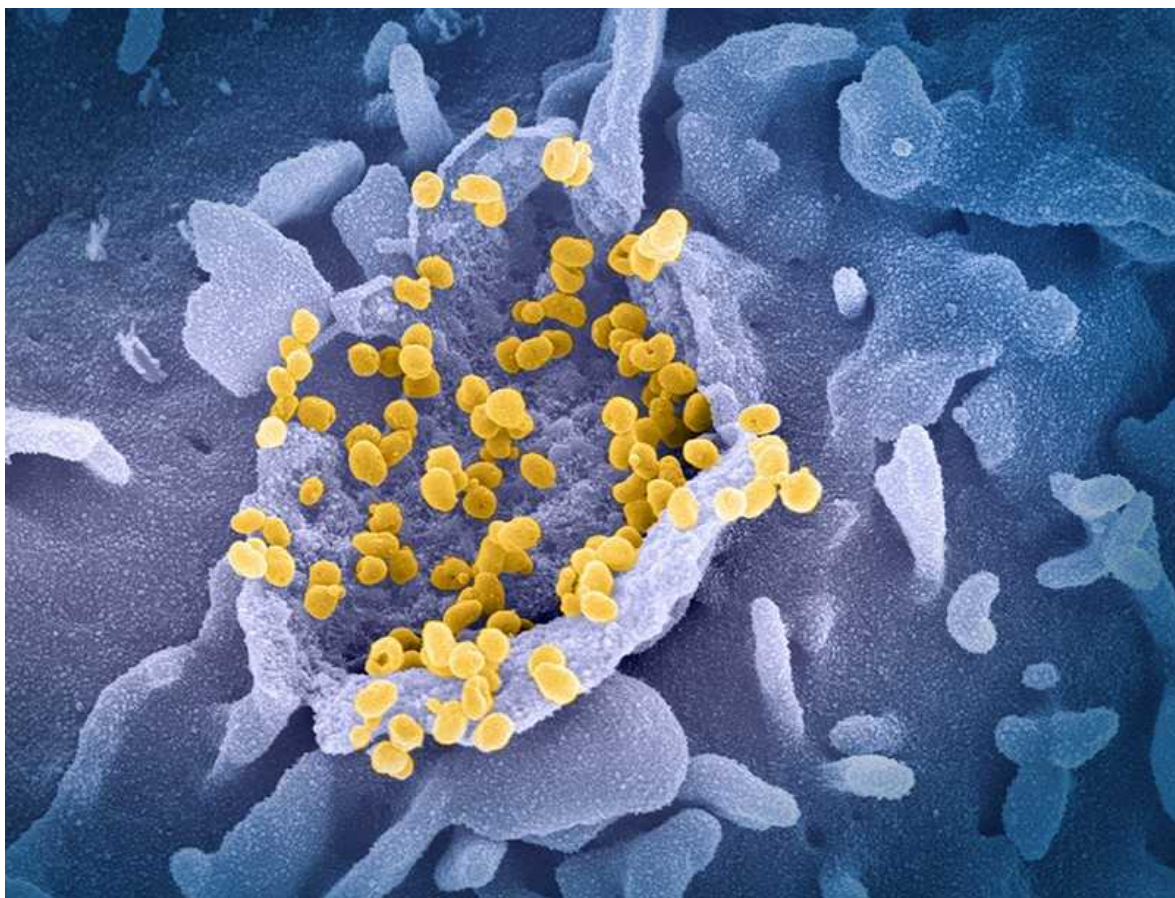
Before the war, about 18.5% of females were naturally tuskless — a trait that made them undesirable to poachers. Among the 91 female elephants that have been born since the war, the researchers show, that fraction has risen to 33%.

Mathematical modelling has confirmed that this shift is the result of hunting pressure: the selective killing of elephants with tusks has led to the birth of more tuskless offspring.

The team noted that tusklessness is seen only in female elephants. This, and the pattern of inheritance of the trait, suggested that it is caused by a mutation on the X chromosome that is fatal to males and dominant in females — just one copy of a mutation is needed to cause it. The researchers searched through the elephants' genomes looking for regions on the X chromosome that differed between those with and without tusks, and that showed signs of recent selection pressure. They identified two likely candidate genes: *AMELX* and *MEPIa*. In humans, these genes are known to be involved in the growth of incisor teeth (the human equivalent of tusks).

For the elephants, selection for tuskless females could have knock-on effects. By looking at DNA in elephant dung, the researchers learnt that

tusked and tuskless animals eat different plants. Elephants are keystone species, so a change in their diet could potentially alter the landscape. And because the tuskless trait is fatal to male offspring, it is likely that fewer elephants will be born overall, which could slow population recovery even though poaching has now been stopped in the park.



Particles of SARS-CoV-2 (yellow; artificially coloured) emerge from a cell.Credit: National Institutes of Health/Science Photo Library

COVID reinfections likely within one or two years

People who have been infected with SARS-CoV-2 [can expect to become reinfected within one or two years](#), unless they take precautions such as getting vaccinated and wearing masks. That's the prediction of modelling based on the genetic relationships between SARS-CoV-2 and other coronaviruses ([J. P. Townsend et al. Lancet Microbe https://doi.org/gmzj22; 2021](https://doi.org/gmzj22)).

Researchers combined genetic data from SARS-CoV-2, three endemic coronaviruses and the closely related coronaviruses SARS-CoV and MERS-CoV to build a viral family tree. They used that tree to model how viral traits have evolved over time, and to estimate the decline in antibody levels after SARS-CoV-2 infection.

The results suggest that the average reinfection risk rises from about 5% four months after initial infection to 50% by 17 months. Natural protection seems to last for less than half as long as it does for the three common-cold coronaviruses. The findings also suggest that people could be reinfected in just a few months if they are not vaccinated.

Further, long-term data will be necessary to show precisely how long natural immunity lasts.

Nature **598**, 545 (2021)

doi: <https://doi.org/10.1038/d41586-021-02902-y>

This article was downloaded by **calibre** from <https://www.nature.com/articles/d41586-021-02902-y>.

| [Section menu](#) | [Main menu](#) |

- NEWS
- 19 October 2021

Attempt to charge Mexican scientists with ‘organized crime’ prompts international outcry

The Mexican government has accused 31 scientists and officials of organized crime and money laundering — allegations that they deny and that many claim are politically motivated.

- [Sara Reardon](#) 0



A number of the accused academics are based at the National Autonomous University of Mexico. Credit: Gerardo Vieyra/NurPhoto/Getty

When the son of astrophysicist José Franco answered the door at their home in Mexico City in June, he didn't know why an agent from Mexico's federal prosecutor's office was asking for verification that his father lived at that address. When he confirmed it, the agent left without explanation. Franco, a researcher at the National Autonomous University of Mexico (UNAM) and former head of the Mexican Academy of Sciences, received no other information about why the agent had visited.

Then, in late September, Franco learnt from national newspaper articles that the government prosecutor was planning to charge him and 30 other Mexican academics and former government administrators with organized crime and money laundering.

The accused to whom *Nature* spoke deny the allegations. But the situation has garnered wide attention in Mexico, because such charges are typically reserved for narcotics traffickers, and are so serious that even just a formal accusation can result in incarceration in a maximum-security prison without the chance of bail until a trial is held.

Since the accusations came to light, the international academic community has rallied behind the 31 individuals. More than 50 universities and professional societies — including the US National Academies of Sciences, Engineering, and Medicine (NASEM) — have written open letters and opinion pieces condemning the prosecution.

Thus far, a judge has refused to grant an arrest warrant and has rejected the charges, saying there isn't enough evidence for a criminal case, but the prosecutor — whose office has not responded to *Nature*'s questions as to why they have attempted to bring such unusual charges in this case — has vowed to continue.

Doubts over claims

The accusations centre on a formerly independent scientific advisory board to the government called the Scientific and Technological Consultative Forum — or Foro Consultivo — that was largely funded by Mexico's top

science agency, the National Council for Science and Technology (Conacyt), and has since been brought under that agency's auspices.

The prosecutor alleges that between 2012 and 2018, before current Mexican president Andrés Manuel López Obrador was in office, Conacyt and the Foro partnered to funnel 471 million pesos (US\$22.9 million) of the agency's money into the Foro.



[Mexican science suffers under debilitating budget cuts](#)

According to the prosecutor's request for an arrest warrant, the 31 individuals linked to the Foro and Conacyt used these funds for travel, buying property, dry cleaning and other purposes not related to Conacyt's mandate.

The accused academics and the judge have pointed out that at the time the expenses were incurred, Conacyt's own constitution mandated that it pay for the advisory panel's operating expenses as well as its research work.

Franco and the other accused parties also say the allegations are baseless, and the money was used for legal purposes — such as buying an office for the Foro's staff members and funding necessary travel to scientific meetings. Furthermore, since the Foro was founded in 2002, Conacyt has approved all its budgets and expenses, which the Foro says have been checked regularly by external auditors.

The accusations come at a time when Mexico's scientific community already feels under fire from López Obrador's administration, the agenda of which has centred on austerity and eliminating corruption. The president has referred to the 31 former officials — and scientists more broadly — as a corrupt, elite group. Early in his administration, officials [sharply curtailed funds](#) for scientists' travel to international meetings, and even to cover electricity for research centres.

‘A lot of fear has been created’

Many scientists believe the latest developments are part of a fear campaign to silence researchers opposing government policies. “The situation is quite alarming,” says David Romero, a geneticist at UNAM in Cuernavaca who is not among the accused. “To apply those kind of charges [to academics and officials] hasn’t occurred before, and this has caused a lot of turmoil in Mexico.”

Academics fear that the case is already harming the public’s opinion of scientists in Mexico. “We share the concern of many members of the international scientific community that our Mexican scientific colleagues are being subjected to harassment and intimidation,” NASEM wrote in a 6 October missive to López Obrador. “In addition to the disturbing human rights aspects of their situation, we are worried that the actions against our colleagues may have a chilling effect on the broader Mexican scientific community.”

Those fears are also shared by the accused. “To some part of the public, we are already guilty of something,” Franco says. “Our names have been put in the spotlight and a lot of fear has been created, not only among us but among the whole scientific community.”

Romero, Franco and some of the seven other accused scientists and officials to whom *Nature* reached out believe that by reporting them to the government, Conacyt is trying to harm the reputations of individuals involved with the Foro, which had criticized budget cuts and other policies.

According to the judge's ruling, in June, Conacyt sent the administration a complaint about possible corruption among former officials, whom the president described in a 24 September speech as a favourite group of the previous regime.



[Violent drug cartels stifle Mexican science](#)

Neither Conacyt nor the government prosecutor have responded to *Nature*'s requests for comment, or to questions about the criticisms levelled against them.

Conacyt [said](#) in a press release that it had complied with its legal duty to report potential crimes and that it did not accuse any particular person. The agency said that it became aware of "irregularities" while building its legal defence when the Foro sued it over austerity-related funding cuts in 2019. Conacyt says its legal department reported these irregularities to both criminal and administrative authorities.

In the statement, Conacyt also decried what it alleges is a "wave of misinformation in the media" related to the allegations, intended to create confusion, polarization and fear in the scientific community.

In August, before the scientists and the public knew about the potential charges, a judge at the country's criminal court threw out the prosecutor's

request to have the 31 people arrested, saying that the prosecution had not supplied enough evidence to support pursuing a criminal case. The prosecutor filed the warrant request again, only to have it rejected a second time on 21 September.

Scientists say there has been discord between the Foro and López Obrador's administration since long before the prosecutor attempted to bring the charges. For example, when Conacyt cut the advisory board's budget in 2019 under austerity measures, the panel sued the agency and won a year of funding.

Conacyt subsequently brought the advisory board under its auspices, essentially stripping it of its independence. That is among many moves that researchers see as attempts to expand Conacyt's political power since director María Elena Álvarez-Buylla Roces took office in 2018. The agency has made other sweeping changes, including suspending scholarships for young researchers. Álvarez-Buylla has not responded to *Nature*'s questions on these matters.

Outcry from academics

“Researchers are very disappointed with the federal government because we have lost everything we have won” in terms of funding and support from previous administrations over recent decades, says Brenda Valderrama, a biotechnology researcher at UNAM in Mexico City and former science minister of the state of Morelos, who is not among the accused academics.

It's a sign of how far the situation has deteriorated that “now we can be officially accused of criminal activities — the worst kind in Mexico”. Although it's conceivable that Conacyt and the Foro might have made administrative errors, she says, that should be investigated by an administrative office, not a criminal court.

“It is grotesque,” says one of the accused researchers, a former Conacyt official who asked not to be named for fear of damaging their legal defence, and who says that current agency officials are trying to distance themselves from previous administrations by accusing their predecessors of crimes.

The researcher says that they are struggling to sleep and that their family has been badly affected by the threat hanging over them, adding that “I’ve never been in that situation in all my life”.

What the government will do next is unclear, given that the judge has twice ruled in the academics’ favour. In a 22 September statement, the prosecutor’s office expressed disappointment with the rulings, and said it would attempt to issue arrest warrants again.

Nature **598**, 547-548 (2021)

doi: <https://doi.org/10.1038/d41586-021-02816-9>

This article was downloaded by **calibre** from <https://www.nature.com/articles/d41586-021-02816-9>

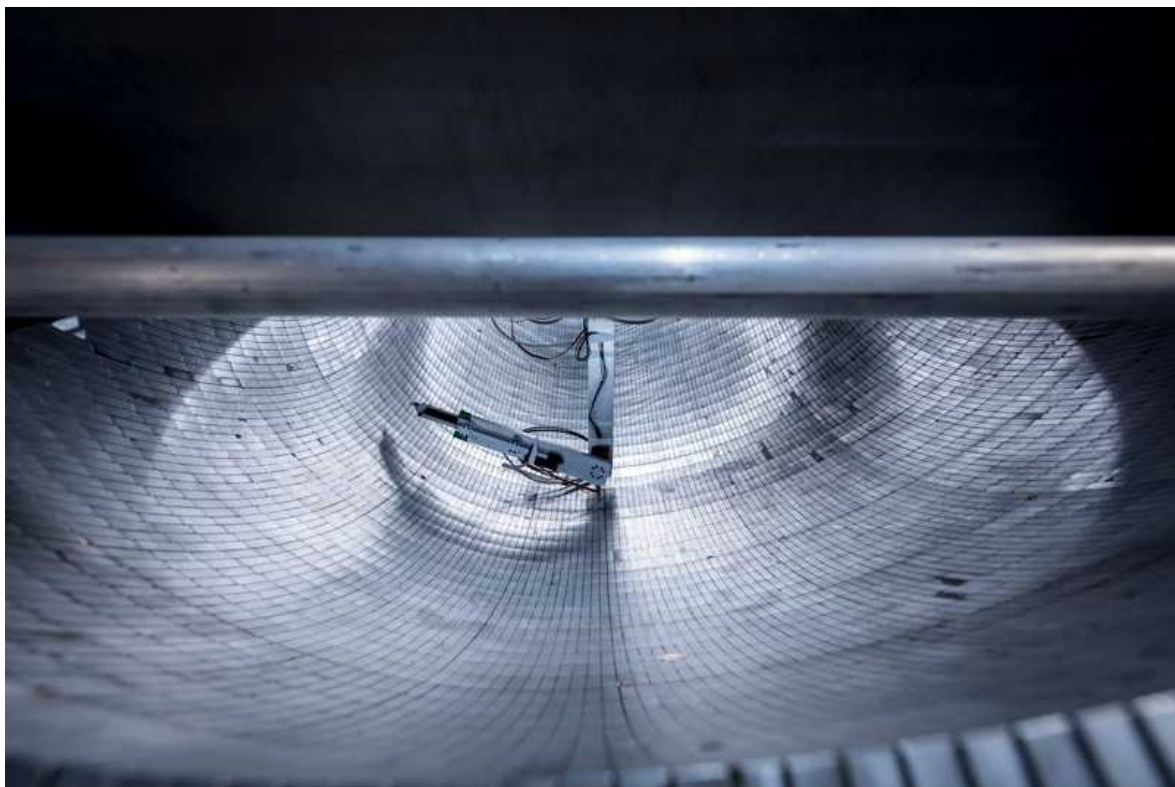
| [Section menu](#) | [Main menu](#) |

- NEWS
- 15 October 2021

Physicists make most precise measurement ever of neutron's lifetime

But decades-long mystery of how long the particles live persists.

- [Davide Castelvecchi](#)



The magnet array for the UCN τ experiment at Los Alamos National Laboratory, where physicists have measured the lifetime of the neutron with the highest ever precision. Credit: Los Alamos National Laboratory

Physicists have measured the lifetime of the neutron more precisely than ever before.

The average time it takes for the subatomic particle to decay is 877.75 seconds, according to an experiment that used magnetic fields to trap ultra-cold neutrons. The results have twice the precision of similar measurements, and are consistent with theoretical calculations. But they do not explain why in an alternative kind of experiment, neutrons last nearly 10 seconds longer.

The latest measurement was presented at a virtual meeting of the American Physical Society on 13 October, and published in *Physical Review Letters*¹.

The result is “very impressive”, says physicist Shannon Hoogerheide, who measures neutron lifetimes using a competing technique at the US National Institute of Standards and Technology (NIST) in Gaithersburg, Maryland.

Random decay

Most neutrons that exist in nature are part of non-radioactive atomic nuclei, where they can essentially last forever. But isolated neutrons, such as those produced by nuclear fission, are unstable and decay into protons. During the process, each decaying neutron emits an electron and an antineutrino.

How long do neutrons live? Physicists close in on decades-old puzzle

Exactly how long it takes for a neutron to decay is random, but the average time is about a quarter of an hour. To get a precise value, Daniel Salvat, an experimental nuclear physicist at Indiana University in Bloomington, and his colleagues built an experiment called UCN τ at the Los Alamos National Laboratory in New Mexico. They slowed neutrons down to ultra-cold temperatures and placed them in a vacuum ‘bottle’, a metal structure shaped like the halfpipe in skateboarding. Magnetic fields at the bottom of the bottle prevented the neutrons from touching the surface, where they would have been lost.

The team kept neutrons in the bottle for periods of between 20 seconds and nearly half an hour, and detected sparks of light each time a neutron decayed. At the end of each cycle, they collected and counted the remaining

neutrons, reloaded the bottle with fresh neutrons and started the process again.

UCN τ began more than ten years ago, but for the newly announced results — based on experimental runs in 2017 and 2018 — the team made several improvements that enabled them to halve their error margins.

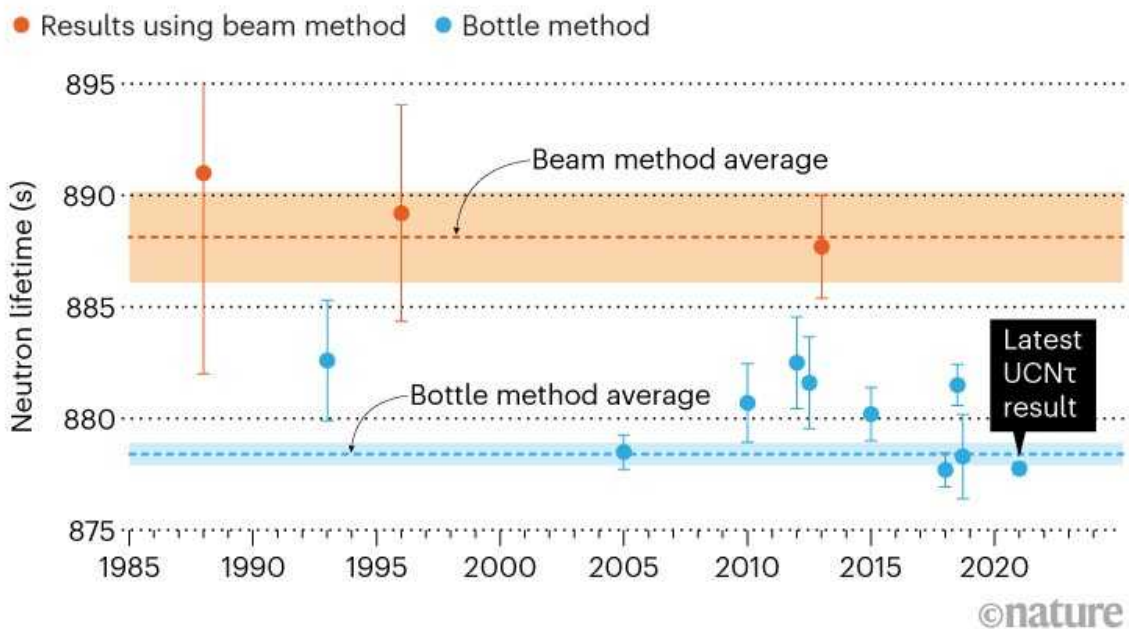
The result's precision is now competitive with calculations based on the standard model, the accepted theory of elementary particles, says Salvat. “For the first time, the experimental precision is starting to approach the precision of the theory,” he says. That means that future improvements could put the standard model itself to the test.

Bottle vs. beam

While some researchers use the ‘bottle’ technique to measure the neutron lifetime, others — such as Hoogerheide — use a method that involves watching the particles decay as they move in a beam². Until about 15 years ago, the results from these two types of experiment largely agreed within their error margins. But as the techniques became more precise, they began to go their separate ways. Neutrons in beams seem to live longer on average (see ‘Unresolved differences’).

UNRESOLVED DIFFERENCES

Mysteriously, neutrons in a beam live several seconds longer on average than do those trapped in a vacuum bottle.



Source: Wietfeldt, F. E. *Atoms* **6**, 70, <https://doi.org/10.3390/atoms6040070> (2018) and Ref. 1

UCN τ 's latest measurement does not help to bridge the gap, says Anatolii Serebrov at the Petersburg Nuclear Physics Institute in Gatchina, Russia. "Even in the light of that new result, the discrepancy remains almost intact," says Serebrov, who led a high-precision bottle experiment in 2005³ that first pointed to a possible discrepancy.

To help solve the neutron-lifetime dilemma, physicist David Lawrence at Johns Hopkins University in Baltimore, Maryland, and his collaborators have been developing a technique to measure it using neutron detectors on space probes. "It would be really useful to have a third way of doing it," he says.

The method relies on the fact that most planetary bodies eject neutrons when hit by cosmic rays. Many of the neutrons fail to escape a planet's gravity and eventually rain back down — but by then, some of those have transformed into protons. Comparing the number of neutrons emitted into space with

those that come back can provide an estimate of the neutron's lifetime⁴. "Some fraction of the neutrons will go up, decay and never come back down," Lawrence says. He adds that the ideal way to do such an experiment would be with a small, dedicated probe in orbit around Venus, because the planet's carbon dioxide atmosphere does not absorb neutrons well.

The UCN τ team has been working on several improvements to increase precision further. Hoogerheide and her colleagues at NIST are doing the same with the beam technique; they expect that its precision can improve by around a factor of 10, she says.

Nature **598**, 549 (2021)

doi: <https://doi.org/10.1038/d41586-021-02812-z>

References

1. 1.

Gonzalez, F. M. *et al. Phys. Rev. Lett.* **127**, 162501 (2021)

2. 2.

Yue, A. T. *et al. Phys. Rev. Lett.* **111**, 222501 (2013).

3. 3.

Serebrov, A. *et al. Physics Letters B* **605**, 72 (2005).

4. 4.

Wilson, J. T. *et al. Phys. Rev. C* **104**, 045501 (2021).

This article was downloaded by **calibre** from <https://www.nature.com/articles/d41586-021-02812-z>

- NEWS
- 22 October 2021

Ancient DNA points to origins of modern domestic horses

Genetic analysis shows that the ancestors of all modern horses lived in the Western Eurasian steppes more than 4,000 years ago.

- [Tosin Thompson](#)



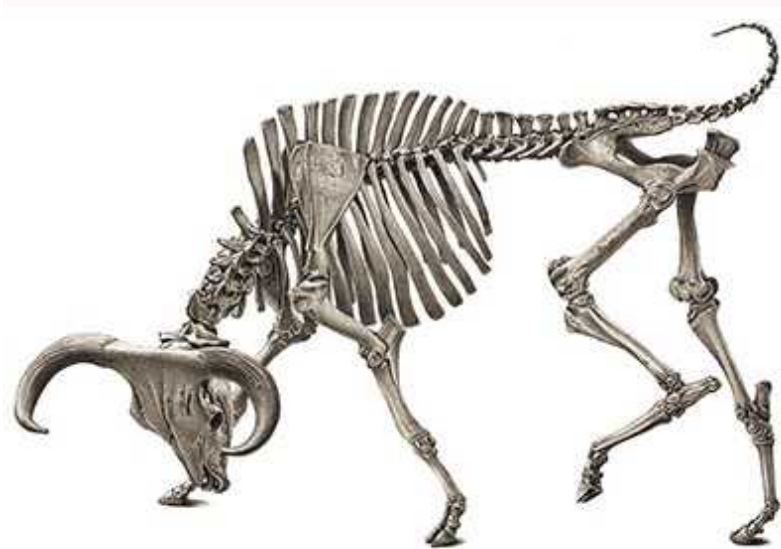
A herd of horses on the steppes of Inner Mongolia.Credit: Ludovic Orlando

Archaeologists have used ancient DNA samples to identify the genetic homeland of modern horses, where the animals were first domesticated

around 4,200 years ago. According to a study published in *Nature* on 20 October¹, modern domestic horses probably originated on the steppes around the Volga and Don rivers, now part of Russia, before spreading across Eurasia, ultimately replacing all pre-existing horse lineages.

“This study has solved a massive mystery, and also fundamentally altered our view of some of the most significant human migrations in prehistory,” says Alan Outram, a bioarchaeologist at the University of Exeter, UK, and a co-author of the work.

Horses shaped much of human development by revolutionizing transport, communication and warfare. But the origins of domestic horses have long been debated because, unlike with other livestock, such as cattle, it is difficult to tell whether bones and other remains belong to domestic horses or wild ones. “Previous work had to be built on indirect evidence, such as killing patterns, tooth damage, traces of consumption of horse milk, symbolic evidence and more,” says lead author Ludovic Orlando, a molecular archaeologist at Paul Sabatier University in Toulouse, France.



What's bred in the bone: the dazzling traits of domesticated animals

Over the past 5 years, Orlando and his team have collected pieces of bone and tooth from ancient horses — amassing more than 2,000 samples from

places where domestic horses could have originated, including Iberia, Anatolia, the steppes of Western Eurasia and Central Asia.

The researchers were able to get complete genome sequences from a subset of around 270 samples. They used radiocarbon dating to determine the ages of samples, and gathered information from field archaeology for cultural context. This allowed them to track various horse populations before, during and after domestication. They found that until around 4,200 years ago, many distinct horse populations inhabited various regions of Eurasia.

“As these populations were differentiated genetically, we could then identify the lineage from which the genetic variation present in modern domestic horses expanded,” says Orlando.

The analysis found that horses with the modern domestic DNA profile lived in the Western Eurasian steppes, especially the Volga–Don region, from the sixth to the third millennia bc. “Populations with modern domestic horse ancestry were marginal at best elsewhere,” says Orlando.

By around 2200–2000 bc, these horses had appeared outside the Western Eurasian steppes — first reaching Anatolia, the lower Danube, Bohemia and Central Asia, and then spreading across Eurasia, replacing all other local horse populations by about 1500 to 1000 bc. “We found that around 4,200 years ago, the horse reproductive pool dramatically expanded, indicating that this was when past breeders started to multiply such horses in large numbers to supply increasing demands for horse-based mobility,” says Orlando. Humans probably rode on horses’ backs before the invention of horse-drawn vehicles: the first spoke-wheeled chariots emerged around 2,000–1,800 bc.

Human migration

The findings also challenge previously held ideas about the role of horses in some early human migrations. Analyses of ancient human genomes have revealed massive migrations from the Western Eurasian steppes into Europe during the third millennium bc, associated with a culture known as the Yamnaya. These people are thought to have helped to spread Indo-European

languages into Europe, and have often been assumed to have ridden horses. “If these numerous people came with as many horses, then we should expect an equivalent shift in the horse ancestry profile,” says Orlando. But the analysis suggests that during this time, there were few domestic-horse ancestors outside the Western Eurasian steppes. This would rule out scenarios in which horses played a part in Yamnaya migration and in the initial spread of Indo-European languages.

“This radically changes our understanding of mass human movements from the steppe into western Europe in the Bronze Age,” says Outram. “It seems that those migrations were not, as had been commonly believed, facilitated by domestic horses.”



Ancient genomes heat up dog domestication debate

The research “addresses long lasting controversies concerning the role of the domestic horse in Bronze Age human expansions”, says Eske Willerslev, an evolutionary geneticist from the University of Copenhagen, Denmark.

Orlando’s team also studied genetic variants that became common in modern domesticated horses from the late third millennium bc. The standout gene was *GSDMC*, which in humans can have mutations associated with hardening of the vertebral discs — a condition that can cause chronic back pain and pain when walking. Another significant gene was *ZFPM1*, which is

essential for development of neurons involved in mood regulation and aggression. The inactivation of *ZFPM1* in mice causes anxiety and fear.

“Two variants of the *GSDMC* and *ZFPM1* genes were selected early on during the domestication process, likely facilitating taming, increasing stress resilience and providing horses with a stronger back,” says Orlando. “These qualities may explain why the new horse type had such a global success.”

Nature **598**, 550 (2021)

doi: <https://doi.org/10.1038/d41586-021-02858-z>

References

1. 1.

Librado, P. *et al.* *Nature* <https://doi.org/10.1038/s41586-021-04018-9> (2021).

This article was downloaded by **calibre** from <https://www.nature.com/articles/d41586-021-02858-z>

- NEWS
- 22 October 2021

Climate change: *Nature* readers say their fears are growing

Poll shows that 80% of respondents are more concerned in the run-up to the COP26 climate meeting than they were ahead of the Paris conference 6 years ago.

- [Quirin Schiermeier](#)



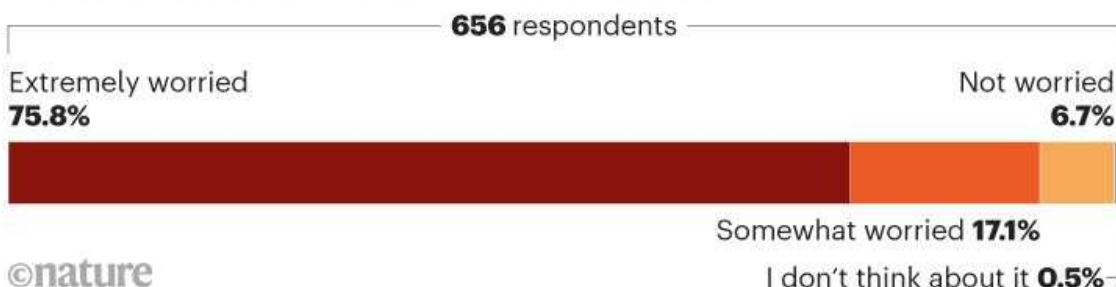
People in Hainan, China, contend with floodwater after a typhoon earlier this month. Severe floods and wildfires are becoming more common as the world warms. Credit: Luo Yunfei/China News Service via Getty

As the governments of almost 200 nations prepare for a pivotal meeting on climate change, scientists have expressed their fears over global warming and lacklustre efforts to curb greenhouse-gas emissions.

With just over a week to go until the 26th Conference of the Parties (COP26) to the United Nations Framework Convention on Climate Change, in Glasgow, UK, 76% of the more than 650 readers who responded to a *Nature* survey said they were extremely worried about climate change (see ‘Extreme concerns’), with nearly 60% saying their worries had greatly increased since the last major climate accord, reached in Paris in 2015 (see ‘Growing fears’).

EXTREME CONCERNS

A great majority of the 656 respondents to a *Nature* poll say they are extremely worried about climate change.



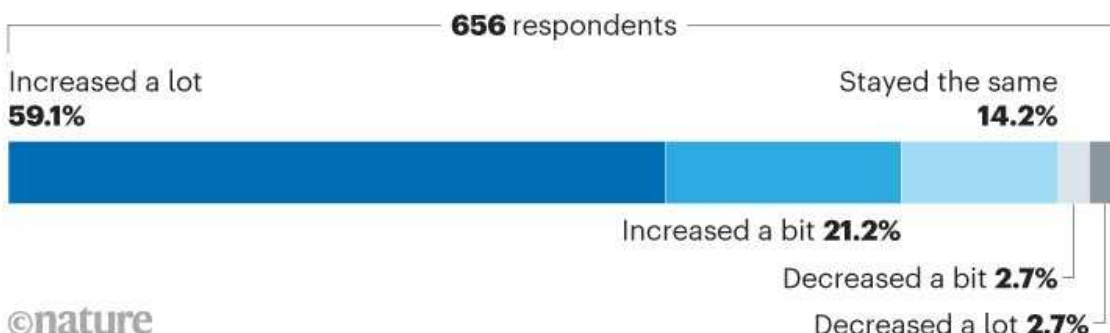
Responses to the reader poll, which were solicited on *Nature*'s website, through the *Nature* Briefing e-mail newsletter and on social media, came from nearly 60 nations. Respondents included a variety of scientists working across different disciplines, as well as some non-scientists (see ‘Breakdown of respondents’).

The results tally with those of larger surveys of the general public this year, including ones conducted in the United Kingdom and the United States, which suggest that concerns over climate change are at an all-time high.

“People are increasingly worried but don’t know what to do about it,” says Cameron Brick, an environmental psychologist at the University of Amsterdam, who has studied the attitudes of people in the United Kingdom to climate change.

GROWING FEARS

80% of poll respondents say their level of worry has increased since the last major international climate summit in Paris in 2015.



©nature

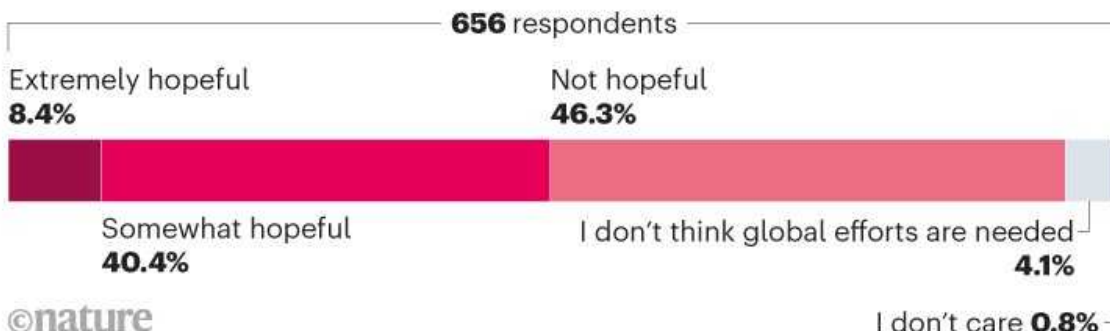
In Paris in 2015, 196 governments agreed to limit global warming to below 2 °C, and preferably below 1.5 °C, relative to pre-industrial temperatures. In Glasgow, governments are expected to adjust their Paris pledges in line with the best available science.

But the world has already warmed by about 1.2 °C compared with pre-industrial times, and scientists think we could exceed 1.5 °C in just 15 years — meaning that without immediate, drastic cuts in greenhouse gases, the Paris goal is very probably out of reach.

Respondents to the survey also expressed a lack of confidence in government pledges to tackle climate change. Fewer than 50% said they are either somewhat hopeful or extremely hopeful of the Glasgow meeting boosting global efforts to tackle climate change (see ‘Hanging on to hope’).

HANGING ON TO HOPE

Just under half of respondents are hopeful that the upcoming COP26 meeting will significantly boost global efforts to tackle climate change.



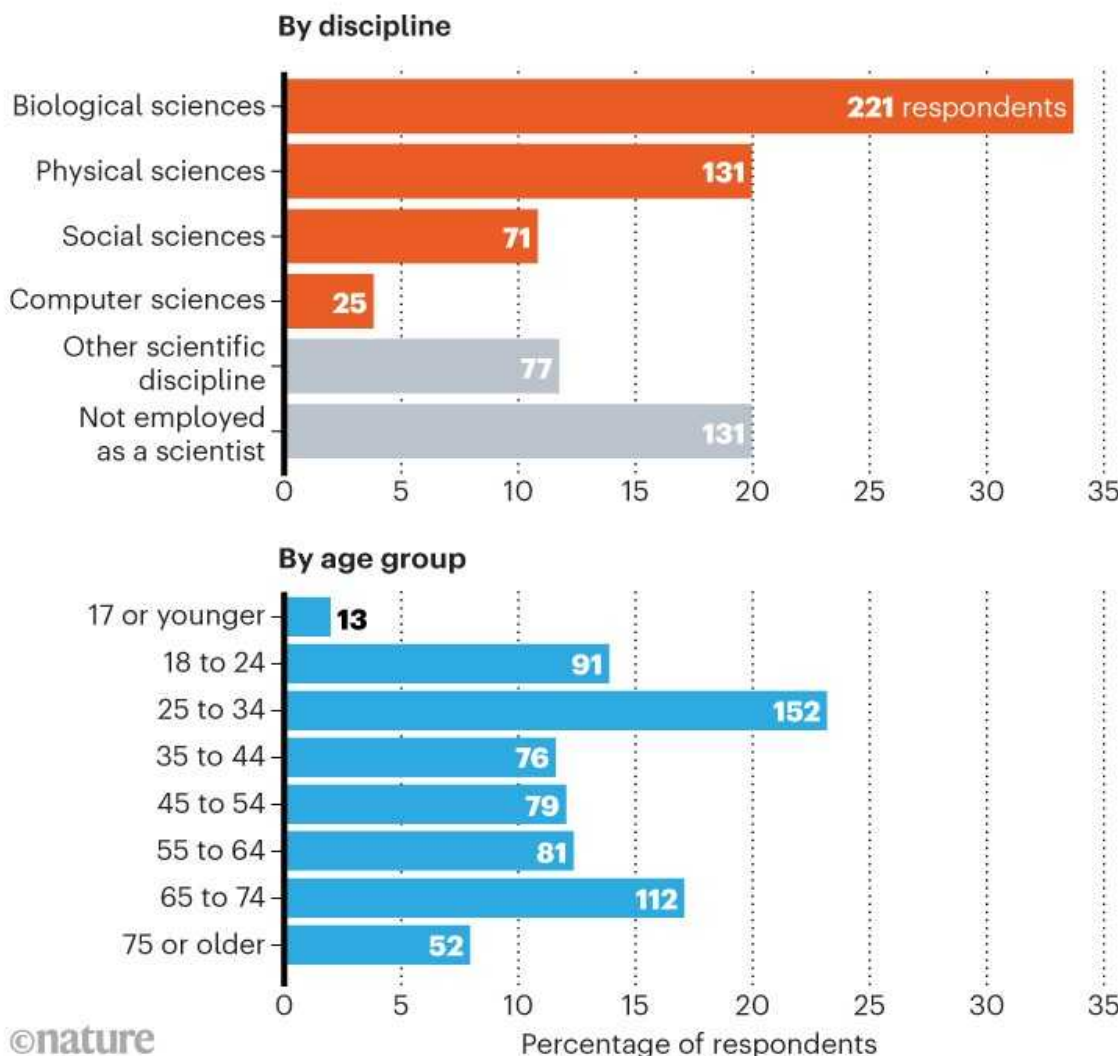
“The *Nature* poll results show that concern is rising, but hope for COP26 lags way behind,” says Brick, who adds that a recent spike in climate concerns has been driven by protests — such as those led by the global grass-roots group Extinction Rebellion — and by the release of the UN Intergovernmental Panel on Climate Change’s [latest alarming report](#) in August.

Widespread uncertainty over how governments should tackle climate change, and the part that individual citizens and households can play, is adding to public confusion and fears, says Brick.

He argues that “there has been a real failure of governments” in terms of effectively communicating positive actions that people can take.

BREAKDOWN OF RESPONDENTS

The 656 readers who participated in *Nature's* survey came from many disciplines and age groups.



Nature **598**, 551 (2021)

doi: <https://doi.org/10.1038/d41586-021-02862-3>

This article was downloaded by **calibre** from <https://www.nature.com/articles/d41586-021-02862-3>

- NEWS
- 20 October 2021

COVID vaccine makers brace for a variant worse than Delta

Companies are updating vaccines and testing them on people to prepare for whatever comes next in the pandemic.

- [Emily Waltz](#)



If an emerging strain of SARS-CoV-2 evades the immunity already conferred by vaccines and infections, vaccine makers say they will act quickly to roll out new jabs.Credit: Chandan Khanna/AFP via Getty

Pfizer's chief executive, Albert Bourla, made a bold promise in June. Standing next to US President Joe Biden at a press conference in St Ives, UK, just before the G7 summit meeting, Bourla said that should the need arise for a new COVID-19 vaccine, his company could get one ready within 100 days.

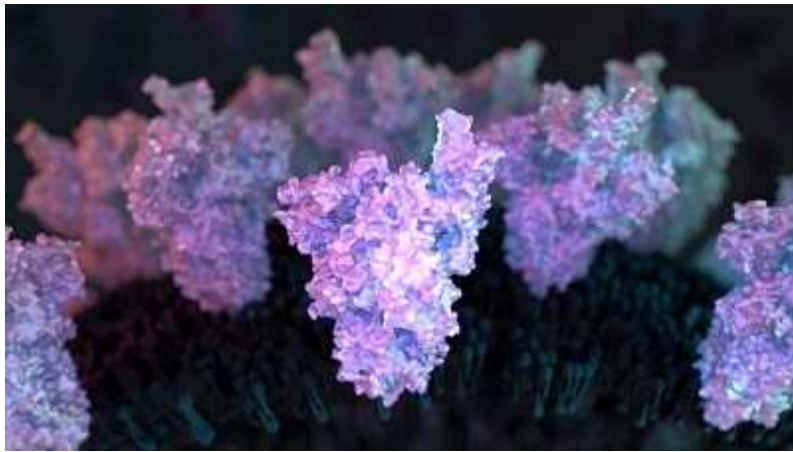
The need he was referring to is the possible emergence of an 'escape variant' — a dominant strain of SARS-CoV-2 that evades the fledgling immunity established through vaccines and previous infections. No such strain has yet been identified, but Pfizer and other leading COVID-19 vaccine makers are gearing up for that scenario.

What does it take to be nimble enough to design and test an updated vaccine against an unknown viral strain, in record time? *Nature* spoke to three COVID-19 vaccine makers — Pfizer, Moderna and AstraZeneca — to find out exactly how they are preparing.

Dress rehearsal

Over the past few months, all three companies have been running dress rehearsals by practising on known SARS-CoV-2 variants. This involves updating their vaccines to match variants such as Beta and Delta, testing them in clinical studies, tuning their internal workflows and coordinating with regulators. Their goal is to learn from these warm-up trials and smooth out kinks in their processes, so that they can move fast if, or when, a true escape variant emerges.

"At some point, inevitably, we're going to have to make variant vaccines — if vaccines are the way population immunity will be maintained — but we're not at the point where we can confidently predict the evolution of the virus," says Paul Bieniasz, a virologist at the Rockefeller University in New York City. "Practising with existing variants seems like a reasonable approach."



Rare COVID reactions might hold key to variant-proof vaccines

The first generation of COVID-19 vaccines seems to be holding up against Delta and other known variants, [at least in preventing severe disease and hospitalization](#). Pfizer, Moderna and AstraZeneca say that their vaccines, which are based on the original SARS-CoV-2 strain that was first detected in Wuhan, China, still offer the best protection against all known variants.

“There really isn’t a need at this time to make a new vaccine that will be more effective, because it looks like the old ones work very well [against] the Delta variant,” says Kathryn Edwards, scientific director of the Vanderbilt Vaccine Research Program at Vanderbilt University Medical Center in Nashville, Tennessee.

If an escape variant emerges, RNA vaccine makers such as Pfizer and Moderna could probably design and synthesize an initial prototype jab against it in [a few days](#). Viral-vector vaccines, such as AstraZeneca’s, could follow closely behind. Making an RNA vaccine typically involves generating a new genetic sequence and encapsulating it in a fatty substance such as a lipid. Viral-vector vaccines are generated by inserting the key genetic sequence into a harmless carrier virus, culturing large quantities of the virus in a bioreactor, and purifying them.



How to redesign COVID vaccines so they protect against variants

But before these shots can be deployed, they will have to be tested in humans, and that will take time. So pharma companies are doing dry runs. Pfizer, with its partner BioNTech, based in Mainz, Germany, is testing a Beta-specific RNA vaccine in a randomized, placebo-controlled clinical trial with up to 930 participants. In August, the companies began a trial of a multivalent vaccine that targets both the Delta and Alpha variants.

“We’re not doing that because we actually think we need a new vaccine for those strains,” says Philip Dormitzer, vice-president and chief scientific officer of viral vaccines and mRNA at Pfizer, based in New York City. “We want to practise all aspects of executing a strain change — the preclinical research, the manufacturing, the clinical testing and the regulatory submissions — so that if we do see a variant out there that truly escapes vaccine immunity, we’re ready to go fast.” Dormitzer says Pfizer currently has no plans to deploy its Beta or Delta vaccines among the public.



Speaking alongside US President Joe Biden on 10 June, Pfizer chief executive Albert Bourla (right) promised that his company would be able to quickly prepare a vaccine against an ‘escape variant’ of SARS-CoV-2. Credit: Brendan Smialowski/AFP via Getty

Moderna, based in Cambridge, Massachusetts, is recruiting cohorts of 300–500 participants to test new RNA vaccines against Beta, Delta and a combination of Beta and the original strain. The company also plans to test a Beta–Delta multivalent vaccine. The purpose is to submit test cases to the US Food and Drug Administration and “establish a process by which this could happen more quickly in the future”, says Jacqueline Miller, a senior vice-president and head of infectious-disease research at Moderna.

Beta is a particular focus because it carries mutations that make it more resistant than any other known variant to neutralization by antibodies created in a person’s body after they’ve been vaccinated. “If there’s another strain that evolves those mutations in the future, we can capitalize on what we’ve already learned from studying the Beta variant,” Miller says.

AstraZeneca, based in Cambridge, UK, has begun a large study of a Beta-specific viral-vector vaccine. Launched in June, the study is enrolling more than 2,800 participants, many of whom have already been vaccinated with either a messenger RNA vaccine or AstraZeneca's first-generation viral-vector vaccine. "We're definitely practising with this one, but we are also developing it, and if it's successful, we will have it ready to use," says Mene Pangalos, executive vice-president of biopharmaceuticals research and development at AstraZeneca.

Real-world effectiveness

Determining the [true efficacy of variant vaccines](#) will be difficult. In regions where COVID-19 vaccine trials are well established, it can be hard to find volunteers who have not yet received a vaccine, yet are willing to enrol in an experimental trial of a new one. There might also be ethical concerns around recruiting placebo groups for randomized controlled trials, given that effective vaccines are available.

"If we're not going to do randomized controlled trials for efficacy, one alternative would be to do immunogenicity studies, plus really robust, well-designed real-world effectiveness studies," says Matthew Hepburn, who until August was the director of COVID-19 vaccine development at the US government's Countermeasures Acceleration Group (formerly Operation Warp Speed) and is now a special adviser at the White House Office of Science and Technology Policy.



COVID vaccine immunity is waning — how much does that matter?

Immunogenicity studies would measure the immune responses triggered by variant vaccines — for instance, an increase in antibody or B-cell levels — and compare those with the effects of the first-generation vaccine. That seems to be where some vaccine makers are heading: on the basis of guidance from European regulators, AstraZeneca will use this approach in its Beta-vaccine trial.

Moderna is also focusing on immunogenicity data, and is collaborating with a hospital system in southern California to collect real-world data on vaccine effectiveness. In these observational studies, participants can choose whether they get a vaccine or not, and researchers monitor the two groups to see how they fare. Such studies “aren’t perfect”, concedes Miller, because the two groups might have different behaviours and risk factors.

How public-health authorities will determine that a variant has escaped — and therefore the world needs a new COVID-19 vaccine — isn’t yet clear. Pangalos offers one way to measure that: “If we start to see lots of people going into the hospital that have been vaccinated, then we have a problem,” he says. “But right now, we’re nowhere near that.”

The World Health Organization has a regimented process for determining when and how to change an influenza vaccine to match an emerging strain.

These decisions are based in part on a long history of monitoring and immunizing against the virus's evolution. "That doesn't exist for COVID," says Hepburn.

Miller hopes that the process of updating a COVID-19 vaccine will eventually become as streamlined as changing a flu vaccine, which typically doesn't require much in the way of clinical studies. And because RNA vaccines can be manufactured more quickly than conventional jabs, she adds, "the idea would be to make that switch even more rapidly than we're able to do with flu".

Nature **598**, 552-553 (2021)

doi: <https://doi.org/10.1038/d41586-021-02854-3>

This article was downloaded by **calibre** from <https://www.nature.com/articles/d41586-021-02854-3>

| [Section menu](#) | [Main menu](#) |

- NEWS Q&A
- 25 October 2021
- Clarification [25 October 2021](#)

‘Politicians shouldn’t meddle’: new chief of Europe’s major research funder shares priorities

Developmental geneticist Maria Leptin hopes to keep the European Research Council true to its founding mission.

- [Quirin Schiermeier](#)



Maria Leptin becomes president of the European Research Council on 1 November. Credit: EMBL PhotoLab

On 1 November, Maria Leptin will [become the new head of the European Research Council](#) (ERC), Europe's premier funding agency for basic research. Leptin, whose background is in developmental genetics, previously served as director of the European Molecular Biology Organization, Europe's life-sciences organization, based at the European Molecular Biology Laboratory (EMBL) in Heidelberg, Germany. She will take over from interim president Jean-Pierre Bourguignon, following the brief and controversial tenure of nanobiologist Mauro Ferrari, who [resigned in April last year](#).

Leptin spoke to *Nature* about her plans for the ERC, its role in European science and its significance for early-career researchers.

What are your top priorities as incoming president?

The ERC is a fantastic organization with fantastic aims and a fantastic staff. I know it well from having been on panels, and I wouldn't dream of coming in and saying we have to change everything. My first aim will be to keep the ERC stable and emphasize its strength. Of course, there are always things that can be improved, such as attaining broader public engagement. The ERC's service to the scientific community might need tweaking, because different fields have different needs.

The ERC aims to be independent from politics. What is your plan to keep the ERC true to its founding mission?

I'm hoping this doesn't need a plan. We have sufficient examples to remind people of how important it is not to meddle with the autonomy of basic research. Everybody recognizes that COVID-19 vaccines were developed so fast because a range of fields, which had been receiving basic-research

funding for a long time, suddenly came together. It illustrates that necessary and topical science comes bottom-up from the best scientists.

New methods have been arising, for instance in genomics or data management and statistics, that allow researchers to do or study things that would have been impossible ten years ago. At the ERC, we will look at all types of research, from the humanities to physics and biology.

How will you promote the value of basic research?

That's really not easy, and I wouldn't say that I have a recipe. The ERC's budget is decided by EU member states but also by the European Parliament, and parliamentarians listen very strongly to their home constituencies. It's clear that the public needs to realize what basic research is about and what it does for them. We will have to think very hard about new routes to get to the public — and it's not just going to be senior people giving lectures. One way to get there is working with locally engaged media experts that reach the people who need to be reached.

Do you envision special ERC programmes, such as on climate or COVID-19 research?

All I can say is give the best researchers a chance to come up with ideas that they want to pursue. When something unforeseen happens in ten years' time, then people will have access to a lot of good stuff that's been done. COVID-19 and climate change are just the best examples we have.

But I would not go for top-down research. We have programmes for that, including the European Innovation Council and the rest of [Horizon Europe](#), the European Union's seven-year research programme. Not all research is there for exploitation. If scientists find out about the history of the Lascaux caves, discover the Higgs boson or work out how people lived in Pompeii, that's just exciting, and people love hearing about it. There is an inherent sympathy for human curiosity in citizens, and I think we have to point that out. It's not just about curing the next disease or saving us from climate change.

ERC funding is very sought after by early-career scientists, but success rates for starting grants are very low (13.5% in 2020). What's your plan to keep young researchers happy?

Well, I think all researchers should be kept happy. Of course I'd like to be able to fund more of them. I also would like to not let them fall off a cliff after getting their first starting grant, when they apply for consolidator or advanced grants and find out it's even tougher to get one (2020 success rates were 13% and 8%, respectively). For every funding call, there are lots of good proposals that cannot be funded. I really would like the award rates go up, but there's only two ways to do this: you have either fewer applications or more money.

An interview for an ERC starting grant is a potentially career-defining moment for an early-career scientist. What's your advice for a nervous applicant?

You'll be nervous; there's nothing you can do about it. If you're not nervous, you might come across as arrogant — which is the worst thing. Be as honest and well-prepared as you can be. The committee will see through gloss and bad preparation. If you have a good project and know the background well, the committee will recognize that.

The United Kingdom and Switzerland are still negotiating access to Horizon Europe. What does this mean for grant applicants from these countries?

We are all desperately hoping that Switzerland and the United Kingdom will associate with Horizon Europe. We care about our colleagues in these

countries and their science, and we want them in the ERC. At the moment, UK-based researchers can apply for funding, but grants can be awarded only once the association agreements have been signed.

Do you think it would be better to keep politics out of science?

It's the prerogative of elected governments to determine what goes on in their constituencies, and if science is part of that they should have a say. But politicians who are not trained in science should not meddle in our day-to-day business, or tell scientists what's right or wrong. I would see it as my duty to explain to politicians what's best, and to get them to realize that. They distribute the money, so we have to make them understand what's good for people, rather than say, "Just stay out."

Nature **598**, 553 (2021)

doi: <https://doi.org/10.1038/d41586-021-02885-w>

This interview has been edited for length and clarity.

Updates & Corrections

- **Clarification 25 October 2021:** This article has been updated to clarify that the ERC's budget is decided by both the European Parliament and EU member states, and that UK-based researchers can currently apply for ERC funding.

This article was downloaded by **calibre** from <https://www.nature.com/articles/d41586-021-02885-w>

- NEWS FEATURE
- 27 October 2021

The shifting sands of ‘gain-of-function’ research

The mystery of COVID’s origins has reignited a contentious debate about potentially risky studies and the fuzzy terminology that describes them.

- [Amber Dance](#) ⁰



Illustration by Kasia Bojanowska

In Greek mythology, the Chimaera was a fire-breathing monster, a horrifying mishmash of lion, goat and snake that laid waste to the countryside. In 2015, virologists led by Ralph Baric at the University of North Carolina in Chapel Hill reported the creation of their own chimaera. They took a version of the coronavirus responsible for the deadly outbreak of severe acute respiratory syndrome (SARS) in the early 2000s — now known as SARS-CoV — and adorned it with surface proteins from a different coronavirus taken from Chinese horseshoe bats. In the laboratory, this particular mash-up was able to break into human cells and also make mice ill¹. This chimaera came with a message: other coronaviruses have the potential to spark a human pandemic. In just a few years’ time, that warning would prove prescient, as a distant cousin of SARS-CoV has now killed more than 4.9 million people worldwide.

“It probably didn’t get the recognition it should have had from the general virology community and people involved in pandemic preparedness,” says Katherine Spindler, a virologist at the University of Michigan Medical

School in Ann Arbor, who was not involved in the work. “Hindsight is 20:20.”

But the 2015 study did raise broad interest for another reason: some wondered whether such an experiment should ever have been attempted. The work was considered by some an example of ‘gain-of-function’ virology, in which scientists bestow new abilities on pathogens to study them.

The term first gained a wide public audience in 2012, after two groups revealed that they had tweaked an avian influenza virus, using genetic engineering and directed evolution, until it could be transmitted between ferrets^{2,3}. Many people were concerned that publishing the work would be tantamount to providing a recipe for a devastating pandemic, and in the years that followed, research funders, politicians and scientists debated whether such work required stricter oversight, lest someone accidentally or intentionally release a lab-created plague. Researchers around the world voluntarily paused some work, but the issue became particularly politicized in the United States.

US funding agencies, which also support research abroad, later imposed a moratorium on gain-of-function research with pathogens while they worked out new protocols to assess the risks and benefits. But many of the regulatory discussions have taken place out of the public eye.



The COVID lab-leak hypothesis: what scientists do and don't know

Now, gain-of-function research is once again centre stage, thanks to SARS-CoV-2 and a [divisive debate about where it came from](#). Most virologists say that the coronavirus probably emerged from repeated contact between humans and animals, potentially in connection with wet markets in Wuhan, China, where the virus was first reported. But a group of scientists and politicians argues that a laboratory origin has not been ruled out. They are demanding investigation of the Wuhan Institute of Virology, where related bat coronaviruses have been extensively studied, to determine whether SARS-CoV-2 could have accidentally leaked from the lab or crossed into humans during collection or storage of samples.

The arguments have highlighted questions about gain-of-function (GOF) research. But the classification is hard to define precisely. “What we mean by the term depends on who’s using the term,” says Gerald Keusch, associate director of the National Emerging Infectious Diseases Laboratories at Boston University in Massachusetts.

Here, *Nature* attempts to elucidate what constitutes GOF, and what science and medicine can learn from it.

The meaning of GOF

What is GOF? Debate over that question got heated at a US Senate hearing in July, when Senator Rand Paul (Republican, Kentucky) and Anthony Fauci, director of the National Institute of Allergy and Infectious Diseases (NIAID), went head-to-head over a 2017 paper⁴ by scientists at the Wuhan Institute. NIAID had supported the research through a New-York-based organization called EcoHealth Alliance. And it had done so at a time when funding for some GOF science was barred. The authors genetically grafted spike proteins — the viral keys that grant access to mammalian cells — from eight different, naturally occurring coronaviruses onto another coronavirus from the wild, called WIV1. They found that these new creations, in lab dishes, could infect monkey kidney cells, as well as human cells, through the same gateway — the widely expressed ACE2 receptor — that is used by SARS-CoV and SARS-CoV-2.

Senator Paul insisted that the work constituted GOF. Fauci was adamant that it did not.

It's no surprise that politicians and scientists would disagree on GOF's meaning, because it can mean different things in different contexts. At its most innocuous, GOF is a classic genetics term to describe mutations that give a gene, RNA or protein new abilities or expression patterns. Gain of function might result in bacteria that are extra sensitive to potassium ions⁵, for example, or an *Arabidopsis* plant with short stems and curly leaves⁶. A complementary approach — loss-of-function — involves disabling a gene to see what happens to organisms that lack it.



Bird-flu research: The biosecurity oversight

The term GOF didn't have much to do with virology until the past decade. Then, the ferret influenza studies came along. In trying to advise the federal government on the nature of such research, the US National Science Advisory Board for Biosecurity (NSABB) borrowed the term — and it stuck, says Gigi Gronvall, a biosecurity specialist at the Bloomberg School of Public Health at Johns Hopkins University in Baltimore, Maryland. From that usage, it came to mean any research that improves a pathogen's abilities to cause disease or spread from host to host.

Virologists do regularly fiddle with viral genes to change them, sometimes enhancing virulence or transmissibility, although usually just in animal or cell-culture models. "People do all of these experiments all the time," says Juliet Morrison, a virologist at the University of California, Riverside. For example, her lab has made mouse viruses that are more harmful to mice than the originals. If only mice are at risk, should it be deemed GOF? And would it be worrying?

The answer is generally no. Morrison's experiments, and many others like them, pose little threat to humans. GOF research starts to ring alarm bells when it involves dangerous human pathogens, such as those on the US government's 'select agents' list, which includes Ebola virus and the bacteria responsible for anthrax and botulism. Other major concerns are

‘pathogens of pandemic potential’ (PPP) such as influenza viruses and coronaviruses. “For the most part, we’re worried about respiratory viruses because those are the ones that transmit the best,” says Michael Imperiale, a virologist at the University of Michigan Medical School. GOF studies with those viruses are “a really tiny part” of virology, he adds.

But this little slice of the field became the focus when the NSABB talked about regulating or monitoring GOF research (see ‘Evolving terminology’). After the ferret flu studies were eventually published, researchers and regulators struggled to determine what sorts of experiment should receive extra scrutiny as a potential biosecurity risk.

Evolving terminology

Scientists started talking about gain of function with respect to virology after a pair of influenza studies raised concerns about publishing risky research. Its definition became narrower as policies evolved.

September 2011

Researchers present work demonstrating that a highly pathogenic avian influenza virus can be made to transmit between ferrets.

January 2012

Influenza researchers voluntarily pause related experiments.

March 2012

The US National Science Advisory Board on Biosecurity (NSABB) recommends full publication of the ‘gain-of-function’ (GOF) influenza studies after previously suggesting that they be redacted.

January 2013

Researchers end the moratorium on influenza research.

February 2013

US government releases a framework for auditing GOF research on highly pathogenic influenza.

October 2014

After a series of sample-handling incidents, the US government pauses funding on GOF research with influenza and coronaviruses as it re-tools oversight.

May 2016

The NSABB issues a new proposal for oversight using a narrow definition of GOF research of concern (GOFROC) that would require evaluation.

December 2017

US government lifts its 2014 ban on funding and releases new guidelines for oversight.

January 2020

The NSABB begins reviewing guidelines for sharing information on GOF research proposals and decisions.

In 2016, the NSABB attempted to clarify matters with a new term, ‘gain-of-function research of concern’ (GOFROC). This category, the committee said, is research that would make a pathogen likely to spread widely or cause significant disease in humans. This, the committee decided, was the only type of GOF work so risky it would require extra regulatory oversight⁷. In 2017, the US Department of Health and Human Services

(HHS) adopted this approach when it devised its framework for reviewing grants on pathogens with pandemic potential.

However, as the war of words between Paul and Fauci shows, the terminology is still hotly debated. The chimeric viruses in the Wuhan Institute study were new viruses made in the lab. But the manipulations that made them did not enhance their ability to cause disease in humans. The starting virus, WIV1, could already infect human cells using ACE2. Although some scientists have argued that [the work does constitute GOF](#), at the time the research was approved, it was evaluated by NIAID and considered exempt from the funding pause.

Last week, leaders at the US National Institutes of Health (NIH) told the US Congress that EcoHealth Alliance had not informed the agency about experiments in Wuhan in 2018 that enhanced the virulence of WIV1 in mice, and that immediately reporting such findings was a condition of the funding. A representative for EcoHealth Alliance says that the data were reported in 2018 and that the organization is working to “promptly address what we believe to be a misconception about the grant’s reporting requirements and what the data from our research showed”. Both EcoHealth Alliance and the NIH have stated that the viruses in question had no role in the emergence of SARS-CoV-2 and that the research doesn’t constitute GOF. But the continued controversy has set off more questions as to whether such research is warranted — and prompted more calls for transparency in how it is reviewed and approved.

Notably, the committee at the HHS charged with reviewing potential GOFROC work has not publicly released any of its deliberations (although details of grant review are typically kept private).

Only a handful of countries even have national policies on oversight for potentially risky biomedical research. And although China has long been a participant in international treaties and conventions on biosecurity, the nation didn’t pass sweeping legislation until 2020. Its law, which took effect this April, requires approvals for research with highly pathogenic microbes by provincial departments of health or rural affairs. But the law does not specifically address GOF studies, and some experts say the rules are vague⁸.

How GOF can help

Despite the ongoing debate, plenty of studies have imparted new functions to viruses, with clear benefit to science and medicine. Since the time when poliovirus was first grown in cultured cells, scientists have [adapted viruses to live in culture](#). This enables production of a large supply of viral material for further study or for vaccine development. This process sometimes diminishes the pathogens' ability to make humans ill. After all, the lab dish contains no immune system, so viruses can streamline their life cycles by dumping costly activities that would normally protect them from host attack, says Stanley Perlman, a physician and virologist at the University of Iowa in Iowa City.

Scientists have also directly modified viruses to create vaccines; the COVID-19 shots from both Oxford–AstraZeneca and Johnson & Johnson are based on adenoviruses harmless to humans that were [modified to produce the SARS-CoV-2 spike protein](#). Researchers have also altered viruses to deliver gene therapies or cancer treatments. “All that great stuff that is going to benefit humanity is a gain of function,” says Vincent Racaniello, a virologist at Columbia University in New York City.



[US officials revisit rules for disclosing risky disease experiments](#)

In addition, scientists routinely give viruses the ability to infect new hosts. Animal research — although fraught with its own set of ethical quandaries — allows scientists to study how pathogens work and to test potential treatments, a necessary precursor to trials in people. That's what Perlman and his collaborators had in mind when they set out to study the coronavirus responsible for Middle East Respiratory Syndrome (MERS-CoV), which emerged as a human pathogen in 2012. They wanted to use mice, but mice can't catch MERS.

The rodents lack the right version of the protein DPP4, which MERS-CoV uses to gain entry to cells. So, the team altered the mice, giving them a human-like version of the gene for DPP4. The virus could now infect the humanized mice, but there was another problem: even when infected, the mice didn't get very ill. "Having a model of mild disease isn't particularly helpful to understand why people get so sick," says collaborator Paul McCray, a paediatric pulmonologist also at the University of Iowa.

So, the group used a classic technique called 'passaging' to enhance virulence. The researchers infected a couple of mice, gave the virus two days to take hold, and then transferred some of the infected lung tissue into another pair of mice. They did this repeatedly — 30 times⁹. By the end of two months, the virus had evolved to replicate better in mouse cells. In so doing, it made the mice more ill; a high dose was deadly, says McCray. That's GOF of a sort because the virus became better at causing disease. But adapting a pathogen to one animal in this way often limits its ability to infect others, says Andrew Pekosz, a virologist at the Bloomberg School of Public Health.

The experiments did make the virus amenable to research, however, and the team shared both it and the engineered mice with others. It led to plenty of new findings. For example, Perlman's team discovered that an immune-system protein called interferon fights the virus, at least in a very specific time window¹⁰. This parallels responses in people with SARS-CoV-2, suggesting that if interferon is provided as a treatment, it should be early in the course of the disease¹¹.

Researchers also used the mouse-adapted MERS-CoV to test new vaccines and treatments. The Iowa team's collaborators tested a vaccine that is a hybrid of parainfluenza virus with the MERS-CoV version of the spike. The vaccine wasn't very effective when injected, but it did protect DPP4-expressing mice from MERS-CoV quite well when provided through the nose¹². Although MERS outbreaks haven't led to sustained transmission, this information has proved valuable in the COVID-19 pandemic: a vaccine with the same design, but against the SARS-CoV-2 spike, works in mice and ferrets¹³ and is now undergoing early clinical trials.

The big questions about GOF

Treatments and vaccines are clear benefits, but what has the body of scientific knowledge gained from basic-science experiments that skate close to, if not cross into, GOF or GOFROC territory?

The initial set of experiments that made GOF a household name revolved around avian influenza, a type known as H5N1. People sometimes catch it from poultry, and it can be fatal, but humans don't typically transmit the virus to one another. Scientists wanted to know, however, what it would take to make that happen. "That's the kind of question you can only answer with a gain-of-function experiment," says Angela Rasmussen, a virologist at the University of Saskatchewan Vaccine and Infectious Disease Organization in Saskatoon, Canada.

Teams in the United States and Japan² and the Netherlands³ set out to test whether the bird virus could possibly evolve into something that's transmissible between mammals, in this case ferrets, which are vulnerable to infection by respiratory viruses and are a common animal model in flu studies. The researchers' strategies included making both specific and random mutations in the viral genome as well as passaging the pathogen through a series of ferrets to encourage it to adapt to the new host — much as McCray and Perlman did with MERS-CoV in mice. The result was that, yes, there are genetic changes that can make avian flu spread from ferret to ferret^{2,3}. The new viruses were weakened and non-lethal, but they sparked a

considerable fuss as science funders, regulators, journals and others debated and deliberated whether the data should even be published.



[US government lifts ban on risky pathogen research](#)

As for whether it was worth it, opinions differ. “Their practical importance, wasn’t, in my mind, very extraordinary,” says David Morens, senior adviser to the director at NIAID. “They don’t help us answer the questions of whether H5N1 might become pandemic or what we would need to do to recognize or prevent it.” (The corresponding authors of these two studies did not respond to, or declined, interview requests from *Nature*.)

Imperiale thinks otherwise: “We learned the determinants of mammalian transmission,” he says. For example, the work supported suspicions that for a flu virus to infect a mammalian host, it must adapt to the temperature of the host’s lungs and to the pH of that host cell’s interior compartments.

The studies also identified several specific mutations that might allow an avian flu virus to turn into a mammalian flu virus, something scientists could watch out for in bird populations. The value of that is somewhat speculative, however. Surveillance of farmed and wild birds is far from universal and avian influenza could, theoretically, evolve to infect humans by an entirely different set of mutations.

As for coronavirus, Baric's 2015 chimaera experiments used a version of SARS-CoV adapted to infect mice, not people, so it might not fit the strictest definition of GOFROC. The chimaera, with the spike from a wild coronavirus called SHC014, was no better at infecting human cells than the original mouse-adapted SARS¹. Baric did not respond to interview requests from *Nature*, but at the time, the authors wrote that “scientific review panels may deem similar studies building chimeric viruses based on circulating strains too risky to pursue”. More recently, [Baric told MIT Technology Review](#) that the work should not be considered gain of function. “We retained function,” Baric said — or even lost function, in that the virus was less able to make mice sick than the original SARS virus.

Baric's studies, and the similar ones carried out by researchers in Wuhan that Rand Paul was concerned about⁵, did predict that a coronavirus could jump to humans and cause a pandemic, years before they were proved right. But the benefits go beyond that, says Rasmussen. “The irony is, these experiments and the work that was done at the Wuhan Institute of Virology, I think, really gave us a lot more information about SARS-CoV-2 than we would have had.”

For example, Baric has pointed to work in his lab suggesting that remdesivir, a drug then in development to fight Ebola, would be a potential treatment for coronavirus infection. In this case, no chimaeras were involved, but the researchers worked with a handful of naturally occurring bat coronaviruses they'd reconstructed in the lab. The team found¹⁴ that the drug protected human cells from these viruses as well as from SARS-CoV and MERS-CoV. It also reduced symptoms in a mouse model infected with SARS-CoV. Remdesivir was quickly applied to people with COVID-19 and is so far the main antiviral in use — [although clinical results have been mixed](#).

Globally, GOFROC experiments will probably continue to be a rarity. But some virologists can envisage valuable experiments with SARS-CoV-2 that could be considered GOF. For example, Morrison thinks that experiments to look for mutations that make SARS-CoV-2 resist vaccines or treatments could be beneficial, so that scientists can be better prepared if such variants emerge. And as scientists attempt to make vaccines that work on all

coronaviruses, it might be useful to test the vaccines' abilities to protect against infection by chimeric viruses that incorporate spikes from various wild specimens, suggests Stephen Goldstein, who studies viral evolution at the University of Utah in Salt Lake City. In fact, Baric has already tested one potential vaccine against a hybrid of mouse-adapted SARS-CoV and a bat coronavirus^{[15](#)}.

The ongoing political debate has meant that some virologists dare not even propose research that might be deemed GOF, says Pekosz. Some are even afraid to talk about it publicly. A survey by *Nature* published earlier this month suggests that scientists who speak out on topics related to the origins of COVID-19 [are subjected to high rates of harassment](#).

With all the challenges inherent in GOF studies, why do them? Because, some virologists say, the viruses are constantly mutating on their own, effectively doing GOF experiments at a rate that scientists could never match. “We can either wait for something to arise, and then fight it, or we can anticipate that certain things will arise, and instead we can preemptively build our arsenals,” says Morrison. “That’s where gain-of-function research can come in handy.”

Nature **598**, 554–557 (2021)

doi: <https://doi.org/10.1038/d41586-021-02903-x>

References

1. 1.

Menachery, V. D. *et al.* *Nature Med.* **21**, 1508–1513 (2015).

2. 2.

Imai, M. *et al.* *Nature* **486**, 420–428 (2012).

3. 3.

Herfst, S. *et al.* *Science* **336**, 1534–1541 (2012).

4. 4.

Hu, B. *et al.* *PLoS Pathog.* **13**, e1006698 (2017).

5. 5.

Kuo, M. M.-C., Saimi, Y. & Kung, C. *EMBO J.* **22**, 4049–4058 (2003).

6. 6.

Want, J. *et al.* *Plant Mol. Biol.* **82**, 71–83 (2013).

7. 7.

National Science Advisory Board for Biosecurity. *Recommendations for the Evaluation and Oversight of Proposed Gain-of-Function Research* (2016).

8. 8.

Cao, C. *J. Law Biosci.* **8**, lsab020 (2021).

9. 9.

Li, K. *et al.* *Proc. Natl Acad. Sci. USA* **114**, E3119–E3128 (2016).

10. 10.

Channappanavar, R. *et al.* *J. Clin. Invest.* **129**, 3625–3639 (2019).

11. 11.

Lee, J. S. & Shin, E.-C. *Nature Rev. Immunol.* **20**, 585–586 (2020).

12. 12.

Li, K. *et al.* *mBio* **11**, e00554-20 (2020).

13. 13.

An, D. *et al.* *Sci. Adv.* **7**, eabi5246 (2021).

14. 14.

Sheahan, T. P. *et al.* *Sci. Transl. Med.* **9**, eal3653 (2017).

15. 15.

Martinez, D. R. *et al.* *Science* **373**, 991–998 (2021).

This article was downloaded by **calibre** from <https://www.nature.com/articles/d41586-021-02903-x>

| [Section menu](#) | [Main menu](#) |

- NEWS FEATURE
- 26 October 2021

The secret lives of cells — as never seen before

Cutting-edge microscopy techniques are allowing researchers to spy on the innards of cells in all their crowded glory.

- [Diana Kwon](#) ⁰



Cryo-electron tomography and related techniques can showcase the insides of cells in striking detail. Credit: S. Albert *et al.*/PNAS ([CC BY 4.0](#))

For a few weeks in 2017, Wanda Kukulski found herself binge-watching an unusual kind of film: videos of the insides of cells. They were made using a technique called cryo-electron tomography (cryo-ET) that allows researchers to view the proteins in cells at high resolution. In these videos, she could see all kinds of striking things, such as the inner workings of cells and the compartments inside them, in unprecedented detail. “I was so overwhelmed by the beauty and the complexity that in the evenings I would just watch them like I would watch a documentary,” recalls Kukulski, a biochemist at the University of Bern, Switzerland.

In recent years, imaging techniques such as cryo-ET have started to enable scientists to see biological molecules in their native environments. Unlike older methods that take individual proteins out of their niches to study them, these techniques provide a holistic view of proteins and other molecules together with the cellular landscape. Although they still have limitations — some researchers say that the resolution of cryo-ET, for example, is too low for molecules to be identified with certainty — the techniques are increasing

in popularity and sophistication. Researchers who turn to them are not only mesmerized by the beautiful images, but also blown away by some of the secrets that are being revealed — such as the tricks bacteria use to infect cells or how mutated proteins drive neurodegenerative diseases such as Parkinson's.

Every peek through the microscope is another chance to explore uncharted cellular terrain, says Grant Jensen, a structural biologist at the California Institute of Technology in Pasadena. "There's definitely a great joy in being able to see something for the first time," he says.

Other researchers share his delight. Elizabeth Villa, a biophysicist at the University of California, San Diego, recalls her overwhelming excitement the first time she saw cell structures with cryo-ET. "It felt as if all of a sudden, we were paparazzi with access we never had before," Villa says.

From crystals to context

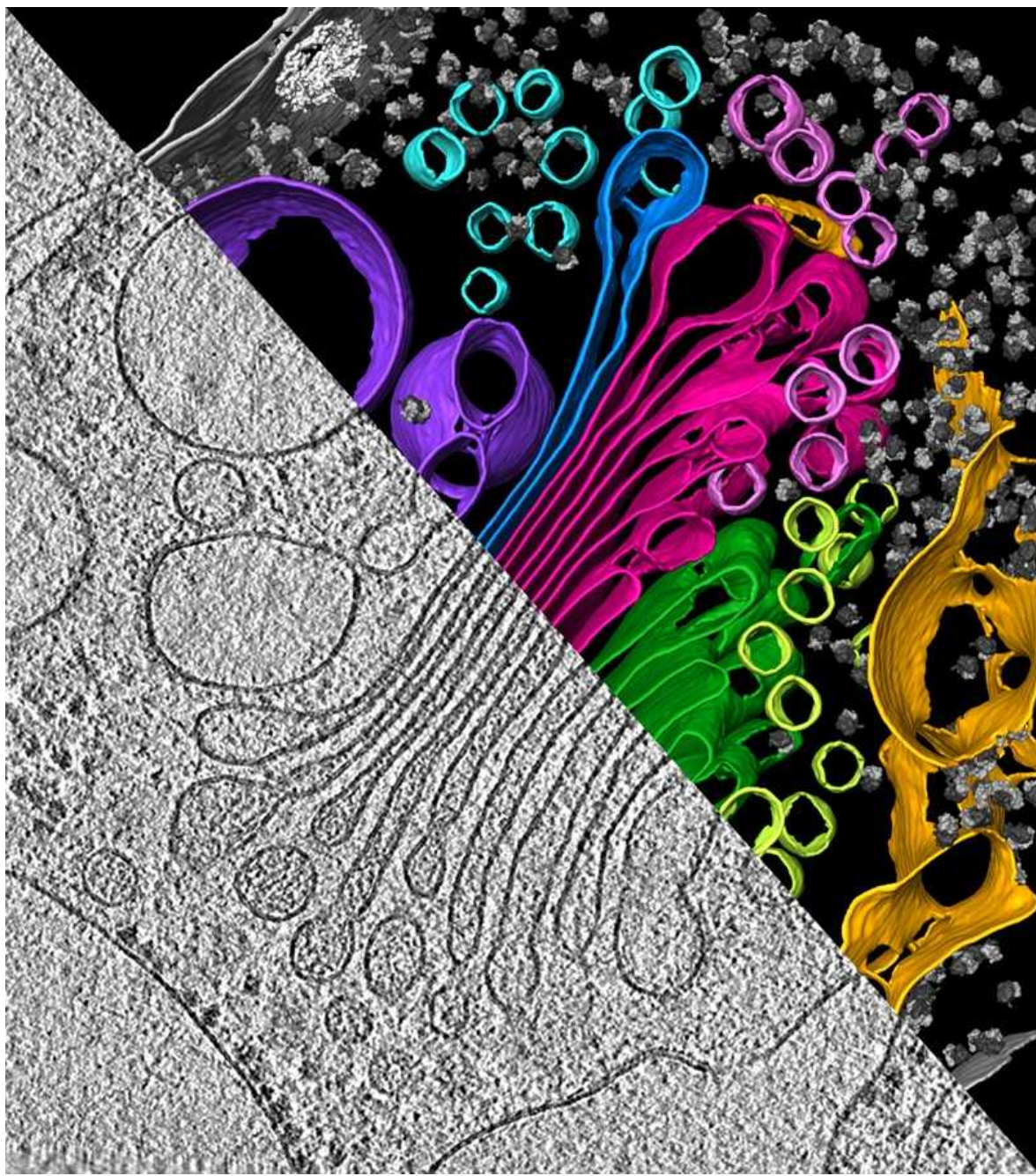
For decades, researchers have relied on a technique called X-ray crystallography to visualize proteins, viruses and other biological entities. The method involves coaxing molecules into forming static, well-ordered crystals and then bombarding the samples with intense X-ray beams. It enabled the discovery of the helical nature of DNA and the structure of more than 100,000 proteins, but it has its limitations: crystallizing molecules is difficult and tedious, and not always possible.

Scientists have overcome these drawbacks using cryo-electron microscopy (cryo-EM), a technique that reveals the structure of biomolecules that have been isolated from their surroundings and then frozen. In cryo-EM, the samples are showered with beams of electrons. Although the technique was initially ridiculed as 'blobology', owing to the blurry images it produced, advances in sample preparation and image processing have increased its resolution enough to visualize individual atoms (around 1.2 ångströms or 1.2×10^{-10} m in size).

As this 'resolution revolution' started to sweep through cryo-EM, around 2013, scientists flocked to the method. So far, researchers have used it to

solve the structures of more than 10,000 biological molecules. Proteins found in cell membranes, in particular, have been of interest, because many of them are important for understanding disease and developing drugs. The advance “opened the door for some of those really talented people to then look for the next richest, most ripe field for big impact advances”, says Jensen. That area happened to be cryo-ET.

Its early proponents sought a technique that could view biological molecules not only in fine detail, but also as they would look inside cells. Like cryo-EM, cryo-ET requires an electron microscope and relies on a sample preparation method known as vitrification: the rapid cooling of the water around a sample so that it freezes into a glass-like state, rather than as ice crystals. Unlike conventional cryo-EM, however, which requires purified samples, investigators can use cryo-ET to capture these molecules *in situ*.



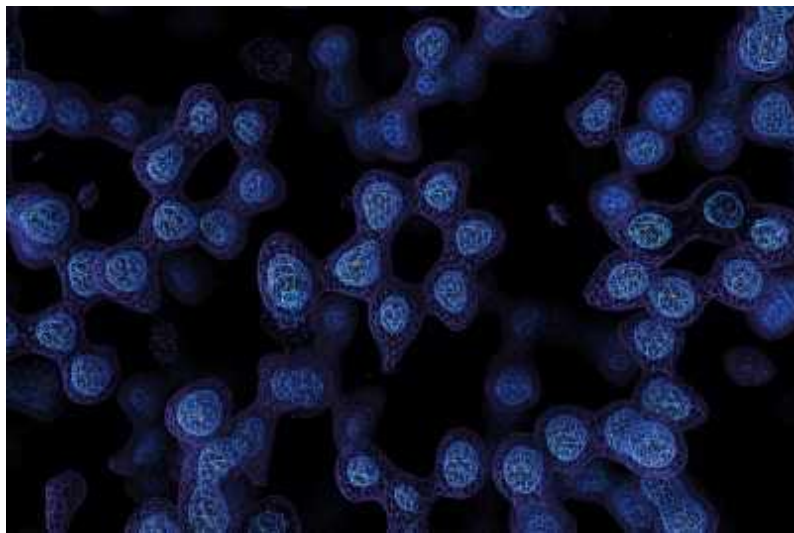
An algal cell reveals its secrets under cryo-ET, showing the endoplasmic reticulum (yellow), which makes proteins, the pouches of the Golgi apparatus (green and magenta), which modifies and packages proteins for transport, and vesicles (small circles, various colours), which carry proteins. Credit: Y. S. Bykkov *et al.*/eLIFE ([CC BY 4.0](#))

With cryo-EM, scientists make a 3D image by taking 2D pictures of lots of isolated molecules in different configurations, and merging the results. With

cryo-ET, by contrast, they take multiple snapshots of a single chunk of material, teeming with molecules, from many different angles, allowing the surroundings to be kept intact.

It's like having a photo of a whole crowd, rather than one person's headshot. This is why Wolfgang Baumeister, a biophysicist at the Max Planck Institute of Biochemistry in Martinsried, Germany, who is one of the pioneers of the technique, and his colleagues have dubbed it "molecular sociology".

And this is how proteins live, after all. "Proteins are social — at any given time a protein is in a complex with about ten other proteins," says Villa. After viewing such interactions with cryo-ET, "I could not stomach the thought of myself studying another protein in isolation," she adds.



[Revolutionary microscopy technique sees individual atoms for first time](#)

Electron tomography itself — the use of an electron microscope to image a specimen from several angles — has been around since the 1960s, but it wasn't until the 1990s that the method began to come into its own. One of the challenges was that streams of electrons are extremely damaging to biological samples, which made it difficult to capture enough snapshots for a clear, crisp image. Scientists have sharpened their pictures using the latest sample-slicing processes and computational methods. For instance, a technique called cryo-focused-ion-beam (cryo-FIB) milling can cut samples into extremely thin slices known as lamellae. Still, the cost and technical expertise needed to use cryo-ET — particularly in combination with

methods such as cryo-FIB milling — can be prohibitive for many laboratories, Baumeister says.

Early demonstrations of cryo-ET from Baumeister's group included snapshots¹ of the cells of *Dictyostelium*, a bacteria-guzzling amoeba that lives in soil. The team revealed, among other things, previously unseen characteristics of intricate protein networks that make up the amoeba's cytoskeleton — such as how individual filaments interact with one another and attach to specific structures on the membranes of *Dictyostelium* cells.

"You can rarely assign biological functions or cellular functions to an individual molecule — the functions arise from the interaction of all the molecules inhabiting a cellular landscape," Baumeister says. "That's where the discovery potential of cryo-ET comes in. Whatever we look at nowadays, there are surprises."

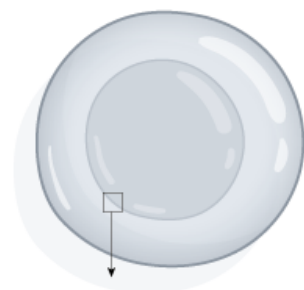
Sociable cells

Much of the early work with cryo-ET was on prokaryotes: single-celled organisms such as bacteria. These cells are usually smaller and thinner than the more complex cells of eukaryotes.

In a study of Jensen's from 2006, for example, he and his team reported the first complete structure of the motor that drives the flagellum, a whip-like appendage in bacteria². Using cryo-ET, they unveiled the architecture of the 20-piece motor in *Treponema primitiva*, a bacterium found in termites' guts, and detailed how these parts were positioned in the bacterial membrane. Jensen and his colleagues have also revealed key details of bacterial pili — protrusions that the microorganisms use for many functions, such as attaching to and secreting substances into cells they infect. Last year, his team released an open-access, digital atlas (see [go.nature.com/3nugs7v](https://doi.org/10.1038/nature25771)) highlighting the many insights cryo-ET has revealed about bacterial and other prokaryotic cells.

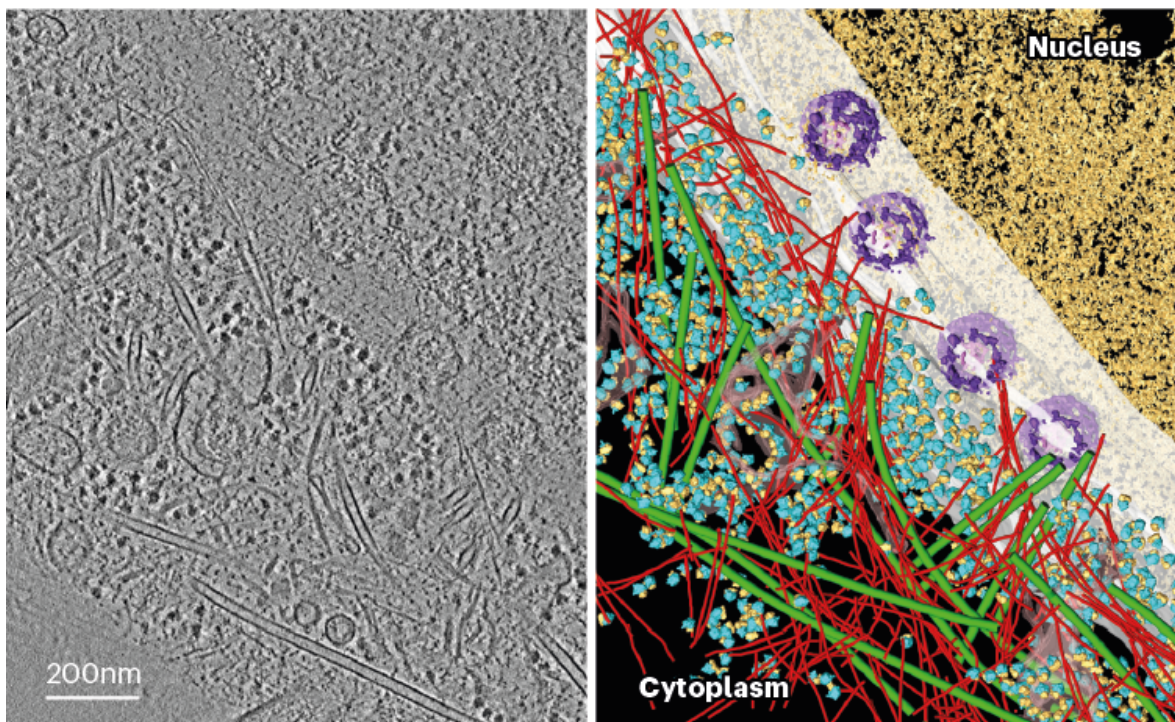
More recently, scientists have moved on to imaging eukaryotic cells — which are palatial in comparison with prokaryotes. This has been possible largely because of the advent of cryo-FIB milling, which allows researchers

to slice cells thinly before placing them under an electron microscope. Baumeister and his colleagues used this mash-up of methods to visualize how molecules were arranged in the vicinity of the nucleus in a human cell³ (see ‘Inside scoop’). Their work revealed how previously unseen, nanometre-thin filaments provided structural support to the nucleus — making it one of the stiffest organelles in animal cells.



INSIDE SCOOP

Researchers used cryo-electron tomography to peer at the boundary of a human cell’s nucleus (left) and pinpoint the structures inside and out (right, annotated view).



- Endoplasmic reticulum, which helps to make proteins
- Actin filaments, which provide structure and shape

- Nuclear envelope or boundary
- Nuclear pore complex, which transports molecules into and out of the nucleus

- Ribosomes, which make proteins
- Microtubules, which maintain shape and aid transport of molecules and cellular structures

Source: Ref. 3

Even with FIB milling, cryo-ET can capture only tiny segments of eukaryotic cells, meaning that scientists need to find a way to pinpoint molecules of interest in a vast and crowded cellular landscape. One solution is to pick out proteins by first fluorescently labelling them under a light microscope, and then zooming into the finer details in specific sections using cryo-ET.

Villa and her colleagues have used this combination of techniques to resolve the architecture of LRRK2, a protein linked to inherited forms of Parkinson's disease⁴. Their work revealed that the mutated version of the protein stuck to components of the cytoskeleton known as microtubules, forming a double helix around them. The team's findings also hinted that mutated LRRK2 might form a configuration that promotes this type of binding — potentially causing problems by blocking molecules that carry important cellular cargo along the microtubules⁵.



The revolution will not be crystallized: a new method sweeps through structural biology

Groups such as Baumeister's have used this method to examine how proteins associated with neurodegenerative diseases such as Huntington's⁶ and motor neuron disease (amyotrophic lateral sclerosis, or ALS)⁷ interact with

components of the cell such as the endoplasmic reticulum (ER), a large piece of cellular machinery that helps to synthesize proteins. Researchers have found that neurotoxic clumps of proteins implicated in these diseases behave very differently to one another inside cells. In Huntington's, for example, aggregates of a mutant form of a protein called huntingtin seem to throw the organization of the ER into disarray, whereas in ALS, aggregates of an abnormal protein impair the cell's biochemistry by activating its protein-degrading machinery.

In the future, scientists hope to use such methods to better understand how therapeutics work, by visualizing how drugs act on the molecular innards of cells. In an early demonstration, Julia Mahamid at the European Molecular Biology Laboratory in Heidelberg, Germany, and her colleagues were able to glimpse antibiotics in a bacterial cell binding to ribosomes — organelles that serve as protein factories⁸. The feat was made possible by pushing the resolution of cryo-ET to 3.5 ångströms.

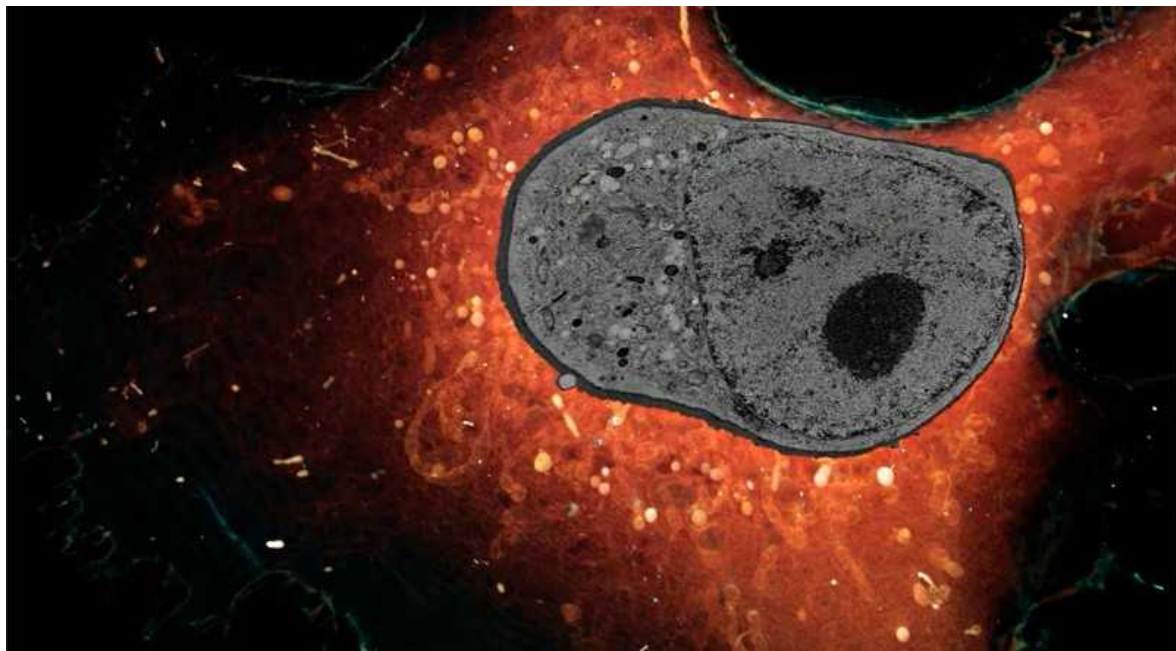
"I think that's probably the state of the art of what's possible [with cryo-ET]," says Kukulski, who was not involved in this work. However, she notes that the ribosome is ubiquitous in the cell and is already well characterized, making it easy to recognize and study. Trying to image lesser-known or rare cellular structures remains an incredibly difficult task, she adds.

Powerful combinations

Cryo-ET is a fast-growing field, but the technique still has a number of limitations. Resolution remains an issue. Although the level of detail has improved drastically in recent years, cryo-ET is unable to attain the atomic-level resolution of cryo-EM. "Cryo-ET is where cryo-EM was in the early 90s, long before it was able to achieve atomic resolution," says Hong Zhou, a biophysicist at the University of California, Los Angeles.

At the current level of performance, it is difficult to correctly identify molecules in a cell using cryo-ET, according to Zhou. So, unless scientists are looking at structures that have previously been well characterized, such as the ribosome, their hypotheses about what they see with the technique

might prove to be incorrect, he adds. “The odds are against you. It’s very easy to make mistakes.”



Whole cells sliced very thinly and imaged with super-resolution microscopy. Credit: Janelia Research Campus HHMI

To circumvent the issue of resolution, Zhou has chosen to try to push the limits of conventional cryo-EM instead. His team recently reported a method called cryoID⁹, which melds cryo-EM with various other techniques. One of these involves breaking open cells in a method that enables proteins to partially remain inside the original cellular milieu; in this way, researchers can view proteins in a near-native state. Despite his current focus on cryo-EM, Zhou says that cryo-ET is the future. “I consider [this method] an intermediate step towards that goal.”

Another limitation of cryo-ET is its narrow sampling. “The best-kept secret of tomography is that when you look at a mammalian cell, a tomograph is less than 0.1% of that cell,” Villa says. This means that large organelles such as the nucleus can be viewed only in tiny segments. To fill this gap, scientists such as Harald Hess, a biophysicist at the Howard Hughes Medical Institute’s Janelia Research Campus in Ashburn, Virginia, are using techniques other than cryo-ET, namely super-resolution fluorescence microscopy and electron microscopy, to visualize entire cells. Using these

methods, Hess and his colleagues are gaining a fresh view into how various cellular components interact¹⁰. In a study published earlier this month, the researchers demonstrated that by using machine learning — a form of artificial intelligence — to help identify these components in many samples, they could map the organization of up to 35 types of organelle¹¹.

Other researchers are combining cryo-ET with another technique called X-ray tomography that can capture images of whole cells. This allows scientists to examine the structure of larger components, such as mitochondria or nuclei, and then zoom in on specific areas of interest.

However, bringing these methods together requires both money and skill. On top of that, both techniques bombard samples with damaging radiation. That makes it a challenge to transfer a sample between them, says Eva Pereiro, a beamline scientist at the ALBA synchrotron facility in Barcelona, Spain, that produces X-rays suitable for tomography.

Some labs have already accomplished this feat. Maria Harkiolaki, principal beam-line scientist at the Diamond Light Source, a synchrotron facility in Didcot, UK, and her colleagues recently published¹² a model of the mechanics of SARS-CoV-2 infection that uses cryo-ET and X-ray tomography to elucidate the process. They captured events at both the level of the cell and individual molecules, and proposed an idea for how the virus replicates in primate cells.

Baumeister thinks that, like cryo-EM, cryo-ET will eventually allow scientists to view biological molecules in atomic detail. Until then, scientists continue to eagerly investigate what insights into the cell might be revealed by cryo-ET and other similar methods. Because these tools can reveal structures that have never been seen before, researchers are often left with new mysteries to solve. “What I love about tomography”, Villa says, “is that we always generate more questions than answers.”

Nature **598**, 558-560 (2021)

doi: <https://doi.org/10.1038/d41586-021-02904-w>

References

1. 1.
Medalia, O. *et al.* *Science* **298**, 1209–1213 (2002).
2. 2.
Murphy, G. E., Leadbetter, J. R. & Jensen, G. J. *Nature* **442**, 1062–1064 (2006).
3. 3.
Mahamid, J. *et al.* *Science* **351**, 969–972 (2016).
4. 4.
Watanabe, R. *et al.* *Cell* **182**, 1508–1518 (2020).
5. 5.
Deniston, C. K. *et al.* *Nature* **588**, 344–349 (2020).
6. 6.
Bäuerlein, F. J. B. *et al.* *Cell* **171**, 179–187 (2017).
7. 7.
Guo, Q. *et al.* *Cell* **172**, 696–705 (2018).
8. 8.
Tegunov, D., Xue, L., Dienemann, C., Cramer, P. & Mahamid, J. *Nature Methods* **18**, 186–193 (2021).
9. 9.
Ho, C.-M. *et al.* *Nature Methods* **17**, 79–85 (2020).

10. 10.

Hoffman, D. P. *et al.* *Science* **367**, eaaz5357 (2020).

11. 11.

Heinrich, L. *et al.* *Nature* <https://doi.org/10.1038/s41586-021-03977-3> (2021).

12. 12.

Mendonça, L. *et al.* *Nature Commun.* **12**, 4629 (2021).

This article was downloaded by **calibre** from <https://www.nature.com/articles/d41586-021-02904-w>

| [Section menu](#) | [Main menu](#) |

Books & Arts

- **Inside the lawsuit that ended US gene patenting** [25 October 2021]
Book Review • How a win in the Supreme Court challenged a linchpin of the genetic-testing industry.
- **Climate lessons from COVID, and the end of paperwork: Books in brief** [15 October 2021]
Book Review • Andrew Robinson reviews five of the week's best science picks.

- BOOK REVIEW
- 25 October 2021

Inside the lawsuit that ended US gene patenting

How a win in the Supreme Court challenged a linchpin of the genetic-testing industry.

- [Heidi Ledford](#)



Protesters outside the US Supreme Court in 2013 as arguments were heard on gene patenting. Credit: Tom Williams/CQ Roll Call

The Genome Defense: Inside the Epic Legal Battle to Determine Who Owns Your DNA Jorge L. Contreras Algonquin (2021)

Not so long ago, if you asked someone about the US Patent and Trademark Office's practice of granting patents on human genes, you'd probably get one of two responses. Biotechnology insiders would shrug — such patents had been standard practice for decades. They were considered a lynchpin of the burgeoning genetic-testing industry. Those less intimate with the inner workings of biotech often had a different reaction: "But that's just ... wrong," said lawyer Chris Hansen. "Who can we sue?"

In 2009, Hansen, a veteran of civil-rights cases at the American Civil Liberties Union (ACLU) in New York City, embarked on a lawsuit that ended gene patenting in the United States. The effort seemed doomed, yet Hansen went on to win at the US Supreme Court, challenging the very idea of what patents are and what they should do.

The unexpected twists and turns of that case — as well as its impact on medicine, and particularly on the lives of women affected by breast and ovarian cancer — are ably and affectingly detailed in *The Genome Defense*. Its author, patent scholar Jorge Contreras, has been a vocal critic of over-reaching patents and the universities that grant exclusive licences to their intellectual property, particularly when they nurture monopolies and sign over responsible stewardship of their patents to the licensee ([J. L. Contreras and J. S. Sherkow *Science* 355, 698-700; 2017](#)).



[Use the patent system to regulate gene editing](#)

That spirit is evident in the book. But readers should note that Contreras is now employed by the University of Utah in Salt Lake City, which historically generated some of the patents that Hansen ultimately decided to challenge. (Contreras took the Utah job after he started the book; he argues that its themes go beyond one set of patents to depict the tensions between the law and the pace of technology.)

Those patents claimed rights to the sequencing of two genes, *BRCA1* and *BRCA2*. Some variations in these are associated with breast and ovarian cancer. The University of Utah licensed some of the relevant patents exclusively to Myriad Genetics in the 1990s. The Salt Lake City company used its intellectual property to create a monopoly on certain tests for cancer risk, and threatened potential competitors with legal action. At the time, the tests cost thousands of dollars and, thanks in no small part to the vagaries of the US health-care system, were not always available to the people who needed them.

Personal stories

The consequences of that lack of access could be devastating. Contreras pulls no punches in detailing the stories of women who were unable to get tested, only to find later that they had a life-threatening cancer that could have been prevented.

But by the 2000s, gene patents were common. In 2005, one team estimated that 20% of the human genome had been patented ([K. Jensen and F. Murray, *Science* 310, 239–240; 2005](#)). Although products of nature are not patentable under US law, some lawyers argued that isolating a gene from its surrounding chromosome fundamentally alters the DNA and therefore constitutes an invention. Another, more utilitarian, defence held that gene patents were necessary to nurture health-care innovation.

There is a reason that few thrillers have been based on patent law. Patents are difficult to digest — sometimes by design. The more ambiguous they are, the more flexibility a patent holder might have to claim that their intellectual property encompasses someone else's invention. “The first part of a patent reads like a scientific paper written by a lawyer, and the last part

reads like a legal document written by a scientist,” writes Contreras. “In both cases, you get the worst of both worlds.”



Racism is baked into patent systems

Thankfully, Contreras spares us the details, pulling out only nuggets that are needed to understand the case. He explains the science and legal arguments clearly and succinctly. (He does a better job of this than did some of the lawyers and justices involved, who trotted out painful analogies throughout the four-year process: genes were likened variously to chocolate-chip cookies, baseball bats and kidneys.)

For me, the most interesting parts of the book were its tangents. The Myriad story highlights the convoluted incentives in the genetic-testing industry that sometimes work against patients’ best interests. I longed to learn more about how the Supreme Court’s decision — as well as other recent decisions from the court on what can and can’t be patented — had affected the industry. The book also lacks any international context for gene patents, which are alive and well in Europe. A 2017 survey of European genetic-testing laboratories found that 14% of non-profit respondents had refrained from offering a genetic test because of patent concerns ([J. Liddicoat et al. Eur. J. Hum. Genet. 27, 997–1007; 2019](#)).

But Contreras succeeds in his main mission: to detail the narrative history of a landmark patent case. The personal stories of key players are rich with detail. We learn about Tania Simoncelli, who, as an ACLU intern with a passion for science and social-justice issues, first brought gene patents to the attention of Hansen. And we encounter Herman Yue, who, at the time that the case was launched, was an intern for a federal district judge, and who just happened to have a doctorate in molecular biology. Yue was pivotal in crafting a surprise early court decision in favour of the ACLU.

Readers are also treated to the inside story of the schism in the US government, with some agencies, most notably the patent office, in favour of gene patents, and the National Institutes of Health, among others, against them. It fell to acting solicitor general Neal Katyal to walk a tightrope between arguing parties, eventually developing a federal government stance: namely, whole-gene sequences as they are found in genomes should not be patentable, but the assembled protein-coding regions of a gene — minus intervening bits of non-coding DNA often scattered throughout — should. The compromise satisfied no one completely.

By 2013, when the Supreme Court issued its unanimous decision in favour of the ACLU, gene patents and Myriad-style testing of single genes were already falling out of fashion. Medical diagnostics had moved on to multi-gene testing, and now, increasingly, the emphasis is on whole-genome sequencing. But this story stands as a guide to the forces that shape an increasingly important industry — and to the vexed influence of patents.

Nature **598**, 561-562 (2021)

doi: <https://doi.org/10.1038/d41586-021-02905-9>

This article was downloaded by **calibre** from <https://www.nature.com/articles/d41586-021-02905-9>

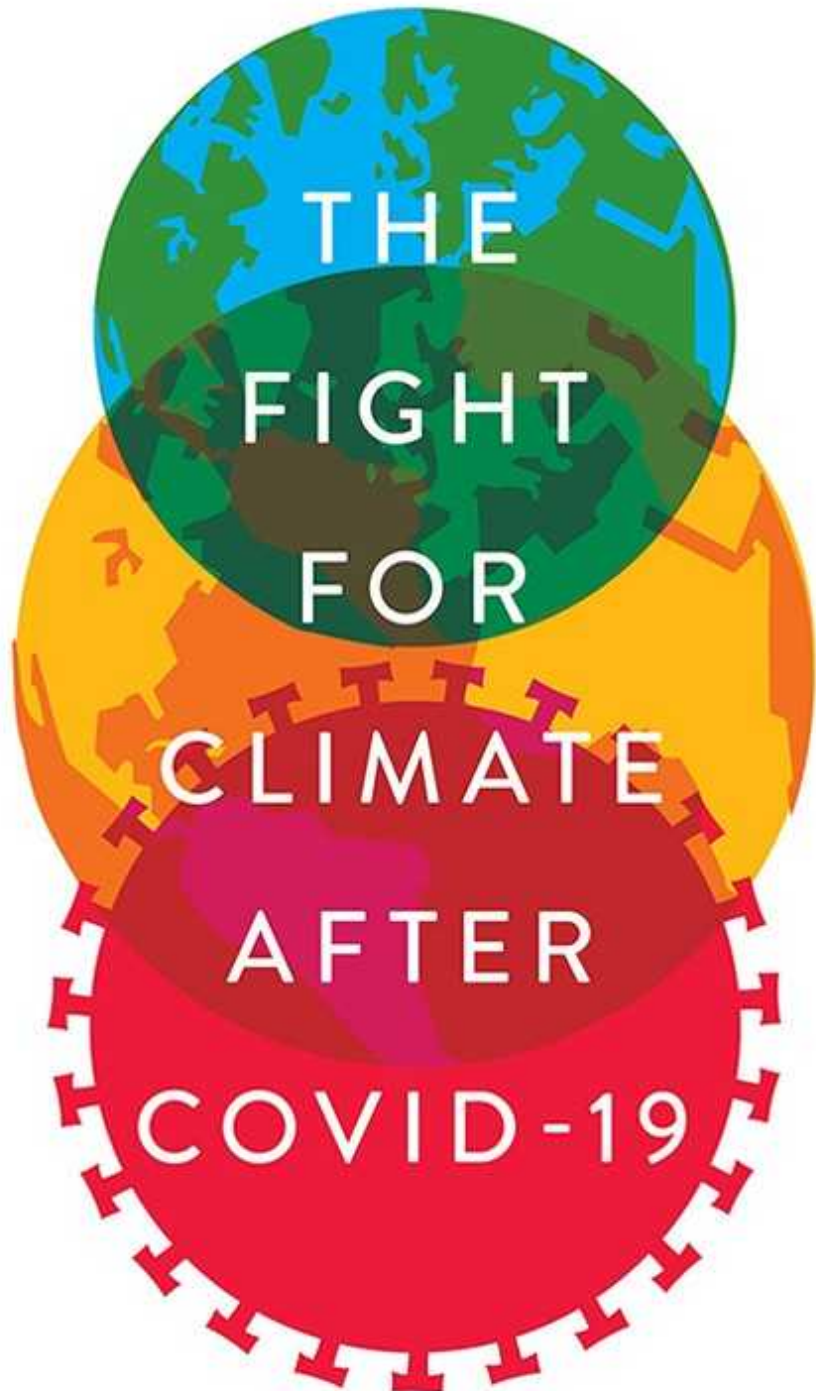
- BOOK REVIEW
- 15 October 2021

Climate lessons from COVID, and the end of paperwork: Books in brief

Andrew Robinson reviews five of the week's best science picks.

- [Andrew Robinson](#) 0

ALICE C. HILL



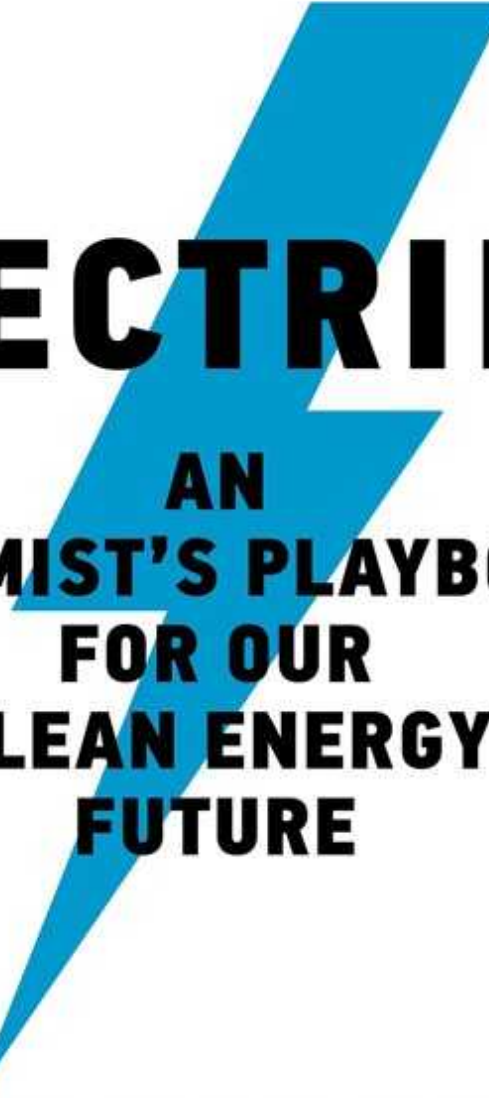
The Fight for Climate after COVID-19

Alice C. Hill *Oxford Univ. Press* (2021)

“No vaccine exists to solve climate change,” writes Alice Hill, a former judge and US government adviser responsible for planning for catastrophic risks, including global warming and biological threats. Nevertheless, she proposes in this formidable analysis, governments trying to mitigate and adapt to global warming can learn from the pandemic. How so? Hill draws out lessons with regard to the importance of early action, cross-border planning and emergency preparation.

"Required reading for an economy-wide
green transition in the USA."

MARIANA MAZZUCATO, AUTHOR OF *MISSION ECONOMY*



ELECTRIFY

AN
OPTIMIST'S PLAYBOOK
FOR OUR
CLEAN ENERGY
FUTURE

SAUL GRIFFITH

Electrify

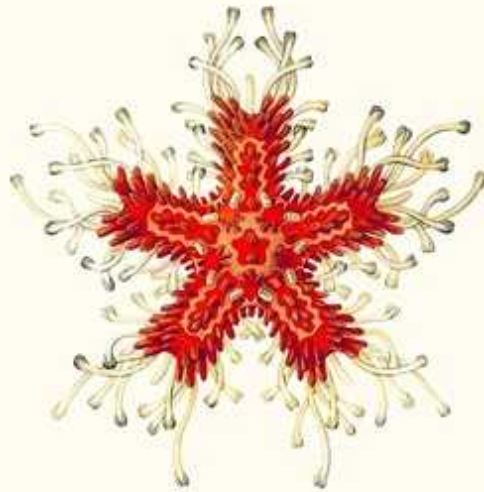
Saul Griffith *MIT Press* (2021)

Engineer, inventor and entrepreneur Saul Griffith calls for all-encompassing electrification in the United States, using renewables to mitigate climate change. He likens it to industrial mobilization during the Second World War, and rewrites Winston Churchill's stirring speech: "We shall fight with our homes, we shall fight with our vehicles, we shall fight with our grid." Based on his earlier analysis of the energy economy, written under government contract, the book demands attention. But how will the required batteries be recycled?

'Who will enjoy reading this book? – Everybody!'
JARED DIAMOND

A (VERY) SHORT HISTORY OF LIFE ON EARTH

4.6 Billion Years
in 12 Chapters



HENRY GEE

A (Very) Short History of Life on Earth

Henry Gee *Picador* (2021)

“Perhaps the most amazing thing about life — apart from its existence — is how quickly it began,” writes Henry Gee, *Nature*’s senior editor specializing in palaeontology. Life appeared in the ocean depths just 100 million years after Earth’s formation, and reached the sunlit surface after another 800 million. His lively, lyrical history covers 4.6 billion years, from bacteria through dinosaurs to mammals including *Homo sapiens*. Humans, Gee says, will eventually become a thin layer in sedimentary rock, to be eroded as dust that sinks to the ocean bottom.

'A brilliant beast of a book.'
DAVID BYRNE

ff

Being You

ANIL SETH

THE
SUNDAY TIMES
BESTSELLER

A New Science of Consciousness

'Insightful and profound. The nature of consciousness is still one of the hardest problems in science, but Seth brings us closer to the answer. This is a hugely important book.'

JIM AL-KHALILI

Being You

Anil Seth *Faber* (2021)

Neuroscientist Anil Seth dates his fascination with consciousness to a childhood jolt while looking in a mirror: the realization that the experience of “being me” would vanish when his physical body ceased to exist. Drawing on philosophy, biology, cognitive science, neuroscience and artificial intelligence, he argues that our brains are prediction machines that constantly invent our world and then correct our mistakes, so that our sense of self derives from our body. He admits: “perhaps it’s not so bad if a little mystery remains” at death.

CASS R. SUNSTEIN

COAUTHOR OF THE NEW YORK TIMES BEST SELLER *NUDGE*

Sludge

What Stops Us
from Getting Things Done
and What to Do about It

Sludge

Cass R. Sunstein *MIT Press* (2021)

In 2016, Americans spent 11.4 billion hours on federal paperwork — much of it unnecessary ‘sludge’. Valued at the average US wage of US\$27 per hour, this equates to 6 times the Department of State’s budget, notes legal scholar Cass Sunstein. Former administrator of a White House office created by the 1980 Paperwork Reduction Act, Sunstein confesses to making little progress. His utterly realistic, surprisingly readable book — partly inspired by the US “war on sludge” during the pandemic — aims to make up for this.

Nature **598**, 562 (2021)

doi: <https://doi.org/10.1038/d41586-021-02833-8>

This article was downloaded by **calibre** from <https://www.nature.com/articles/d41586-021-02833-8>

| [Section menu](#) | [Main menu](#) |

Opinion

- **[Predatory publishers' latest scam: bootlegged and rebranded papers](#)** [26 October 2021]
Comment • To thwart publishing rackets that undermine scholars and scholarly publishing, legitimate journals should show their workings.
- **[COP26: set a minimum global carbon price for emissions](#)**
[26 October 2021]
Correspondence •
- **[Brazil's scientists face 90% budget cut](#)** [25 October 2021]
Correspondence •
- **[Air quality: WHO guidelines could deepen inequities](#)** [26 October 2021]
Correspondence •
- **[Thousands of new and improved mineral symbols](#)** [26 October 2021]
Correspondence •

- COMMENT
- 26 October 2021

Predatory publishers' latest scam: bootlegged and rebranded papers

To thwart publishing rackets that undermine scholars and scholarly publishing, legitimate journals should show their workings.

- [Kyle Siler](#) ⁰,
- [Philippe Vincent-Lamarre](#) ¹,
- [Cassidy R. Sugimoto](#) ² &
- [Vincent Larivière](#) ³

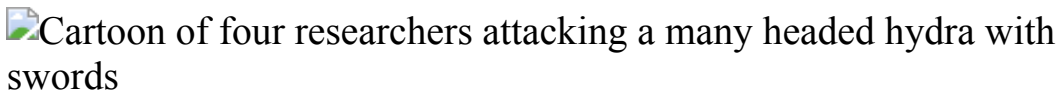


Illustration by David Parkins

In 2018, the US Federal Trade Commission (FTC) won a [US\\$50-million ruling against the publisher OMICS](#) for deceptive business practices. The FTC's investigation found that OMICS accepted and published nearly 69,000 articles in academic disciplines with little or no peer review. The judgement against the infamous publisher, located in Hyderabad, India, proved difficult to enforce. But the ensuing stigma still carries a penalty. In the two years after the FTC filed its complaint, the articles OMICS published under its imprint fell by 40%. After all, a publisher with no reputation is preferable to a publisher with a bad one.

Predatory publishers take publication fees without performing advertised services such as archiving, indexing or quality control. They often use outright deception, such as fake editorial boards or impact factors, to appear legitimate. Researchers might submit work to these outlets naively or

cynically; even unread or sloppy articles are rewarded by some universities' tenure, hiring and promotion decisions. Often, these unvetted articles attract little attention. However, because they sometimes get harvested by non-selective academic search engines such as Google Scholar, they could be found — and read — as part of the scientific corpus.

A year after the FTC judgement, principal scientific adviser to the Government of India Krishnaswamy VijayRaghavan lamented the difficulty of stamping out the “menace” of predatory publishers. He likened them to the Hydra, the creature of Greek myth that sprouts two heads for each one severed.

To get a better look at this many-headed monster, we constructed a database of publishers that have not been indexed in selective bibliographic databases such as Web of Science or Scopus. Currently, this database, called [Lacuna](#), indexes more than 900,000 papers across 2,300 journals from 10 publishers, a small fraction of the fringe of academic publishing. At present it includes mainly journals that falsely advertise peer review and other scholarly services. However, our long-term goal is to index publications across the legitimacy spectrum, from malicious fakes to scrappy, under-resourced start-ups. Already, our preliminary work has uncovered deceptive practices we hadn't anticipated. OMICS branding has been removed from many titles, for example. And predatory journals are re-issuing — seemingly on their own initiative without any consent — actual, peer-reviewed articles that have been published elsewhere.

Better tracking is one strand of a broader strategy to defeat this Hydra. Other strands are better education and incentives for authors submitting manuscripts, and greater transparency around how legitimate journals vet work.

Buried branding

In 2020, OMICS changed hundreds of URLs and overhauled websites and typesetting to remove references to OMICS. It also introduced a ‘Hilaris’ brand. Although the titles of the rebranded journals remained listed on the OMICS web pages, mentions of OMICS are absent on the Hilaris web

pages, as well as those for other subsidiaries. *The Journal of Surgery*, for example, continues under the new brand with the same DOI prefix, ISSN, and editor-in-chief, with no mention of OMICS.

We followed links for the 737 journals listed on the OMICS website. More than 80% (600) are labelled with other brands that are distinct corporate entities. Among the most prominent, Longdom has addresses in Spain and Belgium; Hilaris is also located in Belgium, but at a different address.

iMedPub LTD is located in the United Kingdom. The number of journals has grown faster than the number of publications, suggesting that many journals are shells with little content. Furthermore, the content in the subsidiaries is backdated (see ‘Old articles in new brands’). Although these subsidiaries were incorporated beginning in 2015 and as recently as 2020, articles dating to years before are associated only with the new titles, without any mention of OMICS. (Hilaris, iMedPub, Longdom and OMICS did not respond to our enquiries about backdating and whether this was part of a rebranding practice.)

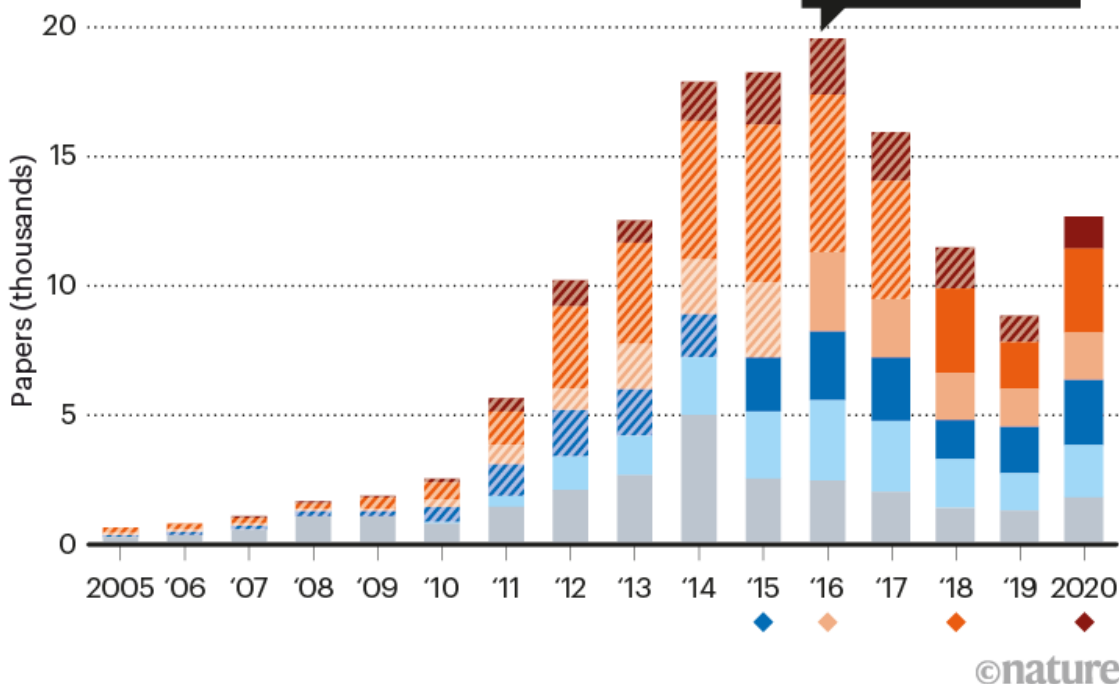
OLD ARTICLES IN NEW BRANDS

In 2018, a US federal judge ruled that the publisher OMICS (began operating in 2008) had engaged in deceptive business practices. A subsequent analysis found OMICS subsidiaries operating under different names, and some had published backdated papers.

OMICS subsidiaries:

- Hilaris ■ Longdom Group ■ Research & Reviews
- iMedPub ■ OMICS Publishing Group ■ Others
- ◆ Date launched or acquired
- ▨ Articles rebranded to before launch or acquisition

US Federal Trade Commission files complaints against OMICS



Source: K. Siller *et al.*

We think OMICS is retconning the publishing histories of many of its journals. Here's an example: *Advances in Pharmacoepidemiology & Drug Safety* published its first issue in 2012 under the OMICS imprint, then removed the OMICS logo in 2015 and appeared as a standalone journal until it was rebranded as a Longdom imprint in 2019. At its inception, Robert H. Howland from the University of Pittsburgh in Pennsylvania and Richard L. Slaughter from Wayne State University in Detroit, Michigan, were listed as editors-in-chief. Howland told the FTC in 2016 that he'd been listed as

©nature

editor without his consent or knowledge. Under Longdom, only Slaughter is listed as editor-in-chief. He died in 2016.

Bootlegged articles

One tactic predatory journals have used is to mimic longstanding legitimate journals online (or sometimes to acquire the titles). Predators rely on the journal's reputation to collect fees¹ without providing scholarly services. In August, scholar Anna Abalkina at the Free University of Berlin reported that a list of COVID-19 publications maintained by the World Health Organization [contained hundreds of papers from three such journals](#), many entirely out of scope. (A journal supposedly about linguistics had papers on COVID-19, nutrition and gestational anaemia).

Indexing for our Lacuna database uncovered another alarming practice: re-publishing bootlegged copies of papers from legitimate sources, under new DOIs, without crediting the original journal, and sometimes not the original author. A researcher perusing what seem to be ‘back issues’ sees real peer-reviewed articles copied from legitimate journals.

Several anomalies led us to discover that at least nine papers in the *Journal of Bone Research and Reports*, under the iMEDPub LTD brand, were directly lifted from the Elsevier journal *Bone Reports*. (We reported this to *Bone Reports*; an Elsevier representative says the matter is now under investigation.) The first clue was the bizarre names of some authors, such as “urban center” and “parliamentarian”. Many author names appeared with an extra character (for example, “John Smitha” and “Mary Jonesb”) — indicating that they were copied from a document containing superscripts.



Predatory journals: no definition, no defence

Some publishing institutions were nonsensical, including “university of canadian province” and “urban center university”. Author affiliations were listed in absurd ways: New Orleans was renamed “point of entry” and North Carolina was dubbed “old North State”. Some authors’ e-mail addresses were those of non-authors. (When we contacted authors of the *Bone Reports* articles, none was aware that their articles had been bootlegged; they responded with a mixture of anger, amusement and bafflement.)

Titles of *Bone Reports* papers were modified by the use of synonyms: for example, “A novel application of the ultrasonic method” became “a completely unique application of the unhearable [sic] technique.” (This particular article was republished in at least two OMICS journals.) Some articles were fully plagiarized from the Elsevier source, with the only difference being redacted sentences. In other cases, words in the Elsevier article were replaced with synonyms, perhaps to create the illusion of originality and evade plagiarism detection. Swaps included “knowledge” for “data” and “intellectual issues” for “cognitive disorders”. More convoluted replacements included incorrectly interpreted acronyms: for example, the common word “an” became “Associate in Nursing”, and “sd” was written as “Mount Rushmore State” (a nickname for the US state of South Dakota) instead of “standard deviation”. Other scholars have identified similar ‘tortured phrases’ in different journals².

To generate these differences, we hypothesize that OMICS used some sort of rudimentary synonym-generating software, or perhaps the works were translated from English to another language and then back to English. Other ‘papers’ were filled with text from unknown sources, perhaps translated from papers in languages other than English. OMICS backdated their mangled copies, creating the illusion that they pre-dated the original, legitimate Elsevier publications.

Market deception

Why go to all this trouble? One possibility is that OMICS is seeding fledgling journals to attract paying customers. Also, OMICS has footnotes in some plagiarized articles claiming that work was presented at predatory conferences, falsely suggesting that these are vibrant, professional events. (The FTC judgement found that such conferences are a significant source of revenue for the company.)

There is evidence that this practice is not limited to OMICS. A team at scholarly-services firm Cabells International compiles lists of predatory publishers and has also identified bootlegging in a hijacked journal (that is, an illegitimate ‘clone’ of a legitimate journal). The fake journal website appeared above its genuine counterpart in web searches, and an article it contained showed page numbers from the original publication, a bright white rectangle where the original journal’s name had been obscured, and even someone’s finger holding a paper being photographed. Other scholars have also found evidence of ‘cloning’ and ‘recycling’ to produce a ‘fictitious archive’ for journals collecting publishing fees³. Our work putting together the Lacuna database should help to identify and track these sorts of practices.

Adaptable foe

Predatory publishing has flourished as more reputable journals charge authors publication fees and scholars remain under intense pressure to publish. OMICS is just the tip of the iceberg of a swiftly evolving fraudulent business model. Following the ruling against OMICS, economist Derek

Pyne at Thompson Rivers University in Kamloops, Canada, remarked that there were hundreds of smaller illegitimate publishers. “Too many … for the FTC to go after.”

Vice-chairman of the India University Grants Commission Bhushan Patwardhan cautioned that predatory publishers are a “determined and adaptable foe”. If a publisher gains notoriety, creating new websites under other brands is cheap, easy, and profitable. The low marginal costs of online publishing allow scam journals to operate from anywhere, particularly where their business practices can operate with impunity. To fight them, it is essential to know how they attract researchers and avoid detection.

By one estimate, respected indexes such as Web of Science cover only about one-third of scholarly publications. Tens of thousands of non-English-language journals are excluded, as are titles that do not meet citation thresholds. And the presence or absence of a journal in those databases is not enough to distinguish between fake or legitimate publishers.

The Lacuna database aims to tabulate published work omitted from major indexing systems: this will enable exploration of shades of legitimacy across scholarly communication and reveal diverse publishing venues, as well as illegitimate, niche and emergent journals.

Though it can be convenient to talk about predatory and legitimate journals, these are not binary classifications. There are different types and degrees of questionable publishing practices⁴. Capturing data for journals that lack indexing and metadata will enable further analysis by librarians, researchers, administrators and policymakers. That will enable understanding of non-indexed publishers of various shades of legitimacy to underpin scientometric insights and inform policies.

Starve the Hydra

Instead of repeatedly severing heads for new ones to regrow, policy that combats predatory publishing should focus on starving the Hydra of resources. Here’s what we recommend.

Audit peer reviews. To determine whether a journal is predatory, evaluators rely on many ‘indirect’ clues, such as dead links on websites, poor English grammar, or lack of listings in institutions such as the Committee on Publishing Ethics (COPE) or the Directory of Open Access Journals (DOAJ). But it is the content of peer review that shows how seriously journals vet submissions. If journals are unwilling to publish their peer reviews, these should be subject to audit by funders.



Do authors comply when funders enforce open access to research?

Falsifying peer review on a large scale would be very difficult for egregious predatory journals. Quasi-predatory journals would reveal poor-quality or ignored reviews. High-status journals coasting on reputation might also be exposed. Even with greater transparency, demarcating legitimate and illegitimate journals will be contentious. However, that demarcation should be based on the most relevant information, not on indirect clues and status signals.

Mandating some form of open peer review dovetails with other initiatives to improve science by sharing data. Breaking open the ‘black box’ would demystify the process and provide new insights⁵. Sharing blinded peer reviews online — or at least confidentially with stakeholders — would allow funders, researchers, librarians and institutions to identify scams and encourage good practices in legitimate journals.

Link quality assurance to funding. Modern universities have systems to vet vendors. They could expand those systems to include payments to journals (both subscription-based and those with article-processing charges). Requirements could include open peer review, as well as adherence to the [Fair Open Access Principles](#), which stipulate explanations of how publishing fees are spent. Mandates from funders have already spurred changes in scholarly publishing, such as those around open access driven by requirements of the US National Institutes of Health, the Bill and Melinda Gates Foundation and the Wellcome.

Instead of relying on third-party lists of acceptable and unacceptable journals (such as Beall's or Cabells' lists, which can stigmatize well-meaning but resource-limited publishers), funders could mandate that publishing fees can only be paid to journals that adhere to transparency rules.

This would require journals to change practices, but digitization means that publishers can collect and archive peer-review data more readily than before. Scientific funders and taxpayers deserve accountability for the billions of dollars invested annually in scholarly publishing. Scholars deciding where to submit work deserve greater transparency about peer review (for example, content, rejection rates and average time to decision). This transparency will both starve the Hydra and improve standards for all journals.

Support good-faith emergent journals. Several platforms — such as the Public Knowledge Project's Open Journal Systems — allow dissemination of journals at a modest cost. SciELO (in Brazil) and Redalyc (in Mexico) are examples of academic-publishing infrastructures that provide quality, low-cost open-access journals for scholars and issues in their native languages. Our preliminary analyses found that academics in Latin America were much less likely to publish in OMICS journals than were those in Central Asia, the Middle East and Africa. New criteria for legitimacy can prevent well-intentioned, emergent journals from being misclassified. Institutionalizing paths to legitimacy for new publishers would lower barriers to entry for disadvantaged scholars and institutions.

Don't reward papers in predatory journals. Many universities and funders unintentionally feed predatory publishers when they put value on

quantity and use ill-informed metrics to gauge quality. Authors who publish in questionable journals span the continuum between well-meaning and naive, to dishonest and complicit⁶. Informing researchers — especially early-career researchers — of the dangers is essential; so is revising policies so that researchers are not tempted to buy ‘easy’ publications.

However, our hope is to move beyond this, by destroying the monster with systemic changes to the scholarly publishing system, rather than placing extra monitoring burdens on individual scholars. If funders and institutions reward transparent quality journals, predatory journals will starve.

Nature **598**, 563–565 (2021)

doi: <https://doi.org/10.1038/d41586-021-02906-8>

References

1. 1.

Moussa, S. *Learn. Publ.* **34**, 688–695 (2021).

2. 2.

Cabanac, G., Labb  , C. & Magazinov, A. Preprint at <https://arxiv.org/abs/2107.06751> (2021).

3. 3.

Abalkina, A. *Scientometrics* **126**, 7123–7148 (2021).

4. 4.

Siler, K. *J. Assoc. Inf Sci. Technol.* **71**, 1386–1401 (2020).

5. 5.

Rennie, D. *Nature* **535**, 31–33 (2016).

6. 6.

Kurt, S. *Learn. Publ.* **31**, 141–147 (2018).

This article was downloaded by **calibre** from <https://www.nature.com/articles/d41586-021-02906-8>

| [Section menu](#) | [Main menu](#) |

- CORRESPONDENCE
- 26 October 2021

COP26: set a minimum global carbon price for emissions

- [Stefano Carattini](#) 0

It would be an unexpected bonus if a ‘floor’ could be set for the price of carbon emissions at the 26th Conference of the Parties (COP26) to the United Nations climate convention, which starts later this month.

Access options

Subscribe to Journal

Get full journal access for 1 year

\$199.00

only \$3.90 per issue

[Subscribe](#)

All prices are NET prices.

VAT will be added later in the checkout.

Tax calculation will be finalised during checkout.

Rent or Buy article

Get time limited or full article access on ReadCube.

from \$8.99

[Rent or Buy](#)

All prices are NET prices.

Additional access options:

- [Log in](#)
- [Learn about institutional subscriptions](#)

Nature **598**, 566 (2021)

doi: <https://doi.org/10.1038/d41586-021-02881-0>

This article was downloaded by **calibre** from <https://www.nature.com/articles/d41586-021-02881-0>

| [Section menu](#) | [Main menu](#) |

- CORRESPONDENCE
- 25 October 2021

Brazil's scientists face 90% budget cut

- [Alicia J. Kowaltowski](#) 0

A proposal to shrink Brazil's federal science budget by more than 90% has now been approved by our president. The immediate future of all ongoing projects, including thousands of research grants, as well as student and researcher fellowships, is uncertain. This in a nation battling crises in energy, public health, climate, water, biodiversity and more.

Access options

Subscribe to Journal

Get full journal access for 1 year

\$199.00

only \$3.90 per issue

[Subscribe](#)

All prices are NET prices.

VAT will be added later in the checkout.

Tax calculation will be finalised during checkout.

Rent or Buy article

Get time limited or full article access on ReadCube.

from \$8.99

Rent or Buy

All prices are NET prices.

Additional access options:

- [Log in](#)
- [Learn about institutional subscriptions](#)

Nature **598**, 566 (2021)

doi: <https://doi.org/10.1038/d41586-021-02882-z>

This article was downloaded by **calibre** from <https://www.nature.com/articles/d41586-021-02882-z>

| [Section menu](#) | [Main menu](#) |

- CORRESPONDENCE
- 26 October 2021

Air quality: WHO guidelines could deepen inequities

- [Forrest Lacey](#)⁰,
- [Rajesh Kumar](#)¹,
- [Gabriele Pfister](#)²,
- [Jean-Francois Lamarque](#)³,
- [Cassandra O'Lenick](#)⁴ &
- [Guy Brasseur](#)⁵

To curb the effects of anthropogenic air pollution on health, the World Health Organization (WHO) has halved its recommended limit for the annual average concentration of fine particulate matter ($PM_{2.5}$) to 5 micrograms per cubic metre. Given that 99% of the world's population is living in areas where such small particulates exceed the WHO's latest threshold, the contribution from natural sources of $PM_{2.5}$ — suspended atmospheric dust, for example — needs to be determined to help countries meet the guidelines.

Access options

Subscribe to Journal

Get full journal access for 1 year

\$199.00

only \$3.90 per issue

Subscribe

All prices are NET prices.
VAT will be added later in the checkout.
Tax calculation will be finalised during checkout.

Rent or Buy article

Get time limited or full article access on ReadCube.

from \$8.99

Rent or Buy

All prices are NET prices.

Additional access options:

- [Log in](#)
- [Learn about institutional subscriptions](#)

Nature **598**, 566 (2021)

doi: <https://doi.org/10.1038/d41586-021-02883-y>

This article was downloaded by **calibre** from <https://www.nature.com/articles/d41586-021-02883-y>.

- CORRESPONDENCE
- 26 October 2021

Thousands of new and improved mineral symbols

- [Laurence N. Warr](#) [ORCID: http://orcid.org/0000-0002-8779-0062](#) 0

A new list of text abbreviations for minerals includes 4,753 compounds with no previous symbol (see [L. N. Warr *Mineral. Mag.* 85, 291–320; 2021](#)). The International Mineralogical Association's Commission on New Minerals, Nomenclature and Classification (IMA-CNMNC) has approved 5,744 standardized abbreviations to cover all IMA-listed minerals. We urge publishers to adopt the system for uniformity and more effective communication.

Access options

Subscribe to Journal

Get full journal access for 1 year

\$199.00

only \$3.90 per issue

[Subscribe](#)

All prices are NET prices.

VAT will be added later in the checkout.

Tax calculation will be finalised during checkout.

Rent or Buy article

Get time limited or full article access on ReadCube.

from \$8.99

[Rent or Buy](#)

All prices are NET prices.

Additional access options:

- [Log in](#)
- [Learn about institutional subscriptions](#)

Nature **598**, 566 (2021)

doi: <https://doi.org/10.1038/d41586-021-02884-x>

This article was downloaded by **calibre** from <https://www.nature.com/articles/d41586-021-02884-x>

| [Section menu](#) | [Main menu](#) |

Work

- **[Academia's ableist mindset needs to change](#)** [25 October 2021]
Career Feature • Four junior researchers with disabilities describe their career experiences to date, and how colleagues can act as allies.
- **[Surmounting challenges with a passion for science](#)** [25 October 2021]
Where I Work • Insight is more important than vision in theoretical physics, says Sofia Qvarfort.

- CAREER FEATURE
- 25 October 2021

Academia's ableist mindset needs to change

Four junior researchers with disabilities describe their career experiences to date, and how colleagues can act as allies.

- [Kendall Powell](#) 0

[Find a new job](#)



Disabled people face many challenges in academia — and that must be corrected. Credit: Andersen Ross Photography

Last year, disabled early-career researchers were under-represented among PhD graduates in science, technology, engineering and maths (STEM) fields.

In the United States, 25% of adults live with a disability, but in 2020 those with impaired hearing or vision earned just 4% of US STEM PhDs, and those with a mobility limitation earned just 1% of STEM PhDs.

A report by the UK Royal Society in January 2021 found that 12.5% of UK STEM graduates had a disability in the 2018–19 academic year, up from 6.1% in 2007–08. This rise is attributed to increases in students reporting mental-health conditions and learning difficulties. Those with physical disabilities comprised roughly 2% of UK STEM graduate students in 2019.

In this second feature to mark National Disability Employment Awareness Month in the United States (October; a similar UK event, Disability History Month, runs from 18 November to 18 December), four disabled early-career researchers recount their own experiences with navigating ableism in academia and how they are surmounting barriers in research spaces. An earlier article focused on disabled group leaders, and how academia's ableist culture — beliefs or practices that devalue and discriminate against people with disabilities (whether physical conditions, mental-health issues, chronic illnesses or cognitive differences) — needs to change (see [*Nature* 598, 221–223; 2021](#)). These junior researchers describe how graduate-student and postdoctoral-researcher colleagues can better advocate for accessibility and inclusiveness in laboratory teams.



Sara Rivera works in the lab.Credit: Sara R. Rivera

SARA RIVERA: Don't make assumptions

Microbial ecologist and postdoctoral researcher at the University of Michigan and the National Oceanic and Atmospheric Administration in Ann Arbor.

I was treated for anxiety, depression and panic attacks after being sexually assaulted during my second undergraduate year at the University of

Michigan in Ann Arbor. I lost my short-term memory. The university's sexual-assault prevention and awareness centre wrote to my professors, explaining the situation and listing steps to help me, including postponing my exams.

I was diagnosed with post-traumatic stress disorder (PTSD) eight months after the attack and was granted some course extensions. I graduated a semester late, and started graduate school at the Scripps Institution of Oceanography in San Diego, California, in 2014, a year later than I had intended. I thought that being in a new place would help, but I left my entire support network and my family back in Michigan.



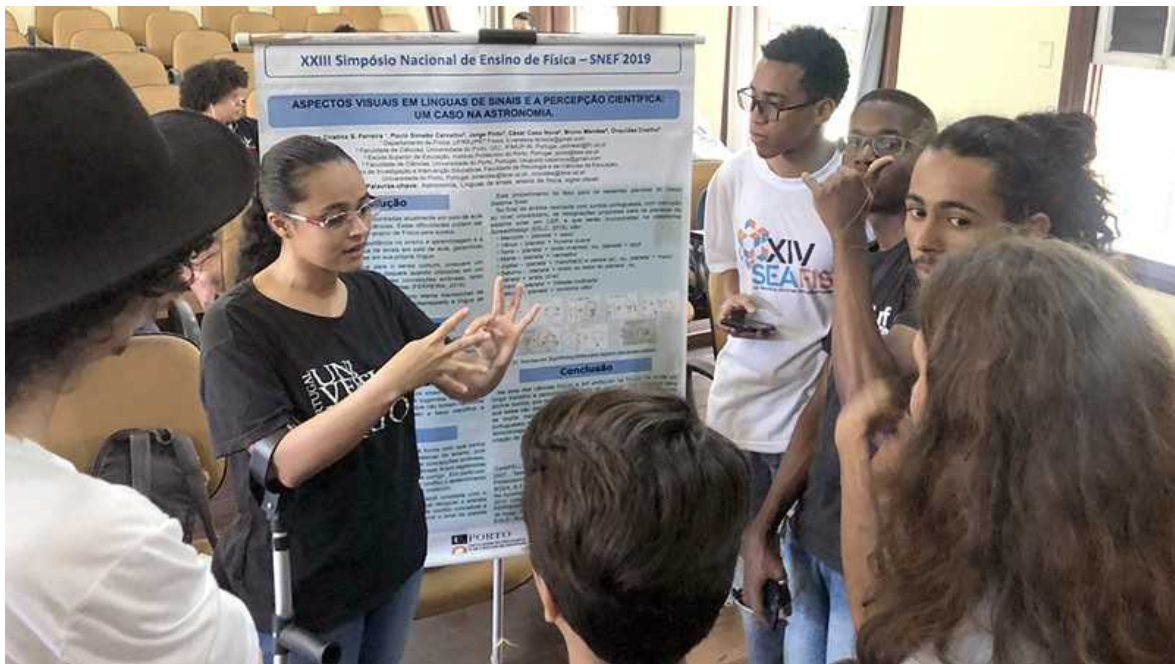
Academia's ableist culture laid bare

Three months into graduate school, I was back in crisis counselling. Graduate school was re-traumatizing in many ways. I had panic attacks going into meetings with my adviser, and I was re-diagnosed with PTSD.

I turned to my established support network at Michigan. A former professor suggested applying for a postdoc that was co-advised by someone at the US National Oceanic and Atmospheric Administration to explore federal research options. I was successful, and began working at Michigan again in 2020.

Once in my new role, I asked about the process for reporting a disability. I told my two postdoctoral advisers, “I have this disability, I have PTSD, and these are some of the accommodations I need.” This is an awkward way to start a new job — but now I work four ten-hour days each week, and I work remotely. I rely on maintaining a schedule to keep my mental health in check. It’s really different having my support network and my family locally. I am Hispanic, and family is hugely important in our culture.

My current adviser is incredibly supportive of people taking time off to deal with their health. I get called out for not scheduling a holiday. Leaves of absence should be normalized. My advice to others is: you don’t know what’s going on with other people. Don’t assume someone is being lazy or doesn’t care. And remember that when someone is struggling with their mental health, it’s hard for them to assess their own mental state. Don’t treat people like crap.



Vanessa Cristina da Silva Ferreira delivers a poster presentation on sign languages and scientific perception. Credit: Roberta Mezine

VANESSA CRISTINA DA SILVA FERREIRA: Create equity for all

Master's student in science and maths education for deaf people at the Federal Rural University of Rio de Janeiro in Seropédica, Brazil.

In 2014, on the first day of my second undergraduate semester at university, I seriously injured my ankle after a car hit me. I had to use a wheelchair for six months, and my mother had to go to classes with me. The next semester was very hard: I was learning to walk again, and I was diagnosed with attention deficit hyperactivity disorder (ADHD).

It took me six years to get my undergraduate degree in physics. I took fewer classes each semester owing to difficulties navigating a huge campus. I had amazing and supportive friends, but not all of my classmates had their attitude.

In one episode, I had a lab class on the second floor, and the elevator was never working. I had to ask friends to help me up the stairs, and then they'd go back and get my wheelchair and my bag — it was a huge operation. For our final-exam experiment, we had to split into two groups because there was not enough equipment. There would be a lottery to see which half of the class had to come back the next day. One friend asked the instructor whether I could go on that day because I had already gotten up the stairs, but another student said it would be unfair to take me out of the lottery.

My professors were all very supportive, but my university did not have an office to deal with disabilities at that time. I asked professors and administrators whether I could have rides between buildings on campus, but they said no. Instead, they suggested that I could study from home by e-mailing my professors and scheduling exams. (This was before the pandemic, so there were no remote lectures.) But I wanted to go to classes. That is my right.



How Zoom helped the neurotypical world hear my autistic voice

I spent a year in Portugal, learning Portuguese sign language and teaching science to a deaf-blind student. My experiences there were very different. The elevators were always working. I asked whether the university needed documentation of my disability, and administrators and my supervisor said, “No, if you say you have it, we trust you.”

I use one crutch for stability because my right leg is weaker than my left one, and my ankle can easily roll and make me fall. I have a lot of pain and cannot walk or sit for too long. I need to take breaks and stretch sometimes during class.

Now, there is a working group on campus to address disabled students' concerns, but they don't always hear us. When I expressed worries about being restricted to remote classes, a senior researcher dismissed my concerns, claiming her 20 years of inclusion-research experience didn't support them. I'm the one who lives with my mobility restrictions and ADHD every day. I cannot put them in a box today because I don't want to think about them. They're part of me.

On the university campus, students and faculty members just need to ask whether people need help. That can solve many problems, but if the disabled person says, “No, thank you,” then they must accept that and not be

offended. Sometimes, we need to go alone or try to do something for ourselves.

After my undergraduate graduation, some students and faculty members with disabilities formed a support and advocacy group. Together, we are in a stronger position to ask the university for better accessibility and for policy changes. In July 2021, we got the university to add accessibility rights to their policies for applying for master's studies.

When I had all these issues with using the wheelchair, I had a lot of support from the cleaners at the university. They asked whether I needed anything and were always smiling and encouraging me. During my honours-thesis presentation, I thanked these women because they were so important to my success. They are people that other people sometimes don't see — just like disabled people.

Some people think that a disability is somehow a privilege, but in reality disabled students need equity — not equality. With equality, we are not getting anywhere. But with equity, all students can access the same facilities and education. We cannot give up, even though it's hard sometimes. I won't be quiet. Disabled people are part of society, and disability is just another human characteristic.



Logan Gin explains a research concept to undergraduate students. Credit: Emma Goodwin

LOGAN GIN: Disability isn't a dirty word

PhD student in biology education at Arizona State University in Tempe studying the undergraduate STEM experiences of students with disabilities.

I have diastrophic dysplasia, a form of dwarfism, which means that I use forearm crutches to get around, and an electric scooter to travel longer

distances. Standing for long periods and reaching things can be challenging. I'm often navigating spaces that weren't built or designed for people with disabilities.

A theme throughout my academic career has been challenging myself in STEM, despite the accessibility issues I face in this arena.

As an undergraduate, I had to navigate the older, hilly campus of my university. Ramps were tacked onto the backs of buildings. I'd enter one lecture hall through a backstage entrance. What message is the university sending?

I wrestled with the challenges for disabled students who want to feel like a part of the STEM community. For biology and chemistry lab classes, all of the benches and fume hoods were made for someone of average height. The course instructors would try to set up a platform or a stool that I could stand on to reach things. But it eventually became a safety issue because I wasn't comfortable reaching for chemicals from these surfaces.

The solution came in the form of my lab partner, another student whom I met early on. We made a great team: he did all the hands-on manipulations, and I did the data collection and analysis. We matched our schedules to take all our lab courses together. He understood what I needed, and I was able to contribute.



Science diversified: Tackling an ‘ableist’ culture in research

When I tell this story, I say I feel very fortunate. But so many people might go into that first-year lab course and have a partner who doesn’t work well with them, or a lab coordinator who is not accommodating, and then they are done with STEM. That’s it.

In many ways, I was turned off by the physical aspects of doing science. I had to consider whether I wanted to continue dealing with the stress of navigating physical spaces. I did not, so I found an alternative field: education research. Now, 99% of my work is on the computer. It was a tough decision, but I made it to preserve my mental and physical health. Now, my goal is to make it easier for those who come after me to navigate those spaces.

There are many fields in science, especially computational sciences, that don’t require physical exertion. But students shouldn’t all be shepherded towards those because they have disabilities. Can we create truly accessible experiences for all students to choose whichever field they wish?

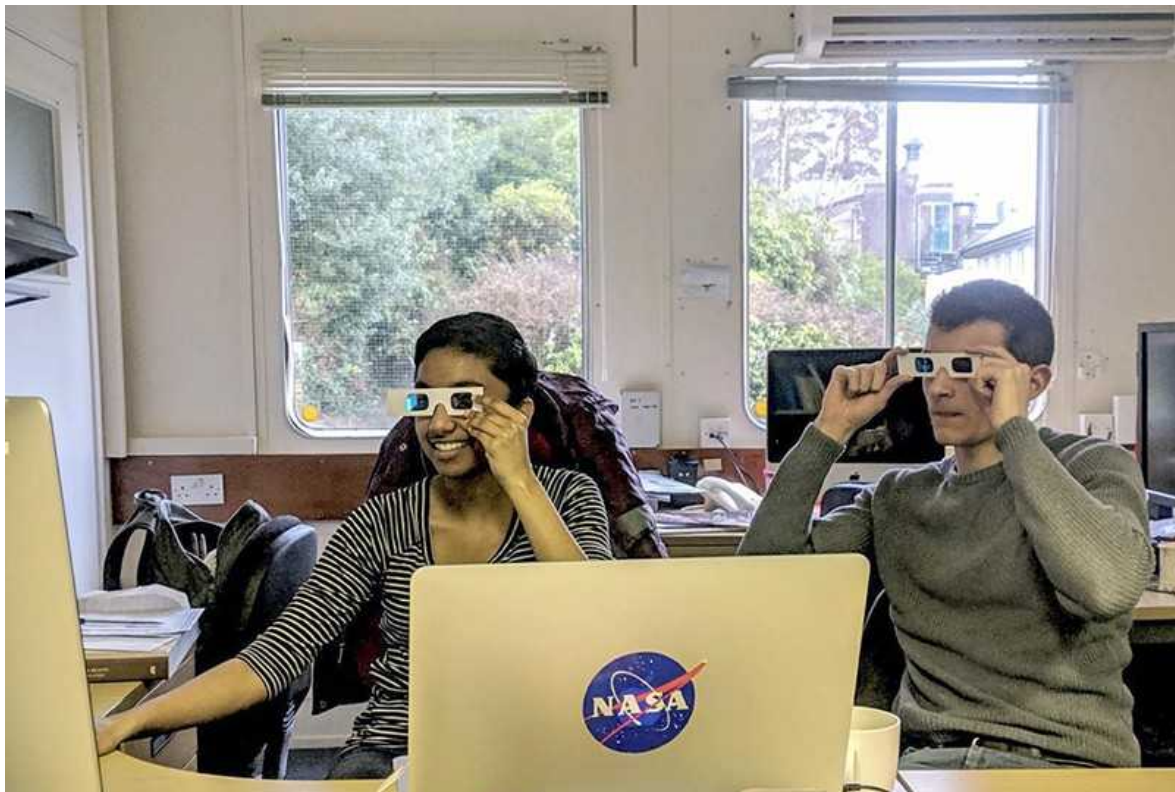
At graduate school, both my PhD adviser and I found it difficult to get the accommodations I needed in our lab group’s space — even simple things, such as a stool to reach the sink. As a graduate student registered with the disability office, I was told, “We only deal with accommodations related to coursework. That’s a human resources (HR) concern because you are an employee.” Then, HR would ping-pong me back to this disability office because I was a student.

In the end, the costs of my accommodations were shared by my advisers and my department, because they wanted me to be successful. What I needed was inexpensive, but other adaptive equipment could be pricey. If principal investigators think it has to come out of their budget, are they going to want to recruit and retain graduate students with disabilities?

The burden is often placed on students to self-advocate with their professors, mentors and the disability office — which takes time, effort and energy. Try to identify people who have your interests in mind. Find individuals who

want to go to bat for you and will challenge ableism in academia. Sometimes people cannot help, but will connect you to those who can.

Checking in about accessibility needs should be a lab-group norm, not a special circumstance. Society is finally at the point where ‘disability’ isn’t a dirty word, but we need to frequently discuss accessibility.



Divya Persaud and a graduate student colleague view 3D imagery of Mars. Credit: Alistair Francis

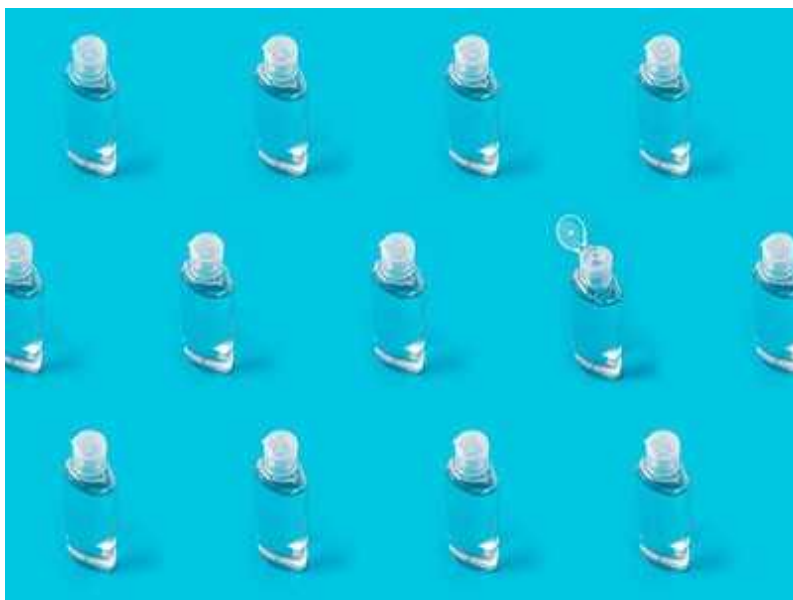
DIVYA PERSAUD: Just ask what we need

PhD student in space and climate physics at University College London, working remotely from Pasadena, California.

I developed a disabling chronic illness about halfway through my undergraduate programme, during which I took three periods of medical leave. I also took a year off before my PhD programme in space and climate physics.

Academia has a big problem with accommodating people with disabilities. Despite registering my disability with my university as an undergraduate, I still struggled to access recorded lectures and had my grades docked for not attending class. I taught myself by reading textbooks, and came in when I could.

I dealt with a lot of hostility. Some professors told me I needed to communicate better, but I didn't want to be explicit about my illness. However, I was not getting the help I needed unless I laid it all on the table. I sometimes advise people to be gruesome: it is pretty common to be dismissed if you won't fully disclose your disability, although you have a right to privacy.



[Why scientists with children who have disabilities need a different career trajectory](#)

One of my informal mentors showed me what true accommodation was. She told me to work from wherever was comfortable. She also treated me as a researcher, which allowed me to see myself as one. I chose mentors who I knew would accommodate me and respect my autonomy. If you are a woman of colour in STEM, like me, informal mentors can help you to stay sane.

My condition is in flux and unpredictable. I often have to cancel commitments at the last minute. On the outside, I look flaky. It's very humbling: I have to prioritize paying attention to my body and say I cannot attend some events in person.

But I've also learnt that people should not apologize constantly. That tells the other person (and you) that it's your fault. Making incessant apologies affects how you view yourself. Instead, I say, "Thank you for your patience," or "I can't 100% commit to this in the next week." Also, be a little assertive. Disclose private details only when it serves to get you something.

If you want to advocate for a disabled peer, just ask what they need. It will be awkward, but that's life. Don't stop asking your disabled friends to go out. Don't do things out of kindness without asking for consent. Don't ever disclose someone's disability to someone else.

And don't assume that everyone in the room is able-bodied. To break the ableism mindset, engage with the work of disabled people: watch TED talks given by disabled scientists and read their words. My go-to activists are Alice Wong, who edited the 2020 book *Disability Visibility*, and Lydia X. Z. Brown, who writes about neurodiversity.

Try to reframe your perspective about people with different needs. Walk into a lab or classroom and consider: what about this space is disabling someone? The chairs? The lack of a ramp? Who can't go on a hiking outing? Is this event, which is being presented in an old London building, excluding people?

I think about this a lot: who are we missing in our field because of disability?

Nature **598**, 693-695 (2021)

doi: <https://doi.org/10.1038/d41586-021-02907-7>

These interviews have been edited for length and clarity.

This article was downloaded by **calibre** from <https://www.nature.com/articles/d41586-021-02907-7>

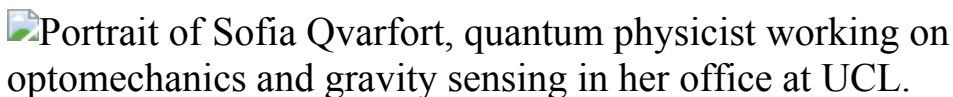
| [Section menu](#) | [Main menu](#) |

- WHERE I WORK
- 25 October 2021
- Correction [26 October 2021](#)

Surmounting challenges with a passion for science

Insight is more important than vision in theoretical physics, says Sofia Qvarfort.

- [Chris Woolston](#)⁰



Sofia Qvarfort is a Marie Skłodowska-Curie Actions Research Fellow at Stockholm University and a Wallenberg Initiative on Networks and Quantum Information Research Fellow at Nordita, Stockholm. Credit: Agnese Abrusci/*Nature*

Theoretical-physics concepts can be hard for anyone to visualize. As a person with albinism, a genetic condition that impairs vision, I face particular challenges. In this picture, taken in June at my former office at University College London, I'm sitting in front of a blackboard filled with mathematical equations describing quantum states. I had to put my face right in front of the chalkboard to make any sense of the scribbles.

I've since moved to my home country of Sweden. I'm navigating my surroundings well. In theoretical physics, thinking is more important than seeing. Experimental quantum physics would have been extremely difficult for me: I can't see the tiny equipment and electronics in quantum laboratories. People with disabilities have to be realistic. I can't do some kinds of experimental work. I can't be a pilot either.

I started [VIP@Uni](#), a website that offers tips and resources for visually impaired people in academia. Academia can be a good option for people with disabilities, because they can achieve a highly valued level of expertise that can help them to find their place in the world.

I still use blackboards, but I now spend more time looking at screens. Computers are an incredible tool for the visually impaired. I can zoom in on any word or image. The switch to virtual conferences during the pandemic was helpful to me. Before, I often had trouble seeing slides at presentations. But at a virtual conference, I can enlarge every slide on my screen.

My work looks at some fundamental questions. In 2020, I co-authored a paper showing that electrons and protons in hydrogen atoms are entangled at a quantum level ([S. Qvarfort et al. New J. Phys. 22, 093062; 2020](#)). It was a very exciting but difficult project. If you're passionate about something, you find ways around the obstacles.

Nature **598**, 698 (2021)

doi: <https://doi.org/10.1038/d41586-021-02908-6>

Updates & Corrections

- **Correction 26 October 2021:** An earlier version of this article misspelt Sofia Qvarfort's surname.

This article was downloaded by **calibre** from <https://www.nature.com/articles/d41586-021-02908-6>

Research

- **[Machine learning enables global solar-panel detection](#)** [27 October 2021]
News & Views • An inventory of the world's solar-panel installations has been produced with the help of machine learning, revealing many more than had previously been recorded. The results will inform efforts to meet global targets for solar-energy use.
- **[Opioid peptide signal in the brain makes mice hungrier for reward](#)** [13 October 2021]
News & Views • Release of opioid peptide in the brain leads food-deprived mice to eat more sugar than do mice that are well fed. This opioid signalling mechanism fine-tunes the reward value of food according to the animal's state.
- **[Bacteria recycle tumour waste to fuel immune cells](#)** [06 October 2021]
News & Views • Key nutrients that are needed by immune cells are scarce in tumours. Engineered cancer-invading bacteria can recycle tumour waste into metabolic fuel to boost anticancer immune responses in mice.
- **[A compact device sustains a fluid of bosons](#)** [27 October 2021]
News & Views • A device that generates exotic fluids of particles at equilibrium conditions and high temperatures could have applications ranging from low-loss electrical cables to memory storage.
- **[From the archive](#)** [26 October 2021]
News & Views • Nature's pages feature musings about the value of studying wetlands, and a report of the excavation of an ancient city in Sicily.
- **[Electroacupuncture activates neurons to switch off inflammation](#)** [13 October 2021]
News & Views • Neurons that express a specific molecular marker are activated by 'electroacupuncture' stimulation. They can then mediate the treatment's anti-inflammatory effects in a mouse model of the inflammatory condition sepsis.
- **[Call for a framework for reporting evidence for life beyond Earth](#)** [27 October 2021]
Perspective • A framework is proposed to start a dialogue on the criteria for assessing claims and supporting evidence for life beyond Earth.

- **A solar C/O and sub-solar metallicity in a hot Jupiter atmosphere** [27 October 2021]
Article • The C/O ratio of the transiting hot Jupiter WASP-77Ab is measured here and found to be approximately solar, though the (C+O)/H ratio is subsolar.
- **Strongly correlated excitonic insulator in atomic double layers** [27 October 2021]
Article • So far only signatures of excitonic insulators have been reported, but here direct thermodynamic evidence is provided for a strongly correlated excitonic insulating state in transition metal dichalcogenide semiconductor double layers.
- **Copper-coordinated cellulose ion conductors for solid-state batteries** [20 October 2021]
Article • By coordinating copper ions with the oxygen-containing groups of cellulose nanofibrils, the molecular spacing in the nanofibrils is increased, allowing fast transport of lithium ions and offering hopes for solid-state batteries.
- **Multicomponent alkene azidoarylation by anion-mediated dual catalysis** [13 September 2021]
Article • A streamlined synthesis of β -arylethylamines using two distinct copper catalysts is reported, and an azide anion is proposed to both react to form the product and facilitate catalyst regeneration.
- **A global inventory of photovoltaic solar energy generating units** [27 October 2021]
Article • A global inventory of utility-scale solar photovoltaic generating units, produced by combining remote sensing imagery with machine learning, has identified 68,661 facilities — an increase of over 400% on previously available asset-level data — the majority of which were sited on cropland.
- **Global potential for harvesting drinking water from air using solar energy** [27 October 2021]
Article • Mapping of the global potential of atmospheric water harvesting using solar energy shows that it could provide safely managed drinking water for a billion people worldwide based on climate suitability.
- **Indo-Pacific Walker circulation drove Pleistocene African aridification** [27 October 2021]
Article • A record of flow-speed variations from an ocean core shows that a key component of Indian Ocean circulation rapidly accelerated 2.1 million years ago, coincident with intensification of Pacific Walker circulation.
- **Spatiotemporal origin of soil water taken up by vegetation** [06 October 2021]

Article • Global inverse modelling of plant water acquisition depth and isotope-based plant water use estimates demonstrate globally prevalent use of precipitation from distant sources, and that water-stressed ecosystems are well suited to using past and remote precipitation.

- **Dairying enabled Early Bronze Age Yamnaya steppe expansions** [15 September 2021]
Article • Analysis of ancient proteins suggests that Early Bronze Age dairy and horse domestication catalysed eastern Yamnaya migrations.
- **The origins and spread of domestic horses from the Western Eurasian steppes** [20 October 2021]
Article • Analysis of 273 ancient horse genomes reveals that modern domestic horses originated in the Western Eurasian steppes, especially the lower Volga-Don region.
- **A neuroanatomical basis for electroacupuncture to drive the vagal–adrenal axis** [13 October 2021]
Article • Neuroanatomical findings demonstrate why electroacupuncture at only specific acupoints can drive the vagal–adrenal axis and treat inflammation in mice.
- **An endogenous opioid circuit determines state-dependent reward consumption** [13 October 2021]
Article • Studies in mice show that μ -opioid peptide receptor regulation of reward consumption in mice acts through a specific dorsal raphe to nucleus accumbens projection and requires enkephalin-producing neurons.
- **Leprosy in wild chimpanzees** [13 October 2021]
Article • Monitoring of western chimpanzee populations in Guinea-Bissau and Côte d'Ivoire reveals the presence of rare and different genotypes of *Mycobacterium leprae*, suggesting greater circulation in wild animals than previously thought.
- **Parallelism of intestinal secretory IgA shapes functional microbial fitness** [13 October 2021]
Article • The functional role of intestinal secretory IgA for host–microbiota interactions is investigated, showing that intestinal bacterial exposure leads to selection of diverse plasma cells that secrete antigen-specific IgA, which predominantly targets bacterial membranes.
- **Metabolic modulation of tumours with engineered bacteria for immunotherapy** [06 October 2021]
Article • Injection of engineered bacteria that convert ammonia to l-arginine into tumours enhance the anti-tumour response in a mouse model and synergize with anti-PD-L1 treatment to clear tumours.
- **The cellular environment shapes the nuclear pore complex architecture** [13 October 2021]

Article • Structure of human nuclear pore complex in its cellular environment reveals a substantially dilated central channel and shows that its nucleoplasmic and cytoplasmic rings restrict channel dimensions and create membrane asymmetry at the inner ring.

- **Structure of Venezuelan equine encephalitis virus in complex with the LDLRAD3 receptor** [13 October 2021]
Article • The structure of the Venezuelan equine encephalitis virus in complex with LDLRAD3 provides insights into the structural basis of alphavirus–receptor interactions.
- **Structure of Venezuelan equine encephalitis virus with its receptor LDLRAD3** [13 October 2021]
Article • The cryo-electron microscopy structure of domain 1 of the LDLRAD3 receptor in complex with virus-like particles of Venezuelan equine encephalitis virus (VEEV) provides insights into the assembly and entry of VEEV and other alphaviruses.
- **KDM5B promotes immune evasion by recruiting SETDB1 to silence retroelements** [20 October 2021]
Article • KDM5B recruits SETDB1 to repress endogenous retroelements such as MMVL30, suppressing anti-tumour immunity, and the depletion of KDM5B induces a robust adaptive immune response and enhances the response to immune checkpoint blockade.
- **Structures of full-length glycoprotein hormone receptor signalling complexes** [22 September 2021]
Article • Cryo-electron microscopy structures of the luteinizing hormone–choriogonadotropin receptor (LHCGR), in complex with Gs and in various states of activation, reveal a distinct mechanism of receptor activation, with implications for drug discovery.

- NEWS AND VIEWS
- 27 October 2021

Machine learning enables global solar-panel detection

An inventory of the world's solar-panel installations has been produced with the help of machine learning, revealing many more than had previously been recorded. The results will inform efforts to meet global targets for solar-energy use.

- [Lynn H. Kaack](#) [ORCID: http://orcid.org/0000-0003-3630-3102](#) 0

Many governments do not maintain a central database listing the size and locations of their country's photovoltaic systems — installations of solar cells that generate electricity. Remote-sensing approaches using machine-learning techniques have the potential to collect these data by detecting such facilities in satellite images. [Writing in *Nature*](#), Kruitwagen *et al.*¹ show how machine learning can be used to mine imagery of the entire globe to produce an inventory of commercial-, industrial- and utility-scale solar installations. The authors locate more than 68,000 such facilities, many of which were not on record.

Access options

Subscribe to Journal

Get full journal access for 1 year

\$199.00

only \$3.90 per issue

Subscribe

All prices are NET prices.
VAT will be added later in the checkout.
Tax calculation will be finalised during checkout.

Rent or Buy article

Get time limited or full article access on ReadCube.

from \$8.99

Rent or Buy

All prices are NET prices.

Additional access options:

- [Log in](#)
- [Learn about institutional subscriptions](#)

Nature **598**, 567–568 (2021)

doi: <https://doi.org/10.1038/d41586-021-02875-y>

References

1. 1.

Kruitwagen, L. *et al.* *Nature* **598**, 604–610 (2021).

2. 2.

Sunter, D. A., Castellanos, S. & Kammen, D. M. *Nature Sustain.* **2**, 71–76 (2019).

3. 3.

Barbose, B., Darghouth, N., O'Shaughnessy, E. & Forrester, S. *Tracking the Sun*, 2021 Edition (Lawrence Berkeley Natl Lab, 2021); <https://emp.lbl.gov/tracking-the-sun>

4. 4.

Malof, J. M., Bradbury, K., Collins, L. M. & Newell, R. G. *Appl. Energy* **183**, 229–240 (2016).

5. 5.

Yuan, J., Yuan, H.-H. L., Omitaomu, O. A. & Bhaduri, B. L. in *2016 Int. Conf Big Data* 2703–2708 (IEEE, 2016).

6. 6.

Ishii, T. *et al.* in *IEEE 23rd Int. Conf Pattern Recognition* 3344–3349 (IEEE, 2016).

7. 7.

Yu, J., Wang, Z., Majumdar, A. & Rajagopal, R. *Joule* **2**, 2605–2617 (2018).

8. 8.

Imamoglu, N., Kimura, M., Miyamoto, H., Fujita, A. & Nakamura, R. Preprint at <https://arxiv.org/abs/1704.06410> (2017).

9. 9.

Hou, X., Wang, B., Hu, W., Yin, L. & Wu, H. Preprint at <https://arxiv.org/abs/1912.03685> (2019).

10. 10.

Rolnick, D. *et al.* Preprint at <https://arxiv.org/abs/1906.05433> (2019).

This article was downloaded by **calibre** from <https://www.nature.com/articles/d41586-021-02875-y>.

| [Section menu](#) | [Main menu](#) |

- NEWS AND VIEWS
- 13 October 2021

Opioid peptide signal in the brain makes mice hungrier for reward

Release of opioid peptide in the brain leads food-deprived mice to eat more sugar than do mice that are well fed. This opioid signalling mechanism fine-tunes the reward value of food according to the animal's state.

- [Lola Welsch](#)⁰ &
- [Brigitte L. Kieffer](#)¹

Eating even a simple snack is much more pleasurable when you are hungry than when you are already well fed. During fasting, complex brain mechanisms evaluate an animal's internal state, as well as the caloric and pleasurable (hedonic) values of the food, to ultimately drive eating. In the brain, several molecular signalling systems act together in this process, including the opioid system, which is composed of several opioid peptides and their receptors. The latter are the targets of opioid drugs such as morphine and heroin that have strong pain-reducing and notoriously addictive properties^{1,2}. The brain's opioid system contributes to the hedonic value of natural rewards such as food, sex and social interactions³, but the exact opioid peptide signal and receptor involved, and where they interact, have been challenging to determine. [Writing in Nature](#), Castro *et al.*⁴ identify an opioid-system-tuned brain circuit that drives hungry mice to eat more of a sugar reward than do well-fed mice.

Access options

[Subscribe to Journal](#)

Get full journal access for 1 year

\$199.00

only \$3.90 per issue

[Subscribe](#)

All prices are NET prices.

VAT will be added later in the checkout.

Tax calculation will be finalised during checkout.

Rent or Buy article

Get time limited or full article access on ReadCube.

from \$8.99

[Rent or Buy](#)

All prices are NET prices.

Additional access options:

- [Log in](#)
- [Learn about institutional subscriptions](#)

Nature **598**, 568-570 (2021)

doi: <https://doi.org/10.1038/d41586-021-02723-z>

References

1. 1.

Corder, G., Castro, D. C., Bruchas, M. R. & Scherrer, G. *Annu. Rev. Neurosci.* **41**, 453–473 (2018).

2. 2.

Darcq, E. & Kieffer, B. L. *Nature Rev. Neurosci.* **19**, 499–514 (2018).

3. 3.

Meier, I. M., Eikemo, M. & Leknes, S. *Curr. Addict. Rep.* **8**, 306–318, (2021).

4. 4.

Castro, D. C. *et al.* *Nature* <https://doi.org/10.1038/s41586-021-04013-0> (2021).

5. 5.

Castro, D. C. & Bruchas, M. R. *Neuron* **102**, 529–552 (2019).

6. 6.

Al-Hasani, R. *et al.* *eLife* **7**, e36520 (2018).

7. 7.

Castro, D. C. & Berridge, K. C. *J. Neurosci.* **34**, 4239–4250 (2014).

8. 8.

Luo, M., Zhou, J. & Liu, Z. *Learn. Mem.* **22**, 452–460 (2015).

9. 9.

Luo, M., Li, Y. & Zhong, W. *Neurobiol. Learn. Mem.* **135**, 40–49 (2016).

10. 10.

Matthews, G. A. *et al.* *Cell* **164**, 617–631 (2016).

This article was downloaded by **calibre** from <https://www.nature.com/articles/d41586-021-02723-z>

| [Section menu](#) | [Main menu](#) |

- NEWS AND VIEWS
- 06 October 2021

Bacteria recycle tumour waste to fuel immune cells

Key nutrients that are needed by immune cells are scarce in tumours. Engineered cancer-invading bacteria can recycle tumour waste into metabolic fuel to boost anticancer immune responses in mice.

- [Laurence C. Chen](#) [ORCID: http://orcid.org/0000-0002-1083-862X⁰](http://orcid.org/0000-0002-1083-862X)
&
- [Yvonne Y. Chen](#) [ORCID: http://orcid.org/0000-0002-5583-119X¹](http://orcid.org/0000-0002-5583-119X)

Harnessing a person's immune system to target a tumour — a type of treatment called cancer immunotherapy — has emerged as a promising treatment option for cancer. T cells are a type of immune cell that has a surveillance function and the capacity to kill foreign or infected cells that are perceived to pose a threat. These properties have cemented T cells as a central pillar of cancer immunotherapy. The generation of an effective antitumour T-cell response depends crucially on the availability of nutrients such as the amino acid l-arginine¹. However, the tumour microenvironment poses a challenge because it is nutrient-poor². [Writing in Nature](#), Canale *et al.*³ show that the treatment of mice with metabolically engineered bacteria produces a local, continuous source of l-arginine in the tumour microenvironment that results in strong, long-lasting antitumour T-cell responses when combined with a form of immunotherapy called checkpoint blockade.

Access options

Subscribe to Journal

Get full journal access for 1 year

\$199.00

only \$3.90 per issue

[Subscribe](#)

All prices are NET prices.

VAT will be added later in the checkout.

Tax calculation will be finalised during checkout.

Rent or Buy article

Get time limited or full article access on ReadCube.

from \$8.99

[Rent or Buy](#)

All prices are NET prices.

Additional access options:

- [Log in](#)
- [Learn about institutional subscriptions](#)

Nature **598**, 570-571 (2021)

doi: <https://doi.org/10.1038/d41586-021-02639-8>

References

1. 1.

Geiger, R. *et al.* *Cell* **167**, 829–842 (2016).

2. 2.

Hou, A. J., Chen, L. C. & Chen, Y. Y. *Nature Rev. Drug Discov.* **20**, 531–550 (2021).

3. 3.

Canale, F. P. *et al.* *Nature* <https://doi.org/10.1038/s41586-021-04003-2> (2021).

4. 4.

Spinelli, J. B. *et al.* *Science* **358**, 941–946 (2017).

5. 5.

Forbes, N. S. *Nature Rev. Cancer* **10**, 785–794 (2010).

6. 6.

Ou, B. *et al.* *Appl. Microbiol. Biotechnol.* **100**, 8693–8699 (2016).

7. 7.

Duong, M. T.-Q. *et al.* *Exp. Mol. Med.* **51**, 152 (2019).

This article was downloaded by **calibre** from <https://www.nature.com/articles/d41586-021-02639-8>

| [Section menu](#) | [Main menu](#) |

- NEWS AND VIEWS
- 27 October 2021

A compact device sustains a fluid of bosons

A device that generates exotic fluids of particles at equilibrium conditions and high temperatures could have applications ranging from low-loss electrical cables to memory storage.

- [Denis Golež](#) ⁰ &
- [Zhiyuan Sun](#) ¹

Imagine that your favourite cinema has just installed a single VIP seat that everybody wants to sit in. If cinema-goers were bosons, a type of elementary particle, they could all fit in this seat at the same time. This is the physics behind Bose–Einstein condensation, a phenomenon that involves a large fraction of the bosons in a gas simultaneously occupying the quantum state with the lowest energy. Bose–Einstein condensates have been achieved in cold atomic gases, a type of gas comprising atoms held at a temperature near absolute zero. But sustaining microkelvin temperatures is far from trivial because of the size of the machinery required. [Writing in Nature](#), Ma *et al.*¹ report a fluid of bosons in equilibrium, generated in a compact solid-state device at temperatures as high as 100 K — well within the reach of an ordinary physics laboratory. However, it remains to be confirmed whether it is indeed a Bose–Einstein condensate.

Access options

Subscribe to Journal

Get full journal access for 1 year

\$199.00

only \$3.90 per issue

[Subscribe](#)

All prices are NET prices.

VAT will be added later in the checkout.

Tax calculation will be finalised during checkout.

Rent or Buy article

Get time limited or full article access on ReadCube.

from \$8.99

[Rent or Buy](#)

All prices are NET prices.

Additional access options:

- [Log in](#)
- [Learn about institutional subscriptions](#)

Nature **598**, 571–572 (2021)

doi: <https://doi.org/10.1038/d41586-021-02876-x>

References

1. 1.

Ma, L. *et al.* *Nature* **598**, 585–589 (2021).

2. 2.

Eisenstein, J. P. & MacDonald, A. H. *Nature* **432**, 691–694 (2004).

3. 3.

Kasprzak, J. *et al.* *Nature* **443**, 409–414 (2006).

4. 4.

Fogler, M. M., Butov, L. V. & Novoselov, K. S. *Nature Commun.* **5**, 4555 (2014).

5. 5.

Xie, M. & MacDonald, A. H. *Phys. Rev. Lett.* **121**, 067702 (2018).

6. 6.

Wang, Z. *et al.* *Nature* **574**, 76–80 (2019).

7. 7.

Su, J.-J. & MacDonald, A. H. *Nature Phys.* **4**, 799–802 (2008).

8. 8.

High, A. E., Novitskaya, E. E., Butov, L. V., Hanson, M. & Gossard, A. C. *Science* **321**, 229–231 (2008).

9. 9.

Sun, Z., Kaneko, T., Golež, D. & Millis, A. J. *Phys. Rev. Lett.* **127**, 127702 (2021).

10. 10.

Rickhaus, P. *et al.* *Science* **373**, 1257–1260 (2021).

- NEWS AND VIEWS
- 26 October 2021

From the archive

Nature's pages feature musings about the value of studying wetlands, and a report of the excavation of an ancient city in Sicily.

50 years ago

Access options

Subscribe to Journal

Get full journal access for 1 year

\$199.00

only \$3.90 per issue

[Subscribe](#)

All prices are NET prices.

VAT will be added later in the checkout.

Tax calculation will be finalised during checkout.

Rent or Buy article

Get time limited or full article access on ReadCube.

from \$8.99

[Rent or Buy](#)

All prices are NET prices.

Additional access options:

- [Log in](#)
- [Learn about institutional subscriptions](#)

Nature **598**, 573 (2021)

doi: <https://doi.org/10.1038/d41586-021-02877-w>

This article was downloaded by **calibre** from <https://www.nature.com/articles/d41586-021-02877-w>

| [Section menu](#) | [Main menu](#) |

- NEWS AND VIEWS
- 13 October 2021

Electroacupuncture activates neurons to switch off inflammation

Neurons that express a specific molecular marker are activated by ‘electroacupuncture’ stimulation. They can then mediate the treatment’s anti-inflammatory effects in a mouse model of the inflammatory condition sepsis.

- [Luis Ulloa](#) [ORCID: http://orcid.org/0000-0002-7702-7549](#) 

Neuronal networks have evolved to control organ functions. A technique called electroacupuncture, in which specific points on the body called acupoints are stimulated electrically, has long been used to activate these networks and thereby modulate the functions of certain organs to treat various disorders. It is a key part of an emerging medical field known as bioelectronic medicine^{1,2}. However, little is known about the neuronal networks that mediate the effects of electroacupuncture at specific acupoints^{1,3}. [Writing in Nature](#), Liu *et al.*⁴ show in mice that a set of neurons expressing the protein Prokr2 are needed for electrical stimulation of a hindlimb acupoint to rein in the unbridled inflammatory responses that characterize lethal sepsis.

Access options

Subscribe to Journal

Get full journal access for 1 year

\$199.00

only \$3.90 per issue

Subscribe

All prices are NET prices.

VAT will be added later in the checkout.

Tax calculation will be finalised during checkout.

Rent or Buy article

Get time limited or full article access on ReadCube.

from \$8.99

Rent or Buy

All prices are NET prices.

Additional access options:

- [Log in](#)
- [Learn about institutional subscriptions](#)

Nature **598**, 573–574 (2021)

doi: <https://doi.org/10.1038/d41586-021-02714-0>

References

1. 1.

Ulloa, L., Quiroz-Gonzalez, S. & Torres-Rosas, R. *Trends Mol. Med.* **23**, 1103–1120 (2017).

2. 2.

Pavlov, V. A. & Tracey, K. J. *Nature Neurosci.* **20**, 156–166 (2017).

3. 3.

Sharma, N. *et al.* *Nature* **577**, 392–398 (2020).

4. 4.

Liu, S. *et al.* *Nature* <https://doi.org/10.1038/s41586-021-04001-4> (2021).

5. 5.

van der Poll, T., van de Veerdonk, F. L., Scicluna, B. P. & Netea, M. G. *Nature Rev. Immunol.* **17**, 407–420 (2017).

6. 6.

Ulloa, L. & Tracey, K. J. *Trends Mol. Med.* **11**, 56–63 (2005).

7. 7.

Torres-Rosas, R. *et al.* *Nature Med.* **20**, 291–295 (2014).

8. 8.

Bassi, G. S. *et al.* *Neurosci. Biobehav. Rev.* **112**, 363–373 (2020).

9. 9.

Vida, G. *et al.* *FASEB J.* **25**, 4476–4485 (2011).

10. 10.

Choi, S. *et al.* *Nature* **587**, 258–263 (2020).

11. 11.

Goldman, N. *et al.* *Nature Neurosci.* **13**, 883–888 (2010).

12. 12.

Liu, S. *et al.* *Neuron* **108**, 436–450 (2020).

13. 13.

Ulloa, L. *Nature Rev. Drug Discov.* **4**, 673–684 (2005).

14. 14.

Wang, H. *et al.* *Nature* **421**, 384–388 (2003).

15. 15.

Huston, J. M. *et al.* *J. Exp. Med.* **203**, 1623–1628 (2006).

This article was downloaded by **calibre** from <https://www.nature.com/articles/d41586-021-02714-0>

| [Section menu](#) | [Main menu](#) |

- Perspective
- [Published: 27 October 2021](#)

Call for a framework for reporting evidence for life beyond Earth

- [James Green](#) ORCID: [orcid.org/0000-0002-4625-9216¹](https://orcid.org/0000-0002-4625-9216),
- [Tori Hoehler²](#),
- [Marc Neveu^{3,4}](#),
- [Shawn Domagal-Goldman⁵](#),
- [Daniella Scalice⁶](#) &
- [Mary Voytek⁷](#)

Nature volume 598, pages 575–579 (2021)

- 1416 Accesses
- 552 Altmetric
- [Metrics details](#)

Subjects

- [Astronomy and planetary science](#)
- [Biological sciences](#)
- [Research management](#)

Abstract

Our generation could realistically be the one to discover evidence of life beyond Earth. With this privileged potential comes responsibility. The magnitude of the question of whether we are alone in the Universe, and the

public interest therein, opens the possibility that results may be taken to imply more than the observations support, or than the observers intend. As life-detection objectives become increasingly prominent in space sciences, it is essential to open a community dialogue about how to convey information in a subject matter that is diverse, complicated and has a high potential to be sensationalized. Establishing best practices for communicating about life detection can serve to set reasonable expectations on the early stages of a hugely challenging endeavour, attach value to incremental steps along the path, and build public trust by making clear that false starts and dead ends are an expected and potentially productive part of the scientific process. Here we endeavour to motivate and seed the discussion with basic considerations and offer an example of how such considerations might be incorporated and applied in a proof-of-concept-level framework. Everything mentioned herein, including the name of the confidence scale, is intended not as a prescription, but simply as the beginning of an important dialogue.

Access options

Subscribe to Journal

Get full journal access for 1 year

\$199.00

only \$3.90 per issue

[Subscribe](#)

All prices are NET prices.

VAT will be added later in the checkout.

Tax calculation will be finalised during checkout.

Rent or Buy article

Get time limited or full article access on ReadCube.

from \$8.99

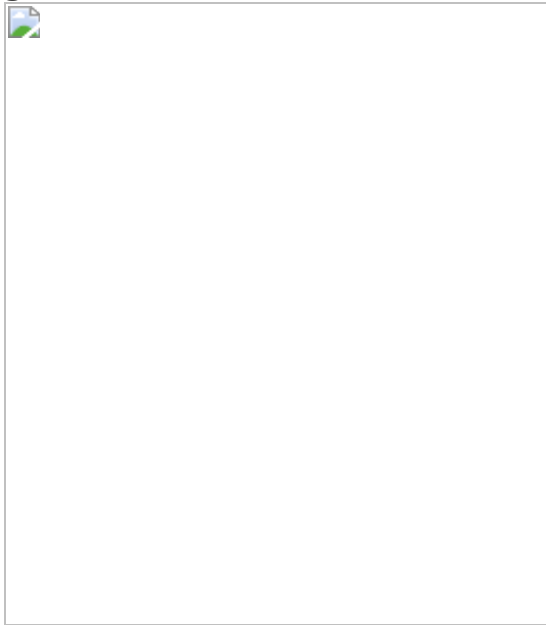
Rent or Buy

All prices are NET prices.

Additional access options:

- [Log in](#)
- [Access through your institution](#)
- [Learn about institutional subscriptions](#)

Fig. 1: The CoLD scale.



References

1. 1.

Crowe, M. *The Extraterrestrial Life Debate: Antiquity to 1915: A Source Book* (Univ. Notre Dame Press, 2008).

2. 2.

Dick, S. J. *Life on Other Worlds: The 20th-Century Extraterrestrial Life Debate* (Cambridge Univ. Press, 1998).

3. 3.

Blastland, M. et al. Five rules for evidence communication. *Nature* **587**, 362–364 (2020). **A commentary on effective science communication.**

4. 4.

National Academies of Sciences, Engineering, and Medicine *An Astrobiology Strategy for the Search for Life in the Universe* (The National Academies Press, 2019).

5. 5.

Neveu, M. et al. The ladder of life detection. *Astrobiology* **18**, 1375–1402 (2018).

6. 6.

Bean, J. L., Abbot, D. S. & Kempton, E. M.-R. A statistical comparative planetology approach to the hunt for habitable exoplanets and life beyond the Solar System. *Astrophys. J. Lett.* **841**, L24 (2017).

7. 7.

Benner, S. A. Defining life. *Astrobiology* **10**, 1021–1030 (2010).

8. 8.

Binzel, R. P. The Torino impact hazard scale. *Planet. Space Sci.* **48**, 297–303 (2000).

9. 9.

Morrison, D. et al. in *Mitigation of Hazardous Comets and Asteroids* (eds Belton, M. et al.) 252–390 (Cambridge Univ. Press, 2004). **A description of the considerations that went into building and updating the Torino scale.**

10. 10.

Beauchamp, P. M. et al. *Technology Readiness Levels: Best Practices Guide* NASA SP-20205003605 (NASA, 2020);
<https://ntrs.nasa.gov/citations/20205003605>

11. 11.

McKay, D. S. et al. Search for past life on Mars: possible relic biogenic activity in Martian meteorite ALH84001. *Science* **273**, 924–930 (1996). **The original report of evidence of life, cast in a binary light, in the Martian meteorite ALH84001.**

12. 12.

Romanek, C. S. et al. Record of fluid–rock interactions on Mars from the meteorite ALH84001. *Nature* **372**, 655–657 (1994).

13. 13.

Sawyer, K. *The Rock from Mars: A Detective Story on Two Planets* (Random House, 2006).

14. 14.

Williford, K. H. et al. *The NASA Mars 2020 Rover Mission and the Search for Extraterrestrial Life. From Habitability to Life on Mars* 275–308 (Elsevier, 2018).

15. 15.

Muirhead, B. K. et al. Mars sample return mission concept status. *Acta Astronaut.* **176**, 131–138 (2020).

16. 16.

Farmer, J. D. & Des Marais, D. J. Exploring for a record of ancient Martian life. *J. Geophys. Res.* **104**, 26977–26995 (1999).

17. 17.

Cady, S. L. et al. Morphological biosignatures and the search for life on Mars. *Astrobiology* **3**, 351–368 (2003).

18. 18.

Bosak, T. et al. Microbial sedimentology of stromatolites in Neoproterozoic cap carbonates. *Paleontol. Soc. Pap.* **19**, 51–76 (2013).

19. 19.

Summons, R. E. & Hallmann, C. in *Treatise on Geochemistry* 2nd edn (eds Falkowski, P. & Freeman, K.) 33–46 (Elsevier, 2014).

20. 20.

Capezzuoli, E., Gandin, A. & Pedley, M. Decoding tufa and travertine (fresh-water carbonates) in the sedimentary record: the state of the art. *Sedimentology* **61**, 1–21 (2014).

21. 21.

Horita, J. Some perspectives on isotope biosignatures for early life. *Chem. Geol.* **218**, 171–186 (2005).

22. 22.

National Academies of Sciences, Engineering, and Medicine *Decadal Survey on Astronomy and Astrophysics 2020* (The National Academies Press, 2021).

23. 23.

Meadows, V. S. et al. Exoplanet biosignatures: understanding oxygen as a biosignature in the context of its environment. *Astrobiology* **18**, 630–662 (2018).

24. 24.

Checlair, J. H. et al. Probing the capability of future direct-imaging missions to spectrally constrain the frequency of Earth-like planets. *Astron. J.* **161**, 150 (2021).

Author information

Affiliations

1. Office of the Chief Scientist, NASA Headquarters, Washington DC, USA

James Green

2. Exobiology Branch, NASA Ames Research Center, Moffett Field, CA, USA

Tori Hoehler

3. Planetary Environments Laboratory, NASA Goddard Space Flight Center, Greenbelt, MD, USA

Marc Neveu

4. Department of Astronomy, University of Maryland, College Park, MD, USA

Marc Neveu

5. Planetary Systems Laboratory, NASA Goddard Space Flight Center, Greenbelt, MD, USA

Shawn Domagal-Goldman

6. NASA Astrobiology Program, Paragon TEC/NASA Headquarters, Washington DC, USA

Daniella Scalice

7. NASA Astrobiology Program, NASA Headquarters, Washington DC,
USA

Mary Voytek

Contributions

All authors contributed to writing the manuscript after many rigorous discussions.

Corresponding author

Correspondence to James Green.

Ethics declarations

Competing interests

The authors declare no competing interests.

Additional information

Peer review information *Nature* thanks Morgan Cable and the other, anonymous, reviewer(s) for their contribution to the peer review of this work.

Publisher's note Springer Nature remains neutral with regard to jurisdictional claims in published maps and institutional affiliations.

Rights and permissions

[Reprints and Permissions](#)

About this article

Cite this article

Green, J., Hoehler, T., Neveu, M. *et al.* Call for a framework for reporting evidence for life beyond Earth. *Nature* **598**, 575–579 (2021).
<https://doi.org/10.1038/s41586-021-03804-9>

- Received: 08 February 2021
- Accepted: 06 July 2021
- Published: 27 October 2021
- Issue Date: 28 October 2021
- DOI: <https://doi.org/10.1038/s41586-021-03804-9>

Share this article

Anyone you share the following link with will be able to read this content:

[Get shareable link](#)

Sorry, a shareable link is not currently available for this article.

[Copy to clipboard](#)

Provided by the Springer Nature SharedIt content-sharing initiative

This article was downloaded by **calibre** from <https://www.nature.com/articles/s41586-021-03804-9>

- Article
- [Published: 27 October 2021](#)

A solar C/O and sub-solar metallicity in a hot Jupiter atmosphere

- [Michael R. Line](#) [ORCID: orcid.org/0000-0001-6247-8323](#)^{1,2},
- [Matteo Brogi](#)^{3,4,5},
- [Jacob L. Bean](#)⁶,
- [Siddharth Gandhi](#)^{3,4},
- [Joseph Zalesky](#) [ORCID: orcid.org/0000-0002-2259-4116](#)¹,
- [Vivien Parmentier](#)⁷,
- [Peter Smith](#)¹,
- [Gregory N. Mace](#)⁸,
- [Megan Mansfield](#)⁹,
- [Eliza M.-R. Kempton](#) [ORCID: orcid.org/0000-0002-1337-9051](#)¹⁰,
- [Jonathan J. Fortney](#)¹¹,
- [Evgenya Shkolnik](#)^{1,2},
- [Jennifer Patience](#)¹,
- [Emily Rauscher](#) [ORCID: orcid.org/0000-0003-3963-9672](#)¹²,
- [Jean-Michel Désert](#)¹³ &
- [Joost P. Wardenier](#) [ORCID: orcid.org/0000-0003-3191-2486](#)⁷

[Nature](#) volume **598**, pages 580–584 (2021)

- 585 Accesses
- 89 Altmetric
- [Metrics details](#)

Subjects

- [Atmospheric chemistry](#)
- [Exoplanets](#)

Abstract

Measurements of the atmospheric carbon (C) and oxygen (O) relative to hydrogen (H) in hot Jupiters (relative to their host stars) provide insight into their formation location and subsequent orbital migration^{1,2}. Hot Jupiters that form beyond the major volatile ($H_2O/CO/CO_2$) ice lines and subsequently migrate post disk-dissipation are predicted have atmospheric carbon-to-oxygen ratios (C/O) near 1 and subsolar metallicities², whereas planets that migrate through the disk before dissipation are predicted to be heavily polluted by infalling O-rich icy planetesimals, resulting in $C/O < 0.5$ and super-solar metallicities^{1,2}. Previous observations of hot Jupiters have been able to provide bounded constraints on either H_2O (refs. [3,4,5](#)) or CO (refs. [6,7](#)), but not both for the same planet, leaving uncertain⁴ the true elemental C and O inventory and subsequent C/O and metallicity determinations. Here we report spectroscopic observations of a typical transiting hot Jupiter, WASP-77Ab. From these, we determine the atmospheric gas volume mixing ratio constraints on both H_2O and CO ($9.5 \times 10^{-5} - 1.5 \times 10^{-4}$ and $1.2 \times 10^{-4} - 2.6 \times 10^{-4}$, respectively). From these bounded constraints, we are able to derive the atmospheric C/H ($(\{0.35\}_{-0.10}^{+0.17}) \times solar$) and O/H ($(\{0.32\}_{-0.08}^{+0.12}) \times solar$) abundances and the corresponding atmospheric carbon-to-oxygen ratio ($C/O = 0.59 \pm 0.08$; the solar value is 0.55). The sub-solar ($C+O/H$) ($(\{0.33\}_{-0.09}^{+0.13}) \times solar$) is suggestive of a metal-depleted atmosphere relative to what is expected for Jovian-like planets¹ while the near solar value of C/O rules out the disk-free migration/C-rich² atmosphere scenario.

Access options

Subscribe to Journal

Get full journal access for 1 year

\$199.00

only \$3.90 per issue

[Subscribe](#)

All prices are NET prices.

VAT will be added later in the checkout.

Tax calculation will be finalised during checkout.

Rent or Buy article

Get time limited or full article access on ReadCube.

from \$8.99

[Rent or Buy](#)

All prices are NET prices.

Additional access options:

- [Log in](#)
- [Access through your institution](#)
- [Learn about institutional subscriptions](#)

Fig. 1: Summary of the planetary atmosphere signal detection.

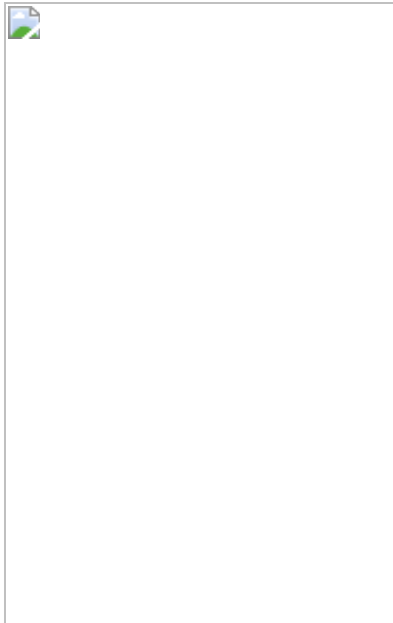


Fig. 2: Summary of the composition and vertical thermal structure constraints, compared to predictions.

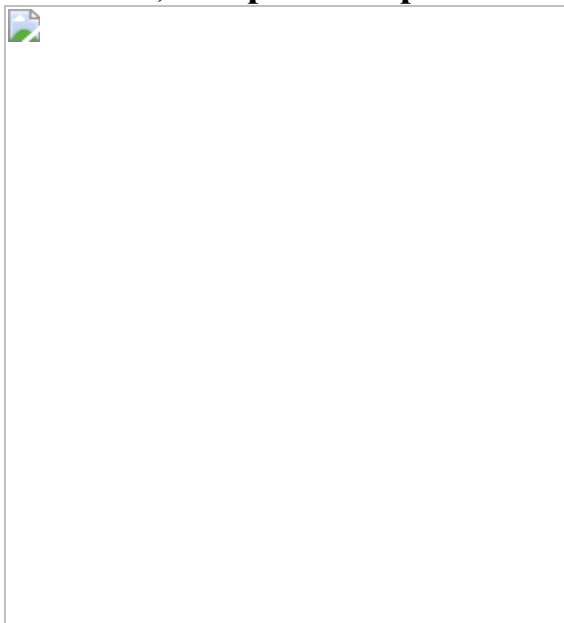
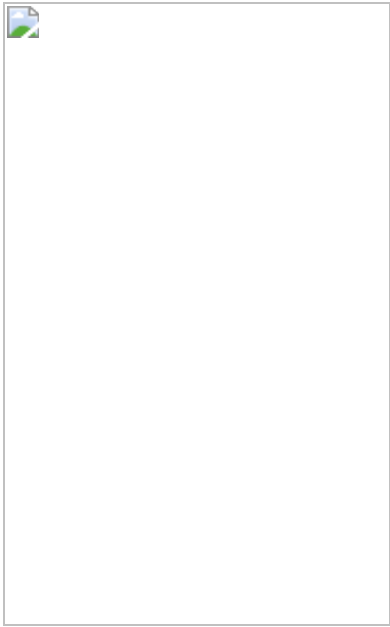


Fig. 3: Comparison of the IGRINS WASP-77Ab abundance constraints with the Solar System planets, exoplanets, and several predictions.



Data availability

The raw PLP extracted IGRINS data files and subsequent data products are available here:

<https://www.dropbox.com/sh/0cxfolfmrs8ip37/AABZYoHr8nuRIHJG84dArX4ea?dl=0>.

Code availability

The IGRINS PLP used to perform the initial reduction and extraction by the instrument team is available at <https://github.com/igrins/plp>. The barycenter correction and planetary phase calculations were made using the python astropy library found here <https://www.astropy.org/>. Python numpy specific tools are noted in the text (for example, the SVD for the PCA). The chemical abundance analysis/physical plausibility assessment made use of the VULCAN chemical kinetics tool.

(<https://github.com/exoclime/VULCAN>). Absorption cross-sections were generated using the HELIOS-K tool (<https://helios-k.readthedocs.io/en/latest/>). Finally, we make available a an end-to-end python2/GPU HRCCS retrieval code example available here <https://www.dropbox.com/sh/0cxfolfmrs8ip37/AABZYoHr8nuRIHJG84dArX4ea?dl=0>, which makes use of the pymultinest nested-sampling package

(<https://johannesbuchner.github.io/PyMultiNest/>), joblib loop parallelization package (<https://joblib.readthedocs.io/en/latest/>), and corner.py (<https://corner.readthedocs.io/en/latest/>).

References

1. 1.

Mordasini, C., van Boekel, R., Molliere, P., Henning, T. & Benneke, B. The imprint of exoplanet formation history on observable present-day spectra of hot Jupiters. *Astrophys. J.* **832**, 41 (2016).

2. 2.

Madhusudhan, N. Exoplanetary atmospheres: key insights, challenges, and prospects. *Ann. Rev. Astron. Astrophys.* **57**, 617–663 (2019).

3. 3.

Tsiaras, A. et al. A population study of gaseous exoplanets. *Astron. J.* **155**, 156 (2018).

4. 4.

Welbanks, L. et al. Mass-metallicity trends in transiting exoplanets from atmospheric abundances of H₂O, Na, and K. *Astrophys. J. Lett.* **887**, L20 (2019).

5. 5.

Gandhi, S., Madhusudhan, N., Hawker, G. & Piette, A. HyDRA-H: simultaneous hybrid retrieval of exoplanetary emission spectra. *Astron. J.* **158**, 228 (2019).

6. 6.

Pelletier, S. et al. Where is the water? Jupiter-like C/H ratio but strong H₂O depletion found on τ Boötis b using SPIRou. *Astron. J.* **162**, 73

(2021).

7. 7.

Brogi, M. & Line, M. R. Retrieving temperatures and abundances of exoplanet atmospheres with high-resolution cross-correlation spectroscopy. *Astron. J.* **157**, 114 (2019).

8. 8.

Maxted, P. F. L. et al. WASP-77 Ab: a transiting hot Jupiter planet in a wide binary system. *Pub. Astron. Soc. Pac.* **125**, 48 (2013).

9. 9.

Park, C. et al. Design and early performance of IGRINS (immersion grating infrared spectrometer). In *Ground-based and Airborne Instrumentation for Astronomy V*, vol. 9147 of *Society of Photo-Optical Instrumentation Engineers (SPIE) Conference Series* (eds Ramsay, S. K., McLean, I. S. & Takami, H.) 91471D (2014).

10. 10.

Mace, G. et al. IGRINS at the Discovery Channel Telescope and Gemini South. In *Ground-based and Airborne Instrumentation for Astronomy VII*, vol. 10702 of *Society of Photo-Optical Instrumentation Engineers (SPIE) Conference Series* (eds. Evans, C. J., Simard, L. & Takami, H.) 107020Q (2018).

11. 11.

Lee, Jae-Joon & Gullikson, Kevin. PLP: v2.1 alpha 3 [Data set]. *Zenodo* <https://doi.org/10.5281/zenodo.56067> (2016)

12. 12.

de Kok, R. J. et al. Detection of carbon monoxide in the high-resolution day-side spectrum of the exoplanet HD 189733b. *Astron. J.* **554**, A82 (2013).

13. 13.

Brogi, M. et al. The signature of orbital motion from the dayside of the planet τ Boötis b. *Nature* **486**, 502–504 (2012).

14. 14.

Birkby, J. L. et al. Detection of water absorption in the day side atmosphere of HD 189733 b using ground-based high-resolution spectroscopy at 3.2 μm . *Mon. Not. R. Astron. Soc.* **436**, L35–L39 (2013).

15. 15.

Lockwood, A. et al. Near-IR direct detection of water vapor in Tau Boötis b. *Astrophys. J. Lett.* **783**, L29 (2014).

16. 16.

Snellen, I. A. G., de Kok, R. J., de Mooij, E. J. W. & Albrecht, S. The orbital motion, absolute mass and high-altitude winds of exoplanet HD209458b. *Nature* **465**, 1049–1051 (2010).

17. 17.

Moses, J. I. Chemical kinetics on extrasolar planets. *Philos. Trans. R. Soc. A* **372**, 20130073 (2014).

18. 18.

Parmentier, V., Fortney, J. J., Showman, A. P., Morley, C. & Marley, M. S. Transitions in the cloud composition of hot Jupiters. *Astrophys. J.* **828**, 22 (2016).

19. 19.

Asplund, M., Grevesse, N., Sauval, A. J. & Scott, P. The chemical composition of the Sun. *Ann. Rev. Astron. Astrophys.* **47**, 481–522 (2009).

20. 20.

Öberg, K. I., Murray-Clay, R. & Bergin, E. A. The effects of snowlines on C/O in planetary atmospheres. *Astrophys. J. Lett.* **743**, L16 (2011).

21. 21.

Madhusudhan, N., Amin, M. A. & Kennedy, G. M. Towards chemical constraints on hot Jupiter migration. *Astrophys. J. Lett.* **794**, L12 (2014)

22. 22.

Madhusudhan, N., Bitsch, B., Johansen, A. & Eriksson, L. Atmospheric signatures of giant exoplanet formation by pebble accretion. *Mon. Not. R. Astron. Soc.* **469**, 4102–4115 (2017).

23. 23.

Booth, R. A., Clarke, C. J., Madhusudhan, N. & Ilee, J. D. Chemical enrichment of giant planets and discs due to pebble drift. *Mon. Not. R. Astron. Soc.* **469**, 3994–4011 (2017).

24. 24.

Kreidberg, L. et al. A precise water abundance measurement for the hot Jupiter WASP-43b. *Astrophys. J. Lett.* **739**, L27 (2014).

25. 25.

Li, C. et al. The water abundance in Jupiter’s equatorial zone. *Nat. Astron.* **4**, 609–616 (2020).

26. 26.

Atreya, S. K. et al. The origin and evolution of Saturn, with exoplanet perspective. Preprint at <https://arxiv.org/abs/1606.04510> (2016).

27. 27.

Thorngren, D. & Fortney, J. J. Connecting giant planet atmosphere and interior modeling: constraints on atmospheric metal enrichment. *Astrophys. J. Lett.* **874**, L31 (2019).

28. 28.

Burrows, A. & Sharp, C. M. Chemical equilibrium abundances in brown dwarf and extrasolar giant planet atmospheres. *Astrophys. J.* **512**, 843–863 (1999).

29. 29.

Giacobbe, P. et al. Five carbon- and nitrogen-bearing species in a hot giant planet’s atmosphere. *Nature* **592**, 205–208 (2021).

30. 30.

Line, M. R. et al. A systematic retrieval analysis of secondary eclipse spectra. I. A comparison of atmospheric retrieval techniques. *Astrophys. J.* **775**, 137 (2013).

31. 31.

Line, M. R. et al. Uniform atmospheric retrieval analysis of ultracool dwarfs. II. Properties of 11 T dwarfs. *Astrophys. J.* **848**, 83 (2017).

32. 32.

Tennyson, J. et al. The 2020 release of the ExoMol database: molecular line lists for exoplanet and other hot atmospheres. *J. Quant. Spectrosc. Radiat. Transf.* **255**, 107228 (2020).

33. 33.

Coles, P. A., Yurchenko, S. N. & Tennyson, J. ExoMol molecular line lists – XXXV. A rotation-vibration line list for hot ammonia. *Mon. Not. R. Astro. Soc.* **490**, 4638–4647 (2019).

34. 34.

Rothman, L. S. et al. HITEMP, the high-temperature molecular spectroscopic database. *J. Quant. Spectrosc. Radiat. Transf.* **111**, 2139–2150 (2010).

35. 35.

Hargreaves, R. J. et al. An accurate, extensive, and practical line list of methane for the HITEMP database. *Astrophys. J. Suppl. Ser.* **247**, 55 (2020).

36. 36.

Li, G. et al. Rovibrational line lists for nine isotopologues of the CO molecule in the X $^1\Sigma^+$ ground electronic state. *Astrophys. J. Suppl. Ser.* **216**, 15 (2015).

37. 37.

Azzam, A. A. A., Tennyson, J., Yurchenko, S. N. & Naumenko, O. V. ExoMol molecular line lists - XVI. The rotation-vibration spectrum of hot H₂S. *Mon. Not. R. Astron. Soc.* **460**, 4063–4074 (2016).

38. 38.

Barber, R. J. et al. ExoMol line lists - III. An improved hot rotation-vibration line list for HCN and HNC. *Mon. Not. R. Astron. Soc.* **437**, 1828–1835 (2014).

39. 39.

Karman, T. et al. Update of the HITRAN collision-induced absorption section. *Icarus* **328**, 160–175 (2019).

40. 40.

Grimm, S. L. & Heng, K. HELIOS-K: an ultrafast, open-source opacity calculator for radiative transfer. *Astrophys. J.* **808**, 182 (2015).

41. 41.

Grimm, S. L. et al. HELIOS-K 2.0 opacity calculator and open-source opacity database for exoplanetary atmospheres. *Astrophys. J. Suppl.* **253**, 30 (2021).

42. 42.

Polyansky, O. L. et al. ExoMol molecular line lists XXX: a complete high-accuracy line list for water. *Mon. Not. R. Astron. Soc.* **480**, 2597–2608 (2018).

43. 43.

Gharib-Nezhad, E. et al. EXOPLINES: molecular absorption cross-section database for brown dwarf and giant exoplanet atmospheres. *Astrophys. J. Suppl. Ser.* **254**, 34 (2021)

44. 44.

Madhusudhan, N. & Seager, S. A temperature and abundance retrieval method for exoplanet atmospheres. *Astrophys. J.* **707**, 24–39 (2009).

45. 45.

Buchner, J. et al. X-ray spectral modelling of the AGN obscuring region in the CDFS: Bayesian model selection and catalogue. *Astron. Astrophys.* **564**, A125 (2014)

46. 46.

Feroz, F., Hobson, M. P. & Bridges, M. MULTINEST: an efficient and robust Bayesian inference tool for cosmology and particle physics. *Mon. Not. R. Astron. Soc.* **398**, 1601–1614 (2009).

47. 47.

Zucker, S. Cross-correlation and maximum-likelihood analysis: a new approach to combining cross-correlation functions. *Mon. Not. R. Astron. Soc.* **342**, 1291–1298 (2003).

48. 48.

Gibson, N. P. et al. Detection of Fe I in the atmosphere of the ultra-hot Jupiter WASP-121b, and a new likelihood-based approach for Doppler-resolved spectroscopy. *Mon. Not. R. Astron. Soc.* **493**, 2215–2228 (2020).

49. 49.

Line, M. R., Knutson, H., Wolf, A. S. & Yung, Y. L. A systematic retrieval analysis of secondary eclipse spectra. II. A uniform analysis of nine planets and their C to O ratios. *Astrophys. J.* **783**, 70 (2014).

50. 50.

Hoeijmakers, H. J. et al. Atomic iron and titanium in the atmosphere of the exoplanet KELT9b. *Nature* **560**, 453–455 (2018).

51. 51.

Brogi, M. et al. Detection of molecular absorption in the dayside of exoplanet 51 Pegasi b? *Astrophys. J.* **767**, 27 (2013).

52. 52.

Beltz, H., Rauscher, E., Brogi, M. & Kempton, E. M. R. A significant increase in detection of high-resolution emission spectra using a three-dimensional atmospheric model of a hot Jupiter. *Astron. J.* **161**, 1 (2021).

53. 53.

Piskorz, D. et al. Ground- and space-based detection of the thermal emission spectrum of the transiting hot Jupiter KELT-2Ab. *Astron. J.* **156**, 133 (2018).

54. 54.

Gharib-Nezhad, E. & Line, M. R. The influence of H₂O pressure broadening in High-metallicity exoplanet atmospheres. *Astrophys. J.* **872**, 27 (2019).

55. 55.

Arcangeli, J. et al. H⁻ opacity and water dissociation in the dayside atmosphere of the very hot gas giant WASP-18b. *Astrophys. J. Lett.* **855**, L30 (2018).

56. 56.

Perez-Becker, D. & Showman, A. P. Atmospheric heat redistribution on hot Jupiters. *Astrophys. J.* **776**, 134 (2013).

57. 57.

Tsai, S.-M. et al. Toward consistent modeling of atmospheric chemistry and dynamics in exoplanets: validation and generalization of the chemical relaxation method. *Astrophys. J.* **862**, 31 (2018).

58. 58.

Fortney, J. J., Lodders, K., Marley, M. S. & Freedman, R. S. A unified theory for the atmospheres of the hot and very hot Jupiters: two classes of irradiated atmospheres. *Astrophys. J.* **678**, 1419–1435 (2008).

59. 59.

Parmentier, V., Showman, A. P. & Fortney, J. J. The cloudy shape of hot Jupiter thermal phase curves. *Mon. Not. R. Astron. Soc.* **501**, 78–108 (2021).

60. 60.

Fortney, J. J. et al. A framework for characterizing the atmospheres of low-mass low density transiting planets. *Astrophys. J.* **775**, 80 (2013).

61. 61.

Pinhas, A., Madhusudhan, N., Gandhi, S. & MacDonald, R. H₂O abundances and cloud properties in ten hot giant exoplanets. *Mon. Not. R. Astron. Soc.* **482**, 1485–1498 (2019).

62. 62.

Fisher, C. & Heng, K. Retrieval analysis of 38 WFC3 transmission spectra and resolution of the normalization degeneracy. *Mon. Not. R. Astron. Soc.* **481**, 4698–4727 (2018).

63. 63.

Feng, Y. K. et al. The impact of non-uniform thermal structure on the interpretation of exoplanet emission spectra. *Astrophys. J.* **829**, 52 (2016).

64. 64.

Line, M. R. et al. Information content of exoplanetary transit spectra: an initial look. *Astrophys. J.* **749**, 93 (2012).

65. 65.

Guillot, T. On the radiative equilibrium of irradiated planetary atmospheres. *Astron. Astrophys.* **520**, A27 (2010).

66. 66.

Gandhi, S. et al. Molecular cross-sections for high-resolution spectroscopy of super-Earths, warm Neptunes, and hot Jupiters. *Mon. Not. R. Astron. Soc.* **495**, 224–237 (2020).

67. 67.

Woods, P. M. & Willacy, K. Carbon isotope fractionation in protoplanetary disks. *Astrophys. J.* **693**, 1360–1378 (2009).

68. 68.

Marboeuf, U., Thiabaud, A., Alibert, Y. & Benz, W. Isotopic ratios D/H and $^{15}\text{N}/^{14}\text{N}$ in giant planets. *Mon. Not. R. Astron. Soc.* **475**, 2355–2362 (2018).

69. 69.

Molliere, P. & Snellen, I. A. G. Detecting isotopologues in exoplanet atmospheres using ground-based high-dispersion spectroscopy. *Astron. Astrophys.* **622**, A139 (2019).

Acknowledgements

M.R.L., J.J.F., J.L.B. and P.S. acknowledge support from NASA XRP grant 80NSSC19K0293. M.R.L. and E.S. acknowledge support from the Nexus for Exoplanet System Science and NASA Astrobiology Institute Virtual Planetary Laboratory (no. 80NSSC18K0829). M.B. and S.G. acknowledge support from the UK Science and Technology Facilities Council (STFC) research grant ST/S000631/1. J.Z. acknowledges support from the NASA FINESST grant 80NSSC19K1420. E.M.-R.K. and E.R. thank the Heising-Simons Foundation for support. J.P.W. acknowledges support from the Wolfson Harrison UK Research Council Physics Scholarship and the UK Science and Technology Facilities Council (STFC). This work used the Immersion Grating Infrared Spectrometer (IGRINS) that was developed under a collaboration between the University of Texas at Austin and the Korea Astronomy and Space Science Institute (KASI) with the financial support of the Mount Cuba Astronomical Foundation, of the US National Science Foundation under grants AST-1229522 and AST-1702267, of the McDonald Observatory of the University of Texas at Austin, of the Korean GMT Project of KASI, and Gemini Observatory. This program, GS-2020B-Q-249, is based on observations obtained at the international Gemini Observatory, a program of NSF's NOIRLab, which is managed by the Association of Universities for Research in Astronomy (AURA) under a cooperative agreement with the National Science Foundation on behalf of the Gemini Observatory partnership: the National Science Foundation (United States), National Research Council (Canada), Agencia Nacional de Investigación y Desarrollo (Chile), Ministerio de Ciencia, Tecnología e Innovación (Argentina), Ministério da Ciência, Tecnologia, Inovações e

Comunicações (Brazil), and Korea Astronomy and Space Science Institute (Republic of Korea). Finally, we acknowledge Research Computing at Arizona State University for providing HPC and storage resources that have significantly contributed to the research results reported within this manuscript.

Author information

Affiliations

1. School of Earth and Space Exploration, Arizona State University, Tempe, AZ, USA

Michael R. Line, Joseph Zalesky, Peter Smith, Evgenya Shkolnik & Jennifer Patience

2. NASA Astrobiology Institute, Virtual Planetary Laboratory Team, Seattle, WA, USA

Michael R. Line & Evgenya Shkolnik

3. Department of Physics, University of Warwick, Coventry, UK

Matteo Brogi & Siddharth Gandhi

4. Centre for Exoplanets and Habitability, University of Warwick, Coventry, UK

Matteo Brogi & Siddharth Gandhi

5. INAF—Osservatorio Astrofisico di Torino, Turin, Italy

Matteo Brogi

6. Department of Astronomy and Astrophysics, University of Chicago, Chicago, IL, USA

Jacob L. Bean

7. Atmospheric, Oceanic, and Planetary Physics, Clarendon Laboratory,
Department of Physics, University of Oxford, Oxford, UK

Vivien Parmentier & Joost P. Wardenier

8. Department of Astronomy, University of Texas at Austin, Austin, TX,
USA

Gregory N. Mace

9. Department of Geophysical Sciences, University of Chicago, Chicago,
IL, USA

Megan Mansfield

10. Department of Astronomy, University of Maryland, College Park, MD,
USA

Eliza M.-R. Kempton

11. Department of Astronomy and Astrophysics, University of California,
Santa Cruz, CA, USA

Jonathan J. Fortney

12. Department of Astronomy, University of Michigan, Ann Arbor, MI,
USA

Emily Rauscher

13. Anton Pannekoek Institute for Astronomy, University of Amsterdam,
Amsterdam, the Netherlands

Jean-Michel Désert

Contributions

M.R.L. conceived of the idea, performed the data analysis and modelling,
and wrote the manuscript. J.Z. (principal investigator) and M.R.L. wrote the

original IGRINS proposal. M.B. provided guidance on the cross-correlation analysis and conceptual framework. J.L.B. provided guidance on the context of the results. S.G. performed an independent Bayesian analysis to confirm the result. G.N.M. ran the PLP pipeline and also assisted in the IGRINS specific observational setup. V.P., P.S., G.M., M.M., E.M.-R.K., J.J.F., E.S., J.P., E.R., J-M.D., J.P.W. and L.P. helped with the original proposal/and or provided valuable insight/comments on the manuscript or through discussions.

Corresponding author

Correspondence to Michael R. Line.

Ethics declarations

Competing interests

The authors declare no competing interests.

Additional information

Peer review information *Nature* thanks Neale Gibson and the other, anonymous, reviewer(s) for their contribution to the peer review of this work. Peer reviewer reports are available.

Publisher's note Springer Nature remains neutral with regard to jurisdictional claims in published maps and institutional affiliations.

Extended data figures and tables

[Extended Data Fig. 1 Summary of the data and PCA procedure.](#)

a, The median per-resolution element signal-to-noise for each order for the night (in red). The blue curve is the median SNR in both time and over an

individual order. **b**, Example raw data cubes (top row)—spectra versus time/frame for representative two orders (25, 5). Stationary tellurics show up as vertical dark streaks. Wavelength dependent gradient is due to the echelle blaze throughput. The PCA/SVD method can remove these stationary features, leaving behind the planetary signal buried in the noise (bottom row). We use these ‘post-PCA’ frames for the subsequent cross-correlation/retrieval analysis (repeated for all 43 use orders).

[Extended Data Fig. 2 Summary of the key opacity sources used in the retrieval analysis.](#)

Absorption cross-sections for the molecules considered in the retrieval analysis (for 0.01 bar, 1,600 K).

[Extended Data Fig. 3 Corner plot summary of the posterior probability distribution from the main-text retrieval analysis.](#)

Note the bounded constraints on water, CO and the isotopic ratio, but upper limits only on the other species. Note, we retrieve [$^{13}\text{C}^{16}\text{O}/^{12}\text{C}^{16}\text{O}$] but plot the inverse, [$^{12}\text{C}^{16}\text{O}/^{13}\text{C}^{16}\text{O}$] to facilitate comparisons to literature reported values (in Extended Data Fig. 6) The inset shows the molecular components of the maximum likelihood model spectrum. Figure generated with corner.py.

[Extended Data Fig. 4 Classic cross-correlation analysis data products.](#)

The model template used to in this cross-correlation analysis is the spectrum resulting from the maximum likelihood solution found by the retrieval analysis. The left column illustrates the gas detections (all gases, H_2O , CO and other— $\text{NH}_3+\text{H}_2\text{S}+\text{HCN}+\text{CH}_4$) in the standard $K_p-\Delta V_{\text{sys}}$ plane, with a slice in V_{sys} along the literature reported K_p at the bottom. The detection maps are constructed by subtracting the mean total CC, then dividing by an ‘off peak’ (a boxed region in the lower left corner of each panel) CC standard deviation. Using this method, only H_2O is strongly

detected, with a hint of CO present at the expected velocities. The right column reproduces analogous products using the log-likelihood formalism⁷ ($\Delta \log L$ relative to the minimum), resulting in a stronger presence of CO. We emphasize that while such maps may be instructive for ‘detecting’ species or ‘atmosphere’, they do not marginalize over all of the degeneracy, nor do they maximize the information content in the data. This is why in our analysis we focus on the results arising from the more comprehensive log-likelihood/retrieval formalism.

Extended Data Fig. 5 Robustness test analyses summary using the H₂O, CO and temperature profile constraints as the metrics for assumption impact.

The top row of histograms and first TP profile histogram demonstrate the lack of impact of temperature profile parameterization. The middle panel of histograms and middle temperature profile panel show that there is little impact due to any presence of temperature heterogeneities on the hemisphere(s) observed during the sequence. Finally, the bottom panel of histograms and last temperature profile panel illustrate the lack of impact of various data analysis and other minor modelling assumptions. In short, the retrieved abundances and temperature profile constraints are largely resilient against most common assumptions.

Extended Data Fig. 6 Bayesian inference/retrieval tool comparison on the IGRINS data.

The temperature profiles are compared in the left most panel and a subset of the abundances in the corner plot on the right. Each model uses slightly different atmospheric parameterization assumptions with the core radiative transfer aspects (solver, opacities) independently developed.

Extended Data Fig. 7 Carbon isotopic abundance analysis.

The top row of histograms compares the constraints from a nominal simplified retrieval model applied to the true data (red) and the reverse-injected data reinjected with ¹³C isotope removed model (black). The upper

limit on the simulated data and bounded constraint arising from the true dataset suggests that there is indeed isotopic information in these IGRINS data. The bottom panel compares the retrieved ^{12}C to ^{13}C ratio (red) to common Solar System bodies (blue, after ref. ⁶⁸) and various reference values (galactic interstellar medium (ISM) components, and Earth (terrestrial), black dashed lines). WASP-77Ab sits anomalously low (enhanced ^{13}C) compared to most Solar System objects.

Extended Data Table 1 Description of the retrieved parameters and uniform prior ranges

Supplementary information

[Peer Review File](#)

Rights and permissions

[Reprints and Permissions](#)

About this article

Cite this article

Line, M.R., Brogi, M., Bean, J.L. *et al.* A solar C/O and sub-solar metallicity in a hot Jupiter atmosphere. *Nature* **598**, 580–584 (2021). <https://doi.org/10.1038/s41586-021-03912-6>

- Received: 04 June 2021
- Accepted: 13 August 2021
- Published: 27 October 2021
- Issue Date: 28 October 2021
- DOI: <https://doi.org/10.1038/s41586-021-03912-6>

Share this article

Anyone you share the following link with will be able to read this content:

[Get shareable link](#)

Sorry, a shareable link is not currently available for this article.

[Copy to clipboard](#)

Provided by the Springer Nature SharedIt content-sharing initiative

This article was downloaded by **calibre** from <https://www.nature.com/articles/s41586-021-03912-6>

| [Section menu](#) | [Main menu](#) |

- Article
- [Published: 27 October 2021](#)

Strongly correlated excitonic insulator in atomic double layers

- [Liguo Ma](#) ORCID: [orcid.org/0000-0002-2690-3094^{1,na1}](https://orcid.org/0000-0002-2690-3094),
- [Phuong X. Nguyen](#)^{1,na1},
- [Zefang Wang](#)¹,
- [Yongxin Zeng](#) ORCID: [orcid.org/0000-0003-1081-1707²](https://orcid.org/0000-0003-1081-1707),
- [Kenji Watanabe](#) ORCID: [orcid.org/0000-0003-3701-8119³](https://orcid.org/0000-0003-3701-8119),
- [Takashi Taniguchi](#) ORCID: [orcid.org/0000-0002-1467-3105³](https://orcid.org/0000-0002-1467-3105),
- [Allan H. MacDonald](#) ORCID: [orcid.org/0000-0003-3561-3379²](https://orcid.org/0000-0003-3561-3379),
- [Kin Fai Mak](#) ORCID: [orcid.org/0000-0002-5768-199X^{1,4,5}](https://orcid.org/0000-0002-5768-199X) &
- [Jie Shan](#) ORCID: [orcid.org/0000-0003-1270-9386^{1,4,5}](https://orcid.org/0000-0003-1270-9386)

[Nature](#) volume **598**, pages 585–589 (2021)

- 2045 Accesses
- 12 Altmetric
- [Metrics details](#)

Subjects

- [Bose–Einstein condensates](#)
- [Quantum fluids and solids](#)
- [Two-dimensional materials](#)

Abstract

Excitonic insulators (EIs) arise from the formation of bound electron–hole pairs (excitons)^{1,2} in semiconductors and provide a solid-state platform for quantum many-boson physics^{3,4,5,6,7,8}. Strong exciton–exciton repulsion is expected to stabilize condensed superfluid and crystalline phases by suppressing both density and phase fluctuations^{8,9,10,11}. Although spectroscopic signatures of EIs have been reported^{6,12,13,14}, conclusive evidence for strongly correlated EI states has remained elusive. Here we demonstrate a strongly correlated two-dimensional (2D) EI ground state formed in transition metal dichalcogenide (TMD) semiconductor double layers. A quasi-equilibrium spatially indirect exciton fluid is created when the bias voltage applied between the two electrically isolated TMD layers is tuned to a range that populates bound electron–hole pairs, but not free electrons or holes^{15,16,17}. Capacitance measurements show that the fluid is exciton-compressible but charge-incompressible—direct thermodynamic evidence of the EI. The fluid is also strongly correlated with a dimensionless exciton coupling constant exceeding 10. We construct an exciton phase diagram that reveals both the Mott transition and interaction-stabilized quasi-condensation. Our experiment paves the path for realizing exotic quantum phases of excitons⁸, as well as multi-terminal exciton circuitry for applications^{18,19,20}.

Access options

Subscribe to Journal

Get full journal access for 1 year

\$199.00

only \$3.90 per issue

[Subscribe](#)

All prices are NET prices.

VAT will be added later in the checkout.

Tax calculation will be finalised during checkout.

Rent or Buy article

Get time limited or full article access on ReadCube.

from \$8.99

[Rent or Buy](#)

All prices are NET prices.

Additional access options:

- [Log in](#)
- [Access through your institution](#)
- [Learn about institutional subscriptions](#)

Fig. 1: Electrical reservoir for interlayer excitons.

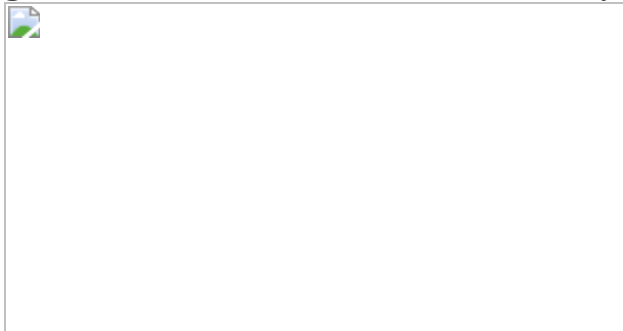


Fig. 2: Exciton and charge compressibility.



Fig. 3: Charge gap energy of the double layer.



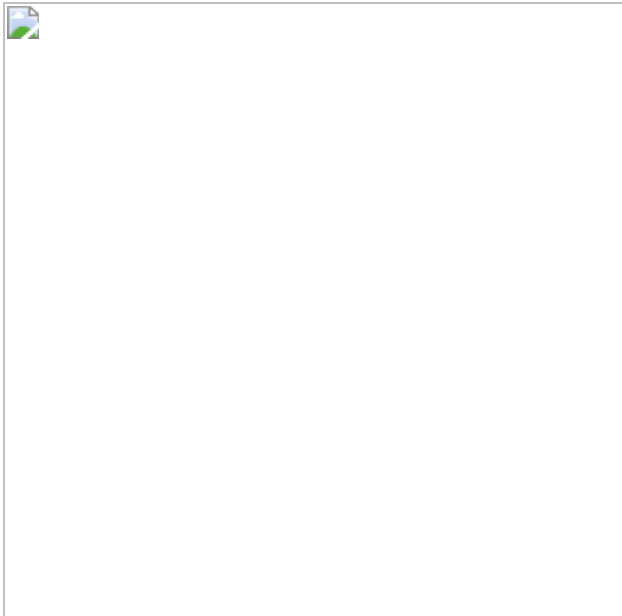
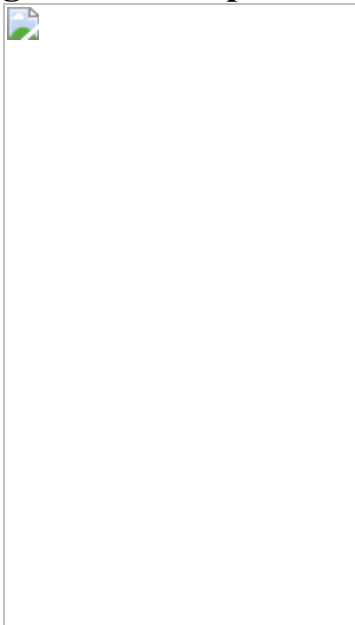


Fig. 4: Exciton phase diagram.



Data availability

The source data that support the findings of this study are available with the paper. [Source data](#) are provided with this paper.

References

1. 1.

Mott, N. F. The transition to the metallic state. *Philos. Mag.* **6**, 287–309 (1961).

2. 2.

Jérôme, D., Rice, T. M. & Kohn, W. Excitonic Insulator. *Phys. Rev.* **158**, 462–475 (1967).

3. 3.

Zhu, X., Littlewood, P. B., Hybertsen, M. S. & Rice, T. M. Exciton condensate in semiconductor quantum well structures. *Phys. Rev. Lett.* **74**, 1633–1636 (1995).

4. 4.

Sun, Z. & Millis, A. J. Topological charge pumping in excitonic insulators. *Phys. Rev. Lett.* **126**, 027601 (2021).

5. 5.

Eisenstein, J. P. & MacDonald, A. H. Bose–Einstein condensation of excitons in bilayer electron systems. *Nature* **432**, 691–694 (2004).

6. 6.

Kogar, A. et al. Signatures of exciton condensation in a transition metal dichalcogenide. *Science* **358**, 1314–1317 (2017).

7. 7.

Butov, L. V. Condensation and pattern formation in cold exciton gases in coupled quantum wells. *J. Phys. Condens. Matter* **16**, R1577–R1613 (2004).

8. 8.

Baranov, M. A., Dalmonte, M., Pupillo, G. & Zoller, P. Condensed matter theory of dipolar quantum gases. *Chem. Rev.* **112**, 5012–5061 (2012).

9. 9.

Z. Hadzibabic, & Dalibard, J. Two-dimensional Bose fluids: an atomic physics perspective. *Riv. del Nuovo Cim.* **34**, 389–434 (2011).

10. 10.

Lozovik, Y. E., Kurbakov, I. L., Astrakharchik, G. E., Boronat, J. & Willander, M. Strong correlation effects in 2D Bose–Einstein condensed dipolar excitons. *Solid State Commun.* **144**, 399–404 (2007).

11. 11.

Ha, L.-C. et al. Strongly interacting two-dimensional Bose gases. *Phys. Rev. Lett.* **110**, 145302 (2013).

12. 12.

Cercellier, H. et al. Evidence for an excitonic insulator phase in 1T-TiSe₂. *Phys. Rev. Lett.* **99**, 146403 (2007).

13. 13.

Seki, K. et al. Excitonic Bose-Einstein condensation in Ta₂NiSe₅. *Phys. Rev. B* **90**, 155116 (2014).

14. 14.

Du, L. et al. Evidence for a topological excitonic insulator in InAs/GaSb bilayers. *Nat. Commun.* **8**, 1971 (2017).

15. 15.

Xie, M. & MacDonald, A. H. Electrical reservoirs for bilayer excitons. *Phys. Rev. Lett.* **121**, 067702 (2018).

16. 16.

Zeng, Y. & MacDonald, A. H. Electrically controlled two-dimensional electron-hole fluids. *Phys. Rev. B* **102**, 085154 (2020).

17. 17.

Burg, G. W. et al. Strongly enhanced tunneling at total charge neutrality in double-bilayer graphene-WSe₂ heterostructures. *Phys. Rev. Lett.* **120**, 177702 (2018).

18. 18.

Su, J.-J. & MacDonald, A. H. How to make a bilayer exciton condensate flow. *Nat. Phys.* **4**, 799–802 (2008).

19. 19.

Yu, E. L. & Yudson, V. I. A new mechanism for superconductivity: pairing between spatially separated electrons and holes. *Zh. Eksp. Teor. Fiz.* **71**, 738–753 (1976).

20. 20.

Dolcini, F. et al. Blockade and counterflow supercurrent in exciton-condensate josephson junctions. *Phys. Rev. Lett.* **104**, 027004 (2010).

21. 21.

Halperin, B. I. & Rice, T. M. Possible anomalies at a semimetal-semiconductor transition. *Rev. Mod. Phys.* **40**, 755–766 (1968).

22. 22.

Kohn, W. & Sherrington, D. Two kinds of bosons and Bose condensates. *Rev. Mod. Phys.* **42**, 1–11 (1970).

23. 23.

Fogler, M. M., Butov, L. V. & Novoselov, K. S. High-temperature superfluidity with indirect excitons in van der Waals heterostructures. *Nat. Commun.* **5**, 4555 (2014).

24. 24.

Wu, F.-C., Xue, F. & MacDonald, A. H. Theory of two-dimensional spatially indirect equilibrium exciton condensates. *Phys. Rev. B* **92**, 165121 (2015).

25. 25.

Skinner, B. et al. Effect of dielectric response on the quantum capacitance of graphene in a strong magnetic field. *Phys. Rev. B* **88**, 155417 (2013).

26. 26.

Z. Sun, T. Kaneko, D. Golež, & Millis, A. J. Second order Josephson effect in excitonic insulators. *Phys. Rev. Lett.* **127**, 127702 (2021).

27. 27.

Wang, Z. et al. Evidence of high-temperature exciton condensation in two-dimensional atomic double layers. *Nature* **574**, 76–80 (2019).

28. 28.

Jauregui, L. A. et al. Electrical control of interlayer exciton dynamics in atomically thin heterostructures. *Science* **366**, 870–875 (2019).

29. 29.

Paik, E. Y. et al. Interlayer exciton laser of extended spatial coherence in atomically thin heterostructures. *Nature* **576**, 80–84 (2019).

30. 30.

Li, J. I. A., Taniguchi, T., Watanabe, K., Hone, J. & Dean, C. R. Excitonic superfluid phase in double bilayer graphene. *Nat. Phys.* **13**, 751–755 (2017).

31. 31.

Liu, X., Watanabe, K., Taniguchi, T., Halperin, B. I. & Kim, P. Quantum Hall drag of exciton condensate in graphene. *Nat. Phys.* **13**, 746–750 (2017).

32. 32.

Rivera, P. et al. Interlayer valley excitons in heterobilayers of transition metal dichalcogenides. *Nat. Nanotechnol.* **13**, 1004–1015 (2018).

33. 33.

Eisenstein, J. P., Pfeiffer, L. N. & West, K. W. Negative compressibility of interacting two-dimensional electron and quasiparticle gases. *Phys. Rev. Lett.* **68**, 674–677 (1992).

34. 34.

De Palo, S., Rapisarda, F. & Senatore, G. Excitonic condensation in a symmetric electron-hole bilayer. *Phys. Rev. Lett.* **88**, 206401 (2002).

35. 35.

López Ríos, P., Perali, A., Needs, R. J. & Neilson, D. Evidence from quantum Monte Carlo simulations of large-gap superfluidity and BCS-BEC crossover in double electron-hole layers. *Phys. Rev. Lett.* **120**, 177701 (2018).

36. 36.

Skinner, B. & Shklovskii, B. I. Anomalously large capacitance of a plane capacitor with a two-dimensional electron gas. *Phys. Rev. B* **82**, 155111 (2010).

37. 37.

Kagan, Y., Kashurnikov, V. A., Krasavin, A. V., Prokof'ev, N. V. & Svistunov, B. V. Quasicondensation in a two-dimensional interacting Bose gas. *Phys. Rev. A* **61**, 043608 (2000).

38. 38.

Xiaomeng Liu, J. I. A. et al. Crossover between strongly-coupled and weakly-coupled exciton superfluids. Preprint at <https://arxiv.org/abs/2012.05916> (2020).

39. 39.

Fallahazad, B. et al. Shubnikov-de Haas oscillations of high-mobility holes in monolayer and bilayer WSe₂: Landau level degeneracy, effective mass, and negative compressibility. *Phys. Rev. Lett.* **116**, 086601 (2016).

40. 40.

Larentis, S. et al. Large effective mass and interaction-enhanced Zeeman splitting of K-valley electrons in MoSe₂. *Phys. Rev. B* **97**, 201407 (2018).

41. 41.

Wang, L. et al. One-dimensional electrical contact to a two-dimensional material. *Science* **342**, 614–617 (2013).

42. 42.

Gong, C. et al. Band alignment of two-dimensional transition metal dichalcogenides: application in tunnel field effect transistors. *Appl. Phys. Lett.* **103**, 053513 (2013).

43. 43.

Ashoori, R. C. et al. Single-electron capacitance spectroscopy of discrete quantum levels. *Phys. Rev. Lett.* **68**, 3088–3091 (1992).

44. 44.

Young, A. F. & Levitov, L. S. Capacitance of graphene bilayer as a probe of layer-specific properties. *Phys. Rev. B* **84**, 085441 (2011).

45. 45.

Wilson, N. R. et al. Determination of band offsets, hybridization, and exciton binding in 2D semiconductor heterostructures. *Sci. Adv.* **3**, e1601832 (2017).

46. 46.

Mak, K. F. & Shan, J. Photonics and optoelectronics of 2D semiconductor transition metal dichalcogenides. *Nat. Photon.* **10**, 216–226 (2016).

47. 47.

Kim, K. et al. Band alignment in WSe₂–graphene heterostructures. *ACS Nano* **9**, 4527–4532 (2015).

48. 48.

Kosterlitz, J. M. & Thouless, D. J. Ordering, metastability and phase transitions in two-dimensional systems. *J. Phys. C Solid State Phys.* **6**, 1181–1203 (1973).

Acknowledgements

We thank E. J. Mueller and C. Dean for fruitful discussions. Research was supported by the US Department of Energy (DOE), Office of Science, Basic Energy Sciences (BES), under award numbers DE-SC0019481 (device fabrication and theoretical analysis) and DE-SC0022058 (optical characterization), the US Office of Naval Research under award number

N00014-21-1-2471 (data analysis) and the National Science Foundation (NSF) under DMR-2004451 (capacitance measurement). Growth of the hBN crystals was supported by the Elemental Strategy Initiative of MEXT, Japan and CREST (JPMJCR15F3), JST. This work was performed in part at the Cornell NanoScale Facility, an NNCI member supported by NSF Grant NNCI-2025233. K.F.M. acknowledges support from the David and Lucille Packard Fellowship.

Author information

Author notes

1. These authors contributed equally: Ligu Ma, Phuong X. Nguyen

Affiliations

1. School of Applied and Engineering Physics, Cornell University, Ithaca, NY, USA

Ligu Ma, Phuong X. Nguyen, Zefang Wang, Kin Fai Mak & Jie Shan

2. Department of Physics, University of Texas at Austin, Austin, TX, USA

Yongxin Zeng & Allan H. MacDonald

3. National Institute for Materials Science, Tsukuba, Japan

Kenji Watanabe & Takashi Taniguchi

4. Laboratory of Atomic and Solid State Physics, Cornell University, Ithaca, NY, USA

Kin Fai Mak & Jie Shan

5. Kavli Institute at Cornell for Nanoscale Science, Ithaca, NY, USA

Kin Fai Mak & Jie Shan

Contributions

L.M. and P.X.N. fabricated the devices, performed the measurements and analysed the data. Z.W. provided assistance in device fabrication. Y.Z. and A.H.M. provided theoretical support for the measurements. K.W. and T.T. grew the bulk hBN crystals. L.M., P.X.N., K.F.M. and J.S. designed the scientific objectives; K.F.M. and J.S. oversaw the project. All authors discussed the results and commented on the manuscript.

Corresponding authors

Correspondence to Kin Fai Mak or Jie Shan.

Ethics declarations

Competing interests

The authors declare no competing financial interests.

Additional information

Peer review information *Nature* thanks Raymond Ashoori, Denis Golez and the other, anonymous, reviewer(s) for their contribution to the peer review of this work. Peer reviewer reports are available.

Publisher's note Springer Nature remains neutral with regard to jurisdictional claims in published maps and institutional affiliations.

Extended data figures and tables

[Extended Data Fig. 1 Optical images of devices 1 and 2.](#)

a, b, Schematic cross-section (upper panels) and optical micrograph (lower panels) of device 1 (**a**) and device 2 (**b**). Constituent layers in the stack include WSe₂ monolayer (red line), MoSe₂ monolayer (yellow line), top

gate (TG, white dashed line), bottom gate (BG, white dash-dotted line) and local gate (LG Mo, white dotted line). The region of interest is shaded brown ('1'). In device 1, the TMD double layers are separated by a thick hBN spacer (blue line) in the contact region ('2'); the thin hBN spacer in the region of interest is not marked. Both electrons and holes are injected into '1' from '2' through one edge (solid black line). In device 2, electrons and holes are injected into '1' from the two long sides separately. The local gate is not shown in the schematics; it heavily dopes the isolated MoSe₂ region to form good contact to the metal electrode. The rectangular yellow bars are Pt electrodes. The scale bar is 5 μm.

Extended Data Fig. 2 Dependence of interlayer bandgap on anti-symmetric gating.

a, Gate dependence of penetration capacitance at 15 K under varying anti-symmetric gating Δ and $V_b = 0$ V. The step falls signify electron doping into the MoSe₂ conduction band (CB) or hole doping into the WSe₂ valence band (VB). The separation between the rising and falling edges determines the bandgap E_G . An additional (small) step on the electron-doping side arises from the presence of a small non-overlapped MoSe₂ monolayer inside the dual-gated device that affects the penetration capacitance. **b**, Interlayer bandgap E_G (symbols) extracted from **a** as a function of Δ . The linear fit (dashed line) has a slope of $\sim 0.21e$. The gap energy extrapolated for $\Delta = 0$ corresponds to the intrinsic bandgap energy \backslash $(\{E\}_{\{\rm G\}}^0 \approx 1.6\{\rm eV\})$.

Extended Data Fig. 3 Tunnelling current, exciton lifetime and electroluminescence (EL).

a, Bias dependence of interlayer tunnelling current of device 1 under anti-symmetric gating $\Delta = 4.6$ V (red), 4.25 V (blue), 4.00 V (black) and 3.75 V (green). The current onset is observed approximately when $eV_b \gtrsim E_G$. **b**, Interlayer tunnelling current over a large bias range at $\Delta = 4.3$ V. The insets illustrate the non-resonant (left) and resonant (right) tunnelling regimes. **c**, Estimated exciton lifetime as a function of V_b from the tunnelling data at Δ

$= 4.6$ V in **a**. **d**, Bias dependence of the EL spectrum (upper) and spectrally integrated EL intensity (lower). The data are acquired simultaneously with the tunnelling current in **b** at equal electron and hole densities at 30 K. The EL at 1.60–1.65 eV arises from intralayer exciton emission in MoSe₂; the feature below 1.60 eV is likely to originate from impurity bound states. Intralayer exciton emission from WSe₂ is not observed, presumably due to quenching from resonant energy transfer. The EL starts to emerge at bias voltages of roughly 1.7 V (red dashed line), when the device enters the resonant tunnelling regime. Both the tunnelling current and the EL intensity increases drastically above 1.7 V.

Extended Data Fig. 4 Determination of the charge gap.

a, b, The penetration capacitance (**a**) and the charge chemical potential of the double layer (**b**) at 15 K as a function of V_g at varying exciton densities. The capacitance peak shows the presence of a charge-incompressible state. The integrated area of the peak gives the chemical potential jump (or the charge gap) at equal electron–hole density. The zero point of the chemical potential shift in **b** has been shifted to $V_g = 0$ V for comparison of different exciton densities. The charge gap closes near the Mott density. **c, d**, Similar to **a, b**, at fixed exciton density $n_X = 2.4 \times 10^{11} \text{ cm}^{-2}$ for different temperatures. The charge gap closes at the ionization temperature.

Extended Data Fig. 5 Exciton compressibility in the high-temperature limit.

a, Inverse interlayer capacitance (or exciton compressibility) as a function of temperature at varying exciton densities. The lines are linear fits in the high-temperature limit, that is, $gn_X/k_B \lesssim T \lesssim T_s$. **b**, Amplitude of the extracted x intercept in **a** as a function of exciton density. A linear fit (blue) gives $g = (2.6 \pm 0.1) \times 10^{-14} \text{ eV cm}^2$. The inset shows the density dependence of the slope extracted from **a** (symbols). The red line is the mean-field result described in the main text. The density range is the same as in the main panel. The vertical error bars are the uncertainty of the linear

fit in **a**. The horizontal error bar is the typical uncertainty of the exciton density from the analysis shown in Fig. [1f](#).

Extended Data Fig. 6 Main results from device 2.

a, b, Normalized penetration capacitance (**a**) and interlayer capacitance (**b**) as a function of bias and gate voltages at 20 K. The Mo layer is grounded and the bias voltage is applied to the W layer. The two red dashed lines denote the conduction band edge of MoSe₂ (vertical line) and the valence band edge of WSe₂ (line with slope +1). The contour plot is flipped horizontally compared to Fig. [2](#) of the main text for device 1, in which the W layer is grounded and the bias voltage is applied to the Mo layer. There the valence band edge of WSe₂ corresponds a vertical line, and the conduction band edge of MoSe₂, a line with slope -1. The two white dashed lines denote the bias voltage at which the charge gap closes (I) and the exciton fluid becomes compressible (II). The difference between the two values (~40 mV) corresponds to the exciton binding energy in the limit of zero exciton density. The exciton binding energy in device 2 with a slightly thinner hBN spacer (roughly 5-layer) is larger than that in device 1 (approximately 25 mV).

Extended Data Fig. 7 Penetration and interlayer capacitances of device 3.

a, b, Penetration capacitance C_P (**a**) and interlayer capacitance C_I (**b**) as a function of bias and gate voltages at 10 K. The device is a MoS₂/WSe₂ double layer with the electron and hole contacts not close by. The Mo layer is grounded. The two red dashed lines denote the conduction band edge of MoS₂ (vertical line) and the valence band edge of WSe₂ (line with slope +1). The charge incompressible region is enclosed by red dashed lines. White dashed lines correspond to the bias voltages at which the charge gap closes and the exciton population is expected to appear, respectively. Exciton injection without creating free charges is not observed, corresponding to negligible C_I in the triangular region bound by the red and

white dashed lines. **c, d**, Same as **b** at 30 K and 50 K, respectively. Thermally assisted exciton injection is observed.

Extended Data Fig. 8 Circuit diagram.

a, Circuit diagram for the penetration capacitance measurement. The red dashed line encloses the sample area. The reference (V_{ref} and C_{ref}) is used to cancel the parasitic background capacitance. The HEMT is biased at voltage V_H . **b**, Equivalent circuit model of C_P in **a**. Here $C_g \approx 2C_{gg}$ is the sample-to-gate geometrical capacitance, which is about twice the gate-to-gate geometrical capacitance C_{gg} .

Extended Data Fig. 9 Equivalent device circuit model for electrostatics simulation.

$C_{Q,M}$ and $C_{Q,W}$ are the quantum capacitances of the MoSe₂ and WSe₂ monolayers, respectively. For details see [Methods](#).

Extended Data Fig. 10 Exciton entropy analysis.

a, Equation of state (chemical potential μ_X versus density n_X) for excitons at varying temperatures T . The data are obtained by integrating the measured interlayer capacitance with respect to exciton density. **b**, Exciton chemical potential of **a**, replotted as a function of temperature at varying exciton densities. **c**, Entropy change per exciton, $(\{\left(\frac{\partial S}{\partial n}\right)_T\})$, as a function of exciton density at varying temperatures (S denoting the 2D exciton entropy density). The data are obtained from **b** by applying the Maxwell's relation, $(\{\left(\frac{\partial \mu}{\partial T}\right)_X\}) = -(\{\left(\frac{\partial S}{\partial n}\right)_T\})$. As density increases, $(\{\left(\frac{\partial S}{\partial n}\right)_T\})$ drops rapidly, followed by a slow decrease. The crossover between the two regimes is correlated with the location of the compressibility peak in Fig. 4b of the main text. It corresponds to a crossover from a non-degenerate to a degenerate exciton fluid. In the latter, the density fluctuations are suppressed and the entropy

change per exciton is substantially reduced. No entropic signature of the 2D superfluid transition is observed. A broad entropy peak is observed near the Mott density, reflecting the presence of a low-temperature Mott critical point. Only a high-temperature crossover is accessed here.

Supplementary information

[Peer Review File](#)

Source data

[Source Data Fig. 1](#)

[Source Data Fig. 2](#)

[Source Data Fig. 3](#)

[Source Data Fig. 4](#)

Rights and permissions

[Reprints and Permissions](#)

About this article

Cite this article

Ma, L., Nguyen, P.X., Wang, Z. *et al.* Strongly correlated excitonic insulator in atomic double layers. *Nature* **598**, 585–589 (2021).
<https://doi.org/10.1038/s41586-021-03947-9>

- Received: 18 April 2021
- Accepted: 24 August 2021

- Published: 27 October 2021
- Issue Date: 28 October 2021
- DOI: <https://doi.org/10.1038/s41586-021-03947-9>

Share this article

Anyone you share the following link with will be able to read this content:

[Get shareable link](#)

Sorry, a shareable link is not currently available for this article.

[Copy to clipboard](#)

Provided by the Springer Nature SharedIt content-sharing initiative

[**A compact device sustains a fluid of bosons**](#)

- Denis Golež
- Zhiyuan Sun

News & Views 27 Oct 2021

This article was downloaded by **calibre** from <https://www.nature.com/articles/s41586-021-03947-9>

| [Section menu](#) | [Main menu](#) |

- Article
- [Published: 20 October 2021](#)

Copper-coordinated cellulose ion conductors for solid-state batteries

- [Chunpeng Yang](#) ORCID: [orcid.org/0000-0001-7075-3356¹](https://orcid.org/0000-0001-7075-3356)^{na1},
- [Qisheng Wu](#) ORCID: [orcid.org/0000-0001-9123-1864²](https://orcid.org/0000-0001-9123-1864)^{na1},
- [Weiqi Xie](#)¹^{na1},
- [Xin Zhang](#)¹,
- [Alexandra Brozena](#) ORCID: [orcid.org/0000-0002-5045-2123¹](https://orcid.org/0000-0002-5045-2123),
- [Jin Zheng](#)³,
- [Mounesha N. Garaga](#)⁴,
- [Byung Hee Ko](#) ORCID: [orcid.org/0000-0002-0934-5182⁵](https://orcid.org/0000-0002-0934-5182),
- [Yimin Mao](#)^{1,6},
- [Shuaiming He](#) ORCID: [orcid.org/0000-0002-6130-0352¹](https://orcid.org/0000-0002-6130-0352),
- [Yue Gao](#)¹,
- [Pengbo Wang](#) ORCID: [orcid.org/0000-0002-5740-6912³](https://orcid.org/0000-0002-5740-6912),
- [Madhusudan Tyagi](#)^{1,6},
- [Feng Jiao](#) ORCID: [orcid.org/0000-0002-3335-3203⁵](https://orcid.org/0000-0002-3335-3203),
- [Robert Briber](#)¹,
- [Paul Albertus](#) ORCID: [orcid.org/0000-0003-0072-0529⁷](https://orcid.org/0000-0003-0072-0529),
- [Chunsheng Wang](#) ORCID: [orcid.org/0000-0002-8626-6381⁷](https://orcid.org/0000-0002-8626-6381),
- [Steven Greenbaum](#)⁴,
- [Yan-Yan Hu](#)^{3,8},
- [Akira Isogai](#) ORCID: [orcid.org/0000-0001-8095-0441⁹](https://orcid.org/0000-0001-8095-0441),
- [Martin Winter](#)¹⁰,
- [Kang Xu](#) ORCID: [orcid.org/0000-0002-6946-8635¹¹](https://orcid.org/0000-0002-6946-8635),
- [Yue Qi](#) ORCID: [orcid.org/0000-0001-5331-1193²](https://orcid.org/0000-0001-5331-1193) &
- [Liangbing Hu](#) ORCID: [orcid.org/0000-0002-9456-9315^{1,12}](https://orcid.org/0000-0002-9456-9315)

[Nature](#) volume **598**, pages 590–596 (2021)

- 13k Accesses
- 218 Altmetric
- [Metrics details](#)

Subjects

- [Batteries](#)
- [Energy](#)

Abstract

Although solid-state lithium (Li)-metal batteries promise both high energy density and safety, existing solid ion conductors fail to satisfy the rigorous requirements of battery operations. Inorganic ion conductors allow fast ion transport, but their rigid and brittle nature prevents good interfacial contact with electrodes. Conversely, polymer ion conductors that are Li-metal-stable usually provide better interfacial compatibility and mechanical tolerance, but typically suffer from inferior ionic conductivity owing to the coupling of the ion transport with the motion of the polymer chains^{1,2,3}. Here we report a general strategy for achieving high-performance solid polymer ion conductors by engineering of molecular channels. Through the coordination of copper ions (Cu^{2+}) with one-dimensional cellulose nanofibrils, we show that the opening of molecular channels within the normally ion-insulating cellulose enables rapid transport of Li^+ ions along the polymer chains. In addition to high Li^+ conductivity (1.5×10^{-3} siemens per centimetre at room temperature along the molecular chain direction), the Cu^{2+} -coordinated cellulose ion conductor also exhibits a high transference number (0.78, compared with 0.2–0.5 in other polymers²) and a wide window of electrochemical stability (0–4.5 volts) that can accommodate both the Li-metal anode and high-voltage cathodes. This one-dimensional ion conductor also allows ion percolation in thick LiFePO_4 solid-state cathodes for application in batteries with a high energy density.

Furthermore, we have verified the universality of this molecular-channel engineering approach with other polymers and cations, achieving similarly high conductivities, with implications that could go beyond safe, high-performance solid-state batteries.

Access options

Subscribe to Journal

Get full journal access for 1 year

\$199.00

only \$3.90 per issue

[Subscribe](#)

All prices are NET prices.

VAT will be added later in the checkout.

Tax calculation will be finalised during checkout.

Rent or Buy article

Get time limited or full article access on ReadCube.

from \$8.99

[Rent or Buy](#)

All prices are NET prices.

Additional access options:

- [Log in](#)
- [Access through your institution](#)
- [Learn about institutional subscriptions](#)

Fig. 1: Structure and ion-transport performance of the Li–Cu–CNF solid-state ion conductor.

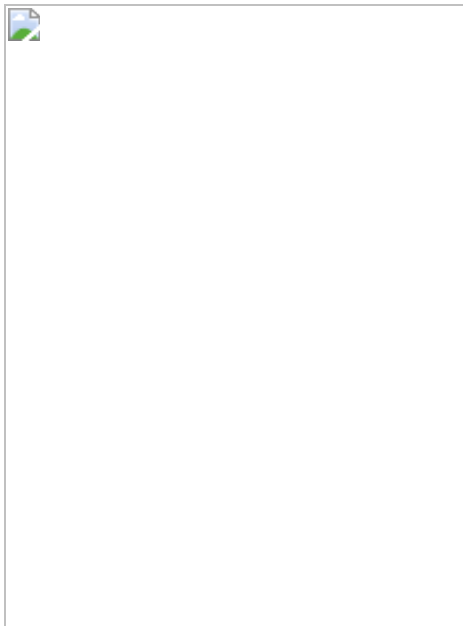


Fig. 2: Structural evolution during the synthesis of Li–Cu–CNF.

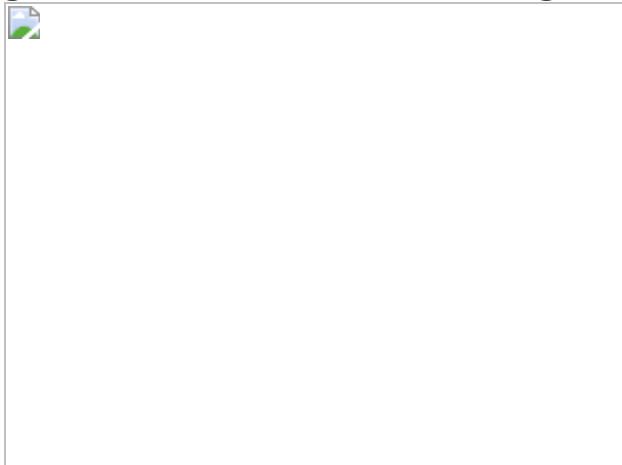


Fig. 3: Li⁺ conductivity and transport mechanism in Li–Cu–CNF.

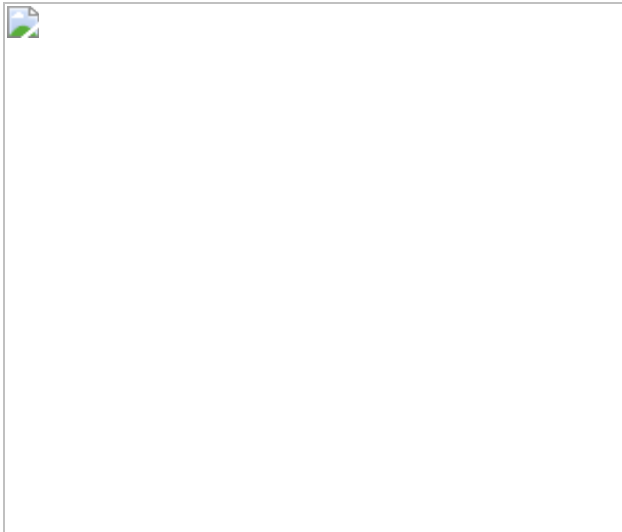
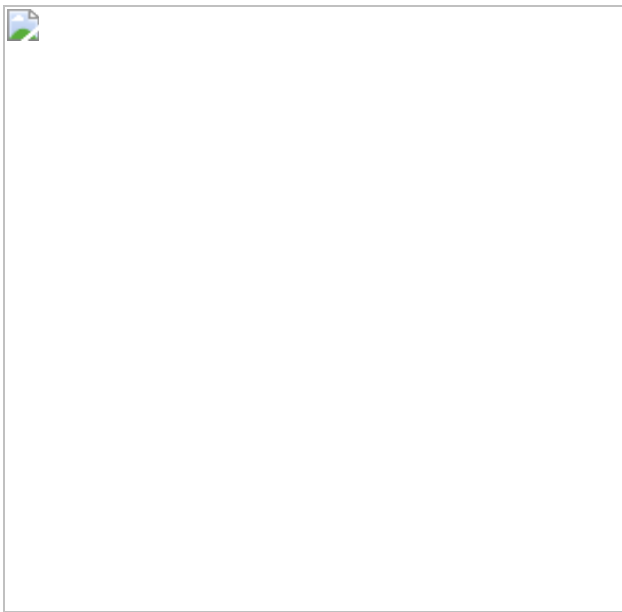


Fig. 4: Demonstration of solid-state Li metal batteries using the Li–Cu–CNF ion conductor.



Data availability

The data that support the findings of this study are available within this article and its [Supplementary Information](#). Additional data are available from the corresponding authors upon reasonable request. [Source data](#) are provided with this paper.

References

1. 1.

Xu, K. Nonaqueous liquid electrolytes for lithium-based rechargeable batteries. *Chem. Rev.* **104**, 4303–4418 (2004).

2. 2.

Long, L., Wang, S., Xiao, M. & Meng, Y. Polymer electrolytes for lithium polymer batteries. *J. Mater. Chem. A* **4**, 10038–10069 (2016).

3. 3.

Gadjourova, Z., Andreev, Y. G., Tunstall, D. P. & Bruce, P. G. Ionic conductivity in crystalline polymer electrolytes. *Nature* **412**, 520–523 (2001).

4. 4.

Croce, F., Appetecchi, G. B., Persi, L. & Scrosati, B. Nanocomposite polymer electrolytes for lithium batteries. *Nature* **394**, 456–458 (1998).

5. 5.

Manthiram, A., Yu, X. & Wang, S. Lithium battery chemistries enabled by solid-state electrolytes. *Nat. Rev. Mater.* **2**, 16103 (2017).

6. 6.

Lopez, J., Mackanic, D. G., Cui, Y. & Bao, Z. Designing polymers for advanced battery chemistries. *Nat. Rev. Mater.* **4**, 312–330 (2019).

7. 7.

Zhao, W., Yi, J., He, P. & Zhou, H. Solid-state electrolytes for lithium-ion batteries: fundamentals, challenges and perspectives. *Electrochem. Energ. Rev.* **2**, 574–605 (2019).

8. 8.

Diederichsen, K. M., McShane, E. J. & McCloskey, B. D. Promising routes to a high Li⁺ transference number electrolyte for lithium ion batteries. *ACS Energy Lett.* **2**, 2563–2575 (2017).

9. 9.

Xue, Z., He, D. & Xie, X. Poly(ethylene oxide)-based electrolytes for lithium-ion batteries. *J. Mater. Chem. A* **3**, 19218–19253 (2015).

10. 10.

Khurana, R., Schaefer, J. L., Archer, L. A. & Coates, G. W. Suppression of lithium dendrite growth using cross-linked polyethylene/poly(ethylene oxide) electrolytes: a new approach for practical lithium-metal polymer batteries. *J. Am. Chem. Soc.* **136**, 7395–7402 (2014).

11. 11.

Mackanic, D. G. et al. Crosslinked poly(tetrahydrofuran) as a loosely coordinating polymer electrolyte. *Adv. Energy Mater.* **8**, 1800703 (2018).

12. 12.

Pan, Q., Smith, D. M., Qi, H., Wang, S. & Li, C. Y. Hybrid electrolytes with controlled network structures for lithium metal batteries. *Adv. Mater.* **27**, 5995–6001 (2015).

13. 13.

Bouchet, R. et al. Single-ion BAB triblock copolymers as highly efficient electrolytes for lithium-metal batteries. *Nat. Mater.* **12**, 452–457 (2013).

14. 14.

Ma, Q. et al. Single lithium-ion conducting polymer electrolytes based on a super-delocalized polyanion. *Angew. Chem. Int. Edn* **55**, 2521–

2525 (2016).

15. 15.

Croce, F., Persi, L., Ronci, F. & Scrosati, B. Nanocomposite polymer electrolytes and their impact on the lithium battery technology. *Solid State Ion.* **135**, 47–52 (2000).

16. 16.

Liu, W., Lin, D., Sun, J., Zhou, G. & Cui, Y. Improved lithium ionic conductivity in composite polymer electrolytes with oxide-ion conducting nanowires. *ACS Nano* **10**, 11407–11413 (2016).

17. 17.

Wan, J. et al. Ultrathin, flexible, solid polymer composite electrolyte enabled with aligned nanoporous host for lithium batteries. *Nat. Nanotechnol.* **14**, 705–711 (2019).

18. 18.

Xu, H. et al. High-performance all-solid-state batteries enabled by salt bonding to perovskite in poly(ethylene oxide). *Proc. Natl Acad. Sci. USA* **116**, 18815–18821 (2019).

19. 19.

Lv, D. et al. Pure cellulose lithium-ion battery separator with tunable pore size and improved working stability by cellulose nanofibrils. *Carbohydr. Polym.* **251**, 116975 (2021).

20. 20.

Zhao, D. et al. Cellulose-based flexible functional materials for emerging intelligent electronics. *Adv. Mater.* **33**, 2000619 (2020).

21. 21.

Dahlström, C. et al. Ion conductivity through TEMPO-mediated oxidized and periodate oxidized cellulose membranes. *Carbohydr. Polym.* **233**, 115829 (2020).

22. 22.

Zugenmaier, P. *Crystalline Cellulose and Derivatives* 1st edn (Springer-Verlag, 2008).

23. 23.

Ogawa, Y. et al. Formation and stability of cellulose–copper–NaOH crystalline complex. *Cellulose* **21**, 999–1006 (2014).

24. 24.

Alava, M. & Niskanen, K. The physics of paper. *Rep. Prog. Phys.* **69**, 669–723 (2006).

25. 25.

Xie, J., Liang, Z. & Lu, Y.-C. Molecular crowding electrolytes for high-voltage aqueous batteries. *Nat. Mater.* **19**, 1006–1011 (2020).

26. 26.

Kimura, K., Motomatsu, J. & Tominaga, Y. Correlation between solvation structure and ion-conductive behavior of concentrated poly(ethylene carbonate)-based electrolytes. *J. Phys. Chem. C* **120**, 12385–12391 (2016).

27. 27.

Nair, J. R., Imholt, L., Brunklaus, G. & Winter, M. Lithium metal polymer electrolyte batteries: opportunities and challenges. *Electrochem. Soc. Interface* **28**, 55–61 (2019).

28. 28.

Shi, S., Qi, Y., Li, H. & Hector, L. G. Defect thermodynamics and diffusion mechanisms in Li_2CO_3 and implications for the solid electrolyte interphase in Li-ion batteries. *J. Phys. Chem. C* **117**, 8579–8593 (2013).

29. 29.

Zheng, J., Tang, M. & Hu, Y.-Y. Lithium ion pathway within $\text{Li}_7\text{La}_3\text{Zr}_2\text{O}_{12}$ -polyethylene oxide composite electrolytes. *Angew. Chem. Int. Edn* **55**, 12538–12542 (2016).

30. 30.

He, X., Zhu, Y., Epstein, A. & Mo, Y. Statistical variances of diffusional properties from ab initio molecular dynamics simulations. *NPJ Comput. Mater.* **4**, 18 (2018).

31. 31.

Kim, B., Lee, J. & Yu, I. Electrical properties of single-wall carbon nanotube and epoxy composites. *J. Appl. Phys.* **94**, 6724–6728 (2003).

32. 32.

Zeng, X.-X. et al. Reshaping lithium plating/stripping behavior via bifunctional polymer electrolyte for room-temperature solid Li metal batteries. *J. Am. Chem. Soc.* **138**, 15825–15828 (2016).

33. 33.

Qiu, J. et al. Enabling stable cycling of 4.2 V high-voltage all-solid-state batteries with PEO-based solid electrolyte. *Adv. Funct. Mater.* **30**, 1909392 (2020).

34. 34.

Saito, T., Kimura, S., Nishiyama, Y. & Isogai, A. Cellulose nanofibers prepared by TEMPO-mediated oxidation of native cellulose.

Biomacromolecules **8**, 2485–2491 (2007).

35. 35.

Ravel, B. & Newville, M. ATHENA, ARTEMIS, HEPHAESTUS: data analysis for X-ray absorption spectroscopy using IFEFFIT. *J. Synchrotron Radiat.* **12**, 537–541 (2005).

36. 36.

Wan, C. et al. Multinuclear NMR study of the solid electrolyte interface formed in lithium metal batteries. *ACS Appl. Mater. Interfaces* **9**, 14741–14748 (2017).

37. 37.

Zou, J., He, H., Dong, J. & Long, Y. A guest/host material of LiCl/H-STI (stilbite) zeolite assembly: preparation, characterization and humidity-sensitive properties. *J. Mater. Chem.* **14**, 2405–2411 (2004).

38. 38.

Zhou, X., Zhao, F., Guo, Y., Rosenberger, B. & Yu, G. Architecting highly hydratable polymer networks to tune the water state for solar water purification. *Sci. Adv.* **5**, eaaw5484 (2019).

39. 39.

Evans, J., Vincent, C. A. & Bruce, P. G. Electrochemical measurement of transference numbers in polymer electrolytes. *Polymer* **28**, 2324–2328 (1987).

40. 40.

Frisch, M. J. et al. Gaussian 16 Rev. AVX2 (Gaussian Inc., Wallingford, CT, 2016).

41. 41.

Adamo, C. & Barone, V. Toward reliable density functional methods without adjustable parameters: The PBE0 model. *J. Chem. Phys.* **110**, 6158–6170 (1999).

42. 42.

Grimme, S., Ehrlich, S. & Goerigk, L. Effect of the damping function in dispersion corrected density functional theory. *J. Comput. Chem.* **32**, 1456–1465 (2011).

43. 43.

BIOVIA. Materials Studio 7.0 (Dassault Systèmes, San Diego, CA, 2013).

44. 44.

Sun, H. et al. COMPASS II: extended coverage for polymer and drug-like molecule databases. *J. Mol. Model.* **22**, 47 (2016).

45. 45.

Nosé, S. A molecular dynamics method for simulations in the canonical ensemble. *Mol. Phys.* **52**, 255–268 (1984).

46. 46.

Berendsen, H. J. C., Postma, J. P. M., Gunsteren, W. F. V., DiNola, A. & Haak, J. R. Molecular dynamics with coupling to an external bath. *J. Chem. Phys.* **81**, 3684–3690 (1984).

47. 47.

Joly, Y. X-ray absorption near-edge structure calculations beyond the muffin-tin approximation. *Phys. Rev. B Condens. Matter Mater. Phys.* **63**, 125120 (2001).

48. 48.

Persson, I. et al. EXAFS study on the coordination chemistry of the solvated copper(II) ion in a series of oxygen donor solvents. *Inorg. Chem.* **59**, 9538–9550 (2020).

49. 49.

Schmidt, D. A. & Miki, K. Structural correlations in liquid water: a new interpretation of IR spectroscopy. *J. Phys. Chem. A* **111**, 10119–10122 (2007).

50. 50.

Wallace, V. M., Dhumal, N. R., Zehentbauer, F. M., Kim, H. J. & Kiefer, J. Revisiting the aqueous solutions of dimethyl sulfoxide by spectroscopy in the mid- and near-infrared: experiments and Car–Parrinello simulations. *J. Phys. Chem. B* **119**, 14780–14789 (2015).

51. 51.

Torres, J. et al. A neutron scattering and electron microscopy study of the structure, wetting, and freezing behavior of water near hydrophilic CuO-nanostructured surfaces. *J. Appl. Phys.* **125**, 025302 (2019).

Acknowledgements

L.H. and C.Y. acknowledge support from the University of Maryland A. James Clark School of Engineering. Q.W. and Y.Q. acknowledge support from the National Science Foundation (NSF) under grant DMR-2054438. Y.-Y.H. acknowledges support from the NSF under grant DMR-1847038. Solid-state NMR experiments were carried out at the National High Magnetic Field Laboratory, which is supported by the NSF through NSF/DMR-1644779 and the State of Florida. The NMR diffusion work at Hunter College was supported in part by the US Office of Naval Research, grant N00014-20-1-2186. This research used resources at the 8-ID Beamline of the National Synchrotron Light Source II, a US Department of Energy Office of Science User Facility operated by Brookhaven National Laboratory under contract no. DE-SC0012704. Access to the High Flux

Backscattering Spectrometer was provided by the Center for High Resolution Neutron Scattering, a partnership between the National Institute of Standards and Technology (NIST) and the NSF under agreement DMR-1508249. Certain commercial equipment, instruments and materials are identified in this paper in order to specify the experimental procedure adequately. Such identification is not intended to imply recommendation or endorsement by the NIST. K.X. acknowledges support from the Joint Centre for Energy Security Research (JCESR), an energy hub funded by the US Department of Energy, Office of Science, Basic Energy Science under IAA SN2020957. We thank F. Lin, D. Hou and Z. Yang from Virginia Tech for providing the NMC811 cathode material.

Author information

Author notes

1. These authors contributed equally: Chunpeng Yang, Qisheng Wu, Weiqi Xie

Affiliations

1. Department of Materials Science and Engineering, University of Maryland, College Park, MD, USA

Chunpeng Yang, Weiqi Xie, Xin Zhang, Alexandra Brozena, Yimin Mao, Shuaiming He, Yue Gao, Madhusudan Tyagi, Robert Briber & Liangbing Hu

2. School of Engineering, Brown University, Providence, RI, USA

Qisheng Wu & Yue Qi

3. Department of Chemistry and Biochemistry, Florida State University, Tallahassee, FL, USA

Jin Zheng, Pengbo Wang & Yan-Yan Hu

4. Department of Physics and Astronomy, Hunter College, City University of New York, New York, NY, USA

Mounesha N. Garaga & Steven Greenbaum

5. Center for Catalytic Science and Technology, Department of Chemical and Biomolecular Engineering, University of Delaware, Newark, DE, USA

Byung Hee Ko & Feng Jiao

6. NIST Center for Neutron Research, National Institute of Standards and Technology (NIST), Gaithersburg, MD, USA

Yimin Mao & Madhusudan Tyagi

7. Chemical and Biomolecular Engineering, University of Maryland, College Park, MD, USA

Paul Albertus & Chunsheng Wang

8. Center of Interdisciplinary Magnetic Resonance, National High Magnetic Field Laboratory, Tallahassee, FL, USA

Yan-Yan Hu

9. Laboratory of Cellulose Chemistry, Department of Biomaterial Sciences, The University of Tokyo, Tokyo, Japan

Akira Isogai

10. MEET Battery Research Center, Institute of Physical Chemistry, University of Münster, Münster, Germany

Martin Winter

11. Battery Science Branch, Energy Science Division, Sensor and Electron Devices Directorate, Army Research Laboratory, Adelphi, MD, USA

Kang Xu

12. Center for Materials Innovation, University of Maryland, College Park, MD, USA

Liangbing Hu

Contributions

L.H. conceived the SPE concept and supervised the project. C.Y. and W.X. designed the experiments and conducted the material synthesis, characterization and electrochemical tests. S.H. and Y.G. also contributed to the material synthesis. Y.Q. and Q.W. carried out the DFT and MD simulations and XANES calculation. X.Z. and R.B. contributed to the structural analysis. M.N.G. and S.G. carried out the NMR analysis and determination of the ion diffusion coefficient. J.Z., P.W. and Y.-Y.H. carried out the ${}^6\text{Li}$ NMR analysis. Y.M. and M.T. carried out the neutron-scattering characterization. B.H.K. and F.J. contributed to the XAS experiment. C.W. provided LiMn_2O_4 material and assisted with testing and evaluating the electrochemical stability window. L.H., C.Y., Y.Q., Q.W., A.B., C.W., A.I., P.A., K.X. and M.W. drafted the paper. All authors contributed to the final manuscript.

Corresponding authors

Correspondence to Yue Qi or Liangbing Hu.

Ethics declarations

Competing interests

The authors declare no competing interests.

Additional information

Peer review information *Nature* thanks Lynden Archer and the other, anonymous, reviewer(s) for their contribution to the peer review of this work.

Publisher's note Springer Nature remains neutral with regard to jurisdictional claims in published maps and institutional affiliations.

Extended data figures and tables

Extended Data Fig. 1 Structural characterization during the synthesis of Li–Cu–CNF.

a–d, Fibre XRD patterns of the CNFs (in the format of densified wood for high-resolution diffraction patterns) after the following treatment steps. **a**, Cu–CNF–NaOH obtained from Cu²⁺-saturated NaOH aqueous solution. Peaks are indexed on the basis of the literature²³. The (003) reflection is observed with a spacing of 0.51 nm, while the (001) and (002) reflections are absent, indicating that the Cu–CNF–NaOH features a threefold symmetric structure along the direction of the cellulose molecular chain. **b**, Cu–CNF washed with water to remove NaOH, demonstrating an amorphous structure. **c**, Cu–CNF after removing water by DMF exchange and evaporating DMF. The fibre XRD pattern shows a mostly amorphous structure with a small angle peak at roughly 2 nm corresponding to cellulose II²², possibly because of a small number of cellulose chains without coordinated Cu that form cellulose II after NaOH is removed. A high q peak at roughly 0.4 nm in the equatorial direction indicates the average molecular chain-to-chain distance of cellulose II. The green arrow in the meridian direction shows a peak corresponding to 0.47 nm in real space. The yellow arrows are pointing to peaks indicating the repeating unit of the Cu–CNF is roughly 1 nm along the cellulose chain. The 0.47 nm and 1 nm repeating distances are absent in all known cellulose structures, and therefore we attribute them to the unique structure of the Cu–CNF. **d**, Li–Cu–CNF after inserting Li⁺ in Cu–CNF and evaporating the solvent. The amorphous cellulose structure is maintained with some weak diffraction peaks of cellulose II. The yellow and green arrows indicate the same peaks as in **c**. **e–h**, XAS analysis of the Cu–CNF and Li–Cu–CNF samples. **e**, **f**,

Cu K-edge X-ray absorption near edge structure (XANES) spectra of: **e**, Cu–CNF, Li–Cu–CNF and a CuO standard; **f**, Cu₂O and Cu standard samples. The green dashed line shows the calculated XANES spectrum of Li–Cu–CNF, in good agreement with the experimentally measured spectrum. Cu–CNF and Li–Cu–CNF show similar yet broadened pre-edge peaks to CuO at 8,986 eV ($1s \rightarrow 3d$ transition), without the characteristic peaks of Cu₂O or Cu metal, indicating that the Cu ions in Cu–CNF and Li–Cu–CNF are of +2 valency. **g**, **h**, Fourier-transformed Cu K-edge extended X-ray absorption fine structure (EXAFS) spectra of: **g**, Cu–CNF; **h**, Li–Cu–CNF. On the basis of the EXAFS spectra, in Cu–CNF and Li–Cu–CNF, the Cu²⁺ are bonded with O atoms with an average bonding distance of 1.97 Å, consistent with that in reported Cu–organic complexes⁴⁸, indicating that the Cu²⁺ is coordinated with the hydroxyl groups of the cellulose molecules.

Extended Data Fig. 2 DFT calculations and MD simulations of the Li–Cu–CNF structure.

a, Assigned COMPASS II force-field types and atomic charges in typical cellulose units for MD simulations. **b**, Optimized atomic structures of the representative systems of Li–Cu–CNF used to evaluate interactions between Li⁺ and different oxygen-containing functional groups and water molecules, and corresponding energy–distance relationships for different Li⁺-bonding environments given by molecular mechanics calculations using COMPASS II FF and DFT calculations. The difference between the total system energy at $r = 10.0$ Å and the minimum energy is taken as the Li⁺-dissociation energy. The Li⁺ is strongly bonded with both anionic COO[−] and RO[−] groups with dissociation energies of more than 5.0 eV. The dissociation energy of the Li⁺ is roughly 3.0 eV for ROH and EO groups, and 1.5 eV for H₂O molecules. The strong interactions between the Li⁺ and one or two oxygen species in cellulose suggest slow Li⁺ movements in the absence of multiple Li–O coordination. In the H₂O molecule, the O atom has an atom type of *o2** and charge of −0.82 *e*, while the H atom has an atom type of *h1o* and a charge of +0.41 *e* for force-field calculations. **c**, To simulate Cu²⁺ coordination in cellulose, we optimized the atomic structure of two AGUs connected by one Cu²⁺ (Cu–(AGU)₂ system) to serve as a

structural building block. Two H atoms are deprotonated by the Cu. The average optimized Cu–O bond length (1.96 Å) is close to that observed in the experiment (1.97 Å), and the calculated XANES of the Cu–(AGU)₂ system is also in good agreement with the experimental measurement (Extended Data Fig. 1e), showing that our computational model for the structure of the Cu–O complex is reasonable. Atom types and atomic charges in force-field calculations are given for Cu and its connected O atoms, which are categorized as ROH for statistics (Fig. 3d in the main text). **d**, Top view of a 2 × 2 supercell of the periodic Cu-coordinated CNF structure as a starting structure for the simulation, built with the most reasonable model that we proposed on the basis of the fibre XRD pattern (Fig. 2c). Every two nearby cellulose chains are connected by one Cu atom through the hydroxyl oxygen atoms. The unit cell is denoted by dashed blue lines. **e**, Top and side views of the Cu–CNF–NaOH. **f**, Top and side views of the amorphous Cu–CNF obtained by removing NaOH aqueous solution from Cu–CNF–NaOH and then equilibrating the system with NPT dynamics simulations. In Cu–CNF, we reserved 144 H₂O molecules to keep an H₂O:AGU ratio of 1:1. **g**, Schematic of the computational approach used to obtain the atomic structure of the final amorphous Li–Cu–CNF model (top and side views).

Extended Data Fig. 3 Bound water analysis of Li–Cu–CNF.

a, ¹H MAS NMR spectra of Li–Cu–CNF with peak deconvolution. **b**, ¹H MAS NMR spectra of Cu–CNF (dried at 30 °C under vacuum for three days to remove water). **c**, FTIR of the pristine CNFs and solid-state Li–Cu–CNF. Both the pristine CNFs and Li–Cu–CNF show a broad –OH stretching peak at roughly 3,300 cm⁻¹. **d**, The –OH stretching peak of Li–Cu–CNF deconvoluted into three bands at 3,464 cm⁻¹, 3,235 cm⁻¹ and 2,886 cm⁻¹, which can be assigned to bound water molecules in different hydrogen-bonding states^{49,50}. **e**, The atomic mean square displacement (MSD) change in CNF and Li–Cu–CNF as a function of temperature, as measured by QENS. The Cu–CNF sample after DMF solvent exchange with some residual DMF (Cu–CNF–DMF) is also shown for comparison. **f**, Elastic neutron-scattering intensity of free water plotted against temperature (60 μl H₂O on Cu foil) upon cooling; data derived from ref. 51. **g**, DSC curve of

Li–Cu–CNF in a cooling process from 30 °C to –30 °C. **h**, Plots of H₂O–H₂O radial distribution function (RDF) (solid lines) and coordination number (dashed lines) in liquid bulk water (red lines) and Li–Cu–CNF (blue lines). The first minimum of the RDF plot for the liquid bulk water system at 3.4 Å (indicated by the black dashed line) was applied to calculate the coordination numbers. The distance is defined as the distance between the O atoms of the H₂O molecules. **i**, Stress–strain curve of Li–Cu–CNF along the direction of the CNF fibre. For more analysis, see Supplementary Discussion [11](#).

Extended Data Fig. 4 Electrochemical stability of Li–Cu–CNF.

a, b, The electrochemical stability window of Li–Cu–CNF was measured by both anodic and cathodic LSV scans at 0.1 mV s^{–1}. **a**, The first three anodic scans from OCV to 5.4 V. **b**, The first three cathodic scans from OCV to 0 V. **c**, Top, reduction and oxidation potentials (versus Li⁺/Li) obtained from DFT calculations for (bottom) different structures representative of the cellulose and Li–Cu–CNF systems, including: (1) glucose; (2) AGU dimer; (3) AGU–COOLi; (4, 5) two isomers of (AGU)₂–COOLi; (6) AGU–CH₂OLi; (7, 8) two isomers of (AGU)₂–CH₂OLi; (9) Cu–(AGU)₂; (10) H₂O dimer; and (11) (AGU)₂–(H₂O)₂. C, H, O, Li and Cu atoms are represented by grey, white, red, purple and blue spheres, respectively. Water molecules are depicted with stick models. The experimental oxidation potential for Li–Cu–CNF (black) and the redox potentials for EC are denoted with dashed lines (blue for reduction and red for oxidation) for reference. See Supplementary Discussion [12](#) for more detailed analysis.

Extended Data Fig. 5 Ionic conductivities and transference numbers of Li–Cu–CNF and Li–CNF.

a, Voltage profile of the galvanostatic Li plating and stripping between two ends of the Li–Cu–CNF with aligned cellulose fibres (length 1 cm) at 0.01 mA. **b**, EIS Nyquist plots of aligned Li–Cu–CNF materials of different lengths, ranging from 1 cm to 3 cm, for measuring the intrinsic conductivity

of Li–Cu–CNF along the direction of the cellulose molecular chain. **c**, Resistance corresponding to the high-frequency semi-circle in **b** of the aligned Li–Cu–CNF with different lengths. **d**, EIS Nyquist plots of the aligned Li–Cu–CNF with a length of 3 cm and cross-sectional area of 0.03 cm² at different temperatures, ranging from 10 °C to 60 °C. **e**, **f**, EIS Nyquist plots of the Li–Cu–CNF paper electrolyte (through-plane) at different temperatures (**e**, 60 °C to 0 °C; **f**, –2 °C to –20 °C); **g**, the corresponding temperature-dependent through-plane ionic conductivity of the Li–Cu–CNF paper electrolyte. **h**, d.c. polarization curve of the Cu²⁺ in the Li–Cu–CNF electrolyte in a Cu//Cu-CNF//Cu cell, showing that the Cu²⁺ conductivity is 1.0×10^{-8} S cm^{−1}, much lower than the Li⁺ conductivity in Li–Cu–CNF. **i**, Simulated structure of Li–CNF by MD. The Li–CNF system consists of 16 cellulose chains surrounded by Li⁺ and water molecules. Different chains are denoted by different colours. Li⁺ ions are indicated by purple spheres and water molecules as stick models. The size of the Li–CNF system is given roughly. The simulations show that, without the participation of Cu²⁺, the Li⁺ and water molecules adsorb only on the surface of the cellulose structures. **j**, d.c. polarization curve, and **k**, EIS Nyquist plots before and after polarization of the Li//Li–Cu–CNF//Li cell. **l**, d.c. polarization curve, and **m**, EIS Nyquist plots before and after polarization of the Li//Li–CNF//Li cell. **n**, Table showing the parameters measured by d.c. polarization and EIS for calculating the Li⁺-transference number.

Extended Data Fig. 6 NMR analysis of Li-coordination environments and diffusion pathways.

a, **b**, ⁶Li NMR spectra and simulations for: **a**, Li–Cu–CNF; **b**, Li–CNF. **c**, **d**, ⁶Li NMR spectra for: **c**, CH₂COOLi·2H₂O, and **d**, LiPF₆, as references for the COO···Li and LiPF₆ peak assignments in Li–Cu–CNF. **e**, **f**, ⁶Li NMR spectra and simulations for: **e**, Li–Cu–CNF, and **f**, Li–CNF after ⁶Li→⁷Li tracer exchange, which was performed by cycling either the Li–Cu–CNF or the Li–CNF electrolyte (natural abundance: 92.4% ⁷Li and 7.6% ⁶Li) between two ⁶Li-enriched metal electrodes (that is, symmetric ⁶Li//Li–Cu–CNF//⁶Li cells). **g**, Table showing the amount of Li⁺ in the different

chemical environments of Li–Cu–CNF and Li–CNF before and after ${}^6\text{Li} \rightarrow {}^7\text{Li}$ tracer exchange, derived from the relative spectral areal integrals of the ${}^6\text{Li}$ resonances in the NMR spectra shown in **a**, **b**, **e**, **f**. The normalized peak area for each sample (Li–Cu–CNF and Li–CNF, before and after ${}^6\text{Li} \rightarrow {}^7\text{Li}$ tracer exchange) can be quantitatively compared between different samples as the normalized peak area is proportional to the amount of ${}^6\text{Li}$ in each individual product. We took the total number of ${}^6\text{Li}$ in the pristine Li–Cu–CNF (before ${}^6\text{Li} \rightarrow {}^7\text{Li}$ tracer exchange) to be 100%, and calculated the ‘relative ${}^6\text{Li}$ number’ of each component by comparing the fitted peak area (Extended Data Fig. [6a](#), [b](#), [e](#), [f](#)) with the total area of ${}^6\text{Li}$ in the pristine Li–Cu–CNF (Extended Data Fig. [6a](#)).

Extended Data Fig. 7 Numerical analyses of MD simulations for Li^+ transport in Li–Cu–CNF.

a, Displacement plots for six Li^+ ions that have displacements of more than 15.0 Å in the simulated Li–Cu–CNF system (Fig. [2i](#)) with an $\text{H}_2\text{O}:AGU$ ratio of 1:1, and indexes of COO/RO atoms that are bonded to the six moving Li^+ ions (Li–O distance less than 2.5 Å). The different colours of the COO/RO atoms indicate they are from different cellulose chains. **b**, Coordination numbers of Li^+ ions coordinating with all available oxygen atoms (Li–O, including the oxygen atoms in cellulose and bound water molecules) and with just water molecules (Li– H_2O) for the six fastest and six slowest Li^+ ions in the Li–Cu–CNF system with an $\text{H}_2\text{O}:AGU$ ratio of 1:1. **c**, MSD plots for Li–Cu–CNF systems with different number of water molecules, and for the Li–CNF system with water molecules on the surface of the CNFs. **d**, Radial distribution functions (RDFs) for Li–Li and COO–RO pairs in Li–Cu–CNF with an $\text{H}_2\text{O}:AGU$ ratio of 1:1. The locations of the first peak of the Li–Li pair and the second peak of the COO–RO pair indicate the Li^+ hopping distance (roughly 3.0 Å) between the residence sites. The first peak of the COO–RO pair indicates the distance between the two O atoms within the same COO group. **e**, MSD plots for Li^+ , COO^- and RO^- groups and Cu^{2+} in the simulated Li–Cu–CNF system with an $\text{H}_2\text{O}:AGU$ ratio of 1:1. The average MSD plots show that Li^+ moves fast

while COO^- , RO^- , and Cu^{2+} in the Li–Cu–CNF backbone move much more slowly. For further analysis, see Supplementary Discussion 13.

Extended Data Fig. 8 The Li–Cu–CNF paper electrolyte and its electrochemical performance.

a, Top-view SEM image of the Li–Cu–CNF paper electrolyte. **b**, Digital photos (top and back) of a permeability test of the Li–Cu–CNF paper electrolyte to demonstrate the denseness. **c**, Li plating/stripping cycling performance of the Li–Cu–CNF paper electrolyte at 0.5 mA cm^{-2} , with 2 h for each plating/stripping half cycle, for a total of 300 h at room temperature. **d**, SEM image and **e**, corresponding EDX spectrum of the Li-metal anode after long-term cycling with the Li–Cu–CNF paper electrolyte. The SEM image of the cycled Li anode shows a fairly smooth surface without Cu particles deposited on the surface. The EDX shows no detectable Cu element on the Li surface, and instead only C, O, F and P, indicating the formation of a solid electrolyte interphase (SEI) on the Li-metal anode.

Extended Data Fig. 9 Demonstration using Li–Cu–CNF as a paper electrolyte and ion-conducting binder for solid-state LiFePO₄ batteries.

a, Fabrication steps for incorporating the cathode material (LiFePO_4 here) with the Li–Cu–CNF ion-conducting binder via the traditional slurry-casting method. The Cu–CNF suspension is first mixed with the cathode material, CNT additive and sodium alginate binder in an aqueous solution to obtain the cathode slurry. The slurry is then cast on aluminium foil using a doctor blade and vacuum dried at 35 °C. The cathode electrodes are then soaked in Li^+ electrolyte to achieve the insertion of Li^+ into the Cu–CNF, followed by vacuum drying to obtain solid electrodes containing the Li–Cu–CNF binder. **b**, **c**, EIS of the solid-state batteries using thick LiFePO_4 cathodes (roughly 120 μm), made by filtration-pressing with the addition of: **b**, Li–Cu–CNF; **c**, Li–CNF. **d**, A pouch solid-state battery made using a Li anode, the Li–Cu–CNF paper SPE, and a LiFePO_4 solid-state cathode

containing the Li–Cu–CNF ion-conducting binder, which shows good flexibility while still powering an LED light.

Extended Data Fig. 10 Electrochemical performances of high-voltage cathodes with the solid-state Li–Cu–CNF electrolyte.

a, b, Typical galvanostatic charge/discharge voltage profile of a solid-state NMC811 cathode with the Li–Cu–CNF electrolyte cycled at 100 mA g⁻¹ and room temperature (**a**); and its discharge capacities during cycling (**b**). **c, d**, Typical galvanostatic charge/discharge voltage profile of the solid-state LiMn₂O₄ cathode with the Li–Cu–CNF electrolyte cycled at 50 mA g⁻¹ and room temperature (**c**); and its discharge capacities during cycling (**d**).

Supplementary information

Supplementary Information

This file contains Supplementary Discussion, including Supplementary Figs. 1–21 and Supplementary Tables 1–8, and additional references.

Source data

Source Data Fig. 1

Source Data Fig. 3

Source Data Fig. 4

Rights and permissions

Reprints and Permissions

About this article

Cite this article

Yang, C., Wu, Q., Xie, W. *et al.* Copper-coordinated cellulose ion conductors for solid-state batteries. *Nature* **598**, 590–596 (2021). <https://doi.org/10.1038/s41586-021-03885-6>

- Received: 23 November 2020
- Accepted: 06 August 2021
- Published: 20 October 2021
- Issue Date: 28 October 2021
- DOI: <https://doi.org/10.1038/s41586-021-03885-6>

Share this article

Anyone you share the following link with will be able to read this content:

[Get shareable link](#)

Sorry, a shareable link is not currently available for this article.

[Copy to clipboard](#)

Provided by the Springer Nature SharedIt content-sharing initiative

[Expanding cellulose](#)

- Sang-Young Lee

News & Views 20 Oct 2021

This article was downloaded by **calibre** from <https://www.nature.com/articles/s41586-021-03885-6>

- Article
- [Published: 13 September 2021](#)

Multicomponent alkene azidoarylation by anion-mediated dual catalysis

- [Ala Bunescu¹](#),
- [Yusra Abdelhamid¹](#) &
- [Matthew J. Gaunt](#) [ORCID: orcid.org/0000-0002-7214-608X¹](#)

[Nature](#) volume **598**, pages 597–603 (2021)

- 9315 Accesses
- 25 Altmetric
- [Metrics details](#)

Subjects

- [Synthetic chemistry methodology](#)
- [Reaction mechanisms](#)

Abstract

Molecules that contain the β-arylethylamine motif have applications in the modulation of pain, treatment of neurological disorders and management of opioid addiction, among others, making it a privileged scaffold in drug discovery^{1,2}. De novo methods for their assembly are reliant on transformations that convert a small class of feedstocks into the target

compounds via time-consuming multistep syntheses^{3,4,5}. Synthetic invention can drive the investigation of the chemical space around this scaffold to further expand its capabilities in biology^{6,7,8,9}. Here we report the development of a dual catalysis platform that enables a multicomponent coupling of alkenes, aryl electrophiles and a simple nitrogen nucleophile, providing single-step access to synthetically versatile and functionally diverse β-arylethylamines. Driven by visible light, two discrete copper catalysts orchestrate aryl-radical formation and azido-group transfer, which underpin an alkene azidoarylation process. The process shows broad scope in alkene and aryl components and an azide anion performs a multifaceted role both as a nitrogen source and in mediating the redox-neutral dual catalysis via inner-sphere electron transfer^{10,11}. The synthetic capabilities of this anion-mediated alkene functionalization process are likely to be of use in a variety of pharmaceutically relevant and wider synthetic applications.

Access options

Subscribe to Journal

Get full journal access for 1 year

\$199.00

only \$3.90 per issue

[Subscribe](#)

All prices are NET prices.

VAT will be added later in the checkout.

Tax calculation will be finalised during checkout.

Rent or Buy article

Get time limited or full article access on ReadCube.

from \$8.99

[Rent or Buy](#)

All prices are NET prices.

Additional access options:

- [Log in](#)
- [Access through your institution](#)
- [Learn about institutional subscriptions](#)

Fig. 1: Background and concept.

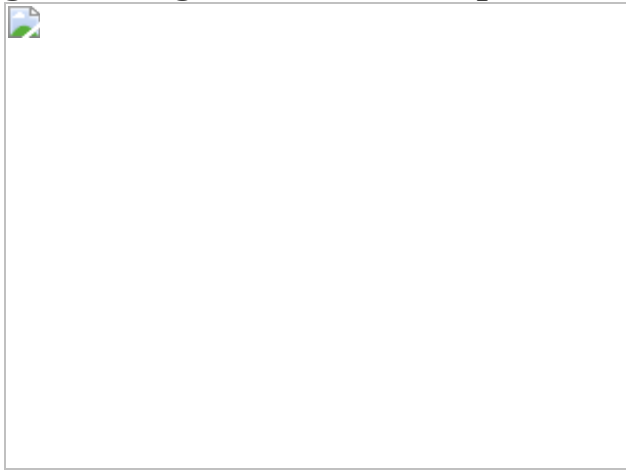


Fig. 2: Development of alkene azidoarylation reaction.

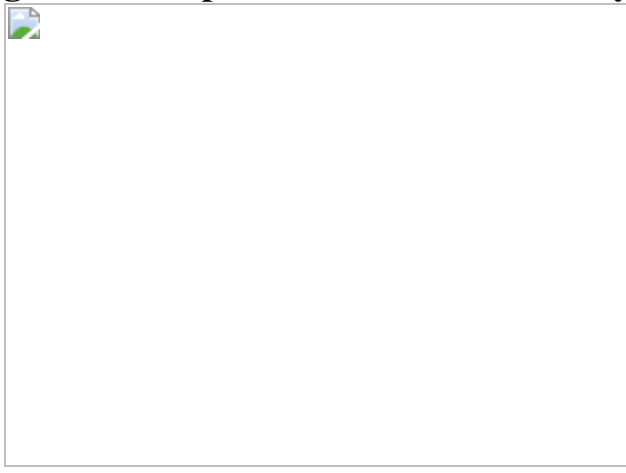


Fig. 3: Scope of alkene azidoarylation reaction.

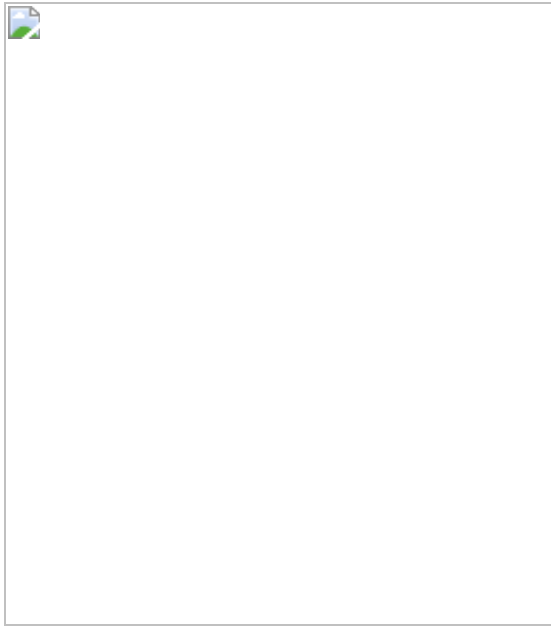


Fig. 4: Alkene azidoarylation as a powerful method to explore the chemical space around the Akt inhibitor CCT128930.

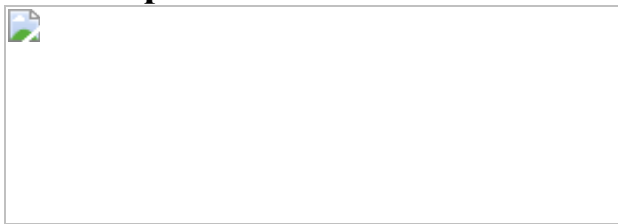
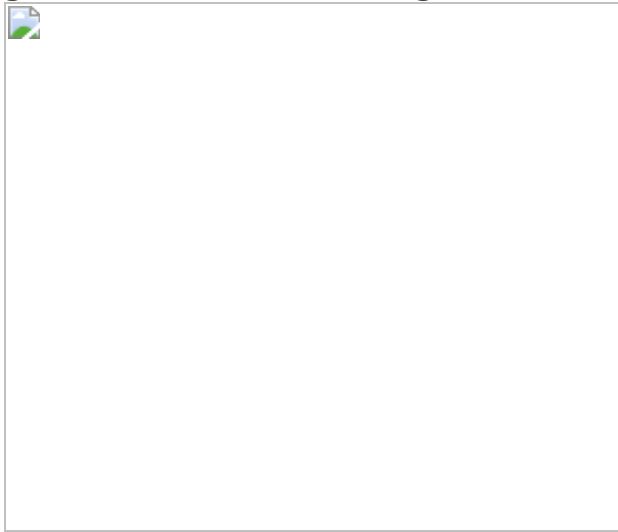


Fig. 5: Mechanistic investigation of the alkene azidoarylation reaction.



Data availability

Materials and methods, optimization studies, experimental procedures, mechanistic studies, ^1H NMR, ^{13}C NMR and ^{19}F NMR spectra, and high-resolution mass spectrometry, infrared, ultraviolet-visible and cyclic voltammetry data are available in the [Supplementary Information](#). Crystallographic data are available free of charge from the Cambridge Crystallographic Data Centre under the reference numbers CCDC 2027142, CCDC 2027143 and CCDC 2032989. Raw data are available from the corresponding author on reasonable request.

References

1. 1.
Freeman, S. & Alder, J. F. Arylethylamine psychotropic recreational drugs: a chemical perspective. *Eur. J. Med. Chem.* **37**, 527–539 (2002).
2. 2.
Dalley, J. W. & Everitt, B. J. Dopamine receptors in the learning, memory and drug reward circuitry. *Semin. Cell Dev. Biol.* **20**, 403–410 (2009).
3. 3.
Barton, D. H. R., Bracho, R. D. & Widdowson, D. A. A new β -arylethylamine synthesis by aryl aldehyde homologation. *J. Chem. Soc. Chem. Commun.* 781a–781a (1973).
4. 4.
Schulze, M. Synthesis of 2-arylethylamines by the curtius rearrangement. *Synth. Commun.* **40**, 1461–1476 (2010).
5. 5.
Bracher, F. Methods for arylation of amines and heteroarenes. *SynOpen* **02**, 0096–0104 (2018).

6. 6.

Müller, T. E., Hultzsch, K. C., Yus, M., Foubelo, F. & Tada, M. Hydroamination: direct addition of amines to alkenes and alkynes. *Chem. Rev.* **108**, 3795–3892 (2008).

7. 7.

Nguyen, T. M., Manohar, N. & Nicewicz, D. A. Anti-Markovnikov hydroamination of alkenes catalyzed by a two-component organic photoredox system: direct access to phenethylamine derivatives. *Angew. Chem. Int. Edn* **53**, 6198–6201 (2014).

8. 8.

Boyington, A. J., Seath, C. P., Zearfoss, A. M., Xu, Z. & Jui, N. T. Catalytic strategy for regioselective arylethylamine synthesis. *J. Am. Chem. Soc.* **141**, 4147–4153 (2019).

9. 9.

Estrada, J. G., Williams, W. L., Ting, S. I. & Doyle, A. G. Role of electron-deficient olefin ligands in a Ni-catalyzed aziridine cross-coupling to generate quaternary carbons. *J. Am. Chem. Soc.* **142**, 8928–8937 (2020).

10. 10.

Haim, A. Role of the bridging ligand in inner-sphere electron-transfer reactions. *Acc. Chem. Res.* **8**, 264–272 (1975).

11. 11.

Rorabacher, D. B. Electron transfer by copper centers. *Chem. Rev.* **104**, 651–698 (2004).

12. 12.

Zeng, W. & Chemler, S. R. Copper(II)-catalyzed enantioselective intramolecular carboamination of alkenes. *J. Am. Chem. Soc.* **129**, 12948–12949 (2007).

13. 13.

Zhang, G., Cui, L., Wang, Y. & Zhang, L. Homogeneous gold-catalyzed oxidative carboheterofunctionalization of alkenes. *J. Am. Chem. Soc.* **132**, 1474–1475 (2010).

14. 14.

Brenzovich, W. E. Jr et al. Gold-catalyzed intramolecular aminoarylation of alkenes: C–C bond formation through bimolecular reductive elimination. *Angew. Chem. Int. Edn* **49**, 5519–5522 (2010).

15. 15.

Schultz, D. M. & Wolfe, J. P. Recent developments in palladium-catalyzed alkene aminoarylation reactions for the synthesis of nitrogen heterocycles. *Synthesis* **44**, 351–361 (2012).

16. 16.

Yang, H.-B., Pathipati, S. R. & Selander, N. Nickel-catalyzed 1,2-aminoarylation of oxime ester-tethered alkenes with boronic acids. *ACS Catal.* **7**, 8441–8445 (2017).

17. 17.

Lerchen, A., Knecht, T., Daniliuc, C. G. & Glorius, F. Unnatural amino acid synthesis enabled by the regioselective cobalt(III)-catalyzed intermolecular carboamination of alkenes. *Angew. Chem. Int. Edn* **55**, 15166–15170 (2016).

18. 18.

Liu, Z. et al. Catalytic intermolecular carboamination of unactivated alkenes via directed aminopalladation. *J. Am. Chem. Soc.* **139**, 11261–

11270 (2017).

19. 19.

van der Puyl, V. A., Derosa, J. & Engle, K. M. Directed, nickel-catalyzed umpolung 1,2-carboamination of alkenyl carbonyl compounds. *ACS Catal.* **9**, 224–229 (2019).

20. 20.

Jiang, H. & Studer, A. Intermolecular radical carboamination of alkenes. *Chem. Soc. Rev.* **49**, 1790–1811 (2020).

21. 21.

Monos, T. M., McAtee, R. C. & Stephenson, C. R. J. Arylsulfonylacetamides as bifunctional reagents for alkene aminoarylation. *Science* **361**, 1369–1373 (2018).

22. 22.

Wang, D. et al. Asymmetric copper-catalyzed intermolecular aminoarylation of styrenes: efficient access to optical 2,2-diarylethylamines. *J. Am. Chem. Soc.* **139**, 6811–6814 (2017).

23. 23.

Heinrich, M. R., Blank, O. & Wölfel, S. Reductive carbodiazenylation of nonactivated olefins via aryl diazonium salts. *Org. Lett.* **8**, 3323–3325 (2006).

24. 24.

Fumagalli, G., Boyd, S. & Greaney, M. F. Oxyarylation and aminoarylation of styrenes using photoredox catalysis. *Org. Lett.* **15**, 4398–4401 (2013).

25. 25.

PrasadHari, D., Hering, T. & König, B. The photoredox-catalyzed meerwein addition reaction: intermolecular amino-arylation of alkenes. *Angew. Chem. Int. Edn* **53**, 725–728 (2014).

26. 26.

Cativiela, C. & Díaz-de-Villegas, M. D. Recent progress on the stereoselective synthesis of acyclic quaternary α -amino acids. *Tetrahedron Asymmetry* **18**, 569–623 (2007).

27. 27.

Venkatraman, J., Shankaramma, S. C. & Balaram, P. Design of folded peptides. *Chem. Rev.* **101**, 3131–3152 (2001).

28. 28.

Hager, A., Vrielink, N., Hager, D., Lefranc, J. & Trauner, D. Synthetic approaches towards alkaloids bearing α -tertiary amines. *Nat. Prod. Rep.* **33**, 491–522 (2016).

29. 29.

Clayden, J., Donnard, M., Lefranc, J. & Tetlow, D. J. Quaternary centres bearing nitrogen (α -tertiary amines) as products of molecular rearrangements. *Chem. Commun.* **47**, 4624–4639 (2011).

30. 30.

Leggans, E. K., Barker, T. J., Duncan, K. K. & Boger, D. L. Iron(III)/NaBH₄-mediated additions to unactivated alkenes: synthesis of novel 20'-vinblastine analogues. *Org. Lett.* **14**, 1428–1431 (2012).

31. 31.

Huang, X., Bergsten, T. M. & Groves, J. T. Manganese-catalyzed late-stage aliphatic C–H azidation. *J. Am. Chem. Soc.* **137**, 5300–5303 (2015).

32. 32.

Bunescu, A., Ha, T. M., Wang, Q. & Zhu, J. Copper-catalyzed three-component carboazidation of alkenes with acetonitrile and sodium azide. *Angew. Chem. Int. Edn* **56**, 10555–10558 (2017).

33. 33.

Fu, N., Sauer, G. S., Saha, A., Loo, A. & Lin, S. Metal-catalyzed electrochemical diazidation of alkenes. *Science* **357**, 575–579 (2017).

34. 34.

Heinrich, M. R. Intermolecular olefin functionalisation involving aryl radicals generated from arenediazonium salts. *Chem. Eur. J.* **15**, 820–833 (2009).

35. 35.

Fischer, H. & Radom, L. Factors controlling the addition of carbon-centered radicals to alkenes—an experimental and theoretical perspective. *Angew. Chem. Int. Edn* **40**, 1340–1371 (2001).

36. 36.

Odian, G. in *Principles of Polymerization* (ed. Odian, G.) 198–349 (Wiley, 2004); <https://doi.org/10.1002/047147875X.ch3>.

37. 37.

Tang, W. et al. Understanding atom transfer radical polymerization: effect of ligand and initiator structures on the equilibrium constants. *J. Am. Chem. Soc.* **130**, 10702–10713 (2008).

38. 38.

Qiu, J., Matyjaszewski, K., Thouin, L. & Amatore, C. Cyclic voltammetric studies of copper complexes catalyzing atom transfer

radical polymerization. *Macromol. Chem. Phys.* **201**, 1625–1631 (2000).

39. 39.

Caldwell, J. J. et al. Identification of 4-(4-aminopiperidin-1-yl)-7*H*-pyrrolo[2,3-*d*]pyrimidines as selective inhibitors of protein kinase B through fragment elaboration. *J. Med. Chem.* **51**, 2147–2157 (2008).

40. 40.

Addie, M. et al. Discovery of 4-amino-*N*[(1*S*)-1-(4-chlorophenyl)-3-hydroxypropyl]-1-(7*H*-pyrrolo[2,3-*d*]pyrimidin-4-yl)piperidine-4-carboxamide (AZD5363), an orally bioavailable, potent inhibitor of Akt kinases. *J. Med. Chem.* **56**, 2059–2073 (2013).

41. 41.

Goel, P. et al. Recent advancement of piperidine moiety in treatment of cancer—a review. *Eur. J. Med. Chem.* **157**, 480–502 (2018).

42. 42.

Suh, S.-E. et al. Site-selective copper-catalyzed azidation of benzylic C–H bonds. *J. Am. Chem. Soc.* **142**, 11388–11393 (2020).

43. 43.

Alfassi, Z. B., Harriman, A., Huie, R. E., Mosseri, S. & Neta, P. The redox potential of the azide/azidyl couple. *J. Phys. Chem.* **91**, 2120–2122 (1987).

44. 44.

Pavlishchuk, V. V. & Addison, A. W. Conversion constants for redox potentials measured versus different reference electrodes in acetonitrile solutions at 25 °C. *Inorg. Chim. Acta* **298**, 97–102 (2000).

45. 45.

Bard, A. *Standard Potentials in Aqueous Solution* (Routledge, 1985).

46. 46.

Zhou, J. & Fu, G. C. Cross-couplings of unactivated secondary alkyl halides: room-temperature nickel-catalyzed Negishi reactions of alkyl bromides and iodides. *J. Am. Chem. Soc.* **125**, 14726–14727 (2003).

47. 47.

Wang, Z., Yin, H. & Fu, G. C. Catalytic enantioconvergent coupling of secondary and tertiary electrophiles with olefins. *Nature* **563**, 379–383 (2018).

Acknowledgements

We thank the Herchel Smith Fund at the University of Cambridge for a postdoctoral fellowship to A.B., the AstraZeneca–University of Cambridge PhD programme for studentship (Y.A.) and the Royal Society for Wolfson Merit Award to M.J.G.

Author information

Affiliations

1. Yusuf Hamied Department of Chemistry, University of Cambridge, Cambridge, UK

Ala Bunescu, Yusra Abdelhamid & Matthew J. Gaunt

Contributions

A.B. and M.J.G. conceived the project. A.B. and Y.A. conducted the experiments. A.B., Y.A. and M.J.G. analysed and interpreted the results. A.B., Y.A. and M.J.G. wrote the manuscript.

Corresponding author

Correspondence to Matthew J. Gaunt.

Ethics declarations

Competing interests

The authors declare no competing interests.

Additional information

Peer review information *Nature* thanks the anonymous reviewer(s) for their contribution to the peer review of this work. Peer reviewer reports are available.

Publisher's note Springer Nature remains neutral with regard to jurisdictional claims in published maps and institutional affiliations.

Supplementary information

[Supplementary Information](#)

This file contains Supplementary Text, Materials and Methods, Figs. 1–40, Tables 1–10 and Refs. 1–155.

[Peer Review File](#)

Rights and permissions

[Reprints and Permissions](#)

About this article

Cite this article

Bunescu, A., Abdelhamid, Y. & Gaunt, M.J. Multicomponent alkene azidoarylation by anion-mediated dual catalysis. *Nature* **598**, 597–603 (2021). <https://doi.org/10.1038/s41586-021-03980-8>

- Received: 16 April 2021
- Accepted: 01 September 2021
- Published: 13 September 2021
- Issue Date: 28 October 2021
- DOI: <https://doi.org/10.1038/s41586-021-03980-8>

Share this article

Anyone you share the following link with will be able to read this content:

[Get shareable link](#)

Sorry, a shareable link is not currently available for this article.

[Copy to clipboard](#)

Provided by the Springer Nature SharedIt content-sharing initiative

This article was downloaded by **calibre** from <https://www.nature.com/articles/s41586-021-03980-8>

- Article
- [Published: 27 October 2021](#)

A global inventory of photovoltaic solar energy generating units

- [L. Kruitwagen](#) [ORCID: orcid.org/0000-0003-2663-395X¹](#),
- [K. T. Story²](#),
- [J. Friedrich](#) [ORCID: orcid.org/0000-0002-7156-532X³](#),
- [L. Byers](#) [ORCID: orcid.org/0000-0002-8178-2483³](#),
- [S. Skillman](#) [ORCID: orcid.org/0000-0002-7626-522X²](#) &
- [C. Hepburn](#) [ORCID: orcid.org/0000-0003-0467-7441¹](#)

[Nature](#) volume 598, pages 604–610 (2021)

- 1267 Accesses
- 205 Altmetric
- [Metrics details](#)

Subjects

- [Climate-change mitigation](#)
- [Energy policy](#)
- [Environmental impact](#)
- [Power stations](#)

Abstract

Photovoltaic (PV) solar energy generating capacity has grown by 41 per cent per year since 2009¹. Energy system projections that mitigate climate

change and aid universal energy access show a nearly ten-fold increase in PV solar energy generating capacity by 2040^{2,3}. Geospatial data describing the energy system are required to manage generation intermittency, mitigate climate change risks, and identify trade-offs with biodiversity, conservation and land protection priorities caused by the land-use and land-cover change necessary for PV deployment. Currently available inventories of solar generating capacity cannot fully address these needs^{1,2,3,4,5,6,7,8,9}. Here we provide a global inventory of commercial-, industrial- and utility-scale PV installations (that is, PV generating stations in excess of 10 kilowatts nameplate capacity) by using a longitudinal corpus of remote sensing imagery, machine learning and a large cloud computation infrastructure. We locate and verify 68,661 facilities, an increase of 432 per cent (in number of facilities) on previously available asset-level data. With the help of a hand-labelled test set, we estimate global installed generating capacity to be 423 gigawatts ($-75/+77$ gigawatts) at the end of 2018. Enrichment of our dataset with estimates of facility installation date, historic land-cover classification and proximity to vulnerable areas allows us to show that most of the PV solar energy facilities are sited on cropland, followed by aridlands and grassland. Our inventory could aid PV delivery aligned with the Sustainable Development Goals.

Access options

Subscribe to Journal

Get full journal access for 1 year

\$199.00

only \$3.90 per issue

[Subscribe](#)

All prices are NET prices.

VAT will be added later in the checkout.

Tax calculation will be finalised during checkout.

Rent or Buy article

Get time limited or full article access on ReadCube.

from \$8.99

[Rent or Buy](#)

All prices are NET prices.

Additional access options:

- [Log in](#)
- [Access through your institution](#)
- [Learn about institutional subscriptions](#)

Fig. 1: Solar PV facilities are detected in remote sensing imagery with machine learning.

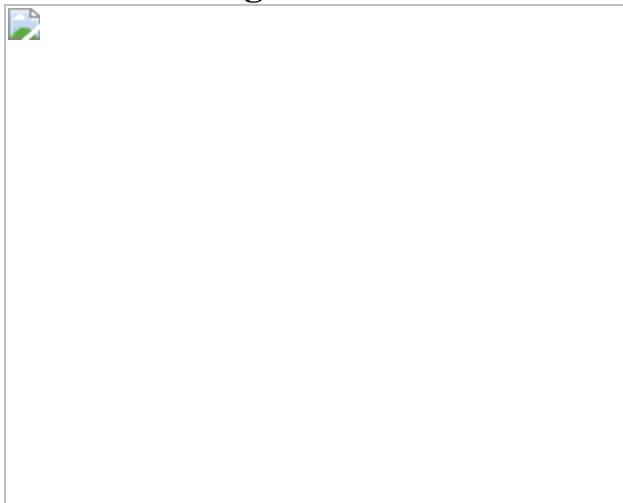


Fig. 2: Aggregated arrangement of the global dataset.

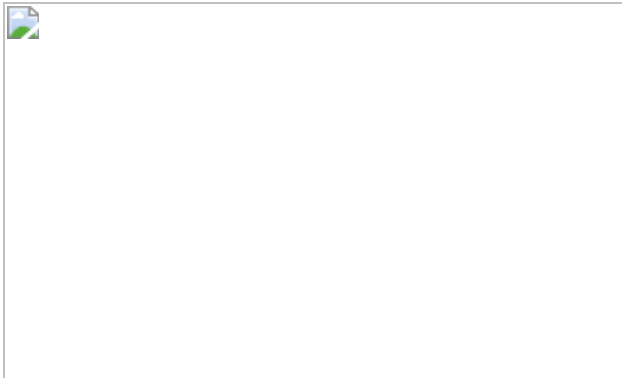


Fig. 3: Pre-existing land cover for new solar PV installations.



Data availability

The dataset is publicly hosted on Zenodo and is available at
<https://zenodo.org/record/5005868>

or <https://doi.org/10.5281/zenodo.5005868>. It will also be visualized and available for download via the World Resources Institute Resource Watch, and the Descartes Labs platform. [Source data](#) are provided with this paper.

Code availability

The code repository is publicly hosted on Github at
<https://github.com/Lkruitwagen/solar-pv-global-inventory>. The code release for this publication is version 1.0.0 and is also hosted on Zenodo at
<https://doi.org/10.5281/zenodo.5045001>.

References

1. 1.

Statistical Review of World Energy 2018 (BP plc., 2018).

2. 2.

World Energy Outlook 2018 (International Energy Agency, 2018).

3. 3.

Renewable Capacity Statistics 2019 (International Renewable Energy Agency, 2019).

4. 4.

Byers, L. et al. *A Global Database of Power Plants* (World Resources Institute, 2018).

5. 5.

Barbose, G. & Darghouth, N. *Tracking the Sun* (Berkeley Lab, 2019);
<https://openpv.nrel.gov/tracking-the-sun>

6. 6.

Yu, J., Wang, Z., Majumdar, A. & Rajagopal, R. DeepSolar: a machine learning framework to efficiently construct a solar deployment database in the United States. *Joule* **2**, 2605–2617 (2018).

7. 7.

Hou, X. et al. Solarnet: a deep learning framework to map solar plants in China from satellite imagery. In *ICLR 2020 Workshop on Tackling Climate Change with Machine Learning* (ICLR, 2020);
<https://www.climatechange.ai/papers/iclr2020/6.html>

8. 8.

Platts, S. G. *World Electric Power Plant Database* (2018);
<https://www.spglobal.com/platts/en/products-services/electric-power/world-electric-power-plants-database>

9. 9.

Electric Plants (IHSMarkit, 2020);
<https://catalogue.datalake.ihsmarkit.com/>

10. 10.

Renewables 2019 (International Energy Agency, 2019);
<https://www.iea.org/reports/renewables-2019>

11. 11.

Bolinger, M., Seel, J. & Robson, D. *Utility-Scale Solar: Empirical Trends in Project Technology, Cost, Performance, and PPA Pricing in the United States* (Berkeley Lab, 2019).

12. 12.

Fukushima, K. Neocognitron: a self-organizing neural network model for a mechanism of pattern recognition unaffected by shift in position. *Biol. Cybern.* **36**, 193–202 (1980).

13. 13.

LeCun, Y. et al. Backpropagation applied to handwritten zip code recognition. *Neural Comput.* **1**, 541–551 (1989).

14. 14.

Krizhevsky, A., Sutskever, I. & Hinton, G. E. Imagenet classification with deep convolutional neural networks. In *Proc. 25th International Conference on Neural Information Processing Systems (NIPS'12)* Vol. 1, 1097–1105 (Curran Associates Inc., 2012).

15. 15.

Zhang, Z., Liu, Q. & Wang, Y. Road extraction by deep residual U-Net. *IEEE Geosci. Remote Sens. Lett.* **15**, 749–753 (2018).

16. 16.

Ishii, T. et al. Detection by classification of buildings in multispectral satellite imagery. In *2016 23rd International Conference on Pattern Recognition (ICPR)* 3344–3349 (IEEE, 2016).

17. 17.

Audebert, N., Le Saux, B. & Lefévre, S. Beyond RGB: very high resolution urban remote sensing with multimodal deep networks. *ISPRS J. Photogramm. Remote Sens.* **140**, 20–32 (2018).

18. 18.

Zuo, J., Xu, G., Fu, K., Sun, X. & Sun, H. Aircraft type recognition based on segmentation with deep convolutional neural networks. *IEEE Geosci. Remote Sens. Lett.* **15**, 282–286 (2018).

19. 19.

Bentes, C., Velotto, D. & Tings, B. Ship classification in TerraSAR-X images with convolutional neural networks. *IEEE J. Ocean. Eng.* **43**, 258–266 (2018).

20. 20.

Gray, M., Watson, L., Ljungwaldh, S. & Morris, E. *Nowhere to Hide: Using Satellite Imagery to Estimate the Utilisation of Fossil Fuel Power Plants* (Carbon Tracker, 2018);
<https://www.carbontracker.org/reports/nowhere-to-hide/>

21. 21.

Wang, A. X., Tran, C., Desai, N., Lobell, D. & Ermon, S. Deep transfer learning for crop yield prediction with remote sensing data. In

Proc. 1st ACM SIGCAS Conference on Computing and Sustainable Societies 50 (ACM, 2018).

22. 22.

Wang, H. et al. Deep learning based ensemble approach for probabilistic wind power forecasting. *Appl. Energy* **188**, 56–70 (2017).

23. 23.

Imamoglu, N., Kimura, M., Miyamoto, H., Fujita, A. & Nakamura, R. Solar power plant detection on multi-spectral satellite imagery using weakly-supervised CNN with feedback features and m-PCNN fusion. Preprint at <https://arXiv.org/abs/1704.06410> (2017).

24. 24.

Malof, J. M., Bradbury, K., Collins, L. M. & Newell, R. G. Automatic detection of solar photovoltaic arrays in high resolution aerial imagery. *Appl. Energy* **183**, 229–240 (2016).

25. 25.

Camilo, J. A., Wang, R., Collins, L. M., Bradbury, K. & Malof, J. M. Application of a semantic segmentation convolutional neural network for accurate automatic detection and mapping of solar photovoltaic arrays in aerial imagery. Preprint at <https://arxiv.org/abs/1801.04018> (2018).

26. 26.

Badrinarayanan, V., Kendall, A. & Cipolla, R. Segnet: A deep convolutional encoder-decoder architecture for image segmentation. Preprint at <https://arxiv.org/abs/1511.00561> (2015).

27. 27.

Simonyan, K. & Zisserman, A. Very deep convolutional networks for large-scale image recognition. In *International Conference on*

Learning Representations (2015); preprint at
<https://arxiv.org/pdf/1409.1556.pdf>

28. 28.

Ronneberger, O., Fischer, P. & Brox, T. U-Net: Convolutional networks for biomedical image segmentation. Preprint at
<https://arxiv.org/abs/1505.04597> (2015).

29. 29.

He, K., Zhang, X., Ren, S. & Sun, J. Deep residual learning for image recognition. Preprint at <https://arxiv.org/abs/1512.03385> (2015).

30. 30.

Wu, G. C. et al. *Power of Place: Land Conservation and Clean Energy Pathways for California* (The Nature Conservancy, 2019).

31. 31.

Konadu, D. et al. Land use implications of future energy system trajectories: the case of the UK 2050 carbon plan. *Energy Policy* **86**, 328–337 (2015).

32. 32.

Turconi, R., Boldrin, A. & Astrup, T. Life cycle assessment (LCA) of electricity generation technologies: overview, comparability and limitations. *Renew. Sustain. Energy Rev.* **28**, 555–565 (2013).

33. 33.

Hernandez, R. et al. Environmental impacts of utility-scale solar energy. *Renew. Sustain. Energy Rev.* **29**, 766–779 (2014).

34. 34.

Bukhary, S., Ahmad, S. & Batista, J. Analyzing land and water requirements for solar deployment in the southwestern United States. *Renew. Sustain. Energy Rev.* **82**, 3288–3305 (2018).

35. 35.

Dias, L., Gouveia, J. P., Loureno, P. & Seixas, J. Interplay between the potential of photovoltaic systems and agricultural land use. *Land Use Policy* **81**, 725–735 (2019).

36. 36.

Grodsby, S. M. & Hernandez, R. R. Reduced ecosystem services of desert plants from ground-mounted solar energy development. *Nat. Sustain.* **3**, 1036–1043 (2020).

37. 37.

Carlisle, J. E., Kane, S. L., Solan, D., Bowman, M. & Joe, J. C. Public attitudes regarding large-scale solar energy development in the U.S. *Renew. Sustain. Energy Rev.* **48**, 835–847 (2015).

38. 38.

Mulvaney, D. Identifying the roots of green civil war over utility-scale solar energy projects on public lands across the American southwest. *J. Land Use Sci.* **12**, 493–515 (2017).

39. 39.

Lamarche, C. et al. Compilation and validation of SAR and optical data products for a complete and global map of inland/ocean water tailored to the climate modeling community. *Remote Sens.* **9**, 36 (2017).

40. 40.

Cherlet, M. et al. *World Atlas of Desertification: Rethinking Land Degradation and Sustainable Land Management* (Publications Office

of the European Union, 2018).

41. 41.

Hersbach, H. et al. The ERA5 global reanalysis. *Q. J. R. Meteorol. Soc.* **146**, 1999–2049 (2020).

Author information

Affiliations

1. Smith School of Enterprise and the Environment, University of Oxford, Oxford, UK

L. Kruitwagen & C. Hepburn

2. Descartes Labs Inc, San Francisco, CA, USA

K. T. Story & S. Skillman

3. World Resources Institute, Washington, DC, USA

J. Friedrich & L. Byers

Contributions

L.K. designed and implemented the machine learning pipeline, designed and implemented the dataset analysis, and wrote the paper draft. K.S. designed the machine learning pipeline and dataset analysis, implemented the SPOT6/7 branch of the machine learning pipeline and wrote the paper draft. J.F. and L.B. contributed to the acquisition of training data and analysis of the dataset. S.S. contributed to the deployment of the machine learning pipeline. C.H. contributed to the analysis of the dataset and wrote the paper draft.

Corresponding author

Correspondence to L. Kruitwagen.

Ethics declarations

Competing interests

K.S. and S.S. are employees and shareholders of Descartes Labs Inc., the company that builds and maintains the cloud computation infrastructure used to conduct this research. J.F. and L.B. are employees of the World Resources Institute, a not-for-profit organization which will host and publicly visualize a copy of our dataset.

Additional information

Peer review information *Nature* thanks Fei Teng, Stefano Ermon, Rebecca R. Hernandez, Lynn Kaack and the other, anonymous, reviewer(s) for their contribution to the peer review of this work.

Publisher's note Springer Nature remains neutral with regard to jurisdictional claims in published maps and institutional affiliations.

Supplementary information

Supplementary Information

This file contains Supplementary Information, including Supplementary Figs. 1–13, Tables 1–10 and references.

Supplementary Data

This file contains the source data for some of the supplementary figures.

Source data

Source Data Fig. 2

Source Data Fig. 3

Rights and permissions

Reprints and Permissions

About this article

Cite this article

Kruitwagen, L., Story, K.T., Friedrich, J. *et al.* A global inventory of photovoltaic solar energy generating units. *Nature* **598**, 604–610 (2021). <https://doi.org/10.1038/s41586-021-03957-7>

- Received: 02 December 2019
- Accepted: 24 August 2021
- Published: 27 October 2021
- Issue Date: 28 October 2021
- DOI: <https://doi.org/10.1038/s41586-021-03957-7>

Share this article

Anyone you share the following link with will be able to read this content:

[Get shareable link](#)

Sorry, a shareable link is not currently available for this article.

[Copy to clipboard](#)

Provided by the Springer Nature SharedIt content-sharing initiative

[Machine learning enables global solar-panel detection](#)

- Lynn H. Kaack

News & Views 27 Oct 2021

This article was downloaded by **calibre** from <https://www.nature.com/articles/s41586-021-03957-7>

| [Section menu](#) | [Main menu](#) |

- Article
- Open Access
- [Published: 27 October 2021](#)

Global potential for harvesting drinking water from air using solar energy

- [Jackson Lord](#) [ORCID: orcid.org/0000-0002-8242-3060](#)¹,
- [Ashley Thomas](#) [ORCID: orcid.org/0000-0003-2098-3801](#)¹,
- [Neil Treat](#)¹,
- [Matthew Forkin](#)¹,
- [Robert Bain](#) [ORCID: orcid.org/0000-0001-6577-2923](#)²,
- [Pierre Dulac](#)³,
- [Cyrus H. Behroozi](#) [ORCID: orcid.org/0000-0002-4067-3707](#)¹,
- [Tilek Mamutov](#)¹,
- [Jillia Fongheiser](#)¹,
- [Nicole Kobilansky](#)¹,
- [Shane Washburn](#)¹,
- [Claudia Truesdell](#)¹,
- [Clare Lee](#)¹ &
- [Philipp H. Schmaelzle](#) [ORCID: orcid.org/0000-0002-5773-596X](#)¹

Nature volume **598**, pages 611–617 (2021)

- 76 Altmetric
- [Metrics details](#)

Subjects

- [Computational science](#)
- [Developing world](#)
- [Geography](#)
- [Technology](#)
- [Water resources](#)

Abstract

Access to safely managed drinking water (SMDW) remains a global challenge, and affects 2.2 billion people^{1,2}. Solar-driven atmospheric water harvesting (AWH) devices with continuous cycling may accelerate progress by enabling decentralized extraction of water from air^{3,4,5,6}, but low specific yields (SY) and low daytime relative humidity (RH) have raised questions about their performance (in litres of water output per day)^{7,8,9,10,11}. However, to our knowledge, no analysis has mapped the global potential of AWH¹² despite favourable conditions in tropical regions, where two-thirds of people without SMDW live². Here we show that AWH could provide SMDW for a billion people. Our assessment—using Google Earth Engine¹³—introduces a hypothetical 1-metre-square device with a SY profile of 0.2 to 2.5 litres per kilowatt-hour (0.1 to 1.25 litres per kilowatt-hour for a 2-metre-square device) at 30% to 90% RH, respectively. Such a device could meet a target average daily drinking water requirement of 5 litres per day per person¹⁴. We plot the impact potential of existing devices and new sorbent classes, which suggests that these targets could be met with continued technological development, and well within thermodynamic limits. Indeed, these performance targets have been achieved experimentally in demonstrations of sorbent materials^{15,16,17}. Our tools can inform design trade-offs for atmospheric water harvesting devices that maximize global impact, alongside ongoing efforts to meet Sustainable Development Goals (SDGs) with existing technologies.

[Download PDF](#)

Main

Ensuring reliable access to safe drinking water for all remains a global challenge, and is formally recognized as an international development priority by 2030 in the United Nations framework for global development priorities, the Sustainable Development Goals 6.1¹⁸. Progress towards this target is measured by the WHO/UNICEF Joint Monitoring Programme (JMP) as the percentage of population using safely managed drinking water (SMDW), where ‘safely managed’ is defined as “an improved source located on the premises, available when needed and free of fecal and priority chemical contamination”^{1,2}. Traditional routes to bring SMDW on premises to currently unserved populations are estimated to cost US\$114 billion per year (from 2015), more than three times the historical financing trend¹⁹. Moreover, there is increasing global interest in solutions that provide safe drinking water without the environmental consequences of increasing reliance on bottled water and that do not require household-level intervention, which has limited adherence^{20,21}. Atmospheric water

harvesting (AWH) shows promise to accelerate decentralized access to underserved communities if a cost-effective, off-grid device can be designed and scaled⁶.

Several classes of off-grid AWH designs exist or are being explored^{8,12,22,23}, as summarized in Table 1. AWH devices are categorized by energy source—active devices use external energy sources whereas passive devices rely solely on atmospheric conditions that allow for pre-condensed dew or fog to be harvested. Passive devices are thus limited to geographic niches where dew or fog can be systematically harvested^{7,12,24}. Active, sorbent-based AWH devices extract water using primarily solar thermal energy in one of two operational modes: diurnal-mode devices extract at night (when RH is higher) and condense during the day (when solar energy is available) in a single daily cycle, requiring a large sorbent bed. By contrast, continuous-mode devices are not limited to a single daily cycle, and need only hold a small amount of water vapour in-process^{3,4}, drastically reducing sorbent mass and device size. This, however, requires extraction at lower RH when solar energy is available, raising questions about performance^{7,8,9,10,11}. Cooler–condenser devices use work (typically electric energy) to actively cool air below its dew point and collect condensation and—if solar-driven—call for photovoltaic (PV) panels. Unlike solar–thermal devices, solar-driven cooler–condenser devices suffer from a steep loss in electric energy conversion. In the context of specific yield, we use kWh to denote primary solar energy prior to thermal and other losses, and kWh_{PV} to denote electrical energy supplied to the device from PV panels after conversion. Unless stated otherwise, ranges of SY refer to RH between 30% and 90% at 20 °C.

Table 1 Suitability of household-scale applications by AWH category

Here we present an assessment of solar-driven, continuous-mode AWH (SC-AWH) using global data. AWH has much lower SY than infrastructural water sources such as desalination²⁵ (approximately 200 l kWh⁻¹). However, SC-AWH devices sized to produce sufficient daily drinking water output for an individual or family could address both the water quality and the water access dimensions of SMDW solutions at the household level.

Geography of the global challenge

To estimate the impact potential of SC-AWH, we first mapped the distribution of the approximately 2.2 billion people without SMDW². Recent studies have used geostatistical techniques to estimate subnational inequalities of safe water and sanitation from a variety of data sources reporting metrics of facility type^{26,27}. Here we use a deterministic method based exclusively on JMP data on drinking water service levels. In this study, we assume that SC-AWH is for drinking water only and

does not replace water for other domestic uses such as hygiene, cooking and sanitation^{[14,28](#)}.

The overall percentage of the population in regions reported by the JMP at the lowest respective available regional hierarchy is shown in Fig. [1a](#). This seamless fabric of national and subnational survey regions gives a spatially continuous picture of the global distribution of people living without SMDW. Sub-Saharan Africa contains the highest total number of people without SMDW, in alignment with previous reports^{[2,29](#)}, followed by regions in South Asia and Latin America.

Fig. 1: Geographic distribution of world population without SMDW.

 [figure1](#)

-
- a**, Percentage share of total population in survey region living without SMDW as reported by the WHO/UNICEF JMP. **b**, Log population density of people without

SMDW from WorldPop at 1 km resolution adjusted by JMP proportions at 1 km resolution. Produced in ArcGIS 10.

The regional proportions from Fig. 1a were applied as a linear weight to each pixel of the WorldPop (2017) 1 km-resolution residential population counts image (<https://www.worldpop.org>). This gives an estimate of the distribution of people without SMDW to a spatial resolution that more closely matches the scales at which climate variables relevant for AWH vary owing to physical geography, such as topography and land cover. The resulting weighted population distribution is shown in Fig. 1b.

Geospatial toolset for AWH assessment

We present a geospatial tool (AWH-Geo) for assessing the global potential for notional SC-AWH devices given available climatic resources. AWH-Geo was built in Google Earth Engine¹³ and is extensible across climate data. For this study, AWH-Geo uses the ERA5-Land climate reanalysis over the 10-year period 2010–2019 (inclusive). ERA5-Land was chosen for its fine resolution (9 km at hourly intervals), global coverage and ability to represent historical synoptic conditions. This period is sufficient to account for interannual variability, although decadal trends are explored in brief in Extended Data Fig. 9. For shorter computation times running their own analysis, the user can adjust the analysis period within the tool.

AWH-Geo takes as input the instantaneous rate of water output as a function of the three dominant environmental variables: (1) global horizontal irradiance from sunlight (GHI (in W m^{-2})), (2) RH (%) and (3) air temperature (T ($^{\circ}\text{C}$)). Secondary climate variables could be incorporated later (for example, downwelling infrared and surface wind speed). We propose an output table with water yield values as a function of binned climate inputs GHI, RH and T , as a way to connect AWH device models or experimental characterizations with geospatial analyses. Water output can be entered in areal harvesting rates (in $1 \text{ h}^{-1} \text{ m}^{-2}$) for abstractions, or as the expected yield of a real device with known collection areas (in 1 h^{-1}). Across all data points of a multi-year climate image time series, AWH-Geo uses the given output table to look up yield values and aggregates water outputs for display as global maps or derived plots. Whereas previous assessments have been limited to relatively small numbers of locations with on-site meteorological data^{7,30} or limited the analysis to a region³¹, the approach presented here is global and spatially continuous. Figure 2 shows a conceptual workflow of AWH-Geo and adjacent processes to produce results in this study.

Fig. 2: Data processing workflow of AWH-Geo.

 **figure2**

Cylinders indicate data stores from Google Earth Engine, the WHO/UNICEF JMP or open online content. Shown are processes (rectangles), geo-images (parallelograms) and outputs (circles).

We first used AWH-Geo to map theoretical upper bounds of solar-driven AWH by constructing output tables from the literature as specific water yields SY (in 1 kWh^{-1}). SY is an evaluative metric for AWH sensitive to RH³², and is the inverse of specific

energy consumption (SEC), which is commonly used for other water and desalination systems. Resulting maps are overlaid with a dot-density representation of the distribution of people without SMDW for visual comparison in Fig. 3.

Fig. 3: Upper bounds water output of solar-driven AWH in relation to global user base.



a–c, Mean daily water output of solar-driven AWH given overall thermodynamic limits of any process³³ ($T_{hot} = 100^\circ\text{C}$) (a), cooler–condenser processes driven by PV³² (b) and example of active sorbent device types (TRP gels from ref. [15](#)) (c). Callout charts in a show select seasonal profiles in bi-weekly intervals of mean output and primary climate drivers: GHI, RH and temperature. Output (in $1 \text{ d}^{-1} \text{ m}^{-2}$) normalized to horizontal device area in sunlight. Real devices will perform below maximum theoretical potentials. Overlaid dot density (red) of 2.2 billion people without SMDW. Placement of dots is spatially arbitrary across the survey region. Produced in ArcGIS 10.

[Source data](#)

Recently, Kim et al. have described the fundamental thermodynamic limits for AWH³³. This model gives the minimum thermal energy required (at a given hot-side temperature level) per unit water output of a black box AWH, corresponding to SY values between 5 and 50 l kWh⁻¹. Kim's thermodynamic limits are mapped in Fig. 3a. Mapping thermodynamic limits is useful to set maximum expectations for SC-AWH output globally and to assess the improvement potential that may exist between existing device performance and fundamental physical limits. Similar analytic approaches have been used to assess condenser-based devices, diurnal devices and dew collectors applied to a specific location or region^{7,12,30,31}. The geographic patterns of output closely follow time-averaged humidity values generally, modified by the availability of sunlight. Notably, the results show significant water production potential throughout much of the world, particularly in the tropics.

Next, we mapped the maximum output of two basic design types. Peeters describes the maximum yield for active cooler-condensers³², giving SYs of $1\text{--}30 \times \{\rm{l}\}$, $\{\rm{kWh}\}_\{\rm{PV}\}^{-1}$ (0.2–6 l kWh⁻¹), plotted using AWH-Geo in Fig. 3b. For sorbent designs, metal organic frameworks (MOFs) and thermo-responsive polymer (TRP) gels¹⁷ show the highest yields at low and high RH, respectively. Zhao et al. demonstrated exceptional performance of a TRP¹⁵ at high RH (0.2–9.3 l kWh⁻¹ (converted to SY by Peeters³²)), generally outperforming MOFs (whose reported maximum³² SYs are around 1 l kWh⁻¹). Global projections for Zhao's TRP are mapped in Fig. 3c.

In addition to annual means, AWH-Geo is capable of deriving metrics useful for analysing seasonal variability of output. Optionally, AWH-Geo exports 90% availability (P90) values across a set of time windows (Methods).

Assessing the global potential

Our coincidence analysis calculates the mean hours per day during which GHI and RH are simultaneously above parametric thresholds. Fig. 4a maps annual means for such daily coincidence hours for the given threshold pairs, interpreted as the operational hours per day (ophd) for a hypothetical device. Important transition areas between tropical and desert regions show the expected trade-off between sunlight and humidity, which generally vary inversely. Very low RH thresholds of 10% increase ophd potential by only 1–2 h from the ophd at 30% RH in arid regions in the Sahel across GHI thresholds, but ophd then falls sharply at higher RH thresholds. This indicates a diminishing return to devices operating below 30%. Coastal areas show promise for consistent 2–4 ophd worldwide above 50% RH.

Fig. 4: AWH technology parameters in relation to global impact targets.

 **figure4**

a, b, Geographic distribution (**a**) and sum (**b**) of population without SMDW living in areas meeting parametric thresholds relevant to operation of SC-AWH devices. Operational hours per day (Ophd) is the mean daily duration of both sunlight (GHI) and RH thresholds exceeded simultaneously. Usage example: a device requiring more than 5 h d^{-1} of sunlight above 400 W m^{-2} must operate down to 40% RH to reach approximately 700 million users. **c, d**, People without SMDW reachable in relation to mean daily output normalized to horizontal device area in sunlight (**c**) and SY profile (**d**). Target curves are hypothetical SY profiles capable of providing 5 l d^{-1} for a given solar collection area. Water output and SY targets scale linearly with device area in sunlight. For demonstration we therefore show that, for a given RH, doubling the area of a device from 1 m^2 to 2 m^2 halves the target SY requirement to achieve SMDW for a target population. ZMW Source profile approximated from the manufacturer's technical specifications sheet³⁵. Note that the full ZMW panel is approximately 3 m^2 . Experimental values for MOFs and sorbents are taken from experiments^{3,36} (0.19 l kWh^{-1} and 0.84 l kWh^{-1}), and TRP is taken from ref. ¹⁵, all converted as in ref.

³² Values for the Bagheri device³⁴ assume work instead of heat input; therefore photovoltaic efficiencies were applied when converting from GHI. Maps are produced in ArcGIS 10.

Source data

Next, we summed the population without access to SMDW segmented by threshold pair using the weighted population image, grouped cumulatively by ophd at whole intervals and shown in Fig. 4b. Inflections of diminishing user potential occur between values of RH between 30 and 50%, GHI between 400 and 600 W m⁻² and ophd between 3 and 5 h. These reflect key spatio-demographic patterns along similar climatic transitions in the tropics, where the bulk of those living without SMDW live—particularly in the tropical savanna of sub-Saharan Africa and the Ganges River Valley in India. A device that could operate above these values has the theoretical potential to serve more than half the world's remaining population lacking access to SMDW.

Next we ran the SY profiles of a collection of SY curves through AWH-Geo, including commercial cooler–condenser devices evaluated by Bagheri³⁴ and a data sheet for the SOURCE panel, a sorbent-based device from company SOURCE, formerly known as Zero Mass Water³⁵ (ZMW).

Figure 4c shows resulting outputs normalized by area (in 1 d⁻¹ m⁻²)—a performance metric advocated by LaPotin et al. ¹¹—as a function of the population without SMDW reached. Steep gradients of the human impact of the output mirror those in the coincidence analysis. Linear SY profiles prioritize performance at low RH, but cap output even in resource-rich climates. The target curves are based on hypothetical SY values similar to those characteristic of sorbent or device profiles that reach 1 billion users at an average of 5 1 d⁻¹ m⁻². Comparing the two target curves demonstrates the expected trade-off between serving more users at low output (linear) and fewer users at high output (logistic).

To further explore trade-offs of the SY curve across different values of RH, we plotted SY values from materials and devices in relation to target curves for reaching 0.5–2.0 billion people without SMDW at 5 1 d⁻¹, the approximate daily drinking water requirements of an individual¹⁴ (Fig. 4d). We based the target curves on a 1 m² device unless otherwise noted, although water output and SY targets scale linearly with device area in sunlight. To demonstrate this, we plotted a version of the 1.0-billion target based on 2 m²—this doubling of the device area halves the SY requirements for the target impacts. The existing devices both follow approximately linear yields across RH below the 0.5-billion impact target curves. MOFs and other sorbents show varied results^{3,36}, although they remain roughly linear. Zhao's exceptional yields at high RH

make up for low performance at low RH (logistic profile), and show the most promise for reaching the largest user base (2.0 billion). Figure 4d compares material and device performance side-by-side to show the gap between present capabilities and theoretical limits, although real devices will be subject to losses that will prevent them from fully reaching idealized material performance or theoretical limits.

Closing the gap

This study presents initial conclusions—developing detailed SC-AWH design criteria will require further work. A device with a 1 m² solar collection area and a SY profile of 0.2–2.5 l kWh⁻¹ (0.1–1.25 l kWh⁻¹ for 2 m²) can serve the SMDW needs of about 1 billion people, assuming continuous harvesting of 2–3 h per day of coincident sunlight of more than 600 W m⁻² and RH above 30%. The shape of the SY curve is critical for SC-AWH to take advantage of coincident humidity and solar energy during key periods of the day, typically during morning and evening hours. A trade-off exists between increasing yields at lower RH (around 30%) for those in climate transition zones (northern sub-Saharan Africa and western India), versus focusing on exponentially higher yields in humid regions such as Bangladesh and equatorial regions.

Researchers and device inventors can cross-reference Fig. 4 when making trade-off decisions between sets of technical specifications and servable regions and people. Recent experiments^{4,5,37} show rapid improvements in multi-cycled sorption material yield, ranging from 0.1 to more than 8.0 l d⁻¹ kg⁻¹ sorbent in outdoor conditions (RH 10–60%, GHI < 1,000 W m⁻²), and show inflections in performance along similar ranges as population distributions^{11,31} (RH 30–50%, GHI 400–600 W m⁻²). Advancements in device efficiencies from innovative design architectures³⁸ and novel high-performance physical sorbents^{15,17,39,40,41} show promise for increasing SC-AWH output. Individual specific yields from materials experiments or prototypes can be plotted in Fig. 4d for benchmarking against target impacts. Validated device performance in outdoor field conditions and published output tables are needed for global researchers to advance progress of AWH.

The long-term averaged output of an AWH device is an important but limited metric. Seasonal, weekly and diurnal variability in output will influence user adoption and market viability. Some seasonal profiles are explored in Extended Data Figs. 4–8. Short periods of shortfall may be supplemented by storage from previous surpluses. Rainfall collection or alternative sources would be required for seasonal shortfall periods, such as those in monsoon climates. Use of multiple water sources and seasonal switching are well established in the literature, although there may be trade-offs with respect to water quality and contamination^{42,43}, reinforcing the need for in-

depth knowledge of existing water access practices when deploying AWHs, with a focus on household water treatment and safe storage.

The hydro-ecological impacts of AWH for drinking water are probably negligible given the scale of the global atmospheric water budget. Serving all 2.2 billion people without SMDW at 10 l d^{-1} sums to approximately $8 \text{ km}^3 \text{ yr}^{-1}$, a mere 0.20% of the net water extraction of global cropland ($4,000 \text{ km}^3 \text{ yr}^{-1}$) and 0.01% of total evapo-transpiration over land⁴⁴ ($65,500 \text{ km}^3 \text{ yr}^{-1}$).

SC-AWH devices have the potential to be low-cost. Most design architectures have few moving parts (for example, a slowly rotating sorbent wheel⁸), and can be constructed from widely available components. Advanced sorbent materials (for example, MOFs or TRP) will need to be mass manufactured to reach cost targets. New high-volume manufacturing methods for MOFs^{45,46} have the potential to drastically reduce costs.

Technology development is only one part of the complex problem of safe water access; user-centric formative research with a wide variety of end users is critical for ensuring that devices are adopted widely. Similar to bottled water²¹ SC_AWH devices could paradoxically undermine efforts to develop permanent piped infrastructure. Product affordability and adoption require parallel financial and socio-cultural efforts such as scaling availability of loans, promoting awareness of waterborne disease risk and increasing women's influence over community decisions^{47,48,49}.

Our analysis demonstrates that daytime climate conditions may in fact be sufficient for continuous-mode AWH operation in world regions with the highest human need. This assessment suggests that focusing device design criteria on maximum impact and reducing costs of off-grid production of drinking water at the household scale is a worthwhile effort.

Methods

Water access data processing

Data on drinking water coverage by region was acquired from the WHO/UNICEF JMP. The JMP acts as official custodian of global data on water supply, sanitation and hygiene² and assimilates data from administrative data, national census and surveys for individual countries, and maintains a database that can be accessed online through their website. We accessed data tables for national and subnational drinking water service levels from <https://washdata.org>.

JMP datasets are not geographically linked to official boundary files. We joined the tables to GIS boundaries obtained from the following open-source collections: GADM (<https://gadm.org>), the Spatial Data Repository of the Demographic and Health Surveys Program of USAID (DHS) and the Global Data Lab of Radboud University (GDL)^{2,50,51,52,53}. Subnational regions reported by the JMP are unstructured, representing various regional administrative levels (province, state, district and others).

The JMP national and subnational data were joined to GIS boundaries using a custom geoprocessing tool built in Python and ArcGIS 10. The tool joins the available JMP subnational-level survey data to the closest name match of regional boundary names from a merged stack of GADM (admin1, admin2 and admin3), DHS and GDL boundaries worldwide. The JMP national-level survey data is then joined to GADM national (admin0) boundaries for countries which have no subnational data available. Finally, the two boundary-joined datasets (national and subnational) are merged, processed and exported as a seamless global fabric of water-stressed-population data at the highest respective spatial resolutions available (Fig. [1a](#)).

JMP does not report the breakdown between the SMDW and basic service level within subnational regions, and instead reports a combined category called ‘at least basic’ (ALB). To estimate the SMDW values in subnational regions, a simple cross-multiplication was performed using the splits at the national level:

$$\$ \$ \{ \{ \backslash rm\{SMDW\} \} \} _\{ \{ \backslash rm\{subnational\} \} \} = \backslash frac\{ \{ \{ \backslash rm\{SMDW\} \} \} _\{ \{ \backslash rm\{national\} \} \} \} \{ \{ \backslash rm\{ALB\} \} \} _\{ \{ \backslash rm\{national\} \} \} \} \{ \backslash times \\ \{ \backslash rm\{ALB\} \} \} _\{ \{ \backslash rm\{subnational\} \} \} , \$ \$$$

where $ALB_{national}$, $ALB_{subnational}$ and $SMDW_{national}$ are known values.

Validation of the cross-estimation of share of SMDW from ALB for subnational regions was conducted on a reference dataset of nationally representative household surveys that collected data on all criteria for SMDW⁵⁴, shown in Extended Data Fig. [2](#). We report regression results of $R^2 = 0.87$ and a standard error of 3.67, indicating a bias which over-reports SMDW share and a probable underestimate of people living without SMDW in our study. This discrepancy comes from JMP calculations of SMDW that rely on the minimum value of multiple drinking water service criteria (free from contamination, available when needed and accessible on premise) rather than considering whether individual households meet all criteria for SMDW⁵⁵.

The fraction of population without SMDW was multiplied by residential population values in the WorldPop top-down unconstrained global mosaic population count of 2017 at 1 km spatial resolution⁵⁶ (<https://www.worldpop.org>). WorldPop was accessed

online as a TIF image and imported to Google Earth Engine. The year 2017 was chosen to more closely match water access data from JMP. The percentages reported by JMP are probably not uniform within most regions⁵⁷, introducing an unknown error to Fig. 1b, but represent the best estimate available to us given the limitations of these regionally reported data.

Climate input and conversion approximations

GHI and reference plane

We used GHI (in W m^{-2}) as solar energy input data. GHI has good availability in climate datasets and introduces the fewest number of assumptions. Since GHI describes the irradiance in a locally horizontal reference plane, this approximation is only exact for devices having a horizontally oriented solar harvesting area. Annually averaged comparisons between horizontal and optimal fixed-tilt panels show negligible differences in direct plus diffuse radiation in tropical latitudes, and ratios below 25% in locations within 50° north and south latitudes⁵⁸. Those seeking precise absolute predictions for tilted devices or higher latitudes are encouraged to adapt the provided code to their specific assumptions.

Conversion from SY to AWH output

As discussed in the main text, solar-driven AWH devices typically have one of two predominant energy inputs: thermal (converted directly from incident sunlight on the device) or electrical (from PV). Here, the energy units used to calculate yield in 1 kWh^{-1} are incident solar energy directly from GHI. The various assumptions are made in relation to the reported values based on their source. The thermal limits³³, target curves, and experimental results reported by TRP¹⁵ and MOFs were assumed to have direct (100%) conversion from sunlight to heat. For the ZMW device, the table provided by the manufacturer accounts for system losses, so the table values were directly converted in our model³⁵. For ref. 34 and the cooler-condenser limits from ref. 32, which both assume work input instead of heat, we applied a typical PV conversion efficiency of 20% to convert from sunlight kWh (GHI) to kWh_{PV} (electrical work) input to the device⁵⁹.

Sufficiently short sorbent cycling times

AWH-Geo assumes continuous or quasi-continuous AWH. AWH-Geo considers each 1-h timestep independently and is thus stateless. Aside from edge cases, this is a safe assumption for mass efficient SC-AWH devices, which typically have time constants

shorter than 1 h, both for sorbent cycling and for most of the thermal time constants. For devices with longer time constants, batch devices or processes with slow (de)sorption kinetics, this assumption may introduce increased error, and may require further adaptation of the provided code.

Climate time-series calculation

AWH-Geo is a resource-assessment tool for AWH. It consists of a geospatial processing pipeline for mapping water production (in litres per unit time) around the world of any solar-driven continuous AWH device that can be characterized by an output table of the form $\text{output} = f(\text{RH}, T, \text{GHI})$.

Output tables show AWH output values in 1 h^{-1} or $1 \text{ h}^{-1} \text{ m}^{-2}$ across permutations of the 3 main climate variables in the following ranges: RH between 0 and 100 % in intervals of 10%, GHI between 0 and $1,300 \text{ W m}^{-2}$ in intervals of 100 W m^{-2} , and T between 0 and 45°C in intervals of 2.5°C (2,145 total output values). The tables are converted into a 3D array image in Google Earth Engine and processed across the climate time-series image collection for the period of interest. Finally, these AWH output values are composited (reduced) to a single time-averaged statistic of interest as an image.

Climate time-series data was acquired from the ERA5-Land climate reanalysis from the European Centre for Medium-Range Weather Forecasts (ECMWF)⁶⁰, accessed from the Google Earth Engine data catalogue. ERA5-Land surface variables were used in 1-h intervals and $0.1^\circ \times 0.1^\circ$ (nominal 9 km). The 10-year analysis period (2010–2019, inclusive) was used for this work, and represents a period long enough to provide a reasonable correction for medium-term interannual climatic variability.

Climate variables GHI and T were matched to ERA5-Land parameters ‘Surface solar radiation downwards’ (converted from cumulative to mean hourly) and ‘2 metre temperature’ (converted from K to $^\circ\text{C}$), respectively. RH was calculated from the ambient and dew point temperature parameters in a relationship derived from the August–Roche–Magnus approximation⁶¹ rearranged as:

$$\$ \$ \text{rm}\{\text{RH}\} = 100 \% \times \frac{\left(\frac{\text{rm}\{e\}}{\text{rm}\{d\}} \right)^{\frac{1}{aT}} - 1}{\left(\frac{\text{rm}\{e\}}{\text{rm}\{d\}} \right)^{\frac{1}{aT}}} \$ \$$$

where a is 17.625 (constant), b is 243.04 (constant), T is the ERA5-Land parameter ‘2 metre temperature’ converted from K to $^\circ\text{C}$, and T_d is the ERA5-Land parameter ‘2 metre dewpoint temperature’ converted from K to $^\circ\text{C}$.

Spot validation of the climate parameters and the mapped output was performed manually in Google Earth Engine across several timesteps in 2016 in Ames, Iowa

(using the Iowa Environmental Mesonet AMES-8-WSW station⁶²) and showed insignificant error (< 5%).

Mapping upper bounds

Figure 3a maps thermodynamic upper bound outputs for SC-AWH based on an equation from Kim et al. ³³, reproduced below.

$$\begin{aligned} & \frac{\dot{Q}_{\min}}{\dot{m}_{\text{water}}(\omega_{\text{air}} - e_{\text{in}}) + e_{\text{out}}(1 - \frac{T_{\text{hot}}}{T_{\text{amb}}})} \\ &= \left[\frac{1}{\omega_{\text{air}} - e_{\text{in}}} \right] \left[\frac{e_{\text{out}}}{e_{\text{out}} - e_{\text{in}}} \right] \times \left(1 - \frac{T_{\text{hot}}}{T_{\text{amb}}} \right)^{-1} \end{aligned}$$

where \dot{Q}_{\min} is the minimum input heat flux (in W_{heat}) required to drive the process, T_{hot} is the temperature (in K) at which the input heat is delivered, T_{amb} is the ambient temperature (in K) at which heat is rejected and water and air exit the process, \dot{m}_{water} is the production rate of liquid water by mass, ω denotes humidity ratios in kg of water per kg of dry air, e denotes specific exergies, which can be looked up for given temperatures and humidities, subscript air,in denotes ambient air drawn in at T_{amb} from which to extract moisture, subscript air,out denotes air exiting the process at T_{hot} after extracting some moisture from it, subscript water,out denotes liquid water exiting the process at T_{hot} as the desired product.

Parameters not present in this formula, but that are in Kim's underlying derivation: this upper limit is obtained for a small recovery ratio ($RR \sim 0$) chosen for numerical stability and for reversible process conditions (entropy generation, $S_{\text{gen}} = 0$).

Kim's model assumes an AWH in which the fundamental energies required are driven by input heat supplied at a temperature T_{hot} . The limit it represents applies independent of the process, number of stages, sorbent choice, and so on, as long as heat drives the process.

We adapt Kim's model to solar energy input, assuming an idealized conversion efficiency from solar irradiance to usable heat of 100%. This idealization retains a robust upper bound without bringing in additional parameters. Literature values for theoretical sun-to-heat efficiency limits range from >99.99 to 95.80% for thermal absorbers, depending on the level of angular selectivity⁶³.

Rearranged, Kim's model yields

$$\$ \$ \frac{\dot{V}_{\text{water}}}{A} \leq E_{\text{GHI}} \times \left(1 - \frac{T_{\text{ambient}}}{T_{\text{hot}}} \right) \times \left(\frac{1}{\omega_{\text{air,in}} - \omega_{\text{air,out}}} + \frac{e_{\text{out}} - e_{\text{in}}}{\rho_{\text{water}}} \right)^{-1} \times \frac{1}{\rho_{\text{water}}} \$ \$$$

where, in addition, $(\dot{V}_{\text{water}}, A)$ is the production rate of liquid water by volume, (A) is the area harvesting sunlight (see approximation section below), (E_{GHI}) is GHI in $\text{W}_{\text{sun}} \text{ m}^{-2}$, and (ρ_{water}) is the density of water.

This is now a function of the three key climate variables: GHI (in the first term), ambient temperature (in the second and hidden in the third term) and RH (entering the third term). This was converted to an output table and processed through the AWH-Geo pipeline and presented in Fig. 3a. While this can be run for any choice of parameter (T_{hot}) , we present figures here for $(T_{\text{hot}}) = 100^\circ\text{C}$, a temperature still achievable in low-cost (non-vacuum) practical devices without tracking or sunlight concentration. Higher driving temperatures increase the upper bound for water output. For the limits analysis, values of RH above 90% are clamped to prevent unrealistically high theoretical outputs as Kim's equation goes to infinity at 100% RH. A further assumption is made that new ambient air is efficiently refreshed.

Figure 3b maps the maximum yield for active cooler-condensers without recuperation of sensible heat—all given work input and an optimum coefficient of performance of the cooling unit at a condenser temperature that maximizes specific yield as modelled by Peeters³², which we digitized from their fig. 11. Peeters chose to set yield to zero whenever frost formation would be expected on the condenser. Since Peeters assumes work input, we convert from solar energy (GHI) to kWh_{PV} as discussed above.

Figure 3c maps Zhao's experimental results from a TRP using a logistic regression curve fit to their reported SYs of 0.21, 3.71 and 9.28 l kWh^{-1} at 30, 60 and 90% RH, respectively¹⁵. The terms of the curve fit are reported in the next section.

Custom yellow to blue map colours are based on www.ColorBrewer.org, by C. A. Brewer, Penn State⁶⁴.

Specific yield and target curves

Two simple characteristic equations, linear and logistic, were used to fit a limited set of SY and RH pairs from laboratory experiments or reported values and plotted through AWH-Geo using calculated output tables. Hypothetical curves of similar form whose terms were adjusted iteratively in AWH-Geo to goal-seek a target output (5 l d^{-1}) and user base, and are reported here (for 1-m² devices). In the following equations, RH in % is taken as a fraction (for example 55% is equivalent to 0.55).

The linear target curve is a simple linear function which crosses the y -axis at zero:

$$\$ \$ \{\mathrm{rm}\{\mathrm{SY}\}\}(\{\mathrm{rm}\{\mathrm{RH}\}\}) = a \times \{\mathrm{rm}\{\mathrm{RH}\}\} \$ \$$$

where a is set to 1.60, 1.86 and 2.60 L/kWh to reach targets of 0.5, 1.0, and 2.0 billion people without SMDW, respectively, and RH is input RH (fractional).

The logistic target curve is a logistic function:

$$\$ \$ \{\mathrm{rm}\{\mathrm{SY}\}\}(\{\mathrm{rm}\{\mathrm{RH}\}\}) = \frac{L}{1 + e^{k(\{\mathrm{rm}\{\mathrm{RH}\}\} - \{\mathrm{rm}\{\mathrm{RH}\}\}_0)}} \$ \$$$

where L is set to 1.80, 2.40 and 4.80 L kWh⁻¹ to reach targets of 0.5, 1.0 and 2.0 billion people without SMDW, respectively, k is the growth rate set to 10.0, and $\{\mathrm{rm}\{\mathrm{RH}\}\}$ and $\{\mathrm{rm}\{\mathrm{RH}\}\}_0$ are input RH (fractional), and 0.60, respectively.

The SY values reported by Zhao for TRPs (which they term ‘SMAG’) were fit to a logistic function of the same form with the following parameters: L set to 9.81 L kWh⁻¹, k set to 11.25 and RH_0 set to 0.645.

The resulting fitted SY profile is expanded into an output table. As with all reports providing SY values instead of full output tables, this forces an assumption of linearity in heat rate (approximately equal to GHI), which may introduce error at lower GHI levels. Zhao reports SY of the TRP material is consistent across temperature below 40 °C—the material’s lower critical solution temperature—above which its performance drops precipitously. Accordingly, we set the SY to 0.1 kWh⁻¹ for temperatures ≥ 40 °C in the output table.

Bagheri reported performance of three existing AWH devices across several climate conditions using an ‘energy consumption rate’ in kWh/L, which can be considered to be the SEC, and the simple reciprocal of SY. Instead of fitting a logistic curve to the reciprocals, we fit an exponential function to the average SEC of the three devices in conditions above 20 °C of the equation:

$$\$ \$ \{\mathrm{rm}\{\mathrm{SEC}\}\}(\{\mathrm{rm}\{\mathrm{RH}\}\}) = 9.03 e^{-2.99 \{\mathrm{rm}\{\mathrm{RH}\}\}} \$ \$$$

where SEC is specific energy consumption in kWh_{PV} l⁻¹ and RH is fractional.

This was applied to RH and taken as reciprocal in an output table and run through AWH-Geo. Since Bagheri reports the equivalent of kWh_{PV}, we scale to adapt to GHI input with a photovoltaic conversion efficiency as discussed above.

For performance of the ZMW device (the company's ~3 m² SOURCE Hydropanel), we used values from the panel production contour plot in the technical specification sheet available from the manufacturer's website³⁵. The decision for inclusion was made owing to the importance as an early example of a SC-AWH product with commercial intent. Values in l per panel per day were taken at each 10% RH step at 5 kWh m⁻², assumed to represent kWh m⁻² d⁻¹, and divided by 15 kWh (~3 m² × 5 kWh m⁻²) to convert to SY in 1 kWh⁻¹. From the resulting SY curve, an output table was generated and processed with AWH-Geo.

Coincidence analysis and population sums

The coincidence analysis was run through AWH-Geo across 70 threshold pairs given the full permutation set of RH from 10 to 100% and GHI from 400 to 700 W m⁻² threshold intervals, using binary image time series. The resulting mean multiplied by 24 represents average hours per day thresholds are met simultaneously, giving ophd. Below is a functional representation of this time-series calculation:

```
$$\{\langle (\{\rm{RH}\})_t, \rm{px} \rangle > \{\rm{RH}\}_{\rm{threshold}}\} \& \{\langle (\rm{simultaneous}) \& (\{\rm{GHI}\})_t, \rm{px} \rangle > \{\rm{GHI}\}_{\rm{threshold}}\} \rangle_{\rm{time}} \langle \rm{average} \rangle $$
```

where $\langle (\{\rm{RH}\})_t, \rm{px} \rangle$ is the RH in the map pixel $\langle \rm{px} \rangle$ at time t , $\{\rm{RH}\}_{\rm{threshold}}$ is the threshold of RH above which the device is assumed to operate, $\langle (\{\rm{GHI}\})_t, \rm{px} \rangle$ is the GHI in the map pixel $\langle \rm{px} \rangle$ at time t , and $\{\rm{GHI}\}_{\rm{threshold}}$ is the threshold of GHI above which the device is assumed to operate.

The population calculation was then conducted on these images in Google Earth Engine.

Zonal statistics were performed on the mean ophd images as integers (0–24) using a grouped image reduction (at 1,000-m scale) summing the population integer counts on the population without SMDW distribution image created previously (derived from WorldPop). This reduction was performed at 1,000 m. Validation was performed in Google Earth Engine on single countries within single ophd zones and showed insignificant error (<2%). The population results were collected as a table (feature

collection) and population was summed cumulatively within stacked ophd zones. These were exported to R for plotting in Fig. 4b.

To assess the sensitivity of results to the choice of climate and population dataset, we performed a coincidence analysis (Fig. 4b) with alternative datasets and provide those results in Extended Data Fig. 1.

As an alternative climate dataset to ERA-5 (1 h, 9 km), we used NASA's Global Land Data Assimilation System (GLDAS) 2.1 at $0.25^\circ \times 0.25^\circ$ spatial resolution (nominally 30 km) and 3 h temporal resolution⁶⁵ during the period concurrent with the main results, 2010–2019. As an alternative population dataset to WorldPop 2017, we used Oak Ridge National Laboratory's LandScan 2017 ambient population counts at 1 km spatial resolution⁶⁶. Two results comparisons were calculated: (1) GLDAS calculated with WorldPop 2017 for direct comparison of climate data input, and (2) GLDAS calculated with LandScan for comparison of climate and population dataset substitution.

The intercomparisons suggest there is negligible sensitivity to the population dataset used, but substantial and systematic sensitivity to the climate dataset used, while all intercomparisons agree in main features and qualitative conclusions. The spatially and temporally ($3\times$) coarser GLDAS dataset consistently results in lower predictions of water output and impact than the finer ERA-5 climate reanalysis. We speculate that the 3-h timesteps of GLDAS are insufficient to capture the performance-critical humidity and GHI dynamics throughout the day (probably morning and evening hours), and, similarly, the 30-km pixels are insufficient to resolve fine-scale climate patterns driven by topographic and other microscale physiographic effects. This illustrates the importance of using high-resolution climate datasets.

Variability statistics of AWH output

To go beyond annual averages and study availability, we introduce a set of metrics we named moving average density 90th percentile (MADP90).

The MADP90-t represents a device's average output rate ($l\ d^{-1}\ m^{-2}$) that will be exceeded for 90% of periods lasting t days at the given location. MADP90 is calculated from the derived P90 value across a probability density function (PDF) of daily mean output during each t -day window in the time series (2010–2019). The result is a scalar that can be mapped spatially. Moving-window periods of 1, 7, 30, 60, 90 and 180 days were examined in this study. MADP90-results are available as additional results and map layers in AWH-Geo.

Extended Data Fig. 3 provides an example set of PDFs for a location in southwest Tanzania. Each of the P90 values correspond to a version of the MADP90 metric

corresponding to a moving window period. The P90 value naturally increases with t in most geographic locations as the PDF tightens its dispersion about the natural (P50) mean.

Data availability

The software and datasets generated during and/or analysed during the current study are available in the following repositories. GitHub: <https://github.com/AWH-GlobalPotential-X/AWH-Geo>; Figshare: <https://doi.org/10.6084/m9.figshare.c.5642992.v1>; JMP Geoprocessor package (Python and ArcGIS geoprocessing model); JMP Geofabric dataset (shapefile); population without SMDW image data layer (geoTiff); upper limit AWH output data layers (geoTiff); coincidence analysis results data tables (Sheets); and output tables used in this study (Sheets). [Source data](#) are provided with this paper.

Code availability

The software used during the current study is available as follows. GitHub: <https://github.com/AWH-GlobalPotential-X/AWH-Geo>; AWH-Geo application: processor and output viewer with source code; population and result data processing scripts.

References

1. 1. Bain, R., Johnston, R., Mitis, F., Chatterley, C. & Slaymaker, T. Establishing Sustainable Development Goal baselines for household drinking water, sanitation and hygiene services. *Water* **10**, 1711 (2018).
2. 2. *Progress on Drinking Water, Sanitation and Hygiene: 2017 Update and SDG Baselines* (World Health Organization and the United Nations Children's Fund, 2017).
3. 3. Hanikel, N. et al. Rapid cycling and exceptional yield in a metal-organic framework water harvester. *ACS Cent. Sci.* **5**, 1699–1706 (2019).
4. 4.

Li, R., Shi, Y., Wu, M., Hong, S. & Wang, P. Improving atmospheric water production yield: enabling multiple water harvesting cycles with nano sorbent. *Nano Energy* **67**, 104255 (2020).

5. 5.

Qi, H. et al. An interfacial solar-driven atmospheric water generator based on a liquid sorbent with simultaneous adsorption–desorption. *Adv. Mater.* **31**, 1903378 (2019).

6. 6.

Humphrey, J. H. et al. The potential for atmospheric water harvesting to accelerate household access to safe water. *Lancet Planet. Health* **4**, e91–e92 (2020).

7. 7.

Gido, B., Friedler, E. & Broday, D. M. Assessment of atmospheric moisture harvesting by direct cooling. *Atmos. Res.* **182**, 156–162 (2016).

8. 8.

Tu, R. & Hwang, Y. Reviews of atmospheric water harvesting technologies. *Energy* **201**, 117630 (2020).

9. 9.

Gould, T. Selling water at \$150/m³ to the world's poorest people – with billionaire backing. *Global Water Intelligence* vol. 21 (21 May 2020).

10. 10.

Kim, H. et al. Adsorption-based atmospheric water harvesting device for arid climates. *Nat. Commun.* **9**, 1191 (2018).

11. 11.

LaPotin, A., Kim, H., Rao, S. R. & Wang, E. N. Adsorption-based atmospheric water harvesting: impact of material and component properties on system-level performance. *Acc. Chem. Res.* **52**, 1588–1597 (2019).

12. 12.

Tu, Y., Wang, R., Zhang, Y. & Wang, J. Progress and expectation of atmospheric water harvesting. *Joule* **2**, 1452–1475 (2018).

13. 13.

Gorelick, N. et al. Google Earth Engine: planetary-scale geospatial analysis for everyone. *Remote Sens. Environ.* **202**, 18–27 (2017).

14. 14.

Gleick, P. H. Basic water requirements for human activities: meeting basic needs. *Water Int.* **21**, 83–92 (1996).

15. 15.

Zhao, F. et al. Super moisture-absorbent gels for all-weather atmospheric water harvesting. *Adv. Mater.* **31**, 1806446 (2019).

16. 16.

Kim, H. et al. Water harvesting from air with metal-organic frameworks powered by natural sunlight. *Science* **356**, 430–434 (2017).

17. 17.

Matsumoto, K., Sakikawa, N. & Miyata, T. Thermo-responsive gels that absorb moisture and ooze water. *Nat. Commun.* **9**, 2315 (2018).

18. 18.

Global Indicator Framework for the Sustainable Development Goals and Targets of the 2030 Agenda for Sustainable Development (United Nations, 2018).

19. 19.

Hutton, G. & Varughese, M. *The Costs of Meeting the 2030 Sustainable Development Goal Targets on Drinking Water, Sanitation, and Hygiene* (Water and Sanitation Program, 2016).

20. 20.

Brown, J. & Clasen, T. High adherence is necessary to realize health gains from water quality interventions. *PLoS ONE* **7**, e36735 (2012).

21. 21.

Cohen, A. & Ray, I. The global risks of increasing reliance on bottled water. *Nat. Sustain.* **1**, 327–329 (2018).

22. 22.

Wahlgren, R. V. Atmospheric water vapour processor designs for potable water production: a review. *Water Res.* **35**, 1–22 (2001).

23. 23.

Zhou, X., Lu, H., Zhao, F. & Yu, G. Atmospheric water harvesting: a review of material and structural designs. *ACS Mater. Lett.* **2**, 671–684 (2020).

24. 24.

Domen, J. K., Stringfellow, W. T., Camarillo, M. K. & Gulati, S. Fog water as an alternative and sustainable water resource. *Clean Tech. Environ. Policy* **16**, 235–249 (2014).

25. 25.

Kim, J., Park, K., Yang, D. R. & Hong, S. A comprehensive review of energy consumption of seawater reverse osmosis desalination plants. *Appl. Energy* **254**, 113652 (2019).

26. 26.

Pullan, R. L., Freeman, M. C., Gething, P. W. & Brooker, S. J. Geographical inequalities in use of improved drinking water supply and sanitation across Sub-Saharan Africa: mapping and spatial analysis of cross-sectional survey data. *PLoS Med.* **11**, e1001626 (2014).

27. 27.

Deshpande, A. et al. Mapping geographical inequalities in access to drinking water and sanitation facilities in low-income and middle-income countries, 2000–17. *Lancet Glob. Health* **8**, e1162–e1185 (2020).

28. 28.

Mujwahuzi, M. R. et al. *Drawers of Water II: 30 Years of Change in Domestic Water Use & Environmental Health in East Africa*. (International Institute for

Environment and Development, 2002).

29. 29.

Roche, R., Bain, R. & Cumming, O. A long way to go—estimates of combined water, sanitation and hygiene coverage for 25 sub-Saharan African countries. *PLoS ONE* **11**, e0171783 (2017).

30. 30.

Beysens, D. Estimating dew yield worldwide from a few meteo data. *Atmos. Res.* **167**, 146–155 (2016).

31. 31.

Mulchandani, A. & Westerhoff, P. Geospatial climatic factors influence water production of solar desiccant driven atmospheric water capture devices. *Environ. Sci. Technol.* **54**, 8310–8322 (2020).

32. 32.

Peeters, R., Vanderschaeghe, H., Rongé, J. & Martens, J. A. Energy performance and climate dependency of technologies for fresh water production from atmospheric water vapour. *Environ. Sci. Water Res. Technol.* **6**, 2016–2034 (2020).

33. 33.

Kim, H., Rao, S. R., LaPotin, A., Lee, S. & Wang, E. N. Thermodynamic analysis and optimization of adsorption-based atmospheric water harvesting. *Int. J. Heat Mass Transfer* **161**, 120253 (2020).

34. 34.

Bagheri, F. Performance investigation of atmospheric water harvesting systems. *Water Res. Industry* **20**, 23–28 (2018).

35. 35.

What Is SOURCE? <https://www.source.co/wp-content/uploads/2020/11/SOURCE-Tech-Spec-Sheet.pdf> (accessed June 2021).

36. 36.

Wang, J. Y., Wang, R. Z., Wang, L. W. & Liu, J. Y. A high efficient semi-open system for fresh water production from atmosphere. *Energy* **138**, 542–551 (2017).

37. 37.

Hanikel, N., Prévot, M. S. & Yaghi, O. M. MOF water harvesters. *Nature Nanotechnology* **15**, 348–355 (2020).

38. 38.

LaPotin, A. et al. Dual-stage atmospheric water harvesting device for scalable solar-driven water production. *Joule* **5**, 166–182 (2021).

39. 39.

Terzis, A. et al. High-frequency water vapor sorption cycling using fluidization of metal-organic frameworks. *Cell Rep. Phys. Sci.* **1**, 100057 (2020).

40. 40.

Logan, M. W., Langevin, S. & Xia, Z. Reversible atmospheric water harvesting using metal-organic frameworks. *Sci. Rep.* **10**, 1492 (2020).

41. 41.

Yilmaz, G. et al. Autonomous atmospheric water seeping MOF matrix. *Sci Adv* **6**, eabc8605 (2020).

42. 42.

Foster, T. & Willetts, J. Multiple water source use in rural Vanuatu: are households choosing the safest option for drinking? *Int. J. Environ. Health Res.* **6**, 579–589 (2018).

43. 43.

Elliott, M. et al. Addressing how multiple household water sources and uses build water resilience and support sustainable development. *npj Clean Water* **2**, 6 (2019).

44. 44.

Oki, T. Global hydrological cycles and world water resources. *Science* **313**, 1068–1072 (2006).

45. 45.

Elhenawy, S. E. M., Khraisheh, M., AlMomaní, F. & Walker, G. Metal-organic frameworks as a platform for CO₂ capture and chemical processes: adsorption, membrane separation, catalytic-conversion, and electrochemical reduction of CO₂. *Catalysts* **10**, 1293 (2020).

46. 46.

DeSantis, D. et al. Techno-economic analysis of metal-organic frameworks for hydrogen and natural gas storage. *Energy Fuels* **31**, 2024–2032 (2017).

47. 47.

Mohapatra, S. & Simon, L. Intra-household bargaining over household technology adoption. *Rev. Econ. Household* **15**, 1263–1290 (2017).

48. 48.

Barstow, C. K. et al. Designing and piloting a program to provide water filters and improved cookstoves in Rwanda. *PLoS ONE* **9**, e92403 (2014).

49. 49.

Daniel, D., Marks, S. J., Pande, S. & Rietveld, L. Socio-environmental drivers of sustainable adoption of household water treatment in developing countries. *npj Clean Water* **9**, 12 (2018).

50. 50.

Smits, J. & Permanyer, I. The Subnational Human Development Database. *Sci. Data* **9**, 190038 (2019).

51. 51.

GADM v3.6. Global Administrative Areas 2020 (University of California, Berkeley, 2020); <https://gadm.org>

52. 52.

Spatial Data Repository, The Demographic and Health Surveys Program (USAID, 2020) <https://spatialdata.dhsprogram.com>

53. 53.

GDL v3.7.0. Global Data Lab Area Database 2020 (Institute for Management Research, Radboud University, 2020); globaldatalab.org

54. 54.

Integrating Water Quality Testing into Household Surveys: Thematic Report on Drinking Water (United Nations Children's Fund and World Health Organization, 2020).

55. 55.

Bain, R., Johnston, R., Khan, S., Hancioglu, A. & Slaymaker, T. Monitoring drinking water quality in nationally representative household surveys in low- and middle-income countries: Cross-sectional analysis of 27 Multiple Indicator Cluster Surveys 2014–2020. *Environ. Health Perspect.* **129**, 97010 (2021).

56. 56.

Lloyd, C. T. et al. Global spatio-temporally harmonised datasets for producing high-resolution gridded population distribution datasets. *Big Earth Data* **3**, 108–139 (2019).

57. 57.

Bain, R., Johnston, R. & Slaymaker, T. Drinking water quality and the SDGs. *npj Clean Water* **3**, 37 (2020).

58. 58.

Jacobson, M. Z. & Jadhav, V. World estimates of PV optimal tilt angles and ratios of sunlight incident upon tilted and tracked PV panels relative to horizontal panels. *Solar Energy* **169**, 55–66 (2018).

59. 59.

Champion photovoltaic module efficiency chart. *National Renewable Energy Laboratory* <https://www.nrel.gov/pv/assets/pdfs/champion-module-efficiencies.20200708.pdf> (2020).

60. 60.

Muñoz Sabater, J. ERA5-Land Hourly Data from 1981 to Present. *Copernicus Climate Change Service (C3S) Climate Data Store (CDS)* <https://doi.org/10.24381/cds.e2161bac> (2019).

61. 61.

Alduchov, O. A. & Eskridge, R. E. Improved Magnus` form approximation of saturation vapor pressure. *J. Appl. Meteorol. Climatol.* **35**, 601–609 (1996).

62. 62.

Iowa Environmental Mesonet (Iowa State University, 2020);
<https://mesonet.agron.iastate.edu/>

63. 63.

Blanco, M. J., Martín, J. G. & Alarcón-Padilla, D. C. Theoretical efficiencies of angular-selective non-concentrating solar thermal systems. *Solar Energy* **76**, 683–691 (2004).

64. 64.

Brewer, C. A. ColorBrewer2. <http://www.ColorBrewer.org> (2020).

65. 65.

Beaudoin, H., Rodell, M. GLDAS Noah Land Surface Model L4 Monthly 0.25 × 0.25 Degree V2.1 (Goddard Earth Sciences Data and Information Services Center, 2020); <https://doi.org/10.5067/SXAVCZFAQLNO>

66. 66.

Rose, A. N., McKee, J. J., Urban, M. L. & Bright, E. A. *LandScan 2017* (Oak Ridge National Laboratory, 2018).

Acknowledgements

We acknowledge contributions from many colleagues, including A. Aron-Gilat, D. Youmans, G.L. Whiting, M. Eisaman, S. Lin, J. Sargent, S. McAlister, S. Chariyasatit, B. Dixon, E. St Jean Duggan, F. Carlsru, K. Stratton, M. McCoy, R. Hessmer, J. Hanna, H. Riley, P. Watson, M. Day, B. Quintanilla-Whyte, A. Ramadan, A. Little and D. Moufarege. We thank the WHO/UNICEF JMP team for guidance on drinking water service estimates, in particular T. Slaymaker, R. Johnston and F. Mitis; the team at Google Earth Engine, in particular S. Ilyushchenko, S. Agarwal, T. Erickson, N. Gorelick, M. Hancher, M. Dixon, M. DeWitt, J. Conkling, N. Clinton, K. Reid, E. Engle, W. Rucklidge and the entire Earth Engine development community for advice;

C. Caywood for code review; B. Schillings and J. Gagne for internal sponsorship at X. Funding was provided by Google LLC.

Author information

Affiliations

1. X, The Moonshot Factory, Mountain View, CA, USA

Jackson Lord, Ashley Thomas, Neil Treat, Matthew Forkin, Cyrus H. Behroozi, Tilek Mamutov, Jillia Fongheiser, Nicole Kobilansky, Shane Washburn, Claudia Truesdell, Clare Lee & Philipp H. Schmaelzle

2. WHO/UNICEF Joint Monitoring Programme, Division of Data, Analytics, Planning and Monitoring, UNICEF, New York, NY, USA

Robert Bain

3. Google Inc., Mountain View, CA, USA

Pierre Dulac

Contributions

P.H.S. and J.L. conceived the study. J.L., P.D., T.M. and N.T. performed analysis and plots. A.T., N.T., J.L., P.H.S., R.B. and C.H.B. developed arguments. J.L., P.H.S., A.T. and R.B. wrote the paper. This study was conducted as a subset of a larger effort at X, led by P.H.S., M.F., N.T. and A.T., to develop a household AWH as a commercial product, which informed the current study: M.F., N.T. and S.W. led prototype development and experimentation, C.H.B. conducted physical modelling, M.F., S.W., C.T., C.L. and others built devices and conducted experiments, A.T., J.F. and N.K. conducted market and user research.

Corresponding authors

Correspondence to Jackson Lord or Philipp H. Schmaelzle.

Ethics declarations

Competing interests

We disclose the following potential competing interests. This work was funded by X, The Moonshot Factory (formerly known as Google[x]). X is a part of Alphabet. Both are for-profit entities. X has filed for patent protection for water-from-air devices, on which multiple authors are listed as inventors. Water-from-air devices may represent significant commercial opportunities upon meeting certain metrics. This work may be pursued further in various ways, including as a possible spinout company in which one or more authors may become founders, officers, shareholders, employees or otherwise involved with a financial interest.

Additional information

Peer review information *Nature* thanks Marisa Escobar and the other, anonymous, reviewer(s) for their contribution to the peer review of this work. Peer reviewer reports are available.

Publisher's note Springer Nature remains neutral with regard to jurisdictional claims in published maps and institutional affiliations.

Extended data figures and tables

[Extended Data Fig. 1 Comparison of coincidence analysis results to input datasets.](#)

Main results from coincidence analysis (Fig. 4b, people without SMDW served by opH/d of coincident climate threshold) with ERA5-Land and WorldPop 2017 datasets compared with results from **(a)** GLDAS 2.1 climate and WorldPop 2017 population, and **(b)** GLDAS 2.1 climate and LandScan 2017 population datasets. Operational hours per day (opH/d) shown across global horizontal irradiance (GHI) and relative humidity (rH) thresholds.

[Extended Data Fig. 2 Validation of SMDW using household surveys reporting SMDW at household-level.](#)

(a) Charted and **(b)** tabulated validation of cross-estimation of percentage safely managed (SM) from at least basic (ALB) drinking water ladders at sub-national (SN) level from national (N) breakdowns using known reference data set at SN level from WHO/UNICEF JMP data. Reference values from nationally representative Multiple Indicator Cluster Surveys integrating water quality testing (ref. SM) compared with our estimates from the JMP Geoprocessor combining JMP sub-national estimates for ALB and national estimates for safely managed drinking water services (est. SM). Ordinary least squares regression (OLS) resulted in standard error (stdErr) as

reported. Sample size $n = 15$. Table **(b)** shows main results (ERA5-Land) population counts after adjustment from regression. Population without safely managed drinking water (SMDW) shown across global horizontal irradiance (GHI) and relative humidity (rH) thresholds.

Extended Data Fig. 3 Visual representation of MADP90 concept from location in Tanzania.

Histograms of moving-averaged output ($L/d/m^2$) across window periods (indicated in days) for a location in Manda, Tanzania. P90 availability value increases as averaging window period increases. P90 values are estimated and for illustrative purposes only.

Extended Data Fig. 4 Select MADP90 metrics of AWH upper bounds.

(a) MADP90-90day, and **(b)** MADP90-7day values (measure of availability through time) globally for AWH thermodynamic upper bounds (Kim 2020), during ten year 2010–2019 (inclusive) analysis period.

Extended Data Fig. 5 Bi-weekly timeseries of AWH output and climate drivers for equatorial profile in Davao, Philippines.

Bi-weekly mean output ($L/d/m^2$), and climate inputs global horizontal irradiance (GHI , plotted from 0–1000 W/m^2), relative humidity (rH , plotted from 0–100 %), and temperature (plotted from 0–100 $^{\circ}C$) of **(a)** AWH thermodynamic upper bounds (Kim 2020) during ten year 2010–2019 (inclusive) analysis period for each bi-weekly interval and **(b)** averaged by bi-weekly period annually during this period, and **(c)** for the 1 billion user linear target curve for each bi-weekly interval. Example of a steady, low variability output profile characteristic of equatorial tropics.

Extended Data Fig. 6 Bi-weekly timeseries of AWH output and climate drivers for tropical savanna profile in Accra, Ghana.

Bi-weekly mean output ($L/d/m^2$), and climate inputs global horizontal irradiance (GHI , plotted from 0–1000 W/m^2), relative humidity (rH , plotted from 0–100 %), and temperature (plotted from 0–100 $^{\circ}C$) of **(a)** AWH thermodynamic upper bounds (Kim 2020) during ten year 2010–2019 (inclusive) analysis period for each bi-weekly interval and **(b)** averaged by bi-weekly period annually during this period, and **(c)** for the 1 billion user linear target curve for each bi-weekly interval. Example of a seasonal wet-dry tropical savanna climate with moderate semi-annual fluctuations of AWH output driven by rH .

[Extended Data Fig. 7 Bi-weekly timeseries of AWH output and climate drivers for tropical savanna profile in Dhaka, Bangladesh.](#)

Bi-weekly mean output ($L/d/m^2$), and climate inputs global horizontal irradiance (GHI , plotted from 0–1000 W/m^2), relative humidity (rH , plotted from 0–100 %), and temperature (plotted from 0–100 °C) of **(a)** AWH thermodynamic upper bounds (Kim 2020) during ten year 2010–2019 (inclusive) analysis period for each bi-weekly interval and **(b)** averaged by bi-weekly period annually during this period, and **(c)** for the 1 billion user linear target curve for each bi-weekly interval. Example of a seasonal wet-dry tropical savanna climate with pronounced semi-annual fluctuations of AWH output driven by rH .

[Extended Data Fig. 8 Bi-weekly timeseries of AWH output and climate drivers for mid-latitude profile in Ulaanbaatar, Mongolia.](#)

Bi-weekly mean output ($L/d/m^2$), and climate inputs global horizontal irradiance (GHI , plotted from 0–1000 W/m^2), relative humidity (rH , plotted from 0–100 %), and temperature (plotted from 0–100 °C) of **(a)** AWH thermodynamic upper bounds (Kim 2020) during ten year 2010–2019 (inclusive) analysis period for each bi-weekly interval and **(b)** averaged by bi-weekly period annually during this period, and **(c)** for the 1 billion user linear target curve for each bi-weekly interval. Example of a mid-latitude climate with pronounced semi-annual fluctuations of AWH output driven by temperature.

[Extended Data Fig. 9 Decadal anomaly of AWH output with logistic SY profile between 2000–2009 and 2010–2019.](#)

(a) Overall mean output ($L/d/m^2$) of 1 billion user target logistic curve at 5 $L/d/m^2$ during ten year 2010–2019 (inclusive) period. **(b)** Ratio (%) anomaly of output of same specific yield (SY , in L/kWh) profile averaged over ten year 2000–2009 (inclusive) period. Red colors indicate increasing AWH output with time between the two decades. Blue colors indicate decreasing AWH output.

Supplementary information

[Peer Review File](#)

Source data

[Source Data Fig. 3](#)

Source Data Fig. 4

Rights and permissions

Open Access This article is licensed under a Creative Commons Attribution 4.0 International License, which permits use, sharing, adaptation, distribution and reproduction in any medium or format, as long as you give appropriate credit to the original author(s) and the source, provide a link to the Creative Commons license, and indicate if changes were made. The images or other third party material in this article are included in the article's Creative Commons license, unless indicated otherwise in a credit line to the material. If material is not included in the article's Creative Commons license and your intended use is not permitted by statutory regulation or exceeds the permitted use, you will need to obtain permission directly from the copyright holder. To view a copy of this license, visit <http://creativecommons.org/licenses/by/4.0/>.

Reprints and Permissions

About this article

Cite this article

Lord, J., Thomas, A., Treat, N. *et al.* Global potential for harvesting drinking water from air using solar energy. *Nature* **598**, 611–617 (2021).
<https://doi.org/10.1038/s41586-021-03900-w>

- Received: 05 February 2021
- Accepted: 11 August 2021
- Published: 27 October 2021
- Issue Date: 28 October 2021
- DOI: <https://doi.org/10.1038/s41586-021-03900-w>

Share this article

Anyone you share the following link with will be able to read this content:

[Get shareable link](#)

Sorry, a shareable link is not currently available for this article.

[Copy to clipboard](#)

Provided by the Springer Nature SharedIt content-sharing initiative

This article was downloaded by **calibre** from <https://www.nature.com/articles/s41586-021-03900-w>

| [Section menu](#) | [Main menu](#) |

- Article
- [Published: 27 October 2021](#)

Indo-Pacific Walker circulation drove Pleistocene African aridification

- [H. J. L. van der Lubbe](#) ORCID: [orcid.org/0000-0001-7545-6502^{1,2}](https://orcid.org/0000-0001-7545-6502),
- [I. R. Hall](#) ORCID: [orcid.org/0000-0001-6960-1419¹](https://orcid.org/0000-0001-6960-1419),
- [S. Barker¹](#),
- [S. R. Hemming](#) ORCID: [orcid.org/0000-0001-8117-2303³](https://orcid.org/0000-0001-8117-2303),
- [T. F. Baars](#) ORCID: [orcid.org/0000-0003-3163-4885⁴](https://orcid.org/0000-0003-3163-4885),
- [A. Starr](#) ORCID: [orcid.org/0000-0003-1854-4412¹](https://orcid.org/0000-0003-1854-4412),
- [J. Just](#) ORCID: [orcid.org/0000-0002-5257-604X⁵](https://orcid.org/0000-0002-5257-604X),
- [B. C. Backeberg^{6,7,8}](#) &
- [J. C. A. Joordens](#) ORCID: [orcid.org/0000-0002-5757-1168^{9,10,11}](https://orcid.org/0000-0002-5757-1168)

Nature volume **598**, pages 618–623 (2021)

- 859 Accesses
- 42 Altmetric
- [Metrics details](#)

Subjects

- [Palaeoceanography](#)
- [Palaeoclimate](#)

Abstract

Today, the eastern African hydroclimate is tightly linked to fluctuations in the zonal atmospheric Walker circulation^{1,2}. A growing body of evidence indicates that this circulation shaped hydroclimatic conditions in the Indian Ocean region also on much longer, glacial–interglacial timescales^{3,4,5}, following the development of Pacific Walker circulation around 2.2–2.0 million years ago (Ma)^{6,7}. However, continuous long-term records to determine the timing and mechanisms of Pacific-influenced climate transitions in the Indian Ocean have been unavailable. Here we present a seven-million-year-long record of wind-driven circulation of the tropical Indian Ocean, as recorded in Mozambique Channel Throughflow (MCT) flow-speed variations. We show that the MCT flow speed was relatively weak and steady until 2.1 ± 0.1 Ma, when it began to increase, coincident with the intensification of the Pacific Walker circulation^{6,7}. Strong increases during glacial periods, which reached maxima after the Mid-Pleistocene Transition (0.9–0.64 Ma; ref. ⁸), were punctuated by weak flow speeds during interglacial periods. We provide a mechanism explaining that increasing MCT flow speeds reflect synchronous development of the Indo-Pacific Walker cells that promote aridification in Africa. Our results suggest that after about 2.1 Ma, the increasing aridification is punctuated by pronounced humid interglacial periods. This record will facilitate testing of hypotheses of climate–environmental drivers for hominin evolution and dispersal.

Access options

Subscribe to Journal

Get full journal access for 1 year

\$199.00

only \$3.90 per issue

[Subscribe](#)

All prices are NET prices.

VAT will be added later in the checkout.

Tax calculation will be finalised during checkout.

Rent or Buy article

Get time limited or full article access on ReadCube.

from \$8.99

[Rent or Buy](#)

All prices are NET prices.

Additional access options:

- [Log in](#)
- [Access through your institution](#)
- [Learn about institutional subscriptions](#)

Fig. 1: Regional oceanographic settings of IODP Site U1476 (2,166 m water depth).

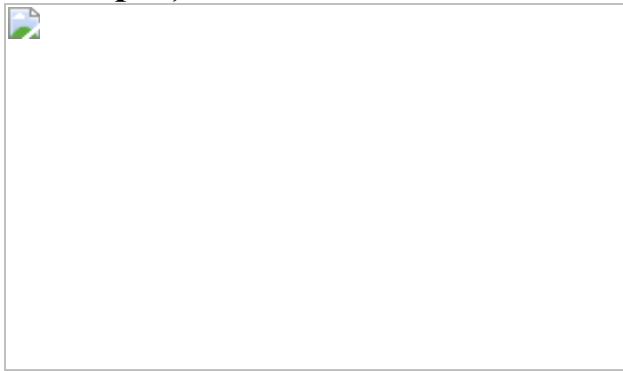
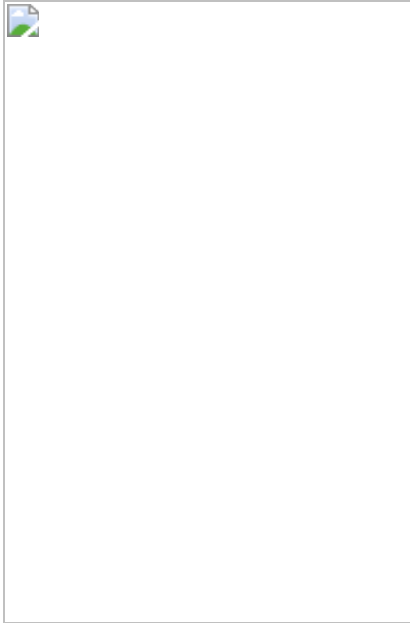


Fig. 2: Climatic and oceanographic records over the past seven million years.



Fig. 3: MCT and eastern African aridity records with distinct glacial and interglacial intervals over the past 3.3 Myr.



Data availability

All new benthic oxygen isotopic and lithogenic grain-size data of the spliced record of IODP Site U1476 are available via www.pangaea.de at <https://doi.org/10.1594/PANGAEA.933831> and <https://doi.org/10.1594/PANGAEA.933833>, respectively.

References

1. 1.

Saji, N., Goswami, B., Vinayachandran, P. & Yamagata, T. A dipole mode in the tropical Indian Ocean. *Nature* **401**, 360–363 (1999).

2. 2.

Tierney, J. E., Smerdon, J. E., Anchukaitis, K. J. & Seager, R. Multidecadal variability in East African hydroclimate controlled by the Indian Ocean. *Nature* **493**, 389–392 (2013).

3. 3.

Kaboth-Bahr, S. et al. Paleo-ENSO influence on African environments and early modern humans. *Proc. Natl Acad. Sci. USA* **118**, e2018277118 (2021).

4. 4.

Maslin, M. A. et al. East African climate pulses and early human evolution. *Quat. Sci. Rev.* **101**, 1–17 (2014).

5. 5.

Trauth, M. H., Larrasoana, J. C. & Mudelsee, M. Trends, rhythms and events in Plio–Pleistocene African climate. *Quat. Sci. Rev.* **28**, 399–411 (2009).

6. 6.

Etourneau, J., Schneider, R., Blanz, T. & Martinez, P. Intensification of the Walker and Hadley atmospheric circulations during the Pliocene–Pleistocene climate transition. *Earth Planet. Sci. Lett.* **297**, 103–110 (2010).

7. 7.

Ravelo, A. C., Andreasen, D. H., Lyle, M., Olivarez Lyle, A. & Wara, M. W. Regional climate shifts caused by gradual global cooling in the Pliocene epoch. *Nature* **429**, 263–267 (2004).

8. 8.

Mudelsee, M. & Schulz, M. The Mid-Pleistocene climate transition: onset of 100 ka cycle lags ice volume build-up by 280 ka. *Earth Planet. Sci. Lett.* **151**, 117–123 (1997).

9. 9.

Hermes, J. & Reason, C. Annual cycle of the South Indian Ocean (Seychelles-Chagos) thermocline ridge in a regional ocean model. *J. Geophys. Res. Oceans* **113**, 1–10 (2008).

10. 10.

Rao, S. A. & Behera, S. K. Subsurface influence on SST in the tropical Indian Ocean: structure and interannual variability. *Dyn. Atmos. Oceans* **39**, 103–135 (2005).

11. 11.

Nicholson, S. E. Climate and climatic variability of rainfall over eastern Africa. *Rev. Geophys.* **55**, 590–635 (2017).

12. 12.

deMenocal, P. B. African climate change and faunal evolution during the Pliocene–Pleistocene. *Earth Planet. Sci. Lett.* **220**, 3–24 (2004).

13. 13.

Levin, N. E. Environment and climate of early human evolution. *Annu. Rev. Earth Planet. Sci.* **43**, 405–429 (2015).

14. 14.

Hall I. R. et al. *South African Climates (Agulhas LGM Density Profile)* (International Ocean Discovery Program, 2017).

15. 15.

Ullgren, J., van Aken, H., Ridderinkhof, H., De, Ruijter, W. The hydrography of the Mozambique Channel from six years of continuous temperature, salinity, and velocity observations. *Deep Sea Res. I* **69**, 36–50 (2012).

16. 16.

Backeberg, B. C. & Reason, C. J. C. A connection between the South Equatorial Current north of Madagascar and Mozambique Channel eddies. *Geophys. Res. Lett.* **37**, 1–6 (2010).

17. 17.

Makarim, S. et al. Previously unidentified Indonesian Throughflow pathways and freshening in the Indian Ocean during recent decades. *Sci. Rep.* **9**, 7364 (2019).

18. 18.

Backeberg, B. C., Penven, P. & Rouault, M. Impact of intensified Indian Ocean winds on mesoscale variability in the Agulhas system. *Nat. Clim. Change* **2**, 608–612 (2012).

19. 19.

Paris, M. L., Subrahmanyam, B., Trott, C. B. & Murty, V. S. N. Influence of ENSO events on the Agulhas leakage region. *Remote Sens. Earth Syst. Sci.* **1**, 79–88 (2018).

20. 20.

Palastanga, V., Van Leeuwen, P. & De, Ruijter, W. A link between low-frequency mesoscale eddy variability around Madagascar and the

large-scale Indian Ocean variability. *J. Geophys. Res. Oceans* **111**, 1–15 (2006).

21. 21.

Ridderinkhof, H. et al Seasonal and interannual variability in the Mozambique Channel from moored current observations. *J. Geophys. Res. Oceans* **115**, 1–18 (2010).

22. 22.

Ridderinkhof, W., Le Bars, D., Von der Heydt, A. & De, Ruijter, W. Dipoles of the south east Madagascar Current. *Geophys. Res. Lett.* **40**, 558–562 (2013).

23. 23.

Yamagami, Y. & Tozuka, T. Interannual variability of South Equatorial Current bifurcation and western boundary currents along the Madagascar coast. *J. Geophys. Res. Oceans* **120**, 8551–8570 (2015).

24. 24.

Jin, X. et al. Influences of Pacific climate variability on decadal subsurface ocean heat content variations in the Indian Ocean. *J. Clim.* **31**, 4157–4174 (2018).

25. 25.

van Oldenborgh, G. J., Doblas-Reyes, F. J., Wouters, B. & Hazeleger, W. Decadal prediction skill in a multi-model ensemble. *Clim. Dyn.* **38**, 1263–1280 (2012).

26. 26.

Herbert, T. D. et al. Late Miocene global cooling and the rise of modern ecosystems. *Nat. Geosci.* **9**, 843–847 (2016).

27. 27.

Groeneveld, J. et al. Australian shelf sediments reveal shifts in Miocene Southern Hemisphere westerlies. *Sci. Adv.* **3**, 1–9 (2017).

28. 28.

Liu, J. et al. Eastern equatorial Pacific cold tongue evolution since the late Miocene linked to extratropical climate. *Sci. Adv.* **5**, 1–7 (2019).

29. 29.

Fedorov, A. et al. Patterns and mechanisms of early Pliocene warmth. *Nature* **496**, 43–49 (2013).

30. 30.

Haug, G. H., Tiedemann, R., Zahn, R. & Ravelo, A. C. Role of Panama uplift on oceanic freshwater balance. *Geology* **29**, 207–210 (2001).

31. 31.

Brierley, C. M. et al. Greatly expanded tropical warm pool and weakened Hadley circulation in the Early Pliocene. *Science* **323**, 1714–1718 (2009).

32. 32.

Tierney, J. E., Haywood, A. M., Feng, R., Bhattacharya, T. & Otto-Bliesner, B. L. Pliocene warmth consistent with greenhouse gas forcing. *Geophys. Res. Lett.* **46**, 9136–9144 (2019).

33. 33.

Cane, M. A. & Molnar, P. Closing of the Indonesian seaway as a precursor to east African aridification around 3–4 million years ago. *Nature* **411**, 157–162 (2001).

34. 34.

Petrick, B. et al. Glacial Indonesian Throughflow weakening across the Mid-Pleistocene climatic transition. *Sci. Rep.* **9**, 16995 (2019).

35. 35.

Karas, C. et al. Mid-Pliocene climate change amplified by a switch in Indonesian subsurface throughflow. *Nat. Geosci.* **2**, 434–438 (2009).

36. 36.

Karas, C., Nürnberg, D., Tiedemann, R. & Garbe-Schönberg, D. Pliocene Indonesian Throughflow and Leeuwin Current dynamics: implications for Indian Ocean polar heat flux. *Paleoceanography* **26**, PA2217 (2011).

37. 37.

Christensen, B. A. et al. Indonesian Throughflow drove Australian climate from humid Pliocene to arid Pleistocene. *Geophys. Res. Lett.* **44**, 6914–6925 (2017).

38. 38.

Chen, Z., Wu, L., Qiu, B., Sun, S. & Jia, F. Seasonal variation of the South Equatorial Current bifurcation off Madagascar. *J. Phys. Oceanogr.* **44**, 618–631 (2014).

39. 39.

Rippert, N., Baumann, K.-H. & Pätzold, J. Thermocline fluctuations in the western tropical Indian Ocean during the past 35 ka. *J. Quat. Sci.* **30**, 201–210 (2015).

40. 40.

Ahn, S., Khider, D., Lisiecki, L. E. & Lawrence, C. A probabilistic Pliocene–Pleistocene stack of benthic $\delta^{18}\text{O}$ using a profile hidden Markov model. *Dyn. Stat. Clim. Syst.* **2**, 1–16 (2017).

41. 41.

Zachos, J., Pagani, M., Sloan, L., Thomas, E. & Billups, K. Trends, rhythms, and aberrations in global climate 65 Ma to present. *Science* **292**, 686–693 (2001).

42. 42.

Ravelo, A. C., Lawrence, K. T., Fedorov, A. & Ford, H. L. Comment on “A 12-million-year temperature history of the tropical Pacific Ocean”. *Science* **346**, 1467 (2014).

43. 43.

Wara, M. W., Ravelo, A. C. & Delaney, M. L. Permanent El Niño-like conditions during the Pliocene warm period. *Science* **309**, 758–761 (2005).

44. 44.

Bjerknes, J. Atmospheric teleconnections from the equatorial Pacific. *Mon. Weather Rev.* **97**, 163–172 (1969).

45. 45.

Emeis, K.-C., Anderson, D. M., Doose, H., Kroon, D., Schulz-Bull, D. Sea-surface temperatures and the history of monsoon upwelling in the northwest Arabian Sea during the last 500,000 years. *Quat. Res.* **43**, 355–361 (1995).

46. 46.

Herbert, T. D., Peterson, L. C., Lawrence, K. T. & Liu, Z. Tropical ocean temperatures over the past 3.5 million years. *Science* **328**, 1530–1534 (2010).

47. 47.

Bobe, R. & Behrensmeyer, A. K. The expansion of grassland ecosystems in Africa in relation to mammalian evolution and the origin of the genus *Homo*. *Palaeogeogr. Palaeoclimatol. Palaeoecol.* **207**, 399–420 (2004).

48. 48.

Kiefer, T., McCave, I. N. & Elderfield, H. Antarctic control on tropical Indian Ocean sea surface temperature and hydrography. *Geophys. Res. Lett.* **33**, 1–5 (2006).

49. 49.

Mohtadi, M., Prange, M., Schefuß, E. & Jennerjahn, T. C. Late Holocene slowdown of the Indian Ocean Walker circulation. *Nat. Commun.* **8**, 1015 (2017).

50. 50.

Faith J. T. et al. Rethinking the ecological drivers of hominin evolution. *Trends Ecol. Evol.* **36**, 797–807 (2021).

51. 51.

Hall I. R., Hemming S. R. & LeVay L. J. *South African Climates (Agulhas LGM Density Profile)* (2016).

52. 52.

Konert, M. & Vandenberghe, J. Comparison of laser grain size analysis with pipette and sieve analysis: a solution for the underestimation of the clay fraction. *Sedimentology* **44**, 523–535 (1997).

53. 53.

Van der Lubbe, H. et al. Sedimentation patterns off the Zambezi River over the last 20,000 years. *Mar. Geol.* **355**, 189–201 (2014).

54. 54.

McCave, I. & Andrews, J. Distinguishing current effects in sediments delivered to the ocean by ice. I. Principles, methods and examples. *Quat. Sci. Rev.* **212**, 92–107 (2019).

55. 55.

Weltje, G. J. & Tjallingii, R. Calibration of XRF core scanners for quantitative geochemical logging of sediment cores: theory and application. *Earth Planet. Sci. Lett.* **274**, 423–438 (2008).

56. 56.

Miramontes, E. et al. The influence of bottom currents on the Zambezi Valley morphology (Mozambique Channel, SW Indian Ocean): in situ current observations and hydrodynamic modelling. *Mar. Geol.* **410**, 42–55 (2019).

57. 57.

Starr, A. et al. Antarctic icebergs reorganize ocean circulation during Pleistocene glacials. *Nature* **589**, 236–241 (2021).

58. 58.

Anthonissen, D. E. & Ogg, J. G. in *The Geologic Time Scale* (eds Gradstein, F. M. et al.) 1083–1127 (Elsevier, 2012).

59. 59.

Tangunan, D. N. et al. The last 1 million years of the extinct genus *Discoaster*: Plio–Pleistocene environment and productivity at Site U1476 (Mozambique Channel). *Palaeogeogr. Palaeoclimatol. Palaeoecol.* **505**, 187–197 (2018).

60. 60.

Lougheed, B. C. & Obrochta, S. P. A rapid, deterministic age-depth modeling routine for geological sequences with inherent depth uncertainty. *Paleoceanogr. Paleoclimatol.* **34**, 122–133 (2019).

61. 61.

Mudelsee, M. Ramp function regression: a tool for quantifying climate transitions. *Comput. Geosci.* **26**, 293–307 (2000).

62. 62.

Huang, Y., Clemens, S. C., Liu, W., Wang, Y. & Prell, W. L. Large-scale hydrological change drove the late Miocene C4 plant expansion in the Himalayan foreland and Arabian Peninsula. *Geology* **35**, 531–534 (2007).

63. 63.

Schott, F. A., Xie, S. P. & McCreary, J. P. Jr Indian Ocean circulation and climate variability. *Rev. Geophys.* **47**, 1–46 (2009).

64. 64.

McCreary, J. P., Kundu, P. K. & Molinari, R. L. A numerical investigation of dynamics, thermodynamics and mixed-layer processes in the Indian Ocean. *Prog. Oceanogr.* **31**, 181–244 (1993).

65. 65.

Centenary Edition of the GEBCO Digital Atlas (IOC, IHO, BODC, 2003).

66. 66.

Mulet, S. et al. The new CNES-CLS18 global mean dynamic topography. *Ocean Sci. Discuss.* **2021**, 1–31 (2021).

67. 67.

Putrasahan, D., Kirtman, B. P. & Beal, L. M. Modulation of SST interannual variability in the Agulhas leakage region associated with ENSO. *J. Clim.* **29**, 7089–7102 (2016).

68. 68.

Abram, N. J. et al. Coupling of Indo-Pacific climate variability over the last millennium. *Nature* **579**, 385–392 (2020).

69. 69.

Rayner, N. A. et al. Global analyses of sea surface temperature, sea ice, and night marine air temperature since the late nineteenth century. *J. Geophys. Res. Atmos.* **108**, 1–29 (2003).

70. 70.

McCave, I., Thornalley, D. & Hall, I. Relation of sortable silt grain-size to deep-sea current speeds: calibration of the ‘mud current meter’. *Deep Sea Res. I* **127**, 1–2 (2017).

71. 71.

McCave, I. N., Manighetti, B. & Robinson, S. G. Sortable silt and fine sediment size/composition slicing: parameters for palaeocurrent speed and palaeoceanography. *Paleoceanography* **10**, 593–610 (1995).

72. 72.

van Aken, H. M., Ridderinkhof, H. & de Ruijter, W. P. North Atlantic deep water in the south-western Indian Ocean. *Deep Sea Res. I* **51**, 755–776 (2004).

73. 73.

Ridderinkhof, H. & De Ruijter, W. Moored current observations in the Mozambique Channel. *Deep Sea Res. II* **50**, 1933–1955 (2003).

74. 74.

Lisiecki, L. E., Raymo, M. E. A Pliocene–Pleistocene stack of 57 globally distributed benthic $\delta^{18}\text{O}$ records. *Paleoceanography* **20**, PA1003 (2005).

75. 75.

Dekens, P. S., Lea, D. W., Pak, D. K., Spero, H. J. Core top calibration of Mg/Ca in tropical foraminifera: refining paleotemperature estimation. *Geochem. Geophys. Geosyst.* **3**, 1–29 (2002).

Acknowledgements

We are grateful to the government of Mozambique for their permission for deep-sea drilling operations in the context of palaeoclimate and palaeoceanography research. This research used samples and data provided by the Integrated Ocean Drilling Program (IODP). We appreciate the entire shipboard party of IODP Expedition 361 ‘South African Climates’ for their tireless efforts at sea. We thank S. Conn, M. Hagen, S. Lordsmith, A. Nederbragt, L. Owen, M. P. Prins, S. Rumping, S. Slater, C. W. Nooitgedacht, F. van Bakel, S. de Bie and C. van Eijbergen for laboratory assistance. Funding for this work was provided in part by the Dutch Research Council (NWO) (Open Programme grant number 824.01.005 to H.J.L.v.d.L., and Talent Programme grant number 016.Vidi.171.049 to J.C.A.J.) and the UK Natural Environment Research Council (grant number NE/P000037/1 to I.R.H. and grant number NE/P000878/1 to S.B.). We acknowledge R. D. Norris and N. Mantke for X-ray fluorescence scanning the spliced record of Site U1476.

Author information

Affiliations

1. School of Earth and Environmental Sciences, Cardiff University,
Cardiff, UK

H. J. L. van der Lubbe, I. R. Hall, S. Barker & A. Starr

2. Department of Earth Sciences, Faculty of Science, Vrije Universiteit
(VU), Amsterdam, the Netherlands

H. J. L. van der Lubbe

3. Earth and Environmental Sciences, Lamont-Doherty Earth Observatory, Palisades, NY, USA

S. R. Hemming

4. Department of Geosciences and Engineering, Delft University of Technology, TU Delft, the Netherlands

T. F. Baars

5. Department of Geosciences, Universität Bremen, Bremen, Germany

J. Just

6. Deltares, Delft, the Netherlands

B. C. Backeberg

7. Nansen Environmental and Remote Sensing Center, Bergen, Norway

B. C. Backeberg

8. Nansen-Tutu Centre for Marine Environmental Research, Cape Town, South Africa

B. C. Backeberg

9. Naturalis Biodiversity Center, Leiden, the Netherlands

J. C. A. Joordens

10. Faculty of Science and Engineering, Maastricht University, Maastricht, the Netherlands

J. C. A. Joordens

11. Faculty of Archaeology, Leiden University, Leiden, the Netherlands

J. C. A. Joordens

Contributions

IODP Expedition 361 was led by I.R.H. and S.R.H. S.B. produced the benthic oxygen isotope record and J.J. produced the X-ray fluorescence bulk chemistry records. H.J.L.v.d.L. and I.R.H. designed the research, H.J.L.v.d.L. performed the grain-size analysis with input from T.F.B. and performed further data analyses with input from I.R.H. and A.S. H.J.L.v.d.L. conducted oceanographic and climatic analyses with input from B.C.B. H.J.L.v.d.L. wrote the manuscript with contributions from I.R.H., J.C.A.J. and A.S. All authors contributed to the data interpretation and commented on the final manuscript. T.F.B. edited the figure layout for publication.

Corresponding authors

Correspondence to H. J. L. van der Lubbe or I. R. Hall.

Ethics declarations

Competing interests

The authors declare no competing interests.

Additional information

Peer review information *Nature* thanks John Andrews, Clara Bolton, Matt O'Regan, Benjamin Petrick and the other, anonymous, reviewer(s) for their contribution to the peer review of this work.

Publisher's note Springer Nature remains neutral with regard to jurisdictional claims in published maps and institutional affiliations.

Extended data figures and tables

Extended Data Fig. 1 Coupled oceanographic and atmospheric circulation of the Indian Ocean region.

a, Surface circulation indicated by mean geostrophic velocities and directions. IODP Site U1476 is situated in the Mozambique Channel, which experiences a net southward flow of the Mozambique Channel Throughflow (MCT). The tropical Indian gyre receives and redistributes inflow from the Indonesian Throughflow (ITF). The main components of the tropical Indian gyre: East African Coastal Current (EACC), Southern Equatorial Current (SEC), Southern Equatorial Counter Current (SECC) and Northeast Madagascar Current (NEMC) are highlighted with a dark grey outline marking the mean extension of the tropical gyre^{63,64}. At ~60°E, the SEC bifurcates into two main branches feeding into the NEMC and the Southeastern Madagascar Current (SEMC) as it crosses bathymetric highs including the Mascarene Plateau, highlighted by the solid grey bathymetric contour at 2,200 m water depth. The SEMC is outside the outline of the tropical gyre as it is part of the anti-cyclonic subtropical gyre. **b**, Mean wind stress (gray arrows) and wind stress curl of the Indian Ocean indicate the basin-wide negative (positive) wind stress curl forcing the tropical (subtropical) gyre. A black line indicates the zero wind stress curl. **c**, Mean dynamic sea surface topography indicating a sea-level low between 10-5°S at the centre of the tropical Indian gyre; the Seychelles–Chagos thermocline ridge (SCTR)⁹. The thicker contour of 1.05 m denotes the northern extent of the subtropical gyre, whereby the blues (reds) highlight lower (higher) sea surfaces, which are associated with the cyclonic (anti-cyclonic) circulation of the tropical (subtropical) gyres. The bathymetric, oceanic (1993-2012) and surface wind data (1979-2019) are derived from: General Bathymetric Chart of the Oceans (GEBCO)⁶⁵, CNES-CLS18 MDT⁶⁶, ERA5 monthly-averaged data on single levels (DOI: 10.24381/cds.6860a573), respectively. These maps are generated with MATLAB and Mapping Toolbox, version 9.8.0.1323502 (R2020a, Natick, Massachusetts: The MathWorks Inc., United States).

Extended Data Fig. 2 Dynamic sea surface topography in meters superimposed by the mean of monthly Indian Ocean sea surface height (SSH) maps.

a, Composite of all monthly SSH between 1999–2019, superimposed on dynamic sea surface topography, marks sea-level low of the SCTR (5°S – 12°S , 45°E – 90°E)⁹. Solid red line refers to cross section along longitude 52°E between latitudes 25 to 5°S , across the SEC, see **b**. **b**, Mean dynamic sea surface gradient at 52°E (red thick line) as marked by solid black line in **a**, **c**, **d**, **e** and **f**. Meridional surface height gradient and associated near-surface pressure gradient south of the SCTR drives (influenced by Coriolis force) the westward deep-reaching South Equatorial Current (SEC). Positive (negative) SSH anomalies formed during ENSO and IOD propagate westward as downwelling (upwelling) Rossby waves in ca. 6 months^{10,19,24,67}. The dynamic sea surface topography averaged over 6 months following positive Indian Ocean Dipole (+IOD), negative Indian Dipole (-IOD), positive El Niño Southern Oscillation (ENSO) - El Niño, and negative ENSO - La Niña are shown in **c**, **d**, **e** and **f**, respectively. **g**, IOD and ENSO time series with solid vertical lines indicating long-term mean with $\pm 1\text{SD}$ and $\pm 2\text{SD}$ (dashed lines). Red dots mark the months that are selected after a positive IOD (**c**) and ENSO (**e**) events, while blue dots mark the months after negative IOD (**d**) and ENSO (**f**) events. SSH anomalies induced by ENSO and IOD often reinforce each other¹⁰, since they are linked at interannual¹ to decadal time-scales⁶³, at least over the last millennium⁶⁸. Sea surface topography, SSH maps, IOD SST index¹, El Niño 3.4 SST Index⁶⁹ are from Ssalto/Duacs-Cnes; <https://www.aviso.altimetry.fr>, https://psl.noaa.gov/gcos_wgsp/Timeseries/DMI/, https://psl.noaa.gov/gcos_wgsp/Timeseries/Nino34. These maps are generated with MATLAB® and Mapping Toolbox, version 9.8.0.1323502 (R2020a, Natick, Massachusetts: The MathWorks Inc., United States).

Extended Data Fig. 3

3d representations of the mean sea surface topography. **a**, **b**, Averaged over 6 months after (**a**) warm (positive) and (**b**) cold (negative) ENSO-IOD phases, respectively induced by regional anti-cyclonic (AC) positive and cyclonic (C) negative wind stresscurls along the equatorial Indian Ocean west of 100°E , which is coupled to the atmospheric Pacific Walker Cell circulation^{10,24}. In contrast, sea surface height (SSH) variability in the

eastern Indian Ocean is derived from the western Pacific Ocean via the Indonesian Throughflow (ITF; Extended Data Figs. 1a, 2c-f). Black arrows indicate schematic representation of the zonal Walker circulation. During positive ENSO phases, the center of atmospheric deep convection shifts eastward, resulting in anomalous descending air masses over the western Pacific Ocean and Maritime Continent⁶³. The corresponding anomalous easterlies induce down-welling Rossby waves in the central Indian Ocean that propagate westward as positive SSH anomalies, increasing the thermocline depth at the SCTR while decreasing the meridional SSH gradient and corresponding SEC in the western Indian Ocean^{10,24} (Extended Data Fig. 2b). Conversely, the SSH gradient and in turn the SEC flow increases during negative ENSO phases. The associated westerlies/easterlies induce upwelling and thermocline shoaling (dark blue) in the western/eastern Indian Ocean, and in turn promote deep atmospheric convection and excess rainfall over the Maritime Continent/eastern Africa via sea atmospheric interactions^{10,17}. The Mozambique Channel Throughflow (MCT) that is related to the westward flow of the SEC north of Madagascar therefore increases following a negative-cold ENSO-IOD phase (b) and vice versa (a).

Extended Data Fig. 4 Precipitation difference (mm/day) of mean precipitation between 2000-2012 minus that of 1979-1999.

The precipitation difference indicates systematically drier conditions in eastern Africa during the last decade¹⁷, which coincides with intensified Southern Equatorial Current (SEC)¹⁷ and Mozambique Channel Throughflow (MCT)⁷⁰. Green triangles indicate the eastern African hominin sites (1. Omo-Turkana Basin, 2. Baringo and Tugen Hills, 3. Kanjera 4. Olorgesailie, 5. Laetoli and Olduvai), from which long-term carbon isotope records of soil carbonates are available serving as long-term proxy of eastern African aridity. The rainfall data is from Global Precipitation Climatology Project (GPCP) monthly precipitation analysis (1979–present; DOI 10.7289/V56971M6) and visualized with MATLAB and Mapping Toolbox, version 9.8.0.1323502 (R2020a, Natick, Massachusetts: The MathWorks Inc., United States).

Extended Data Fig. 5 Flow speed reconstructions using sortable silt mean grain size and abundance in the Mozambique Channel.

a, 3-part diagram of sortable silt properties of flow speed in the Mozambique Channel (Clock-wise). The relationship between sortable silt abundance (% lithogenic fraction between 10-63 μm ; SS%) and mean grain size ($\overline{\{\rm{SS}\}}$)^{54,71,72} for the spliced record from IODP Site U1476¹⁴ and modern surface sediments (64PE304-47, -51, -56, -63, -66 and -68)⁵³. The strong correlation (Pearson's correlation coefficient = 0.79) indicates that sortable silt deposition was subject to current sorting and selective transport⁷¹. The $\overline{\{\rm{SS}\}}$ of U1476 and nearby surface sediments are well within the calibration range for universal near-bottom current flow speed reconstructions⁷¹. The inferred flow speeds for the surface sediment samples using the universal $\overline{\{\rm{SS}\}}$ flow speed calibration correspond to the +2 s.d. from the mean near-bottom currents obtained from nearby mooring stations. The mean flow directions are southwards except for those of the Mozambique undercurrent (MUC) that is confined to the eastern African margin below 1.5 km water depth¹⁵. The $\overline{\{\rm{SS}\}}$ is likely somewhat biased towards higher near bottom flow speeds, as the finest fractions that may have selectively deposited during slow near-bottom current conditions were preferentially removed under intra- and interannually increased near-bottom currents. Additionally, slight deviations from the mean flow speed might be further attributed to the regional nature of the lithogenic sediments, as most $\overline{\{\rm{SS}\}}$ flow speed calibrations are defined for the northern Atlantic Ocean⁷¹. However, the sensitivity is comparable amongst the local calibrations and therefore the inferred relative changes in flow speed are also accurate for the Mozambique Channel, albeit the absolute values may slightly differ. In this study, the coarsest $\overline{\{\rm{SS}\}}$ and in turn highest flow speeds are obtained from near and within the topographic depression, where the continuation of the MUC passes through the Davie Ridge⁷³. **b**, W-E transect across the Mozambique Channel with long-term flow contours (cm s^{-1})¹⁵ as in Fig. 1c, but superimposed by the mean flow speeds of individual moorings of mean near-bottom currents across the Mozambique Channel

(cm s^{-1})²¹⁷³, whereby negative (positive) values reflect southward (northward) flow. **c**, Mozambique Channel bathymetric map with transect across Site IODP U1476 (S2) and the mooring transect (S1) with station (small solid black squares). The mean near-bottom flow speeds vectors recorded at the mooring transect are indicated by dashed⁷³ and solid²¹ lines. The locations of the surface sediment samples are marked by white dots with black outlines (64PE304-47, -51, -56, -63, -66 and -68)⁵³.

Extended Data Fig. 6 Age model of the spliced record of IODP Site U1476.

a, From top to bottom: The chronology of spliced core of IODP Site U1476 is based on the correlation of the $\delta^{18}\text{O}$ benthic record with the global $\delta^{18}\text{O}$ benthic probabilistic stack (Prob-stack)⁴⁰ using 38 tie points for the last ~2 Ma. Benthic $\delta^{18}\text{O}$ record of the spliced record of IODP Site U1476 over the last ~2 Ma (blue) and Prob-stack (black)⁴⁰. Minimal number of tie-points that are used to tune the $\delta^{18}\text{O}$ benthic record of U1476 to Prob-stack are indicated by vertical lines in **a** following a similar approach as⁵⁷. The Prob-stack overlain by the tuned benthic $\delta^{18}\text{O}$ record of the spliced record of IODP Site U1476 demonstrates the similarity between both records. **b**, The age-depth relationship agrees with the biochronology of calcareous nannofossils and planktonic foraminifera with only some minor deviations from the $\delta^{18}\text{O}$ bayesian age model. Bayesian age-modeling⁶⁰ of U1476 with $\pm 1\text{SD}$ (dark grey) and $\pm 2\text{SD}$ (light grey) based on the benthic $\delta^{18}\text{O}$ tuning points and biostratigraphy of calcareous nannofossils over the last 3 Ma with the accumulation rates. The shipboard biostratigraphy of calcareous nannofossils¹⁴, which has been further refined by Tangunan et al.(2018)⁵⁹ displaying internal agreement. **c**, Idem as **b** for the last ~7 Ma, Deviations of the shipboard biochronology of planktonic foraminifera might be partly attributable to the use of general low-latitude calibrations rather than specific calibrations for the tropical western Indian Ocean^{14,51}.

Extended Data Fig. 7 7-Ma long records of sortable silt mean ($\overline{\text{SS}}$) and derived flow speed changes together with lithogenic properties.

The accompanying elemental compositions are obtained through X-ray fluorescence (XRF) analyses of sediments at Site U1476 (Methods). The glacial periods are indicated for the last 5.3 Ma⁷⁴ by vertical light blue bars. The 10-point running means of the lithogenic ln (Zr/Rb) record reflect the relative deposition of dense Zr grains that are sorted, via selective deposition, together with silt-sand sized terrigenous particles, and Rb that is mainly present in clay minerals as substitution for K. Additionally, the 10-point running means of XRF bulk record (ln) Ca/(Ca/Ti) record that represents the relative deposition of carbonates (including foraminiferal shells) versus the terrigenous fraction⁵³. Reconstructed enhancements in flow speed after 2.1 ± 0.1 Ma correspond to increases in coarse-grained lithogenic sediments together with increases in marine carbonates, which suggests selective deposition and removal of the fine-grained lithogenic sediment fractions.

Extended Data Fig. 8 Long-term Sea Surface Temperature (SST) records and Indo-Pacific Walker Cell circulation.

a, Long-term SST records from the Indian and Pacific Ocean. The Mg/Ca-based SST records of DSDP 214³⁵, ODP 709C³⁶, 806 and 847⁴³ that are calculated and corrected for dissolution at depth⁷⁵ are mainly derived from *Globigerinoides sacculifer*, therefore recording temperatures about 20-30 m below the surface. Divergence of the SST records at ~ 2.1 Ma reflects the onset of the modern Indo-Pacific Walker cell circulation. **b**, Representation of present-day coupled Indo-Pacific Walker cell circulation, which is characterized by climatological low-level westerlies¹¹ and easterlies over the equatorial Indian and Pacific Oceans, respectively. The corresponding moisture-laden air masses of both oceans ascend over the Maritime Continent in southeastern Asia and the associated atmospheric deep convection induces excess rainfall. In contrast, the subsiding dry air masses over the cool western Indian Ocean cause arid conditions in eastern Africa. **c**, Ocean map color gradients show climatological mean Sea Surface Temperature (SST) and black arrows represent the atmospheric surface circulation of the Indian and Pacific Ocean basins (ERA5 monthly-averaged data on single levels; <https://doi.org/10.24381/cds.6860a573>). The low-level Pacific easterlies and Indian westerlies are driven by the temperature

contrast between the center of the Indo-Pacific Warm Pool (IPWP; SST >28 °C) and upwelling areas in the eastern Pacific Ocean (Cold tongue) and western Indian Ocean (Seychelles-Chagos Thermocline Ridge (SCTR), western Indian Ocean and Arabian Sea). The yellow dots indicate IODP Site U1476 (this study), and U1337²⁸, DSDP Site 214³⁵, ODP Sites 709C³⁶, 721-722^{12,46,62}, 806 and 847⁴³ providing long-term SST records, as well as sites GeoB12610-2³⁹ and GeoB10038-4⁴⁹ that date back to the Last Glacial Maximum (LGM). The SST map has been derived from NOAA Extended Reconstructed Sea Surface Temperature (ERSST) (Version 5, NOAA National Centers for Environmental Information, DOI:10.7289/V5T72FNM) is plotted with MATLAB and Mapping Toolbox, version 9.8.0.1323502 (R2020a, Natick, Massachusetts: The MathWorks Inc., United States).

Rights and permissions

[Reprints and Permissions](#)

About this article

Cite this article

van der Lubbe, H.J.L., Hall, I.R., Barker, S. *et al.* Indo-Pacific Walker circulation drove Pleistocene African aridification. *Nature* **598**, 618–623 (2021). <https://doi.org/10.1038/s41586-021-03896-3>

- Received: 09 June 2021
- Accepted: 11 August 2021
- Published: 27 October 2021
- Issue Date: 28 October 2021
- DOI: <https://doi.org/10.1038/s41586-021-03896-3>

Share this article

Anyone you share the following link with will be able to read this content:

[Get shareable link](#)

Sorry, a shareable link is not currently available for this article.

[Copy to clipboard](#)

Provided by the Springer Nature SharedIt content-sharing initiative

This article was downloaded by **calibre** from <https://www.nature.com/articles/s41586-021-03896-3>

| [Section menu](#) | [Main menu](#) |

- Article
- [Published: 06 October 2021](#)

Spatiotemporal origin of soil water taken up by vegetation

- [Gonzalo Miguez-Macho](#) ORCID: orcid.org/0000-0002-4259-7883¹
&
- [Ying Fan](#) ORCID: orcid.org/0000-0002-0024-7965²

Nature volume **598**, pages 624–628 (2021)

- 5506 Accesses
- 50 Altmetric
- [Metrics details](#)

Subjects

- [Ecological modelling](#)
- [Plant ecology](#)

Abstract

Vegetation modulates Earth's water, energy and carbon cycles. How its functions might change in the future largely depends on how it copes with droughts^{1,2,3,4}. There is evidence that, in places and times of drought, vegetation shifts water uptake to deeper soil^{5,6,7} and rock^{8,9} moisture as well as groundwater^{10,11,12}. Here we differentiate and assess plant use of four types of water sources: precipitation in the current month (source 1), past precipitation stored in deeper unsaturated soils and/or rocks (source 2),

past precipitation stored in groundwater (source 3, locally recharged) and groundwater from precipitation fallen on uplands via river–groundwater convergence toward lowlands (source 4, remotely recharged). We examine global and seasonal patterns and drivers in plant uptake of the four sources using inverse modelling and isotope-based estimates. We find that (1), globally and annually, 70% of plant transpiration relies on source 1, 18% relies on source 2, only 1% relies on source 3 and 10% relies on source 4; (2) regionally and seasonally, source 1 is only 19% in semi-arid, 32% in Mediterranean and 17% in winter-dry tropics in the driest months; and (3) at landscape scales, source 2, taken up by deep roots in the deep vadose zone, is critical in uplands in dry months, but source 4 is up to 47% in valleys where riparian forests and desert oases are found. Because the four sources originate from different places and times, move at different spatiotemporal scales and respond with different sensitivity to climate and anthropogenic forces, understanding the space and time origins of plant water sources can inform ecosystem management and Earth system models on the critical hydrological pathways linking precipitation to vegetation.

Access options

Subscribe to Journal

Get full journal access for 1 year

\$199.00

only \$3.90 per issue

[Subscribe](#)

All prices are NET prices.

VAT will be added later in the checkout.

Tax calculation will be finalised during checkout.

Rent or Buy article

Get time limited or full article access on ReadCube.

from \$8.99

[Rent or Buy](#)

All prices are NET prices.

Additional access options:

- [Log in](#)
- [Access through your institution](#)
- [Learn about institutional subscriptions](#)

Fig. 1: Schematic of four plant water sources.

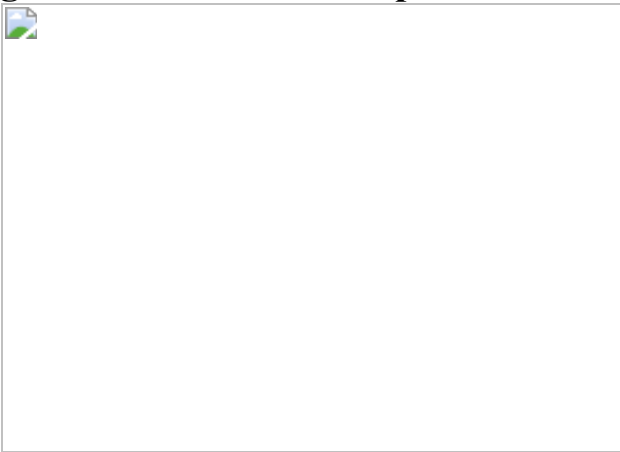


Fig. 2: Modelled fractional source contributions to transpiration.

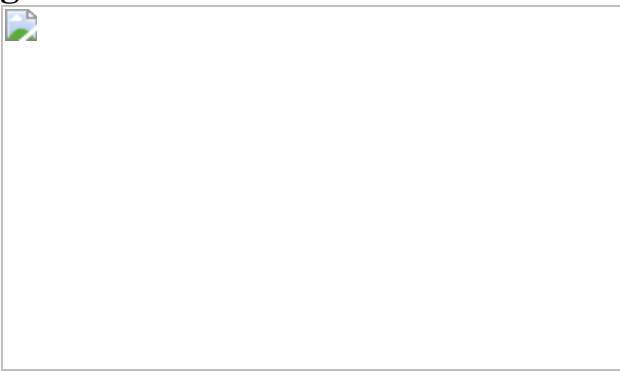


Fig. 3: Monthly source contribution to transpiration for the 12 climate types in the model.

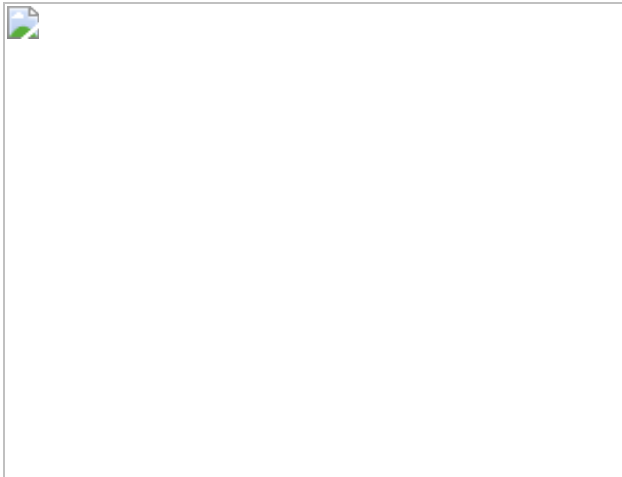
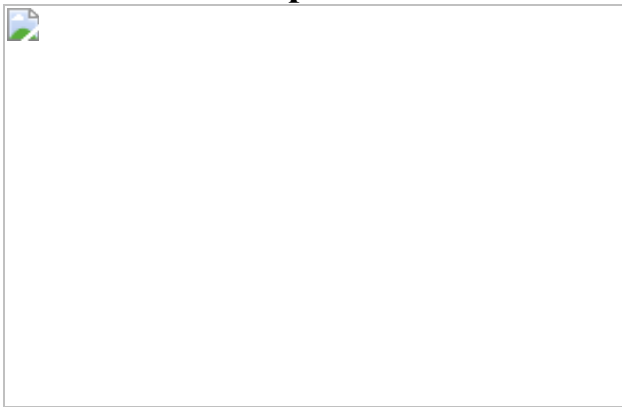


Fig. 4: Modelled source contributions in South America at the continent-to-hillslope scale.



Data availability

All model input data are generated by government and research agencies and are in the public domain. Links to download these data are provided in Supplementary Table 2. Modelled monthly transpiration and source contributions (sources 1, 2, 3 and 4) for each continent and month can be downloaded at the following public repository via ftp: http://thredds-gfnl.usc.es/thredds/catalog/DATA_TRANSOURCES/catalog.html. The isotope compilation can also be found in an Excel spreadsheet at the above ftp site.

Code availability

Our model code, written in Fortran, was uploaded to GitHub:
<https://github.com/gmiguez/MMF-HYDROMODEL>.

References

1. 1.
Graven, H. D. et al. Enhanced seasonal exchange of CO₂ by Northern ecosystems since 1960. *Science* **341**, 1085–1089 (2013).
2. 2.
Humphrey, V. et al. Sensitivity of atmospheric CO₂ growth rate to observed changes in terrestrial water storage. *Nature* **560**, 628–631 (2018).
3. 3.
Bonan, G. B. Forests and climate change: forcings, feedbacks, and the climate benefits of forests. *Science* **320**, 1444–1449 (2008).
4. 4.
Schlesinger, W. H. & Jasechko, S. Agricultural and forest meteorology transpiration in the global water cycle. *Agric. For. Meteorol.* **189–190**, 115–117 (2014).
5. 5.
Dawson, T. E. & Pate, J. S. Seasonal water uptake and movement in root systems of Australian phreatophytic plants of dimorphic root morphology: a stable isotope investigation. *Oecologia* **107**, 13–20 (1996).
6. 6.
Voltas, J., Devon, L., Maria Regina, C. & Juan Pedro, F. Intraspecific variation in the use of water sources by the circum-Mediterranean

conifer *Pinus halepensis*. *New Phytol.* **208**, 1031–1041 (2015).

7. 7.

Grossiord, C. et al. Prolonged warming and drought modify belowground interactions for water among coexisting plants. *Tree Physiol.* **39**, 55–63 (2018).

8. 8.

Rempe, D. M. & Dietrich, W. E. Direct observations of rock moisture, a hidden component of the hydrologic cycle. *Proc. Natl Acad. Sci. USA* **115**, 2664–2669 (2018).

9. 9.

Querejeta, J. I., Estrada-Medina, H., Allen, M. F. & Jiménez-Osornio, J. J. Water source partitioning among trees growing on shallow karst soils in a seasonally dry tropical climate. *Oecologia* **152**, 26–36 (2007).

10. 10.

Evaristo, J. & McDonnell, J. J. Prevalence and magnitude of groundwater use by vegetation: a global stable isotope meta-analysis. *Sci Rep.* **7**, 44110 (2017).

11. 11.

Barbeta, A. & Peñuelas, J. Relative contribution of groundwater to plant transpiration estimated with stable isotopes. *Sci Rep.* **7**, 10580 (2017).

12. 12.

Jobbágy, E. G., Nosetto, M. D., Villagra, P. E. & Jackson, R. B. Water subsidies from mountains to deserts: their role in sustaining groundwater-fed oases in a sandy landscape. *Ecol. Appl.* **21**, 678–694 (2011).

13. 13.

Fan, Y., Miguez-Macho, G., Jobbágy, E. G., Jackson, R. B. & Otero-Casal, C. Hydrologic regulation of plant rooting depth. *Proc. Natl Acad. Sci. USA* **114**, 10572–10577 (2017).

14. 14.

Ellsworth, P. Z. & Sternberg, L. S. L. Seasonal water use by deciduous and evergreen woody species in a scrub community is based on water availability and root distribution. *Ecohydrology* **551**, 538–551 (2015).

15. 15.

Sohel, S. *Spatial and Temporal Variation of Sources of Water Across Multiple Tropical Rainforest Trees*. PhD thesis, Univ. Queensland (2019).

16. 16.

Williams, D. G. & Ehleringer, J. R. Intra- and interspecific variation for summer precipitation use in pinyon-juniper woodlands. *Ecol. Monogr.* **70**, 517–537 (2000).

17. 17.

Allen, S. T., Kirchner, J. W., Braun, S., Siegwolf, R., T. W. & Goldsmith, G. R. Seasonal origins of soil water used by trees. *Hydrol. Earth Syst. Sci.* **23**, 1199–1210 (2019).

18. 18.

David, T. S. et al. Water-use strategies in two co-occurring Mediterranean evergreen oaks: surviving the summer drought. *Tree Physiol.* **27**, 793–803 (2007).

19. 19.

Zencich, S. J., Froend, R. H., Turner, J. V. & Gailitis, V. Influence of groundwater depth on the seasonal sources of water accessed by Banksia tree species on a shallow, sandy coastal aquifer. *Oecologia* **131**, 8–19 (2002).

20. 20.

Naumburg, E., Mata-Gonzalez, R., Hunter, R. G. & Martin, D. W. Phreatophytic vegetation and groundwater fluctuations: a review of current research and application of ecosystem response modeling with an emphasis on Great Basin vegetation. *Environ. Manage.* **35**, 726–740 (2005).

21. 21.

Snyder, K. A. & Williams, D. G. Water sources used by riparian trees varies among stream types on the San Pedro River, Arizona. *Agric. For. Meteorol.* **105**, 227–240 (2000).

22. 22.

Kotttek, M., Grieser, J., Beck, C., Rudolf, B. & Rubel, F. World map of the Köppen–Geiger climate classification updated. *Meteorol. Zeitschrift* **15**, 259–263 (2006).

23. 23.

Eleringer J. R. & Dawson T. Water uptake by plants: perspectives from stable isotope composition. *Plant Cell Environ.* 1073–1082 (1992).

24. 24.

Dawson, T. E., Mambelli, S., Plamboeck, A. H., Templer, P. H. & Tu, K. P. Stable isotopes in plant ecology. *Annu. Rev. Ecol. Syst.* **33**, 507–559 (2002).

25. 25.

Rothfuss, Y. & Javaux, M. Reviews and syntheses: isotopic approaches to quantify root water uptake: a review and comparison of methods. *Biogeosciences* **14**, 2199–2224 (2017).

26. 26.

Orlowski, N. et al. Inter-laboratory comparison of cryogenic water extraction systems for stable isotope analysis of soil water. *Hydrol. Earth Syst. Sci.* **22**, 3619–3637 (2018).

27. 27.

Chen, Y. et al. Stem water cryogenic extraction biases estimation in deuterium isotope composition of plant source water. *Proc. Natl Acad. Sci. USA* **117**, 33345–33350 (2021).

28. 28.

Pastorello, G., Trotta, C., Canfora, E. & Al., E. The FLUXNET2015 dataset and the ONEFlux processing pipeline for eddy covariance data. *Sci. Data* **7**, 225 (2020).

29. 29.

Zhao, Y. & Wang, L. Plant water use strategy in response to spatial and temporal variation in precipitation patterns in China: a stable isotope analysis. *Forests* **9**, 1–21 (2018).

30. 30.

Miguez-Macho, G. & Fan, Y. The role of groundwater in the Amazon water cycle: 2. Influence on seasonal soil moisture and evapotranspiration. *J. Geophys. Res. Atmos.* **117**, (2012).

31. 31.

Poulter, B. et al. Contribution of semi-arid ecosystems to interannual variability of the global carbon cycle. *Nature* **509**, 600–603 (2014).

32. 32.

Ahlstrom, A. et al. The dominant role of semi-arid ecosystems in the trend and variability of the land CO₂ sink. *Science* **348**, 895–899 (2015).

Acknowledgements

This work was supported by grants from the European Commission Seventh Framework Programme (EartH2Observe 603608) to G.M.-M. and grants from the US National Science Foundation (NSF-EAR-825813 and AGS-1852707) to Y.F. All computation was performed at CESGA (Centro de Supercomputación de Galicia) Supercomputer Center at the Universidade de Santiago de Compostela in Galicia, Spain. We thank FLUXNET and the GRDC and their contributors worldwide for providing ET and river flow observations for model validations.

Author information

Affiliations

1. CRETUS, Non-Linear Physics Group, Faculty of Physics,
Universidade de Santiago de Compostela, Galicia, Spain

Gonzalo Miguez-Macho
2. Department of Earth and Planetary Sciences, Rutgers University, New Brunswick, NJ, USA

Ying Fan

Contributions

G.M.-M. performed model simulations and analyses. Y.F. compiled and analysed isotope estimates. Y.F. and G.M.-M. wrote the manuscript.

Corresponding authors

Correspondence to Gonzalo Miguez-Macho or Ying Fan.

Ethics declarations

Competing interests

The authors declare no competing interests.

Additional information

Peer review information *Nature* thanks Adrià Barbeta, Timothy Brodribb, Youri Rothfuss, Ruud Van der Ent and the other, anonymous, reviewer(s) for their contribution to the peer review of this work.

Publisher's note Springer Nature remains neutral with regard to jurisdictional claims in published maps and institutional affiliations.

Extended data figures and tables

[Extended Data Fig. 1 Isotope-based estimates of fractional contribution to plant xylem water.](#)

(a) Source-2 and (b) Source-3+4 (undistinguished isotopically) during dry periods (best sampled). Where species are sampled at the same location (dots overlapping), the highest is displayed on the top.

Extended Data Table 1 Modelled fractional contribution from the four water sources to monthly transpiration as global and hemispheric average

Extended Data Table 2 Modelled fractional contribution of four water sources to monthly transpiration for the 12 climatic types represented in the model, ranked by annual plant uptake of total past precipitation (Source-2+3+4, bold font)

Extended Data Table 3 Modelled plant water source by drainage positions, for low, seasonal and perennial water stress groups
Extended Data Table 4 Isotope-based estimate of vegetation use of past precipitation (past P) (as % xylem water) averaged over each climatic water stress class, with propagated error in parentheses
Extended Data Table 5 Isotope-based estimates of dry period vegetation use of past precipitation along drainage gradient, with propagated error in parentheses
Extended Data Table 6 Isotope-based estimates of dry season vegetation use of past precipitation for eight growth forms with >10 observations, with propagated error term in parentheses; they are loosely ranked by the total plant use of past precipitation (orange)
Extended Data Table 7 Isotope-based estimates of dry season vegetation use of past precipitation for the 10 best sampled genera

Supplementary information

Supplementary Information

This file contains Supplementary Information Sections 1–4, including Supplementary Figs. 1–11, Supplementary Tables 1–4 and Supplementary References. See contents page for full details.

Reporting Summary

Rights and permissions

Reprints and Permissions

About this article

Cite this article

Miguez-Macho, G., Fan, Y. Spatiotemporal origin of soil water taken up by vegetation. *Nature* **598**, 624–628 (2021). <https://doi.org/10.1038/s41586->

021-03958-6

- Received: 24 November 2019
- Accepted: 25 August 2021
- Published: 06 October 2021
- Issue Date: 28 October 2021
- DOI: <https://doi.org/10.1038/s41586-021-03958-6>

Share this article

Anyone you share the following link with will be able to read this content:

[Get shareable link](#)

Sorry, a shareable link is not currently available for this article.

[Copy to clipboard](#)

Provided by the Springer Nature SharedIt content-sharing initiative

This article was downloaded by **calibre** from <https://www.nature.com/articles/s41586-021-03958-6>

| [Section menu](#) | [Main menu](#) |

- Article
- Open Access
- [Published: 15 September 2021](#)

Dairying enabled Early Bronze Age Yamnaya steppe expansions

- [Shevan Wilkin](#) [ORCID: orcid.org/0000-0003-0797-6244](#)^{1,2},
- [Alicia Ventresca Miller](#) [ORCID: orcid.org/0000-0003-4148-4016](#)^{1,3},
- [Ricardo Fernandes](#)^{1,4,5},
- [Robert Spengler](#) [ORCID: orcid.org/0000-0002-5648-6930](#)¹,
- [William T.-T. Taylor](#) [ORCID: orcid.org/0000-0002-0836-7814](#)^{1,6},
- [Dorcas R. Brown](#)⁷,
- [David Reich](#) [ORCID: orcid.org/0000-0002-7037-5292](#)^{8,9,10,11},
- [Douglas J. Kennett](#) [ORCID: orcid.org/0000-0001-6144-7365](#)¹²,
- [Brendan J. Culleton](#)¹³,
- [Laura Kunz](#)¹⁴,
- [Claudia Fortes](#)¹⁴,
- [Aleksandra Kitova](#)¹⁵,
- [Pavel Kuznetsov](#)¹⁶,
- [Andrey Epimakhov](#)^{17,18},
- [Victor F. Zaibert](#)¹⁹,
- [Alan K. Outram](#) [ORCID: orcid.org/0000-0003-3360-089X](#)²⁰,
- [Egor Kitov](#) [ORCID: orcid.org/0000-0002-0159-3288](#)^{21,22},
- [Aleksandr Khokhlov](#)¹⁶,
- [David Anthony](#)^{7,11} &
- [Nicole Boivin](#) [ORCID: orcid.org/0000-0002-7783-4199](#)^{1,23,24,25}

[Nature](#) volume **598**, pages 629–633 (2021)

- 22k Accesses
- 504 Altmetric
- [Metrics details](#)

Subjects

- [Archaeology](#)
- [Proteomics](#)

Abstract

During the Early Bronze Age, populations of the western Eurasian steppe expanded across an immense area of northern Eurasia. Combined archaeological and genetic evidence supports widespread Early Bronze Age population movements out of the Pontic–Caspian steppe that resulted in gene flow across vast distances, linking populations of Yamnaya pastoralists in Scandinavia with pastoral populations (known as the Afanasievo) far to the east in the Altai Mountains^{1,2} and Mongolia³. Although some models hold that this expansion was the outcome of a newly mobile pastoral economy characterized by horse traction, bulk wagon transport^{4,5,6} and regular dietary dependence on meat and milk⁵, hard evidence for these economic features has not been found. Here we draw on proteomic analysis of dental calculus from individuals from the western Eurasian steppe to demonstrate a major transition in dairying at the start of the Bronze Age. The rapid onset of ubiquitous dairying at a point in time when steppe populations are known to have begun dispersing offers critical insight into a key catalyst of steppe mobility. The identification of horse milk proteins also indicates horse domestication by the Early Bronze Age, which provides support for its role in steppe dispersals. Our results point to a potential epicentre for horse domestication in the Pontic–Caspian steppe by the third millennium bc, and offer strong support for the notion that the novel exploitation of secondary animal products was a key driver of the expansions of Eurasian steppe pastoralists by the Early Bronze Age.

[Download PDF](#)

Main

The pastoralist populations of the Eurasian steppe have long been a source of archaeological and historical fascination. Although the later history of steppe pastoralists—including the rise of the Xiongnu and Mongol empires in the east—is reasonably well-established, the early emergence and expansion of pastoralist groups in the steppe occurred before the historical era and has largely been reconstructed on the basis of archaeological and linguistic data^{1,6,7}. More recently, ancient DNA evidence has provided insights into early steppe populations, revealing evidence for a major influx of steppe ancestry into Europe in the Late Neolithic that effectively transformed the European genetic landscape^{1,2,8}. Archaeogenetic data also link these same populations (referred to as Yamnaya) with pastoral Afanasievo populations far to

the east in the Altai Mountains^{1,2} and Mongolia³. Combined archaeological and genetic evidence supports widespread population movements in the Early Bronze Age (about 3300 to 2500 bc) from the Pontic–Caspian steppe that resulted in gene flow across vast distances, linking Yamnaya pastoralist populations in Scandinavia with groups that expanded into Siberia⁹.

Although the Yamnaya expansions are well-established, the driving forces behind them remain unclear. A widely cited theory holds that the early spread of herders across Eurasia was facilitated by a newly mobile pastoral economy that was made possible by a combination of horse traction and bulk wagon transport^{4,5,6}. Together with regular dietary dependence on meat and milk⁵, this opened up the steppe to exploitation and occupation by pastoralist communities. Yet for all its persuasiveness, the model remains inadequately supported by direct archaeological or biomolecular data. Archaeological evidence for the use of bulk wagon transport by the Eneolithic Maikop and Early Bronze Age Yamnaya groups exists in the form of carts and bridling materials¹⁰, but two other critical components of the model—a reliance on domesticated horses and ruminant dairying—remain archaeologically unproven.

The domestication status of Eurasian horses has long been debated^{5,6,11,12,13,14}, and recent archaeogenetic findings¹⁵ have shifted our understanding of early horses at the Eneolithic site of Botai in northern Kazakhstan by identifying them as *Equus przewalskii* rather than the modern-day domestic horse (*Equus caballus*)^{5,6}. Although horses do appear in Early Bronze Age assemblages on the steppe, it remains unclear whether they were being ridden^{7,11,16,17}, or indeed whether they were part of pastoral herds or simply hunted. On the eastern Eurasian steppe, growing evidence suggests that horses were not ridden^{11,12,18} or milked¹⁹ before about 1200 bc, and horses may have been uncommon in early pastoralist assemblages²⁰. Early ruminant dairying on the western steppe has also been inadequately demonstrated, as human stable isotope data from the region suggests—but cannot confirm—dairy consumption^{21,22}. Palaeoproteomics, which is the only method that is able to evince individual dairy consumption (rather than milk production) and provide taxonomic resolution, has so far been minimally applied to steppe populations. Across Yamnaya and Afanasievo populations, dairying evidence is available only for a few individuals from the eastern steppe who have ancestry from western steppe groups; the earliest individual provides only a taxonomically ambiguous ruminant (*Ovis/Bos*) peptide result¹⁹.

To address the heavily debated question of what drove Yamnaya expansions across the steppe^{6,23,24,25}, we conducted proteomic analysis of dental calculus sampled from 56 steppe individuals who span the Eneolithic to Late Bronze Age, and who date from between 4600 and 1700 bc. Our samples from the Eneolithic (about 4600 to 3300 bc) are from 19 individuals from 5 sites: Murzikha 2 (6 individuals), Khvalynsk 1 and

Khvalynsk 2 (9 individuals), Ekaterinovka Mys (1 individual), Lebyazhinka 5 (1 individual) and Khlopkov Bugor (2 individuals) (Fig. 1, Supplementary Fig. 1a). Ancient DNA results from Khvalynsk and other Eneolithic sites in the Volga and northern Caucasus^{2,7,26} support the existence of an Eneolithic population across this region that was genetically similar to the Yamnaya population, but who lacked the additional farmer (Anatolian) ancestry that would arrive later on the steppe⁷. Published stable isotope and archaeological studies applied to Eneolithic populations from the Pontic region point to an economy based on fishing, the gathering of local plants and the keeping of domesticated animals^{6,21,27,28}. Given the importance of the horse in reconstructions of early pastoralist expansions, we also examined dental calculus from two individuals from the well-known site of Botai. With faunal assemblages dominated by horse remains^{11,12,13} and early lipid studies of ceramics indicating horse milking at the site by 3500 bc¹³, the site is central to discussions of early horse milking and dairying in the Eurasian steppe.

Fig. 1: Map showing sites that yielded individuals with preserved ancient proteins.

 **figure1**

a–c, Eneolithic (**a**), Early Bronze Age (**b**) and Middle–Late Bronze Age (**c**) sites in the Pontic–Caspian region, showing the number of individuals with a positive dairy identification out of the total number of individuals with preserved ancient proteins for each site. Strong evidence of preservation of equine or ruminant milk protein

Identifiers are depicted with black animal icons; the single individual with equivocally identified casein peptides is shown with a grey icon. For a map of all sites (including those without preserved proteins), see Supplementary Fig. 1. Base maps were created using QGIS 3.12 (<https://qgis.org/en/site/>), and use Natural Earth vector map data from <https://www.naturalearthdata.com/downloads/>. The horse image is reproduced from ref. 33; sheep silhouette, public domain (<https://thenounproject.com/icon/12538/>).

Our Bronze Age samples come from 35 individuals from 20 sites in the Volga–Ural steppes that can be divided into two chronological groups: the Early Bronze Age (about 3300 to 2500 bc) era of Yamnaya-culture mobile pastoralism^{29,30}; and the Middle–Late Bronze Age transition (about 2500–1700 bc), when chariots, fortified settlements and new western-derived influence genetic ancestries appeared with the Sintashta culture³¹. The cemetery sites and the number of individuals (in parentheses) from the Early Bronze Age are: Krasikovskyi 1 (2) Krasnokholm 3 (1), Krivyanskiy 9 (2), Kutuluk 1 (2), Leshchevskoe 1 (1), Lopatino 1 (1), Mustayevo 5 (2), Nizhnaya Pavlovka (1), Panitskoe (1), Podlesnoe (1), Pyatiletka (1) and Trudovoy (1); and, from the Middle–Late Bronze Age transition, Bolshekaraganskyi (1), Kalinovsky 1 (2), Kamennyi Ambar 5 (3), Krasikovskyi I (1), Krivyanskiy 9 (3), Lopatino 1 and Lopatino 2 (2), Potapovka 1 (1), Shumayevo 2 (1) and Utevka 6 (5) (Supplementary Fig. 1b, c). Archaeological and stable isotope findings^{6,22} indicate that the diet of Early Bronze Age Yamnaya groups was focused on herd animals, specifically cattle, sheep and goat. Horse remains also appear in quantity on a few steppe archaeological sites, but the status of Early Bronze Age horses—whether domesticated or hunted—has remained unclear^{32,33}. The Middle–Late Bronze Age transition saw a shift to greater horse exploitation and chariot use, within the context of an ongoing dietary focus on domesticated livestock.

Of the 56 ancient human dental calculus samples we tested, 55 were successfully extracted and produced identifiable protein data. Of these 55, 48 (87%) were determined to have strong signals for preservation through an assessment of proteins commonly found within the oral cavity; detailed information on this assessment is provided in Methods, Supplementary Table 3.

The earliest samples in our study (about 4600 to 4000 bc) are from 5 Eneolithic sites in southwestern Russia located on or close to the Volga River and its tributaries. Of the samples from these 19 individuals, 11 were successfully extracted and well-preserved, and 10 of these did not show any evidence for dairy consumption (Figs. 1a, 2a). The calculus of one individual contained two peptides specific to bovine (*Bos, Bubalis* and *Bison*) α -S1-casein, a milk curd protein. However, as the only dietary peptides contained in this sample were specific to casein and evidence for the most commonly recovered dairy protein β -lactoglobulin (BLG) was lacking, dairy consumption in this individual could not be confidently confirmed. In general, casein peptides appear to

preserve more poorly than BLG in archaeological calculus, and thus are most often identified together with other dairy protein peptides rather than alone^{19,34,35,36,37}. Additionally, within the two identified casein peptides, there is only one possible amino acid deamidation site, which renders any estimation of the antiquity of these peptides exceedingly challenging. A previously published paper³⁸ demonstrates the extreme variability in deamidation of amino acids in milk proteins, which further limits our ability to confirm the authenticity of this dairy finding. The calculus from the two additional Botai individuals demonstrated adequate preservation, but also lacked evidence for dairy consumption.

Fig. 2: Histogram of taxonomic specificity of dairy peptide spectral matches per individual.

 figure2

a–c, Histograms for individuals with evidence for consumption of dairy, from the Eneolithic (a), Early Bronze Age (b) and Middle and Late Bronze Age (c). PSM, peptide spectral match.

For the Early Bronze Age individuals (dating to the onset of the Yamnaya cultural horizon), dairy peptides were recovered from 15 of the 16 individual calculus samples we analysed (Fig. 1b, 2b). All 15 individuals with positive dairy results contained multiple peptide spectral matches to ruminant dairy proteins (including BLG), and some individuals also contained α -S1 casein, α -S2-casein or both. Although many of the milk peptides were only specific to higher taxonomic levels (such as Pecora, an infraorder within Artiodactyla (cow, sheep, goat, buffalo, yak, reindeer, deer and antelope)), others enabled more specific taxonomic classifications, including to family, genus or species. We found *Ovis*, *Capra* and *Bos* attributions, and the calculus of many individuals contained dairy peptides from several species. Notably, we identified *Equus* milk peptides from the protein BLGI in 2 of 17 Early Bronze Age individuals, both from the southwestern site of Krivanskiy 9 (3305 to 2633 calibrated years bc (Supplementary Table 5 provides individual accelerator mass spectrometry dating information)). Although the genus *Equus* includes horse, donkey and kiang, only horse

species (*E. caballus*, *E. przewalskii*, *Equus hemionus* and *Equus ferus*) are archaeologically attested in the steppe in the Early Bronze Age, supporting the *Equus* identification as horse.

For the Middle–Late Bronze Age transition, calculus samples from 15 of 19 individuals were positive for evidence of ruminant milk consumption (Figs. 1c, 2c). Similar to the Early Bronze Age, we identified BLG, α -S1-casein and α -S2-casein, as well as the whey protein α -lactalbumin. Taxonomic identifications again ranged from the Pecora infraorder to genus-level identifications (including *Ovis* and *Bos*), but without any specific identifications for *Capra* or *Equus*. Supplementary Table 4 provides a full accounting of all identified dairy proteins for each individual.

Overall, our results point to a clear and marked shift in milk consumption patterns between the Eneolithic and Early Bronze Age in the Pontic–Caspian Steppe. The majority of Eneolithic individuals (10 out of 11 (92%)) in our assemblage lack any evidence for milk consumption, whereas the overwhelming majority of Early Bronze Age individuals (15 out of 16 (94%)) contain ample proteomic evidence for dairy consumption in their calculus. Although a single individual at Eneolithic Khvalynsk with somewhat equivocal evidence for the consumption of dairy from cattle may indicate small-scale dairy use, the reliability of this single identification is questionable. Our findings suggest that regular dairy consumption in the Pontic–Caspian Steppe began only at the time of the Eneolithic-to-Early Bronze Age transition. Although neighbouring Eneolithic farming populations in Europe appear to have been dairying³⁹, those living across the steppe frontier did not adopt milking practices, which suggests the presence of a cultural frontier. The proteomic data are in broad agreement with findings from lipid analyses in the Ukraine ([Supplementary Information section 2](#), Supplementary Table 2). They also agree with stable isotope analysis of individuals from Eneolithic-to-Bronze-Age Samara showing a corresponding shift from a heavy reliance on fish, deer and other riverine forest (C3) resources to a greater reliance on terrestrial and grassland (C3 and C4) animal products^{22,40}.

One important advantage of proteomic data is their ability, in some cases, to provide species-specific protein identifications. Our study offers evidence for the Bronze Age milking of sheep, goat and cattle, which fits with evidence for the herding of these animals. The lush valleys of the Pontic–Caspian Steppe provided ample forage and hydration for mixed herds of arid-adapted sheep and goat, as well as more water-reliant cattle^{41,42}. Although a recent study has shown that lactase persistence—which results from the presence of an allele that enables production of lactase into adulthood—was rare in steppe populations of the Early Bronze Age⁴³, we find that the western steppe community was regularly consuming dairy that could have included fresh milk

and/or other processed products with reduced lactose, such as yogurts, cheeses or fermented milk beverages.

Our study of dental calculus from the Eneolithic site of Botai to the east, where early horse milking has been suggested by lipid analysis (albeit equivocally⁴⁴), did not yield milk proteins. Although two samples are insufficient for drawing broad conclusions, this finding does not support widespread milk consumption at the site^{13,45,46}. However, two calculus samples from Early Bronze Age individuals of the Pontic–Caspian region do provide evidence for the consumption of horse milk. Combined with archaeogenetic evidence¹⁵ that places the Botai horses on a different evolutionary trajectory than the domesticated DOM2 *E. caballus* lineage, this finding—if backed up by further sampling and analysis—would seem to firmly shift the focus of sustained early horse domestication on the Eurasian steppe to the Pontic–Caspian region. So far, the oldest horse specimens that carry the DOM2 lineage date to between 2074 to 1625 calibrated years bc, at which time the lineage is archaeologically attested in present-day Russia, Romania and Georgia¹⁵. Our identification of—to our knowledge—the earliest horse milk proteins yet identified on the steppe or anywhere else reveals the presence of domestic horses in the western steppe by the Early Bronze Age, which suggests that the region (where the first evidence for horse chariots later emerged at about 2000 bc⁴⁷) may have been the initial epicentre for domestication of the DOM2 lineage during the late fourth or third millennium bc.

Overall, our findings offer strong support to the notion of a secondary products revolution^{48,49} in the Eurasian steppe by the Early Bronze Age. This change in subsistence economy, indicated by dietary stable isotopes in human bones as well as by proteomics, was accompanied by the widespread abandonment of Eneolithic riverine settlement sites, the appearance of kurgan cemeteries in the previously unexploited arid plateaus between the river valleys, and the inclusion of wheeled vehicles and occasional horse bones in Yamnaya graves. At the same time, the steppe Yamnaya population expanded westward into Europe and eastward to the Altai Mountains (a range of 6,000 km)^{1,3,50}. Although we cannot offer direct insight into the question of horse riding or traction on the basis of our data, evidence for milked horses certainly makes horse domestication more likely, and may indicate that horses had a role in the spread of Yamnaya groups. The triad of animal traction, dairying and horse domestication appears to have had an instrumental role in transforming Pontic–Caspian economies and opening up the broader steppe to human habitation by the Early Bronze Age. If some or even all of these elements were present before the Bronze Age, it is only from this latter period that we witness their intensive and sustained exploitation amongst numerous groups. Although other factors will no doubt also have been important, the emergence of more mobile, pastoralist societies adapted to survival on the cold and arid steppe—where horses may have opened up snow-covered pasturage for other animals¹⁸, and milk would have provided a sustained

source of protein, nutrients and fluids—was undoubtedly critical to the expansion of Bronze Age pastoralists such the Yamnaya groups.

Methods

No statistical methods were used to predetermine sample size. The experiments were not randomized, and investigators were not blinded to allocation during experiments and outcome assessment.

Protein extraction and data analysis methods

Sample collection

Dental calculus was collected at the Department of Archaeology at Samara State University and the Museum at the Institute of Plant and Animal Ecology at the Ural Branch of the Russian Academy of Sciences. Calculus was collected in sterile tubes and hand-carried to the Max Planck Institute for the Science of Human History (MPI-SHH) in Jena. Calculus from the Botai site was sampled at the site; it was collected in sterile tubes and shipped to MPI-SHH. Each calculus sample was removed using a clean dental scaler, and implements were cleaned with alcohol swabs between the sampling of different individuals. Contamination from modern human keratin and environmental collagen that may have occurred owing to previous sampling for ancient DNA or stable isotope analysis was reduced through the use of nitrile gloves during collection, and samples were taken directly from the teeth into clean, 2-ml Eppendorf tubes, in which they were stored until protein extraction in the Palaeoproteomics Laboratory at the MPI-SHH.

Protein extraction

For samples with a ‘Z’ designation, proteins were extracted using a modified low-volume filter-aided sample preparation that has previously been described³⁵. To decrease contamination, 1 ml of 0.5 M EDTA was then added to each sample tube, samples were rotated for 5 min followed by centrifugation at 20,000 rcf for 10 min to remove the any contamination on the outer layer of calculus; the supernatant was then removed and retained. Then, 1 ml of 0.5 M EDTA was added to each decontaminated sample, and the sample was allowed to decalcify on a rotator for 5–7 days at room temperature until completion. After demineralization, samples were centrifuged at top speed (20,000 rcf) for 5 min. Eight hundred µl of EDTA supernatant was removed and stored for future analysis. Separately, 50 µl of urea solution (8 M) was added to a 30-kDa Millipore Microcon filter unit. Samples were denatured, reduced and alkylated with 30 µl of sodium dodecyl sulfate (SDS)-lysis buffer (4% w/v SDS, 100 mM

Tris/HCL pH 8.2 and 0.1 M DTT), incubated at 95 °C for 5 min, and 100 µl of iodoacetamide (IAA) solution (0.5 M IAA and 8 M UA) was added to the filter units and was mixed at 600 rpm for 1 min in the dark. Following incubation, the samples were centrifuged at 14,000g for 10 min. Two hundred µl of UA (8 M) was added to the filter unit, followed by the lysed sample supernatant and units centrifuged for 20 min at 14,000g. UA was used twice to remove the IAA and followed by centrifugation for 12–15 min at top speed. One hundred µl of 0.5 M NaCl was added to each filter unit, spun for 12 min at 14,000g. This step was repeated and the flowthrough discarded. The filter units were transferred to new units, and 120 µl of trypsin solution (3 µl of 0.4 µg µl⁻¹ trypsin in 117 µl of 0.05 M triethylammoniumbicarbonate) was added to each unit. Units were thermomixed at 600 rpm for 1 min and then incubated overnight at 37 °C. Following digestion, samples centrifuged for 20 min at 14,000g and acidified with 5% TFA to a pH of <2.

Stage tips (Thermo Scientific StageTips 200 µl C18 tips) were cleaned with 100% methanol, followed by 60% acetonitrile (ACN) solution (60% ACN, 0.1% TFA and 39.9% ddH₂O). Then, each was equilibrated with 2 washes of 150 µl of 3% ACN solution (3% ACN, 0.1% TFA and 96.9% ddH₂O). Samples were then loaded onto the tips and twice washed with 3% ACN and 0.1% TFA and the flowthrough discarded. Peptides were collected in new tubes from the stage tip with 150 µl 60% ACN solution and each was dried in an evaporator and stored at –80 °C until liquid chromatography with tandem mass spectrometry (LC–MS/MS) analysis.

Samples with a ‘DA’ were extracted using a single pot, solid phase enhanced sample preparation (SP3) modified for archaeological dental calculus samples. One millilitre of 0.5 M EDTA was added to each sample, and samples were then placed on a rotator for 5 min and centrifuged at top speed (20,000 rcf) for 10 min. The entire supernatant was removed and retained, and an additional 500 µl of 0.5 M EDTA for demineralization was added and samples were placed back onto the rotator for 5–7 days.

Following demineralization, samples were centrifuged at 20,000 rcf for 10 min, and 400 µl of the supernatant was removed and retained. To increase denaturation, reduce and alkylate, 200 µl of 6 M guanidine hydrochloride and 30 µl of 40 mM CAA, 100 mM TCEP were added to the pellet and remaining supernatant and mixed through resuspension. Samples were then placed on a heating block (Cell Media, Thermoshaker Pro) and heated to 99 °C for 10 min. Upon removing samples from heat, 20 µl of a 20 µg µl⁻¹ 50/50 mixture of hydrophilic and hydrophobic SeraMag SpeedBeads was added to each sample, and to increase protein–bead adhesion, 350 µl of 100% ethanol was then added to each tube. Samples were then placed on the ThermoMixer for 5 min at 1,000 rpm at 24 °C. Upon removal from the ThermoMixer, tubes were placed on a magnetic rack, which moved the beads to the wall side of the

tube. With the proteins now adhering to the beads, the entire supernatant was removed and retained for possible later analysis. To remove any non-proteinaceous materials, 3 washes of 200 µl 80% ethanol were carried out. Once the beads were thoroughly washed, 100 µl of 100 mM ammonium bicarbonate was added to each tube, as well as 0.2 µg of trypsin. Samples were then placed on the ThermoMixer at 37 °C at 750 rpm. After 10 min, samples were resuspended and left on the ThermoMixer overnight (18 h) for protein digestion. Following digestion, sample tubes were centrifuged at 20,000 rcf for 1 min, and then placed back onto the magnetic rack. The entire supernatant was removed and transferred to a clean tube. Each sample was then acidified with 5% TFA to reduce the pH to <2. Acidified sample tubes were again centrifuged at top speed for five minutes to push any remaining non-proteinaceous materials into a pellet and improve stage tip clean up. Stage tips were prepared with 150 µl MeOH, and centrifuged at 2,000 rcf, followed by 60% ACN, 0.1% TFA and another round of centrifugation. To equilibrate the stage tips, we added 150 µl 3% ACN, 0.1% TFA, followed by another centrifugation step, and these steps were then repeated. Samples were added to each stage tip, and centrifuged for 3 min at 2000 rcf, or until the entire sample had passed the stage tip. This was followed by an additional 2 rinse steps with 3% ACN, 0.1% TFA. Samples were not eluted at the MPI-SHH, but retained on stage tips in the -20°C freezer until shipment to the Functional Genomics Center Zürich at the University of Zürich. A full detailed protocol is available at protocols.io (<https://doi.org/10.17504/protocols.io.bfgrjjv6>).

High performance LC–MS/MS analysis

The samples were sent on stage tips to the Functional Genomics Center. There, the peptides were eluted from the stage tips and dried. After resolubilization in 10 µl of 3% ACN, 0.1% formic acid, the peptide level was normalized using the DeNovix DS-11 Series Spectrophotometer.

LC–MS/MS analysis

For samples with a laboratory identifier that starts with Z (Supplementary Table 3), mass spectrometry analysis was performed on a Q Exactive HF mass spectrometer (Thermo Scientific) equipped with a Digital PicoView source (New Objective) and coupled to a M-Class UPLC (Waters). Solvent composition at the two channels was 0.1% formic acid for channel A and 0.1% formic acid, 99.9% ACN for channel B. Column temperature was 50 °C. For each sample, 4 µl of peptides were loaded on a commercial ACQUITY UPLC M-Class Symmetry C18 Trap column (100 Å, 5 µm, 180 µm × 20 mm, Waters) followed by ACQUITY UPLC M-Class HSS T3 column (100 Å, 1.8 µm, 75 µm × 250 mm, Waters). The peptides were eluted at a flow rate of 300 nl min⁻¹ by a gradient from 5 to 40% B in 62 min. Column was cleaned after the

run by increasing to 98% B and holding 98% B for 5 min before re-establishing the loading condition. Samples were acquired in a given order.

The mass spectrometer was operated in data-dependent mode, acquiring full-scan mass spectra ($350\text{--}1,500\text{ }m/z$) at a resolution of 120,000 at $200\text{ }m/z$ after accumulation to a target value of 3,000,000, and a maximum injection time of 50 ms, followed by higher-energy collision dissociation (HCD) fragmentation on the six most intense signals per cycle. HCD spectra were acquired at a resolution of 120,000 using a normalized collision energy of 28 and a maximum injection time of 247 ms. The automatic gain control was set to 100,000 ions. Charge state screening was enabled. Singly, unassigned and charge states higher than six were rejected. Only precursors with intensity above 18,000 were selected for MS/MS. Precursor masses previously selected for MS/MS measurement were excluded from further selection for 30 s, and the exclusion window was set at 10 ppm. The samples were acquired using internal lock mass calibration on m/z 371.1012 and 445.1200.

For samples with laboratory identifiers starting with DA (Supplementary Table 3), mass spectrometry analysis was performed on a Q Exactive mass spectrometer (Thermo Scientific) equipped with a Digital PicoView source (New Objective) and coupled to a nanoAcquity UPLC (Waters). Solvent composition at the two channels was 0.1% formic acid for channel A and 0.1% formic acid, 99.9% ACN for channel B. Column temperature was 50 °C. For each sample, 4 μl of peptides were loaded on a commercial ACQUITY UPLC M-Class Symmetry C18 Trap column (100 Å, 5 μm , 180 $\mu\text{m}\times 20\text{ mm}$, Waters) followed by ACQUITY UPLC M-Class HSS T3 column (100 Å, 1.8 μm , 75 $\mu\text{m}\times 250\text{ mm}$, Waters). The peptides were eluted at a flow rate of 300 nl min^{-1} by a gradient from 8 to 22% B in 49 min and to 32% B in additional 11 min. Column was cleaned after the run by increasing to 95% B and holding 95% B for 5 min before re-establishing the loading condition. Samples were acquired in a given order.

The mass spectrometer was operated in data-dependent mode, acquiring a full-scan mass spectra ($300\text{--}1,700\text{ }m/z$) at a resolution of 70,000 at $200\text{ }m/z$ after accumulation to a target value of 3,000,000, and a maximum injection time of 110 ms followed by HCD fragmentation on the 12 most intense signals per cycle. HCD spectra were acquired at a resolution of 35,000 using a normalized collision energy of 25 and a maximum injection time of 110 ms. The automatic gain control was set to 50,000 ions. Charge state screening was enabled. Singly, unassigned and charge states higher than seven were rejected. Only precursors with intensity above 9,100 were selected for MS/MS. Precursor masses previously selected for MS/MS measurement were excluded from further selection for 30 s, and the exclusion window was set at 10 ppm. The samples were acquired using internal lock mass calibration on m/z 371.1012 and 445.1200.

As all samples in our study were digested with trypsin, peptides had either an arginine or lysine at the C terminus. This resulted in the C-terminal fragments remaining charged, and therefore identified at a higher intensity than b-ions (Extended Data Fig. 1). The mass spectrometry proteomics data were handled using the local laboratory information management system⁵¹ and all relevant data have been deposited to the ProteomeXchange Consortium via the PRIDE (<http://www.ebi.ac.uk/pride>) partner repository.

Data analysis

To account for as much variation of milk-associated proteins as possible during MS/MS ion searches, a supplementary database of milk protein sequences that had not been reviewed was curated from UniProtKB in addition to those from ancient horses, as previously generated¹⁹. As a previous publication¹⁹, peak lists were generated from raw files by selecting the top 100 peaks using MSConvert from the ProteoWizard software package version 3.0.11781⁵². Sample analysis results were searched using Mascot⁵³ (version 2.6.0) against the Swiss-Prot database in combination with a curated milk protein database¹⁹. Results were exported from Mascot as .csv files, and further processed through an internally created tool, MS-MARGE^{19,54}, to estimate the validity of peptide identifications and summarize the findings. False-discovery rates at both the peptide spectral match and protein level were calculated using MS-MARGE by counting the number of decoy hits after filtering for *e*-value and minimum peptide support, then dividing this value by the number of target hits minus the number of decoys. The resulting value is multiplied by 100 to provide an estimate of the false-discovery rate. For each individual sample, we aimed for a protein false-discovery rate of under 5% and a peptide false-discovery rate of under 2% (Supplementary Table 4). A minimum of two individual peptide spectral matches were required for each specific protein identification, and only peptide spectral matches with an *e* value of below 0.01 were accepted. After filtering criteria were applied, we observed a range of variation in the numbers of proteins identified, with samples ranging from 25 to 196 confidently identified protein families.

Sequence similarities between casein and *Jeotgalicoccus*

During necessary BLAST searches to authenticate the taxonomic specificity of ruminant α -S1 casein peptides, we found identical sequence matches to theoretical proteins for the numerous bacterial firmicute species from the genus *Jeotgalicoccus* (NCBI reference sequence: WP_188349304.1). Upon further investigation, the full amino acid sequence for these hypothetical bacterial proteins is almost identical to ruminant casein sequences, which is probably due to laboratory contamination during the genomic sequencing. As its listing in the NCBI database is not associated with a

publication, we assume this is probably contamination. Supplementary Figure 2 shows the alignment comparing the α -S1 casein sequence for *Bos taurus*, *Bos grunniens*, *Bubalus bubalis* and *Jeotgalicoccus* species.

Proteome preservation assessment with the Oral Signature Screening Database

To confirm the preservation of the calculus from individuals included in this study, the metaproteome from each sample was examined for a combination of specific protein types. Following a previous publication⁶ we compared the data from each sample against the Oral Signature Screening Database (OSSD) to determine the number of common laboratory contaminants, contaminants introduced during handling and curation, regularly recovered human immune proteins found in the oral cavity, and bacterial proteins common to the human oral microbiome. Supplementary Table 3 contains the overall count of OSSD proteins pulled from our filtered results, as well as the result of the oral microbiome protein identifiers + human immune proteins divided by the total number of OSSD proteins multiplied by 100 to find the ‘authenticity’ of oral signature proteins in comparison to the total proteins recovered. To determine who among the individuals passed our screening, we applied a different threshold to each time period. For the Early and Middle Bronze Age, we applied a previously published standard³⁷, and for the Eneolithic period samples we lowered the standard to 40% to take into account increased protein degradation over time. Individuals who had calculus that fell below the authenticity threshold were excluded from the study, but remain listed on the preservation table. Sample authenticity is further supported by an absence of dietary proteins in all positive (archaeological sheep bone with known proteome) and negative controls (extraction blank), as well as the fact that none of the control samples showed any evidence of a typical oral protein signature. Protein preservation varies greatly between different environments and can even differ between individuals at the same site^{37,55}, and this assessment should be conducted on a project-by-project basis.

Bayesian estimates of dietary contributions from freshwater protein and radiocarbon calibration adjusted for freshwater dietary radiocarbon reservoir effects for Eneolithic individuals

Chronologies based on human radiocarbon dates require estimates of individual aquatic dietary intakes, as well as estimates of aquatic radiocarbon reservoir effects of consumed aquatic protein^{56,57}. For the latter, we considered a wide potential variability of between 0 and 1,000 years, which covers previously reported archaeological measurements of coeval terrestrial and aquatic samples and the majority of measurements made on modern freshwater species from our study region⁵⁸. To estimate the dietary contributions from aquatic protein we used the Bayesian mixing

model ReSources developed within the Pandora & IsoMemo initiatives (<https://isomemoapp.com/>). ReSources is a R-based model that follows a similar implementation to the Bayesian mixing model FRUITS⁵⁹. We defined a two-end member model (terrestrial versus freshwater animal protein) with stable nitrogen reference values for these ($\delta^{15}\text{N}_{\text{terrestrial}} = 7.1 \pm 2\text{\textperthousand}$, $\delta^{15}\text{N}_{\text{freshwater}} = 10.6 \pm 1\text{\textperthousand}$) calculated following a literature review of previously reported values for bone collagen extracted from terrestrial and freshwater animal species within the study region^{26,60}. As with previous similar models, protein reference values are corrected for offsets between bone collagen and edible meat, and the implemented model also included a dietary to consumer isotopic offset^{56,57}. For each human bone collagen $\delta^{15}\text{N}$ value, ReSources provided an estimate (expressed as a mean and s.d.) of the dietary intake of freshwater protein. This estimate was included within the Bayesian chronological model OxCal v.4.4 to express the degree of mixing between the terrestrial radiocarbon calibration curve IntCal20 and a freshwater radiocarbon curve^{61,62}. The latter was defined from IntCal20 by adding a uniform prior of between 0 and 1,000 years. Calibrated radiocarbon dates for each individual are expressed as 95% credible intervals. An example of the OxCal code is given below.

Plot()

{

```
Curve("IntCal20","IntCal20.14c");
Curve("FRE","IntCal20.14c");
Delta_R("LocalFRE", U(0,1000));
Mix_Curves("Date1", "IntCal20","LocalFRE", 63,26);
R_Date("OxA-35976", 5965, 20);
Mix_Curves("Date2", "IntCal20","LocalFRE", 36,22);
R_Date("OxA-37350", 4390, 20);
};
```

Radiocarbon sample preparation methods

Bone sample preparation methods for radiocarbon data followed previously described methods⁶³. In brief, the outer bone surfaces were removed manually and all samples were soaked in successive washes of methanol, acetone and dichloromethane for

30 min each at room temperature to remove adhesives and consolidants, and rinsed in $>18.2\text{ M}\Omega\text{ cm}^{-1}$ water. Bones were demineralized in 0.5 N HCl for 24–36 h at 5 °C, and then gelatinized in 0.01 N HCl for 12 h at 60 °C. On the basis of crude gelatin yield and quality, the gelatin was either ultrafiltered (30-kDa MWCO), or hydrolysed for XAD purification. Resulting material was then combusted under vacuum in sealed quartz tubes with CuO and Ag wire, and the resulting CO₂ was converted to graphite using H₂ reduction over an iron catalyst. Radiocarbon content was measured on a 500-kV NEC 1.5SDH-1 compact accelerator, and conventional ages were calculated by normalizing to OXII oxalic acid standards and correcting for fractionation using the δ¹³C ratio measure on the AMS⁶⁴.

Reporting summary

Further information on research design is available in the [Nature Research Reporting Summary](#) linked to this paper.

Data availability

All raw, peak and result protein data have been uploaded to ProteomExchange (<http://www.proteomexchange.org>). Files are available under the project accession: PXD022300, and the project DOI is <https://doi.org/10.6019/PXD022300>. S.W. can also be contacted at shevan.wilkin@iem.uzh.ch.

References

1. 1.
Haak, W. et al. Massive migration from the steppe was a source for Indo-European languages in Europe. *Nature* **522**, 207–211 (2015).
2. 2.
Mathieson, I. et al. Genome-wide patterns of selection in 230 ancient Eurasians. *Nature* **528**, 499–503 (2015).
3. 3.
Jeong, C. et al. A dynamic 6,000-year genetic history of Eurasia's eastern steppe. *Cell* **183**, 890–904 (2020).
4. 4.

Anthony, D. W. & Ringe, D. The Indo-European homeland from linguistic and archaeological perspectives. *Annu. Rev. Linguist.* **1**, 199–219 (2015).

5. 5.

Anthony, D. W. & Brown, D. R. The secondary products revolution, horse-riding, and mounted warfare. *J. World Prehist.* **24**, 131 (2011).

6. 6.

Anthony, D. W. *The Horse, the Wheel, and Language* (Princeton Univ. Press, 2007).

7. 7.

Anthony, D. W. et al. The Eneolithic cemetery at Khvalynsk on the Volga River. *Praehistorische Zeitschrift* (in the press).

8. 8.

Wang, C.-C. et al. Ancient human genome-wide data from a 3000-year interval in the Caucasus corresponds with eco-geographic regions. *Nat. Commun.* **10**, 590 (2019).

9. 9.

Allentoft, M. E. et al. Population genomics of Bronze Age Eurasia. *Nature* **522**, 167–172 (2015).

10. 10.

Reinhold, S. et al. in *Appropriating Innovations: Entangled Knowledge in Eurasia 5000–1500BCE* (eds Stockhammer, P. & Maran, J.) 78–97 (Oxbow Books, 2017).

11. 11.

Rassamakin, Y. in *Late Prehistoric Exploration of the Eurasian Steppe* (eds Levine, M. et al.) 59–182 (McDonald Institute for Archaeological Research, 1999).

12. 12.

Levine, M. A. Botai and the origins of horse domestication. *J. Anthropol. Archaeol.* **18**, 29–78 (1999).

13. 13.

Outram, A. K. et al. The earliest horse harnessing and milking. *Science* **323**, 1332–1335 (2009).

14. 14.

Outram, A. K. et al. Patterns of pastoralism in later Bronze Age Kazakhstan: new evidence from faunal and lipid residue analyses. *J. Archaeol. Sci.* **39**, 2424–2435 (2012).

15. 15.

Gaunitz, C. et al. Ancient genomes revisit the ancestry of domestic and Przewalski's horses. *Science* **360**, 111–114 (2018).

16. 16.

Kohl, P. L. *The Making of Bronze Age Eurasia* (Cambridge Univ. Press, 2007).

17. 17.

de Barros Damgaard, P. et al. The first horse herders and the impact of early Bronze Age steppe expansions into Asia. *Science* **360**, eaar7711 (2018).

18. 18.

Taylor, W. T. T. et al. Early pastoral economies and herding transitions in eastern Eurasia. *Sci. Rep.* **10**, 1001 (2020).

19. 19.

Wilkin, S. et al. Dairy pastoralism sustained Eastern Eurasian steppe populations for 5000 years. *Nat. Ecol. Evol.* **4**, 346–355 (2020).

20. 20.

Frachetti, M. & Benecke, N. From sheep to (some) horses: 4500 years of herd structure at the pastoralist settlement of Begash (south-eastern Kazakhstan). *Antiquity* **83**, 1023–1037 (2009).

21. 21. Schulting, R. J. & Richards, M. P. in *A Bronze Age Landscape in the Russian Steppes: The Samara Valley Project* (eds Anthony, D. W. et al.) 127–148 (Cotsen Institute of Archaeology Press at UCLA, 2016).
22. 22. Ventresca Miller, A. R. & Makarewicz, C. A. Intensification in pastoralist cereal use coincides with the expansion of trans-regional networks in the Eurasian Steppe. *Sci. Rep.* **9**, 8363 (2019).
23. 23. Gimbutas, M. *The Kurgan Culture and the Indo-Europeanization of Europe: Selected Articles from 1952 to 1993* (Study of Man, 1997).
24. 24. Gimbutas, M. in *The Indo-Europeans in the Fourth and Third Millennium* (ed. Polomé, E. C.) 1–60 (Karoma, 1982).
25. 25. Mallory, J. P. *In Search of the Indo-Europeans: Language, Archaeology, and Myth* (Thames and Hudson, 1989).
26. 26. Wang, C. C. et al. Ancient human genome-wide data from a 3000-year interval in the Caucasus corresponds with eco-geographic regions. *Nat. Commun.* **10**, 590 (2019).
27. 27. Shishlina, N. I. et al. Paleoecology, subsistence, and ^{14}C chronology of the Eurasian Caspian steppe Bronze Age. *Radiocarbon* **51**, 481–499 (2009).
28. 28. Gerling, C. *Prehistoric Mobility and Diet in the West Eurasian Steppes 3500 to 300 BC: An Isotopic Approach* (Walter de Gruyter, 2015).
29. 29.

Anthony, D. W. et al. (eds). *A Bronze Age Landscape in the Russian Steppes: The Samara Valley Project* (Cotsen Institute of Archaeology Press at UCLA, 2016).

30. 30.

Kuznetsov, P. F. & Mochalov, O. D. in *A Bronze Age Landscape in the Russian Steppes: The Samara Valley Project* (eds Anthony, D. W. et al.) 71–90 (Cotsen Institute of Archaeology Press at UCLA, 2016).

31. 31.

Hanks, B. K., Epimakhov, A. V. & Renfrew, A. C. Towards a refined chronology for the Bronze Age of the southern Urals, Russia. *Antiquity* **81**, 353–367 (2007).

32. 32.

Kosintsev, P. A. in *Horses and Humans: The Evolution of Human–Equine Relationships* (eds. Olsen, S. L. et al.) 127–135 (BAR, 2006).

33. 33.

Hanks, B. et al. Bronze Age diet and economy: new stable isotope data from the Central Eurasian steppes (2100–1700 BC). *J. Archaeolog. Sci.* **97**, 14–25 (2018).

34. 34.

Hendy, J. et al. Ancient proteins from ceramic vessels at Çatalhöyük West reveal the hidden cuisine of early farmers. *Nat. Commun.* **9**, 4064 (2018).

35. 35.

Jeong, C. et al. Bronze Age population dynamics and the rise of dairy pastoralism on the eastern Eurasian steppe. *Proc. Natl Acad. Sci. USA* **115**, E11248–E11255 (2018).

36. 36.

Charlton, S. et al. New insights into Neolithic milk consumption through proteomic analysis of dental calculus. *Archaeol. Anthropol. Sci.* **11**, 6183–6196 (2019).

37. 37.

Bleasdale, M. et al. Ancient proteins provide evidence of dairy consumption in eastern Africa. *Nat. Commun.* **12**, 632 (2021).

38. 38.

Ramsøe, A. et al. Assessing the degradation of ancient milk proteins through site-specific deamidation patterns. *Sci. Rep.* **11**, 7795 (2021).

39. 39.

Salque, M. et al. Earliest evidence for cheese making in the sixth millennium BC in northern Europe. *Nature* **493**, 522–525 (2013).

40. 40.

Knipper, C. et al. Diet and subsistence in Bronze Age pastoral communities from the southern Russian steppes and the North Caucasus. *PLoS ONE* **15**, e0239861 (2020).

41. 41.

Frachetti, M. D. Multiregional emergence of mobile pastoralism and nonuniform institutional complexity across Eurasia. *Curr. Anthropol.* **53**, 2–38 (2012).

42. 42.

Bendrey, R. Some like it hot: environmental determinism and the pastoral economies of the later prehistoric Eurasian steppe. *Pastoralism: Research, Policy Pract.* **1**, 8 (2011).

43. 43.

Burger, J. et al. Low prevalence of lactase persistence in Bronze Age Europe indicates ongoing strong selection over the last 3,000 years. *Curr. Biol.* **30**, 4307–4315.e13 (2020).

44. 44.

Didier, J. C. *In and Outside the Square: The Sky and the Power of Belief in Ancient China and the World, c. 4500 BC-AD 200 (Sino-Platonic Papers 192)* (3 vols) (ed. Mair, V. H.) (2009).

45. 45.

Miletto, S., Kaiser, E., Rassamakin, Y. & Evershed, R. P. New insights into the subsistence economy of the Eneolithic Dereivka culture of the Ukrainian North-Pontic region through lipid residues analysis of pottery vessels. *J. Archaeol. Sci. Rep.* **13**, 67–74 (2017).

46. 46.

Miletto, S., Kaiser, E., Rassamakin, Y., Whelton, H. & Evershed, R. P. Differing modes of animal exploitation in North-Pontic Eneolithic and Bronze Age societies. *Sci. Technol. Archaeol. Res.* **3**, 112–125 (2017).

47. 47.

Chechushkov, I. V. & Epimakhov, A. V. Eurasian steppe chariots and social complexity during the Bronze Age. *J. World Prehist.* **31**, 435–483 (2018).

48. 48.

Sherratt, A. The secondary exploitation of animals in the Old World. *World Archaeol.* **15**, 90–104 (1983).

49. 49.

Greenfield, H. J. The secondary products revolution: the past, the present and the future. *World Archaeol.* **42**, 29–54 (2010).

50. 50.

Wang, C.-C. et al. Genomic insights into the formation of human populations in East Asia. *Nature* **591**, 413–419 (2021).

51. 51.

Türker, C. et al. B-Fabric: the Swiss Army Knife for life sciences. In *Proc. 13th International Conference on Extending Database Technology* (eds. Manolescu, I. et al.) 717–720 (Association for Computing Machinery, 2010).

52. 52.

Chambers, M. C. et al. A cross-platform toolkit for mass spectrometry and proteomics. *Nat. Biotechnol.* **30**, 918–920 (2012).

53. 53.

Perkins, D. N., Pappin, D. J., Creasy, D. M. & Cottrell, J. S. Probability-based protein identification by searching sequence databases using mass spectrometry data. *Electrophoresis* **20**, 3551–3567 (1999).

54. 54.

Hagan, R. MS-MARGE. Mpi-Shh-mascot report generator, <https://bitbucket.org/rwhagan/ms-marge/src/master/> (2018).

55. 55.

Bleasdale, M., Boivin, N. & Richter, K. K. Oral signature screening database for palaeoproteomic analyses of dental calculus, <https://doi.org/10.5281/zenodo.3698271> (2020).

56. 56.

Fernandes, R., Grootes, P., Nadeau, M.-J. & Nehlich, O. Quantitative diet reconstruction of a Neolithic population using a Bayesian mixing model (FRUITS): the case study of Ostorf (Germany). *Am. J. Phys. Anthropol.* **158**, 325–340 (2015).

57. 57.

Fernandes, R. A simple (R) model to predict the source of dietary carbon in individual consumers. *Archaeometry* **58**, 500–512 (2016).

58. 58.

Svyatko, S. V., Reimer, P. J. & Schulting, R. Modern freshwater reservoir offsets in the Eurasian steppe: implications for archaeology. *Radiocarbon* **59**, 1597–1607 (2017).

59. 59.

Fernandes, R., Millard, A. R., Brabec, M., Nadeau, M.-J. & Grootes, P. Food reconstruction using isotopic transferred signals (FRUITS): a Bayesian model for diet reconstruction. *PLoS ONE* **9**, e87436 (2014).

60. 60.

Shishlina, N. I., van der Plicht, J. & Turetsky, M. A. The Lebyazhinka burial ground (Middle Volga Region, Russia): new ^{14}C dates and the reservoir effect. *Radiocarbon* **60**, 681–690 (2018).

61. 61.
- Ramsey, C. B. Bayesian analysis of radiocarbon dates. *Radiocarbon* **51**, 337–360 (2009).
62. 62.
- Reimer, P. J. et al. The IntCal20 northern hemisphere radiocarbon age calibration curve (0–55 cal kBP). *Radiocarbon* **62**, 725–757 (2020).
63. 63.
- Narasimhan, V. M. et al. The formation of human populations in South and Central Asia. *Science* **365**, eaat7487 (2019).
64. 64.
- Stuiver, M. & Reimer, P. J. Discussion: reporting of ^{14}C data. *Radiocarbon* **19**, 355–363 (1977).

Acknowledgements

We thank the Max Planck Society for providing the funding for this project. D.R. is an Investigator of the Howard Hughes Medical Institute. A.E. was supported by a grant from the Russian Science Federation, grant number 20-18-00402. We thank A. Dittman for insights on protein mass spectra.

Funding

Open access funding provided by Max Planck Society.

Author information

Affiliations

1. Department of Archaeology, Max Planck Institute for the Science of Human History, Jena, Germany

Shevan Wilkin, Alicia Ventresca Miller, Ricardo Fernandes, Robert Spengler, William T.-T. Taylor & Nicole Boivin

2. Institute for Evolutionary Medicine, Faculty of Medicine, University of Zürich,
Zürich, Switzerland

Shevan Wilkin

3. Department of Anthropology, University of Michigan, Ann Arbor, MI, USA

Alicia Ventresca Miller

4. School of Archaeology, University of Oxford, Oxford, UK

Ricardo Fernandes

5. Faculty of Arts, Masaryk University, Brno-střed, Czech Republic

Ricardo Fernandes

6. Department of Anthropology, University of Colorado, Museum of Natural
History, Boulder, CO, USA

William T.-T. Taylor

7. Department of Anthropology, Hartwick College, Oneonta, NY, USA

Dorcas R. Brown & David Anthony

8. Department of Genetics, Harvard Medical School, Boston, MA, USA

David Reich

9. Broad Institute of Harvard and MIT, Cambridge, MA, USA

David Reich

10. Howard Hughes Medical Institute, Harvard Medical School, Boston, MA, USA

David Reich

11. Department of Human Evolutionary Biology, Harvard University, Cambridge,
MA, USA

David Reich & David Anthony

12. Department of Anthropology, University of California, Santa Barbara, CA, USA

Douglas J. Kennett

13. Institutes of Energy and the Environment, The Pennsylvania State University, University Park, PA, USA

Brendan J. Culleton

14. Functional Genomics Centre Zürich, University of Zürich/ETH, Zürich, Switzerland

Laura Kunz & Claudia Fortes

15. Center for Egyptological Studies, Russian Academy of Sciences, Moscow, Russian Federation

Aleksandra Kitova

16. Samara State University of Social Sciences and Education, Samara, Russian Federation

Pavel Kuznetsov & Aleksandr Khokhlov

17. South Ural State University, Chelyabinsk, Russian Federation

Andrey Epimakhov

18. Institute of History and Archaeology, Ural Branch of the Russian Academy of Sciences, Yekaterinburg, Russian Federation

Andrey Epimakhov

19. Institute of Archaeology and Steppe Civilizations, Al-Farabi Kazakh National University, Almaty, Kazakhstan

Victor F. Zaibert

20. Department of Archaeology, University of Exeter, Exeter, UK

Alan K. Outram

21. Center of Human Ecology, Institute of Ethnology and Anthropology, Russian Academy of Sciences, Moscow, Russian Federation

Egor Kitov

22. Faculty of History, Archaeology, and Ethnology, Al-Farabi Kazakh National University, Almaty, Kazakhstan

Egor Kitov

23. School of Social Science, The University of Queensland, Brisbane, Queensland, Australia

Nicole Boivin

24. Department of Anthropology and Archaeology, University of Calgary, Calgary, Alberta, Canada

Nicole Boivin

25. Department of Anthropology, National Museum of Natural History, Smithsonian Institution, Washington, DC, USA

Nicole Boivin

Contributions

S.W. and N.B. designed the study; S.W., A. Khokhlov, E.K., V.F.Z., A.K.O., D.R.B., P.K., A. Kitova and A.E. participated in sample collection; S.W. conducted the protein extractions and analysed the data; L.K. and C.F. ran the samples on the LC–MS/MS; D.R., R.F., B.J.C., D.K., A. Khokhlov and E.K. provided radiocarbon dates; S.W. and N.B. wrote the draft with the help of A.V.M., W.T.-T.T., R.S., D.A., E.K. and A. Khokhlov, and with input from all other co-authors.

Corresponding authors

Correspondence to Shevan Wilkin or Nicole Boivin.

Ethics declarations

Competing interests

The authors declare no competing interests.

Additional information

Peer review information *Nature* thanks the anonymous, reviewer(s) for their contribution to the peer review of this work. Peer reviewer reports are available.

Publisher's note Springer Nature remains neutral with regard to jurisdictional claims in published maps and institutional affiliations.

Extended data figures and tables

Extended Data Fig. 1 MS2 spectra for dairy proteins.

a, BLG peptide specific to *Ovis* or Bovinae for DA420. **b**, BLG I peptide specific to *Equus* for DA420. **c**, *Equus* BLG I peptide for Z438. **d**, MS2 spectra for a *Capra*-specific BLG peptide for Z438. **e**, α-S1 casein from DA430 specific to Bovinae. **f**, Second α-S1 casein peptide specific to Bovidae, also from DA430. Horse, goat and cow images are reproduced from ref. ³⁷; sheep silhouette, public domain (<https://thenounproject.com/icon/12538/>).

Supplementary information

Supplementary Information

This file contains supplementary text, supplementary figures s1 – s2 and supplementary references.

Reporting Summary

Supplementary Table S1

List of all individuals in this study, site names, GPS coordinates.

Supplementary Table S2

Comparison of short and middle chronologies for the Eneolithic to Early Bronze transition in Ukraine and Russia.

Supplementary Table S3

Preservation of individual calculus samples.

Supplementary Table S4

Diary peptides per individual.

Supplementary Table S5

Results for: uncalibrated AMS 14C dates, Bayesian estimates of dietary contributions, and modeled radiocarbon dates.

Peer Review File

Rights and permissions

Open Access This article is licensed under a Creative Commons Attribution 4.0 International License, which permits use, sharing, adaptation, distribution and reproduction in any medium or format, as long as you give appropriate credit to the original author(s) and the source, provide a link to the Creative Commons license, and indicate if changes were made. The images or other third party material in this article are included in the article's Creative Commons license, unless indicated otherwise in a credit line to the material. If material is not included in the article's Creative Commons license and your intended use is not permitted by statutory regulation or exceeds the permitted use, you will need to obtain permission directly from the copyright holder. To view a copy of this license, visit <http://creativecommons.org/licenses/by/4.0/>.

Reprints and Permissions

About this article

Cite this article

Wilkin, S., Ventresca Miller, A., Fernandes, R. *et al.* Dairying enabled Early Bronze Age Yamnaya steppe expansions. *Nature* **598**, 629–633 (2021).
<https://doi.org/10.1038/s41586-021-03798-4>

- Received: 04 April 2021
- Accepted: 05 July 2021
- Published: 15 September 2021
- Issue Date: 28 October 2021
- DOI: <https://doi.org/10.1038/s41586-021-03798-4>

Share this article

Anyone you share the following link with will be able to read this content:

[Get shareable link](#)

Sorry, a shareable link is not currently available for this article.

[Copy to clipboard](#)

Provided by the Springer Nature SharedIt content-sharing initiative

This article was downloaded by **calibre** from <https://www.nature.com/articles/s41586-021-03798-4>

| [Section menu](#) | [Main menu](#) |

- Article
- Open Access
- [Published: 20 October 2021](#)

The origins and spread of domestic horses from the Western Eurasian steppes

- [Pablo Librado¹](#),
- [Naveed Khan^{1,121 nAff120}](#),
- [Antoine Fages¹](#),
- [Mariya A. Kusliy^{1,2}](#),
- [Tomasz Suchan](#) [ORCID: orcid.org/0000-0002-0811-8754^{1,3}](#),
- [Laure Tonasso-Calvière¹](#),
- [Stéphanie Schiavinato¹](#),
- [Duha Alioglu¹](#),
- [Aurore Fromentier¹](#),
- [Aude Perdereau⁴](#),
- [Jean-Marc Aury](#) [ORCID: orcid.org/0000-0003-1718-3010⁵](#),
- [Charleen Gaunitz¹](#),
- [Lorelei Chauvey¹](#),
- [Andaine Seguin-Orlando¹](#),
- [Clio Der Sarkissian¹](#),
- [John Southon⁶](#),
- [Beth Shapiro^{7,8}](#),
- [Alexey A. Tishkin⁹](#),
- [Alexey A. Kovalev](#) [ORCID: orcid.org/0000-0003-2637-3131¹⁰](#),
- [Saleh Alquraishi¹¹](#),
- [Ahmed H. Alfarhan¹¹](#),
- [Khaled A. S. Al-Rasheid](#) [ORCID: orcid.org/0000-0002-3404-3397¹¹](#),
- [Timo Seregely¹²](#),
- [Lutz Klassen¹³](#),
- [Rune Iversen](#) [ORCID: orcid.org/0000-0001-7618-625X¹⁴](#),
- [Olivier Bignon-Lau¹⁵](#),

- [Pierre Bodu](#)¹⁵,
- [Monique Olive](#)¹⁵,
- [Jean-Christophe Castel](#)¹⁶,
- [Myriam Boudadi-Maligne](#)¹⁷,
- [Nadir Alvarez](#)^{18,19},
- [Mietje Germonpré](#) ORCID: orcid.org/0000-0001-8865-0937²⁰,
- [Magdalena Moskal-del Hoyo](#)³,
- [Jarosław Wilczyński](#) ORCID: orcid.org/0000-0002-9786-0693²¹,
- [Sylwia Pospuła](#)²¹,
- [Anna Lasota-Kuś](#)²²,
- [Krzysztof Tunia](#)²²,
- [Marek Nowak](#)²³,
- [Eve Rannamäe](#)²⁴,
- [Urmas Saarma](#)²⁵,
- [Gennady Boeskorov](#)²⁶,
- [Lembi Lõugas](#) ORCID: orcid.org/0000-0003-2011-2141²⁷,
- [René Kysely](#)²⁸,
- [Lubomír Peške](#)²⁹,
- [Adrian Bălășescu](#)³⁰,
- [Valentin Dumitrașcu](#)³⁰,
- [Roxana Dobrescu](#)³⁰,
- [Daniel Gerber](#)^{31,32},
- [Viktória Kiss](#)³³,
- [Anna Szécsényi-Nagy](#)³¹,
- [Balázs G. Mende](#)³¹,
- [Zsolt Gallina](#)³⁴,
- [Krisztina Somogyi](#)³⁵,
- [Gabriella Kulcsár](#)³³,
- [Erika Gál](#) ORCID: orcid.org/0000-0002-4226-3218³³,
- [Robin Bendrey](#)³⁶,
- [Morten E. Allentoft](#)^{37,38},
- [Ghenadie Sirbu](#)³⁹,
- [Valentin Dergachev](#)⁴⁰,
- [Henry Shephard](#)⁴¹,
- [Noémie Tomadini](#)⁴²,
- [Sandrine Grouard](#)⁴²,
- [Aleksei Kasparov](#)⁴³,
- [Alexander E. Basilyan](#)⁴⁴,
- [Mikhail A. Anisimov](#)⁴⁵,

- [Pavel A. Nikolskiy](#)⁴⁴,
- [Elena Y. Pavlova](#)⁴⁵,
- [Vladimir Pitulko](#) [ORCID: orcid.org/0000-0001-5672-2756](#)⁴³,
- [Gottfried Brem](#)⁴⁶,
- [Barbara Wallner](#) [ORCID: orcid.org/0000-0003-4159-0695](#)⁴⁶,
- [Christoph Schwall](#) [ORCID: orcid.org/0000-0002-6310-4056](#)⁴⁷,
- [Marcel Keller](#)^{48,49},
- [Keiko Kitagawa](#) [ORCID: orcid.org/0000-0002-6998-8454](#)^{50,51,52},
- [Alexander N. Bessudnov](#)⁵³,
- [Alexander Bessudnov](#) [ORCID: orcid.org/0000-0002-3785-6342](#)⁴³,
- [William Taylor](#) [ORCID: orcid.org/0000-0002-0836-7814](#)⁵⁴,
- [Jérôme Magail](#) [ORCID: orcid.org/0000-0002-5768-0698](#)⁵⁵,
- [Jamiyan-Ombo Gantulga](#)⁵⁶,
- [Jamsranjav Bayarsaikhan](#)^{57,58},
- [Diimaajav Erdenebaatar](#)⁵⁹,
- [Kubatbeek Tabaldiev](#)⁶⁰,
- [Enkhbayar Mijiddorj](#)⁵⁹,
- [Bazartseren Boldgiv](#) [ORCID: orcid.org/0000-0003-0015-8142](#)⁶¹,
- [Turbat Tsagaan](#) [ORCID: orcid.org/0000-0001-6606-8516](#)⁵⁶,
- [Mélanie Pruvost](#) [ORCID: orcid.org/0000-0001-7824-2155](#)¹⁷,
- [Sandra Olsen](#)⁶²,
- [Cheryl A. Makarewicz](#) [ORCID: orcid.org/0000-0002-1649-336X](#)^{63,64},
- [Silvia Valenzuela Lamas](#) [ORCID: orcid.org/0000-0001-9886-0372](#)⁶⁵,
- [Silvia Albizuri Canadell](#) [ORCID: orcid.org/0000-0001-6194-0475](#)⁶⁶,
- [Ariadna Nieto Espinet](#)⁶⁷,
- [Ma Pilar Iborra](#) [ORCID: orcid.org/0000-0002-4315-7257](#)⁶⁸,
- [Jaime Lira Garrido](#)^{69,70},
- [Esther Rodríguez González](#)⁷¹,
- [Sebastián Celestino](#)⁷¹,
- [Carmen Olària](#)⁷²,
- [Juan Luis Arsuaga](#)^{70,73},
- [Nadiia Kotova](#)⁷⁴,
- [Alexander Pryor](#)⁷⁵,
- [Pam Crabtree](#)⁷⁶,
- [Rinat Zhumataev](#)⁷⁷,
- [Abdesh Toleubaev](#)⁷⁷,
- [Nina L. Morgunova](#)⁷⁸,
- [Tatiana Kuznetsova](#)^{79,80},
- [David Lordkipanize](#)^{81,82},

- [Matilde Marzullo](#)⁸³,
- [Ornella Prato](#)⁸³,
- [Giovanna Bagnasco Gianni](#)⁸³,
- [Umberto Tecchiati](#)⁸³,
- [Benoit Clavel](#)⁴²,
- [Sébastien Lepetz](#)⁴²,
- [Hossein Davoudi](#) ORCID: orcid.org/0000-0002-5236-1444⁸⁴,
- [Marjan Mashkour](#) ORCID: orcid.org/0000-0003-3630-9459^{42,84},
- [Natalia Ya. Berezina](#)⁸⁵,
- [Philipp W. Stockhammer](#)^{86,87},
- [Johannes Krause](#) ORCID: orcid.org/0000-0001-9144-3920^{49,86},
- [Wolfgang Haak](#) ORCID: orcid.org/0000-0003-2475-2007^{49,86,88},
- [Arturo Morales-Muñiz](#)⁸⁹,
- [Norbert Benecke](#)⁹⁰,
- [Michael Hofreiter](#)⁹¹,
- [Arne Ludwig](#) ORCID: orcid.org/0000-0001-7249-9953^{92,93},
- [Alexander S. Graphodatsky](#)²,
- [Joris Peters](#) ORCID: orcid.org/0000-0003-0894-2628^{94,95},
- [Kirill Yu. Kiryushin](#)⁹,
- [Tumur-Ochir Iderkhangai](#)⁵⁹,
- [Nikolay A. Bokovenko](#)⁴³,
- [Sergey K. Vasiliev](#)⁹⁶,
- [Nikolai N. Seregin](#)⁹,
- [Konstantin V. Chugunov](#)⁹⁷,
- [Natalya A. Plasteeva](#)⁹⁸,
- [Gennady F. Baryshnikov](#)⁹⁹,
- [Ekaterina Petrova](#)¹⁰⁰,
- [Mikhail Sablin](#) ORCID: orcid.org/0000-0002-2773-7454⁹⁹,
- [Elina Ananyevskaya](#)¹⁰⁰,
- [Andrey Logvin](#)¹⁰¹,
- [Irina Shevnina](#)¹⁰¹,
- [Victor Logvin](#)¹⁰²,
- [Saule Kalieva](#) ORCID: orcid.org/0000-0003-1901-1001¹⁰²,
- [Valeriy Loman](#) ORCID: orcid.org/0000-0001-6951-0509¹⁰³,
- [Igor Kukushkin](#)¹⁰³,
- [Ilya Merz](#)¹⁰⁴,
- [Victor Merz](#)¹⁰⁴,
- [Sergazy Sakenov](#)¹⁰⁵,
- [Victor Varfolomeyev](#)¹⁰³,

- [Emma Usmanova](#)¹⁰³,
- [Viktor Zaibert](#)¹⁰⁶,
- [Benjamin Arbuckle](#) [ORCID: orcid.org/0000-0002-5445-5516](#)¹⁰⁷,
- [Andrey B. Belinskiy](#)¹⁰⁸,
- [Alexej Kalmykov](#)¹⁰⁸,
- [Sabine Reinhold](#) [ORCID: orcid.org/0000-0002-8107-6300](#)⁹⁰,
- [Svend Hansen](#)⁹⁰,
- [Aleksandr I. Yudin](#)¹⁰⁹,
- [Aleksandr A. Vybornov](#)¹¹⁰,
- [Andrey Epimakhov](#)^{111,112},
- [Natalia S. Berezina](#)¹¹³,
- [Natalia Roslyakova](#) [ORCID: orcid.org/0000-0002-1888-2713](#)¹¹⁰,
- [Pavel A. Kosintsev](#)^{98,114},
- [Pavel F. Kuznetsov](#)¹¹⁰,
- [David Anthony](#)^{115,116},
- [Guus J. Kroonen](#) [ORCID: orcid.org/0000-0002-3708-0476](#)^{117,118},
- [Kristian Kristiansen](#)^{119,120},
- [Patrick Wincker](#) [ORCID: orcid.org/0000-0001-7562-3454](#)⁵,
- [Alan Outram](#) [ORCID: orcid.org/0000-0003-3360-089X](#)⁷⁵ &
- [Ludovic Orlando](#) [ORCID: orcid.org/0000-0003-3936-1850](#)¹

Nature volume **598**, pages 634–640 (2021)

- 36k Accesses
- 1248 Altmetric
- [Metrics details](#)

Subjects

- [Evolutionary genetics](#)
- [Population genetics](#)

Abstract

Domestication of horses fundamentally transformed long-range mobility and warfare¹. However, modern domesticated breeds do not descend from the earliest domestic horse lineage associated with archaeological evidence of bridling, milking and corralling^{2,3,4} at Botai, Central Asia around 3500 bc⁵. Other longstanding candidate

regions for horse domestication, such as Iberia⁵ and Anatolia⁶, have also recently been challenged. Thus, the genetic, geographic and temporal origins of modern domestic horses have remained unknown. Here we pinpoint the Western Eurasian steppes, especially the lower Volga-Don region, as the homeland of modern domestic horses. Furthermore, we map the population changes accompanying domestication from 273 ancient horse genomes. This reveals that modern domestic horses ultimately replaced almost all other local populations as they expanded rapidly across Eurasia from about 2000 bc, synchronously with equestrian material culture, including Sintashta spoke-wheeled chariots. We find that equestrianism involved strong selection for critical locomotor and behavioural adaptations at the *GSDMC* and *ZFPM1* genes. Our results reject the commonly held association⁷ between horseback riding and the massive expansion of Yamnaya steppe pastoralists into Europe around 3000 bc^{8,9} driving the spread of Indo-European languages¹⁰. This contrasts with the scenario in Asia where Indo-Iranian languages, chariots and horses spread together, following the early second millennium bc Sintashta culture^{11,12}.

[Download PDF](#)

Main

We gathered horse remains encompassing all suspected domestication centres, including Iberia, Anatolia and the steppes of Western Eurasia and Central Asia (Fig 1a). The sampling targeted previously under-represented time periods, with 201 radiocarbon dates spanning 44426 to 202 bc, and five beyond 50250 to 47950 bc (Supplementary Table 1).

Fig. 1: Ancient horse remains and their genomic affinities.

 **figure1**

a, Temporal and geographic sampling. The red star indicates the location of the two TURG horses (late Yamnaya context) showing genetic continuity with DOM2. The dashed line indicates the inferred homeland of DOM2 horses in the lower Volga-Don region. Colours refer to regions and/or time periods delineating genetically close horses. The radius of each cylinder is proportional to the number of samples analysed (for <10 specimens; radius constant above this), and the height refers to the time range covered. **b**, Neighbour-joining phylogenomic tree (100 bootstrap pseudo-replicates). Samples are coloured according to **a** and the main phylogenetic clusters are numbered from 1 to 4. **c**, Fold difference between neighbour-joining-based and raw pairwise genetic distances. **d**, Pairwise distance matrix of Struct-f4 genetic affinities between samples. Increasing genetic affinities are indicated by a yellow-to-red gradient. **e**, Struct-f4 ancestry component profiles. **f**, Ancestry profiles of selected key horse groups and samples. PRZE, Przewalski; UP-SFR, Upper Palaeolithic Southern France.

The DNA quality enabled shotgun sequencing of 264 ancient genomes at $0.10\times$ to $25.76\times$ average coverage (239 genomes above $1\times$ coverage), including 16 genomes for

which further sequencing added to previously reported data. Enzymatic¹³ and computational removal of post mortem DNA damage produced high-quality data with derived mutations decreasing with sample age, as expected if mutations accumulate through time (Extended Data Fig. 1). We added ten published modern genomes, and nine ancient genomes characterized with consistent technology or covering relevant time periods and locations, to obtain the most extensive high-quality genome time series for horses.

Pre-domestication population structure

Neighbour-joining phylogenomic inference revealed four geographically defined monophyletic groups (Fig 1b). These closely mirrored clusters identified using an extension of the Struct-f4 method⁵ (Fig 1d–f, Extended Data Fig. 2, [Supplementary Methods](#)), except for the Neolithic Anatolia group (NEO-ANA), where the tree-to-data goodness of fit suggested phylogenetic misplacement (Fig 1c, [Supplementary Methods](#)).

The most basal cluster included *Equus lenensis* (ELEN), a lineage identified in northeastern Siberia from the Late Pleistocene to the late fourth millennium bc^{5,14,15}. A second group covered Europe, including Late Pleistocene Romania, Belgium, France and Britain, and the region from Spain to Scandinavia and Hungary, Czechia and Poland during the sixth-to-third millennium bc. The third cluster comprised the earliest known domestic horses from Botai and Przewalski's horses, as previously reported³, and extended to the Altai and Southern Urals during the fifth-to-third millennium bc. Finally, modern domestic horses clustered within a group that became geographically widespread and prominent following about 2200 bc and during the second millennium bc (DOM2). This cluster appears genetically close to horses that lived in the Western Eurasia steppes (WE) but not further west than the Romanian lower Danube, south of the Carpathians, before and during the third millennium bc. Significant correlation between genetic and geographic distances, and inference of limited long-distance connectivity with estimated effective migration surface¹⁶ (EEMS), confirmed the strong geographic differentiation of horse populations before about 3000 bc (Fig 2a, Extended Data Fig. 3a).

Fig. 2: Horse geographic and genetic affinities.

 **figure2**

a–c, EEMS-predicted migration barriers¹⁶ and average ancestry components found in each archaeological site from before 3000 bc (a), during the third millennium bc (b) and after around 2000 bc (c). The size of the pie charts is proportional to the number of samples analysed in a given location (<10, constant above). Pie chart colours refer

to $K = 6$ ancestry components, averaged per location. Regions inferred as geographic barriers are shown in shades of brown, and regions affected by migrations are shown in shades of blue. The base map was obtained from rworldmap⁴⁶.

Horse ancestry profiles in Neolithic Anatolia and Eneolithic Central Asia, including at Botai, maximized a genetic component (coloured green in Fig. 1e, f) that was also substantial in Central and Eastern Europe during the Late Pleistocene (RONPC06_Rom_m34801) and the fourth or third millennium bc (Figs. 1e, 3a, Extended Data Fig. 4). It was, however, absent or moderately present in the Romanian lower Danube (ENEO-ROM), the Dnieper steppes (Ukr11_Ukr_m4185) and the western lower Volga-Don (C-PONT) populations during the sixth to third millennia bc. This indicates possible expansions of Anatolian horses into both Central and Eastern Europe and Central Asia regions, but not into the Western Eurasia steppes. The absence of typical NEO-ANA ancestry rules out expansion from Anatolia into Central Asia across the Caucasus mountains but supports connectivity south of the Caspian Sea prior to about 3500 bc.

Fig. 3: Population genetic affinities, evolutionary history and geographic origins.

 **figure3**

a, Multi-dimensional scaling plot of f_4 -based genetic affinities. The age of the samples is indicated along the vertical axis. CA, Central Asia. **b**, Horse evolutionary history inferred by OrientAGraph¹⁹ with three migration edges and nine lineages representing key genomic ancestries (coloured as in Fig 1a). The model explains 99.99% of the total variance. The triangular pairwise matrix provides model residuals. The external branch leading to donkey was set to zero to improve visualization. **c**, LOCATOR²⁰ predictions of the geographic region where the ancestors of DOM2, tarpan and modern Przewalski's horses lived. The tarpan and modern Przewalski's horses do not descend from the same ancestral population as modern domestic horses. The map was drawn using the maps R package⁴⁷.

The origins of DOM2 horses

The C-PONT group not only possessed moderate NEO-ANA ancestry, but also was the first region where the typical DOM2 ancestry component (coloured orange in Fig. 1e, f) became dominant during the sixth millennium bc. Multi-dimensional scaling further identified three horses from the western lower Volga-Don region as genetically closest to DOM2, associated with Steppe Maykop (Aygurskii), Yamnaya (Repin) and Poltavka (Sosnovka) contexts, dated to about 3500 to 2600 bc (Figs. 2a, b, 3a). Additionally, genetic continuity with DOM2 was rejected for all horses predating about 2200 bc, especially those from the NEO-ANA group (Supplementary Table 2), except for two late Yamnaya specimens from approximately 2900 to 2600 bc (Turganik (TURG)), located further east than the western lower Volga-Don region (Figs. 2a, b, 3a). These may therefore have provided some of the direct ancestors of DOM2 horses.

Modelling of the DOM2 population with qpADM¹⁷, rotating¹⁸ all combinations of 2, 3 or 4 population donors, eliminated the possibility of a contribution from the NEO-ANA population, but indicated possible formation within the WE population, including a genetic contribution of approximately 95% from C-PONT and TURG horses (Supplementary Table 3). This was consistent with OrientAGraph¹⁹ modelling from nine lineages representing key ancestry combinations, which confirmed the absence of NEO-ANA genetic ancestry in DOM2 and confirmed DOM2 as a sister population to the C-PONT horses (Fig. 3b).

Identifying discrete populations and modelling admixture as single unidirectional pulses, however, was highly challenging given the extent of spatial genetic connectivity. Indeed, the typical DOM2 ancestry component was maximized in the C-PONT group, but declined sharply eastwards (TURG and Central Asia) in the third millennium bc as the proportion of NEO-ANA ancestry increased (Fig. 2a). This suggests a cline of genetic connectivity east of the Western Eurasia steppes and Central Asia, ruling out DOM2 ancestors further east than the western lower Volga-Don and Turganik. A similar genetic cline characterized the region located west of C-PONT, where the typical DOM2 ancestry component declined steadily in the Dnieper steppes, Poland, Turkish Thrace and Hungary in the fifth to third millennia bc. This eliminates the possibility of DOM2 ancestors further west than C-PONT and the Dnieper steppes. Furthermore, patterns of spatial autocorrelations in the genetic data²⁰ indicated Western Eurasia steppes as the most likely geographic location of DOM2 ancestors (Fig. 3c). Combined, our results demonstrate that DOM2 ancestors lived in the Western Eurasia steppes, especially the lower Volga-Don, but not in Anatolia, during the late fourth and early third millennia bc.

Expansion of steppe-related pastoralism

Analyses of ancient human genomes have revealed a massive expansion from the Western Eurasia steppes into Central and Eastern Europe during the third millennium bc, associated with the Yamnaya culture^{8,9,11,12,21}. This expansion contributed at least two thirds of steppe-related ancestry to populations of the Corded Ware complex (CWC) around 2900 to 2300 bc⁸. The role of horses in this expansion remained unclear, as oxen could have pulled Yamnaya heavy, solid-wheeled wagons^{7,22}. The genetic profile of horses from CWC contexts, however, almost completely lacked the ancestry maximized in DOM2 and Yamnaya horses (TURG and Repin) (Figs. 1e, f, 2a, b) and showed no direct connection with the WE group, including both C-PONT and TURG, in OrientAGraph modelling (Fig. 3b, Extended Data Fig. 5).

The typical DOM2 ancestry was also limited in pre-CWC horses from Denmark, Poland and Czechia, associated with the Funnel Beaker and early Pitted Ware cultures (FB/PWC, FB/POL and ENEO-CZE, respectively). DOM2 ancestry reached a maximum 12.5% in one Hungarian horse dated to the mid-third millennium bc and associated with the Somogyvár-Vinkovci Culture (CAR05_Hun_m2458). qpAdm¹⁷ modelling indicated that its DOM2 ancestry was acquired following gene flow from southern Thrace (Kan22_Tur_m2386), but not from the Dnieper steppes (Ukr11_Ukr_m4185) (Supplementary Table 3). Combined with the lack of increased horse dispersal during the early third millennium bc (Fig. 2b, Extended Data Fig. 3b), these results suggest that DOM2 horses did not accompany the steppe pastoralist expansion north of the Carpathians.

By around 2200–2000 bc, the typical DOM2 ancestry profile appeared outside the Western Eurasia steppes in Bohemia (Holubice), the lower Danube (Gordinesti II) and central Anatolia (Acemhöyük), spreading across Eurasia shortly afterwards, eventually replacing all pre-existing lineages (Fig 2c, Extended Data Fig. 3c). Eurasia became characterized by high genetic connectivity, supporting massive horse dispersal by the late third millennium and early second millennium bc. This process involved stallions and mares, indicated by autosomal and X-chromosomal variation (Extended Data Fig. 3d), and was sustained by explosive demographics apparent in both mitochondrial and Y-chromosomal variation (Extended Data Fig. 3e, f). Altogether, our genomic data uncover a high turnover of the horse population in which past breeders produced large stocks of DOM2 horses to supply increasing demands for horse-based mobility from around 2200 bc.

Of note, the DOM2 genetic profile was ubiquitous among horses buried in Sintashta kurgans together with the earliest spoke-wheeled chariots around 2000–1800 bc^{7,9,23,24} (Extended Data Fig. 6). A typical DOM2 profile was also found in Central Anatolia (AC9016_Tur_m1900), concurrent with two-wheeled vehicle iconography from about

1900 bc^{25,26}. However, the rise of such profiles in Holubice, Gordinesti II and Acemhöyük before the earliest evidence for chariots supports horseback riding fuelling the initial dispersal of DOM2 horses outside their core region, in line with Mesopotamian iconography during the late third and early second millennia bc²⁷. Therefore, a combination of chariots and equestrianism is likely to have spread the DOM2 diaspora in a range of social contexts from urban states to dispersed decentralized societies²⁸.

DOM2 biological adaptations

Human-induced DOM2 dispersal conceivably involved selection of phenotypic characteristics linked to horseback riding and chariotry. We therefore screened our data for genetic variants that are over-represented in DOM2 horses from the late third millennium bc (Extended Data Fig. 7). The first outstanding locus peaked immediately upstream of the *GSDMC* gene, where sequence coverage dropped at two L1 transposable elements in all lineages except DOM2. The presence of additional exons in other mammals suggests that independent L1 insertions remodelled the DOM2 gene structure. In humans, *GSDMC* is a strong marker for chronic back pain²⁹ and lumbar spinal stenosis, a syndrome causing vertebral disk hardening and painful walking³⁰.

The second most differentiated locus extended over approximately 16 Mb on chromosome 3, with the *ZFPM1* gene being closest to the selection peak. *ZFPM1* is essential for the development of dorsal raphe serotonergic neurons involved in mood regulation³¹ and aggressive behaviour³². *ZFPM1* inactivation in mice causes anxiety disorders and contextual fear memory³¹. Combined, early selection at *GSDMC* and *ZFPM1* suggests shifting use toward horses that were more docile, more resilient to stress and involved in new locomotor exercise, including endurance running, weight bearing and/or warfare.

Evolutionary history and origins of tarpan horses

Our analyses elucidate the geographic, temporal and biological origins of DOM2 horses. This study features a diverse ancient horse genome dataset, revealing the presence of deep mitochondrial and/or Y-chromosomal haplotypes in non-DOM2 horses (Supplementary Fig 1). This suggests that yet-unsampled divergent populations contributed to forming several lineages excluding DOM2. This was especially true in the Iberian group (IBE), where the expected genetic distance to the donkey was reduced (Extended Data Fig. 5f), but also in NEO-ANA according to OrientAGraph modelling (Fig 3b). Disentangling exact divergence and ancestry contributions of such unsampled lineages is difficult with the currently available data. It can, however, be

stressed that Iberia and Anatolia represent two well-known refugia³³, where populations could have survived and mixed during Ice Ages.

Finally, our analyses have solved the mysterious origins of the tarpan horse, which became extinct in the early 20th century. The tarpan horse came about following admixture between horses native to Europe (modelled as having 28.8–34.2% and 32.2–33.2% CWC ancestry in OrientAGraph¹⁹ and qpAdm¹⁷, respectively) and horses closely related to DOM2. This is consistent with LOCATOR²⁰ predicting ancestors in western Ukraine (Fig 3c) and refutes previous hypotheses depicting tarpans as the wild ancestor or a feral version of DOM2, or a hybrid with Przewalski's horses³⁴.

Discussion

This work resolves longstanding debates about the origins and spread of domestic horses. Whereas horses living in the Western Eurasia steppes in the late fourth and early third millennia bc were the ancestors of DOM2 horses, there is no evidence that they facilitated the expansion of the human genetic steppe ancestry into Europe^{8,9} as previously hypothesized⁷. Instead of horse-mounted warfare, declining populations during the European late Neolithic³⁵ may thus have opened up an opportunity for a westward expansion of steppe pastoralists. Yamnaya horses at Repin and Turganik carried more DOM2 genetic affinity than presumably wild horses from hunter-gatherer sites of the sixth millennium bc (NEO-NCAS, from approximately 5500–5200 bc), which may suggest early horse management and herding practices. Regardless, Yamnaya pastoralism did not spread horses far outside their native range, similar to the Botai horse domestication, which remained a localized practice within a sedentary settlement system^{2,36}. The globalization stage started later, when DOM2 horses dispersed outside their core region, first reaching Anatolia, the lower Danube, Bohemia and Central Asia by approximately 2200 to 2000 bc, then Western Europe and Mongolia soon afterwards, ultimately replacing all local populations by around 1500 to 1000 bc. This process first involved horseback riding, as spoke-wheeled chariots represent later technological innovations, emerging around 2000 to 1800 bc in the Trans-Ural Sintashta culture⁷. The weaponry, warriors and fortified settlements associated with this culture may have arisen in response to increased aridity and competition for critical grazing lands, intensifying territoriality and hierarchy³⁷. This may have provided the basis for the conquests over the subsequent centuries that resulted in an almost complete human and horse genetic turnover in Central Asian steppes^{11,21}. The expansion to the Carpathian basin³⁸, and possibly Anatolia and the Levant, involved a different scenario in which specialized horse trainers and chariot builders spread with the horse trade and riding. In both cases, horses with reduced back pathologies and enhanced docility would have facilitated Bronze Age elite long-distance trade demands and become a highly valued commodity and status symbol,

resulting in rapid diaspora. We, however, acknowledge substantial spatiotemporal variability and evidential bias towards elite activities, so we do not discount additional, harder to evidence, factors in equine dispersal.

Our results also have important implications for mechanisms underpinning two major language dispersals. The expansion of the Indo-European language family from the Western Eurasia steppes has traditionally been associated with mounted pastoralism, with the CWC serving as a major stepping stone in Europe^{39,40,41}. However, while there is overwhelming lexical evidence for horse domestication, horse-drawn chariots and derived mythologies in the Indo-Iranian branch of the Indo-European family, the linguistic indications of horse-keeping practices at the deeper Proto-Indo-European level are in fact ambiguous⁴² ([Supplementary Discussion](#)). The limited presence of horses in CWC assemblages⁴³ and the local genetic makeup of CWC specimens reject scenarios in which horses were the primary driving force behind the initial spread of Indo-European languages in Europe⁴⁴. By contrast, DOM2 dispersal in Asia during the early-to-mid second millennium bc was concurrent with the spread of chariotry and Indo-Iranian languages, whose earliest speakers are linked to populations that directly preceded the Sintashta culture^{11,12,45}. We thus conclude that the new package of chariotry and improved breed of horses, including chestnut coat colouration documented both linguistically ([Supplementary Discussion](#)) and genetically (Extended Data Fig. 8), transformed Eurasian Bronze Age societies globally within a few centuries after about 2000 bc. The adoption of this new institution, whether for warfare, prestige or both, probably varied between decentralized chiefdoms in Europe and urbanized states in Western Asia. The results thus open up new research avenues into the historical developments of these different societal trajectories.

Methods

Radiocarbon dating

A total of 170 new radiocarbon dates were obtained in this study. Dating was carried out at the Keck Carbon Cycle AMS Laboratory, UC Irvine following collagen extraction and ultra-filtration from approximately 1 g of osseous material. IntCal20 calibration⁴⁸ was performed using OxCalOnline⁴⁹.

Genome sequencing

All samples were collected with permission from the organizations holding the collections and documented through official authorization letters for partially destructive sampling from local authorities. Samples were processed for DNA extraction, library construction and shallow sequencing in the ancient DNA facilities of the Centre for Anthropobiology and Genomics of Toulouse (CAGT), France. The overall methodology followed the work from Seguin–Orlando and colleagues⁵⁰. It involved: (1) powdering a total of 100–590 mg of osseous material using the Mixel Mill MM200 (Retsch) Micro-dismembrator; (2) extracting DNA following the procedure Y2 from Gamba and colleagues⁵¹, tailored to facilitate the recovery of even the shortest DNA fragments; (3) treating DNA extracts with the USER (NEB) enzymatic cocktail to eliminate a fraction of post mortem DNA damage¹³; (4) constructing from double-stranded DNA templates DNA libraries in which two internal indexes are added during adapter ligation and one external index is added during PCR amplification; and (5) amplification, purification and quantification of DNA libraries before pooling 20–50 DNA libraries for low-depth sequencing on the Illumina MiniSeq instrument (paired-end mode, 2 × 80). All three indexes of each library were unique in a given sequencing pool.

Raw fastQ files were demultiplexed, trimmed and collapsed when individual read pairs showed significant overlap using AdapterRemoval2⁵² (version 2.3.0), disregarding reads shorter than 25 bp. Processed reads were then aligned against the nuclear and mitochondrial horse reference genomes^{53,54}, and appended with the Y-chromosome contigs from⁵⁵ using the Paleomix bam_pipeline (version 1.2.13.2) with the mapping parameters recommended by Poullet and Orlando⁵⁶. Sequencing reads representing PCR duplicates or showing a mapping quality below 25 were disregarded. DNA fragmentation and nucleotide misincorporation patterns were assessed on the basis of 100,000 random mapped reads using mapDamage2⁵⁷ (version 2.0.8). Paleomix returned provisional estimates of endogenous DNA content and clonality, as defined by the fraction of retained reads mapping uniquely against the horse reference genomes and those mapping

at the same genomic coordinates, respectively. These numbers guided further experimental decisions, including (1) the sequencing effort to be performed per individual library; (2) the preparation of additional libraries from left-over aliquots of USER-treated DNA extracts, or following treatment of DNA extract aliquots with the USER enzymatic cocktail; and (3) the preparation of additional DNA extracts. After initial screening for library content, sequencing was carried out on the Illumina HiSeq4000 instruments from Genoscope (paired-end mode, 2 × 76; France Génomique), except for four samples (BPTDG1_Fra_m11800, Closeau3_Fra_m10400, Novoil1_Kaz_m1832 and Novoil2_Kaz_m1832), for which sequencing was done at Novogene Europe on an Illumina NovaSeq 6000 instrument (S4 lanes, paired-end mode, 2 × 150). Overall, we obtained sequence data for a total of 264 novel ancient horse specimens and 1,029 DNA libraries (980 new), summing up to 31.86 billion sequencing read pairs and 100.82 billion collapsed read pairs, which was sufficient to characterize 226 novel ancient genomes showing a genomic depth-of-coverage of at least 1× (median 2.80-fold, maximum 25.76-fold) (Supplementary Table 1).

Allele sampling, sequencing error rates, genome rescaling and trimming

Following previous work^{5,58}, error rates are defined as the excess of mutations that are private to the ancient genome, relative to a modern genome considered as error-free. Mutations were polarized using an outgroup genome representing a consensus built from seven male specimens of diverse equine species (*Equus africanus somaliensis*, *Equus asinus*, *Equus burchelli*, *Equus grevyi*, *Equus hartmannae*, *Equus hemionus onager* and *Equus kiang*⁵⁹), according to a majority rule in which at maximum 2 of the 7 individuals showed an alternative allele. Minor and major alleles were identified using ANGSD⁶⁰ (version 0.933-86-g3fefdc4, htslib: 1.10.2-106-g9c35744) and the following parameters: -baq 0 - doMajorMinor 2 -uniqueOnly 1 -minMapQ 25 -minQ 30 -minind 7 - doCounts 1 -doMaf 1.

Error rate estimates ranged between 0.000337 and 0.003966 errors per site and revealed that nucleotide C→T and G→A misincorporation rates were

still inflated relative to their reciprocal substitution types (T→C and A→G), despite USER treatment. Therefore, individual BAM alignment files were processed to further reduce nucleotide misincorporation rates. To achieve this, we used PMDtools⁶¹ (version 0.60) to bin apart reads likely containing post mortem DNA damage (--threshold 1; DAM) from those that did not (--upperthreshold 1; NODAM). NODAM-aligned reads were then directly trimmed by 5 bp at their ends, where individual base qualities generally drop. The base quality of aligned DAM reads was first rescaled using mapDamage2⁵⁷ (version 2.0.8), penalizing all instances of potential derivatives of post mortem cytosine deamination, then further trimmed by 10 bp at both ends. The resulting NODAM and DAM aligned reads were merged again to obtain final BAM sequence alignments. Final error rate estimates ranged between 0.000080 and 0.000933 errors per site (Supplementary Table 1).

Uniparentally inherited markers and coat colouration

Mitochondrial genomes for the 264 newly sequenced samples were characterized from quality-filtered BAM alignment files (minMapQ=25, minQ=30), using a majority rule requiring at least five individual reads per position. Their resulting complete mitochondrial genome sequences were aligned together with a total of 193 sequences previously characterized^{3,5,14,15,58,62,63} using mafft⁶⁴ (version 7.407). Sequence alignments were split into six partitions, following previous work⁵, including the control region, all tRNAs, both rRNAs and each codon position considered separately. Maximum-likelihood phylogenetic reconstruction was performed using RAxML⁶⁵ (version 8.2.11) with default parameters, and assessing node support from a total of 100 bootstrap pseudo-replicates. The same partitions were provided as input for BEAST⁶⁶ (version 2.5.1), together with calibrated radiocarbon years (Supplementary Table 1). Specimens lacking direct radiocarbon dates or identified as not belonging to the DOM2 cluster were disregarded (Supplementary Table 1). While the former ensured precise tip-calibration for molecular clock estimation (assuming uncorrelated log-normal relaxed model), the latter prevented misinterpreting spatial variation in the population structure as changes in the effective population size⁶⁷. The best substitution model was

selected from ModelGenerator⁶⁸ (version 0.85) and Bayesian Skyline plots⁶⁹ were retrieved following 1,000,000,000 generations, sampling 1 every 1,000 and disregarding the first 30% as burn-in. Convergence was visually checked in Tracer⁷⁰ (version 1.7.2).

The Y-chromosome maximum-likelihood tree was constructed calling individual haplotypes from trimmed and rescaled BAM sequence alignments against the contigs described by Felkel and colleagues⁵⁵, filtered for single copy MSY regions. The final multifasta sequence alignment included sites covered in at least 20% of the specimens, pseudo-haploidizing each position and filtering out transitions, as done with autosomal data. It was further restricted to specimens showing at least 20% of the final set of positions covered. This represented a total of 3,195 nucleotide transversions for 142 specimens. The final tree was computed using IQtree (version 1.6.12), following AICc selection of the best substitution model and 1,000 ultrafast bootstrap approximation for assessing node support^{71,72}. The Y-chromosome Bayesian skyline plot was obtained following the same procedure as above. Maximum-likelihood trees and Bayesian skyline plots are shown in Supplementary Fig 1 and Extended Data Fig. 3e,f, respectively.

The presence of alleles associated with or causative for a diversity of coat colouration changes was investigated using individual BAM read alignments. For a total of 43 genomic locations representing biallelic SNPs, we simply counted the proportion of reads supporting the associated or causative allele. Results were summarized in the heat map shown in Extended Data Fig. 8, with respect to the sample ordering displayed in the neighbour-joining phylogenetic reconstruction, and limited to those 13 loci that were polymorphic in our horse panel for clarity.

Neighbour-joining phylogeny, genetic continuity and population modelling

Phylogenetic affinities were first estimated by performing a BioNJ tree reconstruction with FastME⁷³ (version 2.1.4), based on the pairwise matrix of genetic distances inferred from the bed2diffs_v1 program¹⁶. Node

supports were assessed using a total of 100 bootstrap pseudo-replicates. The ‘goodness-of-fit’ of the neighbour-joining tree to the data was evaluated by comparing the patristic distances and raw pairwise distances. Patristic distances were obtained from the ape⁷⁴ R package (version 5.5) and their ratios to raw pairwise distances were averaged for each given individual (Fig 1c). Averaged ratios equal to one support perfect phylogenetic placement for the specimen considered.

Genetic continuity between each individual specimen predating about 2200 bc and DOM2 horses was tested following the methodology from Schraiber⁷⁵, which implements a likelihood-ratio test to compare the statistical support for placing DOM2 and the ancient specimen in a direct line of ancestry or as two sister groups. This methodology relies on exact allele frequency estimates within DOM2 and read counts for putatively ancestral ancient samples. To exclude residual sequencing errors within DOM2 horses, we, thus, conditioned these analyses on variants segregating at least as doubletons in positions covered in at least 75% of the DOM2 samples. Linked variation was pruned using Plink⁷⁶ (version v.1.9), with the following parameters, --indep-pairwise 50 10 0.2, which provided a panel of about 1.4 million transversions. Allele frequencies were polarized considering the outgroup genome used for measuring error rates. Results from direct ancestry tests are summarized in Supplementary Table 2.

The complex genetic makeup of some individuals (CAR05_Hun_m2458 and Kan22_Tur_m2386) and/or group of individuals (DOM2) was investigated using the f_4 -statistics-based ancestry decomposition approach implemented in qpAdm¹⁷ (version 7.0), in which one particular (group of) individual(s) is modelled as a linear, additive combination of candidate population sources ('left' populations). We followed the rotating strategy recommended by Harney and colleagues¹⁸ to assess all possible combinations of two, three and four donors ('left') selected from a total of 18 populations. The remaining 14, 15 and 16 populations were used as reference ('right') populations (Supplementary Table 3).

We selected a total of nine horse lineages representing the main phylogenetic clusters, and carrying genetic ancestry profiles representative of the complete dataset, to model the population evolutionary history using

OrientAGraph¹⁹ (version 1.0). By implementing a network orientation subroutine that enables throughout exploration of the graph space, OrientAGraph constitutes a marked advancement in the automated inference of admixture graphs. We considered scenarios from zero to five migration pulses ($M = 0$ to 5 ; Extended Data Fig. 5a–e), and the population model assuming $M = 3$ is represented in Fig 3b. This analysis was conditioned on sites covered at least in one specimen of each population group. This filter yielded a set of 7,936,493 fully orthologous nucleotide transversions.

Struct-f4, ancestry components and multi-dimensional scaling

We extended the Struct-f4 package so as to assess individual genetic affinities within a panel of genomes, and to decompose them into K genetic ancestries. Struct-f4, thus, achieves similar objectives to other clustering methods, such as ADMIXTURE⁷⁷ and Ohana⁷⁸, but does not assume Hardy–Weinberg equilibrium. The latter assumption is known to cause misinterpretation of highly drifted samples as ancestral homogeneous groups instead of highly derived mixtures from multiple populations, as thoroughly described elsewhere⁷⁹. To circumvent this, Struct-f4 relies on the calculation of the widely used f_4 statistics, which were originally devised not only to test for admixture, but also to quantify the drift between the internal nodes of a population tree. The latter provides a direct representation of the true ancestral populations. Overall, Struct-f4 thus implements a more natural and robust (model-free) approach than other clustering alternatives.

Struct-f4 is based on a mixture model that parametrizes the drift that occurred between a given number of K pre-defined ancestral populations, and the mixing coefficient of each individual. Model parameters are estimated using an adaptive Metropolis–Hastings Markov chain Monte Carlo integration, identifying optimal numerical solutions for parameters by means of likelihood maximization. Struct-f4 was validated following extensive coalescent simulations with fastsimcoal2⁸⁰ (version 2.6.0.3). An example of such simulation designed to mimic the complex horse evolutionary history is provided in Extended Data Fig. 2, based on mutation

and recombination rates of 2.3×10^{-8} and 10^{-8} events per generation and bp, respectively. Struct-f4 is implemented in Rcpp and only takes the full set of f_4 -statistics as input to automatically return individual ancestry coefficients, without requiring pre-defined, ad-hoc sets of reference and test populations.

Multi-dimensional scaling was carried out based on the co-ancestry semi-matrix summarizing the drift measured between each pair of individuals, as returned by Struct-f4, removing the domestic donkey outgroup prior to using the cmdscale R function.

Isolation by distance and spatial connectivity

Spatial barriers to gene flow prior to about 3000 bc, between about 3000 and 2000 bc and following about 2000 bc were run using EEMS¹⁶ (built with Eigen version 3.2.2 and Boost version 1.57, and using rEEMSpots version 0.0.0.9000) for 50 million iterations and considering a burn-in of 15 million iterations. Convergence was ensured from visual inspection of likelihood trajectories as well as by the strong correlation obtained between the observed and fitted genetic dissimilarities. Pie-charts depicting the ancestry proportions inferred by Struct-f4 were overlaid on the migration surfaces to facilitate tracking the geographic position of each excavation site, averaging ancestry proportions or using individual ancestry profiles if only one sample was characterized genetically at that location. Spatial pie-chart projection was carried out using the draw.pie R function from the mapplots package⁸¹ (version 1.5.1). The size of each individual pie-chart was commensurate with the number of samples excavated at a given geographic location, provided that the number of samples was lower than 10, while set to a constant maximum radius otherwise.

Partial Mantel tests measuring the correlation between geographic and genomic distances over time were carried out using the ncf R package⁸² (version 1.2.9). This test corrected for the time variation present within each window, similar to the approach described by Loog and colleagues⁸³. Haversine geographic distances between pairs of ancient samples were computed using the geosphere package (version 1.5.10) in R⁸⁴, from the corresponding longitude and latitude coordinates, while radiocarbon date

ages were considered as point estimates (Supplementary Table 1). The matrix of pairwise genetic distances was obtained from the bed2diffs_v1 program provided together with the EEMS software¹⁶. The analysis was carried out for autosomes and the X chromosome separately, so as to investigate possible sex-bias in horse dispersal. Confidence intervals were calculated by sampling with replacement individuals within each time window.

Sliding time windows (step size = 250 years) were broadened forward in time until including at least ten specimens covering two-thirds of the total geographic area sampled in this study. The area delimited by a set or subset of GPS coordinates was calculated using the GeoRange R package⁸⁵ (version 0.1.0) and the age of the window was set to the average age amongst the samples included. Additionally, pairwise distances involving samples located less than 500 km away and separated by less than 500 years were masked in the corresponding matrices to estimate the patterns of isolation by distance between demes, instead of within demes. This whole scheme was designed to prevent regional effects, caused by the over-representation of particular regions in specific time intervals.

The LOCATOR²⁰ program (version 1.2) was run using a geolocated reference panel consisting of all non-DOM2 horses ($n = 136$), except the tarpan and the four Przewalski's horses present in our dataset, and considering nucleotide transversions covered at least in 75% of the samples, for a total of 3,194,008 SNPs. The geographic origin of each DOM2 horse was then estimated from the geographic structure defined by the populations present in the reference panel. Default parameters were used, except that the width of each neural layer was 512 (instead of 256). The best run was selected as the one showing the lowest validation error from a total of 50 independent runs. The analysis was repeated for the tarpan as well as the four Przewalski's horses present in our dataset.

Selection scans

To pinpoint genetic changes potentially underlying biological adaptation within DOM2 horses, we contrasted the frequency of each nucleotide transversion in our dataset ($n = 10,205,277$) in DOM2 ($n = 141$) and non-

DOM2 horses ($n = 142$). The extensive number of samples represented provided unprecedented resolution into patterns of allele frequency differentiation, and encompassed the largest diversity of non-DOM2 horses characterized to date. Weir and Cockerham F_{ST} index values between both groups were calculated using Plink⁷⁶ (version 1.9) and visualized using the GViz R package⁸⁶ (version 1.36.2), together with external genomic tracks provided by the gene models annotated for EquCab3 (Ensembl v0.102) and the interrupted repeats precomputed for the same assembly and stored in the UCSC browser.

Reporting summary

Further information on research design is available in the [Nature Research Reporting Summary](#) linked to this paper.

Data availability

All collapsed and paired-end sequence data for samples sequenced in this study are available in compressed fastq format through the European Nucleotide Archive under accession number [PRJEB44430](#), together with rescaled and trimmed bam sequence alignments against both the nuclear and mitochondrial horse reference genomes. Previously published ancient data used in this study are available under accession numbers [PRJEB7537](#), [PRJEB10098](#), [PRJEB10854](#), [PRJEB22390](#) and [PRJEB31613](#), and detailed in Supplementary Table 1. The genomes of ten modern horses, publicly available, were also accessed as indicated in their corresponding original publications^{59,63,87,88,89}.

Code availability

The Struct-f4 software is available without restriction on Bitbucket (<https://bitbucket.org/plibradosanz/structf4/src/master/>).

References

1. 1.

Kelekna, P. *The Horse in Human History* (Cambridge Univ. Press, 2009).

2. 2.

Outram, A. K. et al. The earliest horse harnessing and milking. *Science* **323**, 1332–1335 (2009)

3. 3.

Gaunitz, C. et al. Ancient genomes revisit the ancestry of domestic and Przewalski's horses. *Science* **360**, 111–114 (2018).

4. 4.

Olsen, S. L. in *Horses and Humans: The Evolution of Human Equine Relationships* (eds Olsen S. L. et al.) 81–113 (Archaeopress, 2006).

5. 5.

Fages, A. et al. Tracking five millennia of horse management with extensive ancient genome time series. *Cell* **177**, 1419-1435.e31 (2019).

6. 6.

Guimaraes, S. et al. Ancient DNA shows domestic horses were introduced in the southern Caucasus and Anatolia during the Bronze Age. *Sci. Adv.* **6**, eabb0030 (2020).

7. 7.

Anthony, D. W. *The Horse, the Wheel and Language* (Princeton Univ. Press, 2007).

8. 8.

Haak, W. et al. Massive migration from the steppe was a source for Indo-European languages in Europe. *Nature* **522**, 207–211 (2015).

9. 9.

Allentoft, M. E. et al. Population genomics of Bronze Age Eurasia. *Nature* **522**, 167–172 (2015).

10. 10.

Demoule, J. P. Mais où sont passés les Indo-Européens ? Le mythe d'origine de l'Occident (Le Seuil, 2014).

11. 11.

de Barros Damgaard, P. et al. 137 ancient human genomes from across the Eurasian steppes. *Nature* **557**, 369–374 (2018).

12. 12.

Narasimhan, V. M. et al. The formation of human populations in South and Central Asia. *Science* **365**, eaat7487 (2019).

13. 13.

Rohland, N., Harney, E., Mallick, S., Nordenfelt, S. & Reich, D. Partial uracil-DNA-glycosylase treatment for screening of ancient DNA. *Philos. Trans. R. Soc. Lond. B* **370**, 20130624 (2015).

14. 14.

Schubert, M. et al. Prehistoric genomes reveal the genetic foundation and cost of horse domestication. *Proc. Natl Acad. Sci. USA* **111**, E5661-E5669 (2014).

15. 15.

Librado, P. et al. Tracking the origins of Yakutian horses and the genetic basis for their fast adaptation to subarctic environments. *Proc.*

Natl Acad. Sci. USA **112**, E6889-E6897 (2015).

16. 16.

Petkova, D., Novembre, J. & Stephens, M. Visualizing spatial population structure with estimated effective migration surfaces. *Nat. Genet.* **48**, 94–100 (2016).

17. 17.

Patterson, N. et al. Ancient admixture in human history. *Genetics* **192**, 1065–1093 (2012).

18. 18.

Harney, É., Patterson, N., Reich, D. & Wakeley, J. Assessing the performance of qpAdm: a statistical tool for studying population admixture. *Genetics* **217**, iyaa045 (2021).

19. 19.

Molloy, E. K., Durvasula, A. & Sankararaman, S. Advancing admixture graph estimation via maximum likelihood network orientation. *Bioinformatics* **37**, i142–i150 (2021).

20. 20.

Battey, C., Ralph, P. L. & Kern, A. D. Predicting geographic location from genetic variation with deep neural networks. *eLife* **9**, e54507 (2020).

21. 21.

de Barros Damgaard, P. et al. The first horse herders and the impact of early Bronze Age steppe expansions into Asia. *Science* **360**, eaar7711 (2018).

22. 22.

Reinhold, S. et al. in *Appropriating Innovations: Entangled Knowledge in Eurasia, 5000–1500 bce* (eds Stockhammer, P. W. & Maran, J.) 78–97 (Oxbow Books, 2017).

23. 23.

Kristiansen, K. in *Trade and Civilization. Economic Networks and Cultural Ties, from Prehistory to the Early Modern Period* (eds Kristiansen, K. et al.) (Cambridge Univ. Press, 2018).

24. 24.

Chechushkov I. V., & Epimakhov, A. V. in *The Puzzle of Indo-European Origins and Dispersals: Archeology, Linguistics and Genetics* (eds Kristiansen, K. et al.) (Cambridge Univ. Press, in the press).

25. 25.

Littauer, M. A., & Crouwel, J. H. The origin of the true chariot. *Antiquity* **70**, 934–939 (1996).

26. 26.

Lindner, S. Chariots in the Eurasian Steppe: a Bayesian approach to the emergence of horse-drawn transport in the early second millennium BC. *Antiquity* **94**, 361–380 (2020).

27. 27.

Moorey, P. R. S. Pictorial evidence for the history of horse-riding in Iraq before the Kassite period. *Iraq* **32**, 36–50 (1970).

28. 28.

Kanne, K. Riding, ruling, and resistance equestrianism and political authority in the Hungarian Bronze Age. *Curr. Anthropol.* (in the press).

29. 29.

Suri, P. et al. Genome-wide meta-analysis of 158,000 individuals of European ancestry identifies three loci associated with chronic back pain. *PLoS Genet.* **14**, e1007601 (2018).

30. 30.

Jiang, H. et al. Two GWAS-identified variants are associated with lumbar spinal stenosis and Gasdermin-C expression in Chinese population. *Sci. Rep.* **10**, 21069 (2020).

31. 31.

Tikker, L. et al. Inactivation of the GATA cofactor ZFPM1 results in abnormal development of dorsal raphe serotonergic neuron subtypes and increased anxiety-like behavior. *J. Neurosci.* **40**, 8669–8682 (2020).

32. 32.

Takahashi, A. & Miczek, K. A. Neurogenetics of aggressive behavior: studies in rodents. *Curr. Top. Behav. Neurosci.* **17**, 3–44 (2014).

33. 33.

Schmitt, T. & Varga, Z. Extra-Mediterranean refugia: the rule and not the exception? *Frontiers Zool.* **9**, 22 (2012).

34. 34.

Spasskaya, N. N., & Pavlinov, I. in *Zoological Research* (Arch. Zoological Museum, Moscow State Univ., 2016).

35. 35.

Colledge, S., Conolly, J., Crema, E., & Shennan, S. Neolithic population crash in northwest Europe associated with agricultural crisis. *Quat. Res.* **92**, 686–707 (2019).

36. 36.

Outram, A. K. & Bogaard, A. *Subsistence and Society in Prehistory: New Directions in Economic Archaeology* (Cambridge Univ. Press, 2019).

37. 37.

Anthony, D. W. in Social Complexity in Prehistoric Eurasia: Monuments, Metals and Mobility (eds Hanks, B. K. & Lindruff, K. M.) Ch. 4 (2009).

38. 38.

Maran, J., Bajenaru, R., Ailincai, S.-C., Popescu, A.-D. & Hansen, S. I. Objects, ideas and travelers. Contacts between the Balkans, the Aegean and Western Anatolia during the Bronze and Early Iron Age. In: *Proc. of the Conference in Tulcea 10-13 November, 2017* (Rudolf Habelt, 2020).

39. 39.

Glob, P. V. *Denmark: An Archaeological History from the Stone Age to the Vikings* (Cornell Univ. Press, 1971).

40. 40.

Gimbutas, M. The first wave of Eurasian Steppe pastoralists into Copper Age Europe. *J. Indo. Eur. Stud.* **5**, 277–338 (1977).

41. 41.

Anthony, D. W. The “Kurgan Culture,” Indo-European origins, and the domestication of the horse: a reconsideration. *Curr. Anthropol.* **27**, 291–313 (1986).

42. 42.

Renfrew, C. They ride horses, don’t they?: Mallory on the Indo-Europeans. *Antiquity* **63**, 843–847 (1989).

43. 43.

Vandkilde, H. *Culture and Change in Central European Prehistory* (Aarhus Univ. Press, 2007).

44. 44.

Häusler, A. in *Indogermanen und das Pferd* (eds Hänsel, B. & Zimmer, S.) 217–257 (Archaeolingua Alapitvany, 1994).

45. 45.

Kroonen, G., Barjamovic, G. & Peyrot, M. Linguistic supplement to de Barros Damgaard et al. 2018: Early Indo-European languages, Anatolian, Tocharian and Indo-Iranian
<https://zenodo.org/record/1240524#.YFtLgGjTVMQ> (2018).

46. 46.

South, A. rworldmap: a new R package for mapping global data. *R J.* **3**, 35-43 (2011).

47. 47.

Brownrigg, R. maps: draw geographical maps. R package version 3.3.0 <https://CRAN.R-project.org/package=maps> (2018).

48. 48.

Reimer, P. et al. The IntCal20 Northern Hemisphere radiocarbon age calibration curve (0–55 cal kBP). *Radiocarbon* **62**, 725 (2020).

49. 49.

Ramsey, C. B. Bayesian analysis of radiocarbon dates. *Radiocarbon* **51**, 337–360 (2009).

50. 50.

Seguin-Orlando, A. et al. Heterogeneous hunter-gatherer and steppe-related ancestries in Late Neolithic and Bell Beaker genomes from present-day France. *Curr. Biol.* **31**, 1072–1083.e10 (2021).

51. 51.

Gamba, C. et al. Comparing the performance of three ancient DNA extraction methods for high-throughput sequencing. *Mol. Ecol. Resour.* **16**, 459–469 (2016).

52. 52.

Schubert, M., Lindgreen, S. & Orlando, L. AdapterRemoval v2: rapid adapter trimming, identification, and read merging. *BMC Res. Notes* **9**, 88 (2016).

53. 53.

Kalbfleisch, T. S. et al. Improved reference genome for the domestic horse increases assembly contiguity and composition. *Commun. Biol.* **1**, 197 (2018).

54. 54.

Xu, X. & Arnason, U. The complete mitochondrial DNA sequence of the horse, *Equus caballus*: extensive heteroplasmy of the control region. *Gene* **148**, 357–362 (1994).

55. 55.

Felkel, S. et al. The horse Y chromosome as an informative marker for tracing sire lines. *Sci. Rep.* **9**, 6095 (2019)

56. 56.

Poulet, M. & Orlando, L. Assessing DNA sequence alignment methods for characterizing ancient genomes and methylomes. *Front. Ecol. Evol.* **8**, 105 (2020).

57. 57.

Jónsson, H., Ginolhac, A., Schubert, M., Johnson, P. L. F. & Orlando, L. mapDamage2.0: fast approximate Bayesian estimates of ancient DNA damage parameters. *Bioinformatics* **29**, 1682–1684 (2013).

58. 58.

Orlando, L. et al. Recalibrating *Equus* evolution using the genome sequence of an early Middle Pleistocene horse. *Nature* **499**, 74–78 (2013).

59. 59.

Jónsson, H. et al. Speciation with gene flow in equids despite extensive chromosomal plasticity. *Proc. Natl Acad. Sci. USA* **111**, 18655–18660 (2014).

60. 60.

Korneliussen, T. S., Albrechtsen, A. & Nielsen, R. ANGSD: analysis of next generation sequencing data. *BMC Bioinformatics* **15**, 356 (2014).

61. 61.

Skoglund, P. et al. Separating endogenous ancient DNA from modern day contamination in a Siberian Neandertal. *Proc. Natl Acad. Sci. USA* **111**, 2229–2234 (2014).

62. 62.

Librado, P. et al. Ancient genomic changes associated with domestication of the horse. *Science* **356**, 442–445 (2017).

63. 63.

Der Sarkissian, C. et al. Evolutionary genomics and conservation of the endangered Przewalski's horse. *Curr. Biol.* **25**, 2577–2583 (2015).

64. 64.

Katoh, K. & Standley, D. M. MAFFT multiple sequence alignment software version 7: improvements in performance and usability. *Mol. Biol. Evol.* **30**, 772–780 (2013).

65. 65.

Stamatakis, A. RAxML version 8: a tool for phylogenetic analysis and post-analysis of large phylogenies. *Bioinformatics* **30**, 1312–1313 (2014).

66. 66.

Bouckaert, R. et al. BEAST 2.5: An advanced software platform for Bayesian evolutionary analysis. *PLoS Comput. Biol.* **15**, e1006650 (2019).

67. 67.

Heller, R., Chikhi, L. & Siegmund, H. R. The confounding effect of population structure on Bayesian skyline plot inferences of demographic history. *PLoS ONE* **8**, e62992 (2013).

68. 68.

Keane, T. M., Creevey, C. J., Pentony, M. M., Naughton, T. J. & McInerney, J. O. Assessment of methods for amino acid matrix selection and their use on empirical data shows that ad hoc assumptions for choice of matrix are not justified. *BMC Evol. Biol.* **6**, 29 (2006).

69. 69.

Drummond, A. J., Rambaut, A., Shapiro, B. & Pybus, O. G. Bayesian coalescent inference of past population dynamics from molecular sequences. *Mol. Biol. Evol.* **22**, 1185–1192 (2005).

70. 70.

Rambaut, A., Drummond, A. J., Xie, D., Baele, G. & Suchard, M. A. Posterior summarization in Bayesian phylogenetics using Tracer 1.7. *Syst Biol* **67**, 901–904 (2018).

71. 71.

Nguyen, L.-T., Schmidt, H. A., von Haeseler, A. & Minh, B. Q. IQ-TREE: a fast and effective stochastic algorithm for estimating maximum-likelihood phylogenies. *Mol. Biol. Evol.* **32**, 268–274 (2015).

72. 72.

Hoang, D. T., Chernomor, O., von Haeseler, A., Minh, B. Q. & Vinh, L. S. UFBoot2: improving the ultrafast bootstrap approximation. *Mol. Biol. Evol.* **35**, 518–522 (2018).

73. 73.

Lefort, V., Desper, R. & Gascuel, O. FastME 2.0: a comprehensive, accurate, and fast distance-based phylogeny inference program. *Mol. Biol. Evol.* **32**, 2798–2800 (2015).

74. 74.

Paradis, E., & Schliep, K. ape 5.0: an environment for modern phylogenetics and evolutionary analyses in R. *Bioinformatics* **35**, 526–528 (2019).

75. 75.

Schraiber, J. Assessing the relationship of ancient and modern populations. *Genetics* **208**, 383–398 (2018).

76. 76.

Purcell, S. et al. PLINK: a tool set for whole-genome association and population-based linkage analyses. *Am. J. Hum. Genet.* **81**, 559–575 (2007).

77. 77.

Alexander, D. H., Novembre, J. & Lange, K. Fast model-based estimation of ancestry in unrelated individuals. *Genome Res.* **19**, 1655–1664 (2009).

78. 78.

Cheng, J. Y., Mailund, T. & Nielsen, R. Fast admixture analysis and population tree estimation for SNP and NGS data. *Bioinformatics* **33**, 2148–2155 (2017).

79. 79.

Lawson, D. J., van Dorp, L. & Falush, D. A tutorial on how not to over-interpret STRUCTURE and ADMIXTURE bar plots. *Nat. Commun.* **9**, 3258 (2018).

80. 80.

Excoffier, L., Dupanloup, I., Huerta-Sánchez, E., Sousa, V. C. & Foll, M. Robust demographic inference from genomic and SNP data. *PLoS Genet.* **9**, e1003905 (2013).

81. 81.

Gerritsen, H. mapplots: data visualisation on maps. R package version 1.5.1 <https://CRAN.R-project.org/package=mapplots> (2018).

82. 82.

Bjornstad, O. N. & Cai, J. ncf: spatial covariance functions. R package version 1.2-9 <http://ento.psu.edu/directory/onb1> (2020).

83. 83.

Loog, L. et al. Estimating mobility using sparse data: application to human genetic variation. *Proc. Natl Acad. Sci. USA* **114**, 12213–12218 (2017).

84. 84.

Hijmans, R. J., Williams, E. & Vennes, C. E.. geosphere: spherical trigonometry. R package version 1.5.1 (2019).

85. 85.

Boyle, J. GeoRange: calculating geographic range from occurrence data. R package version 0.1.0. (2017).

86. 86.

Hahne, F. & Ivanek, R. Visualizing genomic data using Gviz and Bioconductor. *Methods Mol. Biol.* **1418**, 335–351 (2016).

87. 87.

Renaud, G. et al. Improved de novo genomic assembly for the domestic donkey. *Sci. Adv.* **4**, eaaq0392 (2018).

88. 88.

Jagannathan, V. et al. Comprehensive characterization of horse genome variation by whole-genome sequencing of 88 horses. *Anim. Genet.* **50**, 74–77 (2019).

89. 89.

Andersson, L. S. et al. Mutations in DMRT3 affect locomotion in horses and spinal circuit function in mice. *Nature* **488**, 642–646 (2012).

90. 90.

Teufer, M. Ein Scheibenknebel aus Dzarkutan (Südusbekistan). Archäologische Mitteilungen aus Iran und Turan. *Band 31*, 69–142 (1999).

91. 91.

Chechushkov, I. V. *Wheel Complex of the Late Bronze Age Era of Steppe and Forest-Steppe Eurasia (from Dnieper to Irtysh)*. PhD thesis. Department of Archeology and Ethnography of the Federal State Budgetary Institution of Science, Institute of History and Archeology of the Ural Branch of the Russian Academy of Sciences (2013).

Acknowledgements

We thank all members of the AGES group at CAGT. We are grateful for the Museum of the Institute of Plant and Animal Ecology (UB RAS, Ekaterinburg) for providing specimens. The work by G. Boeskorov is done on state assignment of DPMGI SB RAS. This project was supported by the University Paul Sabatier IDEX Chaire d'Excellence (OURASI); Villum Funden miGENEPI research programme; the CNRS 'Programme de Recherche Conjoint' (PRC); the CNRS International Research Project (IRP AMADEUS); the France Génomique Appel à Grand Projet (ANR-10-INBS-09-08, BUCEPHALE project); IB10131 and IB18060, both funded by Junta de Extremadura (Spain) and European Regional Development Fund; Czech Academy of Sciences (RVO:67985912); the Zoological Institute ZIN RAS (AAAA-A19-119032590102-7); and King Saud University Researchers Supporting Project (NSRSP-2020/2). The research was carried out with the financial support of the Russian Foundation for Basic Research (19-59-15001 and 20-04-00213), the Russian Science Foundation (16-18-10265, 20-78-10151, and 21-18-00457), the Government of the Russian Federation (FENU-2020-0021), the Estonian Research Council (PRG29), the Estonian Ministry of Education and Research (PRG1209), the Hungarian Scientific Research Fund (Project NF 104792), the Hungarian Academy of Sciences (Momentum Mobility Research Project of the Institute of Archaeology, Research Centre for the Humanities); and the Polish National Science Centre (2013/11/B/HS3/03822). This project has received funding from the European Union's Horizon 2020 research and innovation programme under the Marie Skłodowska-Curie (grant agreement 797449). This project has received funding from the European Research Council (ERC) under the European Union's Horizon 2020 research and innovation programme (grant agreements 681605, 716732 and 834616).

Author information

Author notes

1. Naveed Khan

Present address: Lundbeck Foundation GeoGenetics Centre,
Copenhagen, Denmark

Affiliations

1. Centre d'Anthropobiologie et de Génomique de Toulouse, Université Paul Sabatier, Toulouse, France

Pablo Librado, Naveed Khan, Antoine Fages, Mariya A. Kusliy, Tomasz Suchan, Laure Tonasso-Calvière, Stéphanie Schiavinato, Duha Alioglu, Aurore Fromentier, Charleen Gaunitz, Lorelei Chauvey, Andaine Seguin-Orlando, Clio Der Sarkissian & Ludovic Orlando

2. Department of the Diversity and Evolution of Genomes, Institute of Molecular and Cellular Biology SB RAS, Novosibirsk, Russia

Mariya A. Kusliy & Alexander S. Graphodatsky

3. W. Szafer Institute of Botany, Polish Academy of Sciences, Kraków, Poland

Tomasz Suchan & Magdalena Moskal-del Hoyo

4. Genoscope, Institut de biologie François-Jacob, Commissariat à l'Energie Atomique (CEA), Université Paris-Saclay, Evry, France

Aude Perdereau

5. Génomique Métabolique, Genoscope, Institut de biologie François Jacob, CEA, CNRS, Université d'Evry, Université Paris-Saclay, Evry, France

Jean-Marc Aury & Patrick Wincker

6. Earth System Science Department, University of California, Irvine, Irvine, CA, USA

John Southon

7. Department of Ecology and Evolutionary Biology, University of California, Santa Cruz, Santa Cruz, CA, USA

Beth Shapiro

8. Howard Hughes Medical Institute, University of California, Santa Cruz, Santa Cruz, CA, USA

Beth Shapiro

9. Department of Archaeology, Ethnography and Museology, Altai State University, Barnaul, Russia

Alexey A. Tishkin, Kirill Yu. Kiryushin & Nikolai N. Seregin

10. Department of Archaeological Heritage Preservation, Institute of Archaeology of the Russian Academy of Sciences, Moscow, Russia

Alexey A. Kovalev

11. Zoology Department, College of Science, King Saud University, Riyadh, Saudi Arabia

Saleh Alquraishi, Ahmed H. Alfarhan & Khaled A. S. Al-Rasheid

12. Institute for Archaeology, Heritage Conservation Studies and Art History, University of Bamberg, Bamberg, Germany

Timo Seregely

13. Museum Østjylland, Randers, Denmark

Lutz Klassen

14. Saxo Institute, section of Archaeology, University of Copenhagen, Copenhagen, Denmark

Rune Iversen

15. ArScAn-UMR 7041, Equipe Ethnologie préhistorique, CNRS, MSH-Mondes, Nanterre Cedex, France

Olivier Bignon-Lau, Pierre Bodu & Monique Olive

16. Muséum d'histoire naturelle, Secteur des Vertébrés, Geneva, Switzerland

Jean-Christophe Castel

17. UMR 5199 De la Préhistoire à l'Actuel : Culture, Environnement et Anthropologie (PACEA), CNRS, Université de Bordeaux, Pessac Cedex, France

Myriam Boudadi-Maligne & Mélanie Pruvost

18. Geneva Natural History Museum, Geneva, Switzerland

Nadir Alvarez

19. Department of Genetics and Evolution, University of Geneva, Geneva, Switzerland

Nadir Alvarez

20. OD Earth & History of Life, Royal Belgian Institute of Natural Sciences, Brussels, Belgium

Mietje Germonpré

21. Institute of Systematics and Evolution of Animals, Polish Academy of Sciences, Kraków, Poland

Jarosław Wilczyński & Sylwia Pospuła

22. Institute of Archaeology and Ethnology Polish Academy of Sciences, Kraków, Poland

Anna Lasota-Kuś & Krzysztof Tunia

23. Institute of Archaeology, Jagiellonian University, Kraków, Poland

Marek Nowak

24. Department of Archaeology, Institute of History and Archaeology,
Tartu, Estonia

Eve Rannamäe

25. Department of Zoology, Institute of Ecology and Earth Sciences,
University of Tartu, Tartu, Estonia

Urmas Saarma

26. Diamond and Precious Metals Geology Institute, SB RAS, Yakutsk,
Russia

Gennady Boeskorov

27. Archaeological Research Collection, Tallinn University, Tallinn,
Estonia

Lembi Lõugas

28. Department of Natural Sciences and Archaeometry, Institute of
Archaeology of the Czech Academy of Sciences, Prague, Czechia

René Kyselý

29. Prague, Czechia

Lubomír Peške

30. Vasile Pârvan Institute of Archaeology, Department of Bioarchaeology,
Romanian Academy, Bucharest, Romania

Adrian Bălăşescu, Valentin Dumitraşcu & Roxana Dobrescu

31. Institute of Archaeogenomics, Research Centre for the Humanities,
Eötvös Loránd Research Network, Budapest, Hungary

Daniel Gerber, Anna Szécsényi-Nagy & Balázs G. Mende

32. Department of Genetics, Eötvös Loránd University, Budapest,
Hungary

Daniel Gerber

33. Institute of Archaeology, Research Centre for the Humanities, Eötvös
Loránd Research Network, Budapest, Hungary

Viktória Kiss, Gabriella Kulcsár & Erika Gál

34. Ásatárs Ltd., Kecskemét, Hungary

Zsolt Gallina

35. Rippl-Rónai Municipal Museum with Country Scope, Kaposvár,
Hungary

Krisztina Somogyi

36. School of History, Classics and Archaeology, University of Edinburgh,
Old Medical School, Edinburgh, UK

Robin Bendrey

37. Trace and Environmental DNA (TrEnD) Lab, School of Molecular and
Life Sciences, Curtin University, Perth, Western Australia, Australia

Morten E. Allentoft

38. Lundbeck Foundation GeoGenetics Centre, GLOBE Institute,
University of Copenhagen, Copenhagen, Denmark

Morten E. Allentoft

39. Department of Academic Management, Academy of Science of Moldova, Chişinău, Republic of Moldova

Ghenadie Sirbu

40. Center of Archaeology, Institute of Cultural Heritage, Academy of Science of Moldova, Chişinău, Republic of Moldova

Valentin Dergachev

41. Archaeological Institute of America, Boston, MA, USA

Henry Shephard

42. Centre National de Recherche Scientifique, Muséum national d'Histoire naturelle, Archéozoologie, Archéobotanique (AASPE), CP 56, Paris, France

Noémie Tomadini, Sandrine Grouard, Benoit Clavel, Sébastien Lepetz & Marjan Mashkour

43. Institute for the History of Material Culture, Russian Academy of Sciences (IHMC RAS), St Petersburg, Russia

Aleksei Kasparov, Vladimir Pitulko, Alexander Bessudnov & Nikolay A. Bokovenko

44. Geological Institute, Russian Academy of Sciences, Moscow, Russia

Alexander E. Basilyan & Pavel A. Nikolskiy

45. Arctic and Antarctic Research Institute, St Petersburg, Russia

Mikhail A. Anisimov & Elena Y. Pavlova

46. Institute of Animal Breeding and Genetics, University of Veterinary Medicine Vienna, Vienna, Austria

Gottfried Brem & Barbara Wallner

47. Department of Prehistory and Western Asian/Northeast African Archaeology, Austrian Archaeological Institute, Austrian Academy of Sciences, Vienna, Austria

Christoph Schwall

48. Estonian Biocentre, Institute of Genomics, University of Tartu, Tartu, Estonia

Marcel Keller

49. Department of Archaeogenetics, Max Planck Institute for the Science of Human History, Jena, Germany

Marcel Keller, Johannes Krause & Wolfgang Haak

50. SFB 1070 Resource Cultures, University of Tübingen, Tübingen, Germany

Keiko Kitagawa

51. Department of Early Prehistory and Quaternary Ecology, University of Tübingen, Tübingen, Germany

Keiko Kitagawa

52. UMR 7194 Muséum National d'Histoire Naturelle, CNRS, UPVD, Paris, France

Keiko Kitagawa

53. Semenov-Tyan-Shanskii Lipetsk State Pedagogical University, Lipetsk, Russia

Alexander N. Bessudnov

54. Museum of Natural History, University of Colorado-Boulder, Boulder, CO, USA

William Taylor

55. Musée d'Anthropologie préhistorique de Monaco, Monaco, Monaco

Jérôme Magail

56. Institute of Archaeology, Mongolian Academy of Sciences,
Ulaanbaatar, Mongolia

Jamiyan-Ombo Gantulga & Turbat Tsagaan

57. Department of Archaeology, Max Planck Institute for the Science of
Human History, Jena, Germany

Jamsranjav Bayarsaikhan

58. Chinggis Khaan Museum, Ulaanbaatar, Mongolia

Jamsranjav Bayarsaikhan

59. Department of Archaeology, Ulaanbaatar State University,
Ulaanbaatar, Mongolia

Diimaajav Erdenebaatar, Enkhbayar Mijiddorj & Tumur-Ochir
Iderkhangai

60. Department of History, Kyrgyz-Turkish Manas University, Bishkek,
Kyrgyzstan

Kubatbeek Tabaldiev

61. Department of Biology, National University of Mongolia, Ulaanbaatar,
Mongolia

Bazartseren Boldgiv

62. Division of Archaeology, Biodiversity Institute, University of Kansas,
Lawrence, KS, USA

Sandra Olsen

63. Institute for Prehistoric and Protohistoric Archaeology, Kiel University, Kiel, Germany

Cheryl A. Makarewicz

64. ROOTS Excellence Cluster, Kiel University, Kiel, Germany

Cheryl A. Makarewicz

65. Archaeology of Social Dynamics, Institutó Milà i Fontanals d'Humanitats, Consejo Superior de Investigaciones Científicas (IMF-CSIC), Barcelona, Spain

Silvia Valenzuela Lamas

66. Departament d'Història i Arqueologia–SERP, Universitat de Barcelona, Barcelona, Spain

Silvia Albizuri Canadell

67. Grup d'Investigació Prehistòrica, Universitat de Lleida, PID2019-110022GB-I00, Lleida, Spain

Ariadna Nieto Espinet

68. Valencia, Spain

Ma Pilar Iborra

69. Departamento de Medicina Animal, Facultad de Veterinaria, Universidad de Extremadura, Cáceres, Spain

Jaime Lira Garrido

70. Centro Mixto UCM-ISCIII de Evolución y Comportamiento Humanos, Madrid, Spain

Jaime Lira Garrido & Juan Luis Arsuaga

71. Instituto de Arqueología (CSIC–Junta de Extremadura), Mérida, Spain

Esther Rodríguez González & Sebastián Celestino

72. Laboratori d'Arqueologia Prehistòrica, Universitat Jaume I, Castelló de la Plana, Spain

Carmen Olària

73. Departamento de Geodinámica, Estratigrafía y Paleontología, Facultad de Ciencias Geológicas, Universidad Complutense de Madrid, Madrid, Spain

Juan Luis Arsuaga

74. Department of Eneolithic and Bronze Age, Institute of Archaeology National Academy of Sciences of Ukraine, Kyiv, Ukraine

Nadiia Kotova

75. Department of Archaeology, University of Exeter, Exeter, UK

Alexander Pryor & Alan Outram

76. Center for the Study of Human Origins, Anthropology Department, New York University, New York, NY, USA

Pam Crabtree

77. Department of Archaeology, Ethnology and Museology, Al Farabi Kazakh National University, Almaty, Kazakhstan

Rinat Zhumataev & Abdesh Toleubaev

78. Scientific Research Department, Orenburg State Pedagogical University, Orenburg, Russia

Nina L. Morgunova

79. Department of paleontology, Faculty of Geology, Moscow State University, Moscow, Russia

Tatiana Kuznetsova

80. Institute of Geology and Petroleum Technologies, Kazan Federal University, Kazan, Russia

Tatiana Kuznetsova

81. Georgian National Museum, Tbilisi, Georgia

David Lordkipanize

82. Tbilisi State University, Tbilisi, Georgia

David Lordkipanize

83. Università degli Studi di Milano, Dipartimento di Beni Culturali e Ambientali, Milan, Italy

Matilde Marzullo, Ornella Prato, Giovanna Bagnasco
Gianni & Umberto Tecchiaty

84. University of Tehran, Central Laboratory, Bioarchaeology Laboratory, Archaeozoology Section, Tehran, Iran

Hossein Davoudi & Marjan Mashkour

85. Research Institute and Museum of Anthropology, Lomonosov Moscow State University, Moscow, Russia

Natalia Ya. Berezina

86. Department of Archaeogenetics, Max Planck Institute for Evolutionary Anthropology, Leipzig, Germany

Philipp W. Stockhammer, Johannes Krause & Wolfgang Haak

87. Institute for Pre- and Protohistoric Archaeology and Archaeology of the Roman Provinces, Ludwig Maximilian University, Munich, Munich, Germany

Philipp W. Stockhammer

88. School of Biological Sciences, The University of Adelaide, Adelaide, South Australia, Australia

Wolfgang Haak

89. Department of Biology, Universidad Autónoma de Madrid, Madrid, Spain

Arturo Morales-Muñiz

90. Eurasia Department of the German Archaeological Institute, Berlin, Germany

Norbert Benecke, Sabine Reinhold & Svend Hansen

91. Evolutionary Adaptive Genomics, Institute of Biochemistry and Biology, Faculty of Mathematics and Science, University of Potsdam, Potsdam, Germany

Michael Hofreiter

92. Department of Evolutionary Genetics, Leibniz-Institute for Zoo and Wildlife Research, Berlin, Germany

Arne Ludwig

93. Albrecht Daniel Thaer-Institute, Faculty of Life Sciences, Humboldt University Berlin, Berlin, Germany

Arne Ludwig

94. ArchaeoBioCenter and Institute of Palaeoanatomy, Domestication Research and the History of Veterinary Medicine, LMU Munich, Munich, Germany

Joris Peters

95. SNSB, State Collection of Anthropology and Palaeoanatomy, Munich, Germany

Joris Peters

96. ArchaeoZOOlogy in Siberia and Central Asia—ZooSCAn International Research Laboratory, Institute of Archeology and Ethnography of the Siberian Branch of the RAS, Novosibirsk, Russia

Sergey K. Vasiliev

97. Department of Eastern European and Siberian Archaeology, State Hermitage Museum, St Petersburg, Russia

Konstantin V. Chugunov

98. Paleoecology Laboratory, Institute of Plant and Animal Ecology, Ural Branch of the Russian Academy of Sciences, Ekaterinburg, Russia

Natalya A. Plasteeva & Pavel A. Kosintsev

99. Zoological Institute, Russian Academy of Sciences, St Petersburg, Russia

Gennady F. Baryshnikov & Mikhail Sablin

100. Department of Archaeology, History Faculty, Vilnius University, Vilnius, Lithuania

Ekaterina Petrova & Elina Ananyevskaya

101. Laboratory for Archaeological Research, Faculty of History and Law, Kostanay State University, Kostanay, Kazakhstan

Andrey Logvin & Irina Shevnina

102. Department of History and Archaeology, Surgut Governmental University, Surgut, Russia

Victor Logvin & Saule Kalieva

103. Saryarka Archaeological Institute, Buketov Karaganda University, Karaganda, Kazakhstan

Valeriy Loman, Igor Kukushkin, Victor Varfolomeyev & Emma Usmanova

104. Toraighyrov University, Joint Research Center for Archeological Studies, Pavlodar, Kazakhstan

Ilya Merz & Victor Merz

105. Faculty of History, L. N. Gumilev Eurasian National University, Nur-Sultan, Kazakhstan

Sergazy Sakenov

106. Institute of Archaeology and Steppe Civilizations, Al-Farabi Kazakh National University, Almaty, Kazakhstan

Viktor Zaibert

107. Department of Anthropology, Alumni Building, University of North Carolina at Chapel Hill, Chapel Hill, NC, USA

Benjamin Arbuckle

108. Nasledie Cultural Heritage Unit, Stavropol, Russia

Andrey B. Belinskiy & Alexej Kalmykov

109. Research Center for the Preservation of Cultural Heritage, Saratov, Russia

Aleksandr I. Yudin

110. Department of Russian History and Archaeology, Samara State University of Social Sciences and Education, Samara, Russia

Aleksandr A. Vybornov, Natalia Roslyakova & Pavel F. Kuznetsov

111. Russian and Foreign History Department, South Ural State University, Chelyabinsk, Russia

Andrey Epimakhov

112. South Ural Department, Institute of History and Archaeology, Ural Branch of the Russian Academy of Sciences, Ekaterinburg, Russia

Andrey Epimakhov

113. Archaeological School, Chuvash State Institute of Humanities, Cheboksary, Russia

Natalia S. Berezina

114. Department of History of the Institute of Humanities, Ural Federal University, Ekaterinburg, Russia

Pavel A. Kosintsev

115. Department of Human Evolutionary Biology, Harvard University, Cambridge, MA, USA

David Anthony

116. Anthropology Faculty, Hartwick College, Oneonta, NY, USA

David Anthony

117. Department of Nordic Studies and Linguistics, University of Copenhagen, Copenhagen, Denmark

Guus J. Kroonen

118. Leiden University Center for Linguistics, Leiden University, Leiden,
The Netherlands

Guus J. Kroonen

119. Department of Historical Studies, University of Gothenburg,
Gothenburg, Sweden

Kristian Kristiansen

120. Lundbeck Foundation GeoGenetics Centre, Copenhagen, Denmark

Kristian Kristiansen

121. Department of Biotechnology, Abdul Wali Khan University, Mardan,
Pakistan

Naveed Khan

Contributions

Designed, conceived and coordinated the study: L.O. Provided samples, reagents and material: A. Perdereau, J.-M.A., B.S., A.A.T., A.A.K., S.A., A.H.A., K.A.S.A.-R., T. Seregély, L.K., R.I., O.B.-L., P.B., M.O., J.-C.C., M.B.-M., N.A., M.G., M.M.-d.H., J.W., S.P., A.L.-K., K. Tunia, M.N., E.R., U.S., G. Boeskorov, L.L., R.K., L.P., A. Bălășescu, V. Dumitrașcu, R.D., D.G., V.K., A.S.-N., B.G.M., Z.G., K.S., G.K., E.G., R.B., M.E.A., G.S., V. Dergachev, H.S., N.T., S.G., A. Kasparov, A.E.B., M.A.A., P.A.N., E.Y.P., V.P., G. Brem, B.W., C.S., M.K., K. Kitagawa, A.N.B., A. Bessudnov, W.T., J.M., J.-O.G., J.B., D.E., K. Tabaldiev, E.M., B.B., T.T., M.P., S.O., C.A.M., S.V.L., S.A.C., A.N.E., M.P.I., J.L.G., E.R.G., S.C., C.O., J.L.A., N. Kotova, A. Pryor, P.C., R.Z., A.T., N.L.M., T.K., D.L., M. Marzullo, O.P., G.B.G., U.T., B.C., S.L., H.D., M. Mashkour, N.Y.B., P.W.S., J.K., W.H., A.M.-M., N.B., M.H., A. Ludwig, A.S.G., J.P., K.Y.K., T.-O.I., N.A.B., S.K.V., N.N.S., K.V.C., N.A.P., G.F.B., E.P., M.S., E.A., A. Logvin, I.S., V. Logvin, S.K., V. Loman, I.K., I.M., V.M., S. Sakenov, V.V., E.U.,

V.Z., B.A., A.B.B., A. Kalmykov, S.R., S.H., A.I.Y., A.A.V., A.E., N.S.B., N.R., P.A.K., P.F.K., D. Anthony, G.J.K., K. Kristiansen, P.W., A.O. and L.O. Performed radiocarbon dating: J.S. Performed wet-lab work: N. Kahn, A. Fages, M.A.K., T. Suchan, L.T.-C., S. Schiavinato, A.F., A. Perdereau, C.G., L.C., A.S.-O and C.D.S., with input from L.O. Analysed genomic data: P.L. and L.O. Analysed uniparental markers: D. Alioglu, with input from P.L. and L.O. Prepared the linguistic index: G.J.K. Interpreted data: P.L. and L.O., with input from B.A., S.R., S.H., D. Anthony, G.J.K., K. Kristiansen and A.O. Wrote the article: L.O., with input from P.L., B.A., S.R., S.H., D. Anthony, G.J.K., K. Kristiansen, A.O. and all co-authors. Wrote the Supplementary Information: P.L., A. Fages, G.J.K. and L.O., with input from all co-authors.

Corresponding author

Correspondence to Ludovic Orlando.

Ethics declarations

Competing interests

The authors declare no competing interests.

Additional information

Peer review information *Nature* thanks Samantha Brooks, Fiona Marshall and the other, anonymous, reviewer(s) for their contribution to the peer review of this work. Peer reviewer reports are available.

Publisher's note Springer Nature remains neutral with regard to jurisdictional claims in published maps and institutional affiliations.

Extended data figures and tables

Extended Data Fig. 1 Proportion of missing derived mutations at sites representing nucleotide transversions.

Proportions are provided relative to the genome of a modern Icelandic⁸⁹ (P5782) horse (Spearman correlation coefficient between total transversion errors and time, R=−0.77 p-value =0).

Extended Data Fig. 2 Struct-f4 validation.

a, Simulated demographic model. A single migration pulse is assumed to have occurred 150 generations ago from population E into B. The magnitude of the migration represents 5% to 25% of the effective size of population B. The model was also simulated in the absence of migration (i.e. m=0%). Five individuals are simulated per population considered, except for the outgroup where only one individual was considered. **b**, Correlation of the expected levels of gene-flow with the predicted E-ancestry component in individuals i belonging to population B, as well as with the average Z-scores of the $f_4(A, B_i; E, \text{Outgroup})$ configurations, which reflects the stochasticity resulting from the simulations, prior to any inference. Each point represents a simulated individual. Colors indicate the 10 independent simulation replicates carried out. **c**, Predicted ancestry profiles in the absence (m=0%) and with gene flow (m=25% and K=7, as per the number of internal nodes immediately ancestral to the 10 extant populations).

Extended Data Fig. 3 Mobility and demographic shifts.

a–c, Correlation between observed pairwise genetic distances between demes as inferred by EEMS¹⁶ and Haversine geographic distances prior to ~3,000 BCE (**a**), during the third millennium BCE (**b**) and after ~2,000 BCE (**c**). **d**, Isolation-by-distance patterns through time inferred from autosomal (red) and X-chromosomal (blue) variation. **e–f**, Bayesian Skyline plots reconstructed from mtDNA (**e**) and Y-chromosomal variation (**f**). The third millennium BCE is highlighted in blue. The red line indicates the median of the 95% confidence range, shown in grey.

Extended Data Fig. 4 Individual ancestry profiles.

a, NJ-tree shown in Fig 1b with sample labels as defined in Supplementary Table 1. **b**, Struct-f4 individual ancestry profiles. **c**, Model likelihood. A total of K=4 to K=9 ancestral populations are assumed. LnL = natural log-likelihood.

Extended Data Fig. 5 OrientAGraph¹⁹ population histories and genetic distances to the domestic donkey.

a–e, OrientAGraph¹⁹ models and residuals assuming M=0 to M=5 migration edges and considering nine lineages representing key genomic ancestries (colored as in Fig 1a). M=3 is shown in Fig 3b. **f**, Pairwise genetic distances between a given horse and the domestic donkey plotted as a function of the age of the horse specimen considered.

Extended Data Fig. 6 Inter-regional trade and chariot networks, marked by horse cheek pieces, connecting Bronze Age steppe societies, mineral rich Caucasian societies and the Old Assyrian trade network during the period 1,950-1,750 BCE.

Documented Near Eastern trade routes are marked with stippled lines (after²³, supplemented with data from^{90,91} and Pavel F. Kuznetsov).

Extended Data Fig. 7 DOM2 selection signatures.

a, Manhattan plot of F_{ST} -differentiation index between DOM2 and non-DOM2 horses along the 31 EquCab3 autosomes. F_{ST} outliers are highlighted using an empirical P -value threshold of 10^{-5} (red dashed line). The two outlier regions on chromosomes 3 and 9 are highlighted within red frames. **b**, F_{ST} -differentiation index and genomic tracks around the *ZFPM1* gene. Depth represents the accumulated number of reads per position within DOM2 (blue) and non-DOM2 (magenta) genomes. **c**, Same as Panel b at *GSDMC*.

Extended Data Fig. 8 Normalized read coverage supporting the presence of causative alleles for coat coloration variation.

Each column represents a particular genome position where genetic polymorphisms associated or causative for coat coloration patterns have been described. The exact EquCab3 genome coordinates are indicated in the locus label. Specimens (rows) are ordered according to their phylogenetic relationships, as shown in Fig 1b. The color gradient is proportional to the fraction of reads carrying the causative variant. Loci that are not covered following trimming and rescaling of individual BAM sequence alignment files are indicated with a white cross.

Supplementary information

Supplementary Methods; Supplementary Discussion; Supplementary Notes

Supplementary Information . This file provides full description of archaeological material and contexts, develops the methodology underlying genome analyses, and summarizes linguistic information on Indo-European equine and Indo-Iranian chariotry terminology. A full list of supplementary references is provided.

Reporting Summary

Peer Review File

Mitochondrial and Y-chromosome phylogenies

Supplementary Fig. 1 This figure provides ML phylogenies mtDNA (a) and the Y-chromosome (b), with full sample labels. Node support is assessed using 100 bootstrap pseudo-replicates.

Supplementary Tables 1–3

Table 1 provides details on archeological contexts and DNA data. Table 2 presents the results of genetic continuity tests, while Table 3 summarizes the best ancestry profiles identified with qpAdm.

Rights and permissions

Open Access This article is licensed under a Creative Commons Attribution 4.0 International License, which permits use, sharing, adaptation, distribution and reproduction in any medium or format, as long as you give appropriate credit to the original author(s) and the source, provide a link to the Creative Commons license, and indicate if changes were made. The images or other third party material in this article are included in the article's Creative Commons license, unless indicated otherwise in a credit line to the material. If material is not included in the article's Creative Commons license and your intended use is not permitted by statutory regulation or exceeds the permitted use, you will need to obtain permission directly from the copyright holder. To view a copy of this license, visit <http://creativecommons.org/licenses/by/4.0/>.

Reprints and Permissions

About this article

Cite this article

Librado, P., Khan, N., Fages, A. *et al.* The origins and spread of domestic horses from the Western Eurasian steppes. *Nature* **598**, 634–640 (2021). <https://doi.org/10.1038/s41586-021-04018-9>

- Received: 04 May 2021
- Accepted: 10 September 2021
- Published: 20 October 2021
- Issue Date: 28 October 2021

- DOI: <https://doi.org/10.1038/s41586-021-04018-9>

Share this article

Anyone you share the following link with will be able to read this content:

[Get shareable link](#)

Sorry, a shareable link is not currently available for this article.

[Copy to clipboard](#)

Provided by the Springer Nature SharedIt content-sharing initiative

This article was downloaded by **calibre** from <https://www.nature.com/articles/s41586-021-04018-9>

| [Section menu](#) | [Main menu](#) |

- Article
- [Published: 13 October 2021](#)

A neuroanatomical basis for electroacupuncture to drive the vagal–adrenal axis

- [Shenbin Liu](#)^{1,2,3,4} na1,
- [Zhifu Wang](#)¹ na1,
- [Yangshuai Su](#)^{1,5},
- [Lu Qi](#)¹,
- [Wei Yang](#)¹,
- [Mingzhou Fu](#)¹,
- [Xianghong Jing](#)⁵,
- [Yanqing Wang](#)^{2,3,4} &
- [Qiufu Ma](#) ORCID: orcid.org/0000-0001-7896-7914¹

[Nature](#) volume **598**, pages 641–645 (2021)

- 17k Accesses
- 256 Altmetric
- [Metrics details](#)

Subjects

- [Neural circuits](#)
- [Neurophysiology](#)

Abstract

Somatosensory autonomic reflexes allow electroacupuncture stimulation (ES) to modulate body physiology at distant sites^{1,2,3,4,5,6} (for example, suppressing severe systemic inflammation^{6,7,8,9}). Since the 1970s, an emerging organizational rule about these reflexes has been the presence of body-region specificity^{1,2,3,4,5,6}. For example, ES at the hindlimb ST36 acupoint but not the abdominal ST25 acupoint can drive the vagal–adrenal anti-inflammatory axis in mice^{10,11}. The neuroanatomical basis of this somatotopic organization is, however, unknown. Here we show that PROKR2^{Cre}-marked sensory neurons, which innervate the deep hindlimb fascia (for example, the periosteum) but not abdominal fascia (for example, the peritoneum), are crucial for driving the vagal–adrenal axis. Low-intensity ES at the ST36 site in mice with ablated PROKR2^{Cre}-marked sensory neurons failed to activate hindbrain vagal efferent neurons or to drive catecholamine release from adrenal glands. As a result, ES no longer suppressed systemic inflammation induced by bacterial endotoxins. By contrast, spinal sympathetic reflexes evoked by high-intensity ES at both ST25 and ST36 sites were unaffected. We also show that optogenetic stimulation of PROKR2^{Cre}-marked nerve terminals through the ST36 site is sufficient to drive the vagal–adrenal axis but not sympathetic reflexes. Furthermore, the distribution patterns of PROKR2^{Cre} nerve fibres can retrospectively predict body regions at which low-intensity ES will or will not effectively produce anti-inflammatory effects. Our studies provide a neuroanatomical basis for the selectivity and specificity of acupoints in driving specific autonomic pathways.

Access options

Subscribe to Journal

Get full journal access for 1 year

\$199.00

only \$3.90 per issue

[Subscribe](#)

All prices are NET prices.
VAT will be added later in the checkout.
Tax calculation will be finalised during checkout.

Rent or Buy article

Get time limited or full article access on ReadCube.

from \$8.99

[Rent or Buy](#)

All prices are NET prices.

Additional access options:

- [Log in](#)
- [Access through your institution](#)
- [Learn about institutional subscriptions](#)

Fig. 1: Characterizing PROKR2^{ADV} neurons.



Fig. 2: Requirement of PROKR2^{ADV} neurons for low-intensity ES to drive the vagal–adrenal anti-inflammatory axis.

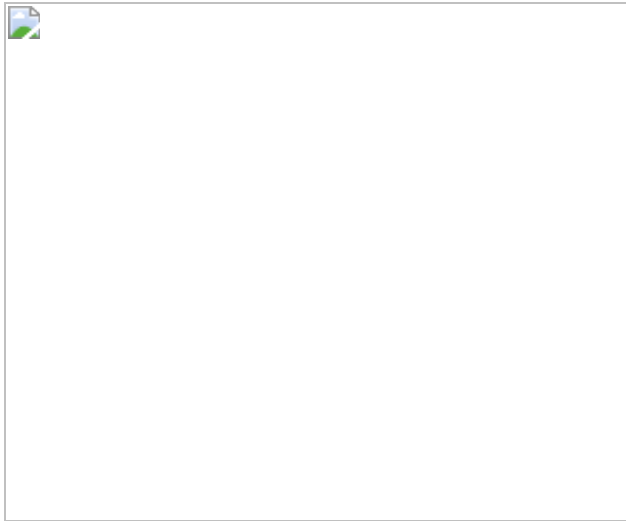


Fig. 3: Activation of PROKR2^{ADV} fibres drives the vagal–adrenal anti-inflammatory axis.



Fig. 4: Requirement of deep-tissue-innervating nerves for anti-inflammatory effects.



Data availability

All data are included in the paper and available from the corresponding author upon request. [Source data](#) are provided with this paper.

References

1. 1.

Kametani, H., Sato, A., Sato, Y. & Simpson, A. Neural mechanisms of reflex facilitation and inhibition of gastric motility to stimulation of various skin areas in rats. *J. Physiol.* **294**, 407–418 (1979).

2. 2.

Sato, A. & Schmidt, R. F. The modulation of visceral functions by somatic afferent activity. *Jpn. J. Physiol.* **37**, 1–17 (1987).

3. 3.

Sato, A. Neural mechanisms of autonomic responses elicited by somatic sensory stimulation. *Neurosci. Behav. Physiol.* **27**, 610–621 (1997).

4. 4.

Li, Y. Q., Zhu, B., Rong, P. J., Ben, H. & Li, Y. H. Neural mechanism of acupuncture-modulated gastric motility. *World J. Gastroenterol.* **13**, 709–716 (2007).

5. 5.

Takahashi, T. Effect and mechanism of acupuncture on gastrointestinal diseases. *Int. Rev. Neurobiol.* **111**, 273–294 (2013).

6. 6.

Ma, Q. Somato-autonomic reflexes of acupuncture. *Med. Acupunct.* **32**, 362–366 (2020).

7. 7.

Chavan, S. S., Pavlov, V. A. & Tracey, K. J. Mechanisms and therapeutic relevance of neuro-immune communication. *Immunity* **46**, 927–942 (2017).

8. 8.

Ulloa, L., Quiroz-Gonzalez, S. & Torres-Rosas, R. Nerve stimulation: immunomodulation and control of inflammation. *Trends Mol. Med.* **23**, 1103–1120 (2017).

9. 9.

Pan, W. X., Fan, A. Y., Chen, S. & Alemi, S. F. Acupuncture modulates immunity in sepsis: toward a science-based protocol. *Auton. Neurosci.* **232**, 102793 (2021).

10. 10.

Torres-Rosas, R. et al. Dopamine mediates vagal modulation of the immune system by electroacupuncture. *Nat. Med.* **20**, 291–295 (2014).

11. 11.

Liu, S. et al. Somatotopic organization and intensity dependence in driving distinct NPY-expressing sympathetic pathways by electroacupuncture. *Neuron* **108**, 436–435 (2020).

12. 12.

Longhurst, J. C. Defining meridians: a modern basis of understanding. *J. Acupunct. Meridian Stud.* **3**, 67–74 (2010).

13. 13.

Yang, F. C. et al. Genetic control of the segregation of pain-related sensory neurons innervating the cutaneous versus deep tissues. *Cell Rep.* **5**, 1353–1364 (2013).

14. 14.

Choi, S. et al. Parallel ascending spinal pathways for affective touch and pain. *Nature* **587**, 258–263 (2020).

15. 15.

Zylka, M. J., Rice, F. L. & Anderson, D. J. Topographically distinct epidermal nociceptive circuits revealed by axonal tracers targeted to *Mrgprd*. *Neuron* **45**, 17–25 (2005).

16. 16.

Ghitani, N. et al. Specialized mechanosensory nociceptors mediating rapid responses to hair pull. *Neuron* **95**, 944–954.e4 (2017).

17. 17.

Sharma, N. et al. The emergence of transcriptional identity in somatosensory neurons. *Nature* **577**, 392–398 (2020).

18. 18.

Kupari, J. et al. Single cell transcriptomics of primate sensory neurons identifies cell types associated with chronic pain. *Nat. Commun.* **12**, 1510 (2021).

19. 19.

Kucera, J. & Walro, J. M. An immunocytochemical marker for early type I muscle fibers in the developing rat hindlimb. *Anat. Embryol. (Berl.)* **192**, 137–147 (1995).

20. 20.

Remick, D. G., Newcomb, D. E., Bolgos, G. L. & Call, D. R. Comparison of the mortality and inflammatory response of two models of sepsis: lipopolysaccharide vs. cecal ligation and puncture. *Shock* **13**, 110–116 (2000).

21. 21.

Kleinlogel, S. et al. Ultra light-sensitive and fast neuronal activation with the Ca^{2+} -permeable channelrhodopsin CatCh. *Nat. Neurosci.* **14**, 513–518 (2011).

22. 22.

Lima, D. in *The Senses: A Comprehensive Reference* Vol. 5 (eds Masland, R. H. et al.) 477–526 (Academic, 2008).

23. 23.

Travagli, R. A. & Anselmi, L. Vagal neurocircuitry and its influence on gastric motility. *Nat. Rev. Gastroenterol. Hepatol.* **13**, 389–401 (2016).

24. 24.

Damarey, B. et al. Imaging of the nerves of the knee region. *Eur. J. Radiol.* **82**, 27–37 (2013).

25. 25.

Quiroz-Gonzalez, S., Segura-Alegria, B., Guadarrama-Olmos, J. C. & Jimenez-Estrada, I. Cord dorsum potentials evoked by electroacupuncture applied to the hind limbs of rats. *J. Acupunct. Meridian Stud.* **7**, 25–32 (2014).

26. 26.

Peng, Z., Nan, G., Cheng, M. & Zhou, K. The comparison of trigger point acupuncture and traditional acupuncture. *World J. Acupunct. Moxibustion* **26**, 1–6 (2016).

27. 27.

Choi, E. M., Jiang, F. & Longhurst, J. C. Point specificity in acupuncture. *Chin. Med.* **7**, 4 (2012).

28. 28.

Xing, J. J., Zeng, B. Y., Li, J., Zhuang, Y. & Liang, F. R. Acupuncture point specificity. *Int. Rev. Neurobiol.* **111**, 49–65 (2013).

29. 29.

Langevin, H. M. & Wayne, P. M. What is the point? The problem with acupuncture research that no one wants to talk about. *J. Altern. Complement. Med.* **24**, 200–207 (2018).

30. 30.

van der Poll, T., van de Veerdonk, F. L., Scicluna, B. P. & Netea, M. G. The immunopathology of sepsis and potential therapeutic targets. *Nat. Rev. Immunol.* **17**, 407–420 (2017).

31. 31.

Gerfen, C. R., Paletzki, R. & Heintz, N. GENSAT BAC Cre-recombinase driver lines to study the functional organization of

cerebral cortical and basal ganglia circuits. *Neuron* **80**, 1368–1383 (2013).

32. 32.

Bourane, S. et al. Identification of a spinal circuit for light touch and fine motor control. *Cell* **160**, 503–515 (2015).

33. 33.

Liu, Y. et al. VGLUT2-dependent glutamate release from peripheral nociceptors is required to sense pain and suppress itch. *Neuron* **68**, 543–556 (2010).

Acknowledgements

We thank D. D. Ginty for critical comments, and W. Lu and B. Zhao for helpful discussions; D. D. Ginty, M. Goulding, S. M. Dymecki, staff at GENSAT/MMRRC at the University of Davis, and the Allen Brain Institute/the Jackson Laboratory for genetically modified mice; and S. Celine for her assistance in histochemical analyses. All experimental data were generated at the Dana-Farber Cancer Institute, and the work was supported primarily by a NIH grant (R01AT010629) and partially by the Harvard/MIT Joint Research Program in Basic Neuroscience and a Wellcome Trust grant (200183/Z/15/Z) to Q.M. S.L.’s salary was supported primarily by a NIH grant (R01AT010629) and partly by the China Postdoctoral Science Foundation (KLF101846) and by the Development Project of Shanghai Peak Disciplines-Integrated Medicine (20150407) during an early period before the NIH grant (R01AT010629) was funded. Y.S.’s and W.Y.’s salary was supported by the China Scholarship Council (CSC no. 201609110039 and CSC no. 20190600178, respectively). Z.W.’s salary was supported by Fujian University of Traditional Chinese Medicine and by the Harvard/MIT Joint Research Program in Basic Neuroscience. Histochemical imaging was supported by Boston Children’s Hospital IDDRC (1U54HD090255).

Author information

Author notes

1. These authors contributed equally: Shenbin Liu, Zhifu Wang

Affiliations

1. Dana-Farber Cancer Institute and Department of Neurobiology, Harvard Medical School, Boston, MA, USA

Shenbin Liu, Zhifu Wang, Yangshuai Su, Lu Qi, Wei Yang, Mingzhou Fu & Qiufu Ma

2. Institute of Acupuncture and Moxibustion, Fudan Institutes of Integrative Medicine, Fudan University, Shanghai, China

Shenbin Liu & Yanqing Wang

3. Department of Integrative Medicine and Neurobiology, School of Basic Medical Science, Fudan University, Shanghai, China

Shenbin Liu & Yanqing Wang

4. Institutes of Brain Science, Fudan University, Shanghai, China

Shenbin Liu & Yanqing Wang

5. Meridians Research Center, Institute of Acupuncture and Moxibustion, China Academy of Chinese Medical Sciences, Beijing, China

Yangshuai Su & Xianghong Jing

Contributions

S.L. and Z.W. jointly performed most experiments. Y.S. helped to determine electric stimulation intensities for driving distinct autonomic pathways. L.Q. helped to characterize the identities of PROKR2^{Cre}-marked sensory neurons. W.Y. determined differential representations of PROKR2^{Cre}-marked DRG neurons at differential axial levels, and M.F. helped to show

innervation of PROKR2^{Cre}-marked sensory neurons in fascial tissues. Q.M. conceptualized and supervised the entire study (with contributions from Y.W. and X.J.). S.L. and Q.M. wrote the manuscript, and all authors edited the manuscript.

Corresponding author

Correspondence to Qiufu Ma.

Ethics declarations

Competing interests

The authors declare no competing interests.

Additional information

Peer review information *Nature* thanks Patrik Ernfors, Kevin Tracey, Luis Ulloa and the other, anonymous, reviewer(s) for their contribution to the peer review of this work. Peer review reports are available.

Publisher's note Springer Nature remains neutral with regard to jurisdictional claims in published maps and institutional affiliations.

Extended data figures and tables

[Extended Data Fig. 1 Intersectional marking and characterization of PROKR2ADV neurons.](#)

a, Schematic description of the intersectional genetic strategy for generating *Prokr2^{Adv}-tdTomato* mice, in which tdTomato expression was confined to PROKR2^{ADV} sensory neurons upon removal of two *STOP* cassettes from the *ROSA26* allele by the Cre and Flpo recombinases. *Advillin^{Flpo}* drove Flpo expression restricted to sensory neurons, such that DRG neurons with developmental coexpression of PROKR2-Cre and ADVILLIN-Flpo were

marked by tdTomato. **b**, Representative sections through suprarenal sympathetic ganglia, adrenal medulla where chromaffin cells were located, the colon that should contain enteric ganglia, and nodose ganglia from *Prokr2^{Adv}-tdTomato* mice. The intersectional genetic strategy only labeled one or two cells per section in nodose ganglia. Arrows indicate tdTomato⁺ fibers, but not somas, likely from DRG neurons or from those rare nodose sensory neurons. In other words, PROKR2^{ADV}-tdTomato did not label any autonomic neurons and adrenal chromaffin cells. n = 5 mice per group. **c**, L4-5 DRG sections from adult *Prokr2^{Adv}-tdTomato* mice. Top panels show double immunostaining of tdTomato (red) with markers for nonpeptidergic neurons (IB4: isolectin B4), proprioceptors (PV: parvalbumin), TRKA-lineage neurons (TRKA), myelinated neurons (NEFH: the neurofilament heavy chain protein), and peptidergic neurons (CGRP: the calcitonin gene-related peptide). Bottom panels show triple staining of tdTomato with NEFH and CGRP. Arrows indicate co-localization. n = 5 mice for each marker. Data are shown as mean ± SEM. Scale bars, 100 μm.

[Source data](#)

[Extended Data Fig. 2 Percentages of PROKR2^{ADV}-tdTomato⁺ neurons in DRGs and their innervation in the spinal cord.](#)

a, Representative sections through cervical (C1-C8), thoracic (T1-T13), lumbar (L1-L6), and sacral (S1-S3) DRGs from the adult *Prokr2^{Adv}-tdTomato* mice. **b**, Percentages of DRG neurons [determined by the expression of TUBB3 (not shown), a pan-neuronal marker] expressing tdTomato along the anterior-posterior axis; n = 4 mice. Note higher representations at the limb levels (e.g., C6-C8 and L3-L6 DRGs that innervate the forelimbs and hindlimbs, respectively) compared with thoracic DRGs. **c, d**, Sections through L4-5 lumbar and T8-10 thoracic levels of the spinal cord from *Prokr2^{Adv}-tdTomato* mice were triple stained [tdTomato (red), the NEFH protein (green) and CGRP(blue)]. tdTomato⁺ terminals were predominantly located in superficial laminae (**c,d**, top boxed panels), but also seen in deep laminae (III-V) (**c,d**, bottom boxed panels). Qualitatively, tdTomato⁺ fibers in the superficial laminae appeared to show more co-staining with CGRP and NEFH, in comparison with those in deep

laminae. n = 5 mice per group. Data are shown as mean ± SEM. Scale bars, 100 μm.

[Source data](#)

Extended Data Fig. 3 Skin innervation by PROKR2^{ADV} neurons in the hindlimb ST36 and abdominal ST25 acupoint regions.

a, Left, schematics showing the ST36 location. Middle: schematic showing of several but not all nerve bundles in the hindleg. Right: a schematic transverse section through the hindlimb ST36 region. TA: the tibialis anterior muscle. “T.”: tibia. “F.”: fibula. G.: gastrocnemius. Cpn: the common peroneal nerve and its deep (d-Cpn) and superficial (s-Cpn) branches. Lcn: the lateral cutaneous nerve. Tn: the tibial nerve. Sn: the sural nerve. **b**, Representative sections through the skin of the ST36 region of *Prokr2^{Adv}-tdTomato* mice. tdTomato⁺ fibers formed circumferential endings surrounding hair follicles (“HF”), without innervation to the epidermis (“Ep.”), in contrast with epidermal presence of TUBB3⁺ nerve fibers (green). DAPI (blue) staining showed cell nuclei. Note that these circumferential endings coexpressed CGRP but lacked detectable expression of the NEFH protein. n = 5 mice. **c**, Representative skin sections through the abdominal ST25 region in *Prokr2^{Adv}-tdTomato* mice. Top: tdTomato⁺ fibers (red) did not innervate the epidermis (“Ep.”), with DAPI (blue) staining cell nuclei. Middle and bottom: NEFH-negative but CGRP-positive tdTomato⁺ fibers formed circumferential endings surrounding hair follicles (“HF”). n = 5 mice. **d, e**, Representative sections through L4-5 lumbar DRGs (d) or through T8-10 thoracic DRGs (e) from *Prokr2^{Adv}-tdTomato* mice, in which DRG neurons innervating the cutaneous tissue of ST36 and ST25 were retrogradely labeled with Fluoro-gold (blue). Note that most retrogradely labeled-PROKR2^{ADV}-tdTomato⁺ neurons in both sets of DRGs coexpressed *Bmpr1b* mRNA (arrows) and low levels of *Nefh* mRNA (arrows). n = 4 mice. The bright-field images of *Nefh* mRNA, which were easier for identification of cells with low versus high levels, were converted to become pseudo green color in merged images. Data are shown as mean ± SEM. Scale bars, 100 μm.

Source data

Extended Data Fig. 4 Innervation patterns by PROKR2^{ADV} neurons in deep fascial tissues at the hindlimb ST36 and abdominal ST25 regions.

a-c, tdTomato⁺ fibers innervated fibula periosteum (**a**, arrow) and the cruciate ligament (**b**, arrow), and tdTomato⁺;NEFH⁺ free nerve endings in the interosseous membrane located between bones (**c**, small arrow). tdTomato signals were, however, not detected in NEFH⁺ fibers (**c**, green, large arrow) passing through the S100⁺ Pacinian corpuscles (**c**, blue, arrowhead). n = 5 (**a, b**) or 2 (**c**) mice. **d**, Representative sections showing PROKR2^{ADV}-tdTomato⁺ fibers that innervated tibia periosteum of the ST36 region, $63.5 \pm 4.1\%$ of which were NEFH⁺ and CGRP⁺. n = 5 mice. **e**, Representative transverse sections through the inner compartment of the tibialis anterior muscle (“TA”) at the ST36 region of *Prokr2^{Adv}-tdTomato* mice. Most tdTomato⁺ fibers coexpressed NEFH (arrows), with few being NEFH-negative (arrowheads). n = 5 mice. **f, g**, Representative sections through L4-5 lumbar DRGs from *Prokr2^{Adv}-tdTomato* mice, in which DRG neurons innervating deep ST36 tissues (deep muscles and possibly bones as well) were retrogradely labeled with Fluoro-gold (blue). Subsets of retrogradely labeled-PROKR2^{ADV}-tdTomato⁺ DRG neurons expressed *Nefh^{High}* (**f**, arrows), *Nefh^{Low}* (**f**, arrowhead), or *Bmpr1b* (**g**, arrow). n = 4 mice. **h**, Representative sections showing higher innervation densities of PROKR2^{ADV}-tdTomato⁺ fibers (arrows) in inner TA, compared with the outer TA muscle at the ST36 site and the abdominal muscle at the ST25 site (one-way ANOVA, n = 5 mice per group; $F_{2, 12} = 25.098$, $P < 0.001$; *post hoc* Tukey’s test: *** $P < 0.001$; NS = not significant, $P = 0.995$). **i, j**, Schematics showing two major subtypes of PROKR2^{ADV} DRG neurons innervating hindlimb ST36 (**i**) and abdominal ST25 regions (**j**). *Nefh^{High}*; *Bmpr1b*⁻ neurons densely innervate deep fascial tissues, including bone periosteum (“Perios.”) plus the space between muscle bundles within the inner TA compartment, but show sparse innervation in the outer TA compartment at the ST36 region and at the abdominal muscle layers of the ST25 region. The *Nefh^{Low}*; *Bmpr1b*⁺ neurons mainly form circumferential

endings around hair follicles at both ST36 and ST25 regions, with few retrogradely labeled from deep fascia (not shown). Thoracic and lumbar DRGs also contain *Nefh*-negative neurons (~40%), and their target tissues remain to be determined since only a small subset (12.3%) of neurons retrogradely labeled from deep ST36 tissues were *Nefh*-negative. T.: tibia; F.: fibula; Ep.: epidermal; De.: dermis; Mus.: muscle; Perit.: peritoneum. Data are shown as mean ± SEM. Scale bars, 100 μm.

[Source data](#)

Extended Data Fig. 5 Intersectional genetic ablation of PROKR2^{ADV} DRG neurons.

a, Schematics of the intersectional genetic strategy for selectively driving the diphtheria toxin receptor (“DTR”) in PROKR2^{Cre}-marked DRG neurons that coexpressed ADVILLIN-Flpo. This was achieved upon removal of two *STOP* cassettes from the intersectional allele of *Tau*, a pan-neural gene. A Cre-dependent *tdTomato* allele driven from the *ROSA26* promoter was included (not shown) to label all PROKR2-Cre⁺ cells with *tdTomato*, within or outside DRGs. **b**, Intraperitoneal injection (“i.p.”) of the diphtheria toxin (“DTX”) in *Prokr2^{Adv}-DTR* mice to create PROKR2^{ADV}-Abl mice, with littermates receiving the same DTX injections as control. **c**, Ablation of PROKR2^{Cre}-*tdTomato*⁺ neurons in lumbar DRGs, as indicated by marked reduction in the percentage of TUBB3⁺ DRG neurons coexpressing *tdTomato*. n = 5 mice per group. Two-side student’s unpaired *t*-test, $t_8 = 35.61$, *** $P < 0.001$. **d**, Representative images through tibia periosteum, showing reduction of TUBB3⁺ and NEFH⁺ fibers in PROKR2^{ADV}-Abl mice compared with control mice (n = 5 mice per group; two-side student’s unpaired *t*-test; for TUBB3: $t_8 = 5.065$, *** $P = 0.001$; for NEFH: $t_8 = 8.122$, *** $P < 0.001$). **e**, Representative images showing the preservation of PROKR2^{Cre}-*tdTomato*⁺ neurons in the spinal cord as well as various brain regions such as the cortex and the striatum. n = 5 mice per group. Data are shown as mean ± SEM. Scale bars, 100 μm.

[Source data](#)

Extended Data Fig. 6 PROKR2^{ADV} neurons were dispensable for high-intensity ES of ST25 to drive sympathetic reflex and to produce anti-inflammatory effects.

a, Without LPS challenge, both control and PROKR2^{ADV}-Abl mice showed virtually non-detectable, indistinguishable levels of TNF- α and IL-6 in serum (two-side student's unpaired *t*-test, n = 5 mice per group; for TNF- α : $t_8 = 0.580$; NS, not significant, $P = 0.578$; for IL-6: $t_8 = 0.151$; NS, $P = 0.884$). **b**, Schematic description of 3.0 mA ES of the abdominal ST25 acupoint that drove spinal-sympathetic reflexes. **c**, No changes in 3.0 mA ST25 ES-evoked Fos (green) induction in ChAT⁺ preganglionic sympathetic efferent neurons in the spinal intermediolateral nuclei ("IML") between control and PROKR2^{ADV}-Abl mice (Two-way ANOVA, n = 5 mice per group, $F_{1, 16} = 0.421$, $P = 0.562$; *post-hoc* Tukey's test: *** $P < 0.001$). **d**, No changes in 3.0 mA ST25 ES-evoked Fos induction in the suprarenal sympathetic ganglia ("g.") (Two-way ANOVA, n = 5 mice per group, $F_{1, 16} = 0.290$, $P = 0.598$; *post-hoc* Tukey's test: *** $P < 0.001$). **e**, No changes in 3.0 mA ST25 ES-induced noradrenaline ("NA") release (two-way ANOVA, n = 6 per group, $F_{1, 20} = 4.093$, $P = 0.057$; *post hoc* Tukey test: *** $P < 0.001$). **f, g**, No changes in 3.0 mA ST25 ES-evoked reduction of LPS-induced TNF- α and IL-6 production (two-way ANOVA, n = 6 mice per group; for TNF- α : $F_{1, 20} = 1.851$, $P = 0.189$; *post-hoc* Tukey test: *** $P < 0.001$; for IL-6: $F_{1, 20} = 5.214$, $P = 0.133$; *post-hoc* Tukey test: *** $P < 0.001$). **h, i**, No marked changes in 1.0 mA ST25 ES-evoked reduction of LPS-induced TNF- α and IL-6 production (two-way ANOVA, n = 5 mice per group; for TNF- α : $F_{1, 16} = 4.357$, $P = 0.053$; *post-hoc* Tukey test: left * $P = 0.014$, right * $P = 0.018$; for IL-6: $F_{1, 16} = 1.019$, $P = 0.328$; *post-hoc* Tukey test: left * $P = 0.013$, right * $P = 0.015$). **j**, Schematics showing that PROKR2^{Cre}-negative sensory neurons preserved in PROKR2^{ADV}-Abl mice were sufficient to drive the spinal-sympathetic anti-inflammatory pathways in response to 1.0-3.0 mA ES of the abdominal ST25 acupoint. Sym. g.: sympathetic ganglia. Data are shown as mean \pm SEM. Scale bars: 100 μ m.

[Source data](#)

Extended Data Fig. 7 3.0 mA ES of ST36 produced anti-inflammatory effects independent of PROKR2^{ADV} neurons.

a, Compared with control littermates, no difference of 3.0 mA ST36 ES-evoked Fos (green) induction in ChAT⁺ (red) sympathetic preganglionic neurons in the spinal intermediolateral nuclei (“IML”) in PROKR2^{ADV}-Abl mice (two-way ANOVA, n = 5 mice per group, $F_{1, 16} = 0.236$, $P = 0.633$; *post-hoc* Tukey’s test: *** $P < 0.001$). **b**, No changes in 3.0 mA ST36 ES-evoked reduction of LPS-induced TNF- α and IL-6 production in PROKR2^{ADV}-Abl mice (two-way ANOVA, n = 5 mice per group; for TNF- α : $F_{1, 16} = 1.392$, $P = 0.255$; *post-hoc* Tukey test: *** $P < 0.001$; for IL-6: $F_{1, 16} = 1.382$, $P = 0.257$; *post-hoc* Tukey test: *** $P < 0.001$). Thus, although PROKR2^{ADV} neurons are necessary for low-intensity ES to drive the vagal-adrenal anti-inflammatory axis, they are dispensable for high-intensity ES to drive spinal-sympathetic anti-inflammatory axis from either ST25 or ST36. Data are shown as mean \pm SEM. Scale bars: 100 μ m.

[Source data](#)

Extended Data Fig. 8 Optogenetic activation of PROKR2^{ADV} neurons inside the hindlimb ST36 region failed to drive sympathetic reflex.

a, Intersectional genetic strategy for generation of *Prokr2^{Adv}-CatCh* (or “*CatCh*”) mice, in which the expression of the calcium translocating channelrhodopsin (*CatCh*, an L132C-mutated channelrhodopsin with enhanced Ca²⁺ permeability) plus the fluorescent protein EYFP was confined to PROKR2^{ADV} DRG neurons defined by co-expression of PROKR2^{Cre} and ADVILLIN^{Flpo}. This was achieved by crossing the intersectional *CatCh* mice (Ai80) with *Prokr2^{Cre}* and *Advillin^{Flpo}* mice. **b, c**, Representative images showing that *CatCh-EYFP* expression was detected in a subset of L4 DRG and EYFP⁺ fibers innervated tibial periosteum. n = 5 mice. **d, e**, Electrophysiological recordings of dissociated DRG neurons from control and *CatCh* mice. Under the voltage clamp mode, blue light

(473 nm) stimulation (10 Hz, 50 µs, 10 mW) resulted in inward currents in 26.3% (15/57) of randomly selected DRG neurons from *CatCh* mice (**d**), and after switching to the current clamp mode, this optical stimulation (10 Hz, 50 µs, 10 mW) reliably produced action potential firing (**e**). None of DRG neurons from control mice produced such inward currents and action potential firing (0/43 = 0%) (**d, e**). n = 3 mice per group. **f, g**, 10 mW (**f**) and 30 mW (**g**) optical stimulation of the hindlimb ST36 region in *CatCh* mice failed to produce an increase of Fos induction in ChAT⁺ preganglionic sympathetic efferent neurons located in the spinal intermediolateral nuclei (“IML”) compared to control mice (n = 5 mice per group, two-side student’s unpaired *t*-test; for 10 mW: $t_8 = 0.362$; NS = not significant, $P = 0.727$; for 30 mW: $t_8 = 0.704$; NS, $P = 0.502$). **h**, Schematics showing how we recorded the left cervical vagal efferent nerve in response to 473 nm optic stimulation at bilateral ST36 sites in control and *CatCh* mice. Note that the distal end of the vagal nerve was transected to block visceral sensory afferent inputs. Data are shown as mean ± SEM. Scale bars: 100 µm.

Source data

Extended Data Fig. 9 Optogenetic activation of hindlimb PROKR2^{ADV} neurons induced Fos in NTS-projecting spinal neurons and in adrenal medulla-projecting DMV efferent neurons.

a, Schematics showing the experimental design for testing if optical stimulation of PROKR2^{ADV} nerve fibers of the hindlimb ST36 region can activate spinal ascending projection neurons retrogradely labeled with Fluoro-gold from the nucleus tractus solitarius (“NTS”) in hindbrain. **b**, 473 nm blue light stimulation of the hindlimb ST36 region was sufficient to evoke Fos induction in NTS-projecting neurons located in the lamina I of the spinal cord in *Prokr2^{Adv}-CatCh* (“*CatCh*”) mice (**b**, arrows), but not in control mice (n = 3 mice per group, two-side student’s unpaired *t*-test, $t_4 = 6.807$, *** $P < 0.001$). This stimulation virtually did not induce any Fos in NTS-projecting neurons located in deep laminae (IV and V) of the spinal cord, in both control ($1.77 \pm 0.24\%$) and *CatCh* ($2.27 \pm 0.43\%$) mice (data

not shown; $n = 3$ mice per group, two-side student's unpaired *t*-test, $t_4 = 1.023$, $P = 0.364$). **c**, Schematics showing the experimental design for testing if optical stimulation of PROKR2^{ADV} nerve fibers of the hindlimb ST36 region can activate a subset of vagal efferent neurons located in the dorsal motor nucleus of the vagus (DMV) that were retrogradely labeled from the adrenal gland with Fluoro-gold. **d**, Optical stimulation of PROKR2^{ADV} neurons of ST36 regions caused an increase in Fos induction in adrenal medulla-projecting DMV neurons compared with control mice ($n = 3$ mice per group, two-side student's unpaired *t*-test, $t_4 = 8.159$, *** $P = 0.001$). Arrows indicate retrogradely labeled DMV neurons with Fos induction. Arrowhead indicates the baseline Fos expression in ChAT-negative cells. **e**, No significant (NS) reduction of LPS-induced TNF- α and IL-6 production following 10 mW or 30 mW optical stimulation of PROKR2^{ADV} fibers at the ST36 site of *CatCh* mice compared with control mice (two-way ANOVA, $n = 5$ mice per group; for TNF- α : $F_{1, 20} = 0.124$; NS, $P = 0.728$; *post-hoc* Tukey test: ** $P = 0.003$, *** $P < 0.001$; for IL-6: $F_{1, 20} = 0.714$; NS, $P = 0.408$; *post-hoc* Tukey test: *** $P < 0.001$). Data are shown as mean \pm SEM. Scale bars: 100 μ m.

Source data

Extended Data Fig. 10 The tibial nerve was dispensable for focal 0.5 mA ST36 ES-evoked anti-inflammatory effects, and the common peroneal nerve was required for 0.5 mA ST36 ES to induce Fos in NTS-projecting spinal neurons.

a, 0.5 mA ST36 ES-evoked reduction of LPS-induced TNF- α and IL-6 in serum, compared with sham 0 mA ES, was unaffected by tibial nerve neurectomy ("TNX") compared with sham surgery ("sham") (two-way ANOVA, $n = 5$ mice per group; for TNF- α : $F_{1, 16} = 0.253$, $P = 0.622$; *post hoc* Tukey's test: left ** $P = 0.002$, right ** $P = 0.005$; for IL-6: $F_{1, 16} = 0.002$, $P = 0.989$; *post hoc* Tukey's test: left ** $P = 0.009$, right ** $P = 0.007$). As described in Extended Data Fig. 3a, the tibial nerve was located posterior to fibula and tibia, and our focal ES of ST36 apparently failed to activate this nerve. This is different from reported activation of this nerve

via a diffuse ES mode¹⁰, in which the electric current entered the left ST36 site and came out of the right ST36 site¹⁰. **b**, 0.5 mA, but not 0 mA control, ES of ST36 induced Fos (green) in Fluoro-gold⁺ retrogradely labeled NTS-projecting neurons (red) located in the lamina I of the spinal cord in sham surgery mice, with arrows indicating co-labeling. This induction was lost in mice with common peroneal neurectomy (“CPX”) (Two-way ANOVA, n = 3 mice per group, $F_{1, 8} = 265.645$, $P < 0.001$; *post-hoc* Tukey’s test: *** $P < 0.001$; NS, not significant, $P = 0.145$). Data are shown as mean ± SEM. Scale bars: 100 μ m.

[Source data](#)

Extended Data Fig. 11 0.5 mA ES at cutaneous or traditional non-acupoint regions failed to suppress inflammation, but ES at the forelimb LI10 acupoint can evoke PROKR2^{ADV} neuron-dependent anti-inflammatory effects.

a, b, low-intensity ES at the superficial ST36 region. Schematics (**a**) showing ES at the superficial, intradermal part of the ST36 region. Two electric needles were inserted through the epidermis (“Ep.”) and into the dermis (“De.”) at ST36 regions, with needles tilted to restrict them within the superficial dermis. This intradermal 0.5-mA ES failed to reduce LPS-induced TNF- α and IL-6 expression compared with sham 0 mA ES in C57BL/6J mice (**b**, n = 5 mice per group; two-side student’s unpaired *t*-test; for TNF- α : $t_8 = 0.218$; NS, not significant, $P = 0.833$; for IL-6: $t_8 = 0.562$; NS, $P = 0.589$). **c, d**, Low-intensity stimulation of the sural nerve. Schematics (**c**) showing ES at the middle region of the posterior hind leg, by inserting electric needles through the Chengjin (BL56) acupoint, with tips flanking the skin-innervating sural nerve (“Sn”). 0.5 mA ES at this acupoint failed to reduce TNF- α and IL-6 compared with sham 0 mA ES in C57BL/6J mice (**d**, n = 5 mice per group; two-side student’s unpaired *t*-test; for TNF- α : $t_8 = 0.375$; NS, $P = 0.718$; for IL-6: $t_8 = 0.721$; NS, $P = 0.491$).

e-j, Low-intensity ES within the gastrocnemius (“G.”) muscle or the semitendinosus (“S.”) muscles. Schematics (**e, h**) showing ES at these two muscles. Two representative images (**f, i**) showing sparse innervation by

$\text{PROKR2}^{\text{ADV}}$ -tdTomato⁺ fibers within these muscles, with the percentages of unit areas showing positive fibers ($0.51 \pm 0.19\%$ for G. and $0.60 \pm 0.11\%$ for S. muscles) comparable to that seen in the outer TA muscle ($0.51 \pm 0.15\%$) and the abdominal wall muscles ($0.59 \pm 0.12\%$) shown in Extended Data Fig. 4h. n = 4 mice. In comparison with sham 0 mA ES, no impact on TNF- α and IL-6 production by 0.5 mA ES in either G. muscle (g, n = 5 mice per group. two-side student's unpaired t-test; for TNF- α : $t_8 = 0.205$; NS, $P = 0.843$; for IL-6: $t_8 = 0.861$; NS, $P = 0.415$) or in S. mucle (j, n = 5 mice per group; two-side student's unpaired t-test; for TNF- α : $t_8 = 0.468$; NS, $P = 0.652$; for IL-6: $t_8 = 0.593$; NS, $P = 0.570$) in C57BL/6J mice. k-m, Low-intensity ES at the forelimb acupoint LI10 (Shousanli). Schematics (k) and the image (l, top) showing ES at the forelimb acupoint LI10.

Representative images (l) showing $\text{PROKR2}^{\text{ADV}}$ -tdTomato⁺ fibers within the deep branch of the radial nerve, and their innervations in radius periosteum, which were prominent at transverse sections at levels slightly distal (e.g., 1 mm) from the LI10 acupoint level. n = 3 mice. (m) Loss of 0.5 mA LI10 ES-evoked reduction of TNF- α and IL-6 in $\text{PROKR2}^{\text{ADV}}$ -Abl mice compared with control mice (two-way ANOVA, n = 5 mice per group; for TNF- α : $F_{1, 16} = 20.384$, $P < 0.001$; post-hoc Tukey test: * $P = 0.011$; NS, $P = 0.562$; for IL-6: $F_{1, 16} = 14.296$, $P = 0.002$; post-hoc Tukey test: ** $P = 0.004$; NS, $P = 0.728$). (n) Loss of 0.5 mA LI10 ES-evoked reduction of TNF- α and IL-6 in mice with subdiaphragmatic vagotomy ("sVX") compared with mice with sham surgery (two-way ANOVA, n = 5 mice per group; for TNF- α : $F_{1, 16} = 22.875$, $P < 0.001$; post-hoc Tukey test: ** $P = 0.004$; NS, $P = 0.697$; for IL-6: $F_{1, 16} = 18.065$, $P = 0.002$; post-hoc Tukey test: ** $P = 0.004$; NS, $P = 0.57$). TA: Anterior tibial muscle; T.: Tibia; F.: Fibula; Fe.: Femur; R.: Radius; U.: Ulna. Data are shown as mean \pm SEM. Scale bars: 100 μm .

[Source data](#)

Supplementary information

[Reporting Summary](#)

Peer Review File

Source data

[Source Data Fig. 1](#)

[Source Data Fig. 2](#)

[Source Data Fig. 3](#)

[Source Data Fig. 4](#)

[Source Data Extended Data Fig. 1](#)

[Source Data Extended Data Fig. 2](#)

[Source Data Extended Data Fig. 3](#)

[Source Data Extended Data Fig. 4](#)

[Source Data Extended Data Fig. 5](#)

[Source Data Extended Data Fig. 6](#)

[Source Data Extended Data Fig. 7](#)

[Source Data Extended Data Fig. 8](#)

[Source Data Extended Data Fig. 9](#)

[Source Data Extended Data Fig. 10](#)

[Source Data Extended Data Fig. 11](#)

Rights and permissions

[Reprints and Permissions](#)

About this article

Cite this article

Liu, S., Wang, Z., Su, Y. *et al.* A neuroanatomical basis for electroacupuncture to drive the vagal–adrenal axis. *Nature* **598**, 641–645 (2021). <https://doi.org/10.1038/s41586-021-04001-4>

- Received: 14 March 2021
- Accepted: 07 September 2021
- Published: 13 October 2021
- Issue Date: 28 October 2021
- DOI: <https://doi.org/10.1038/s41586-021-04001-4>

Share this article

Anyone you share the following link with will be able to read this content:

[Get shareable link](#)

Sorry, a shareable link is not currently available for this article.

[Copy to clipboard](#)

Provided by the Springer Nature SharedIt content-sharing initiative

[**Electroacupuncture activates neurons to switch off inflammation**](#)

- Luis Ulloa

News & Views 13 Oct 2021

This article was downloaded by **calibre** from <https://www.nature.com/articles/s41586-021-04001-4>

| [Section menu](#) | [Main menu](#) |

- Article
- [Published: 13 October 2021](#)

An endogenous opioid circuit determines state-dependent reward consumption

- [Daniel C. Castro](#) ORCID: orcid.org/0000-0001-8036-1313^{1,2,3,4},
- [Corinna S. Osswell](#)^{1,4},
- [Eric T. Zhang](#)^{4,5},
- [Christian E. Pedersen](#)^{4,5},
- [Sean C. Piantadosi](#)^{1,4},
- [Mark A. Rossi](#)^{1,4},
- [Avery C. Hunker](#)⁴,
- [Anthony Guglin](#)^{2,3},
- [Jose A. Morón](#)^{2,3},
- [Larry S. Zweifel](#) ORCID: orcid.org/0000-0003-3465-5331⁴,
- [Garret D. Stuber](#) ORCID: orcid.org/0000-0003-1730-4855^{1,4,6} &
- [Michael R. Bruchas](#) ORCID: orcid.org/0000-0003-4713-7816^{1,2,3,4,5,6}

Nature volume **598**, pages 646–651 (2021)

- 7956 Accesses
- 197 Altmetric
- [Metrics details](#)

Subjects

- [Molecular neuroscience](#)
- [Motivation](#)
- [Neural circuits](#)
- [Reward](#)

Abstract

μ -Opioid peptide receptor (MOPR) stimulation alters respiration, analgesia and reward behaviour, and can induce substance abuse and overdose^{1,2,3}. Despite its evident importance, the endogenous mechanisms for MOPR regulation of consummatory behaviour have remained unknown⁴. Here we report that endogenous MOPR regulation of reward consumption in mice acts through a specific dorsal raphe to nucleus accumbens projection. MOPR-mediated inhibition of raphe terminals is necessary and sufficient to determine consummatory response, while select enkephalin-containing nucleus accumbens ensembles are engaged prior to reward consumption, suggesting that local enkephalin release is the source of the endogenous MOPR ligand. Selective modulation of nucleus accumbens enkephalin neurons and CRISPR–Cas9-mediated disruption of enkephalin substantiate this finding. These results isolate a fundamental endogenous opioid circuit for state-dependent consumptive behaviour and suggest alternative mechanisms for opiate modulation of reward.

Access options

Subscribe to Journal

Get full journal access for 1 year

\$199.00

only \$3.90 per issue

[Subscribe](#)

All prices are NET prices.
VAT will be added later in the checkout.

Tax calculation will be finalised during checkout.

Rent or Buy article

Get time limited or full article access on ReadCube.

from \$8.99

[Rent or Buy](#)

All prices are NET prices.

Additional access options:

- [Log in](#)
- [Access through your institution](#)
- [Learn about institutional subscriptions](#)

Fig. 1: Endogenous MOPR activation in mNAcSh is necessary for potentiating state-dependent consummatory behaviour.



Fig. 2: LDRN^{Penk}-mNAcSh projections make monosynaptic connections and display opioid-dependent spatiotemporal signalling.

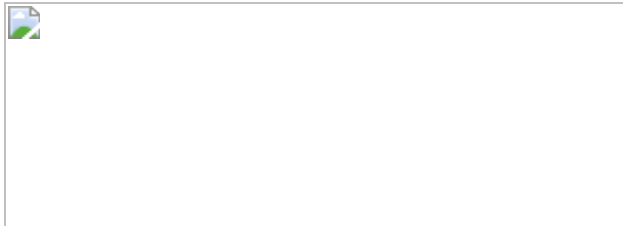


Fig. 3: MOPR activation on LDRN^{MOPR}-mNAcSh is sufficient to potentiate reward consumption.



Fig. 4: mNAcSh enkephalinergic ensembles are modulated by physiological state and reward consumption.

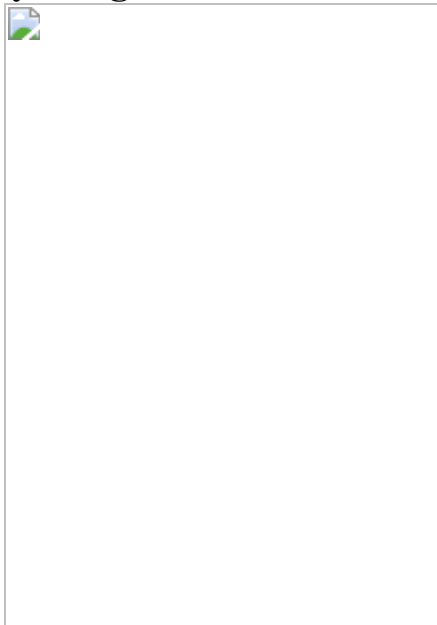
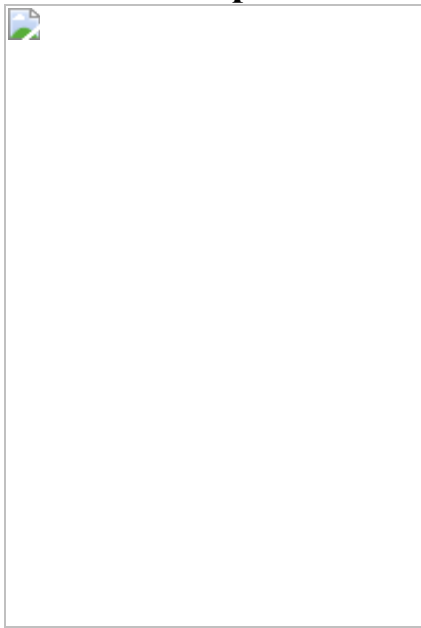


Fig. 5: Endogenous mNAcSh enkephalin is necessary for potentiating reward consumption.



Data availability

The behavioural dataset supporting the current study is available from the author upon request. [Source data](#) are provided with this paper.

Code availability

Custom MATLAB analysis and code was created to appropriately organize, process, and combine photometry and single-photon recording data with associated behavioural data. Analysis code for photometry and single-photon imaging from Figs. [2](#), [4](#) will be made available on Github (<https://github.com/BruchasLab>).

References

1. 1.

Centers for Disease Control and Prevention. CDC grand rounds: prescription drug overdoses—a U.S. epidemic. *Morb. Mortal. Wkly.*

Rep. **61**, 10–13 (2012).

2. 2.

Volkow, N., Benveniste, H. & McLellan, A. T. Use and misuse of opioids in chronic pain. *Annu. Rev. Med.* **69**, 451–465 (2018).

3. 3.

Wei, A. D. & Ramirez, J.-M. Presynaptic mechanisms and KCNQ potassium channels modulate opioid depression of respiratory drive. *Front. Physiol.* **10**, 1407 (2019).

4. 4.

Kelley, A. E., Baldo, B. A. & Pratt, W. E. A proposed hypothalamic-thalamic-striatal axis for the integration of energy balance, arousal, and food reward. *J. Comp. Neurol.* **493**, 72–85 (2005).

5. 5.

Mattison, J. The treatment of the morphine-disease. *Indian Med. Gaz.* **26**, 65–68 (1891).

6. 6.

Herkenham, M. & Pert, C. B. In vitro autoradiography of opiate receptors in rat brain suggests loci of ‘opiatergic’ pathways. *Proc. Natl Acad. Sci. USA* **77**, 5532–5536 (1980).

7. 7.

Massaly, N., Morón, J. A. & Al-Hasani, R. A trigger for opioid misuse: chronic pain and stress dysregulate the mesolimbic pathway and kappa opioid system. *Front. Neurosci.* **10**, 480 (2016).

8. 8.

Castro, D. C. & Bruchas, M. R. A motivational and neuropeptidergic hub: anatomical and functional diversity within the nucleus accumbens shell. *Neuron* **102**, 529–552 (2019).

9. 9.

Hughes, J. et al. Identification of two related pentapeptides from the brain with potent opiate agonist activity. *Nature* **258**, 577–580 (1975).

10. 10.

Simantov, R. & Snyder, H. Isolation and structure identification of a morphine-like peptide ‘enkephalin’ in bovine brain. *Life Sci.* **18**, 781–787 (1976).

11. 11.

Bakshi, V. P. & Kelley, A. E. Feeding induced by opioid stimulation of the ventral striatum: role of opiate receptor subtypes. *J. Pharmacol. Exp. Ther.* **265**, 1253–1260 (1993).

12. 12.

Resendez, S. L. et al. μ -Opioid receptors within subregions of the striatum mediate pair bond formation through parallel yet distinct reward mechanisms. *J. Neurosci.* **33**, 9140–9149 (2013).

13. 13.

Castro, D. C. & Berridge, K. C. Opioid hedonic hotspot in nucleus accumbens shell: mu, delta, and kappa maps for enhancement of sweetness ‘liking’ and ‘wanting’. *J. Neurosci.* **34**, 4239–4250 (2014).

14. 14.

Cui, Y. et al. Targeted expression of μ -opioid receptors in a subset of striatal direct-pathway neurons restores opiate reward. *Nat. Neurosci.* **17**, 254–261 (2014).

15. 15.

Bodnar, R. J., Glass, M. J., Ragnauth, A. & Cooper, M. L. General, μ and κ opioid antagonists in the nucleus accumbens alter food intake under deprivation, glucoprivic and palatable conditions. *Brain Res.* **700**, 205–212 (1995).

16. 16.

Kelley, A. E., Bless, E. P. & Swanson, C. J. Investigation of the effects of opiate antagonists infused into the nucleus accumbens on feeding and sucrose drinking in rats. *J. Pharmacol. Exp. Ther.* **278**, 1499–1507 (1996).

17. 17.

Kramer, T. H. et al. Novel peptidic mu opioid antagonists: pharmacologic characterization in vitro and in vivo. *J. Pharmacol. Exp. Ther.* **249**, 544–551 (1989).

18. 18.

Tervo, D. G. R. et al. A designer AAV variant permits efficient retrograde access to projection neurons. *Neuron* **92**, 372–382 (2016).

19. 19.

Zhao, Z.-Q. et al. Central serotonergic neurons are differentially required for opioid analgesia but not for morphine tolerance or morphine reward. *Proc. Natl Acad. Sci. USA* **104**, 14519–14524 (2007).

20. 20.

Land, B. B. et al. Activation of the kappa opioid receptor in the dorsal raphe nucleus mediates the aversive effects of stress and reinstates drug seeking. *Proc. Natl Acad. Sci. USA* **106**, 19168–19173 (2009).

21. 21.

Nectow, A. R. et al. Identification of a brainstem circuit controlling feeding. *Cell* **170**, 429-442.e11 (2017).

22. 22.

Huang, K. W. et al. Molecular and anatomical organization of the dorsal raphe nucleus. *eLife* **8**, e46464 (2019).

23. 23.

Gunaydin, L. A. et al. Natural neural projection dynamics underlying social behavior. *Cell* **157**, 1535–1551 (2014).

24. 24.

Siuda, E. R. et al. Spatiotemporal control of opioid signaling and behavior. *Neuron* **86**, 923–935 (2015).

25. 25.

Ran, F. A. et al. In vivo genome editing using *Staphylococcus aureus* Cas9. *Nature* **520**, 186–191 (2015).

26. 26.

Hunker, A. C. et al. Conditional single vector CRISPR/SaCas9 viruses for efficient mutagenesis in the adult mouse nervous system. *Cell Rep.* **30**, 4303-4316.e6 (2020).

27. 27.

Al-Hasani, R. et al. In vivo detection of optically-evoked opioid peptide release. *eLife* **7**, e36520 (2018).

28. 28.

Maldonado-Irizarry, C. S., Swanson, C. J. & Kelley, A. E. Glutamate receptors in the nucleus accumbens shell control feeding behavior via the lateral hypothalamus. *J. Neurosci.* **15**, 6779–6788 (1995).

29. 29.

Vachez, Y. M. et al. Ventral arkypallidal neurons inhibit accumbal firing to promote reward consumption. *Nat. Neurosci.* **24**, 379–390 (2021).

30. 30.

Castro, D. C., Terry, R. A. & Berridge, K. C. Orexin in rostral hotspot of nucleus accumbens enhances sucrose ‘liking’ and intake but scopolamine in caudal shell shifts ‘liking’ toward ‘disgust’ and ‘fear’. *Neuropsychopharmacology* **41**, 2101–2111 (2016).

31. 31.

Georgescu, D. et al. The hypothalamic neuropeptide melanin-concentrating hormone acts in the nucleus accumbens to modulate feeding behavior and forced-swim performance. *J. Neurosci.* **25**, 2933–2940 (2005).

32. 32.

Lim, B. K., Huang, K. W., Grueter, B. A., Rothwell, P. E. & Malenka, R. C. Anhedonia requires MC4R-mediated synaptic adaptations in nucleus accumbens. *Nature* **487**, 183–189 (2012).

33. 33.

O’Connor, E. C. et al. Accumbal D1R neurons projecting to lateral hypothalamus authorize feeding. *Neuron* **88**, 553–564 (2015).

34. 34.

Berthoud, H.-R. & Münzberg, H. The lateral hypothalamus as integrator of metabolic and environmental needs: from electrical self-stimulation to opto-genetics. *Physiol. Behav.* **104**, 29–39 (2011).

35. 35.

Corre, J. et al. Dopamine neurons projecting to medial shell of the nucleus accumbens drive heroin reinforcement. *eLife* **7**, e39945 (2018).

36. 36.

Di Chiara, G. & Imperato, A. Drugs abused by humans preferentially increase synaptic dopamine concentrations in the mesolimbic system of freely moving rats. *Proc. Natl Acad. Sci. USA* **85**, 5274–5278 (1988).

37. 37.

Smith, K. S. & Berridge, K. C. The ventral pallidum and hedonic reward: neurochemical maps of sucrose ‘liking’ and food intake. *J. Neurosci.* **25**, 8637–8649 (2005).

38. 38.

Land, B. B. et al. The dysphoric component of stress is encoded by activation of the dynorphin kappa-opioid system. *J. Neurosci.* **28**, 407–414 (2008).

39. 39.

Zelikowsky, M. et al. The neuropeptide Tac2 controls a distributed brain state induced by chronic social isolation stress. *Cell* **173**, 1265–1279.e19 (2018).

40. 40.

Parker, K. E. et al. A paranigral VTA nociceptin circuit that constrains motivation for reward. *Cell* **178**, 653-671.e19 (2019).

41. 41.

Al-Hasani, R. et al. Distinct subpopulations of nucleus accumbens dynorphin neurons drive aversion and reward. *Neuron* **87**, 1063–1077 (2015).

42. 42.

Massaly, N. et al. Pain-induced negative affect is mediated via recruitment of the nucleus accumbens kappa opioid system. *Neuron* **102**, 564–573.e6 (2019).

43. 43.

Fetterly, T. L. et al. Insulin bidirectionally alters NAc glutamatergic transmission: interactions between insulin receptor activation, endogenous opioids, and glutamate release. *J. Neurosci.* **41**, 2360–2372 (2021).

44. 44.

Schmid, C. L. et al. Bias factor and therapeutic window correlate to predict safer opioid analgesics. *Cell* **171**, 1165-1175.e13 (2017).

45. 45.

Singh, J. & Desiraju, T. Differential effects of opioid peptides administered intracerebrally in loci of self-stimulation reward of lateral hypothalamus and ventral tegmental area–substantia nigra. *NIDA Res. Monogr.* **87**, 180–191 (1988).

46. 46.

Lemos, J. C., Roth, C. A. & Chavkin, C. Signaling events initiated by kappa opioid receptor activation: quantification and immunocolocalization using phospho-selective KOR, p38 MAPK, and K_{IR} 3.1 antibodies. *Methods Mol. Biol.* **717**, 197–219 (2011).

47. 47.

Banghart, M. R. & Sabatini, B. L. Photoactivatable neuropeptides for spatiotemporally precise delivery of opioids in neural tissue. *Neuron* **73**, 249–259 (2012).

48. 48.

Banala, S. et al. Photoactivatable drugs for nicotinic optopharmacology. *Nat. Methods* **15**, 347–350 (2018).

49. 49.

Zhang, Y. et al. Battery-free, lightweight, injectable microsystem for in vivo wireless pharmacology and optogenetics. *Proc. Natl Acad. Sci. USA* **116**, 21427–21437 (2019).

50. 50.

Patriarchi, T. et al. Ultrafast neuronal imaging of dopamine dynamics with designed genetically encoded sensors. *Science* **360**, eaat4422 (2018).

51. 51.

Sun, F. et al. A genetically encoded fluorescent sensor enables rapid and specific detection of dopamine in flies, fish, and mice. *Cell* **174**, 481-496.e19 (2018).

52. 52.

Wang, F. et al. RNAscope. *J. Mol. Diagn.* **14**, 22–29 (2012).

53. 53.

Matthes, H. W. et al. Loss of morphine-induced analgesia, reward effect and withdrawal symptoms in mice lacking the μ -opioid-receptor gene. *Nature* **383**, 819–823 (1996).

54. 54.

McCall, J. G. et al. CRH engagement of the locus coeruleus noradrenergic system mediates stress-induced anxiety. *Neuron* **87**, 605–620 (2015).

55. 55.

Resendez, S. L. et al. Visualization of cortical, subcortical and deep brain neural circuit dynamics during naturalistic mammalian behavior with head-mounted microscopes and chronically implanted lenses. *Nat. Protoc.* **11**, 566–597 (2016).

56. 56.

Zhou, P. et al. Efficient and accurate extraction of in vivo calcium signals from microendoscopic video data. *eLife* **7**, e28728 (2018).

Acknowledgements

We thank L. Lawson, D. Blumenthal, M. Chung, T. Hobbs and C. Pizzano for animal colony maintenance; the Bruchas laboratory, Stuber laboratory and multiple trainees and faculty within the NAPE Center for helpful discussions; B. Kieffer for the *Oprm1^{f/f}* mice; and G. Scherrer for the *Penk-Cre* mice. D.C.C. was funded by NIH grants NS007205, DA043999, DA049862 and DA051489. C.E.P. was funded by NIH grant DA051124. M.A.R. was funded by NIH grant DK121883 and a NARSAD Young Investigator Award. J.A.M. was funded by NIH grants DA041781, DA042499 and DA045463. G.D.S. was funded by DA032750, DA038168 and DA048736. M.R.B. was funded by NIH grants R37DA033396 and R61DA051489 and the Mallinckrodt Endowed Professorship. M.R.B., G.D.S. and L.S.Z. were funded by NIH grant P30DA048736.

Author information

Affiliations

1. Department of Anesthesiology and Pain Medicine, University of Washington, Seattle, WA, USA

Daniel C. Castro, Corinna S. Oswell, Sean C. Piantadosi, Mark A. Rossi, Garret D. Stuber & Michael R. Bruchas

2. Departments of Anesthesiology, Neuroscience and Psychiatry,
Washington University School of Medicine, St Louis, MO, USA

Daniel C. Castro, Anthony Guglin, Jose A. Morón & Michael R.
Bruchas
3. Washington University Pain Center, Washington University School of
Medicine, St Louis, MO, USA

Daniel C. Castro, Anthony Guglin, Jose A. Morón & Michael R.
Bruchas
4. Center for Neurobiology of Addiction, Pain, and Emotion, University
of Washington, Seattle, WA, USA

Daniel C. Castro, Corinna S. Oswell, Eric T. Zhang, Christian E.
Pedersen, Sean C. Piantadosi, Mark A. Rossi, Avery C. Hunker, Larry
S. Zweifel, Garret D. Stuber & Michael R. Bruchas
5. Department of Bioengineering, University of Washington, Seattle,
WA, USA

Eric T. Zhang, Christian E. Pedersen & Michael R. Bruchas
6. Department of Pharmacology, University of Washington, Seattle, WA,
USA

Garret D. Stuber & Michael R. Bruchas

Contributions

D.C.C. designed and performed experiments, collected and analysed data, and wrote the manuscript. C.S.O., E.T.Z. and A.G. performed experiments and collected data. M.A.R. collected and analysed electrophysiological data. A.C.H. and L.S.Z. designed and analysed CRISPR virus. C.E.P designed and analysed fibre photometry data. S.C.P. designed and analysed one-photon data. M.R.B. and J.A.M. facilitated resources for generation of *Oprm1^{fl/fl} × Penk* and *Oprm1^{fl/fl} × Pdyn* mouse lines. J.A.M., L.S.Z. and

G.D.S. helped to design experiments, discuss results and write the manuscript. M.R.B. helped lead the design, analysis, oversight of experiments, discuss results, provide resources and write the manuscript.

Corresponding authors

Correspondence to Daniel C. Castro or Michael R. Bruchas.

Ethics declarations

Competing Interests

The authors declare no competing interests.

Additional information

Peer review information *Nature* thanks Brigitte Kieffer, Christian Lüscher and the other, anonymous, reviewer(s) for their contribution to the peer review of this work.

Publisher's note Springer Nature remains neutral with regard to jurisdictional claims in published maps and institutional affiliations.

Extended data figures and tables

[Extended Data Fig. 1 Endogenous MOPR activation in mNAcSh is necessary for potentiating state-dependent consummatory behavior.](#)

a. Placement map of each microinjector tip (blue = intake suppression compared to vehicle-deprived, green = intake enhancement compared to vehicle-deprived). **b.** Schematic of vehicle (ACSF, gray, top) or drug (CTAP, blue, bottom) microinjections into areas surrounding nucleus accumbens (NAc) medial shell. **c.** CTAP (blue) had no effect on ad libitum or hunger enhanced intake compared to vehicle (gray) control days when

injections were outside NAc medial shell ($n = 8$). **d**. In situ hybridization of *Pdyn*, *Penk* and *Oprm1* in NAc medial shell (scale bar = 200 μ m). **e, f**. Quantification of MOPR expression in mNAcSh. **g**. Schematic of *Oprm1*^{f/f} x Pdyn-Cre mouse line cross. **h, i**. In situ hybridization (**h**) and quantification (**i**) of *Pdyn*, *Penk* and *Oprm1* in NAc medial shell (scale bar = 200 μ m) in *Oprm1*^{f/f} x Pdyn-Cre mouse line. **j**. Loss of MOPRs on Pdyn-Cre+ neurons did not disrupt normal ad libitum or food deprived enhanced intake compared to Pdyn-Cre- littermate control mice ($n = 9$ Cre-, 10 Cre+). **k** and **l**. In situ hybridization (**k**) and quantification (**l**) of *Pdyn*, *Penk* and *Oprm1* in NAc medial shell (scale bar = 200 μ m) in *Oprm1*^{f/f} x Penk-Cre mouse line. **m**. Schematic and image of rAAV5-CMV-Cre-GFP injections into NAc medial shell of *Oprm1*^{f/f} mice. **n**. Schematic of combined viral spread map of local MOPR deletion. **o**. Schematic (top) and image (bottom) of AAV2retro-CMV-myc-NLS-Cre or AAV2retro-GFP-Cre injections into NAc (left); retrogradely labeled cells in dorsal raphe nucleus (right). All error bars represent \pm SEM and n = biologically independent mice or cells (**f, i, l**). Medians marked with orange bar. Post hoc p-values are derived from Two-way ANOVA with Sidak multiple comparisons (**c, j**).

Extended Data Fig. 2 Endogenous MOPR activation in mNAcSh is necessary for potentiating state-dependent avoidance behavior.

a. Schematic of elevated zero maze (EZM) test. Mice were tested after habituation to the test room (Unrestrained) or after 30 min of restraint stress (Restraint). **b**. Example heat plots of time spent in the open arms of the EZM in wildtype (WT, left) or *Oprm1* KO (KO, right) after no restraint (top) or 30 min of restraint (bottom). **c**. Unrestrained WT mice spent ~30% of the EZM test in the open arms. Mice exposed to restraint stress significantly reduced their exploration to 10%. Pretreatment with naloxone prevented Restraint induced avoidance. *Oprm1* KO mice did not display open arm avoidance after Restraint. Penk-Cre x cKO mice displayed normal avoidance of the open arms after Restraint ($n = 9$ WT Unrestrained, 9 WT Restrained, 8 *Oprm1* KO Unrestrained, 7 *Oprm1* KO Restrained, 8 *Oprm1*^{f/f} x Penk-Cre- Restrained, 9 *Oprm1*^{f/f} x Penk-Cre+ Restrained). **d**. Schematic of food intake assay after food deprivation or Restraint. **e**. Food

deprived mice showed normal increase in intake relative to their ad libitum test day. Mice exposed to Restraint did not increase food intake relative to their Unrestrained test day (n = 11 deprived, 10 Restrained). All error bars represent \pm SEM and n = biologically independent mice. Medians marked with orange bar. Post hoc p-values are derived from Two-way ANOVA with Sidak multiple comparisons (c, e).

Extended Data Fig. 3 LDRN Penk NAc projections express MOPRs.

a. Retrograde fluorescently tagged cells in amygdala of Penk-Cre+ mouse after injections into nucleus accumbens medial shell. **b.** (left) In situ hybridization of *Oprm1*, *Slc32a1* and *Slc17a6* in DRN (scale bar = 200 μ m). Zoomed in and channel separated images (right) of the red square in the left panel. **c.** Quantification of in situ from panel **b**. **d, e.** Schematic and image of a local injection of AAV2retro-GFP-Cre into nucleus accumbens shell (scale bar = 200 μ m). Zoomed in images of **e** are designated as red (i) and yellow (ii) boxes. **f.** (left) In situ hybridization of *Oprm1*, *Penk* and *Cre* in dorsal raphe nucleus (scale bar = 200 μ m). Zoomed in and channel separated images (right) of the red square in the left panel. **g.** Quantification of in situ from panel **f**. **h.** Schematic of CTb experiment. **i.** Fluorescently tagged CTb was injected into mNAcSh (scale bar = 200 μ m). **j.** CTb tagged cells were observed in dorsal raphe nucleus, including the lateral sites in which enkephalin neurons were labeled in Fig. [2a](#) (scale bar = 200 μ m). Red square shows zoomed in image (right) with labeled cells (depicted by white arrows). All error bars represent \pm SEM and n = biologically independent cells.

Extended Data Fig. 4 Non-DRN sites do not mediate food deprived potentiation of sucrose consumption.

a. Local MOPR deletion in paraventricular thalamus of *Oprm1*^{fl/fl} mice did not reduce food deprived enhanced intake (n = 8, paired t-test $t(7) = 9.634$, $p < 0.001$). **b.** Schematic of local caspase ablations in either ventral pallidum or basomedial amygdala. **c.** Local and cell-type specific ablation of enkephalin neurons in VP or BMA did not reduce food deprived

enhanced intake relative to Cre- control mice ($n = 8$ Cre-, 9 VP, 7 BMA). **d.** Caspase injection site confirmation in ventral pallidum (scale bar = $200\text{ }\mu\text{m}$). AAV2-FLEX-taCas3-TEPp and AAV5-hsyn-EYFP were coinfused for cell-type specific deletion, and non-specific labeling. **e, f.** Schematic and image of a local injection of AAV5-Ef1a-DIO-EYFP into DRN^{Penk} (scale bar = $200\text{ }\mu\text{m}$). **g.** Image of dorsal raphe projection fibers from e (scale bar = $200\text{ }\mu\text{m}$). **h.** oEPSC amplitude was reduced by the application of DNQX ($n = 8$). Blue shaded region indicates duration of optical stimulation. **i.** oIPSC amplitude was reduced by the application of gabazine ($n = 5$). All error bars represent \pm SEM and n = biologically independent mice or cells (**h, i**). Post hoc p-values are derived from Two-way ANOVA with Sidak multiple comparisons (**c**) or two tailed paired t-test (**h, i**).

Extended Data Fig. 5 LDRN^{MOPR}-mNAcSh projection activity is negatively modulated by sucrose consumption in an opioid receptor dependent manner.

- a.** Schematic of photometry and voluntary sucrose consumption paradigm.
- b.** Expression of GCaMP6s in DRN^{Penk} (left, scale bar = $200\text{ }\mu\text{m}$) and fiber placement in mNAcSh (scale bar = $200\text{ }\mu\text{m}$). **c.** FD increases food intake (green) relative to ad libitum intake (white), and is reduced by systemic naloxone (blue, $n = 8$). **d.** Eating microstructure across ad libitum/saline (white), food deprived/saline (green) and food deprived/naloxone (blue) test days. After food deprivation, the majority of sucrose pellets consumed during multi-pellet bouts (left), and more pellets are eaten per multi-pellet bout (right). This shift in eating behavior is blunted by naloxone. **e.** Example of raw 405nm and 470nm channels from photometry experiments.
- f.** Example of raw df/f trace highlighting specific single pellet (black) or multi-pellet (green) intake events during food deprived test day. Colored boxes on top expand color matched portions of the trace below. Orange lines indicate onset of pellet consumption. **g.** Average Z-scored trace aligned to onset of multi-pellet consumption of LDRN^{Penk}-mNAcSh terminals in FD/saline condition (green) and FD/naloxone condition (blue).
- h.** Average Z-scored trace (dark line) and error in on the ad libitum test day. When GCaMP activity is aligned to the onset of each pellet eaten in the ad libitum condition, no significant deviation in activity is observed (black,

top). When aligned to only multi-pellet bout onset, there is no deviation from baseline activity (brown, bottom). **i.** Schematic of regulated food intake paradigm. Two pellets were non-contingently delivered every 90–150 s for 30 min. Mice were tested in either FD/saline or FD/naloxone conditions. **j.** Total number of sucrose pellets eaten in the regulated intake paradigm. Mice ate significantly more pellets on the food deprivation/saline test day (green), which was reduced to baseline levels after systemic naloxone (blue) ($n = 10$). **k.** Average Z-scored trace aligned to onset of multi-pellet consumption of LDRN^{Penk}-mNAcSh. Food deprived/saline trace (green) shows rapid and sustained inhibition. Food deprived/naloxone trace (blue) shows blunted response. **l.** Heatmap of individual trials across all tested mice in food deprived/saline (green) or food deprived/naloxone test days. Orange lines indicate onset of pellet consumption. **m.** Quantification of the average Z-score twenty seconds prior to the onset of multi-pellet pellet bouts versus twenty seconds after the onset. FD/saline traces (green) show significant reductions in GCaMP6s activity whereas FD/naloxone traces (blue) do not ($n = 10$). All error bars represent \pm SEM and n = biologically independent mice. Post hoc p-values are derived from Two-way ANOVA with Sidak multiple comparisons (**c, j, m**).

Extended Data Fig. 6 MOPR activation on LDRN^{MOPR}-mNAcSh is sufficient to enhance consummatory behavior.

a. Schematic of the Tail Immersion Test. Mice were tested at time 0, were injected with morphine (5mg/kg, s.c.), then tested every 10 min for up to 60 min, then again at 90 min. **b.** WT, *Oprm1* KO, and *Oprm1* KO x Penk-Cre rescue mice all show similar baseline responses at time 0. After morphine administration, WT mice significantly increase their latency to flick their tail, whereas *Oprm1* KO and *Oprm1* KO x Penk-Cre show no analgesic response to morphine mice ($n = 5$ WT, 2 *Oprm1* KO, 6 *Oprm1* KO x Penk-Cre rescue; WT/T0 vs *Oprm1* KO/T0 $p = 0.116$, WT/T0 vs *Oprm1* KO x Penk-Cre rescue/T0 $p = 0.063$, WT/T10 vs *Oprm1* KO/T10 $p < 0.001$, WT/T10 vs *Oprm1* KO x Penk-Cre rescue/T10 $p < 0.001$, WT/T90 vs *Oprm1* KO/T90 $p < 0.001$, WT/T90 vs *Oprm1* KO x Penk-Cre rescue/T90 $p < 0.001$). Statistical differences between WT and *Oprm1* KO designated as (***) and differences between WT and *Oprm1* KO x Penk-Cre rescue

designated as (+++). **c**. Raster plots of individual licking events for one mouse, separated by trial. Only trials in which mice licked were included. **d**. Schematic of ChR2 experiments. **e**. Expression of EYFP-tagged ChR2 in LDRNPenk cell bodies (left, scale bar = 200 μ m) and fiber placement in mNAcSh (right, scale bar = 200 μ m). **f**. Penk-Cre- and Penk-Cre⁺ mice licked similar amounts for a sucrose solution in the ad libitum/No Laser condition. ChR2 photo-stimulation did not reduce licking ($n = 7$ Cre-, 6 Cre⁺). **g**. Penk-Cre- and Penk-Cre⁺ mice licked similar amounts for a sucrose solution in the WD/No Laser condition. By contrast, ChR2 photo-stimulation significantly reduced Cre⁺ licking, but not Cre- licking. **h**. Raster plots of individual licking events for one Penk-Cre⁺ mouse in the WD condition, separated by trial. Only trials in which mice licked were included. ChR2 photo-stimulation disrupted lick bout behavior compared to No Laser test days. All error bars represent \pm SEM and n = biologically independent mice or cells (**a**). Post hoc p-values are derived from Two-way ANOVA with Sidak multiple comparisons (**c, f, g**).

Extended Data Fig. 7 mNAcSh enkephalinergic ensembles are modulated by physiological state and potentiate consummatory behavior.

a. Sucrose consumed during ad libitum and food deprived test days ($n = 5$). Miniscope headmount did not disrupt normal intake behaviors. **b**. Examples of individual cell traces aligned to initiation of a multi-pellet bout. **c**. Average trace of all tracked cells aligned to bout consumption on food deprived test day. **d**. TSNE plot of clusters for multi-pellet bouts during the ad libitum state. **e**. Average trace of Onset activated neurons (cluster 1). **f**. Average trace of Pre-onset activated neurons (cluster 2). **g**. Total proportion and overlap of enkephalin neuron subpopulations modulated by multi-pellet bouts (pink), food sniffs (orange), rearing (blue), and grooming (brown). **h**. TSNE (left) and mean Z-scored traces (right) of food sniffing behavior sorted by kmeans clustering. **i**. TSNE (left) and mean Z-scored traces (right) of rearing behavior sorted by kmeans clustering. **j**. TSNE (left) and mean Z-scored traces (right) of grooming behavior sorted by kmeans clustering. All error bars represent \pm SEM (**a**) or SEM is represented by the shaded region surrounding the trace (**c, e, f, h, i, j**).

Extended Data Fig. 8 Modulation of mNAcSh or POMC-containing neurons during sucrose consumption.

a. Schematic of hM3D(Gi) (left) and hM3D(Gq) (right) DREADD experiments. **b.** Fluorescent micrograph of mCherry-tagged enkephalin cells in mNAcSh for hM3D(Gi) (left) and hM3D(Gq) (right) experiments (scale bar = 200 μ m). **c.** CNO injections suppressed hunger enhanced intake in Cre+ mice, but had no effect in Cre- mice (n = 15 Cre-, 12 Cre+). **d.** CNO injections increased intake above the already elevated food deprived intake in Penk-Cre+ mice, but had no effect in Penk-Cre- mice (n = 7 Cre-, 10 Cre+). **e.** Systemic CNO administration (3mg/kg, i.p.) suppressed the already low ad libitum intake in Penk-Cre+ mice, but did not reduce intake in Penk-Cre- mice. **f.** Systemic CNO administration (3mg/kg, i.p.) had no effect on ad libitum intake in Penk-Cre- or Penk-Cre+ mice. **g.** Gq or Gi DREADD injections into arcuate nucleus of POMC-Cre mice. **h.** Micropictograph of mCherry-tagged, DREADD-expressing cells in arcuate nucleus (scale bar = 200 μ m). **i–k.** Neither Gi nor Gq stimulation had an effect on ad libitum or food deprived intake in Cre- or Cre+ mice (n = 7 Cre-, 7 Gq, 9 Gi). All error bars represent \pm SEM and n = biologically independent mice. Post hoc p-values are derived from Two-way ANOVA with Sidak multiple comparisons (c, d, e, f, i, j, k).

Extended Data Fig. 9 Endogenous mu-opioid peptide within mNAcSh is necessary for potentiating consummatory behavior.

a. FISH (scale bar = 200 μ m) of mNAcSh caspase injections. **b.** FISH quantification of (a). **c.** FISH (scale bar = 200 μ m) of mNAcSh CRISPR injections. **d.** FISH quantification of (c). **e.** Schematic of CRISPR virus development and validation. **f.** Sequencing of GFP+ nuclei: (Top) sgPenk sequence with PAM underlined and SaCas9 cut site indicated by black arrow. (Middle) Sanger sequencing results displaying multiple peaks beginning at the SaCas9 predicted cut site. (Bottom) Top ten mutations at cut site with the percent of occurrence on the left. Insertions: underlined. Deletions: marked with “-“. Affected sites after SaCas9 insertion: shaded brown. **g.** Percent of wild type (black), deletions (brown), insertions (pink), and base changes (white) as percent of total reads for GFP+ and GFP-

nuclei. **h**. Frequency distribution of insertions (pink) and deletions (brown) for Penk from GFP+ nuclei. **i**. Sanger sequencing results displaying no unusual peaks beginning at the SaCas9 predicted cut site. **j**. Unilateral hits or bilateral misses of NAc medial shell with the CRISPR mediated deletion of enkephalin did not reduce food deprived enhanced intake ($n = 4$). **k**. Fluorescent micrograph of CRISPR virus expression in dorsal raphe nucleus. **l**. Deletion of enkephalin from dorsal raphe nucleus did not reduce food deprived enhanced intake ($n = 8$) **m**. Deletion of dynorphin in NAc medial shell did not reduce food deprived enhanced intake ($n = 7$). **n**. Heatmap of individual trials across all tested mice in CRISPR/saline (orange) or Control/saline (gray) test days. Orange lines indicate onset of pellet consumption. **o**. Average Z-scored trace aligned to onset of multi-pellet consumption of LDRNPenk-mNAcSh after systemic naloxone injections. Control-treated mice (blue) show blunted inhibition. CRISPR-expressing trace (brown) shows negligible and phasic inhibition. **p**. Heatmap of individual trials across all tested mice in CRISPR/naloxone (orange) or Control/naloxone (blue) test days. **q**. Quantification of the average Z-score twenty seconds prior to the onset of multi-pellet pellet bouts versus twenty seconds after the onset. Neither Control traces (blue) nor CRISPR traces (brown) show significant deviations in GCaMP activity. Some mice did not lick on naloxone treated days and were therefore not included in this analysis (CRISPR $n = 3$, Control $n = 3$). All error bars represent \pm SEM and $n =$ biologically independent mice or cells (**b**, **d**). Post hoc p-values are derived from Two-way ANOVA with Sidak multiple comparisons (**q**) or two-tailed paired t-test (**j**, **l**, **m**).

Extended Data Fig. 10 A LDRN^{MOPR}-mNAcSh^{Penk} circuit mediates potentiation of consummatory behaviors.

Schematic of voluntary sucrose consumption task (upper left) and LDRN-mNAcSh projection (upper right). Effects of LDRN^{MOPR}-mNAcSh^{Penk} manipulations on behavior (lower left) and schematic of hypothesized physiology (lower right).

Extended Data Table 1 Key resources

Extended Data Table 2 Overview of mouse lines and experiments

Extended Data Table 3 Total number of test days per behavior test

Extended Data Table 4 Main figure exact statistics

Supplementary information

Supplementary Discussion

This text considers how the data described in this manuscript are contextualized by known and unknown information. It examines potential circuits, psychological functions, and intracellular signalling mechanisms of interest.

Reporting Summary

Supplementary Video 1

This video demonstrates endoscopic recording of GCaMP6s labelled *Penk-cre* neurons in mNAcSh in an awake and behaving mouse. Behavioural and imaging videos are temporally synchronized.

Source data

Source Data Fig. 1

Source Data Fig. 2

Source Data Fig. 3

Source Data Fig. 5

Rights and permissions

Reprints and Permissions

About this article

Cite this article

Castro, D.C., Oswell, C.S., Zhang, E.T. *et al.* An endogenous opioid circuit determines state-dependent reward consumption. *Nature* **598**, 646–651 (2021). <https://doi.org/10.1038/s41586-021-04013-0>

- Received: 20 January 2021
- Accepted: 09 September 2021
- Published: 13 October 2021
- Issue Date: 28 October 2021
- DOI: <https://doi.org/10.1038/s41586-021-04013-0>

Share this article

Anyone you share the following link with will be able to read this content:

[Get shareable link](#)

Sorry, a shareable link is not currently available for this article.

[Copy to clipboard](#)

Provided by the Springer Nature SharedIt content-sharing initiative

[Opioid peptide signal in the brain makes mice hungrier for reward](#)

- Lola Welsch
- Brigitte L. Kieffer

News & Views 13 Oct 2021

| [Section menu](#) | [Main menu](#) |

- Article
- Open Access
- [Published: 13 October 2021](#)

Leprosy in wild chimpanzees

- [Kimberley J. Hockings](#) ORCID: [orcid.org/0000-0002-6187-644X^{1,2}](https://orcid.org/0000-0002-6187-644X),
- [Benjamin Mubemba](#) ORCID: [orcid.org/0000-0002-5266-3602^{3,4 na1}](https://orcid.org/0000-0002-5266-3602),
- [Charlotte Avanzi](#) ORCID: [orcid.org/0000-0002-1062-4058^{5,6,7,8 na1}](https://orcid.org/0000-0002-1062-4058),
- [Kamilla Pleh](#)^{3,9 na1},
- [Ariane Dux](#)^{3 na1},
- [Elena Bersacola](#) ORCID: [orcid.org/0000-0003-3814-8687^{1,2 na1}](https://orcid.org/0000-0003-3814-8687),
- [Joana Bessa](#)^{2,10 na1},
- [Marina Ramon](#)^{1 na1},
- [Sonja Metzger](#)^{3,9},
- [Livia V. Patrono](#)³,
- [Jenny E. Jaffe](#)^{3,9},
- [Andrej Benjak](#)¹¹,
- [Camille Bonneaud](#)¹,
- [Philippe Busso](#)⁵,
- [Emmanuel Couacy-Hymann](#)¹²,
- [Moussa Gado](#)¹³,
- [Sebastien Gagneux](#) ORCID: [orcid.org/0000-0001-7783-9048^{7,8}](https://orcid.org/0000-0001-7783-9048),
- [Roch C. Johnson](#)^{14,15},
- [Mamoudou Kadio](#)¹⁶,
- [Joshua Lynton-Jenkins](#) ORCID: [orcid.org/0000-0003-1657-7843¹](https://orcid.org/0000-0003-1657-7843),
- [Irina Morozova](#)¹⁷,
- [Kerstin Mätz-Rensing](#)¹⁸,
- [Aissa Regalla](#)¹⁹,
- [Abílio R. Said](#)¹⁹,
- [Verena J. Schuenemann](#)¹⁷,
- [Samba O. Sow](#)¹⁶,
- [John S. Spencer](#)⁶,
- [Markus Ulrich](#)³,
- [Hyacinthe Zoubi](#)²⁰,
- [Stewart T. Cole](#) ORCID: [orcid.org/0000-0003-1400-5585^{5,21}](https://orcid.org/0000-0003-1400-5585),

- [Roman M. Wittig](#) ORCID: [orcid.org/0000-0001-6490-4031^{9,22}](https://orcid.org/0000-0001-6490-4031),
- [Sebastien Calvignac-Spencer](#) ORCID: [orcid.org/0000-0003-4834-0509³](https://orcid.org/0000-0003-4834-0509) &
- [Fabian H. Leendertz](#) ORCID: [orcid.org/0000-0002-2169-7375^{3,23}](https://orcid.org/0000-0002-2169-7375)

Nature volume **598**, pages 652–656 (2021)

- 21k Accesses
- 1484 Altmetric
- [Metrics details](#)

Subjects

- [Anthropology](#)
- [Bacterial infection](#)
- [Pathogens](#)

Abstract

Humans are considered as the main host for *Mycobacterium leprae*¹, the aetiological agent of leprosy, but spillover has occurred to other mammals that are now maintenance hosts, such as nine-banded armadillos and red squirrels^{2,3}. Although naturally acquired leprosy has also been described in captive nonhuman primates^{4,5,6,7}, the exact origins of infection remain unclear. Here we describe leprosy-like lesions in two wild populations of western chimpanzees (*Pan troglodytes verus*) in Cantanhez National Park, Guinea-Bissau and Taï National Park, Côte d'Ivoire, West Africa. Longitudinal monitoring of both populations revealed the progression of disease symptoms compatible with advanced leprosy. Screening of faecal and necropsy samples confirmed the presence of *M. leprae* as the causative agent at each site and phylogenomic comparisons with other strains from humans and other animals show that the chimpanzee strains belong to different and rare genotypes (4N/O and 2F). These findings suggest that *M. leprae* may be circulating in more wild animals than suspected, either as a result of exposure to humans or other unknown environmental sources.

[Download PDF](#)

Main

Leprosy is a neglected tropical disease caused by the bacterial pathogens *M. leprae* and the more recently discovered *Mycobacterium lepromatosis*^{8,9}. In humans, the disease presents as a continuum of clinical manifestations with skin and nerve lesions of increasing severity, from the mildest tuberculoid form (or paucibacillary) to the most severe lepromatous type (or multibacillary)¹⁰. Symptoms develop after a long incubation period ranging from several months to 30 years, averaging 5 years in humans. As a result of sensory loss, leprosy can lead to permanent damage and severe deformity¹¹. Although leprosy prevalence has markedly decreased over recent decades, approximately 210,000 new human cases are still reported every year, of which 2.3% are located in West Africa¹². Transmission is thought to occur primarily between individuals with prolonged and close contact via aerosolized nasal secretions and entry through nasal or respiratory mucosae, but the exact mechanism remains unclear^{13,14}. The role of other routes, such as skin-to-skin contact, is unknown.

Leprosy-causing bacteria were once thought to be obligate human pathogens¹. However, they can circulate in other animal hosts in the wild, such as nine-banded armadillos (*Dasypus novemcinctus*) in the Americas and red squirrels (*Sciurus vulgaris*) in the UK^{2,3}. Although initial infection was most probably incidental and of human origin, secondary animal hosts can subsequently represent a source of infection to humans^{15,16,17,18}. In captivity, nonhuman primates, such as chimpanzees (*Pan troglodytes*)⁴, sooty mangabeys (*Cercocebus atys*)^{5,6} and cynomolgus macaques (*Macaca fascicularis*)⁷, have been known to develop leprosy without any obvious infectious source. However, due to their captive status, it is unclear how they acquired *M. leprae* and whether these species can also contract leprosy in the wild.

Here, we report leprosy infections and their disease course in two wild populations of western chimpanzees (*P. troglodytes verus*) in Cantanhez National Park (CNP), Guinea-Bissau, and in Tai National Park (TNP), Côte d'Ivoire, using a combination of camera trap and veterinary monitoring (Extended Data Fig. 1a and Supplementary Notes 1 and 2). From analyses of faecal samples and postmortem tissues, we identified *M. leprae* as the causative agent of the lesions observed and determined the phylogenetic placement of the respective strains based on their complete genome sequences.

Chimpanzees at CNP are not habituated to human observers, precluding systematic behavioural observations. Longitudinal studies necessitate the use of camera traps, which we operated between 2015 and 2019. Of 624,194 data files (videos and photographs) obtained across 211 locations at CNP (Extended Data Fig. 1b, Extended Data Table 1 and Supplementary Table 1), 31,044 (5.0%) contained chimpanzees. The number of independent events (images separated by at least 60 min) totalled 4,336, and of these, 241 (5.6%) contained chimpanzees with severe leprosy-like lesions, including four clearly identifiable individuals (two adult females and two adult males)

across three communities (Extended Data Fig. 2 and Supplementary Note 2). As with humans, paucibacillary cases in chimpanzees may be present but easily go undetected. Such minor manifestations of leprosy are not reported. All symptomatic chimpanzees showed hair loss and facial skin hypopigmentation, as well as plaques and nodules that covered different areas of their body (limbs, trunk and genitals), facial disfigurement and ulcerated and deformed hands (claw hand) and feet (Fig. 1a–c), consistent with a multibacillary form of the disease. Longitudinal observations showed progression of symptoms across time with certain manifestations similar to those described in humans (such as progressive deformation of the hands) (Extended Data Fig. 2 and Supplementary Videos 1–3). To confirm infection with *M. leprae*, we collected faecal samples and tested them with two nested polymerase chain reaction (PCR) assays targeting the *M. leprae*-specific repetitive element (RLEP) and 18 kDa antigen gene. One out of 208 DNA extracts from CNP was positive in both assays and a second was positive only in the more sensitive RLEP-PCR¹⁹ (Extended Data Table 2, Supplementary Table 2 and Supplementary Note 3). Microsatellite analyses of the two positive samples confirmed that they originated from two distinct female individuals (Supplementary Note 4 and Supplementary Tables 3 and 4). Our results suggest that *M. leprae* is the most likely cause of a leprosy-like syndrome in chimpanzees from CNP.

Fig. 1: Clinical manifestations of leprosy in three chimpanzees at CNP, Guiné-Bissau and TNP, Côte d'Ivoire.

 **figure1**

a–c, Clinical signs of leprosy in two adult female chimpanzees in CNP (images extracted from camera traps). **a**, Rita has large hypopigmented nodules covering the entire body; disfigurement of the face, ears, hands and feet (ulcerated lesions and swelling). **b**, Rita has extensive plaques covering all limbs, with hair loss. **c**, Brinkos has large hypopigmented nodules covering the entire face, with extreme disfigurement of the face and ears, and ulcerated plaques on the arms and the nipples. **d–g**, Clinical signs of leprosy in an adult male chimpanzee, Woodstock, at TNP. **d**, Multiple hypopigmented nodules on the ears, brow ridges, eyelid margins, nostrils, lips and the area between the upper lip and the nose. **e**, Hypopigmentation and swelling of the hands with ulcerations and hair loss on the dorsal side of the joints. **f**, Claw hand with nail loss and abnormal overgrowth of fingernails. **g**, Scrotal reddening and ulceration with fresh blood.

At TNP, chimpanzees are habituated to the presence of researchers and have been followed daily since 1979. In addition, necropsy samples have been collected from all dead individuals recovered since 2000. In June 2018, researchers first noticed leprosy-

like lesions on Woodstock, an adult male chimpanzee from one of the three habituated communities (south) (Extended Data Fig. 1c). The initial small nodules on the ears, lips and under the eye became more prominent and were followed by nodules on the eyebrows, eyelids, nostrils, ears, lips and face. The skin on facial nodules, hands, feet and testicles became hypopigmented and the loss and abnormal growth of nails was observed (Fig 1d–g, Extended Data Fig. 3 and Supplementary Videos 4 and 5).

Mycobacterium leprae DNA was detected in all samples from June 2018 (Extended Data Table 2, Supplementary Table 2 and Supplementary Note 2). Here, continuous noninvasive detection of *M. leprae* was associated with the onset and evolution of a leprosy-like disease.

Retrospective PCR screening of all chimpanzee spleen samples ($n = 38$ individuals) from the TNP necropsy collection led to the identification of *M. leprae* DNA in two further individuals. An adult female from the same community named Zora, who had been killed by a leopard in 2009, tested positive in both PCR assays. The presence of *M. leprae* DNA was confirmed by PCR in various other organs (Extended Data Table 2). Retrospective analyses of photographs taken in the years before her death showed progressive skin hypopigmentation and nodule development since 2007 (Extended Data Fig. 3). Formalin-fixed skin samples (hands and feet) were prepared for histopathological examination using haematoxylin and eosin as well as Fite-Faraco stains. The skin presented typical signs of lepromatous leprosy characterized by a diffuse cutaneous cell infiltration in the dermis and the subcutis clearly separated from the basal layer of the epidermis (Extended Data Fig. 4a). We detected moderate numbers of acid-fast bacilli (single or in clumps) within histiocytes, indicative of *M. leprae* (Extended Data Fig. 4b). As antibodies against the *M. leprae*-specific antigen phenolic glycolipid-I (PGL-I) are a hallmark of *M. leprae* infection in humans²⁰, we also performed a PGL-I lateral flow rapid test²¹ on a blood sample from this individual, which showed strong seropositivity (Extended Data Fig. 4c). Faecal samples collected in the years before Zora's death contained *M. leprae* DNA from 2002 onwards, implying at least 7 years of infection (Extended Data Table 2). In this case, disease manifestations, histopathological findings, serological and molecular data, as well as the overall course of the disease, all unambiguously point towards *M. leprae*-induced leprosy.

To ascertain whether other individuals in the south community of TNP were infected at the time of Zora's death in 2009, cross-sectional screening of contact animals ($n = 32$) was performed by testing all available faecal samples ($n = 176$) collected in 2009 (Supplementary Table 2). Three other chimpanzees were PCR-positive in single samples, including Woodstock. Clinical symptoms of leprosy have not been observed in other individuals, despite daily monitoring of south community members for 20 years and of neighbouring communities for 40 years^{22,23}. Considering that, over this

period, 467 individuals have been observed, it seems that leprosy is a rare disease with low transmission levels in these chimpanzee communities.

To characterize the *M. leprae* strains causing leprosy in wild chimpanzees and to perform phylogenomic comparisons, we selected DNA extracts that were positive in both the RLEP and the less-sensitive 18-kDa PCR, which indicates relatively high levels of *M. leprae* DNA. For TNP, we selected individuals that were positive in multiple samples. Following targeted enrichment using hybridization capture, samples were subjected to Illumina sequencing. Sufficient *M. leprae* genome coverage was obtained for sample GB-CC064 (Guinea-Bissau) and for Zora (Côte d'Ivoire) with mean depth of $39.3\times$ and $25.8\times$, respectively (Extended Data Table 2 and Supplementary Table 5). We generated 21 *M. leprae* genomes from human biopsies from five West African countries (Niger, Mali, Benin, Côte d'Ivoire and Senegal) and depth of coverage ranged from $4.7\times$ to $170\times$. We assembled a dataset that included the genomes generated in this study and all previously available *M. leprae* genomes. Of the total 286 genomes, 64 originated from six West African countries (Extended Data Fig. 5 and Supplementary Note 5).

Bayesian and maximum-parsimony analyses (Extended Data Figs. 6 and 7) place the strain from Guinea-Bissau (GB-CC064) on branch 4, where it clusters outside the standard genotypes 4N, 4O and 4P, but within the so-called 4N/O genotype^{24,25} (Fig. 2a,c). This 4N/O genotype is rare and only comprises five *M. leprae* strains; one strain (Ng13-33) from a patient in Niger, two strains (2188-2007 and 2188-2014) obtained from a single patient in Brazil (of 34 strains in Brazil)²⁶ and two strains from two captive nonhuman primates originating from West Africa (Ch4 and SM1)²⁵. The branching order of these five strains and GB-CC064 was unresolved in our analyses, with a basal polytomy suggestive of star-like diversification within this genotype, and within the group comprising all genotype 4 strains (4N/O, 4N, 4P and 4O). Divergence from the most recent common ancestor for this group is estimated to have occurred in the sixth century ad (mean divergence time, 1,437 years ago, 95% highest posterior density (HPD) 1,132–1,736 years ago). The strain that infected Zora in Côte d'Ivoire, designated TNP-418, belongs to branch 2F, within which, the branching order was also mostly unresolved (Fig. 2a,b). The branch is currently composed of human strains from medieval Europe ($n = 7$) and modern Ethiopia ($n = 2$), and this genotype has thus far never been reported to our knowledge in West Africa. Bayesian analysis estimated a divergence time during the second century ad (mean of 1,873 years ago (95% HPD 1,564–2,204 years ago)), similar to previous predictions²⁷.

Fig. 2: Phylogeny of *M. leprae* strains from human and animal hosts.

 **figure2**

a, Bayesian dated phylogenetic tree of 278 *M. leprae* genomes including the two new chimpanzee strains (in bold red). Hypermutated samples with mutations in the *n*th gene were excluded from the analysis. The tree is drawn to scale, with branch lengths representing years of age. Median estimates of node ages are shown in black above branches; 95% HPD intervals are shown in grey. Some *M. leprae* branches are collapsed to increase readability. **b**, Maximum parsimony tree of branch 2F. **c**, Maximum parsimony tree of the branch 4. The tree was initially constructed using 286 genomes (Supplementary Table 6), including 2 new chimpanzee strains (in bold red) and 21 new genomes from West Africa (in bold), 500 bootstrap replicates and *M. lepromatosis* as outgroup. Sites with missing data were partially deleted (80% genome coverage cutoff), resulting in 4,470 variable sites used for the tree calculation. Subtrees corresponding to branches were retrieved in MEGA7⁶⁵. Corresponding genotypes are indicated on the side of each subtree. Samples are binned according to geographical origin as given in the legend. Scale bars (**b, c**), number of nucleotide

substitutions. Animal silhouettes are available under Public Domain licence at PhyloPic (<http://PhyloPic.org/>).

Samples from Woodstock did not yield enough Illumina reads to reconstruct full genomes for phylogenomic analysis. However, single-nucleotide polymorphisms (SNPs) recovered from the few available Illumina reads and Sanger sequences derived from PCR products allowed us to assign this second *M. leprae* strain from Côte d'Ivoire to the same genotype as TNP-418 (Supplementary Note 5). Overall, phylogenomic analyses show that *M. leprae* strains in chimpanzee populations at CNP and TNP are not closely related.

The finding of *M. leprae*-induced leprosy in wild chimpanzee populations raises the question of the origin(s) of these infections. *Mycobacterium leprae* is considered a human-adapted pathogen and previous cases of leprosy affecting wildlife were compatible with anthroponosis. Therefore, the prime hypothesis would be human-to-chimpanzee transmission. Potential routes of transmission include direct (such as skin-to-skin) contact and inhalation of respiratory droplets and/or fomites, with the assumption that, in all cases, prolonged and/or repeated exposure is required for transmission¹¹. Chimpanzees at CNP are not habituated to humans and are not approached at distances that would allow for transmission via respiratory droplets. Although these chimpanzees inhabit an agroforest landscape and share access to natural and cultivated resources with humans²⁸, present-day human–chimpanzee direct contact is uncommon. The exact nature of historic human–chimpanzee interactions at CNP remains, however, unknown. For example, robust data on whether chimpanzees were kept as ‘pets’ or were hunted for meat are lacking. Long-term human–chimpanzee coexistence in this shared landscape makes humans the most probable source of chimpanzee infection. However, multiple individuals from several chimpanzee communities across CNP show symptomatic leprosy demonstrating that *M. leprae* is now probably transmitted between individuals within this population.

At TNP, the south chimpanzee community is distant from human settlements and agriculture. Human-to-animal transmission of pathogens has been shown at TNP^{29,30} but involved respiratory pathogens (pneumoviruses and human coronavirus OC43) that transmit easily and do not require prolonged exposure. In addition, *M. leprae* is thought to be transmitted from symptomatic humans³¹ and no cases of leprosy have been reported among researchers or local research assistants. Although a human source is impossible to rule out, low human contact coupled with the rarity of the *M. leprae* genotype detected in TNP chimpanzees among human populations in West Africa suggests that recent human-to-chimpanzee transmission is unlikely. This is supported by the absence of drug-resistant mutations (Supplementary Note 6). The relatively old age of the lineage leading to the chimpanzee strain at TNP nevertheless raises the possibility of an ancient human-to-chimpanzee transmission. However, the

human population density 1,500–2,000 years ago was probably even lower than it is currently, making this unlikely. If such an ancient transmission had occurred and the bacterium had persisted for a long time in chimpanzees, it should have spread more broadly as observed in *M. leprae*-infected squirrels and armadillos^{3,16,17}. Therefore, an ancient human-to-chimpanzee transmission is not the most plausible mechanism to explain the presence of *M. leprae* in chimpanzees at TNP.

These findings may be better explained by the presence of a nonhuman leprosy reservoir. As chimpanzees hunt frequently, transmission may originate from their mammalian prey³². Nonhuman primates are the most hunted prey at TNP³³ and are hunted at CNP (Supplementary Note 3). Chimpanzees also consume other mammalian prey such as ungulates. Notably, this scenario assumes that the animal host range of *M. leprae* is even broader than is currently known. Perhaps more intriguingly, an environmental source may be at the origin of chimpanzee infections. Other mycobacteria can survive in water, including *M. ulcerans* and other non-tuberculous mycobacteria^{34,35}, and molecular investigations have reported that *M. leprae* can survive in soil³⁶. Experimental data also show that *M. leprae* multiplies in amoebae³⁷, arthropods³⁸ and ticks³⁹, which could contribute to the persistence of the bacteria in the environment. Testing these hypotheses will require thorough investigation of the distribution of *M. leprae* in wildlife and the environment and so shed light on the overall transmission pathways of the pathogen.

Methods

Study sites

Observational study and sample collections were performed at CNP in southern Guinea-Bissau and TNP in western Côte d'Ivoire (Extended Data Fig. 1a). CNP (1,067 km²) comprises the Cubucaré peninsula in the sector of Bedanda, with the northeast of the park bordering the Republic of Guinea. The landscape at CNP consists of a mosaic of mainly mangroves, subhumid forest patches, savannah grassland and woodland, remnant forest strips dominated by palm groves as well as agriculture⁴⁰. There are approximately 200 villages and settlements within the borders of the park, with an estimated human population of 24,000 individuals who comprise several ethnic groups⁴¹. Chimpanzees are not hunted for consumption within CNP due to local cultural beliefs and taboos⁴² but are sometimes killed in retaliation for foraging on crops^{43,44}. There is a minimum of 12 chimpanzee communities at CNP⁴¹, all unhabituated to researchers, with approximately 35–60 individuals per community^{45,46}. Numerous other wildlife taxa inhabit CNP, including six other nonhuman primate species^{41,47}.

The TNP (5,082 km²) consists of an evergreen lowland rainforest and is the largest remaining primary forest fragment in West Africa. It is home to a wide range of mammals that include 11 different nonhuman primate species^{48,49}. There are no settlements or agricultural areas inside the National Park. As of March 2021, the three habituated communities, north, south and east, comprised 22, 37 and 32 individuals, respectively, although community sizes have varied over time. Systematic health monitoring of these communities has been ongoing since 2000²³.

Longitudinal observations and health monitoring

At CNP, camera traps (Bushnell Trophy Cam models 119774, 119877 and 119875) were deployed at 211 locations, including across different habitat types (forest, mangrove-forest edge and orchards) within the home range of 8 of the 12 putative chimpanzee communities (Supplementary Table 1). Camera traps were set up over six data collection periods from 2015 to 2019 (Extended Data Table 1). Targeted camera traps were deployed to record and monitor chimpanzee behaviour and disease occurrence. To maximize the chances of recording specific behaviours and to identify leprosy-like symptoms in individuals, targeted camera traps were set up in locations that chimpanzees were known to use most often, sometimes in clusters, precluding uniform survey designs. Targeted camera traps were set up in video mode and were active 24 h per day. When triggered, targeted cameras recorded 10 to 60 s of video with a minimum interval of 0.6 s or 2 s, depending on the camera trap model. Furthermore, systematically placed camera traps were used to obtain measures of wildlife occurrence and habitat use across the heterogeneous landscape⁴¹. Systematic camera traps were deployed across central CNP, at a minimum distance of 1 km between sampling points, as well as within the home range of one chimpanzee community (Caiquene-Cadique) and were spaced at least 500 m from one another. The camera traps pointed towards animal paths (often chimpanzee paths), small human paths also used by wildlife and other areas presenting signs of animal activity. Systematic camera traps were set up to record three consecutive photographs when triggered. The GPS coordinates, habitat type, date, time and site description were recorded when setting up individual camera traps (targeted and systematic). Opportunistic observations of chimpanzees at CNP were made in 2013, during which chimpanzees were photographed and/or filmed using digital cameras.

Chimpanzees at TNP are fully habituated to human observers and all individuals in the habituated communities are individually identified. Behavioural and health monitoring of chimpanzees at TNP involves daily observation of habituated individuals by an interdisciplinary team comprising primatologists and veterinarians; investigations of wildlife mortality causes through necropsies on all animal carcasses found in the research area; and the collection of noninvasive samples such as faecal samples, laboratory investigations and the communication of the results to the park

management for corrective and preventive measures²². Abnormalities in behaviour or clinical signs of disease are immediately reported and followed by detailed observation by the on-site veterinarian. To reduce the risk of transmission of human diseases to the chimpanzees, stringent hygiene measures have been put in place, including an initial 5-day quarantine for observers, keeping a distance of at least 7 m and obligatory wearing of masks, with only healthy observers allowed to work in the forest^{50,51}.

Faecal and necropsy sample collection

At CNP, chimpanzee faecal samples were collected between July 2017 and December 2018. The date and putative chimpanzee community were recorded for each faecal sample. As defecation was rarely observed and to prevent the collection of redundant samples from the same individual, we avoided multiple samples found under the same chimpanzee nest and paid special attention if multiple samples were found in proximity on trails^{45,52,53}. All samples were collected with the aid of a wooden spatula and stored at ambient temperature in 15-ml tubes containing NAP buffer⁵⁴. All samples were sent to the Robert Koch Institute for laboratory analysis. Even though chimpanzee faeces are easily distinguishable from those of other species and were found in areas where chimpanzees had recently been present with associated signs such as feeding remains or knuckle prints, we genetically confirmed the presence of chimpanzee DNA in faecal samples that tested positive in either of the *M. leprae* PCRs or the mammal PCR for diet analysis (Supplementary Note 3).

At TNP, the long-term health monitoring programme includes continuous collection of faecal and urine samples from known adult chimpanzees. Faeces are collected right after defecation, transferred to 2-ml cryotubes with the aid of a plastic spatula and frozen in liquid nitrogen the same day. A full necropsy is systematically performed on chimpanzees found dead by the on-site veterinarian. Necropsies follow a standardized biosafety protocol due to the occurrence of anthrax, Ebola and monkeypox in the area. This includes the use of full personal protective equipment and rigorous disinfection measures. Tissue samples of several internal organs are taken if the state of carcass decomposition allows. After collection, all samples are first stored in liquid nitrogen and subsequently shipped on dry ice to the Robert Koch Institute for analyses.

DNA extraction from faeces and necropsy samples

DNA extractions were performed at the Robert Koch Institute in a laboratory that has never been used for molecular *M. leprae* investigations. DNA was extracted from faecal and necropsy samples using the GeneMATRIX stool DNA purification kit (EURx) and the DNeasy Blood and Tissue kit (QIAGEN), respectively, following the manufacturers' instructions. Extracted DNA was then quantified using the Qubit

dsDNA HS Assay kit (Thermo Fisher Scientific) and subsequently stored at -20°C until further use.

Genetic identification of samples from infected chimpanzees at CNP

To determine whether faecal samples positive for *M. leprae* belonged to one or two individuals at CNP, we amplified chimpanzee DNA at 11 microsatellite loci and one sexing marker⁵⁵. Owing to the small quantity of starting DNA, not all loci were amplified and in some cases the amplification quality was low, affecting our ability to confidently interpret allele peak profiles (for example, sample GB-CC064 failed to amplify for 5 out of the 11 loci) (Supplementary Note 4).

Molecular screening of *M. leprae* in faecal and necropsy samples

Mycobacterium leprae DNA was searched for using two nested PCR systems targeting the distinct but conserved repetitive element RLEP and the 18-kDa antigen gene as previously described (Extended Data Table 3). As 37 copies of RLEP are present in the *M. leprae* genome, this assay is considered to be more sensitive than 18 kDa, for which there is only a single copy. To prevent contamination at the laboratory at the Robert Koch Institute and to enable us to identify whether it occurs, we followed these procedures: (1) separate rooms were used for preparation of PCR master mixes and the addition of DNA in the primary PCR; (2) the addition of the primary PCR product in the nested PCR in another separate room; and (3) dUTPs were used for all PCRs instead of dNTPs. For both assays, primary PCRs were performed in 20- μl reactions: up to 200 ng of DNA was amplified using 1.25 U of high-fidelity Platinum Taq polymerase (Thermo Fisher Scientific), 10 \times PCR buffer, 200 μM dUTPs, 4 mM MgCl₂ and 200 nM of both forward and reverse primers. The thermal cycling conditions for the primary and nested PCRs were as follows: denaturation at 95°C for 3 min, followed by 50 cycles of 95°C for 30 s, 55 $^{\circ}\text{C}$ (18 kDa primers) or 58 $^{\circ}\text{C}$ (RLEP primers) for 30 s, and 72 $^{\circ}\text{C}$ for 1 min as well as an elongation step at 72 $^{\circ}\text{C}$ for 10 min. For nested PCRs, 2 μl of a 1:20 dilution of the primary PCR product was used as a template. Molecular-grade water was used as a template-free control. PCR products were visualized on a 1.5% agarose gel stained with GelRed (Biotium). Bands of the expected size were purified using the Purelink Gel extraction kit (Thermo Fisher Scientific). Both RLEP and 18-kDa nested PCR products are too short for direct Sanger sequencing. Therefore, fusion primers (primary PCR primers coupled with M13F and M13R primers) (Extended Data Table 3) were used for further amplification of the cleaned PCR products, applying the same conditions as in the primary PCR, but running only for 25 cycles. The resulting extended PCR products were then enzymatically cleaned using the ExoSAP-IT PCR Product Cleanup assay (Thermo Fisher Scientific) and Sanger sequenced using M13 primers. Resulting

sequences were compared to publicly available nucleotide sequences using the Basic Local Alignment Search Tool (BLAST)⁵⁶.

Histopathology

To further confirm the infection, skin samples were sent to the German Primate Center in Göttingen, Germany for histopathological analyses. Samples were immersion-fixed in 10% neutral-buffered formalin, embedded in paraffin and stained with standard haematoxylin and eosin using the Varistain Gemini staining automat (Thermo Fisher Scientific). Samples were also stained with Fite-Faraco stain for the identification of acid-fast bacilli.

Serology

A whole-blood sample from Zora collected during the necropsy in 2009 was tested for the presence of the *M. leprae*-specific anti-PGL-I antibodies using a chromatographic immunoassay developed for use with human blood following the instructions provided by the test manufacturers with a 1:10 diluted whole-blood sample. This rapid lateral flow test was produced by R. Cho using the synthetic ND-O-BSA antigen with financial support of the NIH/NIAID Leprosy Research Materials contract AI-55262 at Colorado State University. Test results were interpreted at 5 and 10 min. Human serum from a patient with multibacillary leprosy donated by J. S. Spencer, Colorado State University, was used as a positive control. Whole blood collected during the necropsy of a chimpanzee (Olivia) at TNP who died of acute respiratory disease in 2009 was used as a negative control.

Library preparation, genome-wide capture and high-throughput sequencing for nonhuman primate samples

Selected *M. leprae*-positive faecal and necropsy samples (Supplementary Table 2) were converted into dual-indexed libraries using the NEBNext Ultra II DNA Library Prep kit (New England Biolabs)^{57,58}. To reconstruct whole genomes, libraries were target-enriched for *M. leprae* DNA using in-solution hybridization capture with 80-nt RNA baits designed to cover the whole *M. leprae* genome (twofold tiling; design can be shared upon request to the corresponding author) and following the myBaits protocol as previously described²⁵. Around 1.5 µg of each DNA library was captured in single or pooled reactions. Two rounds of 24-h hybridization capture were performed followed by a post-amplification step for each using the KAPA HiFi HotStart Library Amplification kit with 12 to 16 cycles to generate around 200 ng of enriched library per sample. Finally, enriched libraries were purified using the silica-based MinElute reaction cleanup kit (QIAGEN) followed by quantification with the

KAPA library quantification kit (Roche). Libraries were then normalized and pooled across sequencing lanes on an Illumina NextSeq 500 for sequencing with a mid-output kit v.2 for 300 cycles (Illumina).

Sample collection, DNA extraction, library preparation, genome-wide capture and high-throughput sequencing of human specimens

Samples (skin biopsies or DNA extracts) from patients with leprosy from five West African countries who had a positive bacillary index (Niger ($n = 5$), Mali ($n = 8$), Benin ($n = 6$), Côte d'Ivoire ($n = 1$) and Senegal ($n = 1$)) were obtained from the respective National Leprosy Control Programmes in the framework of the leprosy drug-resistance surveillance programmes or from previous investigation⁵⁹.

DNA was extracted from skin biopsies using the total DNA extraction method as described previously⁶⁰. DNA was quantified with a Qubit fluorometer using the Qubit dsDNA BR Assay kit (Thermo Fisher Scientific) before library preparation. DNA libraries were prepared using the KAPA Hyper Prep kit (Roche) as per the manufacturer's recommendation using KAPA Dual-Indexed Adapter (Roche) followed by in-solution capture enrichment with 80-nt RNA baits with 2 \times tiling density for 48 h at 65 °C as described previously⁶⁰. Post-capture amplification was performed with seven cycles. Enriched libraries were purified using a 1 \times ratio of KAPA Pure beads (Roche) followed by quantification with the KAPA library quantification kit (Roche) and quality control of the fragment with the Agilent 2200 TapeStation (Agilent Technologies). Libraries were then normalized and pooled across sequencing lanes on an Illumina NextSeq 500 for sequencing with a high output kit v.2 for 75 cycles (Illumina).

Genomic data analysis

Raw reads were processed as described elsewhere²⁴. Putative unique variants of GB-CC064 and TNP-418 strains were manually checked and visualized using the Integrative Genomics Viewer⁶¹.

Genome-wide comparison and phylogenetic tree

SNPs of the two newly sequenced genomes from chimpanzees were compared to the 263 publicly available *M. leprae* genomes^{25,60,62,63,64} (Supplementary Table 6) and 21 new genomes from West African countries (Supplementary Note 5). Phylogenetic analyses were performed using a concatenated SNP alignment (Supplementary Table 7). Maximum-parsimony trees were constructed in MEGA7⁶⁵ with the 286 genomes available (Supplementary Table 5) using 500 bootstrap replicates and *M.*

*lepromatosis*⁶⁶ as outgroup. Sites with missing data were partially deleted (80% genome coverage cutoff), resulting in 4,470 variable sites used for the tree calculation.

Dating analysis

Dating analyses were performed using BEAST2 (v.2.5.2)⁶⁷ as described previously²⁴ with 278 genomes and an increased chain length from 50 to 100 million. In brief, concatenated SNPs for each sample were used for tip dating analysis (Supplementary Table 7). Hypermutated strains and highly mutated genes associated with drug resistance (in yellow, Supplementary Table 7) were omitted^{24,60}, manual curation of the maximum parsimony and BEAST input file was conducted at the positions described in Supplementary Table 9 for GB-CC064 and TNP-418. Sites with missing data as well as constant sites were included in the analysis, as previously described²⁴. Only unambiguous constant sites (loci where the reference base was called in all samples) were included.

PCR genotyping of insufficiently covered *M. leprae* genomes from positive chimpanzees

The genome coverage for the strain infecting Woodstock was low. To be able to determine the genotype, we identified specific variants from the genome-wide comparison of TNP-418 (the strain infecting Zora, an individual from the same social group) with other strains from branch 2F (Supplementary Table 9). Variants were manually checked and visualized in the partially covered genome from the strain infecting Woodstock using IGV software (Supplementary Table 10). Two variants not covered by high-throughput sequencing data were also selected for specific PCR screening. Primers were designed using the Primer3 web tool (<http://bioinfo.ut.ee/primer3-0.4.0/>) based on Mycobrowser sequences⁶⁸ and are described in Extended Data Table 3. All PCR conditions were the same as in the *M. leprae* screening PCRs except for the primer sets and associated annealing temperatures.

Ethical oversight

For chimpanzees, all data were collected in accordance with Best Practice Disease and Monitoring Guidelines developed by the Section on Great Apes, IUCN SSC Primate Specialist Group (IUCN SSC PSG SGA). The collection of samples was noninvasive. All proposed data collection and analyses adhered strictly to ethics guidelines of the Association for the Study of Animal Behaviour (UK). Ethical approval for targeted leprosy camera trap surveys and faecal sample collection at CNP, Guinea-Bissau, was granted by the University of Exeter, UK. The Institute for Biodiversity and Protected

Areas in Guinea-Bissau approved and collaborated directly on all aspects of this research. Ethical approval for the work by the Taï Chimpanzee Project at TNP was given by the Ethics Commission of the Max Planck Society. The Centre Suisse de Recherches Scientifiques en Côte d'Ivoire collaborates on the research at TNP.

For human participants, this study was carried out under the ethical consent of the World Health Organization Global Leprosy Program surveillance network. All human participants gave written informed consent in accordance with the Declaration of Helsinki.

Reporting summary

Further information on research design is available in the [Nature Research Reporting Summary](#) linked to this paper.

Data availability

Sequence data are available from the National Center for Biotechnology Information Sequence Read Archive, BioProject ([PRJNA664360](#)) and BioSample ([16207289–16207321](#)). BioSample codes for all samples used in this study are given in the [Supplementary Data](#). Other relevant data are available in the Article and its [Supplementary Information](#).

References

1. 1.
Walker, S. L. et al. in *Manson's Tropical Infectious Diseases* 23rd edn, 506–518 (Elsevier, 2014).
2. 2.
Truman, R. Leprosy in wild armadillos. *Lepr. Rev.* **76**, 198–208 (2005).
3. 3.
Avanzi, C. et al. Red squirrels in the British Isles are infected with leprosy bacilli. *Science* **354**, 744–747 (2016).
4. 4.

Suzuki, K., Tanigawa, K., Kawashima, A., Miyamura, T. & Ishii, N. Chimpanzees used for medical research shed light on the pathoetiology of leprosy. *Future Microbiol.* **6**, 1151–1157 (2011).

5. 5.

Meyers, W. M. et al. Leprosy in a mangabey monkey—naturally acquired infection. *Int. J. Lepr. Mycobact. Other Mycobact. Dis.* **53**, 1–14 (1985).

6. 6.

Gormus, B. J. et al. A second sooty mangabey monkey with naturally acquired leprosy: first reported possible monkey-to-monkey transmission. *Int. J. Lepr. Mycobact. Other Mycobact. Dis.* **56**, 61–65 (1988).

7. 7.

Valverde, C. R., Canfield, D., Tarara, R., Esteves, M. I. & Gormus, B. J. Spontaneous leprosy in a wild-caught cynomolgus macaque. *Int. J. Lepr. Mycobact. Other Mycobact. Dis.* **66**, 140–148 (1998).

8. 8.

Han, X. Y. et al. A new *Mycobacterium* species causing diffuse lepromatous leprosy. *Am. J. Clin. Pathol.* **130**, 856–864 (2008).

9. 9.

Han, X. Y. et al. Comparative sequence analysis of *Mycobacterium leprae* and the new leprosy-causing *Mycobacterium lepromatosis*. *J. Bacteriol.* **191**, 6067–6074 (2009).

10. 10.

Ridley, D. S. & Jopling, W. H. Classification of leprosy according to immunity. A five-group system. *Int. J. Lepr. Mycobact. Other Mycobact. Dis.* **34**, 255–273 (1966).

11. 11.

Britton, W. J. & Lockwood, D. N. Leprosy. *Lancet* **363**, 1209–1219 (2004).

12. 12.

World Health Organization. Leprosy (Hansen's disease).
<https://www.who.int/westernpacific/healthtopics/leprosy> (2020).

13. 13.

Araujo, S., Freitas, L. O., Goulart, L. R. & Goulart, I. M. B. Molecular evidence for the aerial route of infection of *Mycobacterium leprae* and the role of asymptomatic carriers in the persistence of leprosy. *Clin. Infect. Dis.* **63**, 1412–1420 (2016).

14. 14.

Lastória, J. C. & Morgado de Abreu, M. A. M. Leprosy: review of the epidemiological, clinical, and etiopathogenic aspects - part 1. *An. Bras. Dermatol.* **89**, 205–218 (2014).

15. 15.

Monot, M. et al. On the origin of leprosy. *Science* **308**, 1040–1042 (2005).

16. 16.

Truman, R. W. et al. Probable zoonotic leprosy in the southern United States. *N. Engl. J. Med.* **364**, 1626–1633 (2011).

17. 17.

Sharma, R. et al. Zoonotic leprosy in the southeastern United States. *Emerg. Infect. Dis.* **21**, 2127–2134 (2015).

18. 18.

da Silva, M. B. et al. Evidence of zoonotic leprosy in Pará, Brazilian Amazon, and risks associated with human contact or consumption of armadillos. *PLoS Negl. Trop. Dis.* **12**, e0006532 (2018).

19. 19.

Donoghue, H. D., Holton, J. & Spigelman, M. PCR primers that can detect low levels of *Mycobacterium leprae* DNA. *J. Med. Microbiol.* **50**, 177–182 (2001).

20. 20.

Stefani, M. M. et al. Assessment of anti-PGL-I as a prognostic marker of leprosy reaction. *Int. J. Lepr. Mycobact. Other Mycobact. Dis.* **66**, 356–364 (1998).

21. 21.

Spencer, J. S. & Brennan, P. J. The role of *Mycobacterium leprae* phenolic glycolipid-I (PGL-I) in serodiagnosis and in the pathogenesis of leprosy. *Lepr. Rev.* **82**, 344–357 (2011).

22. 22.

Leendertz, F. H. et al. Pathogens as drivers of population declines: the importance of systematic monitoring in great apes and other threatened mammals. *Biol. Conserv.* **131**, 325–337 (2006).

23. 23.

Crockford, C., Vigilant, L., Deschner, T., & Leendertz, F. *The Chimpanzees of the Taï Forest: 40 Years of Research* (Cambridge Univ. Press, 2019).

24. 24.

Benjak, A. et al. Phylogenomics and antimicrobial resistance of the leprosy bacillus *Mycobacterium leprae*. *Nat. Commun.* **9**, 352 (2018).

25. 25.

Honap, T. P. et al. *Mycobacterium leprae* genomes from naturally infected nonhuman primates. *PLoS Negl. Trop. Dis.* **12**, e0006190 (2018).

26. 26.

Stefani, M. M. A. et al. Whole-genome sequencing distinguishes between relapse and reinfection in recurrent leprosy cases. *PLoS Negl. Trop. Dis.* **11**, e0005598 (2017).

27. 27.

Schuenemann, V. J. et al. Ancient genomes reveal a high diversity of *Mycobacterium leprae* in medieval Europe. *PLoS Pathog.* **14**, e1006997 (2018).

28. 28.

Hockings, K. J., Parathian, H., Bessa, J. & Frazão-Moreira, A. Extensive overlap in the selection of wild fruits by chimpanzees and humans: implications for the management of complex social-ecological systems. *Front. Ecol. Evol.* **8**, 123 (2020).

29. 29.

Köndgen, S. et al. Pandemic human viruses cause decline of endangered great apes. *Curr. Biol.* **18**, 260–264 (2008).

30. 30.

Patrono, L. V. et al. Human coronavirus OC43 outbreak in wild chimpanzees, Côte d'Ivoire, 2016. *Emerg. Microbes Infect.* **7**, 118 (2018).

31. 31.

Richardus, J. H., Ignotti, E. & Smith, W. C. S. in *International Textbook of Leprosy* (eds Scollard, D. M. & Gillis, T. P.) (2016).

32. 32.

Gogarten, J. F. et al. The ecology of primate retroviruses – an assessment of 12 years of retroviral studies in the Taï National Park area, Côte d'Ivoire. *Virology* **460**, 147–153 (2014).

33. 33.

Boesch, C. & Boesch, H. Hunting behavior of wild chimpanzees in the Taï National Park. *Am. J. Phys. Anthropol.* **78**, 547–573 (1989).

34. 34.

Stinear, T. et al. Identification of *Mycobacterium ulcerans* in the environment from regions in Southeast Australia in which it is endemic with sequence capture-PCR. *Appl. Environ. Microbiol.* **66**, 3206–3213 (2000).

35. 35.

Rabinowitz, P. & Conti, L. *Human-Animal Medicine: Clinical Approaches to Zoonoses, Toxicants and other Shared Health Risks* (Elsevier, 2010).

36. 36.

Lahiri, R. & Adams, L. B. in *International Textbook of Leprosy* (eds. Scollard, D. M. & Gillis, T. P.) (2016).

37. 37.

Wheat, W. H. et al. Long-term survival and virulence of *Mycobacterium leprae* in amoebal cysts. *PLoS Negl. Trop. Dis.* **8**, e3405 (2014).

38. 38.

Neumann, A. et al. Experimental infection of *Rhodnius prolixus* (Hemiptera, Triatominae) with *Mycobacterium leprae* indicates potential for leprosy transmission. *PLoS ONE* **11**, e0156037 (2016).

39. 39.

Ferreira, J. D. S. et al. Ticks as potential vectors of *Mycobacterium leprae*: use of tick cell lines to culture the bacilli and generate transgenic strains. *PLoS Negl. Trop. Dis.* **12**, e0007001 (2018).

40. 40.

Catarino, L. M., Martins, E. S., Pinto-Basto, M. F. & Diniz, M. A. *Plantas Vasculares e Briófitos da Guiné-Bissau* (Instituto de Investigação Científica Tropical, 2006).

41. 41.

Bersacola, E., Hill, C. M. & Hockings, K. J. Chimpanzees balance resources and risk in an anthropogenic landscape of fear. *Sci Rep.* **11**, 4569 (2021).

42. 42.

Parathian, H. E., McLennan, M. R., Hill, C. M., Frazão-Moreira, A. & Hockings, K. J. Breaking through disciplinary barriers: human–wildlife interactions and multispecies ethnography. *Int. J. Primatol.* **39**, 749–775 (2018).

43. 43.

Sousa, C. & Frazão-Moreira, A. in *Etnoecologia em Perspectiva: Natureza, Cultura e Conservação* (eds Alves, A. G. C et al.) 187–200 (NUPEEA, 2010).

44. 44.

Sousa, J., Vicente, L., Gippoliti, S., Casanova, C. & Sousa, C. Local knowledge and perceptions of chimpanzees in Cantanhez National Park, Guinea-Bissau. *Am. J. Primatol.* **76**, 122–134 (2014).

45. 45.

Bessa, J., Sousa, C. & Hockings, K. J. Feeding ecology of chimpanzees (*Pan troglodytes verus*) inhabiting a forest-mangrove-savanna-agricultural matrix at Caiquene-Cadique, Cantanhez National Park, Guinea-Bissau. *Am. J. Primatol.* **77**, 651–665 (2015).

46. 46.

Vieira, W. F., Kerry, C. & Hockings, K. J. A comparison of methods to determine chimpanzee home-range size in a forest–farm mosaic at Madina in Cantanhez National Park, Guinea-Bissau. *Primates* **60**, 355–365 (2019).

47. 47.

Hockings, K. J. & Sousa, C. Human–chimpanzee sympatry and interactions in Cantanhez National Park, Guinea-Bissau: current research and future directions. *Primate Conserv.* **26**, 57–65 (2013).

48. 48.

McGraw, S., Zuberbühler, K. & Noë, R. *Monkeys of the Taï Forest: An African Primate Community* (Cambridge Univ. Press, 2007).

49. 49.

Boesch, C. & Boesch-Achermann, H. *The Chimpanzees of the Taï Forest: Behavioural Ecology and Evolution* (Oxford Univ. Press, 2000).

50. 50.

Gilardi, K. V. K. et al. *Best Practice Guidelines for Health Monitoring and Disease Control in Great Ape Populations* (IUCN, 2015).

51. 51.

Grützmacher, K. et al. Human quarantine: toward reducing infectious pressure on chimpanzees at the Taï Chimpanzee Project, Côte d’Ivoire. *Am. J. Primatol.* **80**, e22619 (2018).

52. 52.

McLennan, M. R. Diet and feeding ecology of chimpanzees (*Pan troglodytes*) in Bulindi, Uganda: foraging strategies at the forest–farm interface. *Int. J. Primatol.* **34**, 585–614 (2013).

53. 53.

McCarthy, M. S. et al. Genetic censusing identifies an unexpectedly sizeable population of an endangered large mammal in a fragmented forest landscape. *BMC Ecol.* **15**, 21 (2015).

54. 54.

Camacho-Sanchez, M., Burraco, P., Gomez-Mestre, I. & Leonard, J. A. Preservation of RNA and DNA from mammal samples under field conditions. *Mol. Ecol. Resour.* **13**, 663–673 (2013).

55. 55.

Borges, F. F. A Country-level Genetic Survey of the IUCN Critically Endangered Western Chimpanzee (*Pan troglodytes verus*) in Guinea-Bissau (Univ. Porto, 2017).

56. 56.

Altschul, S. F., Gish, W., Miller, W., Myers, E. W. & Lipman, D. J. Basic local alignment search tool. *J. Mol. Biol.* **215**, 403–410 (1990).

57. 57.

Mubemba, B. et al. Yaws disease caused by *Treponema pallidum* subspecies *pertenue* in wild chimpanzee, Guinea, 2019. *Infect. Dis. J.* **26**, 1283–1286 (2020).

58. 58.

Patrono, L. V. et al. Monkeypox virus emergence in wild chimpanzees reveals distinct clinical outcomes and viral diversity. *Nat. Microbiol.* **5**, 955–965 (2020).

59. 59.

Monot, M. et al. Comparative genomic and phylogeographic analysis of *Mycobacterium leprae*. *Nat. Genet.* **41**, 1282–1289 (2009).

60. 60.
- Avanzi, C. et al. Population genomics of *Mycobacterium leprae* reveals a new genotype in Madagascar and the Comoros. *Front. Microbiol.* **11**, 711 (2020).
61. 61.
- Robinson, J. T., Thorvaldsdóttir, H., Wenger, A. M., Zehir, A. & Mesirov, J. P. Variant review with the integrative genomics viewer. *Cancer Res.* **77**, e31–e34 (2017).
62. 62.
- Avanzi, C. et al. Emergence of *Mycobacterium leprae* rifampin resistance evaluated by whole-genome sequencing after 48 years of irregular treatment. *Antimicrob. Agents Chemother.* **64**, e00330-20 (2020).
63. 63.
- Guan, Q., Almutairi, T. S., Alhaloui, T., Pain, A. & Alasmari, F. Metagenomics of imported multidrug-resistant *Mycobacterium leprae*, Saudi Arabia, 2017. *Emerg. Infect. Dis.* **26**, 615–617 (2020).
64. 64.
- Tió-Coma, M. et al. Genomic characterization of *Mycobacterium leprae* to explore transmission patterns identifies new subtype in Bangladesh. *Front. Microbiol.* **11**, 1220 (2020).
65. 65.
- Kumar, S., Stecher, G. & Tamura, K. MEGA7: molecular evolutionary genetics analysis version 7.0 for bigger datasets. *Mol. Biol. Evol.* **33**, 1870–1874 (2016).
66. 66.
- Singh, P. et al. Insight into the evolution and origin of leprosy bacilli from the genome sequence of *Mycobacterium lepromatosis*. *Proc. Natl Acad. Sci. USA* **112**, 4459–4464 (2015).
67. 67.
- Volz, E. M. & Siveroni, I. Bayesian phylodynamic inference with complex models. *PLoS Comput. Biol.* **14**, e1006546 (2018).

68. 68.

Kapopoulou, A., Lew, J. M. & Cole, S. T. The MycoBrowser portal: a comprehensive and manually annotated resource for mycobacterial genomes. *Tuberculosis* **91**, 8–13 (2011).

Acknowledgements

The work at CNP was supported by the Darwin Initiative (grant number, 26-018) and the Halpin Trust (UK) to K.J.H. and C.B.; the Fundação para a Ciência e a Tecnologia (FCT), Portugal (FCT EXPL/IVC-ANT/0997/2013; IF/01128/2014) to K.J.H.; and a GCCA+ grant (Áreas Protegidas e Resiliência as Mudanças Climáticas) financed by the European Union to A.R. and A.R.S. E.B. was partly supported by an Oxford Brookes University studentship and grants from Mohamed bin Zayed Species Conservation Fund, Primate Society of Great Britain, International Primatological Society Conservation, Conservation International/Global Wildlife Conservation Primate Action Fund (Ms Constance Roosevelt) and Primate Conservation, Inc. J.B. was supported by a doctoral grant from FCT (SFRH/BD/108185/2015) and the Boise Trust Fund (University of Oxford). M.R. was supported by a studentship funded by the NERC GW4+ Doctoral Training Partnership and the College of Life and Environmental Sciences of the University of Exeter. The work at TNP was supported by the Max Planck Society, which has provided core funding for the Taï Chimpanzee Project since 1997; the work at TNP and all analyses performed on nonhuman primate samples were supported by the German Research Council projects LE1813/10-2, WI2637/4-2 and WI 2637/3-1 within the research group FOR2136 (Sociality and Health in Primates) and LE1813/14-1 (Great Ape Health in Tropical Africa); the ARCUS Foundation grant G-PGM-1807-2491; and the Robert Koch Institute. Work was partly carried out under the Global Health Protection Programme supported by the Federal Ministry of Health on the basis of a decision by the German Bundestag. A part of this Article represents a chapter in the PhD thesis of B.M. who was supported through the Robert Koch Institute's PhD programme. The work on human specimens was supported by the Fondation Raoul Follereau (S.T.C. and C.R.J.), the Heiser Program of the New York Community Trust for Research in Leprosy (J.S.S. and C.A., grant numbers P18-000250) and the Association de Chimiothérapie Anti-Infectieuse of the Société Française de Microbiologie (C.A.). C.A. was also supported by a non-stipendiary European Molecular Biology Organization long-term fellowship (ALTF 1086-2018) and the European Union's Horizon 2020 research and innovation programme under the Marie Skłodowska-Curie grant no. 845479. We thank staff at the Instituto da Biodiversidade e das Áreas Protegidas for their permission to conduct research in Guinea-Bissau and for logistical support; Q. Quecuta, Director of CNP and research assistants and local guards, in particular M. Cassamá, I.T. Camará, D. Indjai, S. Sila, A. Camará, I. Galiza, F. Ndafa, A. Camará and B.S. Vieira for assisting with

data collection and providing advice in CNP; village chiefs, Nalu leaders and Régulos for granting us permission to conduct research; staff at the Ministère de l’Enseignement Supérieur et de la Recherche Scientifique and the Ministère des Eaux et Forêts in Côte d’Ivoire and the Office Ivoirien des Parcs et Réserves for permitting the research at TNP; staff of the Taï Chimpanzee Project and the Centre Suisse de Recherches Scientifiques for support of our work in TNP; S. Lemoine for providing shapefiles on chimpanzee home ranges at TNP; and J. McKinney, N. Dhar, S. Balharry, B. Mangeat and staff at the Gene Expression Core Facility from the Ecole Polytechnique Fédérale de Lausanne for support. The authors thank B. Godley and A. Frazão-Moreira for support in developing research ideas and logistics in Guinea-Bissau; A. Stone for constructive comments on the manuscript; and all the patients and clinical staff who participated in the study.

Funding

Open access funding provided by Robert Koch-Institut.

Author information

Author notes

1. These authors contributed equally: Benjamin Mubemba, Charlotte Avanzi, Kamilla Pleh, Ariane Düx, Elena Bersacola, Joana Bessa and Marina Ramon

Affiliations

1. Centre for Ecology and Conservation, University of Exeter, Penryn, UK
Kimberley J. Hockings, Elena Bersacola, Marina Ramon, Camille Bonneau & Joshua Lynton-Jenkins
2. Centre for Research in Anthropology (CRIA – NOVA FCSH), Lisbon, Portugal
Kimberley J. Hockings, Elena Bersacola & Joana Bessa
3. Project Group Epidemiology of Highly Pathogenic Microorganisms, Robert Koch Institute, Berlin, Germany
Benjamin Mubemba, Kamilla Pleh, Ariane Düx, Sonja Metzger, Livia V. Patrono, Jenny E. Jaffe, Markus Ulrich, Sébastien Calvignac-Spencer & Fabian H. Leendertz

4. Department of Wildlife Sciences, School of Natural Resources, Copperbelt University, Kitwe, Zambia

Benjamin Mubemba

5. Global Health Institute, Ecole Polytechnique Fédérale de Lausanne, Lausanne, Switzerland

Charlotte Avanzi, Philippe Busso & Stewart T. Cole

6. Department of Microbiology, Immunology and Pathology, Colorado State University, Fort Collins, CO, USA

Charlotte Avanzi & John S. Spencer

7. Swiss Tropical and Public Health Institute, Basel, Switzerland

Charlotte Avanzi & Sebastien Gagneux

8. University of Basel, Basel, Switzerland

Charlotte Avanzi & Sebastien Gagneux

9. Taï Chimpanzee Project, Centre Suisse de Recherches Scientifiques, Abidjan, Côte d'Ivoire

Kamilla Pleh, Sonja Metzger, Jenny E. Jaffe & Roman M. Wittig

10. Department of Zoology, University of Oxford, Oxford, UK

Joana Bessa

11. Department for BioMedical Research, University of Bern, Bern, Switzerland

Andrej Benjak

12. Laboratoire National d'Appui au Développement Agricole/Laboratoire Central de Pathologie Animale, Bingerville, Côte d'Ivoire

Emmanuel Couacy-Hymann

13. Programme National de Lutte Contre la Lèpre, Ministry of Public Health, Niamey, Niger

Moussa Gado

14. Centre Interfacultaire de Formation et de Recherche en Environnement pour le Développement Durable, University of Abomey-Calavi, Jericho, Cotonou, Benin
Roch C. Johnson
15. Fondation Raoul Follereau, Paris, France
Roch C. Johnson
16. Centre National d'Appui à la Lutte Contre la Maladie, Bamako, Mali
Mamoudou Kadio & Samba O. Sow
17. Institute of Evolutionary Medicine, University of Zurich, Zurich, Switzerland
Irina Morozova & Verena J. Schuenemann
18. Pathology Unit, German Primate Center, Leibniz-Institute for Primate Research, Göttingen, Germany
Kerstin Mätz-Rensing
19. Instituto da Biodiversidade e das Áreas Protegidas, Dr. Alfredo Simão da Silva (IBAP), Bissau, Guinea-Bissau
Aissa Regalla & Abílio R. Said
20. Programme National d'Elimination de la Lèpre, Dakar, Senegal
Hyacinthe Zoubi
21. Institut Pasteur, Paris, France
Stewart T. Cole
22. Max Planck Institute for Evolutionary Anthropology, Leipzig, Germany
Roman M. Wittig
23. Helmholtz Institute for One Health, Greifswald, Germany
Fabian H. Leendertz

Contributions

Collection and analysis of chimpanzee camera trap data (CNP) was provided by K.J.H., E.B., J.B., M.R., A.R. and A.R.S. Collection of long-term data on chimpanzees and their health (TNP) was provided by R.M.W. and F.H.L. Collection of chimpanzee samples (CNP and TNP) was provided by K.J.H., E.B., J.B., M.R., K.P., A.D., J.E.J., S.M. and F.H.L. Logistics and fieldwork was provided by K.J.H., A.R., A.R.S., E.C.-H., R.M.W. and F.H.L. Necropsies were performed by S.M., A.D., J.E.J. and F.H.L. Histopathological analyses were performed by K.M.-R. Collection and provision of human samples was provided by M.G., R.C.J., M.K., S.O.S., S.T.C. and H.Z. DNA extraction, library preparation, enrichment and whole-genome sequencing was conducted by B.M., C.A., P.B., I.M., V.J.S. and M.U. PCR and SNP data were confirmed by B.M., L.V.P. and C.A. Chimpanzee microsatellite analysis was performed by C.B. and J.L.-J. Computational analysis was performed by C.A., S.C.-S. and B.M. Dating analysis was provided by A.B. Serological investigations were conducted by B.M. and L.V.P. J.S.S. provided material and the protocol for serological investigation. Funding was acquired by K.J.H., C.A., V.J.S., J.S.S., C.B., S.T.C., R.M.W. and F.H.L. K.J.H., C.A., C.B., S.C.S. and F.H.L. wrote the manuscript with considerable input from B.M., K.P., E.B., J.B., M.R., A.D. and L.V.P., with contributions from all authors. All authors approved the submitted manuscript.

Corresponding author

Correspondence to Fabian H. Leendertz.

Ethics declarations

Competing interests

The authors declare no competing interests.

Additional information

Peer review information *Nature* thanks Stephen Gordon and the other, anonymous, reviewer(s) for their contribution to the peer review of this work. Peer reviewer reports are available.

Publisher's note Springer Nature remains neutral with regard to jurisdictional claims in published maps and institutional affiliations.

Extended data figures and tables

Extended Data Fig. 1 Maps of the chimpanzee study sites and chimpanzee communities.

a, Map of the CNP, Guinea-Bissau and the TNP, Côte d'Ivoire, West Africa. **b**, Location of the chimpanzee communities at CNP that were monitored between 2015 and 2019 (1, Caiquene-Cadique; 2, Lautchande; 3, Cambeque; 4, Cabante; 5, Canamine; 6, Madina; 7, Amindara; 8, Guiledje). Estimated home ranges of chimpanzee communities at CNP are shown by 100% minimum convex polygons of direct chimpanzee observations and indirect chimpanzee traces and nests during the study period. Red outline represents chimpanzee communities with at least one individual with clinical manifestations of leprosy, confirmed using molecular analysis; orange outline represents chimpanzee communities with at least one individual with clinical manifestations of leprosy; yellow colour represents monitored communities where clinical manifestations of leprosy have not been observed nor confirmed through molecular analysis. **c**, Location of the three habituated chimpanzee communities monitored at TNP (N, north; S, south; E, east). Estimated home ranges of chimpanzee communities at TNP are shown by 100% minimum convex polygons of direct chimpanzee follows from December 2013 to October 2016. Red outline represents the community with individuals with clinical manifestations of leprosy, confirmed using molecular analysis and serological tests; blue colour represents communities where leprosy has not been recorded.

Extended Data Fig. 2 Disease progression of leprosy in chimpanzees at CNP.

Adult female chimpanzee Rita over the course of 5 years (**a–d**) and disease manifestations in three additional adult chimpanzees (**e–g**). **a**, 2013/05 – Hypopigmentation of skin around the mouth and nose, small nodule on the lower lip and left ear (opportunistically recorded with a video camera before the start of longitudinal health monitoring with camera traps). **b**, 2015/12 – Large nodules between the upper lip and nose, with multiple small nodules on the eyelids, cheek, ears margins, lower lip and brow ridge. Small dry patches with hair loss on the wrists, knees and elbows. **c**, 2017/12 – Nodules increase in number, with apparent swelling and reddening, facial disfigurement and claw hand. Plaques appear on the wrist, knee and elbow joints, with an increase in hair thinning. **d**, 2018/05 – Face and ears completely covered by large nodules, with facial disfigurement and generalized hair loss on limbs and lower back. Nodule formation and swelling of fingers and toes, with disfigurement of hands and feet, and more severe claw hand. Some plaques on the body are ulcerated, and the individual has clear weight loss. **e**, Jimi (Lautchande in 2018/06) – First observation of lesions in 2015. The head is completely covered with multiple nodules of reddish colour, some of which are ulcerated. Ear margins are thickened. Hands and feet present nodules and plaques, and the scrotum is affected

(not visible on picture). **f**, Baaba (Cambeque in 2017/08) – First observation of lesions in 2017. Multiple hypopigmented nodules on the brow ridge, cheek and upper and lower lips. Ears have thickened margins and nodules. There is hair thinning, with multiple small plaques present on the upper and lower limbs, back, abdomen and shoulders. **g**, Brinkos (Caiquene-Cadique in 2018/10) – First observation of lesions in 2015. Facial disfigurement, with the ulceration of nodules and a hanging lower lip. Hands and feet are ulcerated, and fingers are swollen. There are nodules on the nipples, and plaques covering the lower back, shoulders and arm are ulcerated, with hair loss.

Extended Data Fig. 3 Disease progression of leprosy in an adult male chimpanzee at TNP (Woodstock) over the course of 2 years (2018–2020), (a–i) and an adult female chimpanzee at TNP (Zora) over the course of 2008–2009 (j–m).

a, 2017/01 – Woodstock before the appearance of clinical signs. **b**, 2018/06 – First hypopigmented nodules appear on the face (arrows), with swelling and hypopigmentation on both hands, and ulceration on the right hand. **c**, 2018/10 – Existing nodules increase in size and new smaller ones appear (arrows). Development of mucopurulent discharge from the left eye, and lower eyelid is turned outward. Hair loss and ulceration on dorsal part of right wrist and hand. **d**, 2019/04 – Most existing nodules increase in size and become pedunculated, and the nodule under the eye shrinks, and several new nodules appear (see arrows). Suspected start of nasal involvement, and right ear starts to become disfigured. Both hands are slightly swollen and hypopigmented, with the loss of nail plate on the fourth finger of the left hand, and the third and fifth fingers show early stage of abnormal nail overgrowth. **e**, 2019/10 – Facial lesions increase in size, and some become darkly pigmented. New lesions appear on the brow ridge, with nodules above the lips and between the lips, and the nose becomes pedunculated. The loss of nail plate, and nail bed becomes exposed on the first and second fingers of the left hand. **f**, 2020/04 – In general, facial nodules seem smaller than before, and the nodule under the left eye disappears. On the left hand, the nail of the fourth finger shows an advanced stage of abnormal nail overgrowth, and the third and fifth fingernails show early stage of abnormal nail overgrowth. **g**, 2020/07 – Facial nodules seem larger with many hypopigmented, and both ears are swollen and disfigured. Nasal involvement becomes apparent. Both hands are swollen and hypopigmented. Skin ulcerations present on the right hand, with possible claw hand on the left hand. **h**, 2019/04 – Slight hypopigmentation of scrotum. **i**, 2020/07 – Reddening and ulceration of scrotum; fresh blood observed. **j**, 2007/12 – Zora before the appearance of clinical signs of leprosy. **k**, 2008/01 – Appearance of nodules on the right ear and both eyebrow ridges. **l**, 2008/12 – Appearance of nodules on the left ear, and ulceration of the skin at the second, third and fourth proximal interphalangeal joint level of the right hand. **m**, 2009/04 – Nodular lesions on both

ears and brow ridge seem aggravated, with nodular lesions on the lips, and above the mouth (four months before death).

Extended Data Fig. 4 Confirmation of leprosy infection in Zora through histopathology of skin sample and lateral flow test.

a, Lepromatous leprosy, skin with diffuse histiocytic infiltrate in the dermis. The haematoxylin and eosin stain was conducted once; scale bar, 500 µm. **b**, Lepromatous leprosy, skin, acid-fast bacilli in histiocytes. The inflammatory infiltrate consists predominantly of histiocytes admixed with fewer lymphocytes. Histiocytes show foamy or vacuolated cytoplasm and containing bacteria surrounded by a clear zone. Fite-Faraco stain; scale bar, 20 µm. Fite-Faraco stain was conducted once and was controlled by a positive control slide containing mycobacteria. **c**, whole blood from Zora (1) and the positive control (2). **d**, whole blood from a chimpanzee at TNP (Olivia) not infected with *M. leprae*, used as negative control. C, control lane; T, test lane.

Extended Data Fig. 5 Geographical distribution of *M. leprae* genotypes in Africa based on genome data.

The genotype 2F has never been reported in West Africa and is the least identified in Ethiopia. The genotype 4N/O was only reported in one human sample from West Africa. Data included only *M. leprae* genomes (Supplementary Note 5 and Supplementary Table 7). The map was downloaded from <https://www.amcharts.com/svg-maps/> under a free licence and modified for the current figure in Inkscape, an open source digital illustration software package (<https://inkscape.org>).

Extended Data Fig. 6

Best-fitting root analysis using TempEst.

Extended Data Fig. 7 Maximum Likelihood tree to confirm the topological placement of GB-CC064 and TNP-418.

286 genomes (Supplementary Table 6) were used, including the two new chimpanzee strains (in bold red), 500 bootstrap replicates (value in black with the Tamura Nei model and in blue for the general time model) and *M. lepromatosis* as outgroup. Sites with missing data were partially deleted (80% genome coverage cutoff). **a**, Maximum Likelihood tree of the branch 2F. **b**, Maximum Likelihood tree of the branch 4.

Extended Data Table 1 The camera trap (CT) study periods with the focal chimpanzee community within Cantanhez National Park

Extended Data Table 2 Samples (CNP) and animals (TNP) that tested positive for *M. leprae* DNA

Extended Data Table 3 Primers used for the identification of *M. leprae* in chimpanzee tissues and faeces, diet analysis, the genotyping of *M. leprae* strains and confirmation of chimpanzee origin of the samples

Supplementary information

Supplementary Information

This file contains supplementary table and video titles, Supplementary Notes 1–7 and Supplementary References.

Reporting Summary

Peer Review File

Supplementary Tables 1–10

Supplementary Video 1

Videoclip shows adult female chimpanzee, Rita, with claw hand at CNP (dated April 2017).

Supplementary Video 2

Videoclip shows adult female chimpanzee, Rita, at CNP (dated May 2018).

Supplementary Video 3

Videoclip shows adult female chimpanzee, Rita, at CNP (dated November 2018).

Supplementary Video 4

Videoclip shows adult male chimpanzee, Woodstock, at TNP biting his fingernails (dated April 2019).

Supplementary Video 5

Videoclip shows adult male chimpanzee, Woodstock, with claw hand at TNP (dated July 2020).

Rights and permissions

Open Access This article is licensed under a Creative Commons Attribution 4.0 International License, which permits use, sharing, adaptation, distribution and reproduction in any medium or format, as long as you give appropriate credit to the original author(s) and the source, provide a link to the Creative Commons license, and indicate if changes were made. The images or other third party material in this article are included in the article's Creative Commons license, unless indicated otherwise in a credit line to the material. If material is not included in the article's Creative Commons license and your intended use is not permitted by statutory regulation or exceeds the permitted use, you will need to obtain permission directly from the copyright holder. To view a copy of this license, visit <http://creativecommons.org/licenses/by/4.0/>.

Reprints and Permissions

About this article

Cite this article

Hockings, K.J., Mubemba, B., Avanzi, C. *et al.* Leprosy in wild chimpanzees. *Nature* **598**, 652–656 (2021). <https://doi.org/10.1038/s41586-021-03968-4>

- Received: 18 November 2020
- Accepted: 27 August 2021
- Published: 13 October 2021
- Issue Date: 28 October 2021
- DOI: <https://doi.org/10.1038/s41586-021-03968-4>

Share this article

Anyone you share the following link with will be able to read this content:

[Get shareable link](#)

Sorry, a shareable link is not currently available for this article.

[Copy to clipboard](#)

Provided by the Springer Nature SharedIt content-sharing initiative

This article was downloaded by **calibre** from <https://www.nature.com/articles/s41586-021-03968-4>

| [Section menu](#) | [Main menu](#) |

- Article
- [Published: 13 October 2021](#)

Parallelism of intestinal secretory IgA shapes functional microbial fitness

- [Tim Rollenske](#) [ORCID: orcid.org/0000-0003-1982-3253¹](#),
- [Sophie Burkhalter¹](#),
- [Lukas Muerner](#) [ORCID: orcid.org/0000-0001-5972-6410²](#),
- [Stephan von Gunten](#) [ORCID: orcid.org/0000-0002-2753-8738²](#),
- [Jolanta Lukasiewicz³](#),
- [Hedda Wardemann](#) [ORCID: orcid.org/0000-0003-3921-5933^{4 na1}](#) &
- [Andrew J. Macpherson](#) [ORCID: orcid.org/0000-0002-7192-0184^{1 na1}](#)

[Nature](#) volume **598**, pages 657–661 (2021)

- 4525 Accesses
- 175 Altmetric
- [Metrics details](#)

Subjects

- [Antibodies](#)
- [Antimicrobial responses](#)
- [Clonal selection](#)
- [Microbiology](#)
- [Mucosal immunology](#)

Abstract

Dimeric IgA secreted across mucous membranes in response to nonpathogenic taxa of the microbiota accounts for most antibody production in mammals. Diverse binding specificities can be detected within the polyclonal mucosal IgA antibody response^{1,2,3,4,5,6,7,8,9,10}, but limited monoclonal hybridomas have been studied to relate antigen specificity or polyreactive binding to functional effects on microbial physiology in vivo^{11,12,13,14,15,16,17}. Here we use recombinant dimeric monoclonal IgAs (mIgAs) to finely map the intestinal plasma cell response to microbial colonization with a single microorganism in mice. We identify a range of antigen-specific mIgA molecules targeting defined surface and nonsurface membrane antigens. Secretion of individual dimeric mIgAs targeting different antigens in vivo showed distinct alterations in the function and metabolism of intestinal bacteria, largely through specific binding. Even in cases in which the same microbial antigen is targeted, microbial metabolic alterations differed depending on IgA epitope specificity. By contrast, bacterial surface coating generally reduced motility and limited bile acid toxicity. The overall intestinal IgA response to a single microbe therefore contains parallel components with distinct effects on microbial carbon-source uptake, bacteriophage susceptibility, motility and membrane integrity.

Access options

Subscribe to Journal

Get full journal access for 1 year

\$199.00

only \$3.90 per issue

[Subscribe](#)

All prices are NET prices.

VAT will be added later in the checkout.

Tax calculation will be finalised during checkout.

Rent or Buy article

Get time limited or full article access on ReadCube.

from \$8.99

[Rent or Buy](#)

All prices are NET prices.

Additional access options:

- [Log in](#)
- [Access through your institution](#)
- [Learn about institutional subscriptions](#)

Fig. 1: Monoclonal dimeric IgA coats distinct bacterial subpopulations.

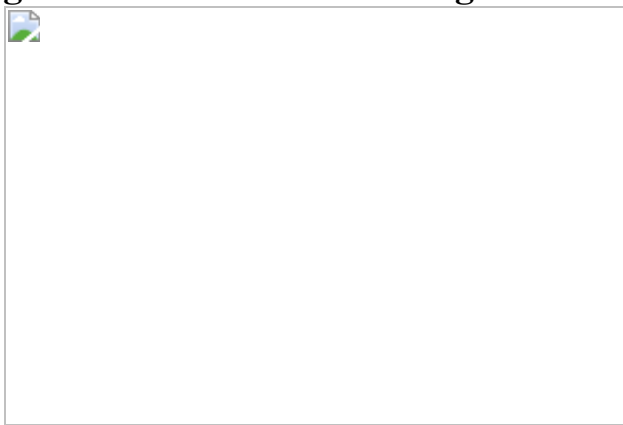


Fig. 2: In vivo mIgA reconstitution of antibody-deficient $J_H^{-/-}$ mice provides a scalable model to study mSIgA function.

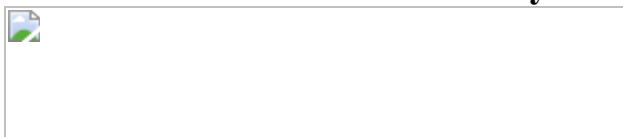
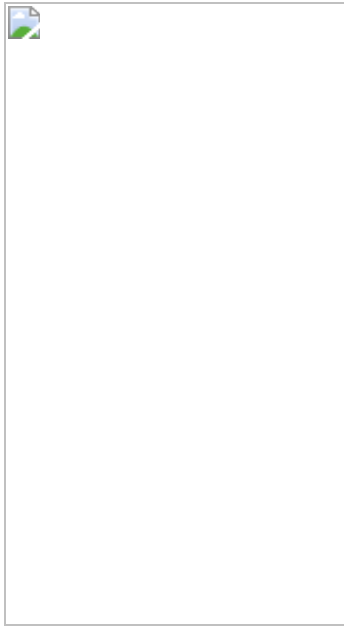


Fig. 3: Surface-binding mSIgA exerts antigen-dependent individual and generic functional alterations in intestinal bacteria.



Data availability

Raw sequence reads are deposited under BioProject [PRJNA702008](#) and are associated with Fig. [3a, d](#) and Extended Data Figs. [6a–d, h–k](#) and [9b](#).

Bacterial sequencing reads were annotated to the *E. coli* genome of strain MG1655 (U00096.2). GO terms and gene set members were extracted from the EcoCyc *E. coli* database at <https://ecocyc.org>. There are no restrictions on data availability. [Source data](#) are provided with this paper.

References

1. 1.

Bunker, J. J. et al. Natural polyreactive IgA antibodies coat the intestinal microbiota. *Science* **358**, eaan6619 (2017).

2. 2.

Moor, K. et al. High-avidity IgA protects the intestine by en chaining growing bacteria. *Nature* **544**, 498–502 (2017).

3. 3.

Benckert, J. et al. The majority of intestinal IgA⁺ and IgG⁺ plasmablasts in the human gut are antigen-specific. *J. Clin. Invest.* **121**, 1946–1955 (2011).

4. 4.

Di Niro, R. et al. *Salmonella* infection drives promiscuous B cell activation followed by extrafollicular affinity maturation. *Immunity* **43**, 120–131 (2015).

5. 5.

Sterlin, D. et al. Human IgA binds a diverse array of commensal bacteria. *J. Exp. Med.* **217**, e20181635 (2020).

6. 6.

Okai, S. et al. High-affinity monoclonal IgA regulates gut microbiota and prevents colitis in mice. *Nat. Microbiol.* **1**, 16103 (2016).

7. 7.

Cullender, T. C. et al. Innate and adaptive immunity interact to quench microbiome flagellar motility in the gut. *Cell Host Microbe* **14**, 571–581 (2013).

8. 8.

Rollenske, T. et al. Cross-specificity of protective human antibodies against *Klebsiella pneumoniae* LPS O-antigen. *Nat. Immunol.* **19**, 617–624 (2018).

9. 9.

Yang, C., Chen-liaw, A., Moran, T. M., Cerutti, A. & Faith, J.J. Immunoglobulin A antibody composition is sculpted to bind the self gut microbiome. Preprint at *bioRxiv* <https://doi.org/10.1101/2020.11.30.405332> (2020).

10. 10.

Macpherson, A. J., Yilmaz, B., Limenitakis, J. P. & Ganal-Vonarburg, S. C. IgA function in relation to the intestinal microbiota. *Annu. Rev. Immunol.* **36**, 359–381 (2018).

11. 11.

Nowosad, C. R. et al. Tunable dynamics of B cell selection in gut germinal centres. *Nature* **588**, 321–326 (2020).

12. 12.

Peterson, D. A., McNulty, N. P., Guruge, J. L. & Gordon, J. I. IgA response to symbiotic bacteria as a mediator of gut homeostasis. *Cell Host Microbe* **2**, 328–339 (2007).

13. 13.

Peterson, D. A. et al. Characterizing the interactions between a naturally primed immunoglobulin A and its conserved *Bacteroides thetaiotaomicron* species-specific epitope in gnotobiotic mice. *J. Biol. Chem.* **290**, 12630–12649 (2015).

14. 14.

Lycke, N., Eriksen, L. & Holmgren, J. Protection against cholera toxin after oral immunization is thymus-dependent and associated with intestinal production of neutralizing IgA antitoxin. *Scand. J. Immunol.* **25**, 413–419 (1987).

15. 15.

Pabst, O. & Slack, E. IgA and the intestinal microbiota: the importance of being specific. *Mucosal Immunol.* **13**, 12–21 (2020).

16. 16.

Nakajima, A. et al. IgA regulates the composition and metabolic function of gut microbiota by promoting symbiosis between bacteria. *J. Exp. Med.* **215**, 2019–2034 (2018).

17. 17.

Joglekar, P. et al. Intestinal IgA regulates expression of a fructan polysaccharide utilization locus in colonizing gut commensal *Bacteroides thetaiotaomicron*. *Mbio* **10**, e02324–19 (2019).

18. 18.

Hapfelmeier, S. et al. Reversible microbial colonization of germ-free mice reveals the dynamics of IgA immune responses. *Science* **328**, 1705–1709 (2010).

19. 19.

Lindner, C. et al. Diversification of memory B cells drives the continuous adaptation of secretory antibodies to gut microbiota. *Nat. Immunol.* **16**, 880–888 (2015).

20. 20.

Maurice, C. F., Haiser, H. J. & Turnbaugh, P. J. Xenobiotics shape the physiology and gene expression of the active human gut microbiome. *Cell* **152**, 39–50 (2013).

21. 21.

Li, H. et al. Mucosal or systemic microbiota exposures shape the B cell repertoire. *Nature* **584**, 274–278 (2020).

22. 22.

Hendrickson, B. A. et al. Altered hepatic transport of immunoglobulin A in mice lacking the J chain. *J. Exp. Med.* **182**, 1905–1911 (1995).

23. 23.

Johansen, F. et al. Absence of epithelial immunoglobulin A transport, with increased mucosal leakiness, in polymeric immunoglobulin receptor/secretory component-deficient mice. *J. Exp. Med.* **190**, 915–922 (1999).

24. 24.

Fransen, F. et al. BALB/c and C57BL/6 mice differ in polyreactive IgA abundance, which impacts the generation of antigen-specific IgA and microbiota diversity. *Immunity* **43**, 527–540 (2015).

25. 25.

Liu, X. & Ferenci, T. Regulation of porin-mediated outer membrane permeability by nutrient limitation in *Escherichia coli*. *J. Bacteriol.* **180**, 3917–3922 (1998).

26. 26.

Yu, F. & Mizushima, S. Roles of lipopolysaccharide and outer membrane protein OmpC of *Escherichia coli* K-12 in the receptor function for bacteriophage T4. *J. Bacteriol.* **151**, 718–722 (1982).

27. 27.

Wardemann, H. et al. Predominant autoantibody production by early human B cell precursors. *Science* **301**, 1374–1377 (2003).

28. 28.

Mouquet, H. & Nussenzweig, M. C. Polyreactive antibodies in adaptive immune responses to viruses. *Cell. Mol. Life Sci.* **69**, 1435–1445 (2011).

29. 29.

Guthmiller, J. J. et al. Polyreactive broadly neutralizing B cells are selected to provide defense against pandemic threat influenza viruses. *Immunity* **53**, 1230–1244 (2020).

30. 30.

Kabbert, J. et al. High microbiota reactivity of adult human intestinal IgA requires somatic mutations. *J. Exp. Med.* **217**, e20200275 (2020).

31. 31.

Wold, A. E. et al. Secretory immunoglobulin A carries oligosaccharide receptors for *Escherichia coli* type 1 fimbrial lectin. *Infect. Immun.* **58**, 3073–3077 (1990).

32. 32.

Stern, R. J. et al. Conversion of dTDP-4-keto-6-deoxyglucose to free dTDP-4-keto-rhamnose by the *rmlC* gene products of *Escherichia coli* and *Mycobacterium tuberculosis*. *Microbiology* **145**, 663–671 (1999).

33. 33.

Weiss, G. L. et al. Architecture and function of human uromodulin filaments in urinary tract infections. *Science* **1010**, 1005–1010 (2020).

34. 34.

Baba, T. et al. Construction of *Escherichia coli* K-12 in-frame, single-gene knockout mutants: the Keio collection. *Mol. Syst. Biol.* **2**, 2006.0008 (2006).

35. 35.

Meuskens, I., Michalik, M., Chauhan, N., Linke, D. & Leo, J. C. A new strain collection for improved expression of outer membrane proteins. *Front. Cell. Infect. Microbiol.* <https://doi.org/10.3389/fcimb.2017.00464> (2017).

36. 36.

Tran, Q.-T. et al. Structure–kinetic relationship of carbapenem antibiotics permeating through *E. coli* OmpC porin. *Proteins* **82**,

2998–3012 (2014).

37. 37.

Lukasiewicz, J. et al. Serological characterization of anti-endotoxin serum directed against the conjugate of oligosaccharide core of *Escherichia coli* type R4 with tetanus toxoid. *FEMS Immunol. Med. Microbiol.* **37**, 59–67 (2003).

38. 38.

Keegan, N., Ridley, H. & Lakey, J. H. Discovery of biphasic thermal unfolding of OmpC with implications for surface loop stability. *Biochemistry* **49**, 9715–9721 (2010).

39. 39.

Schwechheimer, C. & Kuehn, M. J. Outer-membrane vesicles from Gram-negative bacteria: biogenesis and functions. *Nat. Rev. Microbiol.* **13**, 605–619 (2015).

40. 40.

Chen, J. et al. Immunoglobulin gene rearrangement in B cell deficient mice generated by targeted deletion of the JH locus. *Int. Immunol.* **5**, 647–656 (1993).

41. 41.

Meffre, E. et al. Surrogate light chain expressing human peripheral B cells produce self-reactive antibodies. *J. Exp. Med.* **199**, 145–150 (2004).

42. 42.

Ofek, I., Mirelman, D. & Sharon, N. Adherence of *Escherichia coli* to human mucosal cells mediated by mannose receptors. *Nature* **265**, 623–625 (1977).

43. 43.

Busse, C. E., Czogiel, I., Braun, P., Arndt, P. F. & Wardemann, H. Single-cell based high-throughput sequencing of full-length immunoglobulin heavy and light chain genes. *Eur. J. Immunol.* **44**, 597–603 (2014).

44. 44.

Tiller, T., Busse, C. E. & Wardemann, H. Cloning and expression of murine Ig genes from single B cells. *J. Immunol. Methods* **350**, 183–193 (2009).

45. 45.

Li, H. et al. The outer mucus layer hosts a distinct intestinal microbial niche. *Nat. Commun.* **6**, 8292 (2015).

46. 46.

Urdaneta, V. & Casadesús, J. Interactions between bacteria and bile salts in the gastrointestinal and hepatobiliary tracts. *Front. Med.* <https://doi.org/10.3389/fmed.2017.00163> (2017).

47. 47.

Imkeller, K., Arndt, P. F., Wardemann, H. & Busse, C. E. sciReptor: analysis of single-cell level immunoglobulin repertoires. *BMC Bioinform.* **17**, 67 (2016).

48. 48.

Keseler, I. M. et al. The EcoCyc database: reflecting new knowledge about *Escherichia coli* K-12. *Nucleic Acids Res.* **45**, D543–D550 (2017).

Acknowledgements

The Clean Mouse Facility is supported by the Genaxen Foundation, Inselspital and the University of Bern. We thank P. Nicholson, I. Keller, F. Blank, B. Haenni and staff at the flow cytometry, sequencing and microscopy core facilities of the German Cancer Research Center and University of Bern. J. Gärtner, C. Winter, D. Foster, C. Busse and R. Murugan helped with monoclonal antibody production and single-cell Ig-gene sequencing. H. Waller, D. Kalbermatter, K. Lau, R. Glockshuber, B. Yilmaz, J. Leo, C. Piselli, M. Winterhalter and J. Stanisich provided reagents and support. S. Hapfelmeier (University of Bern), provided the smooth *E. coli* strain BW24599. J. Zimmermann, F. Ronchi, H. Li, S. Ganal-Vonarburg, I. D. Young and M. Felber (University of Bern) helped with in vivo experimentation. Grant support was obtained from the Swiss National Science Foundation (310030_179479 and Sinergia CRSII5_177164) and European Research Council (ERC advanced grant HHMM-Neonates project no.742195) to A.J.M.; and through the Swiss National Science Foundation (310030_184757) and Swiss Cancer League/Swiss Cancer Research (KFS-4958-02-2020) to S.v.G. T.R. was supported by a postdoctoral long-term EMBO fellowship (ALTF 1040-2018) and funding from the Bern University Research Foundation.

Author information

Author notes

1. These authors contributed equally: Hedda Wardemann, Andrew J. Macpherson

Affiliations

1. Department of Biomedical Research, University Clinic of Visceral Surgery and Medicine, Inselspital, University of Bern, Bern, Switzerland

Tim Rollenske, Sophie Burkhalter & Andrew J. Macpherson

2. Institute of Pharmacology, University of Bern, Bern, Switzerland

Lukas Muerner & Stephan von Gunten

3. Laboratory of Microbial Immunochemistry and Vaccines, Ludwik Hirschfeld Institute of Immunology and Experimental Therapy, Wroclaw, Poland

Jolanta Lukasiewicz

4. B cell Immunology, German Cancer Research Center, Heidelberg, Germany

Hedda Wardemann

Contributions

T.R. and A.J.M. conceived the project and designed and interpreted experiments. Experiments were carried out by T.R., with support from S.B. L.M. and S.v.G. performed glycan array analysis. J.L. performed LPS structure analysis and provided purified defined LPS samples. H.W. established and supervised the technology for monoclonal antibody selection, expression and analysis. T.R. and A.J.M. wrote the manuscript. All authors approved the manuscript.

Corresponding authors

Correspondence to Tim Rollenske or Andrew J. Macpherson.

Ethics declarations

Competing interests

The authors declare no competing interests.

Additional information

Peer review information *Nature* thanks Sidonia Fagarasan, Maria Rescigno and the other, anonymous, reviewer(s) for their contribution to the peer review of this work. Peer reviewer reports are available.

Publisher's note Springer Nature remains neutral with regard to jurisdictional claims in published maps and institutional affiliations.

Extended data figures and tables

Extended Data Fig. 1 Ig gene and antibody-binding characteristics of monoclonal antibodies derived from intestinal plasma cells of germ-free and transitorily HA107-colonized mice.

a, Strategy to obtain HA107-reactive monoclonal antibodies from lamina propria plasma cells after transient intragastric (i.g.) microbial priming of germ-free wild-type (WT) mice. **b**, Flow cytometric binding analysis of luminal polyclonal SIgA derived from donor mice (each line shows a dilution series from an individual mouse, $n = 6$) to intact live *E. coli* HA107, 21 days after transitory colonization. Red dashed line indicates upper limit of binding from germ-free controls. **c**, Fluorescence-activated cell sorting gate for isolation of IgA⁺ lamina propria plasma cells for single-cell Ig sequencing, analysis and monoclonal Ig expression. **d–g**, Isotype distribution (**d**), clonal expansion (**e**) *IGHV* and *IGKV* gene combination (**f**) and number of *IGHV* somatic hypermutations (**g**) in single lamina propria plasma cell Ig gene repertoires of HA107-primed mice derived from six donor mice (**d–f**) or compared to germ-free controls obtained from six donor mice (**g**), red bar shows mean. $n = 378$ and 379 *IGHV* sequences derived from single plasma cells from germ-free or HA107-exposed animals, respectively (**g**). **h**, Cloning and recombinant antibody expression strategy for monoclonal human IgG1. **i**, Frequency of Igλ light-chain-expressing cells in Ig gene repertoires of HA107-primed mice compared to germ-free controls ($n = 6$ mice), red bar shows mean. **j, k**, Flow cytometric binding analysis of live intact HA107 bacteria surface-coating monoclonal IgG1 and negative control B8-030 (**j**) showing the frequency of surface-binding IgG1 in HA107-associated antibodies and germ-free controls used

at $1 \mu\text{g ml}^{-1}$ within each animal (**k**). **l**, ELISA binding of monoclonal IgG1 derived from HA107-primed mice or germ-free controls used at $1 \mu\text{g ml}^{-1}$ to HA107 lysate. **m**, Clonal expansions of lysate- (grey fill) and surface-binding (dark fill) monoclonal IgG1: the frequencies of B cell clusters are shown separated within the overall populations. **n**, Numbers of IGHV somatic hypermutations in HA107-binding ($n = 22$) and nonbinding ($n = 168$) antibodies and their clonal members derived from HA107-primed mice, red bars show mean values. Statistics show two-sided Mann–Whitney *U*-test (**g, n**). Data are representative of two (**b, c, j, l**) independent experiments.

Extended Data Fig. 2 Antibody-binding characteristics of HA107-binding monoclonal dimeric IgA.

a, Cloning and recombinant antibody expression strategy for mouse dimeric IgA. **b, c, f**, Additional data showing further mIgAs that are not included in Fig. [1a–c](#) due to space limitations. **b**, Individual monoclonal IgA binding to intact live HA107 bacteria by flow cytometry (top panels), or the HA107 lysate (bottom panels) by ELISA. Red dashed lines indicate cutoff for positivity. **c**, Flow cytometry analysis of mIgA binding of non-auxotrophic JM83 parental strain of HA107. **d**, Flow cytometric analysis showing distinctive nonreplicating, replicating and dying subpopulations of JM83 isolated from fresh faecal pellets of antibody-deficient mice ex vivo. **e**, Flow cytometric microscopy of faecal JM83 nonreplicating (top), replicating (middle) and dying (bottom) subpopulations stained with mIgA₄₂₅₀. **f**, Binding of individual monoclonal IgAs to faecal JM83 bacterial nonreplicating, replicating or dying subpopulations gated as in Extended Data Fig. [2d](#). mIgA clone numbers are indicated at the top of each column (**b, c, f**). Data are of one (**e**) or representative of two (**b–d, f**) independent experiments.

Extended Data Fig. 3 Intestinal dimeric mIgAs bind discrete bacterial membrane fractions.

a–d, ELISA binding of individual monoclonal dimeric IgAs ordered as in Fig. [1a–c](#) (**a, b**) or Extended Data Fig. [2b, c, f](#) (**c, d**) to HA107 membrane

fraction (top), cytoplasmic fraction (middle) and purified ribosomes (bottom) (**a**, **c**) or intact outer membrane vesicles (**b**, **d**). mIgA clone numbers are indicated at the top of each column. Red dashed lines indicate upper limit of binding from negative control antibody mIgA_{mGO53}. The insets within the mIgA₄₅₅₉ (**a**, **b**) and the mIgA₄₀₂₅ (**c**, **d**) column show control serum IgG binding from a mouse injected with 10⁸ c.f.u. of *E. coli* HA107 14 days previously.

Extended Data Fig. 4 Intestinal dimeric mIgAs bind discrete membrane-associated antigens.

a, *E. coli* LPS core oligosaccharide structures (*E. coli* O86 (K12), W3110 (K12), O10 (R1), O100 (R2), and O111 (R3))³⁷. K12, R1, R2 and R3 depict core type. R indicates nonstoichiometric substitutions; phosphate group (P); pyrophosphate group (PP); pyrophosphorylethanolamine (PPEtn).

* Indicates heterogeneity of the core OS regarding terminal sugar residues. Blue indicates outer and black indicates inner core region. LA indicates lipid A. **b**, Binding of mIgA₄₀₅₃ to different structures of purified rough and smooth LPS shown in (a). **c**, Flow cytometric analysis of mIgA₄₃₀₈ coating of selective fimbrial (*fim*) gene *E. coli* deletion strains³⁴ and the *E. coli* wild-type (BW25113). **d**, **e**, Flow cytometric binding analysis to *E. coli* wild-type (left) and single gene deletion strains (right) of mIgA₄₂₄₉ (**d**) and mIgA₄₂₅₀ (**e**). **f**, ELISA binding of indicated mIgA to lysates of *E. coli*_{ΔenvZ}, *E. coli*_{ΔompC}, or a series of targeted *E. coli* deletion strains, or the wild-type with normal OmpC expression (details in Supplementary Table 4). **g**, Electron micrograph of the outer membrane vesicle fraction of *E. coli* HA107. Scale bar, 200 nm. **h**, **i**, Flow cytometric binding analysis of mIgA₄₃₀₈ to smooth strain BW24599³² (**h**) and *E. coli* JM83 pre-incubated with and without α-methyl mannoside⁴² to block high mannose binding sites (**i**). **j**, Gene expression ratios assessed by RNA sequencing showing the 20 most upregulated genes from fractionated mIgA₄₃₀₈ coated compared to uncoated HA107 bacteria (left), fimbrial (*fim*) operon members are highlighted (right). **k**, ELISA binding of mIgA₄₂₁₉, mIgA₄₂₅₀ and mIgA₄₅₈₄ to purified recombinant OmpC protein. Each line represents the dilution series of an individual mIgA and the negative control mIgA_{mGO53} is shown

in green. **I**, Surface plasmon resonance affinity measurements of OmpC-binding mIgA₄₂₅₀ (left) and mIgA₄₂₁₉ (right). Antibody affinities (K_D) are shown in the upper left of each panel. Data were obtained from one (**g, j, l**) or are representative of two independent experiments (**b-f, h, i, k**).

Extended Data Fig. 5 IgA secretion and elimination in the in vivo mIgA reconstitution model.

a,b,c IgA concentration measurements of secretion and elimination after i.v. injection by ELISA following injection of monomeric ($n = 2$ mice) or dimeric mIgA in unmanipulated wild-type C57BL/6 ($n = 2$ mice) and dimeric mIgA in C57BL/6 mice ($n = 3$) following bile duct ligation (BDL). Serial measurements from serum (**a**), bile (**b**) or faeces (**c**), individual data points are shown. **d**, Decay of mIgA in serum after injection of different dimeric mIgAs ($n = 3$ for each condition; $\bar{x} \pm \text{s.d.}$). **e**, c.f.u. in colonic/faecal fractions of JM83 at 10.5 h after reconstitution with the indicated mIgA species ($\bar{x} \pm \text{s.d.}$, mSIgA₄₂₅₀ $n = 6$, mSIgA₄₃₀₈ $n = 3$ and mSIgA_{B8-030} $n = 5$ faecal samples from individual mice).

Source Data

Extended Data Fig. 6 Functional consequences of reconstituted mSIgA in vivo and in vitro.

a, OmpC target gene expression from faecal JM83 bacterial RNA Sequencing analysis at 10.5 h following reconstitution with different mIgAs as shown on the x axis ($\bar{x} \pm \text{s.d.}$, mSIgA₄₂₅₀ $n = 8$, mSIgA₄₅₈₄ $n = 10$, mSIgA₄₂₁₉ $n = 4$ and mSIgA_{B8-030} $n = 10$ faecal samples from individual mice). **b**, *ompF* and *lamB* gene expression from faecal JM83 bacterial RNA sequencing at 10.5 h p.i. after mSIgA₄₂₅₀ reconstitution ($\bar{x} \pm \text{s.d.}$, mSIgA₄₂₅₀ $n = 8$ and mSIgA_{B8-030} $n = 10$ faecal samples from individual mice). **c, d**, Venn diagrams of downregulated (**c**) or upregulated genes (**d**) after reconstitution with different OmpC-binding mSIgAs at 10.5 h p.i. **e**, Flow cytometric binding analysis of mIgA-4250 to *ompC*-deficient strain BL21ΔC (top) and BL21ΔCF (bottom) with (right) and without (left)

ectopic OmpC expression^{35,36}. Numbers adjacent to gates indicate bound bacterial frequencies. **f**, [¹⁴C]Glucose uptake in BL21ΔCF bacteria with or without pGOmpC complementation coated with indicated mIgA, ($\bar{x} \pm s.d.$, mSIgA_{B8-030}, $n = 5$ with and 3 without pGOmpC, mSIgA₄₂₅₀ $n = 6$ with and 3 without pGOmpC). **g**, Protection from bacteriophage T4 infection of mIgA-4250-coated OmpC-deletion and complemented bacteria ($\bar{x} \pm s.d.$, $n = 4$ for each condition). **h**, Fimbrial operon members target gene expression from faecal JM83 bacterial RNASeq analysis at 10.5 h following reconstitution with different mIgAs as shown on the *x* axis ($\bar{x} \pm s.d.$, mSIgA₄₃₀₈ $n = 5$ and mSIgA_{B8-030} $n = 10$ faecal samples from individual mice). **i**, Differential gene expression of enriched GO term gene members in faecal JM83 bacteria after reconstitution with fimbriae (fimb.)-binding mSIgA₄₃₀₈ and negative control mSIgA_{B8-030}. Numbers (right *y* axis) identify gene annotations in Supplementary Table 10. **j**, **k**, mSIgA target gene expression from faecal JM83 bacterial RNA sequencing 24 h following mIgA reconstitution, at a time when mSIgA had been almost completely shed from the animal via the faeces ($\bar{x} \pm s.d.$, individual data points are shown). Compare 10.5 h in **a** and **h**. Statistics show two-sided Wald test (**a**, **b**, **h**) and two-sided paired (**f**) and unpaired *t*-test (**g**), **P* < 0.05. Data are from one experiment (**k**) or representative from two experiments (**e**) or pooled from two (**f**, **g**, **j**), four (**a**, **b**, **h**) and five (**c**, **d**, **i**) independent experiments.

Source Data

Extended Data Fig. 7 Bacterial aggregation of mIgA-4308.

a, OD of *E. coli* JM83 grown in the presence of mIgA ($\bar{x} \pm s.d.$, $n = 4$ for each condition, mIgA₄₃₀₈ $P = 0.0054$). **b**, **c**, Bacterial aggregates of *fm*-locked *E. coli* strain AAEC189[pSH2]³³ after addition of mIgA or yeast mannan quantified (**b**) and as representative images (**c**). Box plot shows mean and 25–75th percentiles, whiskers show minimum and maximum value (**b**). mSIgA₄₃₀₈ $n = 68$, mSIgA_{B8-030} $n = 70$, Mannan $n = 58$ and mSIgA₄₂₅₀ $n = 68$. Bar corresponds to 10 μm. Statistics show two-sided

paired *t*-test (**a**) and two-sided unpaired *t*-test (**b**). Data are representative from three experiments (**c**) or pooled from two (**a**) or three (**b**) independent experiments.

[Source Data](#)

Extended Data Fig. 8 Properties of polyreactive monoclonal antibodies derived from plasma cells of germ-free and HA107-primed mice.

a, ELISA binding of monoclonal IgG1 derived from plasma cells of germ-free ($n = 85$ monoclonal antibodies, top) and HA107-primed mice ($n = 91$ monoclonal antibodies, lower row) using standard polyreactivity measurement conditions²⁷ to LPS O111:B4 (left panels), insulin (middle) and double-stranded (ds) DNA (bottom). Red dashed lines show cutoffs according to convention: red and green lines show positive and negative control antibodies mIgG1_{ED38} and mIgG1_{mGO53}, respectively. **b, c**, Polyreactive antibody frequencies among all tested antibodies ordered by donor mouse (**b**) or clonal frequencies for HA107-primed mice (**c**). **d, e**, Summary data of frequency of antibodies that are clonally-expanded among polyreactive (upper left) or nonreactive antibodies (upper right) or including HA107-binders (lower left and right respectively) among all expressed antibodies (**d**) and per HA107-primed donor animal (**e**). Number of antibodies per group is indicated (**d**). $(\bar{x}) \pm$ s.d., $n = 3$ mice for each condition (**e**). **f**, Frequency of polyreactive antibodies within HA107-binding (left) and nonbinding (right) antibodies. Number of antibodies per group is indicated. **g**, ELISA binding of mIgA₄₂₅₀ and mIgA₄₁₈₆ to LPS (left), insulin (middle) and double-stranded (ds) DNA (right). Red dashed lines show cutoffs according to the highest value of the mIgA_{mGO53} negative control, red and green lines show positive and negative control antibodies mIgA_{ED38} and mIgA_{mGO53}, respectively. **h**, Flow cytometric binding analysis of polyreactive (black) and nonpolyreactive (light grey) IgG1 and mIgA to faecal bacteria pooled from C57BL/6 SPF ($n = 6$) or RAG^{-/-} ($n = 2$) animals ($(\bar{x}) \pm$ s.d.). Number of antibodies tested is indicated at the top of each group. Red and green symbols show polyreactive antibodies 4186 and 4250, respectively. **i**, Glycan array

binding of mIgA₄₁₈₆, mIgA₄₂₅₀ and pooled SPF control serum ($n = 3$). **j**, Differential gene expression of enriched GO term gene members in faecal JM83 bacteria after reconstitution with polyreactive mSIgA₄₁₈₆ and negative control mSIgA_{B8-030}. **k**, Differential gene expression of enriched GO terms in faecal JM83 and JW2203(Δ *ompC*) bacteria after reconstitution with polyreactive mSIgA₄₁₈₆, mSIgA₄₂₅₀ and negative control mSIgA_{B8-030}. Statistics show two-sided Fisher's Exact (**d**, **f**), two-sided unpaired *t*-test (**e**) and two-sided Mann–Whitney *U*-test (**h**) + $P_{\text{adj}} < 0.1$. Data are obtained from one (**h**, **k**), representative from two (**g**, **i**) or three (**a**) and pooled from five (**j**, **k**) independent experiments.

Extended Data Fig. 9 Generic functional effects of surface-coating mSIgA.

a, Flow cytometric live/dead analysis to faecal *E. coli* JM83 with (left) or without (right) preincubation with bile acids. **b**, DE flagellar motility genes after indicated mSIgA reconstitution (*P* values mSIgA₄₃₀₈: *flgM* $P = 0.038$, *flhA* $P = 0.036$, *flhB* $P = 0.044$, *flfF* $P = 0.035$, *flfN* $P = 0.048$, *flfO* $P = 0.015$, *flfR* $P = 0.002$, *flfT* $P = 0.003$, *flfZ* $P = 0.037$, *flfI* $P = 0.008$, *flfL* $P = 0.028$, *flfP* $P = 0.042$; mSIgA₄₀₈₁: *flfR* $P = 0.010$, *flfI* $P = 0.035$, *flfP* $P = 0.013$; mSIgA₄₂₅₀: *flgA* $P = 0.028$, *flgB* $P = 0.025$, *flgC* $P = 0.014$, *flgD* $P = 0.042$, *flgF* $P = 0.019$, *flgG* $P = 0.049$, *flhC* $P < 0.001$, *flhD* $P = 0.030$, *flfA* $P = 0.019$, *flfE* $P = 0.025$). Data are representative from two (**a**) or five (**b**) independent experiments.

Supplementary information

Supplementary Information

This file contains Supplementary Tables 1–14 and Supplementary Fig. 1.

Reporting Summary

Peer Review File

Source data

[Source Data Fig. 2](#)

[Source Data Fig. 3](#)

[Source Data Extended Data Fig. 5](#)

[Source Data Extended Data Fig. 6](#)

[Source Data Extended Data Fig. 7](#)

Rights and permissions

[Reprints and Permissions](#)

About this article

Cite this article

Rollenske, T., Burkhalter, S., Muerner, L. *et al.* Parallelism of intestinal secretory IgA shapes functional microbial fitness. *Nature* **598**, 657–661 (2021). <https://doi.org/10.1038/s41586-021-03973-7>

- Received: 16 February 2021
- Accepted: 31 August 2021
- Published: 13 October 2021
- Issue Date: 28 October 2021
- DOI: <https://doi.org/10.1038/s41586-021-03973-7>

Share this article

Anyone you share the following link with will be able to read this content:

[Get shareable link](#)

Sorry, a shareable link is not currently available for this article.

[Copy to clipboard](#)

Provided by the Springer Nature SharedIt content-sharing initiative

This article was downloaded by **calibre** from <https://www.nature.com/articles/s41586-021-03973-7>

| [Section menu](#) | [Main menu](#) |

- Article
- [Published: 06 October 2021](#)

Metabolic modulation of tumours with engineered bacteria for immunotherapy

- [Fernando P. Canale](#) ORCID: orcid.org/0000-0001-5805-6785^{1 na1},
- [Camilla Basso](#)^{1 na1 nAff5},
- [Gaia Antonini](#)¹,
- [Michela Perotti](#)^{1,2},
- [Ning Li](#)³,
- [Anna Sokolovska](#)³,
- [Julia Neumann](#) ORCID: orcid.org/0000-0003-4281-8700¹,
- [Michael J. James](#)³,
- [Stefania Geiger](#)¹,
- [Wenjie Jin](#)^{1,2},
- [Jean-Philippe Theurillat](#)⁴,
- [Kip A. West](#)³,
- [Daniel S. Leventhal](#)³,
- [Jose M. Lora](#)^{3 nAff6},
- [Federica Sallusto](#) ORCID: orcid.org/0000-0003-3750-2752^{1,2} &
- [Roger Geiger](#) ORCID: orcid.org/0000-0002-8016-1669^{1,4}

[Nature](#) volume **598**, pages 662–666 (2021)

- 17k Accesses
- 1 Citations
- 553 Altmetric

- [Metrics details](#)

Subjects

- [Applied immunology](#)
- [Immunotherapy](#)

Abstract

The availability of l-arginine in tumours is a key determinant of an efficient anti-tumour T cell response^{1,2,3,4}. Consequently, increases of typically low l-arginine concentrations within the tumour may greatly potentiate the anti-tumour responses of immune checkpoint inhibitors, such as programmed death-ligand 1 (PD-L1)-blocking antibodies⁵. However, currently no means are available to locally increase intratumoural l-arginine levels. Here we used a synthetic biology approach to develop an engineered probiotic *Escherichia coli* Nissle 1917 strain that colonizes tumours and continuously converts ammonia, a metabolic waste product that accumulates in tumours⁶, to l-arginine. Colonization of tumours with these bacteria increased intratumoural l-arginine concentrations, increased the number of tumour-infiltrating T cells and had marked synergistic effects with PD-L1 blocking antibodies in the clearance of tumours. The anti-tumour effect of these bacteria was mediated by l-arginine and was dependent on T cells. These results show that engineered microbial therapies enable metabolic modulation of the tumour microenvironment leading to enhanced efficacy of immunotherapies.

Access options

Subscribe to Journal

Get full journal access for 1 year

\$199.00

only \$3.90 per issue

Subscribe

All prices are NET prices.
VAT will be added later in the checkout.
Tax calculation will be finalised during checkout.

Rent or Buy article

Get time limited or full article access on ReadCube.

from \$8.99

Rent or Buy

All prices are NET prices.

Additional access options:

- [Log in](#)
- [Access through your institution](#)
- [Learn about institutional subscriptions](#)

Fig. 1: L-Arginine synergizes with PD-L1 blockade to promote MC38 tumour rejection.

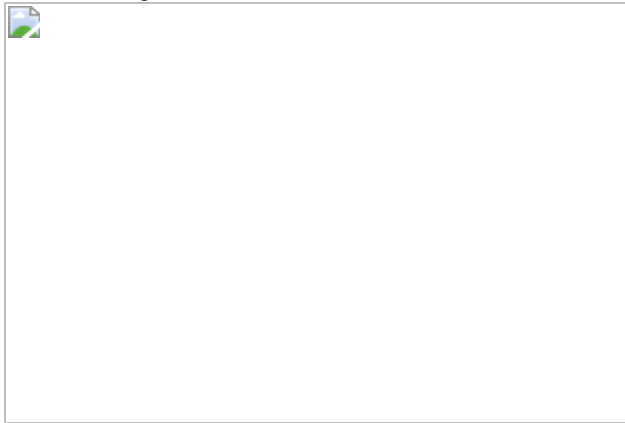


Fig. 2: Metabolically engineered bacteria produce L-arginine and colonize tumours.

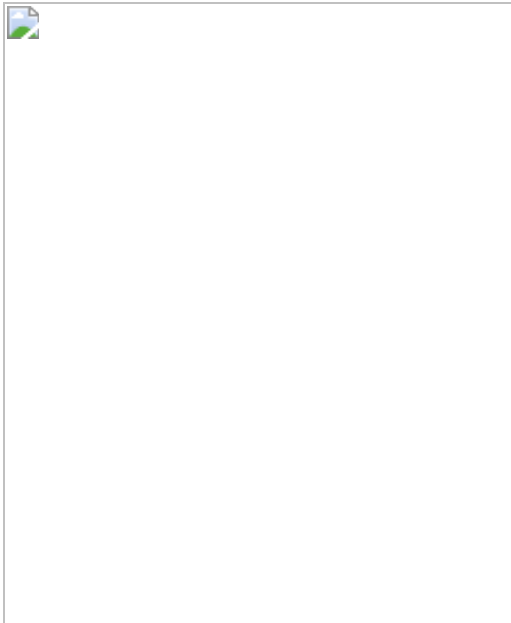


Fig. 3: l-Arg bacteria synergize with PD-L1 blockade to promote MC38 tumour rejection.



Fig. 4: l-Arg bacteria enhance anti-tumour immunity and can be administered systemically.



Data availability

The mass spectrometry proteomics data have been deposited to the ProteomeXchange Consortium via the PRIDE partner repository with the dataset identifier [PXD027167](#). [Source data](#) are provided with this paper.

References

1. 1.

Rodriguez, P. C. & Ochoa, A. C. Arginine regulation by myeloid derived suppressor cells and tolerance in cancer: mechanisms and therapeutic perspectives. *Immunol. Rev.* **222**, 180-191 (2008).

2. 2.

Bronte, V. & Zanovello, P. Regulation of immune responses by l-arginine metabolism. *Nat. Rev. Immunol.* **5**, 641-654 (2005).

3. 3.

Geiger, R. et al. l-Arginine modulates T cell metabolism and enhances survival and anti-tumor activity. *Cell* **167**, 829-842.e813 (2016).

4. 4.

Martí i Líndez, A.-A. M. et al. Mitochondrial arginase-2 is a cell-autonomous regulator of CD8⁺ T cell function and antitumor efficacy. *JCI Insight* **4**, e132975 (2019).

5. 5.

He, X., Lin, H., Yuan, L. & Li, B. Combination therapy with l-arginine and α-PD-L1 antibody boosts immune response against osteosarcoma in immunocompetent mice. *Cancer Biol. Ther.* **18**, 94-100 (2017).

6. 6.

Spinelli, J. B. et al. Metabolic recycling of ammonia via glutamate dehydrogenase supports breast cancer biomass. *Science* **358**, 941-946

(2017).

7. 7.

Forbes, N. S. Engineering the perfect (bacterial) cancer therapy. *Nat. Rev. Cancer* **10**, 785 (2010).

8. 8.

Kitada, T., DiAndreth, B., Teague, B. & Weiss, R. Programming gene and engineered-cell therapies with synthetic biology. *Science* **359**, eaad1067 (2018).

9. 9.

Zhao, G., Jin, Z., Allewell, N. M., Tuchman, M. & Shi, D. Crystal structure of the *N*-acetyltransferase domain of human *N*-acetyl-l-glutamate synthase in complex with *N*-acetyl-l-glutamate provides insights into its catalytic and regulatory mechanisms. *PLoS ONE* **8**, e70369 (2013).

10. 10.

Sancho-Vaello, E., Fernandez-Murga, M. L. & Rubio, V. Mechanism of arginine regulation of acetylglutamate synthase, the first enzyme of arginine synthesis. *FEBS Lett.* **583**, 202-206 (2009).

11. 11.

Rajagopal, B. S., DePonte, J., 3rd, Tuchman, M. & Malamy, M. H. Use of inducible feedback-resistant *N*-acetylglutamate synthetase (*argA*) genes for enhanced arginine biosynthesis by genetically engineered *Escherichia coli* K-12 strains. *Appl. Environ. Microbiol.* **64**, 1805-1811 (1998).

12. 12.

Aebersold, R. & Mann, M. Mass spectrometry-based proteomics. *Nature* **422**, 198-207 (2003).

13. 13.

Malissen, M. et al. Altered T cell development in mice with a targeted mutation of the CD3-epsilon gene. *EMBO J.* **14**, 4641-4653 (1995).

14. 14.

Kurtz, C. B. et al. An engineered *E. coli* Nissle improves hyperammonemia and survival in mice and shows dose-dependent exposure in healthy humans. *Sci. Transl. Med.* **11**, eaau7975 (2019).

15. 15.

Isabella, V. M. et al. Development of a synthetic live bacterial therapeutic for the human metabolic disease phenylketonuria. *Nat. Biotechnol.* **36**, 857-864 (2018).

16. 16.

Malissen, M. et al. Altered T cell development in mice with a targeted mutation of the CD3-epsilon gene. *EMBO J.* **14**, 4641-4653 (1995).

17. 17.

Rappaport, J., Mann, M. & Ishihama, Y. Protocol for micro-purification, enrichment, pre-fractionation and storage of peptides for proteomics using StageTips. *Nat. Protoc.* **2**, 1896-1906 (2007).

18. 18.

Scheltema, R. A. et al. The Q Exactive HF, a benchtop mass spectrometer with a pre-filter, high-performance quadrupole and an ultra-high-field Orbitrap analyzer. *Mol. Cell. Proteomics* **13**, 3698-3708 (2014).

19. 19.

Cox, J. & Mann, M. MaxQuant enables high peptide identification rates, individualized p.p.b.-range mass accuracies and proteome-wide

protein quantification. *Nat. Biotechnol.* **26**, 1367-1372 (2008).

20. 20.

Cox, J. et al. Andromeda: a peptide search engine integrated into the MaxQuant environment. *J. Proteome Res.* **10**, 1794-1805 (2011).

Acknowledgements

R.G. is supported in part by Synlogic, the European Research Council (803150) and Swiss Cancer Research (KFS-4593-08-2018). F.S. is supported by the Helmut Horten Foundation.

Author information

Author notes

1. Camilla Basso

Present address: Ente Ospedaliero Cantonale, Department of Surgery, Università della Svizzera italiana, Bellinzona, Switzerland

2. Jose M. Lora

Present address: Intergalactic Therapeutics, Boston, MA, USA

3. These authors contributed equally: Fernando P. Canale, Camilla Basso

Affiliations

1. Institute for Research in Biomedicine, Università della Svizzera italiana, Bellinzona, Switzerland

Fernando P. Canale, Camilla Basso, Gaia Antonini, Michela Perotti, Julia Neumann, Stefania Geiger, Wenjie Jin, Federica Sallusto & Roger Geiger

2. Institute of Microbiology, ETH Zürich, Zürich, Switzerland

Michela Perotti, Wenjie Jin & Federica Sallusto

3. Synlogic, Cambridge, MA, USA

Ning Li, Anna Sokolovska, Michael J. James, Kip A. West, Daniel S. Leventhal & Jose M. Lora

4. Institute of Oncology Research, Università della Svizzera italiana, Bellinzona, Switzerland

Jean-Philippe Theurillat & Roger Geiger

Contributions

R.G. and J.M.L. conceived the project. F.P.C., C.B., G.A., M.P., S.G., J.N. and W.J. performed experiments with mouse tumour models. N.L. and M.J.J. generated bacterial strains. J.-P.T. analysed tissue sections. A.S. and K.A.W. contributed to discussions. R.G., F.S. and J.M.L. supervised the work. D.S.L., J.M.L. and R.G. wrote the manuscript.

Corresponding author

Correspondence to Roger Geiger.

Ethics declarations

Competing interests

R.G. and J.L. are inventors on a patent application related to l-Arg bacteria. R.G. received research funding from Synlogic. N.L., A.S., M.J, D.S.L, K.A.W. and J.M.L. are or were employees and stockholders of Synlogic.

Additional information

Peer review information *Nature* thanks Jeff Hasty and the other, anonymous, reviewer(s) for their contribution to the peer review of this work.

Publisher's note Springer Nature remains neutral with regard to jurisdictional claims in published maps and institutional affiliations.

Extended data figures and tables

[Extended Data Fig. 1 Intratumoral injections of an L-arginine solution does not affect the growth of MC38 tumors.](#)

(a) MC38 tumors were established in C57BL/6 WT mice. Ten days later, 50 μ l of a saturated L-arginine solution was injected into tumors. This corresponds to 0.25 mg L-arginine/g body weight and is the maximal volume that tumors can take up. Where indicated, mice were treated with 200 μ g anti-PD-L1 antibodies or isotype control antibodies by i.p injection. Mice received a total of four injections (bi-weekly). MC38 tumor growth curves. Values represent mean tumor volume \pm s.e.m. Number of mice are indicated in the graph. Two experiments. **(b)** Same experiment as in **(a)** but survival curves are shown. **(c)** Same experiment as in **(a)** but growth curves of individual mice are shown. **(d)** Example of the gating strategy to quantify CD4 and CD8 T cells used in Figs. [3b,c,f,g](#)

[Source data](#).

[Extended Data Fig. 2 EcN colonization does not affect the growth of MC38 tumors.](#)

MC38 tumors were established in C57BL/6 WT mice. Mice were treated with 5×10^6 CFU EcN (i.t.) or with i.t. injections of PBS, bi-weekly (four treatments in total). MC38 tumor growth curves. Values represent mean tumor volume \pm s.e.m. Number of mice are indicated in the graph. Two experiments

[Source data](#).

Extended Data Fig. 3 The anti-tumor effect of L-Arg bacteria is T cell-dependent.

(a) MC38 tumors were established in C57BL/6 WT mice and in *CD3e*^{-/-} mice and treated via intratumoral injection with 5×10^6 CFUs of L-Arg bacteria or EcN. Tumors were harvested and homogenized after 24 h, and bacterial abundance was measured by CFU assay. n = 2 **(b)** MC38 tumors were established in *CD3e*^{-/-} mice. Tumors of the control group were treated with 5×10^6 CFU EcN (i.t.) twice a week. A second group was treated with 5×10^6 CFU L-Arg bacteria (i.t.) twice a week. A third group received anti-PD-L1 antibodies i.p. and 5×10^6 CFU EcN i.t. (EcN + α -PD-L1) and a fourth group received anti-PD-L1 antibodies i.p. and 5×10^6 L-Arg bacteria i.t (L-Arg-bac. + α -PD-L1). Tumor growth curve. Values represent mean tumor volume \pm s.e.m. n = 5 for each group. **(c)** Survival curves of mice

[Source data.](#)

Extended Data Fig. 4 Effect of bacterial treatments on mouse health.

(a) C57BL/6 WT mice with established MC38 tumors were treated with four i.t. injections of 5×10^6 EcN or L-Arg bacteria, or with PBS. The weight of mice was followed over time. Bars represent the SEM, throughout. **(b)** C57BL/6 WT mice with established MC38 tumors were treated with a single i.v. injection of 5×10^7 EcN or L-Arg bacteria, or with PBS. The weight of mice was followed over time. The number of mice is indicated in the graph. Two experiments (a, b)

[Source data.](#)

Extended Data Fig. 5 Bacterial treatments and PD-L1 blockade have no effect on B16 tumor growth.

C57BL/6 WT mice with established B16.OVA tumors were treated four times with i.t. injections of 5×10^6 EcN or L-Arg bacteria and i.p. injections

of anti-PD-L1 antibodies. Tumor growth curves. Values represent mean tumor volume \pm s.e.m., n = 5

[Source data](#).

Supplementary information

[Reporting Summary](#)

Source data

[Source Data Fig. 1](#)

[Source Data Fig. 3](#)

[Source Data Fig. 4](#)

[Source Data Extended Data Fig. 1](#)

[Source Data Extended Data Fig. 2](#)

[Source Data Extended Data Fig. 3](#)

[Source Data Extended Data Fig. 4](#)

[Source Data Extended Data Fig. 5](#)

Rights and permissions

[Reprints and Permissions](#)

About this article

[Cite this article](#)

Canale, F.P., Basso, C., Antonini, G. *et al.* Metabolic modulation of tumours with engineered bacteria for immunotherapy. *Nature* **598**, 662–666 (2021). <https://doi.org/10.1038/s41586-021-04003-2>

- Received: 16 May 2019
- Accepted: 07 September 2021
- Published: 06 October 2021
- Issue Date: 28 October 2021
- DOI: <https://doi.org/10.1038/s41586-021-04003-2>

Share this article

Anyone you share the following link with will be able to read this content:

[Get shareable link](#)

Sorry, a shareable link is not currently available for this article.

[Copy to clipboard](#)

Provided by the Springer Nature SharedIt content-sharing initiative

[**Bacteria recycle tumour waste to fuel immune cells**](#)

- Laurence C. Chen
- Yvonne Y. Chen

News & Views 06 Oct 2021

This article was downloaded by **calibre** from <https://www.nature.com/articles/s41586-021-04003-2>

- Article
- Open Access
- [Published: 13 October 2021](#)

The cellular environment shapes the nuclear pore complex architecture

- [Anthony P. Schuller](#)^{1,na1},
- [Matthias Wojtynek](#)^{2,3 na1},
- [David Mankus](#) [ORCID: orcid.org/0000-0002-9979-7608](#)⁴,
- [Meltem Tatli](#)²,
- [Rafael Kronenberg-Tenga](#)²,
- [Saroj G. Regmi](#)⁵,
- [Phat V. Dip](#)^{1,6},
- [Abigail K. R. Lytton-Jean](#)⁴,
- [Edward J. Brignole](#)^{1,6},
- [Mary Dasso](#) [ORCID: orcid.org/0000-0002-5410-1371](#)⁵,
- [Karsten Weis](#) [ORCID: orcid.org/0000-0001-7224-925X](#)³,
- [Ohad Medalia](#) [ORCID: orcid.org/0000-0003-0994-2937](#)² &
- [Thomas U. Schwartz](#) [ORCID: orcid.org/0000-0001-8012-1512](#)¹

Nature volume **598**, pages 667–671 (2021)

- 9397 Accesses
- 205 Altmetric
- [Metrics details](#)

Subjects

- [Cryoelectron tomography](#)

Abstract

Nuclear pore complexes (NPCs) create large conduits for cargo transport between the nucleus and cytoplasm across the nuclear envelope (NE)^{1,2,3}. These multi-megadalton

structures are composed of about thirty different nucleoporins that are distributed in three main substructures (the inner, cytoplasmic and nucleoplasmic rings) around the central transport channel^{4,5,6}. Here we use cryo-electron tomography on DLD-1 cells that were prepared using cryo-focused-ion-beam milling to generate a structural model for the human NPC in its native environment. We show that—compared with previous human NPC models obtained from purified NEs—the inner ring in our model is substantially wider; the volume of the central channel is increased by 75% and the nucleoplasmic and cytoplasmic rings are reorganized. Moreover, the NPC membrane exhibits asymmetry around the inner-ring complex. Using targeted degradation of Nup96, a scaffold nucleoporin of the cytoplasmic and nucleoplasmic rings, we observe the interdependence of each ring in modulating the central channel and maintaining membrane asymmetry. Our findings highlight the inherent flexibility of the NPC and suggest that the cellular environment has a considerable influence on NPC dimensions and architecture.

[Download PDF](#)

Main

A combination of X-ray crystallography and electron microscopy (EM) approaches has generated a consensus model for the NPC architecture, characterized by three substructures that span the NE^{4,5,7}. The inner ring (IR) is centrally positioned at the fusion point of the inner and outer nuclear membranes (INM and ONM, respectively) and forms the central channel that connects to phenylalanine–glycine (FG) repeat proteins that create the permeability barrier and facilitate active cargo transport. The cytoplasmic ring (CR) provides a platform for protein and RNA export^{3,8}. The nucleoplasmic ring (NR) shares scaffold nucleoporins (Nups) with the CR and anchors a distinct basket-like structure with diverse functions.

Although all eukaryotes maintain a three-ring NPC structure, the composition and arrangement of the substructures varies between species. In mammalian cells, the IR has five primary subunits: Nup205, Nup188, Nup155, Nup93 and Nup35 (refs. ^{4,5,9}). FG-Nups (Nup54, Nup58 and Nup62) are docked to the IR to create the central channel for transport^{4,5,7}. The CR and NR both contain 16 copies of the Y complex^{10,11,12,13}, which contains a set of elongated helical stack proteins (Nup160, Nup133, Nup107, Nup96 and Nup85) decorated with the beta-propellers Sec13, Seh1, Nup37 and Nup43 (refs. ^{11,12,14}). The principal Y-complex arrangement in both the CR and NR follows a reticulated pattern composed of two eight-membered rings^{12,15}.

Our current understanding of the human NPC structure is based mainly on cryo-electron tomography (cryo-ET) studies of NPCs from purified NEs at 2–6 nm

resolution^{12,15,16}. Cryo-focused-ion-beam (cryo-FIB) milling now enables the study of macromolecular complexes in their native environment¹⁷. NPCs from cryo-FIB-milled yeast^{18,19}, algae²⁰ and human cells^{21,22} show differences compared with previous human NPC structures, including wider IRs. Here we study the architecture of the human NPC from cryo-FIB-milled DLD-1 cells. Our data establish concepts in human NPC architecture that may have previously been interpreted as species-specific differences. Our study shows that the cellular environment substantially influences the diameter of the NPC central channel and emphasizes the modular, although interdependent, architecture of the NPC and its role in shaping the NE.

The architecture of the NPC in DLD-1 cells

We used cryo-FIB-milled lamellae of human DLD-1 cells containing an auxin-inducible degron (AID) tag at the *NUP96* (HGNC symbol: *NUP98*) loci (homozygous *NUP96::Neon-AID*)²³ for the targeted depletion of Nup96. Such Nup96 depletion leads to a loss of both the CR and NR elements, whereas the IR is unaffected. Here we compared native and partially degraded NPC structures. Lamellae were prepared from cells in the absence of auxin (wild-type condition) for cryo-ET imaging and identification of *in situ* NPCs. We extracted 194 NPC-containing subvolumes from 54 tomograms and used subtomogram averaging to obtain a density map of the NPC resolved to ~3.4 nm (Fig. 1 and Extended Data Fig. 1a–c). Our structural analysis revealed a similar three-ring architecture to that observed in previous human models^{12,15,16}. However, the diameter of the central channel is considerably different (Fig. 1c and Extended Data Fig. 2a)—it is about 33% larger (width, about 57 nm) compared with previous models (width, about 43 nm)¹⁵. Furthermore, the outer diameter of the IR is about 105 nm, compared with around 89 nm for semi-purified NPCs. Moreover, we observed a reduced NPC height of 66 nm, compared with 75 nm in previous models. Finally, the distance between the centre of the IR and the distal end of the CR is greater than the distance between the IR and the NR (37 nm versus 29 nm, respectively) (Fig. 1c).

Fig. 1: The NPC structure from human DLD-1 cells.

 **figure1**

a, Tomographic slice from a lamella of a *NUP96::Neon-AID* DLD-1 cell in the absence of auxin (wild-type condition). The slice thickness is 2.7 nm. The arrowheads indicate each of the NPC rings. The arrow indicates an adjacent NPC. Scale bar, 100 nm. **b**, Whole NPC map from DLD-1 cells. Scale bar, 20 nm. **c**, Cross-section of a cryo-ET map with fitted structures for the CR (blue and yellow), IR (orange and magenta) and NR (light blue and gold). The central channel diameter (57 nm), the membrane-to-membrane diameter (105 nm) and the height across the NE (37 nm from IR-CR, 29 nm from IR-NR) are indicated.

We fit structures of nucleoporin subcomplexes into the three rings of the averaged map (Fig. 1c and Extended Data Fig. 1d–f). For the NR and CR, we used a composite Y-complex model derived from overlapping crystal structures and threaded models^{11,14,15,24}. Bending at recognized ‘hinge points’^{10,11,14}, we fit the Y complex (Extended Data Fig. 3a–c). It docks into both the CR and NR in a reticulated pattern of

eight-membered rings (Extended Data Fig. 4a–e). In each ring, we observed considerable density beyond the Y complexes. The additional density in the CR might correspond to Nup358, an expected component of this subassembly¹⁵ (Extended Data Fig. 4b). We also observed density protruding out of the CR towards the centre of the ring at the base of Nup85 (Extended Data Fig. 1d). On the basis of previous cross-linking^{8,25} and cryo-EM/cryo-ET^{26,27} studies, this density is probably occupied by the Nup214–Nup88–Nup62 complex.

For the IR, we first docked the published composite model containing Nup93, Nup188/Nup205, Nup155 and the Nup62–Nup58–Nup54 complex⁹ (Extended Data Fig. 3d,e). Although this model fits well, some elements appear to be shifted, suggesting that flexibility in the IR Nups may account for the larger diameter that we observed (Extended Data Fig. 5a). To better fit the model, we isolated individual Nups and reoriented them locally to create an updated IR model (Extended Data Fig. 5a,b).

The NR is also composed of two eight-membered rings of Y complexes. As in the CR, we identified additional density near the Nup85 arms (Extended Data Fig. 1f), and observed a linker density between the Y rings in agreement with a previous report¹⁵ (Extended Data Fig. 4c). Unique to the NR, we observed density at the base of the Y-complex-containing rings, which extends towards the IR (Extended Data Fig. 5e,f).

Asymmetric nuclear membranes at the NPC

Cross-sections through the cryo-ET map reveal that the NE at the NPC is asymmetric, with a steeper angle at the CR compared with at the NR (about 42° compared with about 28°, respectively), using the IR as a plane of reference (Fig. 2a). This membrane asymmetry is also evident in two-dimensional (2D) orthoslices of eight-fold symmetrized NPCs. In different planes of the NPC, it is readily apparent how the NE is shallower at the nucleoplasmic versus the cytoplasmic surface (Fig. 2b).

Fig. 2: Asymmetric nuclear membrane at the NPC.

 **figure2**

a, Cross-section of the NPC structure. The angles indicate measurements from the membrane distal edge of the IR to the edge of the nuclear membrane at the NR or CR. **b**, 2D orthoslices through the full-NPC average. Top, NPC map; the planes of the 2D slices (bottom) are indicated. Scale bar, 20 nm. Plane 1, at the point of the interaction between the CR Y complex and the membrane. Plane 2, at the point of the interaction between the NR Y complex and the membrane. Plane 3: sSlice in which no Y complexes touch membrane. The slice thickness is 1.4 nm.

Native NPC has a larger central channel

Compared with previous human NPC models, our map displays substantial differences, including larger IR and central channel diameters. Although the IR is

essential for maintaining the architecture of the NPC central channel, it also anchors Nups with flexible, unstructured FG-rich domains that facilitate transport through the channel²⁸. We found that the channel delineated by the IR has a volume that is about 75% larger than previously reported¹⁵ (Fig. 3a). We expect that these differences are due to the preserved cellular environment rather than any cell-type-specific differences, as we observed a similar architecture in HeLa-derived cells (Extended Data Fig. 2a, b). Furthermore, we analysed data from mouse embryonic fibroblasts in which cryo-ETs of NPCs were captured by cryo-FIB milling or cell permeabilization followed by nuclease incubation²⁹. The diameter of NPCs from cryo-FIB cells was again notably larger compared with the diameter of NPCs from permeabilized cells (Extended Data Fig. 2c).

Fig. 3: IR flexibility increases central channel size in native NPCs.

 **figure3**

- a**, Segmentation of the IR from our model and the previous human NPC model. The IR diameter (membrane to membrane) and central channel diameter measurements are indicated. The IR channel volume was calculated as a cylinder with a height of 20 nm.
- b**, Top view of three IR subunits in our model compared with the previous model. **c**,

Schematic showing the lock-and-key-like architecture of the previous model and how the IR subunits have shifted in our model.

In our IR model, Nup205/Nup188 (paralogues that are indistinguishable at this resolution), Nup155 and Nup93 are significantly shifted, whereas the Nup62–Nup58–Nup54 complex is stable (Extended Data Fig. 5b). Propagated through the entire IR, these rearrangements explain how the central channel becomes larger. Adjacent IR subunits are nearly separated compared with previous models in which the subunits were snugly aligned (Fig. 3a, b and Extended Data Fig. 5c, d). The Nup93 and Nup205 subunits of adjacent IR structures form a pseudo-lock-and-key configuration in the constricted IR model; by contrast, here these components shifted to create gaps between the IR subunits (Fig. 3c).

In contrast to the IR, the diameters of the CR and NR are nearly identical to previous models (Extended Data Fig. 4d, e). However, to accommodate a flatter overall assembly, the CR and NR rings flex in relation to the NE. At both the CR and NR, the Y-complex rings are angled more inward towards the central channel (Extended Data Fig. 4f).

Architecture of Nup96-depleted NPCs

To better understand the contribution of each ring to the overall NPC assembly, we next analysed the structure of Nup96-depleted NPCs. We acquired 71 tomograms of cryo-FIB-milled *NUP96::Neon-AID* DLD-1 cells after auxin-induced Nup96 depletion and extracted 163 NPC-containing subvolumes for subtomogram averaging (Extended Data Fig. 6a–f). In two cells, we observed ONM herniations (Extended Data Fig. 6g), indicating dysfunctional assembly of NPCs³⁰. NPCs from this dataset could be divided into the following three classes (Fig. 4a): class 1, with all three rings (17% of particles); class 2, with NR–IR complexes (32%); and class 3, containing only the IR (51%). As we found no CR–IR complexes, this suggests that the CR is more readily removed from the NPC than the NR after Nup96 depletion. Furthermore, the diameters of each unique NPC assembly varied, and assemblies with NR–IR or IR only had significantly larger diameters (Extended Data Fig. 6c). With the reduction from three to two to one ring, the spacing between the eight IR subcomplexes increases (Fig. 4a). In addition to the dilated central channel in IR-only NPCs, a cross-section analysis revealed changes in membrane orientations at the opening surrounding Nup96-depleted NPCs (Fig. 4a). The membrane has a smaller radius of curvature at the ONM–INM fusion, and the NE is more symmetric compared with in wild-type NPCs.

Fig. 4: Ensemble of Nup96-depleted structures reveal the interdependence of the NPC rings and role of the rings in shaping the nuclear membrane.

 figure4

a, NPC structures from *NUP96::Neon-AID* DLD-1 cells in the presence of auxin (Nup96-depleted) compared with wild-type (grey). Class 1 (blue, $n = 27$) contains all three rings. Class 2 (orange, $n = 53$) contains the NR and IR substructures. Class 3 (purple, $n = 83$) contains only the IR. A comparison of IR model docking (middle),

and NE curvature (right) is included. The arrowheads indicate the gaps between adjacent IR subunits. The dashed line is drawn at the midplane of the IR in the cross-sections. **b**, Model of the structural differences between our native NPC structure and the previous structure from purified NEs. **c**, Model of the structural changes caused by Nup96 depletion.

Discussion

The architectural analysis of the NPC is a major challenge for structural biology. To date, the most accurate models of the human NPC are composite structures combining crystal or EM structures and structure-based models of subcomplexes with cryo-ET data of semi-purified, intact NPCs^{9,15,31}. Our study reveals substantial NPC plasticity and shows that the purification of NEs influences the human NPC structure. We considered how the difference in IR diameter between *in situ* versus partially purified NPCs can be explained. As the NPC is integrated into the cellular matrix through the lamina and the cytoskeleton^{32,33}, it is conceivable that tensile forces acting on the NE could cause this change (Fig. 4b). Another consideration is that nuclear transport facilitated by FG-repeat extensions interacting with transport receptors may affect the NPC architecture, as reported in *Xenopus* oocytes³⁴. Furthermore, some FG-Nups stabilize the NPC scaffold³⁵; there could therefore be a yet-to-be discovered connection.

Modulating the IR diameter may be a general property of NPCs as we also observed this phenomenon in mouse embryonic fibroblasts, and it has been reported in *Saccharomyces cerevisiae*¹⁸, *Schizosaccharomyces pombe*¹⁹ and human cells^{21,22}. Moreover, we observed heterogeneity in the IR diameter among individual NPCs. Thus, structural variation is an intrinsic property of the NPC inside cells. IR flexibility could also be important for protein trafficking to the INM, which requires passage through the NPC while membrane anchorage is retained^{18,20,36,37,38}. A wider central channel not only has implications for the maximal size of soluble and membrane-bound cargo that can pass through the NPC, but it also changes the density of the FG repeats that fill the transport channel³⁹. The influence of FG density on transport has been documented⁴⁰. Our NPC model indicates that the FG density in the central channel is lower than previously thought, or that flexibility may be a means to modulate the FG barrier, consistent with suggestions for NPCs from *Chlamydomonas reinhardtii*²⁰ and *S. pombe*¹⁹.

In contrast to the IR diameter change, the CR and NR dimensions are similar to previous studies of semi-purified NPCs, suggesting that the three rings have some independence. Our findings in Nup96-depleted cells support a modular design, but also highlight the interdependence of these modules in regulating the central channel

(Fig. 4c). This may indicate that the CR and NR act as molecular ‘rulers’ to define the upper limit of the IR dimensions, as proposed for *C. reinhardtii*²⁰. However, the fact that the IR is malleable whereas the CR and NR are not also implies that the connections between the distinct rings (IR–NR and IR–CR, respectively) are flexible, explaining different assignments in various reconstructions^{9,12,15,16,18,26,36}.

Our model also exposes the asymmetry of the CR and NR substructures and their effect on the NE, as previously observed in the *Xenopus laevis* NPC²⁶. Furthermore, we observed asymmetry in the nuclear membrane at the NPC, suggesting that the membrane connections between the NR and CR are different. It is possible that ring-specific Nups make interactions with the cytoskeletal/laminar network or with ONM/INM-specific proteins to bring about this asymmetry. Alternatively, the ring-linking densities (such as Nup358 at the CR or the unassigned NR linker) could contort the CR/NR reticulated ring structures differentially, as their diameters are slightly different. Thus, the tension that each ring might impose on the NE may also lead to this asymmetry.

Flexibility of the NPC emerges as a major challenge for achieving true high resolution. In addition to flexibility, architectural heterogeneity might come from NPCs that are assembled from different subsets or stoichiometries of Nups^{41,42}. Thus, the structure described here probably represents just one of several NPC states that are still to be discovered.

Methods

Cell culture and Nup96 depletion

NUP96::Neon-AID DLD-1 cells²³ were grown in standard tissue culture conditions (37 °C with 5% CO₂) using DMEM medium supplemented with 4.5 g l⁻¹ glucose and 4.5 g l⁻¹ sodium pyruvate (Corning), 10% FBS (Gemini Bio) and 2 mM GlutaMAX (Gibco). Next, cells were cultured for 18–24 h on freshly glow-discharged carbon-coated EM gold grids (200 mesh, R1.2/1.3 or R2/1; Quantifoil Micro Tools) before plunge-freezing. For Nup96 depletion, a 250 mM auxin (3-indoleacetic acid, Sigma-Aldrich) solution was added to the cells to a final concentration of 1 mM, followed by incubation at 37 °C for 4–8 h before plunge-freezing. HeLa-derived (*TOR1A/TOR1B/TOR3A*-knockout) cells⁴³ were cultured in the same conditions but never subjected to auxin treatment.

Cryo-FIB milling of lamellae from DLD-1 cells

To prepare lamellae, we used both an Aquilos FIB-SEM system (Thermo Fisher Scientific) and a Crossbeam 540 (Zeiss) with cryo stage (Leica) using similar methods as previously described⁴⁴. On the Aquilos system, grids were loaded into the sample chamber and sputtered with an initial platinum coat (15 s) followed by a second organometallic platinum protective layer using the gas injection system (GIS, 15 s). Samples were tilted to an angle of 15°, and FIB ablation of cellular material was performed in a stepwise manner by focusing the gallium beam at 30 kV on parallel rectangular patterns with over- and under-tilting to the desired thickness as follows: (1) 15°, 500 pA, gap = 3 μm; (2) 16°, 300 pA, gap = 2.2 μm; (3) 14°, 300 pA, gap = 1.5 μm; (4) 15.5°, 100 pA, gap = 0.8 μm; (5) 14.5°, 100 pA, gap = 0.5 μm; (6) 15°, 50 pA, gap = 300 nm; and (7) 15°, 30 pA, gap = 150 nm. The initial width of the lamellae was set to 13 μm but, at each reduced current, we reduced the width by 0.25 μm, for lamellae with a final width of 11–12 μm. Expansion/relief joints to reduce tension at the lamella were milled 3 μm away from the sides of the lamella at step 1 with a 1-μm-wide pattern. A similar procedure was used on the Crossbeam 540 FIB-SEM. Grids were first electron-beam-coated with 2 nm of platinum in an ACE 900 system (Leica) before being loaded into the Crossbeam sample chamber with a VCT 500 (Leica) vacuum transfer system for organometallic platinum coating. FIB ablation was performed using only four stepwise currents and without over- and under-tilting as follows: (1) 700 pA, gap = 3 μm; (2) 300 pA, gap = 1 μm; (3) 100 pA, gap = 400 nm; and (4) 50 pA, gap = 150 nm. In total, we prepared 37 lamellae from non-auxin-treated *NUP96::Neon-AID* DLD-1 cells, and 115 lamellae from auxin-treated cells to obtain our data.

Tilt series acquisition and processing

Cryo-ET datasets were acquired on a Titan Krios G3i operating at 300 keV equipped with a BioQuantum post-column energy filter and a Gatan K3 direct electron detector. Tilt series were acquired at a magnification of ×26,000, resulting in a pixel size of 3.4 Å at the specimen level using Tomo v.5.3.0 (Thermo Fisher Scientific). We used a tilt range of −52° to +68°, starting at +8° with a bidirectional scheme⁴⁵ resulting in a total dose of about 145 electrons per angstrom squared. Tilt series of HeLa cells (*TOR1A/TOR1B/TOR3A*-knockout)⁴³ were acquired with an accumulative dose of about 120 electrons per angstrom squared. Defocus values varied between −5.0 μm to −2.5 μm through the entire data acquisition process. Representative tomograms are included (Supplementary Videos [1](#) and [2](#)).

Tilt series were aligned with 4× binned projections using patch tracking in the IMOD software package⁴⁶. When available, contaminations generated by the FIB process were used as fiducial markers. The contrast transfer function (CTF) was determined and corrected as described previously²⁶, and is summarized here. The mean defocus was estimated by strip-based periodogram averaging for each tilt series. Using the

mean defocus, the tilt angle and axis orientation, the defocus gradient for each projection was determined. CTF correction using the defocus gradient was then performed by phase-flipping each projection image. CTF-corrected stacks were next dose-filtered using the IMOD mtffilter function⁴⁶. NPC coordinates were picked manually using IMOD. During NPC particle picking, the relative orientation of the NPC to the NE was determined to prealign the NPCs. Next, subtomograms of NPCs were reconstructed using IMOD. Detailed imaging parameters are summarized in Extended Data Table 1.

Subtomogram averaging

For the wild-type DLD-1 structure, 194 prealigned NPCs were further aligned using iterative missing-wedge-weighted subtomogram alignment and averaging with the TOM toolbox (tom_corr3d)⁴⁷. Half-set averages were merged after each iteration and used as the template for the next iteration. First, full NPCs were aligned using 8× binned subvolumes and applying eightfold-fold symmetry. This step was repeated using 4× binned subvolumes. Subsequently, these alignments were used to extract the eight asymmetric units (1,552 protomers) for each NPC according to the eight-fold symmetry as previously described⁴⁸. Twice-binned full protomers were aligned and further refined by applying masks for the individual rings (CR, IR and NR). Next, subprotomers were extracted based on the previous alignment step. At this stage, single protomers were manually inspected and missing protomers from incomplete NPCs, misaligned protomers and protomers with a low signal-to-noise ratio were excluded. After this step, 1,252 protomers remained for the subsequent steps. Newly extracted subprotomers were further aligned. Resolution was measured using the 0.5 criterion and soft masks to exclude an artificial contribution to the measured resolution using the Electron Microscopy Data Bank (EMDB) validation server (<https://www.ebi.ac.uk/pdbe/emdb/validation/fsc/>). Subprotomer volumes were *B*-factor sharpened using Relion⁴⁹ with a *B*-factor of $-2,000 \text{ \AA}^2$. The final full NPC model was generated by fitting the subprotomer volumes into the full NPC average using UCSF Chimera⁵⁰.

Averaging of auxin-treated (Nup96-depleted) data was performed similarly. First, 163 full NPCs were aligned using 8× binned subprotomers and applying eight-fold symmetry. Next, NPCs were classified by manually inspecting the subvolumes into three classes containing CR, IR and NR (27 NPCs), IR and NR (53 NPCs), or IR only (83 NPCs). These three classes were further aligned using 8× binned subvolumes at full NPC level using eight-fold symmetry.

For the HeLa (*TOR1A/TOR1B/TOR3A*-knockout) average, 27 NPCs were aligned similar to the wild-type dataset but without dose-filtering of the stacks. After protomer extraction, 36 protomers were excluded and protomers were aligned. The final map

(180 protomers) was generated by fitting the protomer average back into the full NPC map using Chimera.

Model fitting

To create models for the Y complexes in the CR and NR, we performed unbiased global fitting using structural models derived from previously reported human NPC structures^{9,15}. For these complexes, we began with the previously reported model and performed a global fitting analysis as implemented in UCSF Chimera⁵⁰. The fitting was performed independently for the CR and NR using a three-protomer segmented model as our single protomers do not necessarily contain a complete protomer of the eight-fold symmetric NPC (that is, a single protomer may contain half of the Y complex from adjacent protomers). For the IR, a single protomer was used as it contained the entire complex. All fitting runs were performed using Chimera and 1,000,000 random initial placements and local cross-correlation (Chimera's correlation about the mean (CAM)), or a combination of local cross-correlation and overlap (CAM + OVR) was used when local cross-correlation did not provide statistically significant fits (as others have observed)²⁰. We computed fit scores using both metrics for each model but, for the IR, the local cross-correlation (CAM) provided statistical significance to our model, whereas, for the Y complex, the combination metric (CAM + OVR) provided statistical significance. We noted the scores and adjusted *P* values (described below) on the figure for each scoring metric. For each fitting run, the statistical significance was assessed as a *P* value that was calculated from normalized fitting scores. To calculate the *P* values, we transformed the CAM or combined CAM + OVR scores into *Z* scores, derived a two-sided *P* value for each fit and then corrected the *P* values for multiple testing using the conservative Benjamini–Hochberg procedure. This workflow was performed using a Python script running SciPy.stats (for *P* value and *Z*-score analysis)⁵¹, the StatsModels module (for Benjamini–Hochberg analysis)⁵² and Matplotlib (for plots)⁵³.

For the IR complex, we identified a significant fit in the expected position as described in the most recent human structure (Protein Data Bank (PDB): [5IJN](#))⁹, although it was obvious that some of the Nups in this model could be shifted to better fit our density map. We therefore followed a previously described approach²⁰ and optimized the fits by local refitting of individual subunits or domains. For this refinement, we used the option in Chimera to use a map simulated from atoms at a resolution of 25 Å and optimized the fitting for correlation. Using this approach, we fit subcomplexes made of the chains F, G, H, X, Y and Z (two copies of Nup54, Nup58 and Nup62), L, M, N, R, S and T (two additional copies of Nup54, Nup58 and Nup62), each copy of Nup205 (chains D, J, P and V), and the four copies of Nup93 (chains C, I, O and U). To fit the Nup155 chains, we subtracted densities with a radius of 10 Å of the fitted models above from the determined NPC map. In this difference map, we fit the individual

Nup155 copies into the map using the procedure described above (chains E, Q, K, W). The Nup155 chains A and B of [5IJN](#) could not be fit into our map reliably. We next ran a new unbiased global search using this model as the input for completeness.

For the Y complex, we identified a significant fit in the same position as described in the most recent human NPC structure CR and NR (PDB: [5A9Q](#))¹⁵ using a double Y complex as the reference molecule. As the [5A9Q](#) model contains gaps in the heterotetrameric core element of the Y complex called the ‘hub’ (Nup160, Nup85, Nup96 and Sec13), we decided to replace the hub of the [5A9Q](#) model with the hub of a new composite model that we created using published crystal structures and threading models. We first generated an *S. cerevisiae* composite model combining a previous structure of the Y complex hub (Nup120–Nup145N–Sec13–Nup85)¹⁴ (PDB: [4XMM](#)) and the Nup84–Nup133 subcomplex²⁴ (PDB: [6X02](#)). This *S. cerevisiae* Y-complex composite was then used to template the human homologue, using published structures and threading models. The hub of this updated model was then used to rigid-body dock into the CR/NR of our map at the same position that the [5A9Q](#) hub occupied, and the Nup107–Nup133 subcomplex from [5A9Q](#) was kept as is, creating a new complete Y-complex assembly. Fitting was further refined by cutting Nup160 between residue 933 and 934 (ref. [11](#)) and fitting the N-terminal part of Nup160 (Nup160-N) together with Nup37 as a rigid body into our map. The C-terminal part of Nup160 was fit as part of the hub. The CR model was then also placed for the inner Y ring and not further modified. Fitting for the NR Y complex was performed similarly. For the outer Y ring, only the hub and the Nup107–Nup133 subcomplex were separated and fit as individual rigid bodies. For the IR of the NR Y complex, the model without Nup160-N and Nup37 was fit into the map. For fitting of the Nup160-N–Nup37 subcomplex, we subtracted the densities of previously fit models with a radius of 20 Å from the map and fit the subcomplex into the remaining density. After creating the final models for Y complexes in both the CR and NR, we performed another round of unbiased global fitting and identified a similar location at which the Y complex of [5A9Q](#) docked. A final local optimization run maximized density overlap. We strongly urge that the final fits are not interpreted at atomic resolution. Instead, our fitting simply aids in assignment of our density toward understanding how each of the subcomplexes is positioned.

The IR model described above was placed manually into the centre of the IR protomers of the subtomogram maps generated from auxin-treated (Nup96-depleted) cells.

Visualization

Visualizations were performed using UCSF Chimera⁵⁰. Representative tomograms of DLD-1 cells were reconstructed in 8× binned, 12× SIRT-like filtered tomograms in

IMOD⁴⁶. Snapshots of mouse embryonic fibroblast (MEF) NPCs were recorded after manually aligning the NPCs in IMOD Slicer. The orthoslice views of the full-NPC average, wild-type map and auxin maps were taken using tom_volxyz. Scripts were implemented in MATLAB (MathWorks) and using the tom_toolbox⁵⁴.

Local resolution analysis was performed as previously reported²⁶, but also summarized here. To calculate the local resolution of the subprotomers, the full subprotomer volume ($100 \times 100 \times 100$ voxels) was divided into smaller subvolumes (box size, $40 \times 40 \times 40$) along a regular spacing of $4 \times 4 \times 4$. Resolution was measured between the subvolumes of the two half sets and using the 0.5 threshold criterion. Subvolumes were masked with a spherical mask prior to FSC calculation. Data points between measured values were interpolated and visualized using Chimera's Surface color function.

NPC diameter analysis

For diameter measurements, single NPCs were measured using orthoslices at the level of the pore membrane. For the DLD1 and HeLa datasets, aligned NPCs that would proceed to full-NPC averaging in this study were used. For the MEF datasets²⁹, NPCs were manually aligned in IMOD slicer and measured. Distance was measured between the NE at the narrowest point of each NPC manually. When possible, measurement was performed in two orthogonal directions and the average was calculated. Otherwise, only a single measurement was performed per NPC. When measurement was not possible because of strong misalignment or a poor signal-to-noise ratio, no diameter was measured. Scatter plots for NPC diameter analysis were created using Prism 9 (GraphPad).

Statistics and reproducibility

Representative micrographs are provided in Fig. 1a and Extended Data Fig. 6a,f. The micrograph in Fig. 1a highlights the three-ring NPC architecture directly visualized in cryo-ET and was chosen from the dataset of 54 wild-type DLD-1 cell tomograms, all of which reproducibly show a three-ring architecture. The micrograph in Extended Data Fig. 6a was chosen from the auxin-depleted DLD-1 cell dataset (71 tomograms), and this image was specifically chosen because it highlights single-ring NPCs that we describe in this Article. Finally, the micrograph in Extended Data Fig. 6f was specifically chosen to provide the reader with an anecdotal observation that we identified only twice in the dataset (2 out of 73 tomograms) and these tomograms were excluded from subsequent processing (71 tomograms were used for subtomogram averaging).

Reporting summary

Further information on research design is available in the [Nature Research Reporting Summary](#) linked to this paper.

Data availability

Cryo-EM maps for the human DLD-1 NPC have been deposited in the EMDB with the following accession codes: [EMD-12811](#) (CR), [EMD-12812](#) (IR), [EMD-12813](#) (NR) and [EMD-12814](#) (full composite NPC). Coordinate files for the CR, IR and NR docked complexes have been deposited in the PDB with the following accession codes: [7PEQ](#) (CR and NR complex) and [7PER](#) (IR complex). Representative tilt series of lamella from DLD-1 cells have been deposited in the EMDB under accession code [EMPIAR-10700](#) (wild-type, non-depleted cells) and [EMPIAR-10701](#) (Nup96-depleted cells). Density maps for the human NPC from isolated nuclei used for comparison in this study can be found at the EMDB with accession number [EMD-3103](#) (ref. [15](#)), as well as the recent NPC from HIV-infected T cells with accession number [EMD-11967](#) (ref. [22](#)). Moreover, models for the NR and CR Y complexes that we used as templates can be found in the PDB with accession code [5A9Q](#) (ref. [15](#)), as well as the IR complex model with accession code [5IJN](#) (ref. [9](#)).

References

1. 1.

Grossman, E., Medalia, O. & Zwerger, M. Functional architecture of the nuclear pore complex. *Annu. Rev. Biophys.* **41**, 557–584 (2012).

2. 2.

Knockenhauer, K. E. & Schwartz, T. U. The nuclear pore complex as a flexible and dynamic gate. *Cell* **164**, 1162–1171 (2016).

3. 3.

Strambio-De-Castillia, C., Niepel, M. & Rout, M. P. The nuclear pore complex: bridging nuclear transport and gene regulation. *Nat. Rev. Mol. Cell Biol.* **11**, 490–501 (2010).

4. 4.

Hampoelz, B., Andres-Pons, A., Kastritis, P. & Beck, M. Structure and assembly of the nuclear pore complex. *Annu. Rev. Biophys.* **48**, 515–536 (2019).

5. 5.

Lin, D. H. & Hoelz, A. The structure of the nuclear pore complex (an update). *Annu. Rev. Biochem.* **88**, 725–783 (2019).

6. 6.

Schwartz, T. U. The structure inventory of the nuclear pore complex. *J. Mol. Biol.* **428**, 1986–2000 (2016).

7. 7.

Fernandez-Martinez, J. & Rout, M. P. One ring to rule them all? Structural and functional diversity in the nuclear pore complex. *Trends Biochem. Sci.* <https://doi.org/10.1016/j.tibs.2021.01.003> (2021).

8. 8.

Fernandez-Martinez, J. et al. Structure and function of the nuclear pore complex cytoplasmic mRNA export platform. *Cell* **167**, 1215–1228 (2016).

9. 9.

Kosinski, J. et al. Molecular architecture of the inner ring scaffold of the human nuclear pore complex. *Science* **352**, 363–365 (2016).

10. 10.

Kampmann, M. & Blobel, G. Three-dimensional structure and flexibility of a membrane-coating module of the nuclear pore complex. *Nat. Struct. Mol. Biol.* **16**, 782–788 (2009).

11. 11.

Kelley, K., Knockenhauer, K. E., Kabachinski, G. & Schwartz, T. U. Atomic structure of the Y complex of the nuclear pore. *Nat. Struct. Mol. Biol.* **22**, 425–431 (2015).

12. 12.

Bui, K. H. et al. Integrated structural analysis of the human nuclear pore complex scaffold. *Cell* **155**, 1233–1243 (2013).

13. 13.

Lutzmann, M., Kunze, R., Buerer, A., Aebi, U. & Hurt, E. Modular self-assembly of a Y-shaped multiprotein complex from seven nucleoporins. *EMBO J.* **21**, 387–397 (2002).

14. 14.

Stuwe, T. et al. Architecture of the nuclear pore complex coat. *Science* **347**, 1148–1152 (2015).

15. 15.

von Appen, A. et al. In situ structural analysis of the human nuclear pore complex. *Nature* **526**, 140–143 (2015).

16. 16.

Maimon, T., Elad, N., Dahan, I. & Medalia, O. The human nuclear pore complex as revealed by cryo-electron tomography. *Structure* **20**, 998–1006 (2012).

17. 17.

Villa, E., Schaffer, M., Plitzko, J. M. & Baumeister, W. Opening windows into the cell: focused-ion-beam milling for cryo-electron tomography. *Curr. Opin. Struct. Biol.* **23**, 771–777 (2013).

18. 18.

Allegretti, M. et al. In-cell architecture of the nuclear pore and snapshots of its turnover. *Nature* **586**, 796–800 (2020).

19. 19.

Zimmerli, C. E. et al. Nuclear pores constrict upon energy depletion. Preprint at <https://doi.org/10.1101/2020.07.30.228585> (2020).

20. 20.

Mosalaganti, S. et al. In situ architecture of the algal nuclear pore complex. *Nat. Commun.* **9**, 2361 (2018).

21. 21.

Mahamid, J. et al. Visualizing the molecular sociology at the HeLa cell nuclear periphery. *Science* **351**, 969–972 (2016).

22. 22.

Zila, V. et al. Cone-shaped HIV-1 capsids are transported through intact nuclear pores. *Cell* **184**, 1032–1046 (2021).

23. 23.

Regmi, S. G. et al. The nuclear pore complex consists of two independent scaffolds. Preprint at <https://doi.org/10.1101/2020.11.13.381947> (2020).

24. 24.

Nordeen, S. A., Turman, D. L. & Schwartz, T. U. Yeast Nup84-Nup133 complex structure details flexibility and reveals conservation of the membrane anchoring ALPS motif. *Nat. Commun.* **11**, 6060 (2020).

25. 25.

Teimer, R., Kosinski, J., von Appen, A., Beck, M. & Hurt, E. A short linear motif in scaffold Nup145C connects Y-complex with pre-assembled outer ring Nup82 complex. *Nat. Commun.* **8**, 1107 (2017).

26. 26.

Eibauer, M. et al. Structure and gating of the nuclear pore complex. *Nat. Commun.* **6**, 7532 (2015).

27. 27.

Huang, G. et al. Structure of the cytoplasmic ring of the *Xenopus laevis* nuclear pore complex by cryo-electron microscopy single particle analysis. *Cell Res.* **30**, 520–531 (2020).

28. 28.

Hulsmann, B. B., Labokha, A. A. & Gorlich, D. The permeability of reconstituted nuclear pores provides direct evidence for the selective phase model. *Cell* **150**, 738–751 (2012).

29. 29.

Kronenberg-Tenga, R. et al. A lamin A/C variant causing striated muscle disease provides insights into filament organization. *J. Cell Sci.* **134**, jcs256156 (2021).

30. 30.

Thaller, D. J. & Lusk, P. C. Fantastic nuclear envelope herniations and where to find them. *Biochem. Soc. Trans.* **46**, 877–889 (2018).

31. 31.

Lin, D. H. et al. Architecture of the symmetric core of the nuclear pore. *Science* **352**, aaf1015 (2016).

32. 32.

Sapra, K. T. et al. Nonlinear mechanics of lamin filaments and the meshwork topology build an emergent nuclear lamina. *Nat. Commun.* **11**, 6205 (2020).

33. 33.

Turgay, Y. et al. The molecular architecture of lamins in somatic cells. *Nature* **543**, 261–264 (2017).

34. 34.

Feldherr, C., Akin, D. & Moore, M. S. The nuclear import factor p10 regulates the functional size of the nuclear pore complex during oogenesis. *J. Cell Sci.* **111**, 1889–1896 (1998).

35. 35.

Onischenko, E. et al. Natively unfolded FG repeats stabilize the structure of the nuclear pore complex. *Cell* **171**, 904–917 (2017).

36. 36.

Kim, S. J. et al. Integrative structure and functional anatomy of a nuclear pore complex. *Nature* **555**, 475–482 (2018).

37. 37.

Ungrich, R. & Kutay, U. Establishment of NE asymmetry-targeting of membrane proteins to the inner nuclear membrane. *Curr. Opin. Cell Biol.* **34**, 135–141 (2015).

38. 38.

Meinema, A. C. et al. Long unfolded linkers facilitate membrane protein import through the nuclear pore complex. *Science* **333**, 90–93 (2011).

39. 39.

Frey, S., Richter, R. P. & Gorlich, D. FG-rich repeats of nuclear pore proteins form a three-dimensional meshwork with hydrogel-like properties. *Science* **314**, 815–817 (2006).

40. 40.

Frey, S. & Gorlich, D. A saturated FG-repeat hydrogel can reproduce the permeability properties of nuclear pore complexes. *Cell* **130**, 512–523 (2007).

41. 41.

Ori, A. et al. Cell type-specific nuclear pores: a case in point for context-dependent stoichiometry of molecular machines. *Mol. Syst. Biol.* **9**, 648 (2013).

42. 42.

, M. & D’Angelo, M. A. Nuclear pore complex composition: a new regulator of tissue-specific and developmental functions. *Nat. Rev. Mol. Cell Biol.* **13**, 687–699 (2012).

43. 43.

Demircioglu, F. E. et al. The AAA + ATPase TorsinA polymerizes into hollow helical tubes with 8.5 subunits per turn. *Nat. Commun.* **10**, 3262 (2019).

44. 44.

Wagner, F. R. et al. Preparing samples from whole cells using focused-ion-beam milling for cryo-electron tomography. *Nat. Protoc.* **15**, 2041–2070 (2020).

45. 45.

Hagen, W. J. H., Wan, W. & Briggs, J. A. G. Implementation of a cryo-electron tomography tilt-scheme optimized for high resolution subtomogram averaging. *J. Struct. Biol.* **197**, 191–198 (2017).

46. 46.

Kremer, J. R., Mastronarde, D. N. & McIntosh, J. R. Computer visualization of three-dimensional image data using IMOD. *J. Struct. Biol.* **116**, 71–76 (1996).

47. 47.

Forster, F., Medalia, O., Zauberman, N., Baumeister, W. & Fass, D. Retrovirus envelope protein complex structure in situ studied by cryo-electron tomography. *Proc. Natl Acad. Sci. USA* **102**, 4729–4734 (2005).

48. 48.

Beck, M., Lucic, V., Forster, F., Baumeister, W. & Medalia, O. Snapshots of nuclear pore complexes in action captured by cryo-electron tomography. *Nature* **449**, 611–615 (2007).

49. 49.

Scheres, S. H. RELION: implementation of a Bayesian approach to cryo-EM structure determination. *J. Struct. Biol.* **180**, 519–530 (2012).

50. 50.

Pettersen, E. F. et al. UCSF Chimera—a visualization system for exploratory research and analysis. *J. Comput. Chem.* **25**, 1605–1612 (2004).

51. 51.

Virtanen, P. et al. SciPy 1.0: fundamental algorithms for scientific computing in Python. *Nat. Methods* **17**, 261–272 (2020).

52. 52.

Seabold, S. & Perktold, J. statsmodels: econometric and statistical modeling with Python. In *Proc. 9th Python in Science Conference* (2010).

53. 53.

Hunter, J. D. Matplotlib: a 2D graphics environment. *Comput. Sci. Eng.* **9**, 90–95 (2007).

54. 54.

Nickell, S. et al. TOM software toolbox: acquisition and analysis for electron tomography. *J. Struct. Biol.* **149**, 227–234 (2005).

Acknowledgements

We thank the members of the Schwartz, Medalia and Weis laboratories for their discussions throughout this work; and especially M. Eibauer for help with data processing and providing scripts; and staff at the Arnold and Mabel Beckman Foundation for funding to develop the MIT.nano cryo-EM centre. This work was supported by the National Institutes of Health (nos R01-GM77537 and R35-GM141834, to T.U.S.), the Swiss National Science Foundation (nos SNSF 31003A_179418, to O.M.; and SNSF 31003A_179275, to K.W.) and the Helen Hay Whitney Foundation (to A.P.S.).

Author information

Author notes

1. These authors contributed equally: Anthony P. Schuller, Matthias Wojtynek

Affiliations

1. Department of Biology, Massachusetts Institute of Technology, Cambridge, MA, USA

Anthony P. Schuller, Phat V. Dip, Edward J. Brignole & Thomas U. Schwartz

2. Department of Biochemistry, University of Zurich, Zurich, Switzerland

Matthias Wojtynek, Meltem Tatli, Rafael Kronenberg-Tenga & Ohad Medalia

3. Department of Biology, Institute of Biochemistry, ETH Zurich, Zurich, Switzerland

Matthias Wojtynek & Karsten Weis

4. Koch Institute for Integrative Cancer Research, Massachusetts Institute of Technology, Cambridge, MA, USA

David Mankus & Abigail K. R. Lytton-Jean

5. Division of Molecular and Cellular Biology, National Institute of Child Health and Human Development, NIH, Bethesda, MD, USA

Saroj G. Regmi & Mary Dasso

6. MIT.nano, Massachusetts Institute of Technology, Cambridge, MA, USA

Phat V. Dip & Edward J. Brignole

Contributions

A.P.S. and T.U.S. conceived the study. A.P.S. prepared human cryo-FIB samples and acquired the tomography data. M.W. calculated the structures and analysed the data. D.M. and A.K.R.L.-J. assisted in cryo-FIB sample preparation on the Zeiss Crossbeam 540. P.V.D. and E.J.B. helped in cryo-FIB preparation on the Thermo Fisher Scientific Aquilos and cryo-ET data acquisition and processing. M.T. and R.K.-T. prepared MEF samples for diameter analysis. S.R. and M.D. generated the *NUP96::Neon-AID* DLD-1 cell line. A.P.S., M.W, O.M. and T.U.S. wrote the manuscript with input from M.D. Funding was acquired by K.W., O.M. and T.U.S.

Corresponding authors

Correspondence to Ohad Medalia or Thomas U. Schwartz.

Ethics declarations

Competing interests

The authors declare no competing interests.

Additional information

Peer review information *Nature* thanks Benjamin Engel and the other, anonymous, reviewer(s) for their contribution to the peer review of this work. Peer reviewer reports are available.

Publisher's note Springer Nature remains neutral with regard to jurisdictional claims in published maps and institutional affiliations.

Extended data figures and tables

[Extended Data Fig. 1 Details of *in situ* human NPC architecture.](#)

a, Orthoslices through the nucleocytoplasmic axis, CR, and NR for our cryo-ET map of the human NPC from FIB-milled DLD-1 cells. Slice thickness: 3.4 nm. **b**, Fourier

shell correlation curves of the CR, IR, and NR regions in our map. FSC_{0.5} and FSC_{0.143} are indicated as dotted lines. **c**, The local resolution for the CR, IR, and NR protomers is visualized as surface color. **d**, Segment of the CR to highlight fitting of the Y complex structure and several unique features including putative Nup358 density (green arrowheads), extra unassigned density attached to the inner ring of the Y complex Nup85 (black arrowheads), and density we attribute to the Nup214 complex (blue arrowheads). **e**, Segment of the IR from our cryo-ET density with updated model fit inside. **f**, Segment of the NR to highlight fitting of the Y complex structure and several unique features including linker density between the Y complex rings (red arrowheads), unassigned density attached to the inner ring of the Y complex Nup85 (black arrowheads), and linkers between the Y complex inner ring and the IR (purple arrowheads).

Extended Data Fig. 2 Comparison of NPC structures from purified NEs and cryo-FIB suggests the cellular environment impacts NPC architecture and IR diameter.

a, Comparison of human NPC density maps from cryo-FIB and nuclear envelope purification techniques. Measurements for the membrane-to-membrane and IR central channel diameters, as well as the height across the NE are shown. Interestingly, an asymmetric membrane curvature may also exist at human NPCs in HIV-infected cells²², though the angles of the membranes appear different than ours. We refrain from making any speculations about this asymmetry because the deposited map comes from cells infected with HIV-1 virus. **b**, Measurements of NPC diameter from single NPCs in DLD-1 cells (non-auxin treated) as well as HeLa cells (TorsinA/B/3A KO), both prepared by cryo-FIB. Median values from each distribution are indicated as a dotted line and below the plot. **** indicates a two-tailed p-value ≤ 0.0001 from Mann-Whitney U analysis. **c**, Measurements of NPC diameter from single NPCs in MEFs using cryo-FIB or nuclear envelope purification techniques. Median values from each distribution are indicated as a dotted line and below the plot. Representative tomographic slices from intact cells using cryo-FIB milling and from isolated NE preparations are shown. Slice thickness: 8.9 nm.

Extended Data Fig. 3 Systematic fitting of Y complex and Inner Ring complex into the human DLD-1 map.

a, Fitting of the Cytoplasmic Ring Y complex with the previous NPC model (PDB: 5A9Q) compared with our composite model. The details of this fitting are provided in the Methods section. All fitting runs were performed using Chimera with 1,000,000 random initial placements and local cross-correlation (Chimera's correlation about the mean, CAM), or a combination of local cross-correlation and overlap (CAM+OVR)

for scoring. For each model, the top scoring model is shown to the left of a histogram of raw scores. The top scoring model is indicated on the histogram (red arrowhead) with its associated adjusted p-value for two different scoring metrics tested (red text represents the fit identified in the histogram, black represents the alternate metric). Two-sided P-values were corrected for multiple testing using the Benjamini-Hochberg procedure. The resulting composite Y model underwent an additional local optimization step to further improve the density fit (black arrowheads indicate regions that are improved with this step). An overlay of our model and the previous model is also shown in the panel. **b**, Same as **a**, but for the Nuclear Ring Y complex, also starting with PDB [5A9Q](#). **c**, Overlay of our composite Y complex model with that of the previous model. The additional modeled regions in our Y complex model “hub” (Nup160, 85, 96 and Sec13) and are indicated (blue arrowheads). **d**, Fitting of the Inner Ring complex with the previous IR model (PDB: [5IJN](#)) compared with our model. **e**, Overlay of our modified IR complex model with the previous model.

Extended Data Fig. 4 Details of the Y complex assembly in CR and NR.

a, Cartoon model for the human composite Y complex that was docked into the CR of our cryo-ET density map. **b**, Zoom-in view of the docked Y complex model in the CR with additional density connecting the two Y rings attributed to the Nup358 complex (green arrowhead). **c**, Zoom-in view of the docked Y complex model in the NR with additional density connecting the two Y rings (red arrowhead). **d**, Comparison of CR sub-structures from our study and the previous human model. Arrowheads indicate density attributed to the Nup358 complex (green), Nup214 complex (blue), and an unassigned density we observe at the Nup85 arms (black). **e**, Same as **(d)**, but for NR. Black arrowheads indicate similar density at Nup85 arms as in CR. **f**, Comparison of cross-section views of the NPC with dashed red line to indicate the orientation of the Y complexes with respect to the nuclear membranes.

Extended Data Fig. 5 Updated model for native IR.

a, Side-by-side comparison of the previous IR model (PDB: [5IJN](#)) with our updated model to fit the DLD-1 NPC map. **b**, Superimposition of our updated IR model with the previous model shows the rearrangements required to fit our density map. Each pane highlights a different nucleoporin colored in our updated model as in **(a)**, or colored dark grey from the previous model. **c**, Views of three updated IR-models in our map compared with the previous model and human NPC map. **d**, Same as **(c)** but with only models. **e**, Cross-section views of the NR in our map at both high and low threshold to show connectivity with the IR. **f**, Same as **(e)**, though no density can be observed between the CR-IR, likely due to flexibility. Flexibility could explain why the ring-connecting densities, proposed to be Nup155⁹, remain conspicuously poorly resolved in our map compared to the previous human maps^{[12,15,16](#)}. We hypothesize

that this observation may be unique to the more “constricted” IR state observed previously, locking the ring-connecting proteins into a more rigid state. In the same vein, others have shown that NPCs from yeast, both semi-purified³⁶ and in their native state¹⁸, can contain multiple flexible linkers between the outer rings and IR, suggesting this arrangement could provide resilience to the NPC structure.

Extended Data Fig. 6 Details of Nup96-depleted NPC structures.

a, Tomographic slice from a lamella prepared by cryo-FIB of NUP96::Neon-AID DLD-1 cells in the presence of auxin for 4 h (Nup96-depleted). Arrowheads indicate Nup96-depleted NPCs. **b**, Orthoslices across the nucleocytoplasmic axis for the final aligned maps of the three Nup96-depleted NPC classes. **c**, Measurements of NPC diameter from single NPCs in each of the data sets as well as the non-auxin treated (WT). *** indicates a two-tailed p-value ≤ 0.001 and **** indicates a two-tailed p-value ≤ 0.0001 from Mann-Whitney U analysis of each distribution compared with the wild-type condition. Median values from each distribution are indicated as a dotted line and shown above the plot. **d**, Orthoslices across the nucleocytoplasmic axis of single NPCs in each of the three Nup96-depleted NPC classes. Slice thickness is 4.1 nm. **e**, Orthoslices across the nucleocytoplasmic axis of class averages after manual orientation alignment and classification. **f**, Fourier shell correlation curves for the Nup96-depleted NPC classes. FSC_{0.5} and FSC_{0.143} are indicated as dotted lines. **g**, Tomographic slice of Nup96-depleted cells showed instances of NE herniation at the ONM (example indicated by arrow). Slice thickness for all panels except d: 2.7 nm.

Extended Data Table 1 Summary of cryo-ET imaging parameters

Supplementary information

Reporting Summary

Supplementary Video 1: Tomogram from a cryo-FIB-milled NUP96::Neon-AID DLD-1 cell in the absence of auxin (wild-type, non-depleted condition).

. NPC-containing sub-volumes from 54 tomograms were used to obtain the density map of the native NPC described in this study. Scale bar, 100 nm.

Supplementary Video 2: Tomogram from a cryo-FIB milled NUP96::Neon-AID DLD-1 cell in the presence of auxin (Nup96-depleted condition)

. NPC-containing sub-volumes from 71 tomograms were used to obtain the density map of the native NPC described in this study. Scale bar, 100 nm.

[Peer Review File](#)

Rights and permissions

Open Access This article is licensed under a Creative Commons Attribution 4.0 International License, which permits use, sharing, adaptation, distribution and reproduction in any medium or format, as long as you give appropriate credit to the original author(s) and the source, provide a link to the Creative Commons license, and indicate if changes were made. The images or other third party material in this article are included in the article's Creative Commons license, unless indicated otherwise in a credit line to the material. If material is not included in the article's Creative Commons license and your intended use is not permitted by statutory regulation or exceeds the permitted use, you will need to obtain permission directly from the copyright holder. To view a copy of this license, visit <http://creativecommons.org/licenses/by/4.0/>.

[Reprints and Permissions](#)

About this article

Cite this article

Schuller, A.P., Wojtynek, M., Mankus, D. *et al.* The cellular environment shapes the nuclear pore complex architecture. *Nature* **598**, 667–671 (2021).
<https://doi.org/10.1038/s41586-021-03985-3>

- Received: 29 April 2021
- Accepted: 01 September 2021
- Published: 13 October 2021
- Issue Date: 28 October 2021
- DOI: <https://doi.org/10.1038/s41586-021-03985-3>

Share this article

Anyone you share the following link with will be able to read this content:

[Get shareable link](#)

Sorry, a shareable link is not currently available for this article.

[Copy to clipboard](#)

Provided by the Springer Nature SharedIt content-sharing initiative

This article was downloaded by **calibre** from <https://www.nature.com/articles/s41586-021-03985-3>

| [Section menu](#) | [Main menu](#) |

- Article
- Open Access
- [Published: 13 October 2021](#)

Structure of Venezuelan equine encephalitis virus in complex with the LDLRAD3 receptor

- [Katherine Basore](#) ORCID: orcid.org/0000-0001-5974-0968¹,
- [Hongming Ma](#) ORCID: orcid.org/0000-0001-5105-1332²,
- [Natasha M. Kafai](#) ORCID: orcid.org/0000-0002-3115-3400^{1,2},
- [Samantha Mackin](#)^{1,2},
- [Arthur S. Kim](#)^{1,2},
- [Christopher A. Nelson](#) ORCID: orcid.org/0000-0001-8730-4768¹,
- [Michael S. Diamond](#) ORCID: orcid.org/0000-0002-8791-3165^{1,2,3,4} &
- [Daved H. Fremont](#) ORCID: orcid.org/0000-0002-8544-2689^{1,3,4,5}

Nature volume 598, pages 672–676 (2021)

- 2562 Accesses
- 20 Altmetric
- [Metrics details](#)

Subjects

- [Alphaviruses](#)
- [Cryoelectron microscopy](#)

Abstract

LDLRAD3 is a recently defined attachment and entry receptor for Venezuelan equine encephalitis virus (VEEV)¹, a New World alphavirus that causes severe neurological disease in humans. Here we present near-atomic-resolution cryo-electron microscopy reconstructions of VEEV virus-like particles alone and in a complex with the

ectodomains of LDLRAD3. Domain 1 of LDLRAD3 is a low-density lipoprotein receptor type-A module that binds to VEEV by wedging into a cleft created by two adjacent E2–E1 heterodimers in one trimeric spike, and engages domains A and B of E2 and the fusion loop in E1. Atomic modelling of this interface is supported by mutagenesis and anti-VEEV antibody binding competition assays. Notably, VEEV engages LDLRAD3 in a manner that is similar to the way that arthritogenic alphaviruses bind to the structurally unrelated MXRA8 receptor, but with a much smaller interface. These studies further elucidate the structural basis of alphavirus–receptor interactions, which could inform the development of therapies to mitigate infection and disease against multiple members of this family.

[Download PDF](#)

Main

Alphaviruses are enveloped, arthropod-transmitted single-stranded positive-sense RNA viruses that infect many vertebrate hosts, including humans, horses, rodents, birds and fish². Alphaviruses can be categorized on the basis of their clinical syndromes: arthritogenic alphaviruses, such as chikungunya (CHIKV), Ross River, Sindbis (SINV) and O’nyong-nyong, cause arthritis, polyarthralgia and musculoskeletal-associated diseases; encephalitic alphaviruses, including Venezuelan (VEEV), Eastern (EEEV) and Western (WEEV) equine encephalitic viruses, cause meningitis, encephalitis and long-term neurological sequelae in survivors. The global distribution of alphaviruses has increased in recent decades owing to international travel, expansion of mosquito vectors, deforestation and urbanization³.

Alphaviruses enter host cells through receptor-mediated endocytosis⁴. Within the low-pH endosomal compartment, the virion envelope rearranges to enable membrane fusion and nucleocapsid penetration into the cytoplasm⁵. The 12-kilobase alphavirus RNA genome is released after capsid disassembly and is translated from two open reading frames. The structural proteins (capsid, envelope glycoprotein (E)3, E2, 6K and E1) undergo processing and modification in the endoplasmic reticulum–Golgi network. The E2 and E1 proteins facilitate binding to entry factors and subsequent membrane fusion^{6,7,8,9}. The E3 protein is essential for the proper folding of p62 (a precursor to E2) and the formation of the p62–E1 heterodimer^{10,11} but is cleaved by furin-like proteases during maturation¹². Mature E2–E1 heterodimers assemble into trimeric spikes at the plasma membrane before budding and release of the virion from the host cell¹³. The 70-nm-diameter mature alphavirus virion comprises 240 E2–E1 heterodimers that are arranged into 80 trimeric spikes with $T=4$ icosahedral symmetry^{14,15,16}. Twenty of these trimeric spikes sit on the icosahedral

three-fold (i3) symmetry axes, and the other 60 spikes sit on the quasi-three-fold (q3) axes.

Low-density lipoprotein receptor class A domain-containing 3 (LDLRAD3) was recently identified as an attachment and entry receptor for VEEV and shown to be essential for optimal infection in cell culture and pathogenesis in mice¹. LDLRAD3 is a conserved yet poorly characterized cell-surface protein that is expressed in neurons, epithelial cells, myeloid cells and muscle, the endogenous ligand(s) of which remain unknown. Biolayer interferometry experiments established that domain 1 (D1) of LDLRAD3 (LDLRAD3(D1)) binds directly to VEEV, and anti-LDLRAD3 antibodies and LDLRAD3(D1)–Fc fusion proteins block VEEV attachment and infection of cells. Only VEEV uses LDLRAD3 as a receptor, as EEEV, WEEV and other distantly related alphaviruses do not bind to it. How LDLRAD3 engages VEEV, and why only VEEV binds to LDLRAD3 remain unclear. We set out to address these questions using structural, genetic and biophysical approaches.

Cryo-EM structure of LDLRAD3(D1) bound to VEEV

Mammalian-cell-expressed soluble LDLRAD3(D1) was produced in Expi293 cells¹. Cryo-electron micrographs of VEEV virus-like particles (VLPs)¹⁷ with or without bound LDLRAD3(D1) were acquired using a 300 kV Titan Krios system equipped with a Gatan K2 detector (Extended Data Fig. [1a](#) and Supplementary Table [1](#)). Single-particle analysis with imposed icosahedral symmetry yielded reconstructions at resolutions of 4.2 Å and 4.3 Å for the apo and complexed structures, respectively (Fig. [1a, b](#) and Extended Data Fig. [1b](#)). Two-hundred and forty molecules of LDLRAD3(D1) bound to sites on VEEV VLP (100% saturation), each one wedged into a cleft formed between two adjacent E2–E1 heterodimers within each trimeric spike (Fig. [1c](#)). This cleft widens slightly when D1 of LDLRAD3 is bound (Supplementary Video [1](#)). Local resolution estimation performed in RELION revealed heterogeneous resolution; the capsid proteins and membrane proximal regions of the E2–E1 heterodimers were best resolved (about 4 Å) and the membrane distal regions and LDLRAD3(D1) were less-well resolved (about 5–6 Å) (Fig. [1d](#)). To avoid under- and over-sharpening of the reconstructions by conventional global *B*-factor correction, post-processing was performed using DeepEMhancer¹⁸. This resulted in improved continuity and reduced noise in the density (Extended Data Fig. [1e](#)). The visibly clear tracing of the carbon backbone simplified subsequent model building.

Fig. 1: Cryo-EM reconstruction of VEEV VLPs in complex with LDLRAD3(D1).

 **figure1**

a, Coloured surface representation (left) and equatorial cross-section (right) of VEEV VLPs + LDLRAD3(D1). The surfaces are coloured by radial distance in Å, with the density of LDLRAD3 coloured magenta. The white triangle indicates one icosahedral asymmetric unit. The five-fold (i5), three-fold (i3) and two-fold (i2) icosahedral axes of symmetry are indicated by a pentagon, triangles and an oval, respectively. Trimeric spikes are labelled ‘i3’ if coincident with the i3 axes and ‘q3’ if on a quasi-three-fold axis. The black arrows indicate the directions of icosahedral symmetry axes (i2, i3, q3 and i5). Scale bar, 100 Å. **b, c**, Paired electron density of one asymmetric unit of the VEEV–LDLRAD3 complex, coloured by protein: E1 (grey), E2 (cyan), capsid (forest green) and LDLRAD3(D1) (magenta) (**b**) or by local resolution (**c**). Scale bars, 20 Å.

Atomic model building and refinement

LDLRAD3(D1) was identified as an LDL receptor type A (LA) domain by the Pfam database¹⁹. LA domains are approximately 40 amino acids in length and contain 6 disulfide-bound cysteine residues and a cluster of conserved acidic residues that coordinate calcium ions (Fig. 2a). The LA domain architecture is well characterized with over 200 structures in the Protein Data Bank (PDB), revealing a highly conserved fold. The initial model of LDLRAD3(D1) was built from its primary amino acid sequence by threading using the SWISS-MODEL server²⁰ with multiple high-resolution crystal structures of related LA domains as templates. The starting coordinates of the VEEV VLP structural proteins came from a previously built model of the same VEEV strain (PDB: [3J0C](#); ref. ²¹). Both models were docked into the DeepEMhancer modified electron density of the asymmetric unit and underwent manual and computational real-space refinement using COOT²² and PHENIX²³ (Methods), with LDLRAD3(D1) unambiguously oriented with the N terminus proximal to the core of the virus particle (Fig. 2b–d and Supplementary Table 2).

Fig. 2: Atomic model of LDLRAD3 interactions with VEEV.

 **figure2**

a, Structure-based sequence alignment with the labelled secondary structure of various LA domains, including mouse (m) LDLRAD3 domains 1–3, human (h) LDLR CR2 and CR3 (PDB: [5OYL](#) and [5OY9](#), respectively³¹), and human VLDLR-V3 (PDB: [3DPR](#); ref. ³³). Contact residues of LDLRAD3(D1) to the wrapped and intraspike VEEV E2–E1 heterodimers are shaded dark and/or light purple, respectively. Contact residues of the cysteine-rich domain 2 of LDLR (LDLR-CR2) and LDLR-CR3 to glycoprotein G of VSV (VSV G) are shaded green and contact residues of VLDL receptor module 3 (VLDLR-V3) to viral protein 1 (VP1) of human rhinovirus 2 (HRV2) are shaded pink, as determined by PDBePISA (www.ebi.ac.uk/pdbe/pisa/) (Fig. [4c–e](#)). The brackets and rectangles indicate residues that form disulfide bonds and coordinate calcium, respectively. The figure was prepared using ALINE³³. **b**, Ribbon diagram of LDLRAD3(D1) and surface representation of its wrapped and intraspike E2–E1 heterodimers. LDLRAD3(D1) and VEEV E2–E1 are coloured by domain. LDLRAD3(D1) (purple); chain E1: DI (light grey), DII (medium grey), DIII (dark grey) and fusion loop (FL) (orange); chain E2: A domain (cyan), β-linker

(medium blue), B domain (dark cyan) and C domain (blue). The disulfide bonds and calcium ion in the ribbon diagram are coloured yellow and green, respectively. **c**, **d**, Paired isolated views of electron density and a model of LDLRAD3(D1) and its wrapped (**c**) or intraspike (**d**) heterodimers. Wrapped refers to the E2–E1 heterodimer, the fusion loop of which is covered by LDLRAD3. Intraspike refers to the heterodimer adjacent to the wrapped heterodimer but within the same trimeric spike. The naming convention is consistent with previous alphavirus–receptor structural studies²³. The arrows indicate the regions that are magnified in the insets, which contain views of LDLRAD3(D1). Proteins are coloured by domain as described in **b**. N-linked glycans are shown as balls and sticks and coloured by heteroatom. The disulfide bonds and calcium ion are coloured yellow and green, respectively.

The resultant model shows the domains and residues of the VEEV E2–E1 heterodimers at the LDLRAD3-binding interface. The two E2–E1 heterodimers at each binding site were termed ‘wrapped’ and ‘intraspike’, as described previously for the structure of CHIKV²³ in complex with its MXRA8 receptor. At the wrapped heterodimer interface, LDLRAD3 engages domains A and B of E2 (residues 24–28, 70–71, 166–199, 176–177 and 223) and the fusion loop in E1 (residues 85 and 87–92). On the intraspike heterodimer, LDLRAD3 interacts with domain A and the β-linker of E2 (residues 5, 63–64, 79, 92–95, 148, 153–159 and 262–267; Fig. [2c, d](#), Extended Data Figs. [2](#) and [3](#), and Supplementary Table [3](#)). The binding interface is around 900 Å² with equal contributions from the interfaces of the wrapped and intraspike E2–E1 heterodimers. The LDLRAD3 residues at the interaction interface that contribute to binding of the wrapped heterodimer are 29, 34, 36, 38–44, 47, 54–57 and 62. At the intraspike heterodimer interface, residues 28–34, 42–47 and 50–52 form contacts (Supplementary Table [3](#)).

Functional assessment of the atomic model

To assess our model, non-conservative point mutations were introduced throughout D1 of LDLRAD3 and used for complementation experiments in mouse Neuro2a cells lacking *Ldlrad3* ($\Delta Ldlrad3$) and glycosaminoglycan ($\Delta B4galt7$) expression¹; we performed these experiments in cells lacking glycosaminoglycans to minimize background infection, as some alphaviruses also attach to cells through engagement of heparan sulfate moieties^{17,24,25}. Wild-type (WT) LDLRAD3 and single point mutants of LDLRAD3 were transduced into $\Delta B4galt7\Delta Ldlrad3$ Neuro2a cells, which were then inoculated with a chimeric, attenuated SINV–VEEV virus that expresses the structural genes of VEEV Trinidad Donkey (TrD) such that the screen could be performed using flow cytometry at a lower biosafety containment level (BSL2) yet with VEEV structural proteins from a pathogenic subtype IAB isolate. Whereas most mutant forms of LDLRAD3 promoted SINV–VEEV infection, several (including

G33D, M36T, P44R and D57V) did not support infection even though the proteins were expressed on the cell surface at similar levels compared to the WT form of LDLRAD3 (Fig. 3a,b and Extended Data Fig. 4). The residues identified as loss-of-function for infectivity all sit in a pocket of LDLRAD3 that supports direct contact with residues of E2–E1 in both the wrapped and intraspike heterodimers (Supplementary Table 3). Several other mutations in LDLRAD3(D1) that correspond to contact residues (including P32D, N39T, A46K and F56D) appear to show slight increases in infectivity with normal surface expression patterns. Although further studies are required, these changes could enhance the affinity of VEEV binding.

Fig. 3: Experimental assessment of the VEEV–LDLRAD3 model.



a, b, $\Delta B4galt7 \Delta Ldlrad3$ Neuro2a cells complemented with WT *Ldlrad3* or the indicated mutants of *Ldlrad3* were inoculated with chimeric SINV–VEEV–GFP viruses (IAB strain TrD). Subsequently (7.5 h later), the infection levels were assessed (**a**) by monitoring GFP expression using FACS analysis (**b**). Data are mean \pm s.d. of three experiments performed in technical duplicate. Each data symbol is the average of a technical duplicate from one experiment. $n = 3$. Statistical analysis was performed using one-way analysis of variance (ANOVA); * $P = 0.0317$ (N39T) or 0.0453 (R41E), ** $P = 0.0054$, *** $P = 0.001$, **** $P < 0.0001$. The *Ldlrad3* transgene contains an N-terminal Flag tag downstream of the signal sequence for monitoring plasma membrane expression by flow cytometry (Extended Data Fig. 4). **c**, Competition binding analysis of LDLRAD3(D1)–human Fc and anti-VEEV mouse monoclonal antibodies (3B4C-4 and TRD-14) by ELISA. VEEV VLPs were incubated with anti-VEEV monoclonal antibodies (3B4C-4 and TRD-14) or anti-HCV H77.39 isotype control followed by detection with LDLRAD3(D1)–human Fc. Data are mean \pm s.d. of three experiments performed in technical triplicate. Each data symbol is the average of a technical triplicate from one experiment. $n = 3$. Statistical analysis was performed using one-way ANOVA; *** $P = 0.0004$; NS, not significant. OD₄₅₀, optical density at 450 nm. **d**, Ribbon diagram of LDLRAD3(D1) and a surface representation of its wrapped and intraspike E2–E1 heterodimers with labelled epitopes of anti-VEEV mouse monoclonal antibodies (3B4C-4 and TRD-14) and labelled positions of LDLRAD3 mutants. Proteins are coloured by domain. LDLRAD3(D1) (purple); chain E1: DI (light grey), DII (medium grey), DIII (dark grey) and fusion loop (orange); chain E2: A domain (cyan), β -linker (medium blue), B domain (dark cyan) and C domain (blue). Inset: magnified view of the LDLRAD3(D1) ribbon diagram. The positions of mutations that resulted in reduced VEEV infection (G33 (light yellow), M36 (dark green), P44 (light pink) and D57 (dark blue)) are shown as balls and sticks. The N and C termini are labelled, and the disulfide bonds and calcium ion are coloured yellow and green, respectively.

Source data

Several years ago, a high-resolution cryo-electron microscopy (cryo-EM) structure of Fab fragments of the 3B4C-4 mouse monoclonal antibody bound to VEEV was published²⁶. 3B4C-4 binds to the tip of the E2 B domain²⁷ and inhibits cellular attachment and entry of VEEV²⁸. As the principal binding footprint (S177, V179, S180, L181, S184, T214, N216 and K223)²⁶ of this monoclonal antibody is proximal to the LDLRAD3-binding site, we tested whether 3B4C-4 could inhibit binding to LDLRAD3 using a competition binding enzyme-linked immunosorbent assay (ELISA). The 3B4C-4 monoclonal antibody was prebound to VEEV-VLP-coated plates before addition of the LDLRAD3(D1)–human Fc fusion protein. Notably, 3B4C-4 markedly inhibited LDLRAD3(D1) binding, whereas another anti-VEEV monoclonal antibody (TRD-14), which maps to a distinct epitope on the E2 B domain

(G203, G204 and T205; N. Kafai and M. Diamond, unpublished data), did not compete for binding (Fig. 3c). A structural comparison of the monoclonal antibody epitopes on the E2 B domain revealed that 3B4C-4 binds to residues that are immediately adjacent to the LDLRAD3-binding site, probably resulting in steric hindrance (Fig. 3d). By contrast, the TRD-14 epitope is located at the distal end of the E2 B domain.

D2 does not contribute to VEEV binding

D1 of LDLRAD3 is necessary and sufficient to support infection by VEEV¹, but it remains unclear whether D2 also contributes to VEEV binding. To evaluate this question, we expressed soluble LDLRAD3(D1+D2) in Expi293 cells (Extended Data Fig. 5a). Electron micrographs of VEEV VLPs with or without bound LDLRAD3(D1+D2) were acquired using a 300 kV Titan Krios system equipped with a Falcon 4 detector (Supplementary Table 1). Single-particle analysis with imposed icosahedral symmetry yielded a reconstruction at 5.0 Å (Extended Data Fig. 5b). The electron density of D2 of LDLRAD3 was weak and projected away from VEEV (Extended Data Fig. 5c). Binding of purified LDLRAD3(D1+D2) to captured VLPs by surface plasmon resonance yielded a monovalent affinity of approximately 50 nM that was similar to LDLRAD3(D1) (Extended Data Fig. 5d). On the basis of this structural and biophysical analysis, and previous functional data¹, D2 of LDLRAD3 does not appreciably contribute to VEEV binding or infection.

Cell culture infection experiments with mouse and human cells and in vivo pathogenesis studies in mice defined LDLRAD3 as a cell-surface receptor for VEEV that is required for optimal infectivity and induction of encephalitis in mice¹. Here, our single-particle cryo-EM analyses of LDLRAD3 and VEEV VLPs provide structural insights into how VEEV engages with LDLRAD3 to facilitate interactions with target cells. We observed a network of quaternary protein–protein interactions with D1 of LDLRAD3 engaging two E2–E1 heterodimers within one trimeric spike. The specific binding determinants that we observed are supported by structure-guided mutations that we introduced into LDLRAD3, and binding competition studies with LDLRAD3(D1) and a neutralizing monoclonal antibody against VEEV that engages the top of the E2 B domain and directly blocks virus attachment. Our structures indicate that D1 of LDLRAD3 can bind with full occupancy at four distinct sites in the icosahedral asymmetric unit of the mature VEEV VLP.

VEEV binds to LDLRAD3 in a manner that is notably similar to the binding of CHIKV to its receptor MXRA8, which consists of two immunoglobulin-related folds^{23,29,30} (Fig. 4a, b). Although LDLRAD3 and MXRA8 have similar sites of virion engagement, LDLRAD3 forms a significantly smaller interface (about 900 Å²

versus about 2,100 Å²) even though the monovalent affinity of virus–receptor binding is similar²³ (Extended Data Fig. 5d). Inspection of the contact residues indicates that LDLRAD3 makes greater use of hydrophobic residues to bind to VEEV compared with the use of hydrophobic residues by MXRA8 when binding to CHIKV (about 40% versus about 24% of interface residues, respectively). Approximately 65% of the receptor contact positions on VEEV spikes are shared with CHIKV (Extended Data Figs. 2 and 3). Both receptors effectively shield the hydrophobic fusion loop from solvent access, and all seven of the VEEV E1 contact residues are conserved with CHIKV E1. We speculate that the common positioning of these receptors near the fusion loop might function to modulate viral fusion during endocytosis. However, the primary contact residues used by LDLRAD3 and MXRA8 are not conserved; notably, MXRA8 has a substantial number of histidine residues (7% of the ectodomain) and LDLRAD3(D1) has no histidine residues.

Fig. 4: Comparisons of VEEV–LDLRAD3 with other virus–receptor complexes.



a, Surface representation of the wrapped (dark grey) and intraspike E2–E1 (light grey) heterodimers of CHIKV, labelled by domain and coloured by determinants of MXRA8 receptor binding. Positions of determinants specific to MXRA8 are coloured cyan; positions shared with LDLRAD3 are yellow. The MXRA8 binding interface is about 2,100 Å². **b**, Surface representation of the wrapped (dark grey) and intraspike E2–E1 (light grey) heterodimers of VEEV, labelled by domain and coloured by determinants of LDLRAD3 receptor binding. Positions of determinants specific to LDLRAD3 are coloured magenta; positions shared with MXRA8 are coloured yellow. The LDLRAD3(D1) binding interface is about 900 Å². **c–e**, Paired, ribbon and surface diagrams of virus–LDLR structures. The calcium ions and tryptophan residues are coloured light green and yellow, respectively. **c**, Fragments of domains of the wrapped and intraspike E2–E1 heterodimers of VEEV (fusion loop of E1 (orange), domain A of E2 (cyan), β-linker of E2 (medium blue), domain B of E2 (dark cyan)) at the interface of LDLRAD3(D1) (grey). After VEEV binding, 29.0% of the solvent-accessible surface area (SASA) of LDLRAD3(D1) is lost. **d**, Fragments of VSV G (green) at the interface of LDLR-CR2 (grey) (PDB: [5OYL](#); ref. ³¹). After VSV binding, 25.3% of the SASA of LDLR-CR2 is lost. **e**, Loops from two different copies of viral protein 1 (VP1; light and dark pink) from human rhinovirus 2 (HRV2) engage VLDLR-V3 (grey) (PDB: [3DPR](#); ref. ³²). After HRV2 binding, 13.1% of the SASA of VLDLR-V3 is lost.

The distinct receptor specificities of VEEV and CHIKV can probably be explained by the low level of sequence conservation of the E2-binding residues (26% of 35 LDLRAD3 contact positions). Our structural analysis also suggests why LDLRAD3 is a receptor for VEEV but not for WEEV and EEEV—other related encephalitic alphaviruses. Other than the aforementioned conserved contact site in the E1 fusion loop (100% conservation for 7 residues), the receptor determinants in E2 of VEEV generally are not conserved in WEEV and EEEV (17% and 23% identity, respectively, for 35 contact residues; Extended Data Figs. [2](#) and [3](#)). By contrast, these determinants are essentially conserved among VEEV complex members, which probably explains why LDLRAD3 supports infection of all of the VEEV strains (IAB, IC and ID) that we tested¹.

LDL-receptor family members mediate the entry of several viruses belonging to different families. High-resolution structures have been solved for LDL receptor (LDLR) LA domains in complex with vesicular stomatitis virus (VSV) and human rhinovirus (HRV)^{[31,32](#)}. Notably, an unrelated negative stranded rhabdovirus (VSV) and non-enveloped picornavirus (HRV) engage the same tryptophan residue near the calcium-binding site of the conserved cysteine-rich domain that also is a major contact for LDLRAD3 (Trp47) (Figs. [2a](#), Fig. [4c–e](#)). Thus, evolutionarily distinct viruses have evolved similar structural strategies for engaging related members of a protein superfamily to enable entry into target cells. As such, it is plausible that structure-

guided design of small-molecule inhibitors could prevent entry of viruses from multiple families.

Methods

Recombinant LDLRAD3 protein generation and purification

Monomeric LDLRAD3 ectodomain constructs were prepared as previously described¹. In brief, mouse LDLRAD3(D1) (residues 18–70) and LDLRAD3(D1+D2) (residues 18–112) were cloned into the pCDNA3.4 vector (Thermo Fisher Scientific) with the native signal peptide sequence, followed by an HRV 3C cleavage site (LEVLFQGP) and the mouse IgG2b Fc region. The RAP chaperone protein (residues 1–357; GenBank: [NM_002337](#)) was cloned into the pCDNA3.4 vector. Expi293 cells (50 ml) were seeded at 1.5×10^6 cells per ml, then transfected with 50 µg of LDLRAD3 and 10 µg of RAP in diluted Opti-MEM with complexed with ExpiFectamine 293 transfection reagent (Thermo Fisher Scientific). Cells were supplemented with ExpiFectamine 293 transfection enhancers 1 and 2 to boost transfection levels 1 d later. The supernatant was collected 4 d after transfection. Protein was purified using protein A Sepharose 4B (Thermo Fisher Scientific) and then dialysed into 1× HBS with 1 mM CaCl₂ and EDTA-free protease inhibitors (Roche). The cleaved monomeric LDLRAD3 ectodomain was obtained after incubation with HRV 3C protease (Thermo Fisher Scientific) at a 1:10 ratio overnight at 4 °C and then purified by sequential protein A Sepharose 4B and Superdex 75 size exclusion (GE Healthcare) chromatography in 20 mM HEPES pH 7.4, 150 mM NaCl and 0.01% NaN₃.

Cryo-EM sample preparation, data collection and single-particle reconstruction

VEEV VLPs³³ (gift from K. Carlton and J. Mascola, Vaccine Research Center of the National Institutes of Allergy and Infectious Diseases) with and without cleaved LDLRAD3(D1) or LDLRAD3(D1+D2) in molar excess were flash-cooled on lacey carbon grids in liquid ethane using an FEI Vitrobot (Thermo Fisher Scientific). Videos of the VEEV VLPs alone and with LDLRAD3(D1) samples were recorded using the EPU software (Thermo Fisher Scientific) using a K2 Summit electron detector (Gatan) mounted onto a Bioquantum 968 GIF Energy Filter (Gatan) attached to a Titan Krios microscope operating at 300 keV with an electron dose of $35 \text{ e}^- \text{ Å}^{-2}$ and a magnification of $\times 105,000$. Videos of VEEV VLPs with cleaved LDLRAD3(D1+D2) were recorded using a Falcon 4 Direct Electron Detector (Thermo Fisher Scientific) with a magnification of $\times 59,000$. Videos from all of the samples were corrected for beam-induced motion using MotionCor2 (ref. [34](#)). Contrast transfer function

parameters of the electron micrographs were estimated using Gctf³⁵, and particles were auto-picked using crYOLO³⁶. Single-particle analysis, specifically reference-free 2D classification, 3D refinement, video refinement, Bayesian polishing, post-processing and local resolution estimation were performed using RELION-3.1 (ref. ³⁷). Post-processing of maps for model building and figure presentation was performed using DeepEMhancer¹⁸. Further information for all of the samples is provided in Supplementary Table 1. Structural visualization of the electron maps was performed using ChimeraX³⁸.

Model building and refinement

The initial models of the VEEV structural proteins (E1, E2, transmembrane regions and capsid) with or without LDLRAD3 were constructed by docking the coordinates of the previously built model of VEEV strain TC-83 (PDB: [3J0C](#); ref. ²¹) and the model of LDLRAD3(D1) predicted by SWISS-MODEL server²⁰ into the electron density of the asymmetric units of the cryo-EM maps using the fitmap command in ChimeraX. N-linked glycans and coordinated calcium ions were built manually using COOT²². The model underwent real-space refinement in PHENIX²³ using the default parameters plus Morphing and secondary-structure, rotamer and torsion restraints with the initial model as the reference. Bond and angle restraints were also applied for the modelled N-linked glycans and calcium ions. After optimization, coordinates of the asymmetric units were checked using MolProbity. Contact residues were identified, and buried surface areas were calculated using PDBePISA (www.ebi.ac.uk/pdbe/pisa/).

Surface plasmon resonance

The binding kinetics and affinity of cleaved LDLRAD3(D1) or LDLRAD3(D1+D2) to VEEV VLPs were measured using the Biacore T200 system (GE Healthcare).

Experiments were performed at $30 \mu\text{l min}^{-1}$ and 25°C using HBS-P (0.01 M HEPES pH 7.4, 0.15 M NaCl, 3 mM EDTA, 0.005% (v/v) Surfactant P20) plus 1 mM CaCl₂ as running buffer. VEEV-57 monoclonal antibody (anti-VEEV E2, N. Kafai and M. Diamond, unpublished results) was immobilized onto a CM5 sensor chip (GE Healthcare) using standard amine coupling chemistry, and VEEV VLPs were captured. LDLRAD3 proteins were injected over a range of concentrations (1 μM to 16 nM) for 300 s, followed by a 600-s dissociation period. The sensor chip was regenerated after each analyte concentration with 60 s of 10 mM glycine, pH 1.7. Before the next analyte concentrated was tested, VEEV VLPs were recaptured; the response units of captured VLPs were consistent for each cycle. All sensorgrams were double-reference-subtracted using the reference flow cell (immobilized VEEV-57 monoclonal antibody, no captured VLP) and the running-buffer blank sample. The kinetic profiles and

steady-state equilibrium concentration curves were fitted using a global 1:1 binding algorithm with a drifting baseline using BIAevaluation v.3.1 (GE Healthcare).

Infection assay

A comprehensive mutation library was generated using gene synthesis by mutating a single amino acid in D1 of the LDLRAD3 protein. The amino acids that are essential for maintaining the structural integrity of LDLRAD3 (the cysteines forming disulfide bonds, the amino acids coordinating the calcium and those forming the hydrophobic core) were kept intact³⁹. The substitutions were determined using the BLOSUM scoring matrix⁴⁰ and a list of these is provided in Supplementary Table 4. The mutants were cloned into lentivirus vector pLV-EF1a-IRES-Hygro (Addgene, 85134) between the BamHI and MluI restriction enzyme sites (Genscript). An N-terminal Flag tag was added to each LDLRAD3 mutant to monitor protein expression. *ΔB4galt7 ΔLdlrad3* Neuro2a cells were transduced with each LDLRAD3 mutant and, 7 d later, were inoculated with SINV–VEEV (TrD)–GFP¹ (gift of W. Klimstra, University of Pittsburgh) infection at a multiplicity of infection of 20 for 7.5 h. Cells were stained with anti-Flag antibodies (1:2,000 dilution, Cell Signaling Technology, D6W5B) to measure the surface expression levels of the WT and mutant forms of LDLRAD3. Inoculated and stained cells were analysed using the MACSQuant Analyzer 10 (Miltenyi Biotec), and all flow cytometry data were processed using FlowJo (FlowJo).

Competition binding ELISA

Nunc MaxiSorp plates (Thermo Fisher Scientific) were coated with 2 µg ml⁻¹ of capture monoclonal antibody (mouse anti-VEEV-1A4A)⁴¹ in 100 µl of sodium bicarbonate coating buffer (0.1 M Na₂CO₃, pH 9.3) and incubated overnight at 4 °C. Plates were washed four times with PBS and incubated with 150 µl of blocking buffer (PBS, 4% BSA) for 1 h at room temperature. VEEV VLPs were diluted to 1 µg ml⁻¹ in PBS containing 2% BSA and added (100 µl per well) to plates for 1 h at room temperature. After four additional PBS washes, 50 µl of mouse anti-VEEV monoclonal antibody (3B4C-4 or TRD-14) at 20 µg ml⁻¹ in PBS with 2% BSA was added to plates for 30 min at room temperature to allow for binding to VEEV VLPs. Then, 50 µl of human LDLRAD3(D1)–Fc at 20 µg ml⁻¹ was added directly, with no additional washes. One hour later, the plates were washed four times with PBS and incubated with 100 µl per well 1:5,000 horseradish-peroxidase-conjugated goat anti-human IgG (H+L; Jackson ImmunoResearch) diluted in PBS with 2% BSA for 1 h at room temperature for detection of LDLRAD3(D1)–Fc binding. The plates were washed four times with PBS and then incubated with 100 µl of 3,3',5,5'-tetramethylbenzidine substrate (Thermo Fisher Scientific) for 3 min at room temperature before quenching by addition of 50 µl of 2 N H₂SO₄. Absorbance was

read at an optical density of 450 nm using the TriStar Microplate Reader (Berthold Technologies).

Statistical analysis

Statistical significance was assigned when $P < 0.05$ using Prism (v.8, GraphPad) and is indicated in each of the figure legends. Cell culture or ELISA experiments were analysed using one-way ANOVA.

Reporting summary

Further information on research design is available in the [Nature Research Reporting Summary](#) linked to this paper.

Data availability

All data supporting the findings of this study are available within the paper and its Supplementary Information. All structures have been deposited in the PDB and Electron Microscopy Data Bank databases (PDB: [7N1I](#), [7N1H](#); EMDB: [24117](#), [24116](#), [24394](#)). [Source data](#) are provided with this paper.

References

1. 1.

Ma, H. et al. LDLRAD3 is a receptor for Venezuelan equine encephalitis virus. *Nature* **588**, 308–314 (2020).

2. 2.

Weaver, S. C. & Barrett, A. D. T. Transmission cycles, host range, evolution and emergence of arboviral disease. *Nat. Rev. Microbiol.* **2**, 789–801 (2004).

3. 3.

Zaid, A. et al. Arthritogenic alphaviruses: epidemiological and clinical perspective on emerging arboviruses. *Lancet Infect. Dis.* **21**, e123–e133 (2021).

4. 4.

Marsh, M. & Helenius, A. Virus entry into animal cells. *Adv. Virus Res.* **36**, 107–151 (1989).

5. 5.

Kielian, M., Chanel-Vos, C. & Liao, M. Alphavirus entry and membrane fusion. *Viruses* **2**, 796–825 (2010).

6. 6.

Lescar, J. et al. The fusion glycoprotein shell of Semliki Forest virus: an icosahedral assembly primed for fusogenic activation at endosomal pH. *Cell* **105**, 137–148 (2001).

7. 7.

Smith, T. J. et al. Putative receptor binding sites on alphaviruses as visualized by cryoelectron microscopy. *Proc. Natl Acad. Sci. USA* **92**, 10648–10652 (1995).

8. 8.

Zhang, W., Heil, M., Kuhn, R. J. & Baker, T. S. Heparin binding sites on Ross River virus revealed by electron cryo-microscopy. *Virology* **332**, 511–518 (2005).

9. 9.

Basore, K. et al. Cryo-EM structure of Chikungunya virus in complex with the Mxra8 receptor. *Cell* **177**, 1725–1737 (2019).

10. 10.

Carleton, M., Lee, H., Mulvey, M. & Brown, D. T. Role of glycoprotein PE2 in formation and maturation of the Sindbis virus spike. *J. Virol.* **71**, 1558–1566 (1997).

11. 11.

Mulvey, M. & Brown, D. T. Involvement of the molecular chaperone BiP in maturation of Sindbis virus envelope glycoproteins. *J. Virol.* **69**, 1621–1627 (1995).

12. 12.

Heidner, H. W., Knott, T. A. & Johnston, R. E. Differential processing of Sindbis virus glycoprotein PE2 in cultured vertebrate and arthropod cells. *J. Virol.* **70**, 2069–2073 (1996).

13. 13.

Leung, J. Y. S., Ng, M. M. L. & Chu, J. J. H. Replication of alphaviruses: a review on the entry process of alphaviruses into cells. *Adv. Virol.* **2011**, 249640 (2011).

14. 14.

Holland Cheng, R. et al. Nucleocapsid and glycoprotein organization in an enveloped virus. *Cell* **80**, 621–630 (1995).

15. 15.

Kostyuchenko, V. A. et al. The structure of Barmah Forest virus as revealed by cryo-electron microscopy at a 6-Angstrom resolution has detailed transmembrane protein architecture and interactions. *J. Virol.* **85**, 9327–9333 (2011).

16. 16.

Paredes, A. M. et al. Three-dimensional structure of a membrane-containing virus. *Proc. Natl Acad. Sci. USA* **90**, 9095–9099 (1993).

17. 17.

Tanaka, A. et al. Genome-wide screening uncovers the significance of *N*-sulfation of heparan sulfate as a host cell factor for Chikungunya virus infection. *J. Virol.* **91**, e00432-17 (2017).

18. 18.

Sanchez-Garcia, R. et al. DeepEMhancer: a deep learning solution for cryo-EM volume post-processing. *Commun. Biol.* **4**, 1–8 (2021).

19. 19.

Mistry, J. et al. Pfam: the protein families database in 2021. *Nucleic Acids Res.* **49**, D412–D419 (2021).

20. 20.

Waterhouse, A. et al. SWISS-MODEL: homology modelling of protein structures and complexes. *Nucleic Acids Res.* **46**, W296–W303 (2018).

21. 21.

Zhang, R. et al. 4.4 Å cryo-EM structure of an enveloped alphavirus Venezuelan equine encephalitis virus. *EMBO J.* **30**, 3854–3863 (2011).

22. 22.

Emsley, P., Lohkamp, B., Scott, W. G. & Cowtan, K. Features and development of Coot. *Acta Crystallogr. D* **66**, 486–501 (2010).

23. 23.

Afonine, P. V. et al. Towards automated crystallographic structure refinement with phenix.refine. *Acta Crystallogr. D* **68**, 352–367 (2012).

24. 24.

Ryman, K. D. et al. Heparan sulfate binding can contribute to the neurovirulence of neuroadapted and nonneuroadapted Sindbis viruses. *J. Virol.* **81**, 3563–3573 (2007).

25. 25.

Gardner, C. L., Ebel, G. D., Ryman, K. D. & Klimstra, W. B. Heparan sulfate binding by natural eastern equine encephalitis viruses promotes neurovirulence. *Proc. Natl Acad. Sci. USA* **108**, 16026–16031 (2011).

26. 26.

Porta, J. et al. Locking and blocking the viral landscape of an alphavirus with neutralizing antibodies. *J. Virol.* **88**, 9616–9623 (2014).

27. 27.

Johnson, B. J. B., Brubaker, J. R., Roehrig, J. T. & Trent, D. W. Variants of Venezuelan equine encephalitis virus that resist neutralization define a domain of the E2 glycoprotein. *Virology* **177**, 676–683 (1990).

28. 28.

Roehrig, J. T., Hunt, A. R., Kinney, R. M. & Mathews, J. H. In vitro mechanisms of monoclonal antibody neutralization of alphaviruses. *Virology* **165**, 66–73 (1988).

29. 29.

Song, H. et al. Molecular basis of arthritogenic alphavirus receptor MXRA8 binding to Chikungunya virus envelope protein. *Cell* **177**, 1714–1724 (2019).

30. 30.

Zhang, R. et al. Mxra8 is a receptor for multiple arthritogenic alphaviruses. *Nature* **557**, 570–574 (2018).

31. 31.

Nikolic, J. et al. Structural basis for the recognition of LDL-receptor family members by VSV glycoprotein. *Nat. Commun.* **9**, 1029 (2018).

32. 32.

Verdaguer, N., Fita, I., Reithmayer, M., Moser, R. & Blaas, D. X-ray structure of a minor group human rhinovirus bound to a fragment of its cellular receptor protein. *Nat. Struct. Mol. Biol.* **11**, 429–434 (2004).

33. 33.

Ko, S. Y. et al. A virus-like particle vaccine prevents equine encephalitis virus infection in nonhuman primates. *Sci. Transl. Med.* **11**, eaav3113 (2019).

34. 34.

Zheng, S. Q. et al. MotionCor2: anisotropic correction of beam-induced motion for improved cryo-electron microscopy. *Nat. Methods* **14**, 331–332 (2017).

35. 35.

Zhang, K. Gctf: real-time CTF determination and correction. *J. Struct. Biol.* **193**, 1–12 (2016).

36. 36.

Wagner, T. et al. SPHIRE-crYOLO is a fast and accurate fully automated particle picker for cryo-EM. *Commun. Biol.* **2**, 218 (2019).

37. 37.

Zivanov, J. et al. New tools for automated high-resolution cryo-EM structure determination in RELION-3. *eLife* **7**, e42166 (2018).

38. 38.

Pettersen, E. F. et al. UCSF ChimeraX: structure visualization for researchers, educators, and developers. *Protein Sci.* **30**, 70–82 (2021).

39. 39.

Fass, D., Blacklow, S., Kim, P. S. & Berger, J. M. Molecular basis of familial hypercholesterolaemia from structure of LDL receptor module. *Nature* **388**, 691–693 (1997).

40. 40.

Henikoff, S. & Henikoff, J. G. Amino acid substitution matrices from protein blocks. *Proc. Natl Acad. Sci. USA* **89**, 10915–10919 (1992).

41. 41.

Roehrig, J. T. & Mathews, J. H. The neutralization site on the E2 glycoprotein of Venezuelan equine encephalomyelitis (TC-83) virus is composed of multiple conformationally stable epitopes. *Virology* **142**, 347–356 (1985).

Acknowledgements

We thank J. Fitzpatrick and M. Rau of the Washington University Center for Cellular Imaging and J. Errico for assistance with cryo-EM data collection and processing. We acknowledge K. Carlton and J. Mascola from the Vaccine Research Center of the National Institutes of Allergy and Infectious Diseases (NIH) for a gift of the VEEV VLPs. This study was supported by NIH grants R01AI164653 and T32AI007172 and contract HHSN272201700060C (CSGID).

Author information

Affiliations

1. Department of Pathology & Immunology, Washington University School of Medicine, St Louis, MO, USA

Katherine Basore, Natasha M. Kafai, Samantha Mackin, Arthur S. Kim, Christopher A. Nelson, Michael S. Diamond & Daved H. Fremont

2. Department of Medicine, Washington University School of Medicine, St Louis, MO, USA

Hongming Ma, Natasha M. Kafai, Samantha Mackin, Arthur S. Kim & Michael S. Diamond

3. Department of Molecular Microbiology, Washington University School of Medicine, St Louis, MO, USA

Michael S. Diamond & Daved H. Fremont

4. The Andrew M. and Jane M. Bursky Center for Human Immunology and Immunotherapy Programs, Washington University School of Medicine, St Louis, MO, USA

Michael S. Diamond & Daved H. Fremont

5. Department of Biochemistry & Molecular Biophysics, Washington University School of Medicine, St Louis, MO, USA

Daved H. Fremont

Contributions

K.B. performed the cryo-EM reconstructions and asymmetric unit atomic modelling with support from C.A.N. and D.H.F. A.S.K. engineered and purified the LDLRAD3 proteins. H.M. performed the SINV–VEEV infection experiments. N.M.K. and S.M. designed and performed antibody inhibition studies. K.B. performed data analysis. M.S.D. and D.H.F. obtained funding for the studies. K.B., M.S.D. and D.H.F. wrote the initial manuscript draft, and the other authors provided editorial comments.

Corresponding authors

Correspondence to Michael S. Diamond or Daved H. Fremont.

Ethics declarations

Competing interests

M.S.D. is a consultant for Inbios, Vir Biotechnology, Fortress Biotech and Carnival Corporation and on the Scientific Advisory Board of Moderna and Immunome. The Diamond laboratory has received unrelated funding support in sponsored research

agreements from Moderna, Vir Biotechnology and Emergent BioSolutions. D.H.F. is a founder of Courier Therapeutics and has received unrelated funding support from Emergent BioSolutions and Mallinckrodt Pharmaceuticals.

Additional information

Peer review information *Nature* thanks the anonymous reviewers for their contribution to the peer review of this work. Peer reviewer reports are available.

Publisher's note Springer Nature remains neutral with regard to jurisdictional claims in published maps and institutional affiliations.

Extended data figures and tables

Extended Data Fig. 1 Quality assessment of cryo-EM maps.

a, Representative electron micrograph (micrograph number, 1453) of VEEV VLPs. Scale bar, 500 Å. **b**, Fourier shell correlation (FSC) plots for VEEV VLPs alone (left) and with LDLRAD3(D1) (right). **c**, Side views of the unsharpened (left), globally sharpened by RELION postprocessing (middle) or modified by DeepEMhancer (right) electron densities of one asymmetric unit of VEEV–LDLRAD3 complex. The maps are coloured by radial distance from the VLP center, with LDLRAD3(D1) shown in purple, analogous to in Fig. 1b.

Source data

Extended Data Fig. 2 Sequence alignment of E2 proteins of the VEEV complex and other alphaviruses.

Amino acid sequence alignment of E2 proteins of various VEEV strains (IAB strain TC-83, AAB02517; IAB strain TrD, AAC19322; IC strain INH9813, AJP13627; ID strain ZPC738, AUV65225) and other alphaviruses (EEEV strain FL93-939, ABL84687; WEEV strain CBA87, ABD98014; SINV strain Girdwood, AUV65223; CHIKV strain 37997, ABX40011). Structure-based sequence alignments were performed between alphaviruses that do (group 1, left margin) or do not (groups 2 and 3, left margin) use LDLRAD3 as a receptor for infection using PROMALS3D with VEEV numbering. The figure was prepared using ESPript 3.0. Domains are coloured (A (light cyan), B (medium cyan), C (blue) and β linker (medium cyan)) and indicated above the sequence, along with the secondary structure features and nomenclature (PDB: [3J0C](#); ref. [21](#)). Red boxes indicate residues that are 100% conserved; white boxes and red letters indicate homologous residues within the specific group; white

boxes and black letters indicate non-conserved residues. Determinants of receptor binding to the individual E2–E1 heterodimers are indicated by stars below the alignment and are coloured magenta if specific to LDLRAD3, cyan if specific to MXRA8, or yellow if shared between the two receptors. Wrapped denotes contacts to the wrapped E2–E1 heterodimer, the fusion loop of which is covered by LDLRAD3(D1) or MXRA8. Intraspike refers to the intraspike heterodimer, which is adjacent to the wrapped heterodimer but within the same trimeric spike. Contact residues were determined using PDBePISA.

[Extended Data Fig. 3 Sequence alignment of E1 proteins of the VEEV complex and other alphaviruses.](#)

Amino acid sequence alignment of E1 proteins of various VEEV strains (IAB strain TC-83, AAB02517; IAB strain TrD, AAC19322; IC strain INH9813, AJP13627; ID strain ZPC738, AUV65225) and other alphaviruses (EEEV strain FL93-939, ABL84687; WEEV strain CBA87, ABD98014; SINV strain Girdwood, AUV65223; CHIKV strain 37997, ABX40011). Structure-based sequence alignments were performed between alphaviruses that do (group 1, left margin) or do not (groups 2 and 3, left margin) use LDLRAD3 as a receptor using PROMALS3D with VEEV numbering. The figure was prepared using ESPript 3.0. Domains are coloured (I (light grey), II (medium grey), III (dark grey) and fusion loop (orange)) and indicated above the sequence, along with the secondary structure features and nomenclature (PDB: [3J0C](#); ref. [21](#)). Red boxes indicate residues that are 100% conserved; white boxes and red letters indicate homologous residues within the specific group; white boxes and black letters indicate non-conserved residues. Determinants of receptor binding to the individual E2–E1 heterodimers are indicated by stars below the alignment and are coloured magenta if specific to LDLRAD3, cyan if specific to MXRA8 or yellow if shared between the two receptors. Wrapped denotes contacts to the wrapped E2–E1 heterodimer, the fusion loop of which is covered by LDLRAD3(D1) or MXRA8. Intraspike refers to the intraspike heterodimer, which is adjacent to the wrapped heterodimer but within the same trimeric spike. Contact residues were determined using PDBePISA.

[Source data](#)

[Extended Data Fig. 4 Expression of LDLRAD3\(D1\) mutants on the cell surface and the effect on SINV–VEEV infection.](#)

$\Delta B4galt7 \Delta Ldlrad3$ Neuro2a cells complemented with indicated non-conservative point mutations of *Ldlrad3* in D1 (encoding an N-terminal Flag tag) were inoculated with chimeric SINV–VEEV–GFP viruses (IAB strain TrD). Then, 7.5 h later, the levels of cell surface expression of LDLRAD3 (via anti-Flag; **a, c**) or SINV–VEEV–

GFP infection (via GFP; **b**) were assessed by flow cytometry. **a**, Data are mean \pm s.d. of three experiments performed in technical duplicate. Each data symbol is the average of a technical duplicate from one experiment. **b, c**, Representative flow cytometry contour plots for each indicated LDLRAD3 mutant.

[Source data](#)

[Extended Data Fig. 5 D2 of LDLRAD3 does not contribute to VEEV binding.](#)

a, Cartoon schematic of LDLRAD3 with labelled ectodomains and amino (n) and carboxy (c) termini. D1 is coloured in a rainbow spectrum of blue to red. **b**, Fourier shell correlation plots for VEEV VLP with LDLRAD3(D1+D2). **c**, Electron density of one asymmetric unit of VEEV–LDLRAD3(D1+D2) complex coloured by protein: E1 (grey), E2 (cyan), capsid (forest green) and LDLRAD3(D1+D2) (purple). Density map viewed at a low contour level to show weak density for D2 of LDLRAD3. A ribbon diagram of docked LDLRAD3(D1) model is shown with the amino to carboxy termini in a rainbow spectrum of blue to red. The cysteine residues and the acidic residues responsible for calcium ion coordination are shown as balls and sticks. The disulfide bonds and calcium ion are coloured yellow and green, respectively. Inset: magnified view of LDLRAD3 with the weak density for D2 circled. **d**, Representative surface plasmon resonance sensograms with the binding parameters of LDLRAD3(D1+D2) (left) and LDLRAD3(D1) (right) to VEEV VLPs. $n = 4$ experiments. Data are mean \pm s.e.m. A 1:1 binding model (red traces) was used to fit the experimental curves (black traces).

[Source data](#)

Supplementary information

[Supplementary Tables 1–4](#)

[Reporting Summary](#)

[Supplementary Video 1](#)

Movement of VEEV after LDLRAD3(D1) binding. Morphing of asymmetric unit maps of VEEV with and without bound LDLRAD3(D1), coloured by protein: E1 (grey), E2 (cyan), capsid (forest green) and LDLRAD3(D1) (purple).

[Peer Review File](#)

Source data

[Source Data Fig. 3](#)

[Source Data Extended Data Fig. 1](#)

[Source Data Extended Data Fig. 4](#)

[Source Data Extended Data Fig. 5](#)

Rights and permissions

Open Access This article is licensed under a Creative Commons Attribution 4.0 International License, which permits use, sharing, adaptation, distribution and reproduction in any medium or format, as long as you give appropriate credit to the original author(s) and the source, provide a link to the Creative Commons license, and indicate if changes were made. The images or other third party material in this article are included in the article's Creative Commons license, unless indicated otherwise in a credit line to the material. If material is not included in the article's Creative Commons license and your intended use is not permitted by statutory regulation or exceeds the permitted use, you will need to obtain permission directly from the copyright holder. To view a copy of this license, visit <http://creativecommons.org/licenses/by/4.0/>.

[Reprints and Permissions](#)

About this article

Cite this article

Basore, K., Ma, H., Kafai, N.M. *et al.* Structure of Venezuelan equine encephalitis virus in complex with the LDLRAD3 receptor. *Nature* **598**, 672–676 (2021).
<https://doi.org/10.1038/s41586-021-03963-9>

- Received: 26 May 2021
- Accepted: 26 August 2021
- Published: 13 October 2021
- Issue Date: 28 October 2021

- DOI: <https://doi.org/10.1038/s41586-021-03963-9>

Share this article

Anyone you share the following link with will be able to read this content:

[Get shareable link](#)

Sorry, a shareable link is not currently available for this article.

[Copy to clipboard](#)

Provided by the Springer Nature SharedIt content-sharing initiative

This article was downloaded by **calibre** from <https://www.nature.com/articles/s41586-021-03963-9>

| [Section menu](#) | [Main menu](#) |

- Article
- [Published: 13 October 2021](#)

Structure of Venezuelan equine encephalitis virus with its receptor LDLRAD3

- [Bingting Ma¹ ✉](#),
- [Cuiqing Huang^{2,3} ✉](#),
- [Jun Ma² ✉](#),
- [Ye Xiang](#) ORCID: orcid.org/0000-0003-0230-9522¹ &
- [Xinzheng Zhang](#) ORCID: orcid.org/0000-0002-0114-0270^{2,3}

Nature volume **598**, pages 677–681 (2021)

- 2836 Accesses
- 30 Altmetric
- [Metrics details](#)

Subjects

- [Alphaviruses](#)
- [Cryoelectron microscopy](#)

Abstract

Venezuelan equine encephalitis virus (VEEV) is an enveloped RNA virus that causes encephalitis and potentially mortality in infected humans and equines¹. At present, no vaccines or drugs are available that prevent or cure

diseases caused by VEEV. Low-density lipoprotein receptor class A domain-containing 3 (LDLRAD3) was recently identified as a receptor for the entry of VEEV into host cells². Here we present the cryo-electron microscopy structure of the LDLRAD3 extracellular domain 1 (LDLRAD3-D1) in complex with VEEV virus-like particles at a resolution of 3.0 Å. LDLRAD3-D1 has a cork-like structure and is inserted into clefts formed between adjacent VEEV E2–E1 heterodimers in the viral-surface trimer spikes through hydrophobic and polar contacts. Mutagenesis studies of LDLRAD3-D1 identified residues that are involved in the key interactions with VEEV. Of note, some of the LDLRAD3-D1 mutants showed a significantly increased binding affinity for VEEV, suggesting that LDLRAD3-D1 may serve as a potential scaffold for the development of inhibitors of VEEV entry. Our structures provide insights into alphavirus assembly and the binding of receptors to alphaviruses, which may guide the development of therapeutic countermeasures against alphaviruses.

Access options

Subscribe to Journal

Get full journal access for 1 year

\$199.00

only \$3.90 per issue

[Subscribe](#)

All prices are NET prices.

VAT will be added later in the checkout.

Tax calculation will be finalised during checkout.

Rent or Buy article

Get time limited or full article access on ReadCube.

from \$8.99

[Rent or Buy](#)

All prices are NET prices.

Additional access options:

- [Log in](#)
- [Access through your institution](#)
- [Learn about institutional subscriptions](#)

Fig. 1: Overall structure of the VEEV VLP–LDLRAD3-D1 complex.

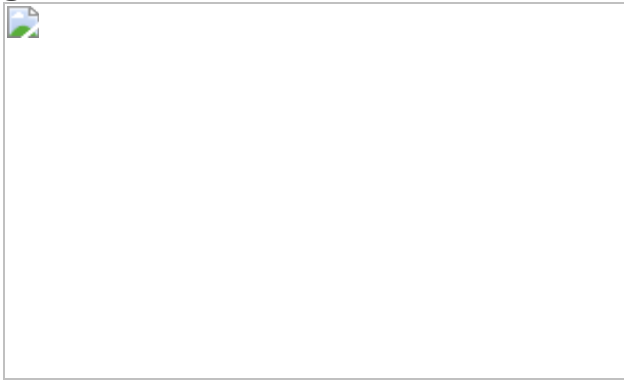


Fig. 2: Detailed contacts between VEEV VLP and the bound LDLRAD3-D1.

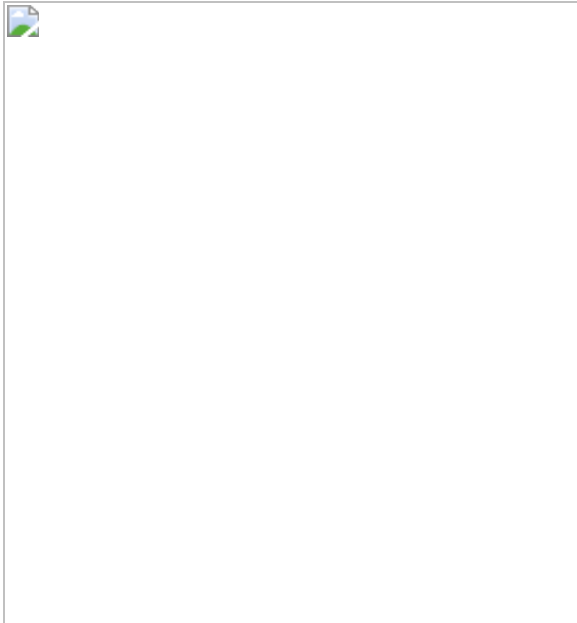
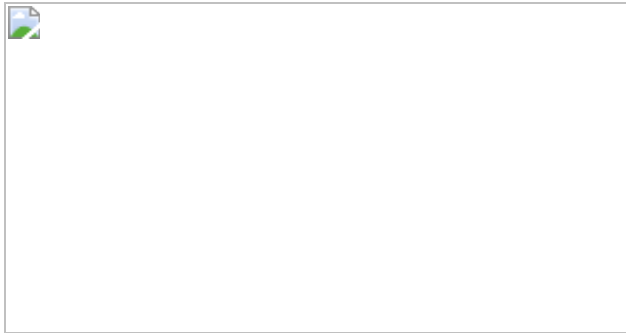


Fig. 3: Structure and organization of the VEEV E1, E2 and capsid proteins.



Data availability

The atomic coordinates and electron microscopy maps have been deposited into the PDB (<http://www.pdb.org>) and the Electron Microscopy Data Bank (EMDB), respectively. The deposited data include the cryo-EM maps and PDB coordinates for an asymmetric unit ([EMD-31567](#), [7FFF](#)), the twofold block ([EMD-31568](#), [7FFL](#)) and the fivefold block ([EMD-31569](#), [7FFN](#)) of the VEEV VLP–LDLRAD3-D1 complex and an asymmetric unit ([EMD-31566](#), [7FFE](#)), the twofold block ([EMD-31571](#), [7FFQ](#)) and the fivefold block ([EMD-31570](#), [7FFO](#)) of VEEV VLP. All other relevant data are available from the corresponding authors upon reasonable request.

References

1. 1.

Taylor, K. G. & Paessler, S. Pathogenesis of Venezuelan equine encephalitis. *Vet. Microbiol.* **167**, 145–150 (2013).

2. 2.

Ma, H. et al. LDLRAD3 is a receptor for Venezuelan equine encephalitis virus. *Nature* **588**, 308–314 (2020).

3. 3.

Strauss, J. H. & Strauss, E. G. The alphaviruses: gene expression, replication, and evolution. *Microbiol. Rev.* **58**, 491–562 (1994).

4. 4.

Suhrbier, A., Jaffar-Bandjee, M. C. & Gasque, P. Arthritogenic alphaviruses—an overview. *Nat. Rev. Rheumatol.* **8**, 420–429 (2012).

5. 5.

Carossino, M., Thiry, E., de la Grandière, A. & Barrandeguy, M. E. Novel vaccination approaches against equine alphavirus encephalitides. *Vaccine* **32**, 311–319 (2014).

6. 6.

Zacks, M. A. & Paessler, S. Encephalitic alphaviruses. *Vet. Microbiol.* **140**, 281–286 (2010).

7. 7.

Sharma, A. & Knollmann-Ritschel, B. Current understanding of the molecular basis of Venezuelan equine encephalitis virus pathogenesis and vaccine development. *Viruses* **11**, 164 (2019).

8. 8.

Bronze, M. S., Huycke, M. M., Machado, L. J., Voskuhl, G. W. & Greenfield, R. A. Viral agents as biological weapons and agents of bioterrorism. *Am. J. Med. Sci.* **323**, 316–325 (2002).

9. 9.

Lescar, J. et al. The fusion glycoprotein shell of Semliki Forest virus: an icosahedral assembly primed for fusogenic activation at endosomal pH. *Cell* **105**, 137–148 (2001).

10. 10.

Li, L., Jose, J., Xiang, Y., Kuhn, R. J. & Rossmann, M. G. Structural changes of envelope proteins during alphavirus fusion. *Nature* **468**, 705–708 (2010).

11. 11.

Roussel, A. et al. Structure and interactions at the viral surface of the envelope protein E1 of Semliki Forest virus. *Structure* **14**, 75–86 (2006).

12. 12.

Voss, J. E. et al. Glycoprotein organization of Chikungunya virus particles revealed by X-ray crystallography. *Nature* **468**, 709–712 (2010).

13. 13.

Chen, L. et al. Implication for alphavirus host-cell entry and assembly indicated by a 3.5 Å resolution cryo-EM structure. *Nat. Commun.* **9**, 5326 (2018).

14. 14.

Cheng, R. H. et al. Nucleocapsid and glycoprotein organization in an enveloped virus. *Cell* **80**, 621–630 (1995).

15. 15.

Hasan, S. S. et al. Cryo-EM structures of eastern equine encephalitis virus reveal mechanisms of virus disassembly and antibody neutralization. *Cell Rep.* **25**, 3136–3147 (2018).

16. 16.

Kostyuchenko, V. A. et al. The structure of Barmah Forest virus as revealed by cryo-electron microscopy at a 6-angstrom resolution has detailed transmembrane protein architecture and interactions. *J. Virol.* **85**, 9327–9333 (2011).

17. 17.

Pletnev, S. V. et al. Locations of carbohydrate sites on alphavirus glycoproteins show that E1 forms an icosahedral scaffold. *Cell* **105**, 127–136 (2001).

18. 18.

Zhang, R. et al. 4.4 Å cryo-EM structure of an enveloped alphavirus Venezuelan equine encephalitis virus. *EMBO J.* **30**, 3854–3863 (2011).

19. 19.

Sun, S. et al. Structural analyses at pseudo atomic resolution of Chikungunya virus and antibodies show mechanisms of neutralization. *Elefé* **2**, e00435 (2013).

20. 20.

Zhang, W. et al. Aura virus structure suggests that the T=4 organization is a fundamental property of viral structural proteins. *J. Virol.* **76**, 7239–7246 (2002).

21. 21.

Jose, J., Snyder, J. E. & Kuhn, R. J. A structural and functional perspective of alphavirus replication and assembly. *Future Microbiol.* **4**, 837–856 (2009).

22. 22.

Holmes, A. C., Basore, K., Fremont, D. H. & Diamond, M. S. A molecular understanding of alphavirus entry. *PLoS Pathog.* **16**, e1008876 (2020).

23. 23.

Vancini, R., Hernandez, R. & Brown, D. Alphavirus entry into host cells. *Prog. Mol. Biol. Transl. Sci.* **129**, 33–62 (2015).

24. 24.

Zhang, R. et al. Mxra8 is a receptor for multiple arthritogenic alphaviruses. *Nature* **557**, 570–574 (2018).

25. 25.

Basore, K. et al. Cryo-EM structure of chikungunya virus in complex with the Mxra8 receptor. *Cell* **177**, 1725–1737 (2019).

26. 26.

Song, H. et al. Molecular basis of arthritogenic alphavirus receptor MXRA8 binding to chikungunya virus envelope protein. *Cell* **177**, 1714–1724 (2019).

27. 27.

Fass, D., Blacklow, S., Kim, P. S. & Berger, J. M. Molecular basis of familial hypercholesterolaemia from structure of LDL receptor module. *Nature* **388**, 691–693 (1997).

28. 28.

Ivanova, L. & Schlesinger, M. J. Site-directed mutations in the Sindbis virus E2 glycoprotein identify palmitoylation sites and affect virus budding. *J. Virol.* **67**, 2546–2551 (1993).

29. 29.

Ko, S. Y. et al. A virus-like particle vaccine prevents equine encephalitis virus infection in nonhuman primates. *Sci. Transl. Med.* **11**, eaav3113 (2019).

30. 30.

Jiang, L. et al. Potent neutralization of MERS-CoV by human neutralizing monoclonal antibodies to the viral spike glycoprotein. *Sci. Transl. Med.* **6**, 234ra259 (2014).

31. 31.

Wu, C., Huang, X., Cheng, J., Zhu, D. & Zhang, X. High-quality, high-throughput cryo-electron microscopy data collection via beam tilt and astigmatism-free beam-image shift. *J. Struct. Biol.* **208**, 107396 (2019).

32. 32.

Zheng, S. Q. et al. MotionCor2: anisotropic correction of beam-induced motion for improved cryo-electron microscopy. *Nat. Methods* **14**, 331–332 (2017).

33. 33.

Rohou, A. & Grigorieff, N. CTFFIND4: Fast and accurate defocus estimation from electron micrographs. *J. Struct. Biol.* **192**, 216–221 (2015).

34. 34.

Zivanov, J. et al. New tools for automated high-resolution cryo-EM structure determination in RELION-3. *Elife* **7**, e42166 (2018).

35. 35.

Ludtke, S. J., Baldwin, P. R. & Chiu, W. EMAN: semiautomated software for high-resolution single-particle reconstructions. *J. Struct. Biol.* **128**, 82–97 (1999).

36. 36.

Pettersen, E. F. et al. UCSF Chimera—a visualization system for exploratory research and analysis. *J. Comput. Chem.* **25**, 1605–1612 (2004).

37. 37.

Afonine, P. V. et al. Real-space refinement in PHENIX for cryo-EM and crystallography. *Acta Crystallogr. D* **74**, 531–544 (2018).

38. 38.

Kucukelbir, A., Sigworth, F. J. & Tagare, H. D. Quantifying the local resolution of cryo-EM density maps. *Nat. Methods* **11**, 63–65 (2014).

Acknowledgements

We thank the Tsinghua University Branch of the China National Center for Protein Sciences (Beijing) for providing the facility support; L. Q. Zhang for providing the vectors; L. Kong for cryo-EM data storage and back-up; and D. J. Zhu and M. J. Zhao for discussions of cryo-EM data processing. Cryo-EM data collection was carried out at the Center for Biological Imaging, Core Facilities for Protein Science at the Institute of Biophysics (IBP), Chinese Academy of Sciences (CAS). We thank X. J. Huang, B. L. Zhu, X. J. Li, L. H. Chen, F. Sun and other staff members at the Center for Biological Imaging (IBP, CAS). This work was supported by funds from the Ministry of Science and Technology of China (grants 2017YFA0504700 and 2016YFA0501100); the Spring Breeze Fund of Tsinghua University; the National Natural Science Foundation of China (grants 31925023, 21827810, 31861143027, 31930069 and 31470721); the Strategic Priority Research Program of the Chinese Academy of Sciences (XDB37040101); the Key Research Program of Frontier Sciences at the Chinese Academy of Sciences (ZDBS-LY-SM003); the Beijing Frontier Research Center for Biological Structure; and the Beijing Advanced Innovation Center for Structure Biology to Y.X. and X.Z. J.M. is supported by the Youth Innovation Promotion Association of CAS (no. 2019094) and the Beijing Nova Program (no. Z201100006820033).

Author information

Author notes

1. These authors contributed equally: Bingting Ma, Cuiqing Huang, Jun Ma

Affiliations

1. Beijing Advanced Innovation Center for Structural Biology, Beijing Frontier Research Center for Biological Structure, Center for Infectious Disease Research, Department of Basic Medical Sciences, School of Medicine, Tsinghua University, Beijing, P. R. China

Bingting Ma & Ye Xiang

2. National Laboratory of Biomacromolecules, CAS Center for Excellence in Biomacromolecules, Institute of Biophysics, Chinese Academy of Sciences (CAS), Beijing, P. R. China

Cuiqing Huang, Jun Ma & Xinzheng Zhang

3. University of Chinese Academy of Sciences, Beijing, P. R. China

Cuiqing Huang & Xinzheng Zhang

Contributions

B.M. prepared the VEEV VLPs and developed the protein expression and purification procedures for LDLRAD3-D1, performed the mutagenesis and BLI analysis and helped with the cryo-EM grid and manuscript preparation. C.H. prepared the cryo-EM grids, collected the cryo-EM data and calculated the structures. J.M. built the atomic model and helped with the cryo-EM grid preparation, cryo-EM data collection and manuscript preparation. Y.X. oversaw the preparation of the VEEV VLPs and LDLRAD3-D1 and the mutagenesis assay. X.Z oversaw the cryo-EM structure determination. Y.X. and X.Z. initiated the project, planned and analysed experiments, supervised the research and wrote the manuscript with input from all co-authors.

Corresponding authors

Correspondence to Ye Xiang or Xinzheng Zhang.

Ethics declarations

Competing interests

A patent application applied by Tsinghua University and the Institute of Biophysics, Chinese Academy of Sciences with Y.X., X.Z., B.M. and C.H. listed as the inventors on the LDLRAD3-D1 core and the LDLRAD3-D1 mutants is pending.

Additional information

Peer review information *Nature* thanks the anonymous reviewers for their contribution to the peer review of this work. Peer reviewer reports are available.

Publisher's note Springer Nature remains neutral with regard to jurisdictional claims in published maps and institutional affiliations.

Extended data figures and tables

[Extended Data Fig. 1 Preparation of the VEEV VLP and LDLRAD3-D1.](#)

a, Left: A schematic diagram showing the VEEV polyprotein and cleavage sites that result in the VEEV structural proteins that assemble into VLPs. Middle: Negative staining electron microscopy analysis of the purified VEEV VLPs. Right: SDS-PAGE analysis of the purified VEEV VLPs. **b**, Left: Schematic diagrams of the domain organization of LDLRAD3 and the construct used to produce the recombinant LDLRAD3-D1-Fc fusion protein. Right: SDS-PAGE analysis of the purified LDLRAD3-D1-Fc recombinant protein under reducing and non-reducing conditions.

[Extended Data Fig. 2 Cryo-EM reconstruction of VEEV VLP and the complex of VEEV VLP with LDLRAD3-D1.](#)

a, A typical cryo-EM image of the VEEV VLP complexed with LDLRAD3-D1. **b**, A reconstructed map of the VEEV VLP complexed with

LDLRAD3-D1 at a resolution of 4.1 Å shows the q3 E1/E2 trimeric spikes surrounding the icosahedral 5-fold axes, the i3 E1/E2 trimeric spikes sitting on the icosahedral 3-fold positions, and the positions of the four E1-E2-E3-C assemblies (1, 2, 3 and 4) in the asymmetric unit. **c**, Diagrams showing the positions of the 5-fold and 2-fold blocks used for the block-based subregion reconstructions of the VEEV VLP. The two blocks were refined and reconstructed separately and cover the complete icosahedral asymmetric unit. **d**, Fourier shell coefficient curves calculated between the odd and even half maps show that the map resolutions of the two reconstructed blocks are 3.03 and 3.06 Å, respectively. The threshold used was 0.143. **e**, The local resolution maps of the two reconstructed blocks calculated with the software Resmap³⁸. **f**, The work flow used for the cryo-EM data processing and block-based reconstructions of VEEV VLP and the complex of VEEV VLP with LDLRAD3-D1.

Extended Data Fig. 3 Representative densities of VEEV VLP and the bound LDLRAD3-D1.

a–d, The density maps are contoured at 0.025 e[−] per Å³.

Extended Data Fig. 4 Structural comparisons between the receptor-bound and receptor-free VEEV E proteins, overall shape of LDLRAD3-D1 and the low-pH-treated VEEV VLP with the bound LDLRAD3-D1.

a, Ribbon diagrams showing the LDLRAD3-D1 bound and free VEEV E2 structures. LDLRAD3-D1 and VEEV E2 are shown in ribbons and coloured pink and green, respectively. Upon binding LDLRAD3-D1, conformational changes were observed at residues H96 and H156 of E2. In addition, the E2 loop that involves residues 57-64 becomes ordered in the complex structure owing to the establishment of the salt bridges between R64 of E2 and D54 and D50 of LDLRAD3-D1. **b**, Ribbon and schematic diagrams showing the elliptical cylinder shape of LDLRAD3-D1. The ribbon of LDLRAD3-D1 is coloured blue through the rainbow spectrum to red (from N to C). **c**, Cryo-EM images of the low pH treated VEEV VLP complexed with LDLRAD3-

D1 showing the aggregated particles, which is an indication for the exposure of the fusion loop.

Extended Data Fig. 5 Sequence alignments of LDLRAD3 with its orthologues and other members of the LDL receptor family.

a, Sequence alignments of the human LDLRAD3 domain 1 and the LDL-receptor class A domains of human LRP1, LRP2, VLDLR, LRP5, LRP1B, LRP4, LRP12, LRP10, LRP6, LDLR, and LRP8. Conserved residues are boxed and coloured red. Completely conserved residues are shown in white on a red background. Triangles indicate residues of LDLRAD3-D1 shown to be critical in the interactions with VEEV VLP. **b**, Sequence alignments of the mouse (*Mus musculus*), horse (*Equus caballus*), human (*Homo sapiens*), chimpanzee (*Pan troglodytes*), rhesus macaque (*Macaca mulatta*), cattle (*Bos taurus*), pig (*Sus scrofa*), dog (*Canis lupus familiaris*), chicken (*Gallus gallus*), duck (*Oxyura jamaicensis*), and turkey (*Meleagris gallopavo*) LDLRAD3 ectodomains. Conserved residues are boxed and coloured red. Completely conserved residues are shown in white on a red background. Triangles indicate the residues of LDLRAD3-D1 shown to be critical in the interactions with VEEV VLP. Stars indicate the D-x-S-D-E calcium binding motif of LDLRAD3.

Extended Data Fig. 6 BLI analyses of the binding of LDLRAD3-D1 or its mutants to VEEV VLP.

BLI analysis showing the representative binding and disassociation curves of LDLRAD3-D1 and mutants N30A, I31A, N34A, N39A, R41A, R41N, R41L, W47G, W47F, W47I, D50G, D54G, F56G, and D57G to VEEV VLP. The K_D value displayed for each sample is the mean value of two independent measurements.

Extended Data Fig. 7 Sequence alignments of the E1 proteins from different alphaviruses.

Sequence alignments of the E1 proteins from VEEV (AAB02517.1), WEEV (UniProt ID: P13897), EEEV (UniProt ID: P08768), ONNV

(UniProt ID: O90369), SINV (UniProt ID: P03316), CHIKV (UniProt ID: Q5XXP3), MAYV (UniProt ID: Q8QZ72), and RRV (UniProt ID: P08491). Conserved residues are boxed and coloured red. Completely conserved residues are shown in white on a red background. Diamonds underneath the alignments indicate residues involved in the interactions between the VEEV E1 and E2. Red diamonds indicate residues that participate in the formation of hydrogen bonds at the VEEV E1-E2 interfaces. Triangles indicate residues of VEEV VLP involved in the interactions with LDLRAD3-D1. Red triangles indicate residues of VEEV VLP that participate in the formation of hydrogen bonds with LDLRAD3-D1. Rectangles indicate residues of CHIKV VLP that participate in the interactions with the receptor MXRA8. Red rectangles indicate residues of CHIKV VLP involved in the formation of hydrogen bonds with MXRA8. Stars indicate residues involved in the interactions between the VEEV capsid protein and E1. Red stars indicate residues of VEEV E1 that participate in the formation of hydrogen bonds with VEEV capsid protein.

Extended Data Fig. 8 Sequence alignments of the E2 proteins from different alphaviruses.

Sequence alignments of the E2 proteins from VEEV (AAB02517.1), WEEV (UniProt ID: P13897), EEEV (UniProt ID: P08768), ONNV (UniProt ID: O90369), SINV (UniProt ID: P03316), CHIKV (UniProt ID: Q5XXP3), MAYV (UniProt ID: Q8QZ72), and RRV (UniProt ID: P08491). Conserved residues are boxed and coloured red. Completely conserved residues are shown in white on a red background. Diamonds indicate residues of VEEV VLP involved in the interactions between E1 and E2. Red diamonds indicate residues of VEEV VLP that participate in the formation of hydrogen bonds at the VEEV E1-E2 interfaces. Triangles indicate residues of VEEV VLP that participate in the interactions with LDLRAD3-D1. Red triangles indicate residues of VEEV VLP that participate in the formation of hydrogen bonds with LDLRAD3-D1. Rectangles indicate residues of CHIKV VLP that participate in the interactions with the receptor MXRA8. Red rectangles indicate residues of CHIKV VLP that participate in the formation of hydrogen bonds with MXRA8. Stars indicate residues involved in the interactions between the

VEEV capsid protein and E2. Red stars indicate residues of VEEV E2 that participate in the formation of hydrogen bonds with VEEV capsid protein.

Extended Data Fig. 9 Sequence alignments of the capsid proteins from different alphaviruses.

Sequence alignments of the capsid proteins from VEEV (AAB02517.1), WEEV (UniProt ID: P13897), EEEV (UniProt ID: P08768), ONNV (UniProt ID: O90369), SINV (UniProt ID: P03316), CHIKV (UniProt ID: Q5XXP3), MAYV (UniProt ID: Q8QZ72), and RRV (UniProt ID: P08491). Conserved residues are boxed and coloured red. Completely conserved residues are shown in white on a red background. Diamonds underneath the alignments indicate residues involved in the interactions between the VEEV capsid and E1. Red diamonds indicate residues that participate in the formation of hydrogen bonds at the VEEV capsid-E1 interfaces. Triangles underneath the alignments indicate residues involved in the interactions between the VEEV capsid and E2. Red triangles indicate residues that participate in the formation of hydrogen bonds at the VEEV capsid-E2 interfaces.

Extended Data Table 1 Cryo-EM data collection and validation statistics

Supplementary information

Supplementary Information

This file contains Supplementary Figure 1 and Supplementary Tables 1–3

Reporting Summary

Peer Review File

Rights and permissions

[Reprints and Permissions](#)

About this article

Cite this article

Ma, B., Huang, C., Ma, J. *et al.* Structure of Venezuelan equine encephalitis virus with its receptor LDLRAD3. *Nature* **598**, 677–681 (2021).
<https://doi.org/10.1038/s41586-021-03909-1>

- Received: 19 May 2021
- Accepted: 13 August 2021
- Published: 13 October 2021
- Issue Date: 28 October 2021
- DOI: <https://doi.org/10.1038/s41586-021-03909-1>

Share this article

Anyone you share the following link with will be able to read this content:

[Get shareable link](#)

Sorry, a shareable link is not currently available for this article.

[Copy to clipboard](#)

Provided by the Springer Nature SharedIt content-sharing initiative

This article was downloaded by **calibre** from <https://www.nature.com/articles/s41586-021-03909-1>

- Article
- [Published: 20 October 2021](#)

KDM5B promotes immune evasion by recruiting SETDB1 to silence retroelements

- [Shang-Min Zhang¹](#),
- [Wesley L. Cai¹](#) nAff12,
- [Xiaoni Liu^{1,2}](#),
- [Durga Thakral²](#),
- [Jiesi Luo^{3,4}](#),
- [Lok Hei Chan¹](#),
- [Meaghan K. McGeary](#) [ORCID: orcid.org/0000-0002-8505-7158^{1,2}](#),
- [Eric Song](#) [ORCID: orcid.org/0000-0001-5448-5865⁵](#),
- [Kim R. M. Blenman^{2,6,7}](#),
- [Goran Micevic²](#),
- [Shlomit Jessel⁶](#),
- [Yangyi Zhang^{1,8}](#),
- [Mingzhu Yin^{1,8}](#),
- [Carmen J. Booth](#) [ORCID: orcid.org/0000-0002-2153-738X⁹](#),
- [Lucia B. Jilaveanu^{6,7}](#),
- [William Damsky](#) [ORCID: orcid.org/0000-0003-0975-4071^{2,7}](#),
- [Mario Sznol^{2,7}](#),
- [Harriet M. Kluger^{6,7,10}](#),
- [Akiko Iwasaki](#) [ORCID: orcid.org/0000-0002-7824-9856^{5,7,10,11}](#),
- [Marcus W. Bosenberg](#) [ORCID: orcid.org/0000-0003-0166-1612^{1,2,4,5,7,10}](#) &
- [Qin Yan](#) [ORCID: orcid.org/0000-0003-4077-453X^{1,4,7,10}](#)

[Nature](#) volume **598**, pages 682–687 (2021)

- 7648 Accesses
- 62 Altmetric
- [Metrics details](#)

Subjects

- [Epigenetics](#)
- [Melanoma](#)

Abstract

Tumours use various strategies to evade immune surveillance^{1,2}. Immunotherapies targeting tumour immune evasion such as immune checkpoint blockade have shown considerable efficacy on multiple cancers^{3,4} but are ineffective for most patients due to primary or acquired resistance^{5,6,7}. Recent studies showed that some epigenetic regulators suppress anti-tumour immunity^{2,8,9,10,11,12}, suggesting that epigenetic therapies could boost anti-tumour immune responses and overcome resistance to current immunotherapies. Here we show that, in mouse melanoma models, depletion of KDM5B—an H3K4 demethylase that is critical for melanoma maintenance and drug resistance^{13,14,15}—induces robust adaptive immune responses and enhances responses to immune checkpoint blockade. Mechanistically, KDM5B recruits the H3K9 methyltransferase SETDB1 to repress endogenous retroelements such as *MMVL30* in a demethylase-independent manner. Derepression of these retroelements activates cytosolic RNA-sensing and DNA-sensing pathways and the subsequent type-I interferon response, leading to tumour rejection and induction of immune memory. Our results demonstrate that KDM5B suppresses anti-tumour immunity by epigenetic silencing of retroelements. We therefore reveal roles of KDM5B in heterochromatin regulation and immune evasion in melanoma, opening new paths for the development of

KDM5B-targeting and SETDB1-targeting therapies to enhance tumour immunogenicity and overcome immunotherapy resistance.

Access options

Subscribe to Journal

Get full journal access for 1 year

\$199.00

only \$3.90 per issue

[Subscribe](#)

All prices are NET prices.

VAT will be added later in the checkout.

Tax calculation will be finalised during checkout.

Rent or Buy article

Get time limited or full article access on ReadCube.

from \$8.99

[Rent or Buy](#)

All prices are NET prices.

Additional access options:

- [Log in](#)
- [Access through your institution](#)
- [Learn about institutional subscriptions](#)

Fig. 1: Depletion of KDM5B induces anti-tumour immunity in a manner dependent on the adaptive immune system.

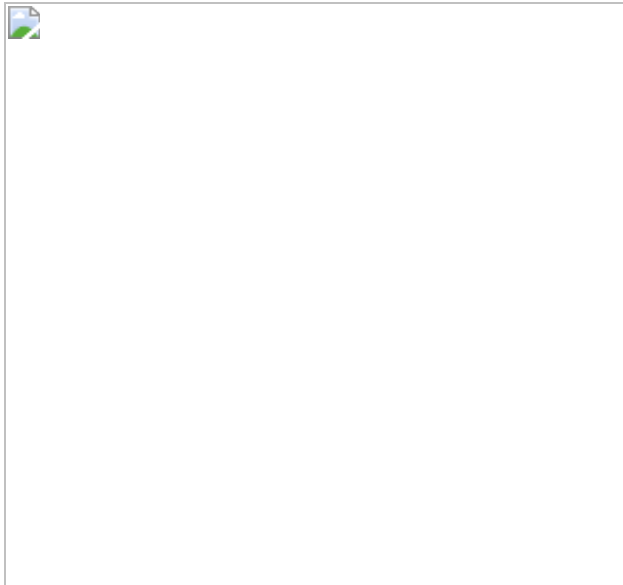


Fig. 2: Deletion of *Kdm5b* activates the type-I interferon response through both cytosolic RNA-sensing and DNA-sensing pathways.

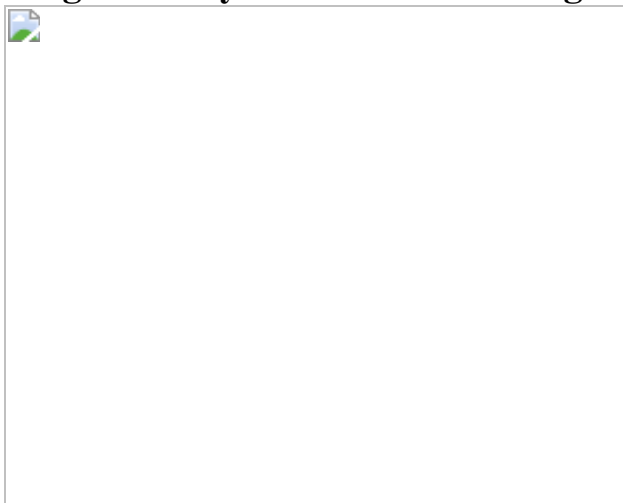


Fig. 3: Deletion of *Kdm5b* derepresses endogenous retroelements, which can be reverse transcribed into cDNAs.

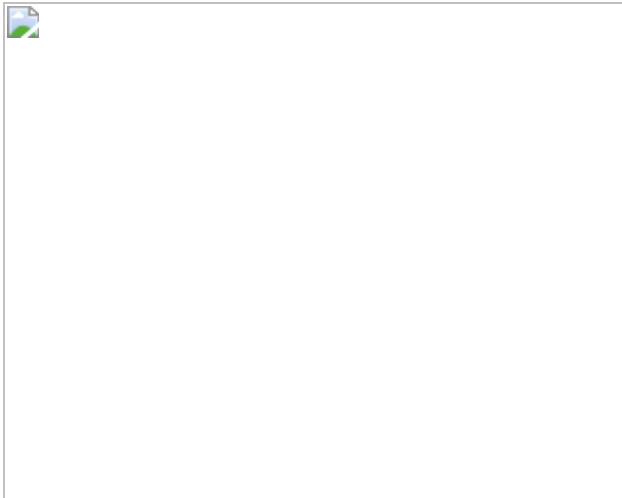
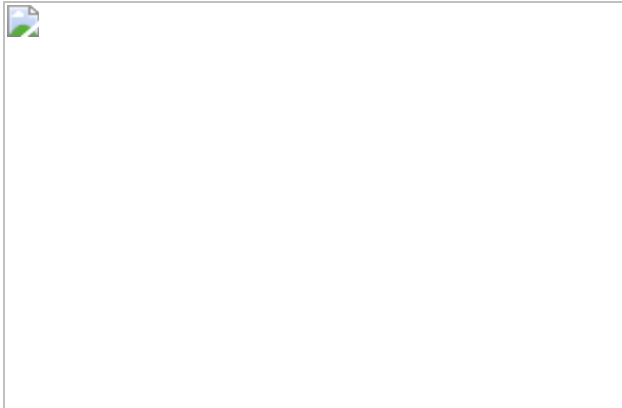


Fig. 4: KDM5B suppresses the expression of retroelements by recruiting the H3K9 methyltransferase SETDB1.



Data availability

All epigenomic sequencing data of this study have been deposited at the Gene Expression Omnibus database under accession number [GSE161065](#). [Source data](#) are provided with this paper.

Code availability

Custom codes have been deposited in GitHub (https://github.com/wesleylcai/zhang_nature_2021).

References

1. 1.
Chen, D. S. & Mellman, I. Elements of cancer immunity and the cancer-immune set point. *Nature* **541**, 321–330 (2017).
2. 2.
Cao, J. & Yan, Q. Cancer epigenetics, tumor immunity, and immunotherapy. *Trends Cancer* **6**, 580–592 (2020).
3. 3.
Topalian, S. L., Drake, C. G. & Pardoll, D. M. Immune checkpoint blockade: a common denominator approach to cancer therapy. *Cancer Cell* **27**, 450–461 (2015).
4. 4.
Topalian, S. L. et al. Safety, activity, and immune correlates of anti-PD-1 antibody in cancer. *N. Engl. J. Med.* **366**, 2443–2454 (2012).
5. 5.
Hugo, W. et al. Genomic and transcriptomic features of response to anti-PD-1 therapy in metastatic melanoma. *Cell* **165**, 35–44 (2016).
6. 6.
Sharma, P., Hu-Lieskovan, S., Wargo, J. A. & Ribas, A. Primary, adaptive, and acquired resistance to cancer immunotherapy. *Cell* **168**, 707–723 (2017).
7. 7.
Ribas, A. & Wolchok, J. D. Cancer immunotherapy using checkpoint blockade. *Science* **359**, 1350–1355 (2018).
8. 8.

Chiappinelli, K. B. et al. Inhibiting DNA methylation causes an interferon response in cancer via dsRNA including endogenous retroviruses. *Cell* **162**, 974–986 (2015).

9. 9.

Roulois, D. et al. DNA-demethylating agents target colorectal cancer cells by inducing viral mimicry by endogenous transcripts. *Cell* **162**, 961–973 (2015).

10. 10.

Sheng, W. et al. LSD1 ablation stimulates anti-tumor immunity and enables checkpoint blockade. *Cell* **174**, 549–563 (2018).

11. 11.

Pan, D. et al. A major chromatin regulator determines resistance of tumor cells to T cell-mediated killing. *Science* **359**, 770–775 (2018).

12. 12.

Ishizuka, J. J. et al. Loss of ADAR1 in tumours overcomes resistance to immune checkpoint blockade. *Nature* **565**, 43–48 (2019).

13. 13.

Roesch, A. et al. A temporarily distinct subpopulation of slow-cycling melanoma cells is required for continuous tumor growth. *Cell* **141**, 583–594 (2010).

14. 14.

Roesch, A. et al. Overcoming intrinsic multidrug resistance in melanoma by blocking the mitochondrial respiratory chain of slow-cycling JARID1B^{high} cells. *Cancer Cell* **23**, 811–825 (2013).

15. 15.

Liu, X. et al. KDM5B promotes drug resistance by regulating melanoma-propagating cell subpopulations. *Mol. Cancer Ther.* **18**, 706–717 (2019).

16. 16.

Kearney, C. J. et al. Tumor immune evasion arises through loss of TNF sensitivity. *Sci. Immunol.* **3**, eaar3451 (2018).

17. 17.

Trujillo, J. A., Sweis, R. F., Bao, R. & Luke, J. J. T cell-inflamed versus non-T cell-inflamed tumors: a conceptual framework for cancer immunotherapy drug development and combination therapy selection. *Cancer Immunol. Res.* **6**, 990–1000 (2018).

18. 18.

Wang, J. et al. UV-induced somatic mutations elicit a functional T cell response in the YUMMER1.7 mouse melanoma model. *Pigment Cell Melanoma Res.* **30**, 428–435 (2017).

19. 19.

Held, M. A. et al. Characterization of melanoma cells capable of propagating tumors from a single cell. *Cancer Res.* **70**, 388–397 (2010).

20. 20.

Kalbasi, A. et al. Uncoupling interferon signaling and antigen presentation to overcome immunotherapy resistance due to JAK1 loss in melanoma. *Sci. Transl. Med.* **12**, eabb0152 (2020).

21. 21.

King, D. P. & Jones, P. P. Induction of Ia and H-2 antigens on a macrophage cell line by immune interferon. *J. Immunol.* **131**, 315–318 (1983).

22. 22.

Mu, X., Ahmad, S. & Hur, S. Endogenous retroelements and the host innate immune sensors. *Adv. Immunol.* **132**, 47–69 (2016).

23. 23.

Ahmad, S. et al. Breaching self-tolerance to Alu duplex RNA underlies MDA5-mediated inflammation. *Cell* **172**, 797–810 (2018).

24. 24.

Mehdipour, P. et al. Epigenetic therapy induces transcription of inverted SINEs and ADAR1 dependency. *Nature* **588**, 169–173 (2020).

25. 25.

Kong, Y. et al. Transposable element expression in tumors is associated with immune infiltration and increased antigenicity. *Nat. Commun.* **10**, 5228 (2019).

26. 26.

Ye, X. et al. Endogenous retroviral proteins provide an immunodominant but not requisite antigen in a murine immunotherapy tumor model. *Oncimmunology* **9**, 1758602 (2020).

27. 27.

Cao, J. et al. Histone demethylase RBP2 is critical for breast cancer progression and metastasis. *Cell Rep.* **6**, 868–877 (2014).

28. 28.

Horton, J. R. et al. Structural basis for KDM5A histone lysine demethylase inhibition by diverse compounds. *Cell Chem. Biol.* **23**, 769–781 (2016).

29. 29.

Griffin, G. K. et al. Epigenetic silencing by SETDB1 suppresses tumour intrinsic immunogenicity. *Nature* **595**, 309–314 (2021).

30. 30.

Yin, M. et al. Potent BRD4 inhibitor suppresses cancer cell-macrophage interaction. *Nat. Commun.* **11**, 1833 (2020).

31. 31.

Kluger, H. M. et al. PD-L1 studies across tumor types, its differential expression and predictive value in patients treated with immune checkpoint inhibitors. *Clin. Cancer Res.* **23**, 4270–4279 (2017).

32. 32.

Kluger, H. M. et al. Characterization of PD-L1 expression and associated T-cell infiltrates in metastatic melanoma samples from variable anatomic sites. *Clin. Cancer Res.* **21**, 3052–3060 (2015).

33. 33.

Blenman, K. R. M. & Bosenberg, M. W. Immune cell and cell cluster phenotyping, quantitation, and visualization using in silico multiplexed images and tissue cytometry. *Cytometry A* **95**, 399–410 (2019).

34. 34.

Treger, R. S. et al. Human APOBEC3G prevents emergence of infectious endogenous retrovirus in mice. *J. Virol.* **93**, e00728-19 (2019).

35. 35.

Bolger, A. M., Lohse, M. & Usadel, B. Trimmomatic: a flexible trimmer for Illumina sequence data. *Bioinformatics* **30**, 2114–2120 (2014).

36. 36.

Dobin, A. et al. STAR: ultrafast universal RNA-seq aligner. *Bioinformatics* **29**, 15–21 (2013).

37. 37.

Karolchik, D. et al. The UCSC Table Browser data retrieval tool. *Nucleic Acids Res.* **32**, D493–D496 (2004).

38. 38.

Liao, Y., Smyth, G. K. & Shi, W. featureCounts: an efficient general purpose program for assigning sequence reads to genomic features. *Bioinformatics* **30**, 923–930 (2014).

39. 39.

Love, M. I., Huber, W. & Anders, S. Moderated estimation of fold change and dispersion for RNA-seq data with DESeq2. *Genome Biol.* **15**, 550 (2014).

40. 40.

Storer, J., Hubley, R., Rosen, J., Wheeler, T. J. & Smit, A. F. The Dfam community resource of transposable element families, sequence models, and genome annotations. *Mob. DNA* **12**, 2 (2021).

41. 41.

Pertea, M. et al. StringTie enables improved reconstruction of a transcriptome from RNA-seq reads. *Nat. Biotechnol.* **33**, 290–295 (2015).

42. 42.

Tjeldnes, H. & Labun, K. ORFik: open reading frames in genomics (2021); <https://github.com/Roleren/ORFik>

43. 43.

Andreatta, M. & Nielsen, M. Gapped sequence alignment using artificial neural networks: application to the MHC class I system. *Bioinformatics* **32**, 511–517 (2016).

44. 44.

Nielsen, M. et al. Reliable prediction of T-cell epitopes using neural networks with novel sequence representations. *Protein Sci.* **12**, 1007–1017 (2003).

45. 45.

Krueger, F. Trim Galore (2019).

46. 46.

Langmead, B. & Salzberg, S. L. Fast gapped-read alignment with Bowtie 2. *Nat. Methods* **9**, 357–359 (2012).

47. 47.

Li, H. et al. The Sequence Alignment/Map format and SAMtools. *Bioinformatics* **25**, 2078–2079 (2009).

48. 48.

Zhang, Y. et al. Model-based analysis of ChIP-Seq (MACS). *Genome Biol.* **9**, R137 (2008).

49. 49.

Ramirez, F. et al. deepTools2: a next generation web server for deep-sequencing data analysis. *Nucleic Acids Res.* **44**, W160–W165 (2016).

50. 50.

Gu, Z., Eils, R. & Schlesner, M. Complex heatmaps reveal patterns and correlations in multidimensional genomic data. *Bioinformatics* **32**, 2847–2849 (2016).

51. 51.

Pohl, A. & Beato, M. bwtool: a tool for bigWig files. *Bioinformatics* **30**, 1618–1619 (2014).

52. 52.

Heinz, S. et al. Simple combinations of lineage-determining transcription factors prime cis-regulatory elements required for macrophage and B cell identities. *Mol. Cell* **38**, 576–589 (2010).

53. 53.

Wei, J. et al. Genome-wide CRISPR screens reveal host factors critical for SARS-CoV-2 infection. *Cell* **184**, 76–91 (2021).

54. 54.

Tokuyama, M. et al. ERVmap analysis reveals genome-wide transcription of human endogenous retroviruses. *Proc. Natl Acad. Sci. USA* **115**, 12565–12572 (2018).

55. 55.

Patro, R., Duggal, G., Love, M. I., Irizarry, R. A. & Kingsford, C. Salmon provides fast and bias-aware quantification of transcript expression. *Nat. Methods* **14**, 417–419 (2017).

56. 56.

Canadas, I. et al. Tumor innate immunity primed by specific interferon-stimulated endogenous retroviruses. *Nat. Med.* **24**, 1143–1150 (2018).

57. 57.

Herquel, B. et al. Trim24-repressed VL30 retrotransposons regulate gene expression by producing noncoding RNA. *Nat. Struct. Mol. Biol.* **20**, 339–346 (2013).

58. 58.

West, A. P. et al. Mitochondrial DNA stress primes the antiviral innate immune response. *Nature* **520**, 553–557 (2015).

Acknowledgements

We thank members of the Yan, Bosenberg and Iwasaki laboratories for their discussion and support; J. J. Ishizuka for discussions; R. Halaban for providing the human melanoma cell lines used in this study; Q. Xiao for help with some FACS analysis; F. J. Rauscher III from the Wistar Institute for providing pCMV.Flag-SETDB1 (wild-type and catalytically inactive mutant) plasmids; M. Zhong for performing the sequencing at Yale Stem Cell Center Genomics Core facility, which was supported by the Connecticut Regenerative Medicine Research Fund and the Li Ka Shing Foundation; staff at the Yale Center for Genome Analysis for performing part of the Illumina sequencing; and staff at the Comparative Pathology Research Core for Histology Service and Amos Brooks at Yale Pathology Tissue Services for histology and immunohistochemistry services. These studies were supported in part by grants from the NIH Yale SPORE in Skin Cancer, NCI P50 CA121974 (to M.W.B., H.M.K., M.S. and Q.Y.), P01 CA128814 (to M.W.B.), R01 CA237586 (to Q.Y.), R01 CA227473 and R01 CA216846 (to H.M.K.), Department of Defense W81XWH-13-1-0235 (to Q.Y.) and W81XWH-16-1-0306 and W81XWH-20-1-0360 (to S.-M.Z.), a pilot grant from Yale Cancer Center and NCI P30 CA016359 (to M.W.B., Q.Y. and A.I.), the Melanoma Research Foundation (to M.W.B. and Q.Y.), the Lung Cancer Research Foundation-LUNGevity and Melanoma Research Alliance Award 308721 (to L.B.J.) and the Melanoma Research Alliance Young Investigator Award (to K.R.M.B.).

Author information

Author notes

1. Wesley L. Cai

Present address: Hillman Cancer Center, University of Pittsburgh Medical Center, Pittsburgh, PA, USA

Affiliations

1. Department of Pathology, Yale School of Medicine, New Haven, CT, USA

Shang-Min Zhang, Wesley L. Cai, Xiaoni Liu, Lok Hei Chan, Meaghan K. McGeary, Yangyi Zhang, Mingzhu Yin, Marcus W. Bosenberg & Qin Yan

2. Department of Dermatology, Yale School of Medicine, New Haven, CT, USA

Xiaoni Liu, Durga Thakral, Meaghan K. McGeary, Kim R. M. Blenman, Goran Micevic, William Damsky, Mario Sznol & Marcus W. Bosenberg

3. Section of Cardiovascular Medicine, Department of Internal Medicine, Yale Cardiovascular Research Center, Yale School of Medicine, New Haven, CT, USA

Jiesi Luo

4. Yale Stem Cell Center, Yale School of Medicine, New Haven, CT, USA

Jiesi Luo, Marcus W. Bosenberg & Qin Yan

5. Department of Immunobiology, Yale School of Medicine, New Haven, CT, USA

Eric Song, Akiko Iwasaki & Marcus W. Bosenberg

6. Department of Medicine, Yale School of Medicine, New Haven, CT, USA

Kim R. M. Blenman, Shlomit Jessel, Lucia B. Jilaveanu & Harriet M. Kluger

7. Yale Cancer Center, Yale School of Medicine, New Haven, CT, USA

Kim R. M. Blenman, Lucia B. Jilaveanu, William Damsky, Mario Sznol, Harriet M. Kluger, Akiko Iwasaki, Marcus W. Bosenberg & Qin Yan

8. Department of Dermatology, Hunan Engineering Research Center of Skin Health and Disease, Hunan Key Laboratory of Skin Cancer and Psoriasis, Xiangya Hospital, Central South University, Changsha, China

Yangyi Zhang & Mingzhu Yin

9. Department of Comparative Medicine, Yale School of Medicine, New Haven, CT, USA

Carmen J. Booth

10. Yale Center for Immuno-Oncology, Yale School of Medicine, New Haven, CT, USA

Harriet M. Kluger, Akiko Iwasaki, Marcus W. Bosenberg & Qin Yan

11. Howard Hughes Medical Institute, Chevy Chase, MD, USA

Akiko Iwasaki

Contributions

S.-M.Z., M.W.B. and Q.Y. conceived and designed the study. S.-M.Z. performed most of the experiments with help from X.L., W.L.C., L.H.C., M.K.M., J.L., S.J., Y.Z. and M.Y.; W.L.C. performed most of the bioinformatics analysis. D.T. and M.K.M. performed some RNA-seq analysis. K.R.M.B. performed capturing, quantification and analytical analysis for TMA. E.S. contributed to neoantigen analysis. G.M. performed

some TCGA bioinformatics analysis. L.B.J. performed TMA staining. M.S. and H.M.K. provided clinical patient samples. C.J.B. performed histology analysis and captured immunohistochemistry images. W.D. and A.I. provided input on study design and data analysis. S.-M.Z., M.W.B. and Q.Y. wrote the manuscript.

Corresponding authors

Correspondence to Marcus W. Bosenberg or Qin Yan.

Ethics declarations

Competing interests

The authors declare no competing interests.

Additional information

Peer review information *Nature* thanks Daniel De Carvalho, Lélia Delamarre and Didier Trono for their contribution to the peer review of this work. Peer reviewer reports are available.

Publisher's note Springer Nature remains neutral with regard to jurisdictional claims in published maps and institutional affiliations.

Extended data figures and tables

Extended Data Fig. 1 KDM5B expression is negatively correlated with anti-tumor immunity, and depletion of KDM5B in mouse melanoma tumor cells induces strong anti-tumor immunity and enhances response to anti-PD-1 treatment.

a, Spearman correlation coefficient scores of selected genes negatively correlated with KDM5B gene expression from the melanoma TCGA dataset, categorized by their functions. **b**, Box plot showing expression

levels of *CD8A*, *CD8B*, *IFNG*, *TNF*, *CXCL9* and *CXCL10* in samples from patients with melanoma from the TCGA dataset are higher in “KDM5B low” group (lowest quartile) than in “KDM5B high” (highest quartile) group. Statistical significance was computed with the unpaired two-sided Student’s t test. **c**, Immunofluorescence staining of pre-treatment melanoma samples with a melanoma cocktail (S100, HMB45 -green), KDM5B (red), and DAPI (blue). Images A-C are representative images from 3 independent non-responders to anti-PD-1 treatment; Images D-F are representative images from 3 independent responders. Cell-specific KDM5B expression levels of KDM5B and melanoma markers in the tumor microenvironment are displayed in 2D dot plots in non-responders (G) and responders (H). Each dot represents the mean fluorescent intensities of a single cell for KDM5B and the melanoma marker cocktail. Cells that are positive for both KDM5B and melanoma marks are in the upper right quadrants. (I) displays the frequency and distribution of expression levels of KDM5B in responders (green) and non-responders (red). MGLI = mean grey level intensity. Cutoff values for positive settings are denoted by the horizontal and vertical bars. Scale bar = 100 μ m. **d**, Survival curves of C57BL/6 mice subcutaneously injected with 500,000 control (black) ($n = 6$) or *Kdm5b*^{-/-} (*Kdm5b* sg) (red) ($n = 6$) YUMMER1.7 cells. Mice injected with *Kdm5b*^{-/-} cells had completely regressed tumors, and were re-challenged with control tumor cells on day 45 after initial tumor injection. Data are representative of two independent experiments. Log-rank test for survival curves, ** $p = 0.004$. **e**, Tumor growth curves of C57BL/6 mice injected with polyclonal YUMMER1.7 cells with stable lentiviral Ctl sg ($n = 5$), *Kdm5b* sg1 ($n = 5$) or *Kdm5b* sg2 ($n = 5$), with western blot analyses (insert) showing knockout efficacy of KDM5B. Data are representative of two independent experiments. Data are mean \pm SEM. 2-way ANOVA analysis for comparison at day 18 after tumor injection, *** $p < 0.0001$. For gel source data, see Supplementary Fig. 1. **f**, Representative images of immunofluorescent staining of CD3 (green), Melan A (red) and DAPI (blue) (left) and Quantification of CD3⁺ cells per view field (3-5 view fields per tumor; each dot represents the mean for each tumor; 5 tumors per group) (right) from Ctl, *Kdm5b* sg1 and *Kdm5b* sg2 YUMMER1.7 tumors harvested at day 14 after injection. scale bar = 200 μ m. Quantification data are mean \pm SD; Unpaired two-sided Student’s t-test, ** $p = 0.0081$ for Ctl vs sg1; ** $p = 0.0063$ for Ctl vs sg2. **g**, Quantitation of the percentages of CD4⁺

and CD8⁺ cells in total CD45⁺ immune cells using flow cytometry analysis of control and *Kdm5b* sgRNA tumors. Unpaired two-sided Student's t-test for each comparison, **p* = 0.036 for CD4⁺%; **p* = 0.024 for CD8⁺%. Data are representative of two independent experiments. Data are mean± SD. **h**, Representative flow cytometry plots showing CD8⁺ T cells in Ctl and *Kdm5b* sg YUMMER1.7 tumors harvested at day 14 after tumor injection. **i**, Representative immunohistochemical staining of CD8 (CD8⁺ T cells) and cleaved caspase-3 in control and *Kdm5b* sg YUMMER1.7 tumors at day 14 after injection. scale bar = 100 μm. Data are representative of three independent experiments. **j,k**, Tumor growth curves (**j**) and survival curves (**k**) of C57BL/6 mice injected with single clones of *Kdm5b*^{-/-} YUMMER1.7 cells, WT (*n* = 5), 1G8 (*n* = 5), 4B5 (*n* = 5), 4H1(*n* = 5) and 4H3(*n* = 5) are clone numbers. Statistical significance of tumor growth curves was analysed using two-way ANOVA, ****p*<0.0001. Data are representative of two independent experiments. Data are mean± SEM. Statistical significance of tumor survival was analysed with log-rank (Mantel-Cox) test. ***p* = 0.0018. **l**, Tumor growth curves of wild-type C57BL/6J (B6) mice injected with control (Ctl) (*n* = 4) or *Kdm5b*^{-/-} (*Kdm5b* sg) (*n* = 4) YUMMER1.7 cells or *Rag1*^{-/-} mice injected with control (*n* = 5) or *Kdm5b*^{-/-} YUMMER1.7 cells (*n* = 4). Data represent one experiment. Data are mean ± SEM. ****p*<0.0001. **m**, Tumor growth curves of WT (*n* = 5) and *Kdm5b*^{-/-} YUMM1.7 (*n* = 4) in *Rag1*^{-/-} mice. Western blot of the cell lines is shown on the right. Data represent one experiment. Data are mean ± SEM. 2-way ANOVA analysis for comparison at day 25 after tumor injection, ****p*<0.0001. For gel source data, see Supplementary Fig. 1. **n**, Tumor growth curves of C57BL/6J (B6) mice that rejected *Kdm5b*^{-/-} YUMMER1.7 tumors (Challenged B6) rechallenged with YUMM1.7 (*n* = 6) or *Kdm5b*^{-/-} YUMM1.7 (*n* = 5) cells compared with age matched Naïve B6 mice injected with YUMM1.7 (*n* = 5) or *Kdm5b*^{-/-} YUMM1.7 (*n* = 5) cells. Data represent one experiment. Data are mean ± SEM. 2-way ANOVA analysis for comparison of tumor size at day 25. n.s., not significant; ****p*<0.0001. **o**, Survival curves of C57BL/6J (B6) mice that rejected *Kdm5b*^{-/-} YUMMER1.7 tumors (Challenged B6) rechallenged with *Kdm5b*^{-/-} YUMM1.7 cells and treated with anti-CD8 antibody (*n* = 4) or IgG control (*n* = 4). Data represent one experiment. Statistical significance of tumor survival was analysed with log-rank

(Mantel-Cox) test. ** $p = 0.0067$. **p**, Tumor growth curves of C57BL/6 mice injected with wild-type YUMM1.7 cells treated with IgG control ($n = 10$) or anti-PD-1 antibody ($n = 10$); or $Kdm5b^{-/-}$ YUMM1.7 cells treated with IgG control ($n = 9$) or anti-PD-1 antibody ($n = 10$). Data are representative of two independent experiments. Data are mean \pm SEM. 2-way ANOVA analysis for comparison at day 18. n.s., not significant; *** $p < 0.0001$. **q**, Spider plots of tumor growth data shown in **p**.

[Source data](#)

Extended Data Fig. 2 Depletion of KDM5B in mouse melanoma cells activates the type I interferon response through both RNA and DNA sensing pathways.

a, Gene set enrichment analysis comparing RNA-seq data from $Kdm5b^{-/-}$ ($Kdm5b$ sg) YUMMER1.7 cells with control YUMMER1.7 cells. Shown are selected top upregulated pathways (FDR ≤ 0.05). **b**, Western blot analyses of DNA and RNA sensors, as well as signalling proteins involved in the type I IFN pathway. T-, total; p-, phosphorylated. For gel source data, see Supplementary Fig. 1. **c**, RT-qPCR analyses of ISGs in $Ifigr1^{-/-}$ YUMMER1.7 mouse melanoma cells with Ctl sg, $Kdm5b$ sg1 and $Kdm5b$ sg2. **d**, RT-qPCR analyses of ISGs (left) and western blot analyses (right) of YUMM1.7 mouse melanoma cells with Ctl sg and $Kdm5b$ sg. For gel source data, see Supplementary Fig. 1. **e**, RT-qPCR analyses of ISGs in 1445 mouse melanoma cells with Ctl shRNA and $Kdm5b$ shRNA. **f**, Western blot analyses of the indicated cell lines used in Figure 2b and Extended Data Fig. 2g. For gel source data, see Supplementary Fig. 1. **g**, RT-qPCR analyses of selected ISGs in the indicated YUMMER1.7 cells treated with 10 ng/ml IFN γ for 24h. Data are mean \pm SD. **h**, Western blot analyses of the indicated cell lines, used in Figure 2c. For gel source data, see Supplementary Fig. 1. **i**, RT-qPCR analyses (left) and western blot analyses (right) of YUMM1.7- $Kdm5b$ sg cells with Ctl sg, *Sting1* sg, *Ddx58* (RIG-I gene) sg, *Mda5* sg, *Mavs* sg, or *Cgas* sg. For gel source data, see Supplementary Fig. 1. **j**, RT-qPCR analyses of IRF9 in 1445- $Kdm5b$ sg cells with Ctl sg, *Sting1* sg, *Ddx58* sg, *Mda5* sg, *Mavs* sg, or *Cgas* sg. **k**, RT-qPCR analyses of ISGs from YUMM1.7- $Kdm5b$ sg cells treated with Ctl

siRNA, *Sting1* siRNA or *Mavs* siRNA for 3 days. **1**, RT-qPCR analyses of ISGs from 1445 cells with Ctl shRNA treated with Ctl siRNA, 1445 cells with *Kdm5b* shRNA treated with Ctl siRNA, *Sting1* siRNA, or *Mavs* siRNA cells for 3 days. Data are means \pm SEM. **m**, Tumor growth curve (left) and survival curve (right) of C57BL/6 mice injected with YUMMER1.7 cells of the indicated genotypes, WT ($n=5$), *Kdm5b*^{-/-}-*Mda5*^{-/-} *Cgas*^{-/-}-C1 ($n=4$), *Kdm5b*^{-/-}-*Mda5*^{-/-} *Cgas*^{-/-}-C3 ($n=4$), *Kdm5b*^{-/-} ($n=5$). C1 and C3 are clone numbers. Data represent one experiment. Data are mean \pm SEM. 2-way ANOVA analysis for comparison at day 20. n.s., not significant; *** $p<0.0001$. Log-rank test for survival curves. ** $p=0.004$ for C1 vs *Kdm5b*^{-/-}; ** $p=0.005$ for C3 vs *Kdm5b*^{-/-}; * $p=0.023$ for C3 vs WT. Unpaired two-sided Students' *t* tests were performed for all RT-qPCR data (**c-e,g, i-l**). n.s., not significant; * $p<0.05$; ** $p<0.01$; *** $p<0.001$; *** $p<0.0001$.

Source data

Extended Data Fig. 3 Deletion of KDM5B in mouse melanoma cells increases MHC-I expression, and induces expression of genes involved in antigen processing/presentation and endogenous retroelements.

a-c, Flow cytometry analysis for MHC-I levels (left) and RT-qPCR analyses of MHC-I genes and genes involved in antigen processing and presentation (right) in YUMMER1.7 cells with Ctl sg, *Kdm5b* sg1 or sg2 (**a**), YUMM1.7 cells with Ctl sg, *Kdm5b* sg1 or sg2 (**b**), and YUMM3.3 cells with Ctl shRNA or *Kdm5b* shRNA (**c**). Data are mean \pm SEM. **d,e**, RT-qPCR analyses of retroelements in YUMM1.7 cells (**d**) and 1445 cells (**e**) with Ctl shRNA or *Kdm5b* shRNA. Data are mean \pm SEM. Statistical analysis was done with unpaired two-sided Student's *t* test. * $p<0.05$, ** $p<0.01$, *** $p<0.001$ and *** $p<0.0001$.

Extended Data Fig. 4 Deletion of KDM5B induces endogenous retroelement expression and forms dsRNA.

a,b, Immunofluorescence staining of dsRNA with J2 antibody (red) and DAPI (blue) in WT or *Kdm5b*^{-/-} YUMMER1.7 cells, using a confocal microscope (**a**) (scale bar = 50 µm) and 1445 cells with Ctl shRNA or *Kdm5b* shRNA (**b**) (scale bar = 50 µm). **c**, Immunofluorescence staining of dsRNA with J2 antibody (red) and DAPI (blue) of WT or *Kdm5b* sg YUMMER1.7 tumors harvested 14 days after tumor injection (scale bar = 100 µm). **d**, Immunofluorescence staining (left) and quantification (right) of dsRNA with J2 antibody (red) and DAPI (blue) of representative patients as responder or non-responder to ICB (scale bar = 100 µm). MGLI= mean grey level intensity. **e**, Volcano plots comparing inverted repeats in YUMMER1.7 cells with *Kdm5b* sg vs YUMMER1.7 cells with Ctl sg. **f**, Western blot analyses of *Kdm5b* sg YUMMER1.7 cells treated with 20 µM of reverse transcriptase inhibitors (RTi) for 48h. For gel source data, see Supplementary Fig. 1. **g**, qPCR analyses of retroelements from DNA isolated from cytosolic (cyto) lysate versus from nuclear lysate. Data are mean ± SD. **h**, Relative copy number of mitochondrial (mito) DNA quantified by qPCR analyses with Dloop primers. Data are mean ± SD. **i**, RT-qPCR analyses of *MMVL30-int*, *RLTR6_Mm* and *Isg15* in *Kdm5b*^{-/-} cells with the indicated doxycycline (Dox) inducible shRNAs. Data are mean ± SEM. p values for **g-i** were calculated using unpaired two-sided Students' *t* tests. n.s., not significant; ***p*<0.01; ****p*<0.001; *****p*<0.0001.

Extended Data Fig. 5 KDM5B represses retroelement expression in a demethylase-independent manner.

a,b, ChIP–qPCR analyses of WT and *Kdm5b*^{-/-} (KO) YUMMER1.7 cells. Data are mean± SEM. **c,d**, Western blot (**c**) and RT-qPCR analyses of retroelements and ISGs (**d**) in YUMMER1.7 treated with 1 µM, 3 µM and 5 µM of KDM5i (CPI-48 and KDM5-C70) for 7 days. For gel source data, see Supplementary Fig. 1. **e**, RT-qPCR analyses of retroelements and ISGs (left) and western blot analyses (right) of YUMMER1.7 cells treated with DMSO or EZH2 inhibitors (5 µM EPZ6438, 5 µM GSK343) for 10 days. For gel source data, see Supplementary Fig. 1. **f**, RT-qPCR analyses (left) and western blot analyses (right) of YUMMER1.7 cells treated with DMSO or chaetocin (10, 20, and 30 nM), an inhibitor of H3K9me3 methyltransferases, for 3 days. **g,h**, ChIP–qPCR analyses of WT and

Kdm5b^{-/-} (KO) YUMMER1.7 cells. **i,j**, RT-qPCR analyses (**i**) and western blot analyses (**j**) of YUMMER1.7 cells with Ctl sg, *G9a* sg (1-3) or *Suv39h1* sg (1-3). For gel source data, see Supplementary Fig. [1](#). **k**, RT-qPCR analyses of *MMVL30* in YUMMER1.7 cells with Ctl sg, *G9a* sg (1-3), *Suv39h1* sg (1-3), and *Setdb1* sg (1-3). **l**, Western blot analyses of YUMMER1.7 cells with Ctl sg or *Setdb1* sg (1-3). For gel source data, see Supplementary Fig. [1](#). **m**, ChIP-qPCR analyses of WT YUMMER1.7 cells with GFP, *Kdm5b*^{-/-} YUMMER1.7 cells, with GFP control, or reconstituted expression of WT-KDM5B or catalytically inactive mutant (MT) KDM5B. For **a,b, d-h, i,k,m**, data are means ± SEM. Statistical analysis was done with unpaired two-sided Student's t test. n.s. not significant, **p*<0.05, ***p*<0.01, ****p*<0.001 and *****p*<0.0001.

Extended Data Fig. 6 KDM5B directly binds to the retroelements induced by *Kdm5b* loss.

a, Genomic annotations of *Kdm5b* binding peaks from KDM5B ChIP-seq in YUMMER1.7 cells. **b**, Heatmaps of input-subtracted KDM5B, SETDB1 and H3K9me3 ChIP-seq signal averaged across all loci per retroelement in YUMMER1.7 cells, sorted by KDM5B binding intensity. Top 10 significantly increased retroelements plus “*MMERVK10C-int*, *RLTR6-int*, and *RLTR6B_Mm*“ are labeled. **c**, Violin plots of RNA-seq analysis showing differential expressed endogenous retroelements categorized in classes (three classes of ERVs, LINEs and SINEs) in 1445 mouse melanoma cells with *Kdm5b* sg vs. Ctl sg. **d**, Input-subtracted KDM5B ChIP-seq signal averaged across all loci per retroelement in 1445 cells. KDM5B signal on retroelements were sorted by intensity. Top 10 significantly increased retroelements are labeled. **e**, Venn diagram showing overlapping ChIP-seq binding regions shared between KDM5B and SETDB1. KDM5B only peaks, n = 25,315; Shared peaks, n = 66,503; SETDB1 only peaks, n = 16,934. **f**, Box plot showing RNA-seq log₂ Fold Change (FC) of (*Kdm5b*^{-/-} vs WT) for four different categories of TE located within overlapping regions between KDM5B and SETDB1. **g**, Venn diagram showing overlapping ChIP-seq binding regions shared among KDM5B, SETDB1 and H3K9me3. **h,i**, Western blot analyses of KDM5B (**h**) or SETDB1 (**i**) immunoprecipitates from nuclear extracts of 1445

mouse melanoma cells, MC38 mouse colon cancer cells or YUMM1.7 mouse melanoma cells. For gel source data, see Supplementary Fig. 1.

Extended Data Fig. 7 ChIP-seq and ATAC-seq analyses of epigenomic changes induced by *Kdm5b* loss.

a. Aggregated RNA-seq, KDM5B, SETDB1, H3K9me3, H3K4me3 and H3K4me2 ChIP-seq signals of *MMVL30-int* loci in WT and *Kdm5b*^{-/-} (KO) YUMMER1.7 cells. **b-c.** IGV (Integrative Genomic Viewer) screenshots of KDM5B, SETDB1, H3K9me3, H3K4me3, and H3K4me2 ChIP-seq signals from WT and *Kdm5b*^{-/-} YUMMER1.7 cells. **d.** Volcano plot showing ATAC-seq signals from WT and *Kdm5b*^{-/-} YUMMER1.7 cells; Peaks enriched significantly in *Kdm5b*^{-/-} cells are in red and enriched significantly in WT cells are in blue (FDR < 0.05). Significant changed *MMVL30-int* loci are marked in black. **e.** Box plot showing ATAC-seq log₂ Fold Change of (*Kdm5b*^{-/-} vs WT YUMMER1.7) for four different categories of TE. **f.** Pie charts showing proportion of increased or unchanged ATAC peaks within KDM5B domains in *Kdm5b*^{-/-} vs WT YUMMER1.7 cells. **g.** Comparison of ATAC-seq signals among baseline or IFNγ treated *Kdm5b*^{-/-} (KO) and WT YUMMER1.7 cells. **h-l.** Motif sequences (left) and top 5 best matched transcription factor (TF) with corresponding p value (right) from *de novo* motif analysis of KDM5B binding regions (**h**), increased ATAC seq peaks in *Kdm5b*^{-/-} (KO) compared to WT YUMMER1.7 cells (**i**), increased ATAC seq peaks in IFNγ treated *Kdm5b*^{-/-} compared to WT YUMMER1.7 cells (**j**), retroelements within KDM5B binding regions, with increased ATAC seq peaks in *Kdm5b*^{-/-} cells compared to WT YUMMER1.7 cells (**k**), and retroelements within KDM5B binding regions, with increased ATAC seq peaks in IFNγ treated *Kdm5b*^{-/-} (KO) YUMMER1.7 compared to IFNγ treated WT YUMMER1.7 cells (**l**).

Extended Data Fig. 8 KDM5B regulates SETDB1 protein stability and is required for the recruitment of SETDB1 to retroelements, some of which encode potential antigens.

a, Western blot analyses of SETDB1 in cytosolic and nuclear extracts from *Kdm5b*^{-/-} YUMMER1.7 cells treated with DMSO, 5 μM or 10 μM proteasome inhibitor MG132 for 21 h. For gel source data, see Supplementary Fig. 1. **b**, Western blot analyses of YUMMER1.7 cells with GFP, *Kdm5b*^{-/-} YUMMER1.7 cells with GFP, WT SETDB1, or MT SETDB1. For gel source data, see Supplementary Fig. 1. **c**, RT-qPCR analyses of retroelements and ISGs in *Kdm5b*^{-/-} YUMMER1.7 cells with GFP, WT SETDB1, or MT SETDB1, in the absence or presence of 100 nM IFN γ for 24 h. **d**, H3K9me3 ChIP–qPCR analyses of *Kdm5b*^{-/-} YUMMER1.7 cells with GFP, SETDB1, WT KDM5B or MT KDM5B. **e-d**, Data are means ± SEM. Statistical analysis was done with unpaired two-sided Student's *t* test. P values for **c** are from comparison to the GFP control with the same IFN γ treatment status. n.s. not significant; * $p<0.05$; ** $p<0.01$; *** $p<0.001$ and **** $p<0.0001$. **e,f**, Kaplan–Meier survival curves (**e**) and spider plots of tumor growth (**f**) of C57BL/6 mice injected with *Kdm5b*^{-/-} YUMMER1.7 cells with GFP ($n=6$) or SETDB1 ($n=6$). *P* values were determined using the log-rank test, n.s. not significant. **g**, Flow cytometry analysis for MuLV envelope protein (Env) in YUMMER1.7 cells with Ctl sg or *Kdm5b* sg. **h**, Quantification of flow cytometry analysis for P15E⁺CD8⁺ T cells in YUMMER1.7 tumors with Ctl sg ($n=3$) or *Kdm5b* sg ($n=7$). Data are means ± SEM. Statistical analysis was done with unpaired two-sided Student's *t* test. n.s. not significant. **i**, Quantification showing the percentage of retroelement encoded peptides that were exchanged onto H2-K^b in vitro.

Source data

Extended Data Fig. 9 Knockdown of KDM5B in human melanoma cells induces ISGs and ERVs through RIG-I and MAVS.

a,b, RT-qPCR analyses of ERVs and ISGs in YURIF (**a**) or YUDOSO (**b**) with Ctl or KDM5B shRNA. **c**, RT-qPCR analyses of ISGs (left) and western blot analyses of DNA and RNA sensors and the type I IFN pathway (right) in YUDOSO human melanoma cells with KDM5B shRNA and Ctl sg, *TLR3* sg, *RIG-I (DDX58)* sg, *MDA5* sg, *CGAS* sg, *MAVS* sg, or *STING1*

sg. For gel source data, see Supplementary Fig. 1. Data are means \pm SEM. Statistical analysis was done with unpaired two-sided Student's t test. ** $p<0.01$, *** $p<0.001$ and **** $p<0.0001$.

Extended Data Fig. 10 Correlation analysis of human ERVs with KDM5B expression and selected epigenetic regulators with patient response to anti-PD-1 treatment, and the working model summarizing the mechanistic findings.

a, Heatmap showing highly differential expressed human ERVs in patient biopsies prior to anti-PD-1 treatment. Samples were ranked by *KDM5B* expression, with patient responses to anti-PD-1 treatment annotated (PD, progressive disease; PR, partial response; CR, complete response). **b**, *ERVmap_2637* expression is inversely correlated with *KDM5B* expression in patient cohort described in panel **a**. Gray zone represents 95% confidence interval for the linear model prediction. **c-k**, Box plot showing expression of *ERVmap_2637* (**c**), *KDM5A* (**d**), *KDM5C* (**e**), *KDM5D* (**f**), *EZH2* (**g**), *KDM1A* (**h**), *DNMT1* (**i**), *DNMT3B* (**j**) and *SETDB1* (**k**) in patient cohort described in panel **a**. Statistical analysis was done with unpaired two-sided Student's t test. **l**, The working model showing that KDM5B suppresses anti-tumor responses by recruiting SETDB1 to inhibit endogenous retroelements and type I interferon response. This panel is created with BioRender.com.

Supplementary information

Supplementary Figs. 1 and 2

Supplementary Fig. 1 shows gel source data. Supplementary Fig. 2 shows the gating strategies used.

Reporting Summary

Peer Review File

Supplementary Tables 1–18

Source data

[Source Data Fig. 1](#)

[Source Data Fig. 2](#)

[Source Data Fig. 4](#)

[Source Data Extended Data Fig. 1](#)

[Source Data Extended Data Fig. 2](#)

[Source Data Extended Data Fig. 8](#)

Rights and permissions

[Reprints and Permissions](#)

About this article

Cite this article

Zhang, SM., Cai, W.L., Liu, X. *et al.* KDM5B promotes immune evasion by recruiting SETDB1 to silence retroelements. *Nature* **598**, 682–687 (2021).
<https://doi.org/10.1038/s41586-021-03994-2>

- Received: 04 October 2020
- Accepted: 03 September 2021
- Published: 20 October 2021
- Issue Date: 28 October 2021

- DOI: <https://doi.org/10.1038/s41586-021-03994-2>

Share this article

Anyone you share the following link with will be able to read this content:

[Get shareable link](#)

Sorry, a shareable link is not currently available for this article.

[Copy to clipboard](#)

Provided by the Springer Nature SharedIt content-sharing initiative

This article was downloaded by **calibre** from <https://www.nature.com/articles/s41586-021-03994-2>

| [Section menu](#) | [Main menu](#) |

- Article
- [Published: 22 September 2021](#)

Structures of full-length glycoprotein hormone receptor signalling complexes

- [Jia Duan](#)^{1,2 na1},
- [Peiyu Xu](#) [ORCID: orcid.org/0000-0003-3590-4037](#)^{1,2 na1},
- [Xi Cheng](#) [ORCID: orcid.org/0000-0003-3735-645X](#)^{1 na1},
- [Chunyou Mao](#) [ORCID: orcid.org/0000-0001-5349-8592](#)^{3,4,5,6 na1 nAff12},
- [Tristan Croll](#)⁷,
- [Xinheng He](#) [ORCID: orcid.org/0000-0001-7813-5480](#)^{1,2},
- [Jingjing Shi](#)¹,
- [Xiaodong Luan](#) [ORCID: orcid.org/0000-0002-1279-5432](#)^{8,9,10},
- [Wanchao Yin](#) [ORCID: orcid.org/0000-0002-6889-4907](#)¹,
- [Erli You](#)¹,
- [Qiufeng Liu](#)¹,
- [Shuyang Zhang](#) [ORCID: orcid.org/0000-0002-1532-0029](#)^{8,9,10},
- [Hualiang Jiang](#) [ORCID: orcid.org/0000-0003-0656-6315](#)^{1,2,11},
- [Yan Zhang](#) [ORCID: orcid.org/0000-0003-2189-0244](#)^{3,4,5,6},
- [Yi Jiang](#) [ORCID: orcid.org/0000-0002-0723-1413](#)^{1,2} &
- [H. Eric Xu](#) [ORCID: orcid.org/0000-0002-6829-8144](#)^{1,2,11}

Nature volume **598**, pages 688–692 (2021)

- 4468 Accesses
- 34 Altmetric

- [Metrics details](#)

Subjects

- [Cryoelectron microscopy](#)
- [Hormones](#)

Abstract

Luteinizing hormone and chorionic gonadotropin are glycoprotein hormones that are related to follicle-stimulating hormone and thyroid-stimulating hormone^{1,2}. Luteinizing hormone and chorionic gonadotropin are essential to human reproduction and are important therapeutic drugs^{3,4,5,6}. They activate the same G-protein-coupled receptor, luteinizing hormone–choriogonadotropin receptor (LHCGR), by binding to the large extracellular domain³. Here we report four cryo-electron microscopy structures of LHCGR: two structures of the wild-type receptor in the inactive and active states; and two structures of the constitutively active mutated receptor. The active structures are bound to chorionic gonadotropin and the stimulatory G protein (G_s), and one of the structures also contains Org43553, an allosteric agonist⁷. The structures reveal a distinct ‘push-and-pull’ mechanism of receptor activation, in which the extracellular domain is pushed by the bound hormone and pulled by the extended hinge loop next to the transmembrane domain. A highly conserved 10-residue fragment (P10) from the hinge C-terminal loop at the interface between the extracellular domain and the transmembrane domain functions as a tethered agonist to induce conformational changes in the transmembrane domain and G-protein coupling. Org43553 binds to a pocket of the transmembrane domain and interacts directly with P10, which further stabilizes the active conformation. Together, these structures provide a common model for understanding the signalling of glycoprotein hormone receptors and a basis for drug discovery for endocrine diseases.

Access options

[Subscribe to Journal](#)

Get full journal access for 1 year

\$199.00

only \$3.90 per issue

[Subscribe](#)

All prices are NET prices.

VAT will be added later in the checkout.

Tax calculation will be finalised during checkout.

Rent or Buy article

Get time limited or full article access on ReadCube.

from \$8.99

[Rent or Buy](#)

All prices are NET prices.

Additional access options:

- [Log in](#)
- [Access through your institution](#)
- [Learn about institutional subscriptions](#)

Fig. 1: Cryo-EM structure of the CG–LHCGR–G_s complexes.

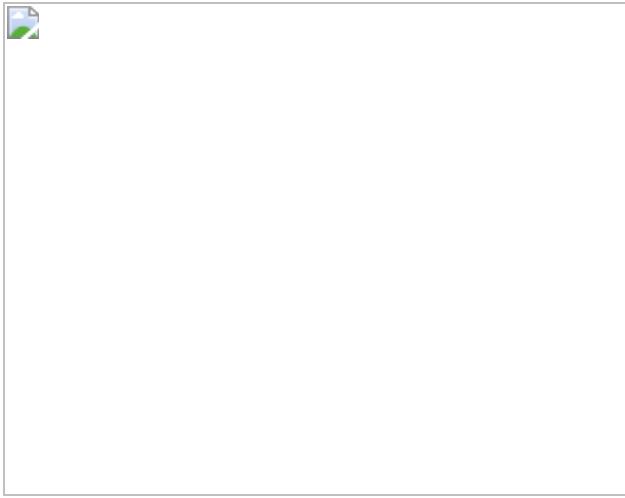


Fig. 2: Interactions between CG and LHCGR.



Fig. 3: Basis for hormone-induced receptor activation.

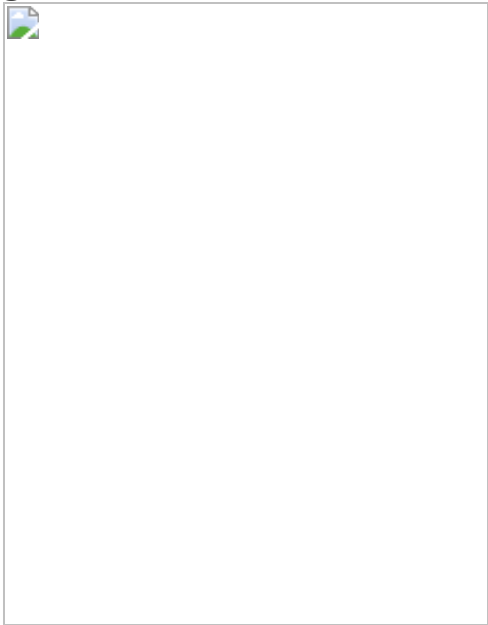


Fig. 4: Interactions between the LHCGR ECD and TMD.

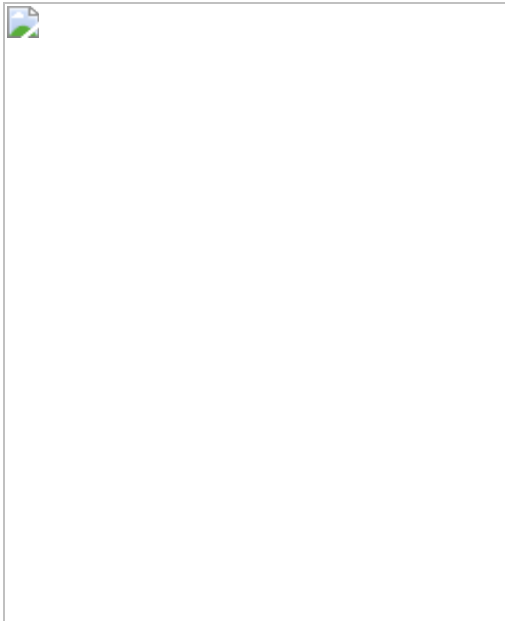
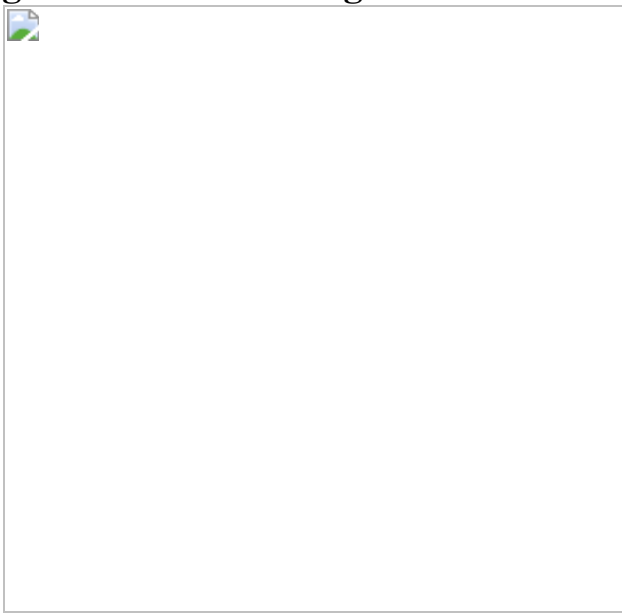


Fig. 5: Basis for the regulation of LHCGR by Org43553.



Data availability

The density maps and structure coordinates have been deposited in the Electron Microscopy Database (EMDB) and the PDB with accession numbers as follows: [EMD-31596](#), PDB [7FIG](#) for the CG–LHCGR(S277I)–G_s complex; [EMD-31597](#) and [7FIH](#) for the CG–Org43553–LHCGR(S277I)–G_s complex; [EMD-31598](#) and [7FII](#) for the CG–

LHCGR(WT)–G_s complex; and [EMD-31599](#) and [7FIJ](#) for the LHCGR (inactive) structure.

References

1. 1.
Pierce, J. G. & Parsons, T. F. Glycoprotein hormones: structure and function. *Annu. Rev. Biochem.* **50**, 465–495 (1981).
2. 2.
Fan, Q. R. & Hendrickson, W. A. Structural biology of glycoprotein hormones and their receptors. *Endocrine* **26**, 179–188 (2005).
3. 3.
Casarini, L., Santi, D., Brigante, G. & Simoni, M. Two hormones for one receptor: evolution, biochemistry, actions, and pathophysiology of LH and hCG. *Endocr. Rev.* **39**, 549–592 (2018).
4. 4.
Jiang, X., Dias, J. A. & He, X. Structural biology of glycoprotein hormones and their receptors: insights to signaling. *Mol. Cell. Endocrinol.* **382**, 424–451 (2014).
5. 5.
Themmen, A. P. N. & Huhtaniemi, I. T. Mutations of gonadotropins and gonadotropin receptors: elucidating the physiology and pathophysiology of pituitary–gonadal function. *Endocr. Rev.* **21**, 551–583 (2000).
6. 6.
Troppmann, B., Kleinau, G., Krause, G. & Gromoll, J. Structural and functional plasticity of the luteinizing hormone/choriogonadotrophin

receptor. *Hum. Reprod. Update* **19**, 583–602 (2013).

7. 7.

van Koppen, C. J. et al. A signaling-selective, nanomolar potent allosteric low molecular weight agonist for the human luteinizing hormone receptor. *Naunyn Schmiedebergs Arch. Pharmacol.* **378**, 503–514 (2008).

8. 8.

Nakabayashi, K., Kudo, M., Kobilka, B. & Hsueh, A. J. Activation of the luteinizing hormone receptor following substitution of Ser-277 with selective hydrophobic residues in the ectodomain hinge region. *J. Biol. Chem.* **275**, 30264–30271 (2000).

9. 9.

Jiang, X. et al. Structure of follicle-stimulating hormone in complex with the entire ectodomain of its receptor. *Proc. Natl Acad. Sci. USA* **109**, 12491–12496 (2012).

10. 10.

Wu, H., Lustbader, J. W., Liu, Y., Canfield, R. E. & Hendrickson, W. A. Structure of human chorionic gonadotropin at 2.6 Å resolution from MAD analysis of the selenomethionyl protein. *Structure* **15**, 545–558 (1994).

11. 11.

Fan, Q. R. & Hendrickson, W. A. Structure of human follicle-stimulating hormone in complex with its receptor. *Nature* **433**, 269–277 (2005).

12. 12.

Okada, T. et al. Functional role of internal water molecules in rhodopsin revealed by X-ray crystallography. *Proc. Natl Acad. Sci.*

USA **99**, 5982–5987 (2002).

13. 13.

Staus, D. P. et al. Allosteric nanobodies reveal the dynamic range and diverse mechanisms of G-protein-coupled receptor activation. *Nature* **535**, 448–452 (2016).

14. 14.

Ballesteros, J. A. & Weinstein, H. in *Receptor Molecular Biology* Vol. 25 (ed. Sealfon, S. C.) 366–428 (Elsevier, 1995).

15. 15.

Costagliola, S. et al. Tyrosine sulfation is required for agonist recognition by glycoprotein hormone receptors. *EMBO J.* **21**, 504–513 (2002).

16. 16.

Bruser, A. et al. The activation mechanism of glycoprotein hormone receptors with implications in the cause and therapy of endocrine diseases. *J. Biol. Chem.* **291**, 508–520 (2016).

17. 17.

Schulze, A. et al. The intramolecular agonist is obligate for activation of glycoprotein hormone receptors. *FASEB J.* **34**, 11243–11256 (2020).

18. 18.

Jiang, X. et al. Evidence for follicle-stimulating hormone receptor as a functional trimer. *J. Biol. Chem.* **289**, 14273–14282 (2014).

19. 19.

Carpenter, B., Nehme, R., Warne, T., Leslie, A. G. & Tate, C. G. Structure of the adenosine A_{2A} receptor bound to an engineered G

protein. *Nature* **536**, 104–107 (2016).

20. 20.

Maeda, S., Qu, Q., Robertson, M. J., Skiniotis, G. & Kobilka, B. K. Structures of the M1 and M2 muscarinic acetylcholine receptor/G-protein complexes. *Science* **364**, 552–557 (2019).

21. 21.

Kang, Y. et al. Cryo-EM structure of human rhodopsin bound to an inhibitory G protein. *Nature* **558**, 553–558 (2018).

22. 22.

Liang, Y. L. et al. Dominant negative G proteins enhance formation and purification of agonist–GPCR–G protein complexes for structure determination. *ACS Pharmacol. Transl. Sci.* **1**, 12–20 (2018).

23. 23.

Rasmussen, S. G. et al. Crystal structure of the β_2 adrenergic receptor–G_s protein complex. *Nature* **477**, 549–555 (2011).

24. 24.

Wortmann, L. et al. Discovery of BAY-298 and BAY-899: tetrahydro-1,6-naphthyridine-based, potent, and selective antagonists of the luteinizing hormone receptor which reduce sex hormone levels in vivo. *J. Med. Chem.* **62**, 10321–10341 (2019).

25. 25.

Mastronarde, D. N. Automated electron microscope tomography using robust prediction of specimen movements. *J. Struct. Biol.* **152**, 36–51 (2005).

26. 26.

Zheng, S. Q. et al. MotionCor2: anisotropic correction of beam-induced motion for improved cryo-electron microscopy. *Nat. Methods* **14**, 331–332 (2017).

27. 27.

Zhang, K. Gctf: real-time CTF determination and correction. *J. Struct. Biol.* **193**, 1–12 (2016).

28. 28.

Scheres, S. H. RELION: implementation of a Bayesian approach to cryo-EM structure determination. *J. Struct. Biol.* **180**, 519–530 (2012).

29. 29.

Kucukelbir, A., Sigworth, F. J. & Tagare, H. D. Quantifying the local resolution of cryo-EM density maps. *Nat. Methods* **11**, 63–65 (2014).

30. 30.

Punjani, A., Rubinstein, J. L., Fleet, D. J. & Brubaker, M. A. cryoSPARC: algorithms for rapid unsupervised cryo-EM structure determination. *Nat. Methods* **14**, 290–296 (2017).

31. 31.

Pettersen, E. F. et al. UCSF Chimera—a visualization system for exploratory research and analysis. *J. Comput. Chem.* **25**, 1605–1612 (2004).

32. 32.

Grant, T., Rohou, A. & Grigorieff, N. *cisTEM*, user-friendly software for single-particle image processing. *Elife* **7**, e35383 (2018).

33. 33.

Emsley, P. & Cowtan, K. Coot: model-building tools for molecular graphics. *Acta Crystallogr. D* **60**, 2126–2132 (2004).

34. 34.

Croll, T. I. ISOLDE: a physically realistic environment for model building into low-resolution electron-density maps. *Acta Crystallogr. D* **74**, 519–530 (2018).

35. 35.

Adams, P. D. et al. PHENIX: a comprehensive Python-based system for macromolecular structure solution. *Acta Crystallogr. D* **66**, 213–221 (2010).

36. 36.

Chen, V. B. et al. MolProbity: all-atom structure validation for macromolecular crystallography. *Acta Crystallogr. D* **66**, 12–21 (2010).

37. 37.

Pettersen, E. F. et al. UCSF ChimeraX: structure visualization for researchers, educators, and developers. *Protein Sci.* **30**, 70–82 (2021).

38. 38.

Wang, R. Y. et al. Automated structure refinement of macromolecular assemblies from cryo-EM maps using Rosetta. *Elife* **5**, e17219 (2016).

39. 39.

Sali, A. & Blundell, T. L. Comparative protein modelling by satisfaction of spatial restraints. *J. Mol. Biol.* **234**, 779–815 (1993).

40. 40.

Wu, E. L. et al. CHARMM-GUI Membrane Builder toward realistic biological membrane simulations. *J. Comput. Chem.* **35**, 1997–2004 (2014).

41. 41.

Lee, J. et al. CHARMM-GUI input generator for NAMD, GROMACS, AMBER, OpenMM, and CHARMM/OpenMM simulations using the CHARMM36 additive force field. *J. Chem. Theory Comput.* **12**, 405–413 (2016).

42. 42.

Jorgensen, W. L., Chandrasekhar, J., Madura, J. D., Impey, R. W. & Klein, M. L. Comparison of simple potential functions for simulating liquid water. *J. Chem. Phys.* **79**, 926–935 (1983).

43. 43.

Guvench, O. et al. CHARMM additive all-atom force field for carbohydrate derivatives and its utility in polysaccharide and carbohydrate-protein modeling. *J. Chem. Theory Comput.* **7**, 3162–3180 (2011).

44. 44.

MacKerell, A. D. et al. All-atom empirical potential for molecular modeling and dynamics studies of proteins. *J. Phys. Chem. B* **102**, 3586–3616 (1998).

45. 45.

Abraham, M. J. et al. GROMACS: high performance molecular simulations through multi-level parallelism from laptops to supercomputers. *SoftwareX* **1-2**, 19–25 (2015).

46. 46.

Páll, S., Abraham, M. J., Kutzner, C., Hess, B. & Lindahl, E. in *Solving Software Challenges for Exascale* (eds Markidis, S. & Laure, E.) 3–27 (Springer, 2015).

47. 47.

Bussi, G., Donadio, D. & Parrinello, M. Canonical sampling through velocity rescaling. *J. Chem. Phys.* **126**, 014101 (2007).

48. 48.

Aoki, K. M. & Yonezawa, F. Constant-pressure molecular-dynamics simulations of the crystal-smectic transition in systems of soft parallel spherocylinders. *Phys. Rev. A* **46**, 6541–6549 (1992).

49. 49.

Hess, B. P-LINCS: a parallel linear constraint solver for molecular simulation. *J. Chem. Theory Comput.* **4**, 116–122 (2008).

50. 50.

Darden, T., York, D. & Pedersen, L. Particle mesh Ewald: An $N \cdot \log(N)$ method for Ewald sums in large systems. *J. Chem. Phys.* **98**, 10089–10092 (1993).

Acknowledgements

The cryo-EM data were collected at the Cryo-Electron Microscopy Research Center, Shanghai Institute of Materia Medica (SIMM) and Shuimu BioSciences. We thank the staff at the SIMM Cryo-Electron Microscopy Research Center and Shuimu BioSciences for their technical support. This work was partially supported by Ministry of Science and Technology (China) grants (2018YFA0507002 to H.E.X. and 2019YFA0508800 to Y.Z.); the Shanghai Municipal Science and Technology Major Project (2019SHZDZX02 to H.E.X.); the CAS Strategic Priority Research Program (XDB08020303 to H.E.X.); the National Natural Science Foundation of China (31770796 to Y.J. and 81922071 to Y.Z.); the

National Science and Technology Major Project ‘Key New Drug Creation and Manufacturing Program’ (2018ZX09711002 to Y.J. and H.J.); Wellcome Trust grant 209407/Z/17/Z; the National Key R&D Program of China (2020YFC0861000 to S.Z.); the CAMS Innovation Fund for Medical Sciences (2020-I2M-CoV19-001 to S.Z.); the Tsinghua University–Peking University Center for Life Sciences (045-160321001 to S.Z.); the Science and Technology Commission of Shanghai Municipal (20431900100 to H.J.); the Jack Ma Foundation (2020-CMKYGG-05 to H.J.); Shanghai Sailing Program (19YF1457600 to Q.L.); the Zhejiang Province Science Fund for Distinguished Young Scholars (LR19H310001 to Y.Z.); the MOE Frontier Science Center for Brain Science & Brain-Machine Integration, Zhejiang University (to Y.Z.); and The Youth Innovation Promotion Association of Chinese Academy of Science (2018319 to X.C.).

Author information

Author notes

1. Chunyou Mao

Present address: Department of General Surgery, Sir Run Run Shaw Hospital, Zhejiang University School of Medicine, Hangzhou, China

2. These authors contributed equally: Jia Duan, Peiyu Xu, Xi Cheng, Chunyou Mao

Affiliations

1. The CAS Key Laboratory of Receptor Research and State Key Laboratory of Drug Research, Shanghai Institute of Materia Medica, Chinese Academy of Sciences, Shanghai, China

Jia Duan, Peiyu Xu, Xi Cheng, Xinheng He, Jingjing Shi, Wanchao Yin, Erli You, Qiu Feng Liu, Hualiang Jiang, Yi Jiang & H. Eric Xu

2. University of Chinese Academy of Sciences, Beijing, China

Jia Duan, Peiyu Xu, Xinheng He, Hualiang Jiang, Yi Jiang & H. Eric Xu

3. Department of Biophysics and Department of Pathology of Sir Run Run Shaw Hospital, Zhejiang University School of Medicine, Hangzhou, China

Chunyou Mao & Yan Zhang

4. Liangzhu Laboratory, Zhejiang University Medical Center, Hangzhou, China

Chunyou Mao & Yan Zhang

5. MOE Frontier Science Center for Brain Research and Brain-Machine Integration, Zhejiang University School of Medicine, Hangzhou, China

Chunyou Mao & Yan Zhang

6. Zhejiang Provincial Key Laboratory of Immunity and Inflammatory Diseases, Hangzhou, China

Chunyou Mao & Yan Zhang

7. Cambridge Institute for Medical Research, Department of Haematology, University of Cambridge, Cambridge, UK

Tristan Croll

8. School of Medicine, Tsinghua University, Beijing, China

Xiaodong Luan & Shuyang Zhang

9. Department of Cardiology, Peking Union Medical College Hospital, Peking Union Medical College and Chinese Academy of Medical Sciences, Beijing, China

Xiaodong Luan & Shuyang Zhang

10. Tsinghua–Peking Center for Life Sciences, Tsinghua University,
Beijing, China

Xiaodong Luan & Shuyang Zhang

11. School of Life Science and Technology, ShanghaiTech University,
Shanghai, China

Hualiang Jiang & H. Eric Xu

Contributions

J.D. designed the expression constructs, purified the LHCGR proteins, prepared the final samples for negative-stain microscopy and data collection towards the structures, conducted functional studies and participated in figure and manuscript preparation. P.X. performed cryo-EM grid preparation, cryo-EM data collection, map calculations and model building and participated in figure preparation. X.C. and X.H. analysed the molecular dynamics simulations and participated in figure preparation. C.M. processed the datasets of Org43553-bound LHCGR and inactive LHCGR and built the model for the inactive structure. T.C. helped to build and refine the structure model. J.S. and E.Y. synthesized Org43553 and compound 26. W.Y. designed G-protein constructs. X.L and S.Z. coordinated electron microscopy data collection. Q.L. performed detergent and lipid screen experiments. H.J. supervised and coordinated molecular dynamics experiments. Y.Z. supervised C.M. in data processing and figure preparation. Y.J. supervised the studies, performed the structural analysis and participated in manuscript preparation. H.E.X. conceived and supervised the project, analysed the structures and wrote the manuscript with input from all authors.

Corresponding authors

Correspondence to Yan Zhang, Yi Jiang or H. Eric Xu.

Ethics declarations

Competing interests

The authors declare no competing interests.

Additional information

Peer review information *Nature* thanks Torsten Schöneberg and the other, anonymous, reviewer(s) for their contribution to the peer review of this work. Peer reviewer reports are available.

Publisher's note Springer Nature remains neutral with regard to jurisdictional claims in published maps and institutional affiliations.

Extended data figures and tables

[Extended Data Fig. 1 Cryo-EM images and single-particle reconstruction of the CG–LHCGR–G_s complex.](#)

a, Size-exclusion chromatography elution profile and SDS-PAGE of the CG–LHCGR–G_s complex. Red star indicates the monomer peak of the complex. For gel source data, see Supplementary Fig. 1 (Experiments were repeated three times with similar results). **b**, Cryo-EM micrograph, reference-free 2D class averages, and flowchart of cryo-EM data analysis of the CG–LHCGR–G_s complex. **c**, Cryo-EM map of the CG–LHCGR–G_s complex coloured by local resolutions from 2.0 Å (blue) to 5.0 Å (red). The ‘gold-standard’ Fourier shell correlation (FSC) curve indicates that the overall resolution of the electron density map of the CG–LHCGR–G_s complex is 3.9 Å.

[Extended Data Fig. 2 Cryo-EM image and single-particle reconstruction of the Org43553–CG–LHCGR–G_s complex.](#)

a, Size-exclusion chromatography elution profile and SDS-PAGE of the Org43553–CG–LHCGR–G_s complex. Red star indicates the monomer peak

of the two complex. For gel source data, see Supplementary Fig. 1 (Experiments were repeated three times with similar results). **b**, Cryo-EM micrograph, reference-free 2D class averages, and flowchart of cryo-EM data analysis of the Org43553–CG–LHCGR–G_s complex. Org43553–CG–LHCGR–G_s complex coloured by local resolutions from 2.0 Å (blue) to 5.0 Å (red). The ‘gold-standard’ Fourier shell correlation (FSC) curves indicate that the overall resolution of the Org43553–CG–LHCGR–G_s complex is 3.18 Å (Focused refinement) and 3.3 Å (Global refinement), respectively. **d**, Cryo-EM density map and model of the Org43553–CG–LHCGR–G_s complex. The regions of the cryo-EM density map with all transmembrane helices, H8 and hinge C terminus are shown.

Extended Data Fig. 3 Cryo-EM images and single-particle reconstruction of the Org43553–CG–LHCGR(WT)–G_s complex and inactive LHCGR, and electron microscopy maps for the inactive LHCGR structure.

a, b, Size-exclusion chromatography elution profiles and SDS-PAGEs of the Org43553–CG–LHCGR(WT)–G_s complex (left panel) and inactive LHCGR (right panel). Red stars indicate the monomer peaks of the two proteins. For gel source data, see Supplementary Fig. 1 (Experiments were repeated three times with similar results). **c, d**, Cryo-EM micrograph, reference-free 2D class averages, and flowchart of cryo-EM data analysis of the Org43553–CG–LHCGR(WT)–G_s complex (**c**) and inactive LHCGR (**d**). **e, f**, Cryo-EM maps of the Org43553–CG–LHCGR(WT)–G_s complex (**e**) and inactive LHCGR (**f**) coloured by local resolutions from 2.0 Å (blue) to 5.0 Å (red). The “Gold-standard” Fourier shell correlation (FSC) curves indicate that the overall resolution of the electron density map of the Org43553–CG–LHCGR(WT)–G_s complex is 4.3 Å (**e**) and inactive LHCGR is 3.8 Å (**f**). **g**, Cryo-EM density map and model of the inactive LHCGR. The regions of the cryo-EM density map with all transmembrane helices and H8 are shown.

Extended Data Fig. 4 Structural features of LHCGR.

a, Ribbon presentation of CG α and CG β subunits stabilized by cysteine-knots. Disulfide bonds are shown as yellow sticks. **b**, Ribbon presentation of CG α and CG β subunits. The C terminus of the CG β subunit, known as ‘seat belt’ highlighted in red, circulates the CG α subunit. **c**, A ‘hand-clasp’ binding fashion of CG to LHCGR from different views. CG α and CG β subunits are shown in a surface presentation, and LHCGR is displayed as a ribbon. **d**, Structural comparison of free human CG (PDB code: 1HCN, green–yellow) with receptor-bound CG (light sea green), the conformational changes in four segments are highlighted in red rectangle. **e**, Structural comparison of seat belt between CG–LHCGR and FSH–FSHR (PDB code: 1XWD). The residue P107 in CG β and P101 in FSH β are shown as sticks. **f**, Conformational comparison of TM6 of inactive LHCGR with inactive rhodopsin (PDB code: 1L9H, left panel) and inactive β_2 AR (PDB code: 5JQH, right panel). **g**, Electrostatic potential surface of CG. The positively charged pockets that interact with the hinge loop are highlighted in red circles. **h**, Concentration–response curves for point mutants at S277. Data from three independent experiments are presented as the mean \pm s.e.m. **i**, The putative interaction between S277 in the hinge helix and N351 in the P10 region based on the model of the Org43553–CG–LHCGR–G_s complex.

Extended Data Fig. 5 Sequence alignment of glycoprotein hormones and related receptors.

a, Sequence alignment of human FSHR, LHR and TSHR in the region of the hormone-binding domain. Residues only interact with CG β (light sea green), CG α (pink), and both CG α and CG β subunits (light blue) are highlighted. Residues that determine LHCGR specificity were labeled with asterisks. **b**, Sequence alignment of human CG, LH, TSH and FSH β -subunit. CG β residues interacted with LHCGR are highlighted in light sea green. **c**, The α -subunit sequence of glycoprotein hormones. CG α residues interacted with LHCGR are highlighted in pink.

Extended Data Fig. 6 Molecular dynamics simulations showing hormone-induced receptor activation.

a, Representative snapshots from the CG-bound receptor simulation and inactive receptor simulation, respectively. The receptor is shown as cartoon, the CG is shown as surface, the phosphate groups of the lipid membrane are shown as spheres, three ECD residues N107, D157 and E206 are shown as sticks. **b**, Changes of ECD orientations observed in the different simulations as a function of time. Tilting angle of the ECD with respect to the z-axis (membrane normal) and the minimal distance from an ECD residue (D157, N107, or E206) to the membrane. **c**, Structural alignment of the CG–LHCGR complex onto the FSH–FSHR-ECD dimer (PDB code: 1WXD, left panel) shows that the two TMD from each complex is pointed in the opposite direction and cannot be on the same membrane layer. **d**, Structural alignment of the CG–LHCGR complex onto the FSH–FSHR-ECD trimer (PDB code: 4AY9, right panel) shows that the TMD from the CG–LHCGR complex will clash with the neighbouring ECD in the trimeric arrangement. The trimeric FSH–FSHR ECD was shown in surface presentation, with each monomeric complex in a single colour (red, yellow, green). The CG–LHCGR is shown as a ribbon and is aligned onto the yellow ECD complex but is clashed with the red ECD complex.

[Extended Data Fig. 7 The binding pocket of Org43553 in the top half of the TMD.](#)

a, Two views of the Org43553-binding pocket in the representative structures of molecular dynamics Simulation 1 and 2. Org43553 is shown as sticks, and LHCGR is depicted by surface. **b**, The interactions between I585, S604 and Org43553 in the cryo-EM structure and the representative structures of simulation 1 and simulation 2. Org43553 is shown as sticks, and LHCGR is shown as cartoon. **c**, The time-course curve of the shortest distance between the heavy atoms of I585, S604 and Org43553 during simulation 1 and 2. **d**, The distribution of the root mean square deviation (RMSD) from the cryo-EM ligand pose in simulations of Org43553-bound LHCGR system. **e**, Comparison of the Org43553-binding pocket with other agonist-binding pockets of class A GPCRs. β_2 AR (PDB code: 3SN6); β_1 AR (PDB code: 2Y03); A2aR (PDB code: 3QAK); 5HT1B (PDB code: 4IAR); Org43553, tomato; β_2 AR-agonist, yellow; β_1 AR-agonist, cyan; A2aR-agonist, lime green; 5HT1B-agonist, magenta.

Extended Data Table 1 Cryo-EM data collection, refinement and validation statistics

Extended Data Table 2 CG-induced activation of wild type LHCGR and LHCGR with site-directed mutations

Extended Data Table 3 Sequence alignment of residues from the four conserved motifs in class A GPCRs

Supplementary information

Supplementary Information

This file contains Supplementary Fig. 1, the uncropped blots and Supplementary Table 1, model building references of the LHCGR and CG models in the CG–Org43553–LHCGR(S277I)–G_s complex.

Reporting Summary

Peer Review File

Rights and permissions

Reprints and Permissions

About this article

Cite this article

Duan, J., Xu, P., Cheng, X. *et al.* Structures of full-length glycoprotein hormone receptor signalling complexes. *Nature* **598**, 688–692 (2021). <https://doi.org/10.1038/s41586-021-03924-2>

- Received: 18 November 2020
- Accepted: 18 August 2021

- Published: 22 September 2021
- Issue Date: 28 October 2021
- DOI: <https://doi.org/10.1038/s41586-021-03924-2>

Share this article

Anyone you share the following link with will be able to read this content:

[Get shareable link](#)

Sorry, a shareable link is not currently available for this article.

[Copy to clipboard](#)

Provided by the Springer Nature SharedIt content-sharing initiative

This article was downloaded by **calibre** from <https://www.nature.com/articles/s41586-021-03924-2>

| [Section menu](#) | [Main menu](#) |

Amendments & Corrections

- [**Author Correction: A molecular single-cell lung atlas of lethal COVID-19**](#) [08 October 2021]
Author Correction •
- [**Author Correction: Structural basis of ketamine action on human NMDA receptors**](#) [14 October 2021]
Author Correction •
- [**Publisher Correction: Dysregulation of brain and choroid plexus cell types in severe COVID-19**](#) [08 October 2021]
Publisher Correction •
- [**Publisher Correction: Demonstration of reduced neoclassical energy transport in Wendelstein 7-X**](#) [12 October 2021]
Publisher Correction •

- Author Correction
- [Published: 08 October 2021](#)

Author Correction: A molecular single-cell lung atlas of lethal COVID-19

- [Johannes C. Melms](#) ORCID: orcid.org/0000-0002-5410-6586^{1,2} na1,
- [Jana Biermann](#) ORCID: orcid.org/0000-0002-8907-4633^{1,2} na1,
- [Huachao Huang](#)^{3,4,5} na1,
- [Yiping Wang](#)^{1,2} na1,
- [Ajay Nair](#) ORCID: orcid.org/0000-0003-4521-5614⁵ na1,
- [Somnath Tagore](#)⁶ na1,
- [Igor Katsyy](#)⁷ na1,
- [André F. Rendeiro](#)^{8,9} na1,
- [Amit Dipak Amin](#)^{1,2} na1,
- [Denis Schapiro](#)^{10,11},
- [Chris J. Frangieh](#)^{11,12},
- [Adrienne M. Luoma](#)¹³,
- [Aveline Filliol](#)⁵,
- [Yinshan Fang](#)^{3,4,5},
- [Hiranmayi Ravichandran](#)^{9,14,15},
- [Mariano G. Clausi](#)¹⁶,
- [George A. Alba](#)¹⁷,
- [Meri Rogava](#)^{1,2},
- [Sean W. Chen](#)^{1,2},
- [Patricia Ho](#) ORCID: orcid.org/0000-0002-4622-8188^{1,2},
- [Daniel T. Montoro](#)^{18,19},
- [Adam E. Kornberg](#)²,
- [Arnold S. Han](#)²,

- [Mathieu F. Bakhoum](#) ORCID: [orcid.org/0000-0001-8989-8205²⁰](https://orcid.org/0000-0001-8989-8205),
- [Niroshana Anandasabapathy](#)^{9,21,22},
- [Mayte Suárez-Fariñas](#) ORCID: [orcid.org/0000-0001-8712-3553^{23,24}](https://orcid.org/0000-0001-8712-3553),
- [Samuel F. Bakhoum](#)^{25,26},
- [Yaron Bram](#)²⁷,
- [Alain Borczuk](#)^{28,29},
- [Xinzheng V. Guo](#)¹⁶,
- [Jay H. Lefkowitch](#)⁷,
- [Charles Marboe](#)⁷,
- [Stephen M. Lagana](#)⁷,
- [Armando Del Portillo](#)⁷,
- [Emily J. Tsai](#)⁵,
- [Emmanuel Zorn](#) ORCID: [orcid.org/0000-0001-9985-8389²](https://orcid.org/0000-0001-9985-8389),
- [Glen S. Markowitz](#)⁷,
- [Robert F. Schwabe](#)^{5,30},
- [Robert E. Schwartz](#) ORCID: [orcid.org/0000-0002-5417-5995^{27 na2}](https://orcid.org/0000-0002-5417-5995),
- [Olivier Elemento](#)^{8,9,15 na2},
- [Anjali Saqi](#)^{7 na2},
- [Hanina Hibshoosh](#)^{7 na2},
- [Jianwen Que](#) ORCID: [orcid.org/0000-0002-6540-6701^{3,4,5,31 na2}](https://orcid.org/0000-0002-6540-6701) &
- [Benjamin Izar](#) ORCID: [orcid.org/0000-0003-2379-6702^{1,2,31,32 na2}](https://orcid.org/0000-0003-2379-6702)

Nature volume **598**, page E2 (2021)

- 978 Accesses
- 3 Altmetric
- [Metrics details](#)

Subjects

- [Cellular signalling networks](#)
- [Infection](#)
- [SARS-CoV-2](#)

The [Original Article](#) was published on 29 April 2021

[Download PDF](#)

Correction to: *Nature* <https://doi.org/10.1038/s41586-021-03569-1>

Published online 19 April 2021

In the version of this Article originally published, an oversight led to author Emily J. Tsai (Division of Cardiology, Department of Medicine, Columbia University Irving Medical Center, New York, NY, USA) not appearing in the author list or Author contributions section. This individual had a significant role in coordinating and facilitating performance of rapid autopsies, the research importance of which is noted throughout the text. The Author contributions section has been amended to include the text “E.J.T. facilitated rapid autopsy specimen collection.” The original Article has been corrected online.

Author information

Author notes

1. These authors contributed equally: Johannes C. Melms, Jana Biermann, Huachao Huang, Yiping Wang, Ajay Nair, Somnath Tagore, Igor Katsyy, André F. Rendeiro, Amit Dipak Amin
2. These authors jointly supervised this work: Robert E. Schwartz, Olivier Elemento, Anjali Saqi, Hanina Hibshoosh, Jianwen Que, Benjamin Izar

Affiliations

1. Department of Medicine, Division of Hematology/Oncology, Columbia University Irving Medical Center, New York, NY, USA

Johannes C. Melms, Jana Biermann, Yiping Wang, Amit Dipak Amin, Meri Rogava, Sean W. Chen, Patricia Ho & Benjamin Izar

2. Columbia Center for Translational Immunology, Columbia University Irving Medical Center, New York, NY, USA

Johannes C. Melms, Jana Biermann, Yiping Wang, Amit Dipak Amin, Meri Rogava, Sean W. Chen, Patricia Ho, Adam E. Kornberg, Arnold S. Han, Emmanuel Zorn & Benjamin Izar

3. Columbia Center for Human Development, Columbia University Irving Medical Center, New York, NY, USA

Huachao Huang, Yinshan Fang & Jianwen Que

4. Division of Digestive and Liver Diseases, Columbia University Irving Medical Center, New York, NY, USA

Huachao Huang, Yinshan Fang & Jianwen Que

5. Department of Medicine, Columbia University Irving Medical Center, New York, NY, USA

Huachao Huang, Ajay Nair, Aveline Filliol, Yinshan Fang, Emily J. Tsai, Robert F. Schwabe & Jianwen Que

6. Department of Systems Biology, Columbia University Irving Medical Center, New York, NY, USA

Somnath Tagore

7. Department of Pathology and Cell Biology, Columbia University Irving Medical Center, New York, NY, USA

Igor Katsyv, Jay H. Lefkowitch, Charles Marboe, Stephen M. Lagana, Armando Del Portillo, Glen S. Markowitz, Anjali Saqi & Hanina Hibshoosh

8. Institute for Computational Biomedicine, Weill Cornell Medicine, New York, NY, USA

André F. Rendeiro & Olivier Elemento

9. Caryl and Israel Englander Institute for Precision Medicine, Weill Cornell Medicine, New York, NY, USA

André F. Rendeiro, Hiranmayi Ravichandran, Niroshana Anandasabapathy & Olivier Elemento

10. Laboratory of Systems Pharmacology, Harvard Medical School, Boston, MA, USA

Denis Schapiro

11. Klarman Cell Observatory, Broad Institute of MIT and Harvard, Cambridge, MA, USA

Denis Schapiro & Chris J. Frangieh

12. Department of Electrical Engineering and Computer Science, Massachusetts Institute of Technology, Cambridge, MA, USA

Chris J. Frangieh

13. Department of Cancer Immunology and Virology, Dana-Farber Cancer Center, Boston, MA, USA

Adrienne M. Luoma

14. Department of Physiology and Biophysics, Weill Cornell Medical College, New York, NY, USA

Hiranmayi Ravichandran

15. WorldQuant Initiative for Quantitative Prediction, Weill Cornell Medicine, New York, NY, USA

Hiranmayi Ravichandran & Olivier Elemento

16. Human Immune Monitoring Core, Columbia University Irving Medical Center, New York, NY, USA

Mariano G. Clausi & Xinzheng V. Guo

17. Department of Medicine, Division of Pulmonary and Critical Care,
Massachusetts General Hospital, Boston, MA, USA

George A. Alba

18. Cell Circuits, Broad Institute of MIT and Harvard, Cambridge, MA,
USA

Daniel T. Montoro

19. Systems Biology, Harvard Medical School, Boston, MA, USA

Daniel T. Montoro

20. Department of Ophthalmology, University of California San Diego, La
Jolla, CA, USA

Mathieu F. Bakhoum

21. Department of Dermatology, Weill Cornell Medical College, New
York, NY, USA

Niroshana Anandasabapathy

22. Meyer Cancer Center, Weill Cornell Medical College, New York, NY,
USA

Niroshana Anandasabapathy

23. Department of Genetics and Genomic Science, Icahn School of
Medicine at Mount Sinai, New York, NY, USA

Mayte Suárez-Fariñas

24. Department of Population Health Science and Policy, Icahn School of
Medicine at Mount Sinai, New York, NY, USA

Mayte Suárez-Fariñas

25. Human Oncology and Pathogenesis Program, Memorial Sloan Kettering Cancer Center, New York, NY, USA

Samuel F. Bakhoum

26. Department of Radiation Oncology, Memorial Sloan Kettering Cancer Center, New York, NY, USA

Samuel F. Bakhoum

27. Division of Gastroenterology and Hepatology, Department of Medicine, Weill Cornell Medicine, New York, NY, USA

Yaron Bram & Robert E. Schwartz

28. Department of Pathology and Laboratory Medicine, Weill Cornell Medicine, New York, NY, USA

Alain Borczuk

29. Department of Medicine, Weill Cornell Medicine, New York, NY, USA

Alain Borczuk

30. Institute of Human Nutrition, Columbia University, New York, NY, USA

Robert F. Schwabe

31. Herbert Irving Comprehensive Cancer Center, Columbia University Irving Medical Center, New York, NY, USA

Jianwen Que & Benjamin Izar

32. Program for Mathematical Genomics, Columbia University, New York, NY, USA

Benjamin Izar

Corresponding authors

Correspondence to Jianwen Que or Benjamin Izar.

Rights and permissions

[Reprints and Permissions](#)

About this article

Cite this article

Melms, J.C., Biermann, J., Huang, H. *et al.* Author Correction: A molecular single-cell lung atlas of lethal COVID-19. *Nature* **598**, E2 (2021).
<https://doi.org/10.1038/s41586-021-03921-5>

- Published: 08 October 2021
- Issue Date: 28 October 2021
- DOI: <https://doi.org/10.1038/s41586-021-03921-5>

Share this article

Anyone you share the following link with will be able to read this content:

[Get shareable link](#)

Sorry, a shareable link is not currently available for this article.

[Copy to clipboard](#)

Provided by the Springer Nature SharedIt content-sharing initiative

This article was downloaded by **calibre** from <https://www.nature.com/articles/s41586-021-03921-5>

| [Section menu](#) | [Main menu](#) |

- Author Correction
- [Published: 14 October 2021](#)

Author Correction: Structural basis of ketamine action on human NMDA receptors

- [Youyi Zhang](#) ORCID: [orcid.org/0000-0001-7558-6454^{1,2 na1}](https://orcid.org/0000-0001-7558-6454),
- [Fei Ye](#) ORCID: [orcid.org/0000-0003-4119-3219^{3 na1}](https://orcid.org/0000-0003-4119-3219),
- [Tongtong Zhang](#) ORCID: [orcid.org/0000-0002-2414-8048^{1,2 na1}](https://orcid.org/0000-0002-2414-8048),
- [Shiyun Lv](#) ORCID: [orcid.org/0000-0001-8779-9430^{1,2}](https://orcid.org/0000-0001-8779-9430),
- [Liping Zhou](#)^{2,4},
- [Daohai Du](#) ORCID: [orcid.org/0000-0002-6623-7778⁴](https://orcid.org/0000-0002-6623-7778),
- [He Lin](#)⁵,
- [Fei Guo](#)⁴,
- [Cheng Luo](#) ORCID: [orcid.org/0000-0003-3864-8382^{2,4}](https://orcid.org/0000-0003-3864-8382) &
- [Shujia Zhu](#) ORCID: [orcid.org/0000-0001-8358-2859^{1,2,6}](https://orcid.org/0000-0001-8358-2859)

[Nature](#) volume **598**, page E3 (2021)

- 664 Accesses
- 2 Altmetric
- [Metrics details](#)

Subjects

- [Cryoelectron microscopy](#)
- [Ion channels in the nervous system](#)

The [Original Article](#) was published on 28 July 2021

[Download PDF](#)

Correction to: *Nature* <https://doi.org/10.1038/s41586-021-03769-9>

Published online 28 July 2021

This Article has been amended to make two clarifications. The second sentence of the Abstract paragraph, now reading “Ketamine is a racemic mixture containing equal parts of *R*- and *S*-ketamine, with the *S*-enantiomer having greater affinity for the NMDA receptor (Ebert, B., Mikkelsen, S., Thorkildsen, C. & Borgbjerg, F. M. Norketamine, the main metabolite of ketamine, is a non-competitive NMDA receptor antagonist in the rat cortex and spinal cord. *Eur. J. Pharmacol.* **333**, 99–104 (1997)),” was changed from “Ketamine is a racemic mixture of *S*- and *R*-ketamine enantiomers, with *S*-ketamine isomer being the more active antidepressant (Jelen, L. A., Young, A. H. & Stone, J. M. Ketamine: a tale of two enantiomers. *J. Psychopharmacol.* **35**, 109–123 (2021)).”

In Fig. 1f, the *y*-axis label now reading “Inhibition (%)" was changed from “Inhibition relative to 10 μM [³H]-MK-801 (%).” The authors note that accurate concentrations of [³H]-MK-801 are noted in the Methods, subsection “Ligand-binding assay,” particularly as “[³H]MK-801 (10 nM for GluN1–GluN2A_{EM} receptor and rat cortex; 50 nM for GluN1–GluN2B_{EM} receptor).” The original Article has been corrected online.

Author information

Author notes

1. These authors contributed equally: Youyi Zhang, Fei Ye, Tongtong Zhang

Affiliations

1. Institute of Neuroscience, State Key Laboratory of Neuroscience, CAS
Center for Excellence in Brain Science and Intelligence Technology,
Chinese Academy of Sciences, Shanghai, China

Youyi Zhang, Tongtong Zhang, Shiyun Lv & Shujia Zhu

2. University of Chinese Academy of Sciences, Beijing, China

Youyi Zhang, Tongtong Zhang, Shiyun Lv, Liping Zhou, Cheng
Luo & Shujia Zhu

3. College of Life Sciences and Medicine, Zhejiang Sci-Tech University,
Hangzhou, China

Fei Ye

4. Drug Discovery and Design Center, the Center for Chemical Biology,
State Key Laboratory of Drug Research, Shanghai Institute of Materia
Medica, Chinese Academy of Sciences, Shanghai, China

Liping Zhou, Daohai Du, Fei Guo & Cheng Luo

5. Criminal Investigation Technology Department, The Third Research
Institute of Ministry of Public Security, Shanghai, China

He Lin

6. Shanghai Center for Brain Science and Brain-Inspired Intelligence
Technology, Shanghai, China

Shujia Zhu

Corresponding authors

Correspondence to Cheng Luo or Shujia Zhu.

Rights and permissions

[Reprints and Permissions](#)

About this article

Cite this article

Zhang, Y., Ye, F., Zhang, T. *et al.* Author Correction: Structural basis of ketamine action on human NMDA receptors. *Nature* **598**, E3 (2021).
<https://doi.org/10.1038/s41586-021-04038-5>

- Published: 14 October 2021
- Issue Date: 28 October 2021
- DOI: <https://doi.org/10.1038/s41586-021-04038-5>

Share this article

Anyone you share the following link with will be able to read this content:

[Get shareable link](#)

Sorry, a shareable link is not currently available for this article.

[Copy to clipboard](#)

Provided by the Springer Nature SharedIt content-sharing initiative

This article was downloaded by **calibre** from <https://www.nature.com/articles/s41586-021-04038-5>

- Publisher Correction
- [Published: 08 October 2021](#)

Publisher Correction: Dysregulation of brain and choroid plexus cell types in severe COVID- 19

- [Andrew C. Yang](#) [ORCID: orcid.org/0000-0002-6756-4746](#)^{1,2,3} na1,
- [Fabian Kern](#) [ORCID: orcid.org/0000-0002-8223-3750](#)⁴ na1,
- [Patricia M. Losada](#)³,
- [Maayan R. Agam](#)³,
- [Christina A. Maat](#)³,
- [Georges P. Schmartz](#)⁴,
- [Tobias Fehlmann](#) [ORCID: orcid.org/0000-0003-1967-2918](#)⁴,
- [Julian A. Stein](#)⁵,
- [Nicholas Schaum](#)³,
- [Davis P. Lee](#)³,
- [Kruti Calcuttawala](#)³,
- [Ryan T. Vest](#)³,
- [Daniela Berdnik](#)³,
- [Nannan Lu](#)³,
- [Oliver Hahn](#)³,
- [David Gate](#) [ORCID: orcid.org/0000-0003-0481-9657](#)³,
- [M. Windy McNerney](#)⁶,
- [Divya Channappa](#)³,
- [Inma Cobos](#)^{3,7},
- [Nicole Ludwig](#)⁸,
- [Walter J. Schulz-Schaeffer](#) [ORCID: orcid.org/0000-0001-5886-2322](#)⁵,

- [Andreas Keller](#) [ORCID: orcid.org/0000-0002-5361-0895^{3,4 na2}](#) &
- [Tony Wyss-Coray](#) [ORCID: orcid.org/0000-0001-5893-0831^{2,3,9,10 na2}](#)

[*Nature*](#) volume **598**, page E4 (2021)

- 830 Accesses
- 2 Altmetric
- [Metrics details](#)

The [Original Article](#) was published on 21 June 2021

[Download PDF](#)

Correction to: *Nature* <https://doi.org/10.1038/s41586-021-03710-0>

Published online 7 June 2021

In the version of this Article initially published, a labeling error appeared in Fig. 4d. On the far right *x*-axis label, the last term, “Cognitive,” was incorrect. This has been replaced with the original label “Interneuron.”

The original Article has been corrected online.

Author information

Author notes

1. These authors contributed equally: Andrew C. Yang, Fabian Kern
2. These authors jointly supervised this work: Andreas Keller, Tony Wyss-Coray

Affiliations

1. Department of Bioengineering, Stanford University School of Medicine, Stanford, CA, USA

Andrew C. Yang

2. ChEM-H, Stanford University, Stanford, CA, USA

Andrew C. Yang & Tony Wyss-Coray

3. Department of Neurology and Neurological Sciences, Stanford University School of Medicine, Stanford, CA, USA

Andrew C. Yang, Patricia M. Losada, Maayan R. Agam, Christina A. Maat, Nicholas Schaum, Davis P. Lee, Kruti Calcuttawala, Ryan T. Vest, Daniela Berdnik, Nannan Lu, Oliver Hahn, David Gate, Divya Channappa, Inma Cobos, Andreas Keller & Tony Wyss-Coray

4. Chair for Clinical Bioinformatics, Saarland University, Saarbrücken, Germany

Fabian Kern, Georges P. Schmartz, Tobias Fehlmann & Andreas Keller

5. Institute for Neuropathology, Saarland University Hospital and Medical Faculty of Saarland University, Homburg, Germany

Julian A. Stein & Walter J. Schulz-Schaeffer

6. Department of Psychiatry, Stanford University School of Medicine, Stanford, CA, USA

M. Windy McNerney

7. Department of Pathology, Stanford University School of Medicine, Stanford, CA, USA

Inma Cobos

8. Department of Human Genetics, Saarland University, Homburg, Germany

Nicole Ludwig

9. Wu Tsai Neurosciences Institute, Stanford University, Stanford, CA, USA

Tony Wyss-Coray

10. Paul F. Glenn Center for the Biology of Aging, Stanford University School of Medicine, Stanford, CA, USA

Tony Wyss-Coray

Corresponding authors

Correspondence to Andreas Keller or Tony Wyss-Coray.

Rights and permissions

[Reprints and Permissions](#)

About this article

Cite this article

Yang, A.C., Kern, F., Losada, P.M. *et al.* Publisher Correction: Dysregulation of brain and choroid plexus cell types in severe COVID-19. *Nature* **598**, E4 (2021). <https://doi.org/10.1038/s41586-021-04080-3>

- Published: 08 October 2021
- Issue Date: 28 October 2021
- DOI: <https://doi.org/10.1038/s41586-021-04080-3>

Share this article

Anyone you share the following link with will be able to read this content:

[Get shareable link](#)

Sorry, a shareable link is not currently available for this article.

[Copy to clipboard](#)

Provided by the Springer Nature SharedIt content-sharing initiative

This article was downloaded by **calibre** from <https://www.nature.com/articles/s41586-021-04080-3>

| [Section menu](#) | [Main menu](#) |

- Publisher Correction
- Open Access
- [Published: 12 October 2021](#)

Publisher Correction: Demonstration of reduced neoclassical energy transport in Wendelstein 7-X

- [C. D. Beidler](#) [ORCID: orcid.org/0000-0002-4395-239X¹](#),
- [H. M. Smith¹](#),
- [A. Alonso](#) [ORCID: orcid.org/0000-0001-6863-8578²](#),
- [T. Andreeva¹](#),
- [J. Baldzuhn¹](#),
- [M. N. A. Beurskens¹](#),
- [M. Borchardt](#) [ORCID: orcid.org/0000-0003-4514-7391¹](#),
- [S. A. Bozhenkov¹](#),
- [K. J. Brunner](#) [ORCID: orcid.org/0000-0002-0974-0457¹](#),
- [H. Damm](#) [ORCID: orcid.org/0000-0001-9423-1608¹](#),
- [M. Drevlak¹](#),
- [O. P. Ford](#) [ORCID: orcid.org/0000-0002-5646-4758¹](#),
- [G. Fuchert¹](#),
- [J. Geiger](#) [ORCID: orcid.org/0000-0003-4268-7480¹](#),
- [P. Helander¹](#),
- [U. Hergenhahn](#) [ORCID: orcid.org/0000-0003-3396-4511^{1 nAff5}](#),
- [M. Hirsch¹](#),
- [U. Höfel](#) [ORCID: orcid.org/0000-0003-0971-5937¹](#),
- [Ye. O. Kazakov](#) [ORCID: orcid.org/0000-0001-6316-5441³](#),
- [R. Kleiber](#) [ORCID: orcid.org/0000-0002-2261-2855¹](#),

- [M. Krychowiak](#)¹,
- [S. Kwak](#)¹,
- [A. Langenberg](#) ORCID: orcid.org/0000-0002-2107-5488¹,
- [H. P. Laqua](#)¹,
- [U. Neuner](#)¹,
- [N. A. Pablant](#)⁴,
- [E. Pasch](#)¹,
- [A. Pavone](#)¹,
- [T. S. Pedersen](#) ORCID: orcid.org/0000-0002-9720-1276¹,
- [K. Rahbarnia](#) ORCID: orcid.org/0000-0002-5550-1801¹,
- [J. Schilling](#) ORCID: orcid.org/0000-0002-6363-6554¹,
- [E. R. Scott](#) ORCID: orcid.org/0000-0002-1389-1151¹,
- [T. Stange](#)¹,
- [J. Svensson](#)¹,
- [H. Thomsen](#) ORCID: orcid.org/0000-0002-6835-1494¹,
- [Y. Turkin](#) ORCID: orcid.org/0000-0002-6127-9266¹,
- [F. Warmer](#) ORCID: orcid.org/0000-0001-9585-5201¹,
- [R. C. Wolf](#) ORCID: orcid.org/0000-0002-2606-5289¹,
- [D. Zhang](#)¹ &
- [the W7-X Team](#)

Nature volume **598**, page E5 (2021)

- 353 Accesses
- 2 Altmetric
- [Metrics details](#)

The [Original Article](#) was published on 11 August 2021

[Download PDF](#)

Correction to: *Nature* <https://doi.org/10.1038/s41586-021-03687-w>
Published online 11 August 2021

In the original version of this Article, in the fifth paragraph of the section titled “Qneo for W7-X discharge 20180918.045,” errors appeared in reference to the configurations shown in the curves of Fig. 3a and associated Fig. 3b–e panels. In the sentence originally reading “This comparison is provided in **Fig. 3a** for the configurations (**Fig. 3b**) W7-X standard, (**Fig. 3c**) W7-X high-mirror, (**Fig. 3d**) LHD $R_0 = 3.6$ m, and (**Fig. 3e**) LHD $R_0 = 3.75$ m....,” the references to Fig. 3b–e should instead have referred to the lettered curves “b,c,d,e” shown in the graph of Fig. 3a. The text has now been amended to read: “This comparison is provided in **Fig. 3a** for the configurations (b) W7-X standard, (c) W7-X high-mirror, (d) LHD $R_0 = 3.6$ m, and (e) LHD $R_0 = 3.75$ m....”

Additionally, a member of the W7-X Team was incorrectly listed as “M. Sanchez”; their name has been corrected to “E. Sánchez.”

The original Article has been corrected online.

Author information

Author notes

1. U. Hergenhahn

Present address: Fritz-Haber-Institut der Max-Planck-Gesellschaft, Berlin, Germany

Affiliations

1. Max-Planck-Institut für Plasmaphysik, Greifswald, Germany

C. D. Beidler, H. M. Smith, T. Andreeva, J. Baldzuhn, M. N. A. Beurskens, M. Borchardt, S. A. Bozhenkov, K. J. Brunner, H. Damm, M. Drevlak, O. P. Ford, G. Fuchert, J. Geiger, P. Helander, U. Hergenhahn, M. Hirsch, U. Höfel, R. Kleiber, M. Krychowiak, S. Kwak, A. Langenberg, H. P. Laqua, U. Neuner, E. Pasch, A. Pavone, T. S. Pedersen, K. Rahbarnia, J. Schilling, E. R. Scott, T. Stange, J. Svensson, H. Thomsen, Y. Turkin, F. Warmer, R. C. Wolf, D. Zhang, I.

Abramovic, S. Äkäslompolo, J. Alcusón, P. Aleynikov, K.
Aleynikova, A. Ali, J. P. Bähner, M. Banduch, A. Benndorf, C.
Biedermann, M. Blatzheim, T. Bluhm, D. Böckenhoff, L.-G.
Böttger, H.-S. Bosch, R. Brakel, C. Brandt, T. Bräuer, H. Braune, K.-J.
Brunner, R. Burhenn, R. Bussiahn, B. Buttenschön, V. Bykov, A.
Carls, N. Chaudhary, M. Cole, M. Czerwinski, S. Degenkolbe, C. P.
Dhard, A. Dinklage, P. Drewelow, G. Ehrke, M. Endler, J. Fellinger, Y.
Feng, B. Geiger, D. Gradic, M. Grahl, H. Grote, O. Grulke, P.
Hacker, D. Hartmann, D. Hathiramani, B. Hein, P. Helander, S.
Henneberg, U. Hergenhahn, A. Hölting, Z. Huang, M. Jakubowski, H.
Jenzsch, J.-P. Kallmeyer, U. Kamionka, C. Killer, T. Klinger, J.
Knauer, A. Könies, R. König, P. Kornejew, J.-P. Koschinsky, R.
Krampitz, J. Krom, G. Kühner, P. A. Kurz, H. Laqua, R. Laube, C.
Li, J.-F. Lobsien, J. Loizu Cisquella, A. Lorenz, H. Maaßberg, S.
Marsen, M. Marushchenko, P. McNeely, A. Mishchenko, B. Missal, A.
Mollen, T. Mönnich, D. Moseev, M. Nagel, D. Naujoks, H.
Niemann, T. Nishizawa, C. Nührenberg, J. Nührenberg, J. W.
Oosterbeek, M. Otte, N. Panadero, T. S. Pedersen, V. Perseo, D.
Pilopp, S. Pingel, G. Plunk, A. Puig Sitjes, F. Purps, F. Reimold, J.
Riemann, K. Risse, D. Rondeshagen, P. Rong, L. Rudischhauser, K.
Rummel, T. Rummel, A. Runov, N. Rust, J. Schacht, F. Schauer, G.
Schlisio, M. Schneider, W. Schneider, P. Scholz, M. Schröder, T.
Schröder, R. Schroeder, B. Shanahan, P. Sinha, C. Slaby, A. Spring, U.
Stridde, H. Trimino Mora, I. Vakulchyk, S. Valet, P. van Eeten, H.
Viebke, R. Vilbrandt, A. von Stechow, A. Vorköper, F. Wagner, Z.
Wang, L. Wegener, T. Wegner, G. Weir, J. Wendorf, U. Wenzel, A.
Werner, F. Wilde, T. Windisch, M. Winkler, A. Winter, R. C. Wolf, P.
Xanthopoulos, M. Zanini, J. Zhu & A. Zocco

2. Laboratorio Nacional de Fusion, CIEMAT, Madrid, Spain

A. Alonso, A. Alonso, E. Ascasibar, E. Blanco, I. Calvo, A. Cappa, F. Castejon, A. de la Pena, H. Esteban, T. Estrada, J. Fontdecaba, J. García Regaña, C. Guerard, J. Hernandez Sanchez, C. Hidalgo, D. Loesser, K. McCarthy, L. Pacios Rodriguez, N. Panadero Alvarez, E. Sánchez, B. van Milligen, J.-L. Velasco & H. Zhang

3. Laboratory for Plasma Physics (LPP), École royale militaire/Koninklijke Militaire School (ERM/KMS), Brussels, Belgium

Ye. O. Kazakov, F. Durodie, A. Goriaev, J. Ongena, B. Schweer, M. Vergote, M. Vervier & T. Wauters

4. Princeton Plasma Physics Laboratory, Princeton, NJ, USA

N. A. Pablot, D. Gates, B. Israeli, S. Langish, S. Lazerson, D. Mikkelsen, J. Mittelstaedt, H. Neilson, A. Reiman, M. Sibilia & M. Zarnstorff

5. Wigner Research Centre for Physics, Budapest, Hungary

G. Anda, G. Cseh, T. Ilkei, G. Kocsis, G. Náfrádi, S. Récsei, V. Szabó, T. Szabolics, T. Szepesi, Z. Szökefalvi-Nagy, S. Tulipán, L. Vanó & S. Zoletnik

6. Massachusetts Institute of Technology, Cambridge, MA, USA

S. G. Baek, S. Ballinger, E. Edlund, M. Porkolab, J. Terry & A. White

7. Max Planck Institute for Plasma Physics, Garching, Germany

M. Balden, B. Böswirth, J. Boscaro, M. Dibon, S. Elgeti, H. Frerichs, H. Greuner, B. Heinemann, P. Junghanns, P. Lang, M. Mayer, B. Mendelevitch, R. Neu, R. Nocentini, S. Obermayer, G. Orozco, P. Pölöskei, R. Riedl, V. Rohde, R. Stadler, J. Tretter, A. J. van Vuuren & M. Zilker

8. University of Wisconsin Madison, Madison, WI, USA

T. Barbui, F. Effenberg, E. Flom, J. Green, T. Kremeyer, O. Schmitz, L. Stephey & V. Winters

9. Institute for Energy and Climate Research – Plasma Physics, Research Center Jülich, Jülich, Germany

W. Behr, W. Biel, V. Borsuk, S. Brezinsek, J. Cai, A. Charl, J. Coenen, G. Czymek, T. Dittmar, P. Drews, A. Freund, Y. Gao, X. Han, M. Henkel, K. P. Hollfeld, D. Höschen, M. Hubeny, M. Jia, A. Kirschner, M. Knaup, A. Knieps, A. Krämer-Flecken, M. Lennartz, C. Li, Y. Li, Y. Liang, C. Linsmeier, S. Liu, O. Marchuk, P. Mertens, O. Neubauer, D. Nicolai, G. Offermanns, J. Ölmanns, M. Rack, D. Reiter, G. Satheeswaran, F. Schluck, H. Schmitz, S. Sereda, J. Thomas, B. Unterberg, E. Wang, N. Wang & Y. Wei

10. The Australian National University, Canberra, Australian Capital Territory, Australia
B. Blackwell, J. H. Matthew & A. Wright
11. Technical University of Denmark, Kongens Lyngby, Denmark
L.-G. Böttger, O. Grulke, S. K. Nielsen, M. Salewski, M. Stejner & A. Tancetti
12. Eindhoven University of Technology, Eindhoven, Netherlands
H. Brand, J. Howard, S. Paqay, J. Proll & M. Zuin
13. University of Cagliari, Cagliari, Italy
B. Cannas & F. Pisano
14. Consorzio RFX, Padova, Italy
L. Carraro & N. Vianello
15. Instituto de Plasmas e Fusao Nuclear, Lisbon, Portugal
B. Carvalho
16. CEA Cadarache, Saint-Paul-lez-Durance, France
D. Chauvin, A. da Silva, H. Fernandes, B. Goncalves, A. Grosman, M. Houry, V. Moncada, T. Ngo, S. Renard & J. M. Travere

17. Ioffe Physical-Technical Institute of the Russian Academy of Sciences,
St Petersburg, Russian Federation

F. Chernyshev

18. Oak Ridge National Laboratory, Oak Ridge, TN, USA

M. Cianciosa, M. J. Cole, J. H. Harris, J. Lore, A. Lumsdaine & D. A.
Spong

19. University of Salerno, Fisciano, Italy

R. Citarella & V. Giannella

20. ENEA Centro Ricerche Frascati, Frascati, Italy

G. Claps & F. Cordella

21. Institute of Plasma Physics and Laser Microfusion, Warsaw, Poland

A. Czarnecka, W. Figacz, T. Fornal, A. Galkowski, M. Gruca, S.
Jablonski, J. Kacmarczyk, N. Krawczyk, M. Kubkowska, G.
Pelka & L. Ryc

22. University of Szczecin, Szczecin, Poland

K. Czerski & M. Slezcka

23. University of Milano-Bicocca, Milan, Italy

A. da Molin

24. Auburn University, Auburn, AL, USA

D. Ennis, D. Maurer, J. Schmitt & P. Traverso

25. Karlsruhe Institute of Technology, Eggenstein-Leopoldshafen,
Germany

W. H. Fietz, G. Gantenbein, M. Huber, H. Hunger, S. Illy, J. Jelonnek, T. Kobarg, R. Lang, W. Leonhardt, M. Losert, A. Meier, D. Mellein, D. Papenfuß, A. Samartsev, T. Scherer, A. Schlaich, W. Spiess, M. Thumm, S. Wadle & J. Weggen

26. National Institute for Fusion Science, Toki, Japan

T. Funaba, X. Huang, K. Ida, H. Kasahara, N. Kenmochi, S. Masuzaki, T. Morisaki, K. Ogawa, B. Peterson, S. Ryosuke, R. Sakamoto, S. Satake, C. Suzuki, N. Tamura, H. Tsuchiya, T. Tsujimura, H. Yamada, I. Yamada, R. Yasuhara & M. Yokoyama

27. Universidad Carlos III de Madrid, Madrid, Spain

A. Gogoleva & L. Vela

28. Greifswald University, Greifswald, Germany

P. Helander, T. Klinger & T. S. Pedersen

29. Institute for Surface Process Engineering and Plasma Technology,
University of Stuttgart, Stuttgart, Germany

T. Jesche, W. Kasperek, M. Krämer, C. Lechte, B. Plaum, F. Remppel, H. Röhlinger, B. Roth, K.-H. Schlüter, S. Wolf & A. Zeitler

30. Austrian Academy of Science, Vienna, Austria

F. Köchl & R. Schrittwieser

31. Institute for Nuclear Research, Kiev, Ukraine

Y. Kolesnichenko & V. Lutsenko

32. Technical University of Berlin, Berlin, Germany

F. Köster & R. C. Wolf

33. University of Opole, Opole, Poland

I. Ksiazek & E. Pawelec

34. Aalto University, Espoo, Finland

T. Kurki-Suonio & S. Sipliä

35. University of Maryland, College Park, MA, USA

M. Landreman

36. Physikalisch Technische Bundesanstalt (PTB), Braunschweig,
Germany

A. Lücke, H. Schumacher & B. Wiegel

37. Kyoto University, Kyoto, Japan

T. Mizuuchi, S. Murakami & F. Sano

38. Istituto di Fisica del Plasma “Piero Caldirola”, Milan, Italy

M.-E. Puiatti & M. Romé

39. Culham Centre for Fusion Energy, Abingdon, UK

S. Schmuck

40. Los Alamos National Laboratory, Los Alamos, NM, USA

G. Wurden

Consortia

the W7-X Team

- I. Abramovic
- , S. Äkäslompolo
- , J. Alcusón
- , P. Aleynikov

- , K. Aleynikova
- , A. Ali
- , A. Alonso
- , G. Anda
- , T. Andreeva
- , E. Ascasibar
- , J. P. Bähner
- , S. G. Baek
- , M. Balden
- , J. Baldzuhn
- , M. Banduch
- , T. Barbui
- , W. Behr
- , C. D. Beidler
- , A. Benndorf
- , M. N. A. Beurskens
- , C. Biedermann
- , W. Biel
- , B. Blackwell
- , E. Blanco
- , M. Blatzheim
- , S. Ballinger
- , T. Bluhm
- , D. Böckenhoff
- , B. Böswirth
- , L.-G. Böttger
- , M. Borchardt
- , V. Borsuk
- , J. Boscary
- , H.-S. Bosch
- , S. A. Bozhenkov
- , R. Brakel
- , H. Brand
- , C. Brandt
- , T. Bräuer
- , H. Braune
- , S. Brezinsek

- , K.-J. Brunner
- , R. Burhenn
- , R. Bussiahn
- , B. Buttenschön
- , V. Bykov
- , J. Cai
- , I. Calvo
- , B. Cannas
- , A. Cappa
- , A. Carls
- , L. Carraro
- , B. Carvalho
- , F. Castejon
- , A. Charl
- , N. Chaudhary
- , D. Chauvin
- , F. Chernyshev
- , M. Cianciosa
- , R. Citarella
- , G. Claps
- , J. Coenen
- , M. Cole
- , M. J. Cole
- , F. Cordella
- , G. Cseh
- , A. Czarnecka
- , K. Czerski
- , M. Czerwinski
- , G. Czymek
- , A. da Molin
- , A. da Silva
- , H. Damm
- , A. de la Pena
- , S. Degenkolbe
- , C. P. Dhard
- , M. Dibon
- , A. Dinklage

- , T. Dittmar
- , M. Drevlak
- , P. Drewelow
- , P. Drews
- , F. Durodie
- , E. Edlund
- , F. Effenberg
- , G. Ehrke
- , S. Elgeti
- , M. Endler
- , D. Ennis
- , H. Esteban
- , T. Estrada
- , J. Fellinger
- , Y. Feng
- , E. Flom
- , H. Fernandes
- , W. H. Fietz
- , W. Figacz
- , J. Fontdecaba
- , O. P. Ford
- , T. Fornal
- , H. Frerichs
- , A. Freund
- , G. Fuchert
- , T. Funaba
- , A. Galkowski
- , G. Gantenbein
- , Y. Gao
- , J. García Regaña
- , D. Gates
- , B. Geiger
- , J. Geiger
- , V. Giannella
- , A. Gogoleva
- , B. Goncalves
- , A. Goriaev

- , D. Gradic
- , M. Grahl
- , J. Green
- , H. Greuner
- , A. Grosman
- , H. Grote
- , M. Gruca
- , O. Grulke
- , C. Guerard
- , P. Hacker
- , X. Han
- , J. H. Harris
- , D. Hartmann
- , D. Hathiramani
- , B. Hein
- , B. Heinemann
- , P. Helander
- , S. Henneberg
- , M. Henkel
- , U. Hergenhahn
- , J. Hernandez Sanchez
- , C. Hidalgo
- , M. Hirsch
- , K. P. Hollfeld
- , U. Höfel
- , A. Höltig
- , D. Höschen
- , M. Houry
- , J. Howard
- , X. Huang
- , Z. Huang
- , M. Hubeny
- , M. Huber
- , H. Hunger
- , K. Ida
- , T. Ilkei
- , S. Illy

- , B. Israeli
- , S. Jablonski
- , M. Jakubowski
- , J. Jelonnek
- , H. Jenzsch
- , T. Jesche
- , M. Jia
- , P. Junghanns
- , J. Kacmarczyk
- , J.-P. Kallmeyer
- , U. Kamionka
- , H. Kasahara
- , W. Kasparek
- , Ye. O. Kazakov
- , N. Kenmochi
- , C. Killer
- , A. Kirschner
- , R. Kleiber
- , T. Klinger
- , J. Knauer
- , M. Knaup
- , A. Knieps
- , T. Kobarg
- , G. Kočsics
- , F. Köchl
- , Y. Kolesnichenko
- , A. Könies
- , R. König
- , P. Kornejew
- , J.-P. Koschinsky
- , F. Köster
- , M. Krämer
- , R. Krampitz
- , A. Krämer-Flecken
- , N. Krawczyk
- , T. Kremeyer
- , J. Krom

- , M. Krychowiak
- , I. Ksiazek
- , M. Kubkowska
- , G. Kühner
- , T. Kurki-Suonio
- , P. A. Kurz
- , S. Kwak
- , M. Landreman
- , P. Lang
- , R. Lang
- , A. Langenberg
- , S. Langish
- , H. Laqua
- , H. P. Laqua
- , R. Laube
- , S. Lazerson
- , C. Lechte
- , M. Lennartz
- , W. Leonhardt
- , C. Li
- , C. Li
- , Y. Li
- , Y. Liang
- , C. Linsmeier
- , S. Liu
- , J.-F. Lobsien
- , D. Loesser
- , J. Loizu Cisquella
- , J. Lore
- , A. Lorenz
- , M. Losert
- , A. Lücke
- , A. Lumsdaine
- , V. Lutsenko
- , H. Maaßberg
- , O. Marchuk
- , J. H. Matthew

- , S. Marsen
- , M. Marushchenko
- , S. Masuzaki
- , D. Maurer
- , M. Mayer
- , K. McCarthy
- , P. McNeely
- , A. Meier
- , D. Mellein
- , B. Mendelevitch
- , P. Mertens
- , D. Mikkelsen
- , A. Mishchenko
- , B. Missal
- , J. Mittelstaedt
- , T. Mizuuchi
- , A. Mollen
- , V. Moncada
- , T. Mönnich
- , T. Morisaki
- , D. Moseev
- , S. Murakami
- , G. Náfrádi
- , M. Nagel
- , D. Naujoks
- , H. Neilson
- , R. Neu
- , O. Neubauer
- , U. Neuner
- , T. Ngo
- , D. Nicolai
- , S. K. Nielsen
- , H. Niemann
- , T. Nishizawa
- , R. Nocentini
- , C. Nührenberg
- , J. Nührenberg

- , S. Obermayer
- , G. Offermanns
- , K. Ogawa
- , J. Ölmanns
- , J. Ongena
- , J. W. Oosterbeek
- , G. Orozco
- , M. Otte
- , N. A. Pablant
- , L. Pacios Rodriguez
- , N. Panadero
- , N. Panadero Alvarez
- , D. Papenfuß
- , S. Paqay
- , E. Pasch
- , A. Pavone
- , E. Pawelec
- , T. S. Pedersen
- , G. Pelka
- , V. Perseo
- , B. Peterson
- , D. Pilopp
- , S. Pingel
- , F. Pisano
- , B. Plaum
- , G. Plunk
- , P. Pölöskei
- , M. Porkolab
- , J. Proll
- , M.-E. Puiatti
- , A. Puig Sitjes
- , F. Purps
- , M. Rack
- , K. Rahbarnia
- , S. Récsei
- , A. Reiman
- , F. Reimold

- , D. Reiter
- , F. Remppel
- , S. Renard
- , R. Riedl
- , J. Riemann
- , K. Risse
- , V. Rohde
- , H. Röhlinger
- , M. Romé
- , D. Rondeshagen
- , P. Rong
- , B. Roth
- , L. Rudischhauser
- , K. Rummel
- , T. Rummel
- , A. Runov
- , N. Rust
- , L. Ryc
- , S. Ryosuke
- , R. Sakamoto
- , M. Salewski
- , A. Samartsev
- , E. Sánchez
- , F. Sano
- , S. Satake
- , J. Schacht
- , G. Satheeswaran
- , F. Schauer
- , T. Scherer
- , J. Schilling
- , A. Schlaich
- , G. Schlisiö
- , F. Schlück
- , K.-H. Schlüter
- , J. Schmitt
- , H. Schmitz
- , O. Schmitz

- , S. Schmuck
- , M. Schneider
- , W. Schneider
- , P. Scholz
- , R. Schrittwieser
- , M. Schröder
- , T. Schröder
- , R. Schroeder
- , H. Schumacher
- , B. Schweer
- , E. R. Scott
- , S. Sereda
- , B. Shanahan
- , M. Sibilia
- , P. Sinha
- , S. Sipliä
- , C. Slaby
- , M. Slezcka
- , H. M. Smith
- , W. Spiess
- , D. A. Spong
- , A. Spring
- , R. Stadler
- , T. Stange
- , M. Stejner
- , L. Stephey
- , U. Stridde
- , C. Suzuki
- , J. Svensson
- , V. Szabó
- , T. Szabolics
- , T. Szepesi
- , Z. Szökefalvi-Nagy
- , N. Tamura
- , A. Tancetti
- , J. Terry
- , J. Thomas

- , H. Thomsen
- , M. Thumm
- , J. M. Travere
- , P. Traverso
- , J. Tretter
- , H. Trimino Mora
- , H. Tsuchiya
- , T. Tsujimura
- , S. Tulipán
- , Y. Turkin
- , B. Unterberg
- , I. Vakulchyk
- , S. Valet
- , L. Vanó
- , P. van Eeten
- , B. van Milligen
- , A. J. van Vuuren
- , L. Vela
- , J.-L. Velasco
- , M. Vergote
- , M. Vervier
- , N. Vianello
- , H. Viebke
- , R. Vilbrandt
- , A. von Stechow
- , A. Vorköper
- , S. Wadle
- , F. Wagner
- , E. Wang
- , N. Wang
- , Z. Wang
- , F. Warmer
- , T. Wauters
- , L. Wegener
- , J. Weggen
- , T. Wegner
- , Y. Wei

- , G. Weir
- , J. Wendorf
- , U. Wenzel
- , A. Werner
- , A. White
- , B. Wiegel
- , F. Wilde
- , T. Windisch
- , M. Winkler
- , A. Winter
- , V. Winters
- , S. Wolf
- , R. C. Wolf
- , A. Wright
- , G. Wurden
- , P. Xanthopoulos
- , H. Yamada
- , I. Yamada
- , R. Yasuhara
- , M. Yokoyama
- , M. Zanini
- , M. Zarnstorff
- , A. Zeitler
- , D. Zhang
- , H. Zhang
- , J. Zhu
- , M. Zilker
- , A. Zocco
- , S. Zoletnik
- & M. Zuin

Corresponding author

Correspondence to C. D. Beidler.

Rights and permissions

Open Access This article is licensed under a Creative Commons Attribution 4.0 International License, which permits use, sharing, adaptation, distribution and reproduction in any medium or format, as long as you give appropriate credit to the original author(s) and the source, provide a link to the Creative Commons license, and indicate if changes were made. The images or other third party material in this article are included in the article's Creative Commons license, unless indicated otherwise in a credit line to the material. If material is not included in the article's Creative Commons license and your intended use is not permitted by statutory regulation or exceeds the permitted use, you will need to obtain permission directly from the copyright holder. To view a copy of this license, visit <http://creativecommons.org/licenses/by/4.0/>.

Reprints and Permissions

About this article

Cite this article

Beidler, C.D., Smith, H.M., Alonso, A. *et al.* Publisher Correction: Demonstration of reduced neoclassical energy transport in Wendelstein 7-X. *Nature* **598**, E5 (2021). <https://doi.org/10.1038/s41586-021-04023-y>

- Published: 12 October 2021
- Issue Date: 28 October 2021
- DOI: <https://doi.org/10.1038/s41586-021-04023-y>

Share this article

Anyone you share the following link with will be able to read this content:

[Get shareable link](#)

Sorry, a shareable link is not currently available for this article.

[Copy to clipboard](#)

Provided by the Springer Nature SharedIt content-sharing initiative

This article was downloaded by **calibre** from <https://www.nature.com/articles/s41586-021-04023-y>.

| [Section menu](#) | [Main menu](#) |

Collections